Advanced Structured Materials

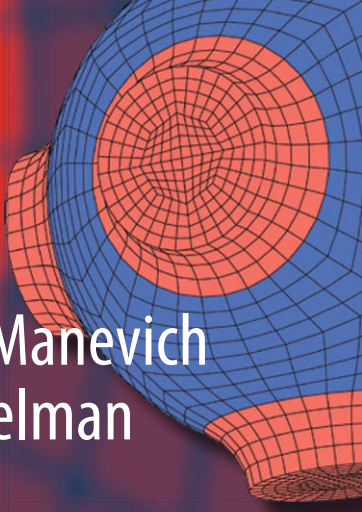

Igor V. Andrianov · Arkadiy I. Manevich
Yuri V. Mikhlin · Oleg V. Gendelman
Editors

Problems of Nonlinear Mechanics and Physics of Materials

Springer

Advanced Structured Materials

Volume 94

Common engineering materials reach in many applications their limits and new developments are required to fulfil increasing demands on engineering materials. The performance of materials can be increased by combining different materials to achieve better properties than a single constituent or by shaping the material or constituents in a specific structure. The interaction between material and structure may arise on different length scales, such as micro-, meso- or macroscale, and offers possible applications in quite diverse fields.

This book series addresses the fundamental relationship between materials and their structure on the overall properties (e.g. mechanical, thermal, chemical or magnetic etc.) and applications.

The topics of *Advanced Structured Materials* include but are not limited to

- classical fibre-reinforced composites (e.g. class, carbon or Aramid reinforced plastics)
- metal matrix composites (MMCs)
- micro porous composites
- micro channel materials
- multilayered materials
- cellular materials (e.g. metallic or polymer foams, sponges, hollow sphere structures)
- porous materials
- truss structures
- nanocomposite materials
- biomaterials
- nano porous metals
- concrete
- coated materials
- smart materials

Advanced Structures Material is indexed in Google Scholar and Scopus.

More information about this series at http://www.springer.com/series/8611

Igor V. Andrianov · Arkadiy I. Manevich
Yuri V. Mikhlin · Oleg V. Gendelman
Editors

Problems of Nonlinear Mechanics and Physics of Materials

Springer

Editors
Igor V. Andrianov
Institut für Allgemeine Mechanik
RWTH Aachen University
Aachen
Germany

Yuri V. Mikhlin
Department of Applied Mathematics
National Technical University
Kharkov
Ukraine

Arkadiy I. Manevich
Department of Theoretical
and Computational Mechanics
Dnepropetrovsk National University
Dnipro
Ukraine

Oleg V. Gendelman
Faculty of Mechanical Engineering
Technion—Israel Institute of Technology
Haifa
Israel

ISSN 1869-8433 ISSN 1869-8441 (electronic)
Advanced Structured Materials
ISBN 978-3-319-92233-1 ISBN 978-3-319-92234-8 (eBook)
https://doi.org/10.1007/978-3-319-92234-8

Library of Congress Control Number: 2018941999

Printed on acid-free paper

This Springer imprint is published by the registered company Springer Nature Switzerland AG
The registered company address is: Gewerbestrasse 11, 6330 Cham, Switzerland

This book is dedicated to
Professor Leonid I. Manevitch
On the occasion of His 80th birthday

Preface

This volume is a collection of papers contributed by colleagues and disciples as a tribute to eminent scientist, Prof. Leonid Isakovich Manevitch on the occasion of his 80th birthday. The researches of Prof. Manevitch cover various fields of mechanics and physics, in particular, Mechanics of Solids, Nonlinear Dynamics, Polymer Materials and Nanostructures, Condensed Matter Mechanics and Physics (L. I. Manevitch's scientific achievements are outlined in the Appendix to this volume).

Working as a Professor at Dnepropetrovsk University (Ukraine) and later as a Researcher and Head of Laboratory of Polymer Physics and Mechanics in N. N. Semenov Institute of Chemical Physics in Moscow, he brought up many pupils and created well-known and highly branched scientific school that made a significant contribution to the aforementioned fields of science.

This book contains articles by well-known scientists who actively work in the fields where Prof. Manevitch was very active over almost six decades. Geographically, this volume covers researches from Canada, France, Germany, Israel, Italy, Poland, Russia, Ukraine, UK, and USA. It includes 27 articles divided into the following sections:

I. Stationary and nonstationary dynamics of oscillators and oscillatory chains;
II. Molecular dynamics of polymer crystals and nanostructures;
III. Condensed matter mechanics and physics;
IV. Theory of beams, plates, and shells;
V. Theory of elasticity and thermo-elasticity.

Appendix contains short survey of scientific achivements of L. Manevitch, prepared by I. Andrianov, O. Gendelman, A. Manevich, Yu. Mikhlin and V. Smirnov.

We believe that this Festschrift will be of great interest to researchers and practitioners in the abovementioned areas.

Köln, Germany — Igor V. Andrianov
Haifa, Israel — Oleg V. Gendelman
Dnepr, Ukraine — Arkadiy I. Manevich
Kharkov, Ukraine — Yuri V. Mikhlin

Contents

Contributors

Igor V. Andrianov Institute of General Mechanics, RWTH Aachen University, Aachen, Germany

Arkadii Arinstein Department of Mechanical Engineering, Technion, Israel Institute of Technology, Haifa, Israel

Jan Awrejcewicz Department of Automatics, Biomechanics and Mechatronics, Łódź University of Technology, Łódź, Poland

N. K. Balabaev Institute of Mathematical Problems of Biology, Keldysh Institute of Applied Mathematics, Russian Academy of Sciences, Pushchino, Moscow Region, Russia

L. A. Bergman University of Illinois, Urbana, IL, USA

Alexander A. Berlin N. N. Semenov Institute of Chemical Physics, Russian Academy of Sciences, Moscow, Russia

Vladyslav V. Danishevskyy Department of Structural Mechanics and Strength of Materials, Prydniprovska State Academy of Civil Engineering and Architecture, Dnipro, Ukraine

M. Eriten University of Wisconsin-Madison, Madison, WI, USA

A. Yu. Evkin Software for Structures, Toronto, Canada

Oleg V. Gendelman Faculty of Mechanical Engineering, Technion, Haifa, Israel

Valeriy V. Ginzburg Dow Chemical Company, Midland, MI, USA

V. Guillot University Lyon, ENTPE, Vaulx-en-Velin, rue Maurice Audin, France

Julius D. Kaplunov School of Computing and Mathematics, Keele University, Keele, Staffordshire, UK

V. Kislovsky Faculty of Mechanical Engineering, Technion Israel Institute of Technology, Technion City, Haifa, Israel

S. Koblik Indianapolis, IN, USA

Irina P. Koroleva (Kikot) Semenov Institute of Chemical Physics, Russian Academy of Sciences, Moscow, Russia

Yuriy A. Kosevich Semenov Institute of Chemical Physics, Russian Academy of Sciences, Moscow, Russia; Plekhanov Russian University of Economics, Moscow, Russia

Michael I. Kotelyanskii Rudolph Technologies Inc., Mount Olive, NJ, USA

Margarita A. Kovaleva Semenov Institute of Chemical Physics, Russian Academy of Sciences, Moscow, Russia

Natalya A. Kovaleva N. N. Semenov Institute of Chemical Physics, Moscow, Russia

Vasiliy L. Krasovsky Pridneprovskaja State Academy of Civil Engineering and Architecture, Dnipro, Ukraine

Anna G. Kryvoruchko Department of Theoretical and Computational Mechanics, Oles Honchar Dnipro National University, Dnipro, Ukraine

M. Kurt Stevens Institute of Technology, Hoboken, NJ, USA

C.-H. Lamarque University Lyon, ENTPE, Vaulx-en-Velin, rue Maurice Audin, France

Vladimir V. Loboda Department of Theoretical and Computational Mechanics, Oles Honchar Dnipro National University, Dnipro, Ukraine

Arkadiy I. Manevich Dniepr National University, Dniepr, Ukraine

Leonid I. Manevitch Department Polymer and Composite Materials, Semenov Institute of Chemical Physics, Russian Academy of Sciences, Moscow, Russia

Bernd Markert Institute of General Mechanics, RWTH Aachen University, Aachen, Germany

Mikhail A. Mazo Department Polymer and Composite Materials, N. N. Semenov Institute of Chemical Physics, Russian Academy of Sciences, Moscow, Russia

D. M. McFarland University of Illinois, Urbana, IL, USA; Zhejiang University of Technology, Hangzhou, Zheijiang, China

Yuri V. Mikhlin Kharkiv Polytechnic Institute, National Technical University, Kharkiv, Ukraine

A. Mojahed University of Illinois, Urbana, IL, USA

K. J. Moore University of Illinois, Urbana, IL, USA

Eduard F. Oleinik Department Polymer and Composite Materials, Semenov Institute of Chemical Physics, Russian Academy of Sciences, Moscow, Russia

Valery N. Pilipchuk Wayne State University, Detroit, MI, USA

Katarina Yu. Plaksiy Kharkiv Polytechnic Institute, National Technical University, Kharkiv, Ukraine

Danila Prikazchikov School of Computing and Mathematics, Keele University, Keele, UK

Giuseppe Rega Department of Structural and Geotechnical Engineering, Sapienza University of Rome, Rome, Italy

Sergey N. Rudnev Department Polymer and Composite Materials, Semenov Institute of Chemical Physics, Russian Academy of Sciences, Moscow, Russia

Gayane V. Rudneva Kharkiv Polytechnic Institute, National Technical University, Kharkiv, Ukraine

Olga B. Salamatina Department Polymer and Composite Materials, Semenov Institute of Chemical Physics, Russian Academy of Sciences, Moscow, Russia

Alexander V. Savin Semenov Institute of Chemical Physics, Russian Academy of Sciences, Moscow, Russia

Valeria Settimi Department of Structural and Geotechnical Engineering, Sapienza University of Rome, Rome, Italy

Alla Ye. Sheveleva Department of Computational Mathematics, Oles Honchar Dnipro National University, Dnipro, Ukraine

Itzik B. Shiroky Faculty of Mechanical Engineering, Technion, Haifa, Israel

Tatyana V. Shmatko Kharkiv Polytechnic Institute, National Technical University, Kharkiv, Ukraine

Valeri V. Smirnov Semenov Institute of Chemical Physics, Russian Academy of Sciences, Moscow, Russia

Roman Starosta Poznan University of Technology, Institute of Applied Mechanics, Poznań, Poland

Y. Starosvetsky Faculty of Mechanical Engineering, Technion Israel Institute of Technology, Technion City, Haifa, Israel

Ivan A. Strelnikov N. N. Semenov Institute of Chemical Physics, Russian Academy of Sciences, Moscow, Russia

Leyla Sultanova School of Computing and Mathematics, Keele University, Keele, UK

Grażyna Sypniewska-Kamińska Poznan University of Technology, Institute of Applied Mechanics, Poznań, Poland

A. Ture Savadkoohi University Lyon, ENTPE, Vaulx-en-Velin, rue Maurice Audin, France

Robert A. Turusov Semenov Institute of Chemical Physics, Russian Academy of Sciences, Moscow, Russia

A. F. Vakakis University of Illinois, Urbana, IL, USA

Elena A. Zubova N. N. Semenov Institute of Chemical Physics, Moscow, Russia

Part I
Stationary and Non-stationary Dynamics of Oscillators and Oscillatory Chains

Wide Frequency Higher-Order Dynamic Model for Transient Waves in a Lattice

Igor V. Andrianov, Vladyslav V. Danishevskyy, Julius D. Kaplunov and Bernd Markert

Abstract Propagation of transient waves through a periodic elastic lattice is considered. Asymptotic solutions are used to describe the effective dynamic properties of the structure at frequencies close to the continuous and anti-continuous limits. Matching the asymptotic solutions by two-point Padé approximants, we derive a new dynamic equation that is applicable in a wide frequency range. An advantage of the proposed approach is that all the macroscopic parameters can be determined explicitly in terms of the microscopic properties of the medium. Dispersion diagram is evaluated and the propagation of transient waves induced by pulse and harmonic loads is studied. The developed analytical model is verified by comparison with data of numerical simulations.

1 Introduction

In the last years there has been a rapid growth in research interest in the dynamic response of multi-scale heterogeneous media and structures. This increased attention is motivated, primarily, by remarkable properties of mechanical composites

I. V. Andrianov · B. Markert
Institute of General Mechanics, RWTH Aachen University, Templergraben 64, 52056 Aachen, Germany
e-mail: igor.andrianov@gmail.com

B. Markert
e-mail: markert@iam.rwth-aachen.de

V. V. Danishevskyy (✉)
Department of Structural Mechanics and Strength of Materials, Prydniprovska State Academy of Civil Engineering and Architecture, Chernyshevskogo 24a, Dnipro 49600, Ukraine
e-mail: vladyslav.danishevskyy@gmail.com

J. D. Kaplunov
School of Computing and Mathematics, Keele University, Staffordshire ST5 5BG, UK
e-mail: j.kaplunov@keele.ac.uk

I. V. Andrianov et al. (eds.), *Problems of Nonlinear Mechanics and Physics of Materials*, Advanced Structured Materials 94,
https://doi.org/10.1007/978-3-319-92234-8_1

and metamaterials (see, for example, a review by Zheludev and Kivshar [1]). The potential engineering applications include noise control devices, vibration reduction and seismic isolation, negative refraction and flat lenses, waves focusing materials, acoustic diodes, acoustically invisible cloaks. Recent progress in the field is outlined by Maldovan [2] and Hussein et al. [3].

The specific dynamic behaviour of heterogeneous media can not be described properly in terms of the classical continuous elasticity, so refined gradient approaches are required. These approaches can be interpreted as either phenomenological or analytical.

Phenomenological models are based on allowing the medium additional internal degrees of freedom (e.g., considering a system of micro particles and postulating some interactions between them). The origins of the phenomenological elasticity were introduced by Cosserats and Le Roux more than 100 years ago. Later on, various models were developed and specified; for a detailed review of the subject we refer to Askes and Aifantis [4]. A disadvantage of the phenomenological approaches is that the relationships between micro- and macroscale properties are not known a priori. Hence, the macroscopic parameters of the model are usually expected to be deduced from experimental observations.

Analytical approaches address directly non-local (e.g., discrete) problems and can employ different types of the homogenisation procedure [5]. Using non-local models (for example, a lattice with a physically justified interaction potential) gives a possibility to predict relationships between the microscopic and macroscopic parameters on a rigorous theoretical basis. Transformation of non-local models into gradient ones can be justified by a continuous approximation of corresponding integral or pseudo-differential operators [6].

The approaches discussed above allows evaluation of higher-order dynamic equations that are applicable only in some limiting cases, namely, in the vicinity of resonant frequencies of the unit cells. Here we propose a new macroscopic model, which can describe the behaviour of a heterogeneous medium in a wide frequency range. The developed procedure is based on asymptotic solutions obtained at the low- and at the high-frequency limits, which are further matched using the method of two-point Padé approximants [7]. The derived higher-order equation captures precisely the dispersive properties of the medium. Moreover, it can also be applied to solving macroscopic boundary value problems.

As an illustrative example, we consider the dynamic response of a monatomic lattice subjected to external pulse and harmonic loads. Discrete lattice-type models are widely used to describe vibrations in crystals [8], in foams [9], in cellular structures and bone tissues [10]. Some novel applications include modelling of polymer molecules, atomic lattices (e.g., graphene), and nanocrystalline materials [11, 12]. Discrete models can also appear in engineering, e.g., for simulating lightweight truss structures with attached masses (like overhead power cables) or interactions of railway coaches.

The important feature of the pulse load problem is that during the transient wave propagation the coupling forces between the particles can exceed sufficiently the magnitude of the initial excitation. This effect is caused by a spatial redistribution

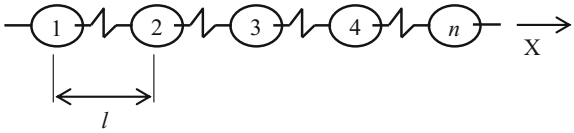

Fig. 1 Monatomic lattice under consideration

of energy due to the heterogeneity of the structure and it can never be observed in homogeneous media. One of the earliest studies of this problem was presented by Filimonov et al. [13]. Some recent results can be found, for example, in papers by Metrikine [14], Askes et al. [15], Andrianov et al. [16] and references therein. The analytical model developed in our study exhibits excellent agreement with the direct numerical solution.

The paper is organised as follows. In Sect. 2, we consider dispersion properties of the lattice and obtain the higher-order dynamic equation. In Sect. 3, the proposed macroscopic model is used to study transient waves propagation. Concluding remarks are given in Sect. 4.

2 Monatomic Lattice and the Higher-Order Dynamic Equation

Let us consider an infinite lattice consisting of identical particles of the mass m connected by massless springs of rigidity c (Fig. 1). The equation of motion reads

$$m\frac{d^2u_n}{dT^2} + c(2u_n - u_{n+1} - u_{n-1}) = 0, \tag{1}$$

where u is the displacement; n is the index number of the particle, $n = 0, \pm1, \pm2, \ldots$; T is the time variable. The time-harmonic wave is represented by the expression

$$u = A\exp(-ikn)\exp(i\,\Omega\,T), \tag{2}$$

where A is the amplitude; k is the non-dimensional wave number; Ω is the angular frequency. Substituting (2) into (1), we obtain the dispersion relation as follows

$$\omega^2 = 4\sin^2(k/2), \tag{3}$$

where ω is the non-dimensional frequency, $\omega^2 = \Omega^2$ m/c.

A simple analysis of formula (3) shows that wave propagation is allowed in the frequency range $0 < \omega < 2$. At the long-wave (so called continuous) limit, as $k \to 0$, the frequency vanishes, $\omega \to 0$, so no vibrations occur and the motion is simply a rigid body translation. The opposite (anti-continuous) limit, $k \to \pi$, describes a standing wave with zero group velocity and non-zero frequency, $\omega \to 2$.

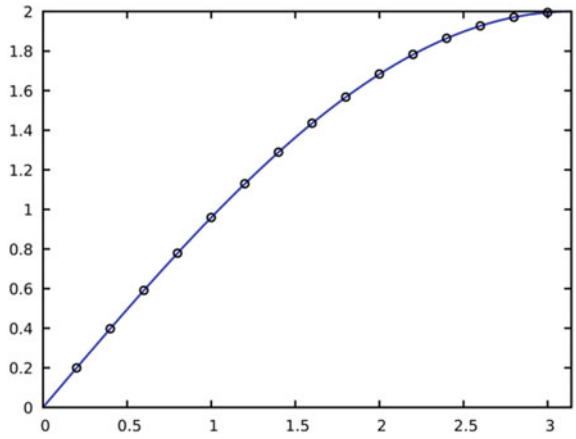

Fig. 2 Dispersion relation of the lattice. Solid curves—exact solution (3), circles—Padé approximant (6)

This regime can be considered as a "hidden" or "trapped" mode, in the sense that no energy is transmitted on macro scale, but on micro scale the lattice exhibits saw-tooth oscillations. As $\omega > 2$, the wave number k becomes complex. Then the spectrum of the lattice exhibits a band gap and the signal decays exponentially with an attenuation coefficient equal to the imaginary part of the wave number.

In the limiting cases discussed above, the dispersion relation (3) can be expressed by asymptotic relations

$$\omega^2 \sim k^2 \,\text{as}\, k \to 0, \tag{4}$$

$$\omega^2 \sim 4 - (\pi - k)^2 \,\text{as}\, k \to \pi. \tag{5}$$

Matching expressions (4) and (5) with the help of two-point Padé approximants [7], we obtain

$$\omega^2 \approx \frac{a_1 k^2 + a_2 k^4}{1 + a_3 k^2 + a_4 k^4}. \tag{6}$$

Here the coefficients $a_1, \ldots, a_4$ are determined in such a way that the leading terms of the power series expansions of Padé approximant (6) at $k \to 0$ and $k \to \pi$ must coincide with formulas (4) and (5) up to $O\left(k^2\right)$, $O\left[(\pi - k)^2\right]$ accordingly. Fulfilling this condition, we derive

$$a_1 = 1, \quad a_2 = \frac{64 - \pi^4}{\pi^6}, \quad a_3 = \frac{\pi^2 - 8}{4\pi^2}, \quad a_4 = \frac{64 + 4\pi^2 - \pi^4}{4\pi^6}.$$

In Fig. 2, formula (6) is compared with the exact dispersion relation (3). We note that the numerical results are essentially indistinguishable.

For any real k, the denominator of the derived Padé approximant does not equal zero. Therefore, expression (6) can be rewritten as follows

$$\omega^2 - a_1 k^2 - a_2 k^4 + a_3 \omega^2 k^2 + a_4 \omega^2 k^4 = 0. \tag{7}$$

Let us introduce the continuous coordinate X scaled in such a way that $X = nl$ at the nodes of the lattice, where l is the distance between the particles. Using non-dimensional variables, the time-harmonic solution (2) reads

$$u = A \exp(-ikx) \exp(i\,\omega\, t),$$

where $x = X/l$; $t = T(c/m)^{1/2}$; $k = 2\pi\, l/L$, L is the wave length. Then one can easily show

$$\frac{\partial^2 u}{\partial x^2} = -k^2 u, \quad \frac{\partial^4 u}{\partial x^4} = k^4 u, \quad \frac{\partial^2 u}{\partial t^2} = -\omega^2 u, \quad \frac{\partial^4 u}{\partial x^2 \partial t^2} = \omega^2 k^2 u, \quad \frac{\partial^6 u}{\partial x^4 \partial t^2} = -\omega^2 k^4 u. \tag{8}$$

Making use of expressions (8), the dispersion relation (7) allows us to obtain a higher-order differential equation that describes wave propagation in the entire region of the wave number $0 \le k \le \pi$:

$$a_1 \frac{\partial^2 u}{\partial x^2} - \frac{\partial^2 u}{\partial t^2} - a_2 \frac{\partial^4 u}{\partial x^4} + a_3 \frac{\partial^4 u}{\partial x^2 \partial t^2} - a_4 \frac{\partial^6 u}{\partial x^4 \partial t^2} = 0. \tag{9}$$

Equation (9) includes three dispersive terms and may be considered as a generalisation of double-dispersive equations, which were employed by many authors to simulate elastic waves in waveguides with a free lateral surface (see, for example, [17] and references therein). In the theory of waves in structured solids, double- and triple-dispersion equations can be obtained by imposing some additional internal degrees of freedom on the system (see, for example, a review by Berezovski et al. [18]). It should be noted that such non-local models include a number of phenomenological parameters, which for real materials remain usually unknown. Whereas, the approach proposed in this paper allows us to evaluate all the coefficients of Eq. (9) theoretically basing on the information about the internal structure of the medium and its properties. The developed macroscopic model is able to describe the long-wave case and, at the same time, it is valid in a high-frequency domain in the vicinity of the stop-band threshold.

3 Dynamic Response to External Loads

Equation (9) can be applied to solving boundary value problems. As a benchmark test, let us study the dynamic response of the semi-infinite ($x \ge 0$) lattice to an external load applied at the edge $x = 0$.

We consider two types of excitations: a pulse load and a harmonic load. The initial and the boundary conditions read

$$u|_{t=0} = \frac{\partial u}{\partial t}|_{t=0} = 0; \tag{10}$$

$$a_1\frac{\partial u}{\partial x} - a_2\frac{\partial^3 u}{\partial x^3} + a_3\frac{\partial^3 u}{\partial x \partial t^2} - a_4\frac{\partial^5 u}{\partial x^3 \partial t^2}|_{x=0} = -p_0(t)l; \tag{11}$$

$$u \to 0,\ \frac{\partial u}{\partial x} \to 0 \text{ as } x \to \infty; \tag{12}$$

where the function $p_0(t)$ describes the external excitation. For the pulse load $p_0(t) = p\,\delta(t)$ and for the harmonic load $p_0(t) = p\sin(\omega t)$. Here $p = P/(cl)$; P is the amplitude of the external force; $\delta(t)$ is the Dirac delta function.

Boundary conditions (11), (12) come naturally from the physical reasons. It should be noted that Eq. (9) includes the fourth-order spatial derivatives and, consequently, additional boundary conditions are required. This is a typical difficulty that arises when higher-order models, derived originally for infinite media, are applied to bounded domains. Kaplunov and Pichugin [19] have shown that general solutions of the higher-order models combine contributions of long wave solutions associated with the macroscopic problem and short wave solutions localised in the vicinity of boundaries. The latter are induced particularly by the presence of higher-order derivative terms. The short wave solutions describe extraneous boundary layers that have no physical sense. Therefore, additional boundary conditions for Eq. (9) should be formulated in such a way to eliminate spurious short wave solutions. For the monatomic lattice this principle yields:

$$\left.\frac{\partial^2 u}{\partial x^2}\right|_{x=0} = 0. \tag{13}$$

Problem (9)–(13) can be solved by applying the Laplace transform

$$u_s(x,s) = \int_0^\infty u(x,t)\exp(-st)dt.$$

In the Laplace domain we obtain

$$-s^2u_s + \left(a_1 + s^2a_3\right)\frac{d^2u_s}{dx^2} - \left(a_2 + s^2a_4\right)\frac{d^4u_s}{dx^4} = 0; \tag{14}$$

$$\left(a_1 + s^2a_3\right)\frac{du_s}{dx} - \left(a_2 + s^2a_4\right)\frac{d^3u_s}{dx^3}\bigg|_{x=0} = -pl \text{ for the pulse load}, \tag{15}$$

$$\left(a_1 + s^2a_3\right)\frac{du_s}{dx} - \left(a_2 + s^2a_4\right)\frac{d^3u_s}{dx^3}\bigg|_{x=0} = -pl\frac{\omega}{s^2+\omega^2} \text{ for the harmonic load};$$

$$\left.\frac{d^2u_s}{dx^2}\right|_{x=0} = 0; \tag{16}$$

$$u_s \to 0,\ \frac{du_s}{dx} \to 0 \text{ as } x \to \infty. \tag{17}$$

A general solution of Eq. (14) that meets the boundary conditions (17) read

$$u_s = C_1 \exp(-\kappa_1 x) + C_2 \exp(-\kappa_2 x). \tag{18}$$

Substituting (18) into (14), we get a characteristic equation for κ_1, κ_2 as follows

$$\left(a_2 + s^2 a_4\right)\kappa^4 - \left(a_1 + s^2 a_3\right)\kappa^2 + s^2 = 0. \tag{19}$$

In order to implement conditions (17), we have to choose two positive roots of Eq. (19) such that $\mathrm{Re}(\kappa_1, \kappa_2) > 0$ for $\mathrm{Re}(s) > 0$. Then we obtain

$$\kappa_{1,2} = \sqrt{\frac{a_1 + s^2 a_3 \pm \sqrt{s^4\left(a_3^2 - 4a_4\right) + 2s^2(a_1 a_3 - 2a_2) + a_1^2}}{2\left(a_2 + s^2 a_4\right)}}. \tag{20}$$

Substituting (18), (20) into the boundary conditions (15), (16) provides us with a system of two linear equations for the constants C_1, C_2, which yields for the pulse load

$$C_1 = \frac{\kappa_2 pl}{D_1 + s^2 D_2}, \quad C_2 = -\frac{\kappa_1^2}{\kappa_2^2} C_1;$$

and for the harmonic one

$$C_1 = \frac{\kappa_2 pl\, \omega}{\left(D_1 + s^2 D_2\right)\left(s^2 + \bar{\omega}^2\right)}, \quad C_2 = -\frac{\kappa_1^2}{\kappa_2^2} C_1;$$

where $D_1 = -a_1\kappa_1^2 + \left(a_1 - a_2\kappa_1^2\right)\kappa_1\kappa_2 + a_2\kappa_1^2\kappa_2^2$, $D_2 = -a_3\kappa_1^2 + \left(a_3 - a_4\kappa_1^2\right)\kappa_1\kappa_2 + a_4\kappa_1^2\kappa_2^2$.

The inverse Laplace transform is determined by the integral

$$u(x,t) = \frac{1}{2\pi i} \int_{\gamma - i\infty}^{\gamma + i\infty} u_s(x,s) \exp(st) ds. \tag{21}$$

Here γ is a real positive constant that has to be larger than the real parts of all singularities of the function u_s. Since the derived solution has no singularities at the right half-plane of the complex s-plane, we may choose any positive value of γ. In the examples below integral (21) is evaluated numerically in *Maple* with $\gamma = 0.1$.

Numerical results for the pulse load problem are presented at Fig. 3 ($t = 20,\ p = 1$). The analytical solution is verified by a numerical simulation of the discrete lattice performed by the Runge-Kutta fourth-order method. Three types of higher-order boundary conditions are examined. Additional solutions are evaluated, when instead of Eq. (13) one assumes $\partial u/\partial x|_{x=0} = 0$ or $\partial^3 u/\partial x^3|_{x=0} = 0$. We can observe that Eq. (13) ensures the best accuracy of the obtained results (see Fig. 3b). The case of the harmonic load is presented at Fig. 4 $\left(\omega^2 = 2\right)$.

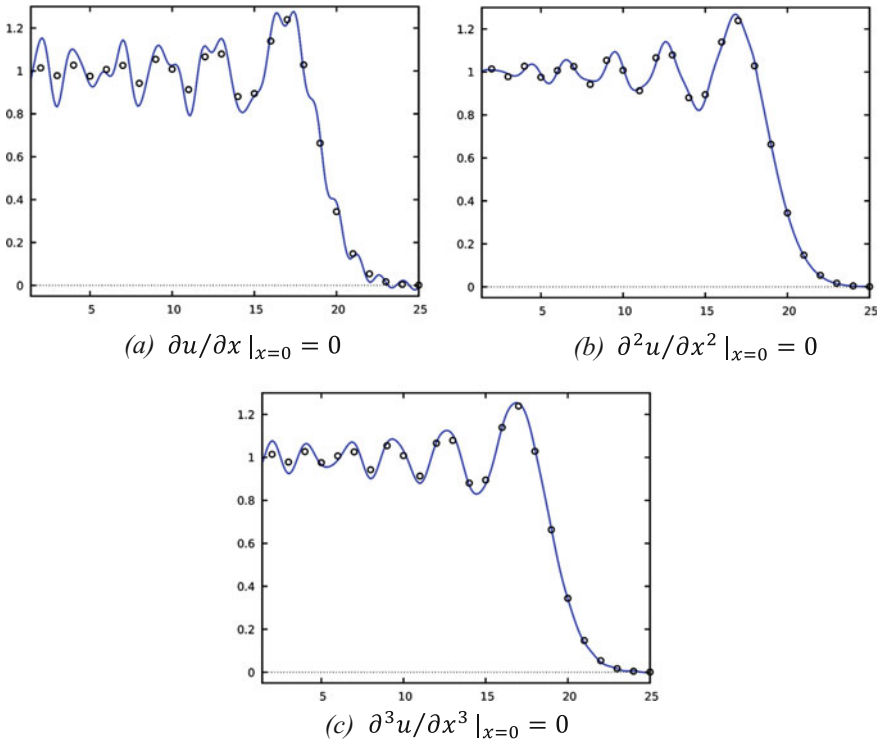

Fig. 3 Dynamic response of the lattice to the pulse load. Solid curves—analytical solution employing different boundary conditions; dots—data of the numerical simulation. **a** $\partial u/\partial x|_{x=0}= 0$, **b** $\partial^2 u/\partial x^2|_{x=0}= 0$, **c** $\partial^3 u/\partial x^3|_{x=0}= 0$

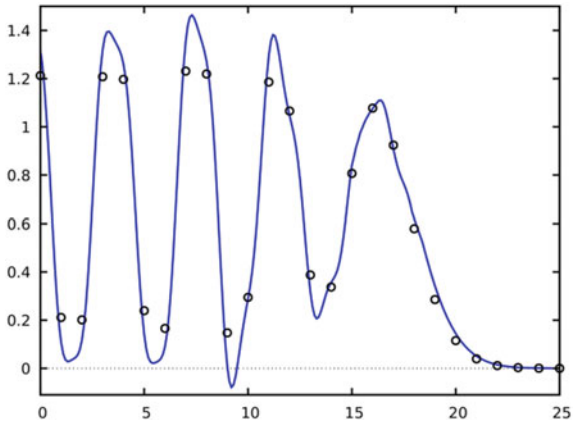

Fig. 4 Dynamic response of the lattice to the harmonic load. Solid curves—analytical solution; dots—data of the numerical simulation

It should be noted that the profile of the transient waves in the lattice is qualitatively similar to the wave fronts appearing in plates and shells (see, for example, Kaplunov et al. [20] and references therein). This displays an analogue between the propagation of elastic waves in heterogeneous media and in thin wave guides [21].

4 Conclusions

A new approach to predict the dynamic behaviour of periodically heterogeneous elastic structures is proposed. As an illustrative example, a monatomic lattice was considered. Asymptotic solutions were employed to approximate the dispersion properties at the low- and high-frequency limits. Matching the limiting solutions by the method of two-point Padé approximants, we have derived a new higher-order dynamic equation valid in the entire frequency range. The developed model encapsulates information about the microstructure and, in contrary to many phenomenological theories of gradient elasticity, all its coefficients can be determined on a rigorous theoretical basis.

The proposed macroscopic equation captures the dispersive properties of the lattice. Moreover, it can also be applied to solving boundary value problems. The propagation of transient waves excited by pulse and harmonic loads was studied. An important feature of the pulse load problem is that, due to a spatial redistribution of energy, the internal forces arising in a heterogeneous medium can be higher than the magnitude of the initial excitation. This effect is crucial for the dynamic failure of structures. The developed analytical model demonstrates excellent agreement with the direct numerical solutions.

The proposed approach can be further generalised to continuous and multi-dimensional structures.

Acknowledgements This work has received funding from the European Union's Horizon 2020 research and innovation programme under Marie Sklodowska-Curie grant agreement no. 655177. We also acknowledge the financial support of the Exploratory Research Space at RWTH Aachen University through Theodore von Kármán Fellowship (for V.V. Danishevskyy).

References

1. Zheludev, N.I., Kivshar, Yu.S.: From metamaterials to metadevices. Nat. Mater. **11**, 917–924 (2012)
2. Maldovan, M.: Sound and heat revolution in phononics. Nature **503**, 209–217 (2013)
3. Hussein, M.I., Leamy, M.J., Ruzzene, M.: Dynamics of phononic materials and structures: historical origins, recent progress, and future outlook. Appl. Mech. Rev. **66**, 040802 (2014)
4. Askes, H., Aifantis, E.C.: Gradient elasticity in statics and dynamics: An overview of formulations, length scale identification procedures, finite element implementations and new results. Int. J. Solids Struct. **48**, 1962–1990 (2011)

5. Andrianov, I.V., Awrejcewicz, J., Weichert, D.: Improved continuous models for discrete media. Math. Prob. Eng. **2010**, 986242 (2010)
6. Kunin, I.A.: Elastic Media with Microstructure. 1. One-dimensional Models. Springer, Berlin, New York (1982)
7. Baker, G.A., Graves-Morris, P.: Padé Approximants, 2nd edn. Cambridge University Press, Cambridge (1996)
8. Kittel, C.: Introduction to Solid State Physics, 8th edn. Wiley, New York (2005)
9. Cantat, I., Cohen-Addad, S., Elias, F., Graner, F., Höhler, R., Pitois, O.: Foams: Structure and Dynamics. Oxford University Press, Oxford (2013)
10. Gibson, L.J., Ashby, M.F., Harley, B.A.: Cellular Materials in Nature and Medicine. Cambridge University Press, Cambridge (2010)
11. Friesecke, G., James, R.D.: A scheme for the passage from atomic to continuum theory for thin films, nanotubes and nanorods. J. Mech. Phys. Solids **48**, 1519–1540 (2000)
12. Potapov, A.I., Pavlov, I.S., Lisina, S.A.: Acoustic identification of nanocrystalline media. J. Sound Vib. **322**, 564–580 (2009)
13. Filimonov, A.M., Kurchanov, P.F., Myshkis, A.D.: Some unexpected results in the classical problem of vibrations of the string with n beads when n is large. C.R. Acad. Sci. Paris **313**(1), 961–965 (1991)
14. Metrikine, A.V.: On causality of the gradient elasticity models. J. Sound Vib. **297**, 727–742 (2006)
15. Askes, H., Metrikine, A.V., Pichugin, A.V., Bennett, T.: Four simplified gradient elasticity models for the simulation of dispersive wave propagation. Philos. Mag. **88**, 1–11 (2008)
16. Andrianov, I.V., Starushenko, G.A., Weichert, D.: Numerical investigation of 1D continuum dynamical models of discrete chain. Z. Angew. Math. Mech. **92**, 945–954 (2012)
17. Porubov, A.V.: Amplification of Nonlinear Strain Waves in Solids. World Scientific, Singapore (2003)
18. Berezovski, A., Engelbrecht, J., Berezovski, M.: Waves in microstructured solids: a unified viewpoint of modeling. Acta Mech. **220**, 349–363 (2011)
19. Kaplunov, J.D., Pichugin, A.V.: On rational boundary conditions for higher-order long-wave models. In: IUTAM Symposium on Scaling in Solid Mechanics. IUTAM Bookseries **10**, 81–90 (2009)
20. Kaplunov, J.D., Nolde, E.V., Rogerson, G.A.: A low-frequency model for dynamic motion in pre-stressed incompressible elastic structures. Proc. R. Soc. Lond. A **456**, 2589–2610 (2000)
21. Craster, R.V., Joseph, L.M., Kaplunov, J.: Long-wave asymptotic theories: The connection between functionally graded waveguides and periodic media. Wave Motion **51**, 581–588 (2014)

Analysis of the Beating States in the System of Nonlinearly Coupled Parametrically Forced Oscillators

V. Kislovsky and Y. Starosvetsky

Abstract Present study focuses on the special response regimes of resonant energy transfer emerging in the system of two nonlinearly coupled, parametrically forced oscillators. Assuming the 1:1 internal resonant interaction we find the special conditions on the system parameters leading to the formation of these special dynamical states in the un-damped as well as the weakly damped cases. Numerical simulation of the model under consideration is in a complete agreement with the analytical predictions derived in the study.

1 Introduction

The well-known phenomenon of resonant energy transfer [1–10] remains one of the most intensively studied subjects in various aspects of applied physics and engineering. This phenomenon is ubiquitous in a wide variety of physical and engineering problems. Obviously, the predictive capacity of the well-known analytical and semi-analytical methods applied for the analysis of nonstationary system response regimes is quite limited.

Thus the common approaches which have been proven to be successful in studying the weakly nonstationary processes appear to be quite inappropriate for the analysis of highly nonstationary regimes [1]. Quite recently, the concept of *Limiting Phase Trajectories* (LPTs) has been proposed by Manevitch et al. [11–14] which was intended to analyse the regimes of resonant energy transfer [11–22].

In the present paper we analyse the resonant mechanisms of formation and destruction of special states of recurrent energy transfer exhibited by the two-oscillator model subject to a parametric excitation. Using the multi-time-scale expansion under a 1:1

V. Kislovsky · Y. Starosvetsky (✉)
Faculty of Mechanical Engineering, Technion Israel Institute of Technology,
32000 Technion City, Haifa, Israel
e-mail: staryuli@technion.ac.il

V. Kislovsky
e-mail: victotach@gmail.com

I. V. Andrianov et al. (eds.), *Problems of Nonlinear Mechanics and Physics of Materials*, Advanced Structured Materials 94,
https://doi.org/10.1007/978-3-319-92234-8_2

resonance conditions we derive the slow flow model. The derived slow model is analysed further and the special conditions on the system parameters, which guarantee the existence of special beating states, are obtained for the undamped as well as the damped cases. We note that the results of numerical simulations of the original system are found to be in a perfect agreement with the analysis.

2 Model

The basic model under consideration comprises the system of two parametrically forced and nonlinearly coupled oscillators. The non-dimensional equations of motion read

$$\begin{aligned} \ddot{x}_1 + \varepsilon\lambda\dot{x}_1 + [(1+\varepsilon\sigma) - \varepsilon A\ \cos(2t)]x_1 &= \varepsilon(x_2 - x_1)^3 \\ \ddot{x}_2 + \varepsilon\lambda\dot{x}_2 + [(1+\varepsilon\sigma) + \varepsilon A\ \cos(2t)]x_2 &= \varepsilon(x_1 - x_2)^3 \end{aligned} \tag{1}$$

where μ_1, μ_2 are the parameters of nonlinear coupling, σ is the frequency detuning parameter, A stands for the amplitude of the parametric forcing and ε is a formal small system parameter ($0 < \varepsilon \ll 1$) which scales the magnitude of the damping, forcing, frequency mismatch and the coupling terms.

The ultimate goal of the present study is to analyze the mechanisms of formation and destruction of some special regimes of synchronized beating states manifested by the complete energy exchanges between the two parametrically forced oscillators.

3 Slow Flow Model

To derive the slow flow model we follow the standard procedure (see e.g. [1–10]) of complexification and the regular multi-scale expansion. To this end the complex variables are introduced as follows

$$\psi_1 = \dot{x}_1 + ix_1,\ \psi_2 = \dot{x}_2 + ix_2. \tag{2}$$

Substituting (2) into (1) we use the multi-scale expansion in the form

$$\psi_i = \psi_{i0}(\tau_0, \tau_1) + \varepsilon\psi_{i1}(\tau_0, \tau_1) + O(\varepsilon^2),\ \frac{\partial}{\partial t} = \frac{\partial}{\partial \tau_0} + \varepsilon\frac{\partial}{\partial \tau_1} + \ldots. \tag{3}$$

Following the steps of the standard multi-scale analysis [1–10] up to the first order ($O(\varepsilon)$) one arrives at the following slow flow model,

$$\psi_{i0} = \varphi_i(\tau_1)\exp(i\tau_0), i = 1, 2$$
$$\varphi_1' = \frac{i\sigma}{2}\varphi_1 + \frac{iA}{4}\varphi_1^* - \frac{\lambda}{2}\varphi_1 - \frac{3i}{8}|\varphi_2 - \varphi_1|^2(\varphi_2 - \varphi_1)$$
$$\varphi_2' = \frac{i\sigma}{2}\varphi_2 - \frac{iA}{4}\varphi_2^* - \frac{\lambda}{2}\varphi_2 - \frac{3i}{8}|\varphi_2 - \varphi_1|^2(\varphi_1 - \varphi_2) \quad (4)$$

4 Non-dissipative Case ($\lambda = 0$)

Let us start the analysis from a non-dissipative case. It can be shown that for the non-dissipative case System (4) possesses the following conserved quantities

$$M = \varphi_1\varphi_2^* + \varphi_1^*\varphi_2$$
$$H = \sigma\left(|\varphi_1|^2 + |\varphi_2|^2\right) + \frac{A}{4}\left(\varphi_1^2 + \varphi_1^{*2} - \varphi_2^2 - \varphi_2^{*2}\right) + \frac{3}{8}|\varphi_2 - \varphi_1|^4. \quad (5)$$

It is convenient to introduce the slow-flow model coordinates in their polar form

$$\varphi_k = N_k(\tau_1)\exp(i\delta_k(\tau_1)), k = 1, 2 \quad (6)$$

Further, using the conserved quantity M, one arrives at the following important relation

$$N_1N_2\cos\Delta = M,\ \Delta = \delta_1 - \delta_2 \quad (7)$$

It is worthwhile noting that the regimes of complete energy exchanges between the coupled oscillators must satisfy $M = 0$, as these special regimes recurrently path through the localized states (i.e. $N_1\left(\tau_1^*\right) = 0, N_2\left(\tau_1^*\right) > 0$ and $N_1\left(\tau_1^{**}\right) > 0, N_2\left(\tau_1^{**}\right) = 0$). This observation immediately brings us to the following stationary values of the relative phase.

$$\Delta = \frac{\pi}{2} + \pi n, n = 0, \pm1, \pm2, \ldots \quad (8)$$

Using $M = 0$ one can easily show that the second conserved quantity (H) takes the following simplified form,

$$H = \sigma N + \frac{A}{2}N\cos(2\delta_1) + \frac{3}{8}N^2 \quad (9)$$

where $N = N_1^2 + N_2^2$. In Fig. 1 we plot the phase portrait (N vs. δ_1). As one can infer from the observation of the phase portrait of Fig. 1, there exist several types of beating regimes (BR). Let us start with the simplest BR which corresponds to the fixed point of the phase portrait (Fig. 1). In fact this regime is characterized by the stationarity of the norm $\left(N(\tau_1) = N_1^2 + N_2^2 = const\right)$ and is denoted on Fig. 1

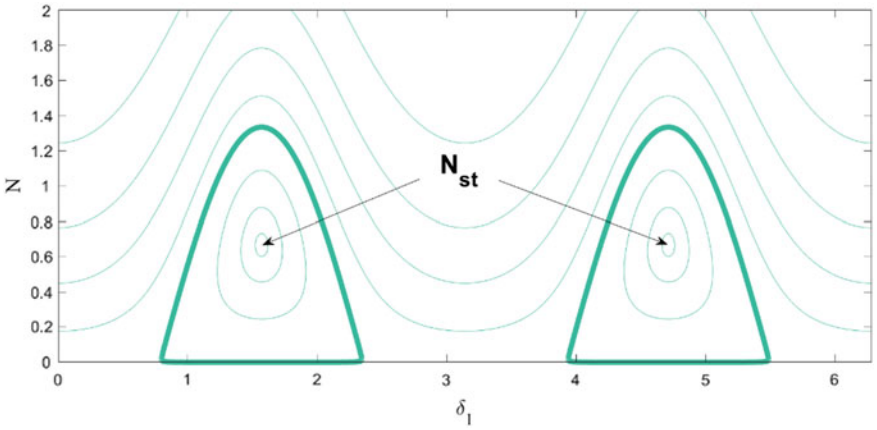

Fig. 1 Phase portrait of N versus δ_1. System parameters: $A = 1, \sigma = 0$

as N_{st}. This regime can be attributed to the classical beating response where equal amount of energy is being exchanged between the coupled, parametrically forced oscillators.

We illustrate the time-histories of this response in Fig. 2a. Slight mismatch from the fixed point obviously brings to the modulations of $N(t)$. Two types of the trajectories can be distinguished in this case (i.e. phase locked and those with the drifting phase). Additional special trajectory, which separates between the phase locked orbits and the orbits with the phase drift, is denoted with the bold line on the phase portrait of Fig. 1. This trajectory is a separatrix which is characterized by the infinitely long, complete energy exchange between the oscillators. In Fig. 2 we illustrate the time histories of the slow and the full models corresponding to the four distinct beating states of the system namely, stationary (i.e. $N(\tau_1) = const$) (Fig. 2a), near stationary (Fig. 2b), essentially nonstationary (Fig. 2c) and finally a close to separatrix (Fig. 2d) beating state.

The fixed point of the diagram of Fig. 1 can be calculated directly from (9). Thus setting $\cos(2\delta_1) = \pm 1$ in (9) one arrives at the following expressions for the stationary values (fixed point) of N, δ_1 and $H = h_{ST}$

$$
\begin{aligned}
&N_{1ST} = \frac{2}{3}\{A - 2\sigma\},\ \delta_{1ST} = \frac{\pi}{2} - \delta_{2ST} \\
&N_{2ST} = -\frac{2}{3}\{A + 2\sigma\},\ \delta_{2ST} = \pi k, k = 0, \pm 1, \pm 2, \ldots .
\end{aligned} \tag{10}
$$

From the results of (10) one can directly obtain the conditions for the existence of stationary beating regimes (SBS), which read

$$
\begin{aligned}
&A/2 > \sigma \quad -\text{1st stable BS}\,(N = N_{1ST}) \\
&-A/2 > \sigma \ -\text{2nd unstable BS}\,(N = N_{2ST}).
\end{aligned} \tag{11}
$$

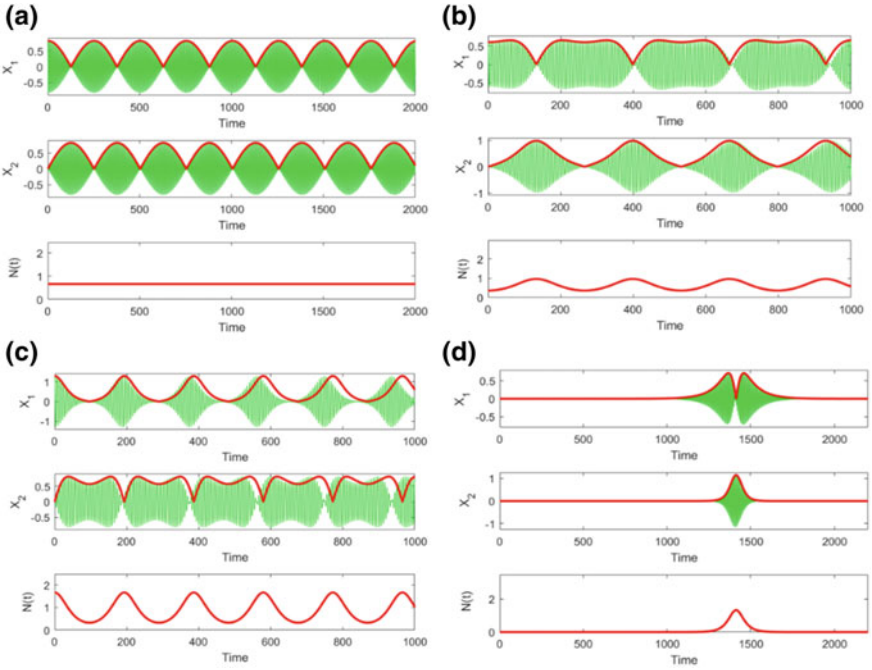

Fig. 2 Time histories of the original model (1) (green thin-line) and the slow-flow model (4) (bold red line), **a** stationary regime ($N = N_{ST}$), **b** weakly nonstationary, **c** essentially nonstationary, **d** near separatrix

Analytical description of the beating states under consideration can be further derived from the slow flow model (4) using (8). Thus, substituting (6) into (4) and splitting into the real and imaginary parts one has

$$\begin{aligned}
\delta_1' &= \frac{\sigma}{2} + \frac{A}{4}\cos(2\delta_1) + \frac{3}{8}\left(N_1^2 + N_2^2\right) \\
\delta_2' &= \frac{\sigma}{2} - \frac{A}{4}\cos(2\delta_2) + \frac{3}{8}\left(N_1^2 + N_2^2\right) \\
N_1' &= \frac{A}{4}N_1\sin(2\delta_1) \mp \frac{3}{8}\left(N_1^2 + N_2^2\right)N_2 \\
N_2' &= -\frac{A}{4}N_2\sin(2\delta_2) \pm \frac{3}{8}\left(N_1^2 + N_2^2\right)N_1.
\end{aligned} \tag{12}$$

Using (8) in (12) and performing some trivial algebraic manipulations one arrives at the following reduced model,

$$N' = \frac{A}{2}\sin(2\delta_1)N$$
$$\delta_1' = \frac{\sigma}{2} + \frac{A}{4}\cos(2\delta_1) + \frac{3}{8}N. \tag{13}$$

Obviously enough, the dynamics of (13) is depicted by (9) and has been discussed above. Let us consider the third and the fourth equations of (12) under the assumption (8),

$$N_1' = \frac{A}{4}N_1\sin(2\delta_1) \mp \frac{3}{8}\left(N_1^2 + N_2^2\right)N_2$$
$$N_2' = \frac{A}{4}N_2\sin(2\delta_1) \pm \frac{3}{8}\left(N_1^2 + N_2^2\right)N_1. \tag{14}$$

Analytical solution of the classical BR shown in Fig. 2a is derivable from (14). Noting that this BS satisfies $\left(N = N_{ST}, \delta_1 = \frac{\pi}{2} + \pi n\right)$ we end up with the following linear system:

$$N_1' = \mp\frac{3}{8}N_{ST}N_2,\ N_2' = \pm\frac{3}{8}N_{ST}N_1 \tag{15}$$

System (15) can be immediately replaced with the second order ODE (linear oscillator),

$$N_1'' + \left(\frac{9}{64}N_{ST}^2\right)N_1 = 0 \tag{16}$$

Solution of (16) yields the harmonic response for both amplitudes (N_1, N_2)

$$N_1 = \sqrt{N_{ST}}\cos\left(\frac{3}{8}N_{ST}\tau_1\right),\ N_2 = \sqrt{N_{ST}}\sin\left(\frac{3}{8}N_{ST}\tau_1\right) \tag{17}$$

Thus recalling that the solution of the separatrix corresponds to the special case of $H = 0$ which satisfies,

$$N = -\frac{8}{3}\sigma - \frac{8A}{6}\cos(2\delta_1) \tag{18}$$

We complete the present chapter with the computation of simple periodic regimes of (1). To this end we resort to the complex form (4). Further, seeking for the stationary solutions we set both time derivatives of (4) to zero which yields the following set of equations,

$$0 = \frac{i\sigma}{2}\varphi_1 + \frac{iA}{4}\varphi_1^* - \frac{\lambda}{2}\varphi_1 - \frac{3i}{8}|\varphi_2 - \varphi_1|^2(\varphi_2 - \varphi_1)$$
$$0 = \frac{i\sigma}{2}\varphi_2 - \frac{iA}{4}\varphi_2^* - \frac{\lambda}{2}\varphi_2 - \frac{3i}{8}|\varphi_2 - \varphi_1|^2(\varphi_1 - \varphi_2) \tag{19}$$

Further analysis of (19) is easier in the new set of complex coordinates

$$w = \varphi_1 - \varphi_2,\ z = \varphi_1 + \varphi_2 \tag{20}$$

Substituting (20) into (19) one has,

$$\sigma w + \frac{A}{2} z^* + \frac{3}{2} w|w|^2 = 0, \quad \sigma z + \frac{A}{2} w^* = 0 \tag{21}$$

Solutions of (21) can be readily obtained, reading the following

$$\begin{aligned} &(1)\, 0 < \sigma < \frac{A}{2} : |w| = \left[\frac{A^2 - 4\sigma^2}{6\sigma}\right]^{1/2}, \quad |z| = \frac{A}{2\sigma}\left[\frac{A^2 - 4\sigma^2}{6\sigma}\right]^{1/2} \\ &(2)\, \sigma < -\frac{A}{2} : |w| = \left[\frac{A^2 - 4\sigma^2}{6\sigma}\right]^{1/2}, \quad |z| = -\frac{A}{2\sigma}\left[\frac{A^2 - 4\sigma^2}{6\sigma}\right]^{1/2} \\ &\vartheta_z + \vartheta_w = \pi m \end{aligned} \tag{22}$$

and in the original coordinates,

$$\begin{aligned} \varphi_1 &= -\frac{|w|}{2}\left[\frac{A}{2\sigma}\exp\left(-i\vartheta_w\right) - \exp\left(i\vartheta_w\right)\right], \quad \varphi_2 \\ &= -\frac{|w|}{2}\left[\frac{A}{2\sigma}\exp\left(-i\vartheta_w\right) + \exp\left(i\vartheta_w\right)\right], \quad \vartheta_w \\ &\in [0, 2\pi] \end{aligned} \tag{23}$$

We note that the solutions of (23) exist only in the certain ranges of frequency detuning parameter $0 < \sigma < \frac{A}{2}$ and $\sigma < -\frac{A}{2}$. In Fig. 3 we plot the time histories of the stationary (simple periodic) regimes of the original model (1) corresponding to the analytical solutions given by (23). Stability analysis as well as the bifurcation structure of these periodic regimes is beyond the scope of the present paper and will be published elsewhere.

5 Dissipative Case

It can be shown that for the dissipative case System (4) satisfies the following first order ODE,

$$\frac{dM}{d\tau_1} = -\lambda M,\ M = \varphi_1\varphi_2^* + \varphi_1^*\varphi_2. \tag{24}$$

Thus as is obvious from (24), $M \to 0$ as $\tau_1 \to \infty$. In what follows, we demonstrate the emergence of special, stationary BRs as attractive/repelling solutions. Again

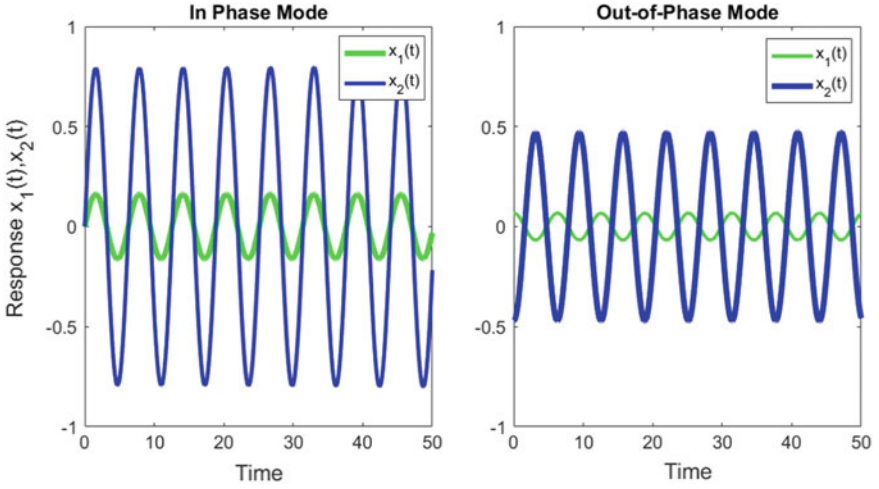

Fig. 3 Simple periodic regimes of the original model. System parameters: $A = 1.5$, $\varepsilon = 0.05$ (1) (**Left Panel**) ($\sigma = 0.5$) (**Right Panel**) ($\sigma = -1$)

seeking for the steady-state beating response regimes (BRs) we study the dynamics of (4) satisfying $M = 0$. This immediately yields the following stationary solutions of the relative phase,

$$\Delta = \frac{\pi}{2} + \pi n,\ n = 0, 1, 2, \ldots \quad (\Delta = \delta_1 - \delta_2). \tag{25}$$

Further, using (25) we write down (4),

$$\begin{aligned} N_1' &= \frac{A}{4} N_1 \sin(2\delta_1) \mp \frac{3}{8}\left(N_1^2 + N_2^2\right) N_2 - \frac{\lambda}{2} N_1 \\ N_2' &= -\frac{A}{4} N_2 \sin(2\delta_2) \pm \frac{3}{8}\left(N_1^2 + N_2^2\right) N_1 - \frac{\lambda}{2} N_2 \\ \delta_1' &= \frac{\sigma}{2} + \frac{A}{4}\cos(2\delta_1) + \frac{3}{8}\left(N_1^2 + N_2^2\right) \\ \delta_2' &= \frac{\sigma}{2} - \frac{A}{4}\cos(2\delta_2) + \frac{3}{8}\left(N_1^2 + N_2^2\right). \end{aligned} \tag{26}$$

Using (25) in (26) and some rather trivial algebraic manipulations, System (26) can be further reduced and reads,

$$\begin{aligned} N' &= \left(\frac{A}{2}\sin(2\delta_1) - \lambda\right) N \\ \delta_1' &= \frac{\sigma}{2} + \frac{A}{4}\cos(2\delta_1) + \frac{3}{8} N. \end{aligned} \tag{27}$$

The stationary BRs of (27) read the following,

$$N_{1ST} = -\frac{2}{3}\left\{2\sigma - \sqrt{A^2 - 4\lambda^2}\right\}, \quad \delta_{1ST} = \frac{1}{2}\left(\pi - \arcsin\left(\frac{2\lambda}{A}\right)\right)$$
$$N_{2ST} = -\frac{2}{3}\left\{2\sigma + \sqrt{A^2 - 4\lambda^2}\right\}, \quad \delta_{2ST} = \frac{1}{2}\arcsin\left(\frac{2\lambda}{A}\right). \tag{28}$$

where the pair (δ_{1ST}, N_{1ST}) stands for the stable stationary BS solution (stable focus) while (δ_{2ST}, N_{2ST}) for the unstable one (saddle). From (28) one can directly infer the conditions for the existence of the BS solutions,

$$\begin{aligned} \text{Stable BS solution: } A^2 \geq 4\left(\sigma^2 + \lambda^2\right),\ \sigma > 0 \\ A^2 \geq 4\lambda^2,\ \sigma < 0\,. \\ \text{Un - stable BS solution: } A^2 \leq 4\left(\sigma^2 + \lambda^2\right),\ \sigma < 0 \end{aligned} \tag{29}$$

As is evident from (29) both stable and unstable BR solutions coexist in the range

$$2\lambda \leq A \leq 2\left(\sigma^2 + \lambda^2\right)^{1/2}, \sigma < 0. \tag{30}$$

Analytical description of the stationary beating states can be derived from (26) using (28) which reduces to the solution of the following second order linear ODE,

$$N_1'' + \left(\frac{9}{64}N_{ST}^2\right)N_1 = 0. \tag{31}$$

The solution of (31) reads,

$$N_1 = \sqrt{N_{ST}}\cos\left(\frac{3}{8}N_{ST}\tau_1\right),\ N_2 = \sqrt{N_{ST}}\sin\left(\frac{3}{8}N_{ST}\tau_1\right). \tag{32}$$

As is clear from the analysis brought above, there exists a single stable and unstable beating regimes (SBR and UBR). Additionally, it can be shown that the stationary response regimes corresponding to a simple periodic motion do not exist in the dissipative case under consideration. In Fig. 4 (left panel) we plot the phase plane corresponding to the reduced order model (27) and in Fig. 4 (right panel) we plot the time histories of the response of the original model (1) (for the same system parameters). As is clear from the results of Fig. 4, starting a bit off the stable beating regime the system is being gradually attracted to this special dynamical state ending up with recurrent complete energy exchanges between the parametrically forced oscillators. This result of numerical simulation of the full model is in a complete agreement with the analytical model (see the right panel of Fig. 4).

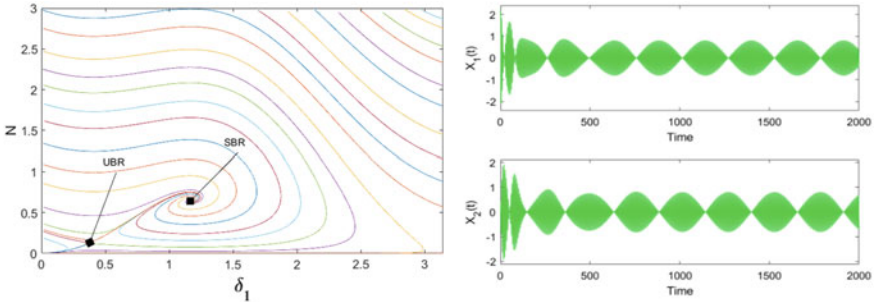

Fig. 4 (**Left Panel**) Phase plane, System (27) (**Right Panel**) Stable beating response of the original model. System parameters: $A = 0.55, \quad \sigma = -0.3, \quad \varepsilon = 0.05$

6 Conclusions

We analysed the special mechanisms of formation and destruction of special beating regimes exhibited by the two-oscillator model subject to a parametric excitation. We separately treated the non-dissipative as well as the weakly dissipative cases. In the former we presented the analysis for the special family of beating regimes (BRs) characterized by the complete energy exchange between the coupled oscillators. Among all the regimes of nonlinear beats characterized by the complete energy exchanges between the oscillators, we singled out the special types of regimes satisfying $\left(N = |\varphi_1(\tau_1)|^2 + |\varphi_2(\tau_1)|^2 = const\right)$. We derived the formation of both stable and unstable regimes of that kind which have been characterized by the uniform, recurrent excitations emerging on each parametrically forced oscillator. Additional, special beating regime which has been revealed in the analysis is the regime manifested by a one-cycle, complete energy exchange between the oscillators which occurs in the infinitely long time. Along with the beating states of the system we also analysed the family of (simple) localized periodic regimes exhibiting the in- and out-of-phase motion. We found analytically the ranges in the system parameter space for their existence. In the weakly dissipative case we have shown analytically that the only, non-trivial, steady state solution emerging in the system under consideration is the regime of nonlinear beats manifested by the complete energy exchanges between the parametrically forced oscillators. We depicted these regimes analytically and found the necessary conditions on the system parameters for the existence of these unique, stable solutions.

Acknowledgements Authors are grateful to Prof. L.I. Manevitch and Dr. M. Kovaleva from N.N. Semenov Institute of Chemical Physics, Moscow, Russia, for fruitful discussions.

References

1. Vakakis, A.F.: Nonlinear Targeted Energy Transfer in Mechanical and Structural Systems. Springer (2008)
2. Hasselmann, K.: On the non-linear energy transfer in a gravity-wave spectrum, Part 3, Evaluation of the energy flux and swell-sea interaction for a Neumann spectrum. J. Fluid Mech. **15**(3), 385–398 (1963)
3. Benney, D.J., Saffman, P.G.: Nonlinear interactions of random waves in a dispersive medium. Proc. R. Soc. A **289**, 301 (1966)
4. Benney, D.J., Newell, A.C.: Random wave closures. Stud. Appl. Math. **48**(1), 29–53 (1969)
5. Newell, A.C.: Wave turbulence is almost always intermittent at either small or large scales. Stud. Appl. Math. **108**(1), 39–64 (2002)
6. Newell, A.C., Nazarenko, S., Biven, L.: Wave turbulence and intermittency. Physica D **152**, 520–550 (2001)
7. Kadomtsev, B.B.: Plasma Turbulence. Academic Press, New York (1965)
8. Lvov, Y.V., Tabak, E.G.: Hamiltonian formalism and the GarrettMunk spectrum of internal waves in the ocean. Phys. Rev. Lett. **87**(16), 168501 (2001)
9. Lvov, Y.V., Binder, R., Newell, A.C.: Quantum weak turbulence with applications to semiconductor lasers. Physica D **121**(3–4), 317–343 (1998)
10. Lvov, Y.V., Newell, A.C.: Finite flux solutions of the quantum Boltzmann equation and semiconductor lasers. Phys. Rev. Lett. **84**(9), 1894–1897 (2000)
11. Manevitch, L.I.: New approach to beating phenomenon in coupled nonlinear oscillatory chains. Arch. Appl. Mech. **77**(5), 301–312 (2007)
12. Manevitch, L.I., Kovaleva, A.S., Manevitch, E.L., Shepelev, D.S.: Limiting phase trajectories and non-stationary resonance oscillations of the Duffing oscillator. Part 1. A non-dissipative oscillator. Commun. Nonlinear Sci. Numer. Simul. **16**(2), 1089–1097 (2011)
13. Manevitch, L.I., Kovaleva, A.S., Manevitch, E.L., Shepelev, D.S.: Limiting phase trajectories and nonstationary resonance oscillations of the Duffing oscillator. Part 2. A dissipative oscillator. Commun. Nonlinear Sci. Numer. Simul. **16**(2), 1098–1105 (2011)
14. Starosvetsky, Y., Manevitch, L.I.: Nonstationary regimes in a Duffing oscillator subject to biharmonic forcing near a primary resonance. Phys. Rev. E **83**(4), 046211 (2011)
15. Manevitch, L.I., Kovaleva, M.A., Pilipchuk, V.N.: Non-conventional synchronization of weakly coupled active oscillators. Europhys. Lett. **101**(5), 50002 (2013)
16. Manevitch, L.I., Musienko, A.I.: Limiting phase trajectories and energy exchange between anharmonic oscillator and external force. Nonlinear Dyn. **58**(4), 633–642 (2009)
17. Manevitch, L.I., Kovaleva, A.: Nonlinear energy transfer in classical and quantum systems. Phys. Rev. E **87**(2), 022904 (2013)
18. Manevitch L.I., Gendelman, O.V.: Tractable Models of Solid Mechanics. Springer (2011)
19. Starosvetsky, Y., Ben-Meir, Y.: Nonstationary regimes of homogeneous Hamiltonian systems in the state of sonic vacuum. Phys. Rev. E **87**(6), 062919 (2013)
20. Kovaleva, A., Manevitch, L., Manevitch, E.: Intense energy transfer and superharmonic resonance in a system of two coupled oscillators. Phys. Rev. E **81**(5), 056215 (2010)
21. Kovaleva, A., Manevitch, L.I.: Limiting phase trajectories and emergence of autoresonance in nonlinear oscillators. Phys. Rev. E **88**, 024901 (2013)
22. Kovaleva, A., Manevitch, L.I.: Internal autoresonance in coupled oscillators with slowly decaying frequency. Phys. Rev. E **96**, 032213 (2017)

Is Energy Localization Possible in the Conditions of Non-local Acoustic Vacuum?

Irina P. Koroleva (Kikot) and Leonid I. Manevitch

Abstract We present results of analytical and numerical study of planar dynamics of a membrane consisting of one longitudinal and N transversal strings without a preliminary stretching with uniformly distributed discrete masses. In the previous paper it was shown that in the most significant case of predominantly transversal dynamics an effective non-local axial force is formed in longitudinal string and equations of motion cannot be linearized. Therefore the membrane oscillates in the conditions of "non-local" acoustic vacuum and can be used as an efficient energy trap. Adequate analytical description of non-stationary resonance dynamics at such conditions is achieved in terms of limiting phase trajectories (LPT) corresponding to maximum possible energy exchange between different parts (clusters) of the membrane. We have revealed also in these terms the conditions of energy localization in the initially excited cluster. Analytical results are confirmed by numerical simulation data.

1 Introduction

It was shown recently [1] that in the limit of low energy a fixed-fixed chain of linearly coupled particles performing in-plane transverse oscillations possesses strongly nonlinear dynamics due to geometric nonlinearity, forming a nonlinear acoustic vacuum. This designation denotes the fact that the speed of sound as defined in the sense of classical acoustic theory is zero in that medium, so the resulting equations of motion lack any linear stiffness components. However a significant feature of the considered system was the presence of strongly non-local terms in the governing equations of motion (in the sense that each equation directly involves all particle displacements), in-spite of the fact that the physical spring-mass chain has only local (nearest-neighbor) interactions between the particles. These non-local terms consti-

I. P. Koroleva (Kikot) (✉) · L. I. Manevitch
Semenov Institute of Chemical Physics RAS, 119991, 4 Kosygin street, Moscow, Russia
e-mail: irakikotx@gmail.com

L. I. Manevitch
e-mail: manevitchleonid3@gmail.com

I. V. Andrianov et al. (eds.), *Problems of Nonlinear Mechanics and Physics of Materials*, Advanced Structured Materials 94,
https://doi.org/10.1007/978-3-319-92234-8_3

tute a time- dependent effective speed of sound for this medium, which is completely tunable with energy. A rich structure of resonance manifolds of varying dimensions were identified in the nonlinear sonic vacuum, and 1:1 resonance interactions are studied asymptotically to prove the possibility of strong energy exchanges between nonlinear modes.

One of distinctive features of the chain without transversal strings was that its nonlinear normal modes NNMs [2] could be exactly determined in the limit of acoustic vacuum. Moreover, the analysis has shown that the number of NNMs in this case was equal to the dimensionality of the configuration space and that no NNM bifurcations were possible. In addition, the most intensive 1:1 resonance intermodal interaction was realized by two NNMs with the highest wave numbers. However, the unstretched string model considered in [1] is in some sense a special case, since one of the most significant features of dynamical systems with homogeneous potential is that the number of NNMs may exceed the number of degrees of freedom due to mode bifurcations [3]. One can expect that such NNM bifurcations will also lead to drastic modification of the non-stationary resonance dynamics of the acoustic vacuum described by Limiting Phase Trajectories(LPTs) [4], corresponding to maximum energy exchange between different parts of the system. Thus it is of great interest to consider an extension of the nonlinear acoustic vacuum developed in [1] so that the modified system has the capacity to undergo NNM bifurcations. Such a study can provide us with the opportunity to investigate how these bifurcations can affect the non-stationary resonant dynamics corresponding to resonant energy exchange and localization.

First example of localized excitations in many-particle systems in the conditions of acoustic vacuum was presented in the paper [5]. It was the chain with integer power elastic characteristic different from unity, and the solitary wave solutions were obtained. The following studies dealt with solitary waves(compactons) in the uncompressed granular chain [6] and breathers in purely cubic without [7] or with [8] anchor spring. In all these cases, as well as in the paper [9], devoted to two-particle systems, the authors dealt with “local” acoustic vacuum.

Contrary to this, the current paper deals with the case of non-local acoustic vacuum, because as we mentioned above, the elastic terms depend on all particle displacements. The case of the membrane with one longitudinal and two transversal strings questions was considered in our previous paper [10]. Here we present an extension to much more complicated system with arbitrary finite number of discrete masses.

2 The Model and Equations of Motion

Lets consider an unstretched membrane with one longitudinal and N transversal strings with uniformly distributed equal masses (see Fig. 1). The equations of motion may be presented as

$$m\frac{d^2U_j}{dt^2} + T_j\cos\theta_j - T_{j+1}\cos\theta_{j+1} = 0,\ j = 1,\ldots,N,$$
$$m\frac{d^2V_j}{dt^2} + cV_j^3 + T_j\sin\theta_j - T_{j+1}\sin\theta_{j+1} = 0,\ j = 1,\ldots,N, \quad (1)$$

with U_j, V_j being longitudinal and transversal displacements of jth mass, respectively; θ_j is angle between jth segment and its equilibrium position. The effect of transversal strings is described by cubic term.

The tensile forces are proportional to deformations and may be written as

$$T_j = K\frac{1}{l}\left[(U_j - U_{j-1}) + \frac{1}{2l}(V_j - V_{j-1})^2\right],$$

with l being equilibrium length of one segment and K being stiffness coefficient.

We consider the case when amplitude of transversal oscillations a is much smaller then equilibrium length, that is $\varepsilon = a/l \ll 1$ may be considered as small parameter. Also we introduce the slow time scale $\tau_0 = \varepsilon t$, because we consider low-frequency dynamics. Comparing orders of different terms in (1), we obtain for the first equation that inertial term may be neglected, so the tensile forces in all segments are approximately equal to each other and therefore are equal to their mean value:

$$T = < T_j > = \frac{1}{N+1}K\frac{1}{2l^2}\sum_{s=0}^{N}(V_{s+1} - V_s)^2 \quad (2)$$

This mechanism of nonlocal force formation was discussed in more detailed in the paper [1]. Analogous simplification in continuum limit is refered to as Kirchhoff model [11, 12]. Considering the second equation in system (1), we obtain the following equation system for transversal motion (parameter $\mu = \frac{K}{Cl^3}$ describes relation between longitudinal and transversal string stiffnesses):

$$\frac{d^2v_j}{d\tau_0^2} + \frac{v_j^3}{\mu} + \frac{\sum_{s=0}^{N}(v_{s+1} - v_s)^2}{2(N+1)}\left(2v_j - v_{j+1} - v_{j-1}\right) = 0,\ v_0 = v_{N+1} = 0, \quad (3)$$

where $V_j = \varepsilon v_j$, v_j are normalized displacements, and $\omega_0 = \sqrt{\frac{K}{lm}}$.

3 Nonlinear Normal Modes

It was shown in the paper [1] that for oscillatory chain (which corresponds to a particular case of membrane with only one longitudinal string and with no transversal strings)in the conditions of acoustic vacuum the dynamical system has exactly N

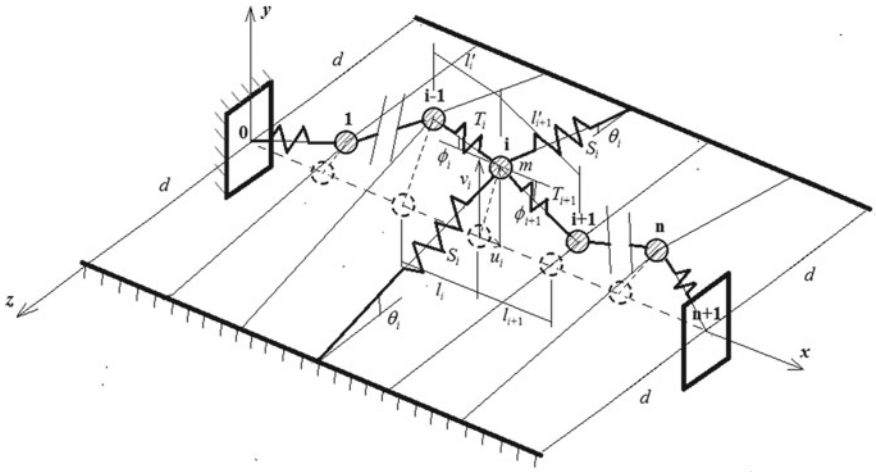

Fig. 1 Oscillator chain with elastic support (reprinted from [10] with permission from Elsevier)

NNMs, which moreover coincides with normal modes of harmonic string, that is have sine-like form. When transversal strings are present it isn't the case: the spatial distribution of the displacements in considered system is no more exactly sine-like. However, we can use homogenity of system (3) to search the stationary solutions, that is solutions of the form $v_j(t) = A(t)C_j$. Let's substitute this into the Eq. (3):

$$\ddot{A}(t)C_j + \frac{1}{\mu}A^3(t)C_j^3 + \frac{1}{2(N+1)}A^3(t)\sum_{s=0}^{N}(C_{s+1} - C_s)^2\left(2C_j - C_{j+1} - C_{j-1}\right) = 0,$$

$$C_0 = C_{N+1} = 0;\ j = 1, N. \tag{4}$$

Due to homogenity we can separate the variables:

$$\frac{\ddot{A}}{A^3(t)} = -\frac{\frac{1}{\mu}C_j^3 + \frac{1}{2(N+1)}\sum_{s=0}^{N}(C_{s+1} - C_s)^2\left(2C_j - C_{j+1} - C_{j-1}\right)}{C_j},\ j = 1, N.$$

Since the left hand side depends only on time t and the right hand side depends only on index j, they both should be equal to constant.

$$-\frac{\frac{1}{\mu}C_j^3 + \frac{1}{2(N+1)}\sum_{s=0}^{N}(C_{s+1} - C_s)^2\left(2C_j - C_{j+1} - C_{j-1}\right)}{C_j} = B,\ j = 1, N.$$

We can also renormalize (by the factor $\sqrt[3]{B}$) the variables C_j and get the following equations for coefficients C_j:

$$\frac{\frac{1}{\mu}C_j^3 + \frac{1}{2(N+1)}\sum_{s=0}^{N}(C_{s+1}-C_s)^2\left(2C_j - C_{j+1} - C_{j-1}\right)}{C_j} = 1,\ j = 1, N \qquad (5)$$

This is a system of N nonlinear algebraic equations with N variables C_j, $j = 1, N$. We can solve it numerically.

Such approach has been used in the case of $N = 10$ particles for finding the mode profiles for $k = N - 1$, $k = N$th modes. These two modes are considered because as will be shown further, their interaction is the most important for description of intensive energy exchange and localization. The result is shown in the Fig. 2. We can see that the mode profiles are very close to sine-like form.

4 Two-Mode Approximation

Given the essential (non-linearizable) stiffness nonlinearity of the dynamical system (3) we resort to a previously elaborated methodology (see, for example, [1, 10]) based on the assumption of a resonance between the NNMs, to study analytically its stationary and non-stationary dynamics. To this end, we re-write system (3) as,

$$\left(\ddot{v_j} + \omega^2 v_j\right) + \varepsilon_1\gamma\left(\frac{1}{\mu}v_j^3 - \omega^2 v_j + \frac{2v_j - v_{j-1} - v_{j+1}}{2(N+1)}\sum_{s=0}^{N}(v_{s+1}-v_s)^2\right) = 0,\ j = 1, N. \qquad (6)$$

Here ω is a supposed resonance frequency. Combination in the right hand side should be small since we consider a system near resonance. It is reflected by introducing the small parameter $\varepsilon_1 \ll 1$. We introduce a bookkeeping parameter $\gamma = \varepsilon_1^{-1}$ to provide an equivalence of systems (3) and (6). We introduce complex variables:

$$\psi_j = \dot{v_j} + i\omega v_j,\ \Phi_j = \psi_{j+1} - \psi_j,\ j = 1, \ldots, N.$$

Then

$$\dot{\psi}_j - i\omega\psi_j = -\varepsilon_1\gamma\left\{\frac{1}{\mu}\left(\frac{\psi_j - \psi_j^*}{2i\omega}\right)^3 + \frac{i\omega}{2}(\psi_j - \psi_j^*)\right.$$

$$\left. + \frac{1}{2(N+1)}\left[\left(\frac{\Phi_{j-1} - \Phi_{j-1}^*}{2i\omega}\right) - \left(\frac{\Phi_j - \Phi_j^*}{2i\omega}\right)\right]\sum_{s=0}^{N}\left(\frac{\Phi_s - \Phi_s^*}{2i\omega}\right)^2\right\},\ j = 1, N.$$

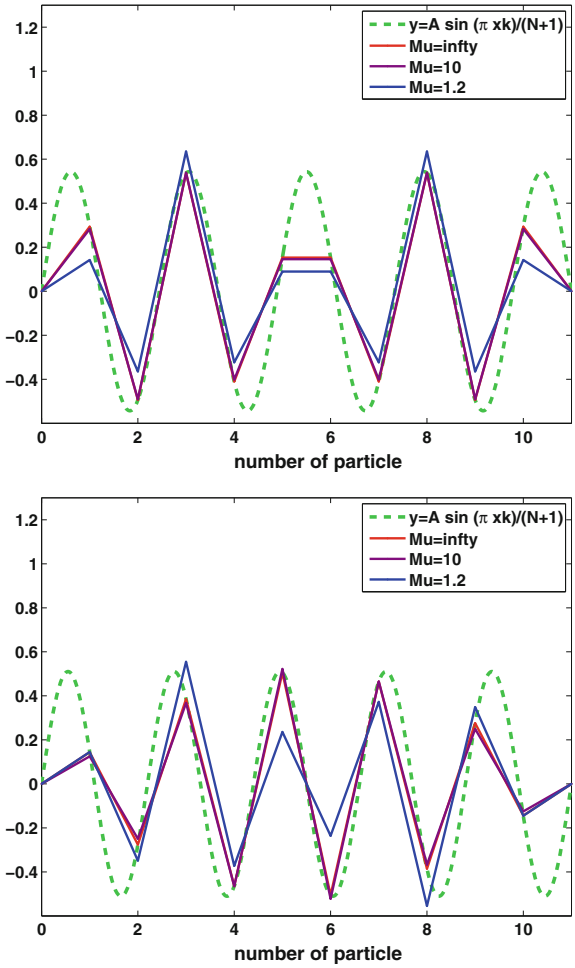

Fig. 2 Profiles of exact modes for $\mu = \infty$, $\mu = 10$, $\mu = 1.2$ for $N-1$, Nth modes. The chain consists of $N = 10$ particles

Applying a procedure of multiscale expansion we introduce a super-slow time scale $\tau_1 = \varepsilon_1 \tau_0$. Taking into account that $\frac{d}{d\tau_0} = \frac{\partial}{\partial \tau_0} + \varepsilon_1 \frac{\partial}{\partial \tau_1} + \cdots$, we are looking for a solution in the following form: $\psi_j = \psi_{j0} + \varepsilon_1 \psi_{j1} + \cdots$, $j = 1, N$. We substitute this expansion into system (6) and equate the terms of each order by parameter ε_1 to zero. In the first approximation we get: $\psi_{j0} = e^{i\omega\tau_0}\varphi_j(\tau_1)$, $j = 1, N$. We substitute this expression into the equation for complex variables and consider next order of smallness. To avoid appearance of secular terms while inegrating over time τ_0, coefficient before $e^{i\omega\tau_0}$ should be zero. Thus we obtain the system which determines the "amplitude" functions $\varphi_j(\tau_1)$, $j = 1, N$ in super-slow time τ_1:

$$\frac{\partial\varphi_{j,0}}{\partial\tau_1}+\gamma\frac{3\varphi_{j,0}|\varphi_{j,0}|^2}{8\mu i\omega^3}-\frac{\gamma}{4(N+1)i\omega}(2\varphi^*_{j,0}-\varphi^*_{j-1,0}-\varphi^*_{j+1,0})\sum_{s=0}^{N}\frac{(\varphi_{s+1,0}-\varphi_{s,0})^2}{4\omega^2}$$

$$-\frac{\gamma}{4i\omega}\frac{1}{(N+1)}(2\varphi_{j,0}-\varphi_{j-1,0}-\varphi_{j+1,0})\sum_{s=0}^{N}\frac{|\varphi_{s+1,0}-\varphi_{s,0}|^2}{2\omega^2}+\gamma\frac{i\omega}{2}\varphi_{j,0}=0,\ j=1,N.$$

Now $\varphi_j^m=a_m(\tau_0)exp\left(\frac{i\pi jm}{N+1}\right)$ is an exact solution of these equations. Also $\varphi_j^m=a_m(\tau_0)exp\left(-\frac{i\pi jm}{N+1}\right)$ is an exact equation. Sine-like expression $\varphi_j^m=a_m(\tau_0)\sin\frac{\pi jm}{N+1}$ is an exact solution only in the case when the transversal strings are absent. Also it satisfies the boundary conditions (fixed ends). That's because we are looking for a solution in two-mode approximation as $\varphi_j=\sin\frac{j\pi m}{N+1}A_m+\sin\frac{j\pi k}{N+1}A_k=\frac{e^{\frac{ij\pi m}{N+1}}-e^{\frac{-ij\pi m}{N+1}}}{2i}\dot{A}_m+\frac{e^{\frac{ij\pi k}{N+1}}-e^{\frac{-ij\pi k}{N+1}}}{2i}\dot{A}_k$. Projecting these equations onto the two NNMs (equating the coefficient before $e^{\frac{ij\pi m}{N+1}}$ to zero) we obtain following:

$$\begin{aligned}
&\dot{A}_m-\frac{3i\gamma}{32\mu\omega^3}\cdot\left(3A_m|A_m|^2+2A_k^2A_m^*+4A_m|A_k|^2\right)\\
&+\frac{i\gamma}{32\omega^3}\omega_m^2\left[3\omega_m^2|A_m|^2A_m+2\omega_k^2|A_k|^2A_m+\omega_k^2A_k^2A_m^*\right]+\gamma\tfrac{i\omega}{2}A_m=0\\
&\dot{A}_k-\frac{3i\gamma}{32\mu\omega^3}\cdot\left(3A_k|A_k|^2+2A_m^2A_k^*+4A_k|A_m|^2\right)\\
&+\frac{i\gamma}{32\omega^3}\omega_k^2\left[3\omega_k^2|A_k|^2A_k+2\omega_m^2|A_m|^2A_k+\omega_m^2A_m^2A_k^*\right]+\gamma\tfrac{i\omega}{2}A_k=0.
\end{aligned}\tag{7}$$

Here for shortness and convenience we denote $\omega_k^2=4\sin^2\frac{\pi k}{2(N+1)}$.

The obtained system is integrable because besides the integral of energy it possesses a second integral

$$N=|A_m|^2+|A_k|^2,\tag{8}$$

that can be verified directly. Due to existence of the second integral it is possible to introduce angular variables:

$$A_m=\sqrt{N}\cos\theta e^{i\delta_1},\ A_k=\sqrt{N}\sin\theta e^{i\delta_2}.$$

Here θ and $\Delta=\delta_1-\delta_2$ characterize relationship between amplitudes of the two NNMs and phase shift between them respectively.

Equations (8) in angular variables can be written as follows:

$$\begin{aligned}
&\tfrac{1}{2}\sin2\theta\dot{\Delta}=\tfrac{3\gamma N}{32\mu\omega^3}\left(\tfrac{1}{4}\sin4\theta+\tfrac{1}{2}\sin4\theta\cos2\Delta\right)\\
&+\tfrac{\gamma N}{32\omega^3}\left(\tfrac{3}{2}\sin2\theta(\omega_k^4\sin^2\theta-\omega_m^4\cos^2\theta)+\tfrac{1}{4}\omega_m^2\omega_k^2\sin4\theta(\cos2\Delta+2)\right)
\end{aligned}\tag{9}$$

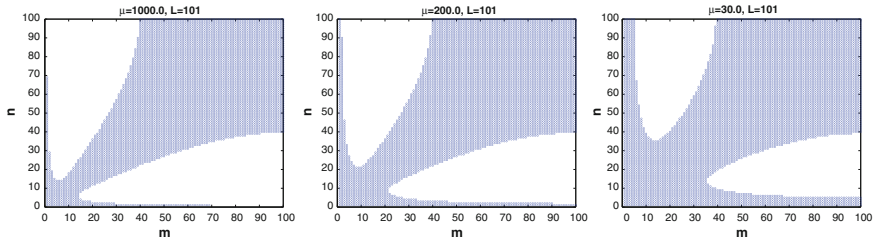

$\mu = 1000$; $\mu = 200$ $\mu = 30$

Fig. 3 Resonance domain for different μ. Chain consists of $N = 100$ particles

$$\dot{\theta} = \frac{3\gamma N}{32\mu\omega^3} \sin 2\theta \sin 2\Delta + \frac{\gamma N}{32\omega^3}\omega_k^2\omega_m^2 \frac{1}{2} \sin 2\theta \sin 2\Delta$$

Occurence of resonance is defined by existence of stationary point of this system. From the second equation we get: $\Delta_e = \pi/2$. Substituting this value into the equation for θ, we get:

$$-\frac{3}{2\mu}\cos 2\theta + \left[\frac{3}{2}\left(\omega_k^4 \sin^2\theta - \omega_m^4 \cos^2\theta\right) - \frac{1}{2}\omega_m^2\omega_k^2 \cos 2\theta\right] = 0.$$

Hence we get an expression for stationary value of θ:

$$tg^2\theta_e = \frac{\frac{3}{\mu} + 3\omega_m^4 - \omega_m^2\omega_k^2}{\frac{3}{\mu} + 3\omega_k^4 - \omega_m^2\omega_k^2}.$$

This expression leads to real value of $tg\theta$ when

$$\frac{\frac{3}{\mu} + 3\omega_m^4 - \omega_m^2\omega_k^2}{\frac{3}{\mu} + 3\omega_k^4 - \omega_m^2\omega_k^2} > 0.$$

In fact, this inequality is the condition of resonance occurence. Corresponding resonance domains for different values of μ are shown in the Fig. 3. We see that presence of transversal strings increases essentially the quantity of resonances.

5 Cluster Variables

The significant case deals with the possibility of the energy exchange between different parts of the system. We'll show that adequate description of the energy exchange and localization in the considered system can be achieved by introducing cluster variables, corresponding to combinations of two resonant NNMs. We introduce clus-

ter variables $Y_1 = \frac{A_m + A_k}{2}$, $Y_2 = \frac{A_m - A_k}{2}$. The motion equations (8) in these variables accept the following view:

$$\begin{gathered}
\dot{Y}_1 - \tfrac{3i\gamma}{32\mu\omega^3}\left(9Y_1|Y_1|^2 + Y_2^2 Y_1^* + 2Y_1|Y_2|^2\right) - \gamma\tfrac{i\omega}{2}Y_1 \\
+\tfrac{i\gamma}{64\omega^3}\left(3AY_1|Y_1|^2 + 6CY_2|Y_1|^2 + BY_2^2Y_1^* + 3CY_1^2Y_2^* + 2BY_1|Y_2|^2 + 3CY_2|Y_2|^2\right) = 0 \\
\dot{Y}_2 - \tfrac{3i\gamma}{32\mu\omega^3}\left(9Y_2|Y_2|^2 + Y_1^2Y_2^* + 2Y_2|Y_1|^2\right) - \gamma\tfrac{i\omega}{2}Y_2 \\
+\tfrac{i\gamma}{64\omega^3}\left(3AY_2|Y_2|^2 + 6CY_1|Y_2|^2 + BY_1^2Y_2^* + 3CY_2^2Y_1^* + 2BY_2|Y_1|^2 + 3CY_1|Y_1|^2\right) = 0
\end{gathered} \tag{10}$$

Here we introduce denotations, similar to those in the previous paper [13]: $A = \left(\omega_k^2 + \omega_m^2\right)^2$, $B = 3\omega_k^4 - 2\omega_k^2\omega_m^2 + 3\omega_m^4$, $C = \omega_m^4 - \omega_k^4$, $M = \frac{3}{4\mu}$.

Similarly to the case of modal variables, the obtained system is integrable because besides the integral of energy it possesses a second integral

$$N = |Y_1|^2 + |Y_2|^2, \tag{11}$$

that enables to introduce angular variables:

$$Y_1 = \sqrt{N}\cos\theta e^{i\delta_1},\ Y_2 = \sqrt{N}\sin\theta e^{i\delta_2}.$$

Here θ and $\Delta = \delta_1 - \delta_2$ characterize relationship between amplitudes of two clusters and phase shift between them.

In these variables we obtain following system:

$$\begin{gathered}
\frac{1}{2}\sin 2\theta\dot{\Delta} = M\left(-\frac{7}{4}\sin 4\theta + \frac{1}{4}\sin 4\theta\cos 2\Delta\right) \\
-\frac{1}{2}\left(\frac{3A}{4}\sin 4\theta - \frac{B}{4}\sin 4\theta(\cos 2\Delta + 2) - 3C\cos 2\theta\cos\Delta\right) \\
\dot{\theta} = \frac{3}{2\mu}\sin 2\theta\sin 2\Delta + \frac{1}{2}\left(B\sin\theta\cos\theta\sin 2\Delta + 3C\sin\Delta\right).
\end{gathered} \tag{12}$$

Here overdot denotes differentiation with respect to normalized (for convenience) time $\tau_1^* = \frac{\gamma N}{32\omega^3}\tau_1$.

This first-order system of real equations possesses the energy integral:

$$\begin{gathered}
H = -M\left(\frac{9}{2}\sin^4\theta + \frac{9}{2}\cos^4\theta + \frac{1}{4}\sin^2 2\theta(\cos 2\Delta + 2)\right) \\
+\frac{1}{2}\left(-\frac{3A}{2}(\sin^4\theta + \cos^4\theta) - 3C\sin 2\theta\cos\Delta - B\sin^2\theta\cos^2\theta(\cos 2\Delta + 2)\right),
\end{gathered} \tag{13}$$

hence it is integrable. In angular variables the stationary (equilibrium) points correspond to NNMs of initial system.

6 Phase Plane

In this section we focus mostly on two modes with highest wavenumbers (i.e. $(N-1)$th and Nth modes) because in this case cluster variables have the most intuitive sense: Y_1 corresponds to one half of the longitudinal string and Y_2 — to another half. However the same analysis may be held for any pair of resonant modes.

Due to existence of the integral of motion the simplest way of investigation is to study a topology of phase plane. First of all let us note that the point ($\theta = \pi/4$, $\Delta = \pi$), which corresponds to the $N-1$th mode, is always unstable and has saddle type (it can be derived analytically from hamiltonian (13). The stability of the point $\theta = \pi/4$, $\Delta = 0$, which corresponds to Nth NNM, will be discussed further.

Comparing phase planes for different values of parameter μ we reveal two dynamical transitions which are reflected in the phase plane topology. The first one is caused by instability and bifurcation of the highest NNM (the point $\theta = \pi/4$, $\Delta = 0$). It leads to appearance of two additional NNMs and a separatrix which encircles them. When $\mu > \mu_{cr1}$ (as in a particular case also, when there is no transversal strings, $1/\mu = 0$), there are four critical points. When $\mu < \mu_{cr1}$, a bifurcation is observed: the point ($\theta = \pi/4$, $\Delta = 0$) (corresponding to in-phase motion of clusters) becomes unstable and two additional equilibrium points appear. These equilibrium points correspond to predominant stationary energy localization on one of clusters. The critical value of the parameter μ can be found analytically from the condition

$$\left.\frac{\partial^2 H}{\partial \theta^2}\right|_{\theta=\pi/4,\,\Delta=0} = 0. \tag{14}$$

Hence

$$\mu_{cr1} = \frac{3}{-A+2C+B}.$$

In the case of two highest modes (i.e. $(N-1)$th and Nth) for the membrane with $N = 10$ transversal strings $\mu_{cr1} = 2.65$.

The first topological transition is a significant stage of the system evolution (in parametric space). This stage precedes to second topological transition which leads to spontaneous energy localization on initially excited cluster, when $\mu < \mu_{cr2}$ (complete energy exchange becomes impossible). It is possible to find a critical value μ_{cr2} analytically from the condition of coincidence of separatrix and LPT: $H(\pi/4, 0) = H(0, \pi)$. Hence

$$\mu_{cr2} = \frac{3}{-A+4C+B}.$$

For two highest NNMs $\mu_{cr2} = 1.35$ if $N = 10$.

The obtained results are confirmed by numerical integration of initial system (3) with initial conditions corresponding to excitation of one cluster which is formed by resonance interaction of two highest modes ($v_j = \sin\frac{\pi j(N-1)}{N+1} + \sin\frac{\pi jN}{N+1}$) (see Fig. 4).

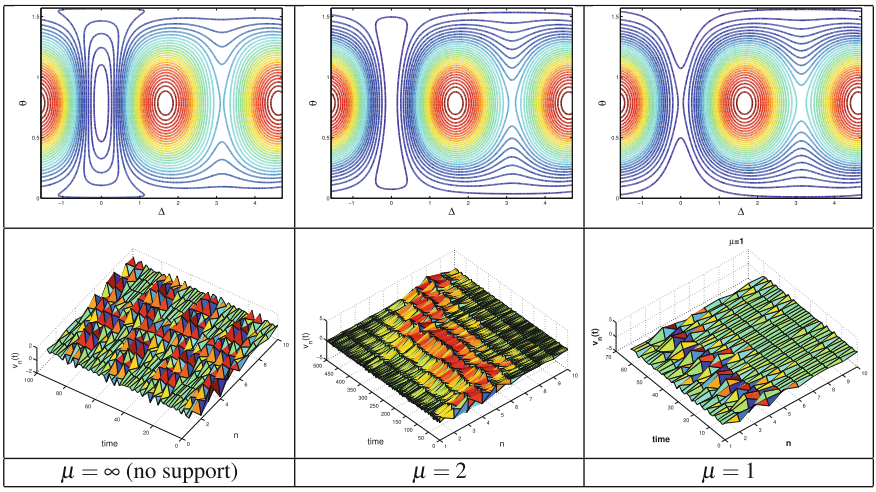

Fig. 4 Energy exchange and energy localization in initial variables and corresponding phase plane in angular variables

When $\mu < \mu_{cr2}$ the energy localization is realized; when $\mu > \mu_{cr1}$ we observe complete energy exchange. Between two critical values $\mu_{cr2} < \mu < \mu_{cr1}$ the energy exchange is still possible but takes more time (see time scale on the plots.)

6.1 Analytical Description of LPT

Complete energy exchange between clusters described by LPT is a fundamental non-stationary process very important in applications. Therefore it is desirable though challenging to describe the process analytically. It can be done in angular variables satisfying the Eq. (12). Since LPT is given by

$$H(\theta, \Delta) = H(0, 0),$$

where hamiltonian is defined as (13), we obtain following equation:

$$-M\left(\frac{9}{2}\sin^4\theta + \frac{9}{2}\cos^4\theta + \frac{1}{4}\sin^2 2\theta(\cos 2\Delta + 2)\right)$$

$$-\frac{3A}{4}(\sin^4\theta + \cos^4\theta) - \frac{3C}{2}\sin 2\theta\cos\Delta - \frac{B}{2}\frac{\sin^2 2\theta}{4}(\cos 2\Delta + 2) = -\frac{9}{2}M - \frac{3A}{4}.$$

It enables to define relationship between θ and Δ on LPT:

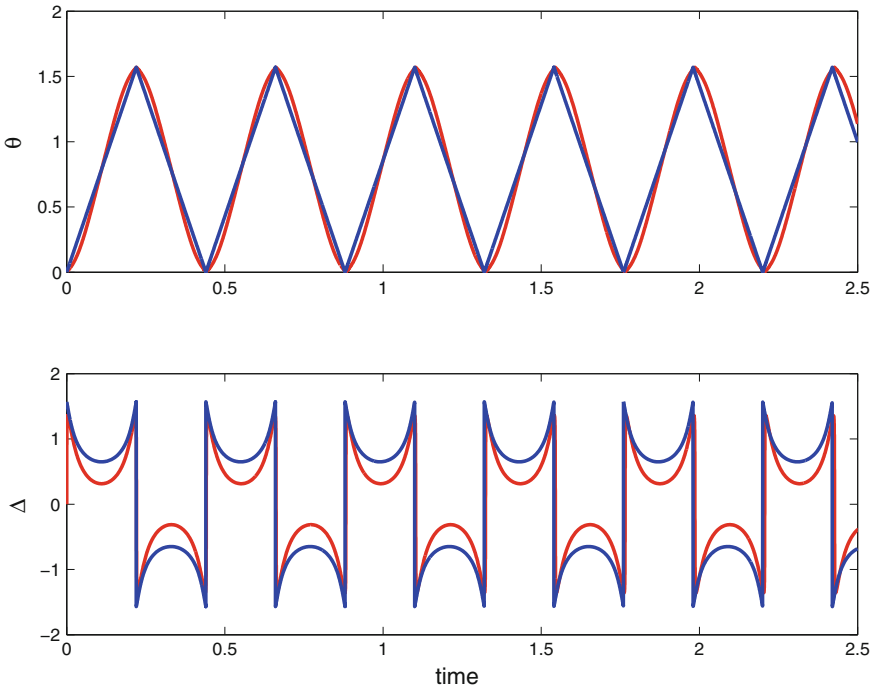

Fig. 5 Comparison of numerical simulation of the system (12) (red lines) and analytical approximation (15) (blue lines) for LPT; $\mu = 3$, $N = 10$, two last modes are considered

$$-M\left(-\frac{9}{4}\sin^2 2\theta + \frac{1}{4}\sin^2 2\theta(\cos 2\Delta + 2)\right)$$

$$+\frac{1}{2}\left(\frac{3A}{4}\sin^2 2\theta - 3C\sin 2\theta\cos\Delta - \frac{B}{4}\sin^2 2\theta(\cos 2\Delta + 2)\right) = 0.$$

Hence either $\theta = 0, \theta = \pi/2$, that corresponds to straight lines of LPT, or

$$\cos\Delta = \frac{\frac{3}{2}C - \sqrt{\left(\frac{3}{2}C\right)^2 + (2M - \frac{B}{8} + \frac{3A}{8})(2M + B)\sin^2 2\theta}}{(-M - \frac{B}{2})\sin 2\theta}.$$

Therefore, we get analytical representation of LPT:

$$\theta = \frac{\pi}{2}\tau(t/a),$$

$$\Delta = -arccos\left(\frac{\frac{3}{2}C - \sqrt{\left(\frac{3}{2}C\right)^2 + (2M - \frac{B}{8} + \frac{3A}{8})(2M + B)\sin^2 \pi\tau}}{(-M - \frac{B}{2})\sin\pi\tau}\right). \quad (15)$$

Here τ is a saw-tooth function with the period $T = 2a$:

$$\tau(\tau_1) = 0.5\,((2/\pi)arcsin(\sin(\pi\,\tau_1/a - \pi/2)) + 1)\,,$$

$e(\tau)$ is its derivative in sense of generalized functions: $e(\tau_1) = d\tau/d\tau_1$. Period may be found (as an integral) from temporal equation for θ:

$$T = 2a = 2\int\limits_0^{\pi/2} \frac{d\theta}{M\sin 2\theta\sin 2\Delta + \frac{1}{2}\,(B\sin\theta\cos\theta\sin 2\Delta + 3C\sin\Delta)}.$$

We refer the reader to [14] for more detailed description of non-smooth basic function technique.

The comparison of numerical simulation of the system (12) and analytical approximation (15) for LPT is shown in the Fig. 5. One can see very good agreement between numerical and analytical results.

7 Conclusions

The adequate analysis of strongly modulated processes in nonlinear dynamics goes out of framework of the conventional paradigm. The concept of Limiting Phase Trajectories which turns out to be an alternative to Nonlinear Normal Modes concept gives an efficient tool for such analysis. The mathematical content of this concept is closely connected with non-smooth transformations [14].

In particular, we reveal that for a membrane consisting of one longitudinal and N transversal strings in conditions of "non-local" acoustic vacuum there exists a regular regime of complete energy exchange between different domains of the longitudinal string (clusters) and nonstationary energy localization on the excited cluster, alongside with NNMs and stationary energy localization (predominantly localized NNMs). These regimes have been described analytically, and corresponding thresholds in parametric space were defined. Possibility of existence of different regimes in the same system is due to transversal strings, that enables also to widen essentially the resonance domain. Therefore, the considered membrane can be used as an efficient energy sink.

Acknowledgements We are grateful to the Russian Foundation for Basic Research (Grants No. 17-01-00582, 16-02-00400) for financial support of this work.

References

1. Manevitch, L.I., Vakakis, A.F.: Nonlinear oscillatory acoustic vacuum. SIAM J. **74**, 1742–1762 (2014)
2. Vakakis, A.F., Manevitch, L.I., Mikhlin, Y.V., Pilipchuk, V.N., Zevin, A.A.: Normal Modes and Localization in Nonlinear Systems. Wiley, New York (1996)
3. Rosenberg, R.M.: On nonlinear vibrations of systems with many degrees of freedom. Adv. Appl. Mech. **9**, 156–243 (1966)
4. Manevitch, L., Kovaleva, A., Smirnov, V., Starosvetsky, Y.: Nonstationary Resonant Dynamics of Oscillatory Chains and Nanostructures. Springer Science and Business Media, Berlin (2017)
5. Nesterenko, V.F.: Nonlinear waves in sonic vacuum. Fizika gorenia i vzryva **28**(3), 121–123 (1992). (in russian)
6. Nesterenko, V.: Propagation of nonlinear compression pulses in granular media. J. Appl. Mech. Tech. Phys. **24**, 733–743 (1983)
7. Kivshar, Y.S.: Intrinsic localized modes as solitons with a compact support. Phys. Rev. E **48**(1), 43–45 (1993)
8. Rosenau, P., Pikovsky, A.: Breathers in strongly anharmonic lattices. Phys. Rev. E **89**(022,924) (2014)
9. Starosvetsky, Y., Ben-Meir, Y.: Nonstationary regimes of homogeneous hamiltonian systems in the state of sonic vacuum. Phys. Rev. E **87**(062,919) (2013)
10. Koroleva(Kikot), I., Manevitch, L., Vakakis, A.F.: Non-stationary resonance dynamics of a nonlinear sonic vacuum with grounding supports. J. Sound Vib. **357**, 349–364 (2015)
11. Kauderer, H.: Nichtlineare Mechanik. Springer, Berlin (1958)
12. Kirchhoff, G.: Vorlesungen ber Mathematische Physik. Erster Band, Mechanik (1897)
13. Koroleva(Kikot), I.P., Manevitch, L.I.: Oscillatory chain with grounding support in conditions of acoustic vacuum. Rus. J. Nonlinear Dyn. **11**(3), 487–502 (2015). (in russian)
14. Pilipchuk, V.N.: Nonlinear Dynamics: Between Linear and Impact Limits, vol. 52. Springer Science and Business Media, Berlin (2010)

Phase Dynamics of Intrinsic Localized Modes in Two Weakly Coupled Nonlinear Chains and Correspondence Between Periodic Tunneling of Classical and Quantum Objects

Yuriy A. Kosevich

Abstract We present a brief survey of the phase-coherent dynamics of intrinsic localized modes (discrete breathers) in a system of two weakly coupled nonlinear chains and its comparison with periodic tunneling of a quantum particle in a double-well potential and with macroscopic quantum tunneling of two weakly linked Bose–Einstein condensates. We consider the dynamics of relative phase of two classically-tunneling intrinsic localized modes in weakly coupled nonlinear chains and show that the dynamics of the relative phase in the $\pi/2$ tunneling mode coincides exactly with the experimentally observed dynamics of the relative phase of a quantum particle, periodically tunneling in a double-well potential. The observed coincidence demonstrates the correspondence between the dynamics of classical localized excitations in two weakly coupled nonlinear chains and tunneling dynamics of quantum object in the double-well potential. We show that in both $\pi/2$ and winding tunneling modes, the relative phase experiences periodic jumps by π in the instants of complete depopulation of one of the weakly coupled chains or potential wells. The connection of the observed phase dynamics with the non-quantum uncertainty principle is discussed.

Keywords Intrinsic localized modes · Weakly coupled anharmonic chains · Dynamics of relative phase · $\pi/2$ tunneling mode · Winding tunneling mode · Periodic tunneling · Classical and quantum objects · Non-quantum uncertainty principle

Yu. A. Kosevich (✉)
Semenov Institute of Chemical Physics, Russian Academy of Sciences,
ul. Kosygina 4, 119991 Moscow, Russia
e-mail: yukosevich@gmail.com

Yu. A. Kosevich
Plekhanov Russian University of Economics, Stremyanny per. 36,
117997 Moscow, Russia

I. V. Andrianov et al. (eds.), *Problems of Nonlinear Mechanics and Physics of Materials*, Advanced Structured Materials 94,
https://doi.org/10.1007/978-3-319-92234-8_4

1 Introduction

Tunneling through a barrier is purely quantum mechanical phenomenon. On a macroscopic scale it is realized in Josephson effect between two weakly coupled phase-coherent condensates. The latter can be two superconductors separated by a thin barrier [1], two reservoirs of superfluid helium connected by nanoscopic apertures [2, 3], or two weakly linked Bose–Einstein condensates in a macroscopic double-well potential (single bosonic Josephson junction) [4]. In this Chapter we discuss the profound analogy between classical phase-coherent dynamics of intrinsic localized modes (ILMs) in two weakly coupled nonlinear chains and tunneling dynamics of quantum objects. Corresponding equations of *classical tunneling dynamics* of two weakly coupled ILMs (wandering breathers) were obtained in the first papers in this field [5–7] and were later applied to a great variety of nonlinear mechanical systems [8]. Here we show that the dynamics of the relative phase of the ILMs in two weakly coupled nonlinear chains in the $\pi/2$ tunneling mode, first described in [5–7], exactly coincides with the experimentally observed dynamics of the relative phase of a quantum particle periodically tunneling in a double-well potential, which revealed the abrupt changes (jumps) of the phase between the $\pi/2$ and $-\pi/2$ values at the instants when the particle is fully localized in one of the coupled potential wells [9]. We show that in both $\pi/2$ and winding tunneling modes, the relative phase experiences periodic jumps by π in the instants of complete depopulation of one of two weakly coupled chains or potential wells.

Nonlinear excitations (solitons, kink-solitons, intrinsic localized modes and discrete breathers) can be created most easily in low-dimensional (1D and quasi-1D) systems [10–20]. Recent experiments have demonstrated the existence of intrinsic localized modes and discrete breathers in various systems such as coupled nonlinear optical waveguides [21], low-dimensional crystals [22], antiferromagnetic materials [23], micromechanical oscillator arrays [24, 25], Josephson junction arrays [26, 27], photonic structures and micromechanical systems [28], α-helices [29, 30], and α-uranium [31]. Slowly-moving ILMs and supersonic kink-solitons were also described in 1D nonlinear chains [15, 17, 32–37] and quasi-1D polymer crystals [38]. One-dimensional arrays of magnetic or optical microtraps for BECs of ultracold quantum gases with tunneling coupling provide a new field for the studies of coherent nonlinear dynamics in low-dimensional systems [39, 40].

Here, we discuss another conceptual aspect of classical nonlinear excitations by considering the analogy between dynamics of *phase-coherent* ILMs, either stationary or slowly-moving, in two weakly coupled nonlinear chains and quantum tunneling dynamics of a quantum particle periodically tunneling in a double-well potential [9] and of two weakly linked macroscopic condensates in a single bosonic Josephson junction [5–7]. There are two qualitatively different dynamical regimes of the coupled ILMs or discrete breathers, the nonlinear Rabi-like oscillations of the low-amplitude ILMs between the chains (*tunneling* ILM), and one-chain-localization (nonlinear self-trapping) for the high-amplitude ILM. These two regimes, which are separated by a separatrix mode with zero rate of energy and excitation exchange, are analogous to the two regimes in nonlinear dynamics of macroscopic Bose–Einstein

condensates in a single bosonic Josephson junction [4]. Phase-coherent dynamics of the coupled classical ILMs is described by a pair of equations completely similar to that for Bose–Einstein condensates in a single bosonic Josephson junction [41, 42]. The considered evolution of the relative phase of two weakly coupled ILMs is analogous to the evolution of relative quantum-mechanical phase between two macroscopic condensates, which was directly measured in a single bosonic Josephson junction by means of interference [4]. Moreover, the separatrix in the excitation exchange between macroscopic phase-coherent ensembles of particles in weakly coupled classical chains with "repulsive" nonlinearity can be considered as a nonlinear dynamical model of the reversible interaction-induced superfluid-Mott-insulator transition, which was observed in Bose–Einstein condensate in a lattice with tunneling intersite coupling [43].

2 Model

Following [5–7], we consider two identical linearly coupled identical anharmonic chains (with unit lattice period), which we model with the Fermi-Pasta-Ulam (β-FPU) Hamiltonian:

$$H = \sum_n \left[\sum_{i=1}^{2} \left[\frac{1}{2} p_n^{(i)2} + \frac{1}{2}(u_{n+1}^{(i)} - u_n^{(i)})^2 + \frac{1}{4}\beta\ (u_{n+1}^{(i)} - u_n^{(i)})^4 \right] + \frac{1}{2} C (u_n^{(1)} - u_n^{(2)})^2 \right], \tag{1}$$

where $u_n^{(i)}$ is displacement of the nth particle from its equilibrium position in the ith chain, $p_n^{(i)} = \dot{u}_n^{(i)}$ is particle momentum, β and C are, respectively, dimensionless intra-chain nonlinear and inter-chain linear force constants (in units of intra-chain linear force constant). We assume that the coupling is weak, $C \ll 1$, and do not include the nonlinear inter-chain interaction. Hamiltonian (1) describes, e.g., purely transverse particle motion [15].

We are interested in high-frequency and therefore short-wavelength dynamics of the coupled chains, when the displacements of the nearest-neighbour particles are mainly anti-phase. For this case we introduce continuous envelope-functions for the particle displacements in the chains, $u_n^{(i)} = f_i(x)(-1)^n$, $\partial f_i / \partial x \ll 1$, where $x = n$ is a continuous spatial coordinate along the ith chain, which allow us to write partial differential equations for $f_i(x,t)$, see, e.g., [11, 15, 33, 34, 44]. Then from Hamiltonian (1) we get the following equations for $f_i(x,t)$, $i = 1, 2$:

$$\ddot{f}_i + (4 + C) f_i + \frac{\partial^2 f_i}{\partial x^2} + 16\beta f_i^3 - C f_{3-i} = 0. \tag{2}$$

In order to deal with the amplitude and phase of the coupled nonlinear excitations, it is useful to introduce complex wave fields $\Psi(x,t)_i$ for each chain, cf. [44]:

$$f_i(x,t) = \frac{1}{2}\left[\Psi_i(x,t)\exp(-i\omega_m t) + \Psi_i(x,t)^*\exp(i\omega_m t)\right], \tag{3}$$

where $\omega_m = \sqrt{4+C} \approx 2 + C/4$ is characteristic frequency slightly above the maximal phonon frequency of isolated chains (equal to 2 in each chain). Assuming that characteristic frequencies of the fields $\Psi(x,t)_i$ are small in comparison with ω_m, from Eqs. (2) and (3) we get the following coupled nonlinear-Schrödinger-type equations for $\Psi(x,t)_i$, $i = 1, 2$:

$$-i\omega_m\dot{\Psi}_i + \frac{1}{2}\frac{\partial^2\Psi_i}{\partial x^2} + 6\beta \mid \Psi_i \mid^2 \Psi_i = \frac{C}{2}\Psi_{3-i}, \tag{4}$$

and complex-conjugated equations for Ψ_i^*. Similar Schrödinger-type and nonlinear-Schrödinger-type equations for complex envelope functions of classical displacement fields were obtained in [44, 45].

Using Eq. (4), one can readily show the existence of the following integrals of motion and inter-chain flux:

$$N_s = \int \left[\mid \Psi_1 \mid^2 + \mid \Psi_2 \mid^2\right] dx \equiv N_1 + N_2, \tag{5}$$

$$E_s = \int [\sum_{i=1}^{2}(3\beta \mid \Psi_i \mid^4 - \frac{1}{2} \mid \frac{\partial\Psi_i}{\partial x} \mid^2) - \frac{1}{2}C(\Psi_1\Psi_2^* + \Psi_2\Psi_1^*)]dx, \tag{6}$$

$$P_{sx} = -\frac{i}{2}\int \sum_{i=1}^{2}\left[\Psi_i\frac{\partial\Psi_i^*}{\partial x} - \Psi_i^*\frac{\partial\Psi_i}{\partial x}\right]dx, \tag{7}$$

$$J_i = \frac{iC}{2\omega_m}\int \left[\Psi_i\Psi_{3-i}^* - \Psi_i^*\Psi_{3-i}\right]dx = -J_{3-i}, \tag{8}$$

which describe, respectively, the total number of excitations, total energy, total momentum along the chain axis, and total inter-chain flux of excitations (which conserves the total number of them, $\dot{N}_i + J_i = 0$), cf. [44]. The existence of these integrals of motion and inter-chain flux demonstrates that the exchange of energy between two coupled nonlinear systems is a coherent phenomenon, which depends, in general, on the initial conditions.

3 Tunneling Dynamics of Weakly Coupled ILMs

To describe a *slowly-moving* ILM, tunneling between two weakly coupled nonlinear chains with positive (repulsive) anharmonic force constant β, we assume the following form for the complex fields Ψ_1 and Ψ_2 [5–7]:

$$\Psi_1 = \Psi_{max} \frac{\exp[i(kx - \Omega t)]}{\cosh[\kappa_1(x - Vt)]} \cos\Theta \exp(-\frac{i}{2}\Delta), \tag{9}$$

$$\Psi_2 = \Psi_{max} \frac{\exp[i(kx - \Omega t)]}{\cosh[\kappa_2(x - Vt)]} \sin\Theta \exp(\frac{i}{2}\Delta), \tag{10}$$

where $\Omega > 0$ describes a shift of the ILM frequency ω with respect to ω_m, $V \ll 1$ and $k \ll 1$ are the velocity and wavenumber related with the moving ILM, κ_i describe inverse localization lengths. Here $\Delta = \Delta(t - kx/\omega)$ stands for the *reduced phase* of the lattice excitations in the coupled chains, while the parameter $\Theta = \Theta(t - kx/\omega)$ describes the *relative population* (population imbalance) of the two chains $z = (n_1 - n_2)/(n_1 - n_2) = \cos 2\Theta$, where $n_i = |\Psi_1|^2$ is local density of excitations in the ith chain, and $n_1 + n_2 = |\Psi_{max}|^2 = const$.

Parameters Δ and Θ determine the inter-chain flux of excitations, cf. Eq. (8):

$$J_1 = -J_2 = \frac{C\Psi_{max}^2}{2\omega_m} \int \frac{\sin 2\Theta \sin\Delta}{\cosh[\kappa_1(x - Vt)]\cosh[\kappa_2(x - Vt)]} dx. \tag{11}$$

The *relative phase* Φ, which we will compare below with the relative phase in quantum tunneling dynamics, is defined as

$$\Phi = \arg\left[\frac{\Psi_2}{\Psi_1}\right] = \arg\left[\tan\theta \exp(i\Delta)\right]. \tag{12}$$

It is worth underlining that the relative and reduced phases Φ and Δ coincide in the case of tunneling dynamics, in which the tunneling object does not reach during its evolution the state of complete depopulation of one of the weakly coupled atomic chains or potential wells, which corresponds to $|z| = 1$. Such tunneling dynamics, with equal relative and reduced phases, was realized, e.g., in Ref. [4] for the Bose–Einstein condensate in weakly linked double-well potential (bosonic Josephson junction).

Using Eqs. (4), (9) and (10), after some algebra we obtain dispersion equations for the introduced parameters,

$$\Omega = \frac{1}{2\omega_m}[3\beta\Psi_{max}^2 - k^2 - C\frac{\cos\Delta}{\sin(2\Theta)}], V = \frac{\partial\Omega}{\partial k}, \tag{13}$$

$$\kappa_1^2 = 6\beta\Psi_{max}^2\langle\cos^2\Theta\rangle, \quad \kappa_2^2 = 6\beta\Psi_{max}^2\langle\sin^2\Theta\rangle, \tag{14}$$

and evolution equations for the phases Θ and Δ:

$$\dot{\Theta} = \frac{C}{2\omega_m}\sin\Delta, \tag{15}$$

$$\dot{\Delta} = \frac{3\beta\Psi_{max}^2}{\omega_m}\cos(2\Theta) + \frac{C}{\omega_m}\cos\Delta\cot(2\Theta). \tag{16}$$

Angular brackets in Eq. (14) denote the time-averaged and therefore time-independent quantities, which take into account the possibility of the integration along the trajectory of the slowly-moving ILM in the integrals like that given by Eqs. (5)–(8). In the derivation of Eqs. (15) and (16), it was assumed explicitly that the ratio $\frac{\cosh[\kappa_1(x-Vt)]}{\cosh[\kappa_2(x-Vt)]}$ is equal to one. The latter is valid for small-amplitude ILMs with long localization lengths, $\kappa_{1,2} \ll 1$. In this case the above assumption, which is exact for the central region of the ILMs, $x\text{-}Vt \approx 0$, will be (approximately) valid for a large number of particles, which form weakly localized tunneling ILM in weakly coupled nonlinear chains.

Equations (15) and (16) can be written in an equivalent form for the reduced relative phase Δ and relative population of the two chains $z = (n_1 - n_2)/(n_1 + n_2) = \cos 2\Theta$, which are canonically conjugate, except the point of $|z| = 1$, see below:

$$\dot{z} = -\frac{\partial H_{eff}}{\partial \Delta} = -\frac{C}{\omega_m}\sqrt{1-z^2}\sin\Delta, \tag{17}$$

$$\dot{\Delta} = \frac{\partial H_{eff}}{\partial z} = \frac{3\beta\Psi_{max}^2}{\omega_m}z + \frac{C}{\omega_m}\frac{z}{\sqrt{1-z^2}}\cos\Delta, \tag{18}$$

with the following effective Hamiltonian [which has the dimension of frequency]:

$$H_{eff} = \frac{3\beta\Psi_{max}^2}{2\omega_m}z^2 - \frac{C}{\omega_m}\sqrt{1-z^2}\cos\Delta. \tag{19}$$

The very same equations were derived in [41, 42] in connection with theoretical studies, based on macroscopic quantum Gross–Pitaevskii equation, of coherent atomic tunneling and coherent oscillations between two weakly coupled Bose–Einstein condensates, which were later used in the analysis of the experimental realization of a single bosonic Josephson junction [4]. In our case, Eqs. (17) and (18) describe the exchange of lattice excitations between the chains rather than atomic tunneling. One can consider such excitation exchange as a classical counterpart of macroscopic quantum tunneling dynamics.

It is noteworthy that the equations, which are similar to Eqs. (15) and (16), describe the dynamics of two weakly coupled identical nonlinear oscillators. Therefore the tunneling intrinsic localized modes can be considered as weakly coupled phase-coherent nonlinear *macroscopic oscillators*.

Equations (15) and (16) can be solved analytically for the given initial conditions. [For the weak coupling, in the following we assume $\omega_m = 2$]. Using the ansatz,

$$\cos\Delta = A(t)/\sin(2\Theta), \tag{20}$$

where $A = 0$ for $\Theta = 0$, we get from Eqs. (15) and (16):

$$\dot{A} = -(3\beta\Psi_{max}^2/C)\sin(4\Theta)\dot{\Theta}. \tag{21}$$

We are seaking for a solution of Eqs. (15) and (16) with the initial condition $\Theta(0) = 0$, which corresponds to zero complex field Ψ_2 in the second chain at t=0 and which is realized in our simulations. For $\Theta(0) = 0$ and $A(0) = 0$, we obtain

$$\begin{aligned} A &= -\frac{3\beta\Psi_{max}^2}{2C}\sin^2(2\Theta), \\ \cos\Delta &= -\frac{3\beta\Psi_{max}^2}{2C}\sin(2\Theta) = -\frac{3\beta\Psi_{max}^2}{2C}\sqrt{1-z^2}, \end{aligned} \tag{22}$$

which corresponds to $\Delta(0) = \pi/2$ (or $\Delta(0) = -\pi/2$). Then Eqs. (15) and (16) take the following form:

$$\dot{\Theta} = \frac{C}{4}\sin\Delta, \quad \dot{\Delta} = \frac{3\beta\Psi_{max}^2}{4}\cos(2\Theta). \tag{23}$$

Finally, from Eqs. (22) and (23) we get the following two equivalent pendulum equations:

$$\ddot{\delta} + \frac{C^2}{4}\sin\delta = 0 \tag{24}$$

- for $\delta = 2\Delta - \pi$, and

$$\ddot{\Xi} + \Omega_0^2 \sin\Xi = 0 \tag{25}$$

- for $\Xi = 4\Theta$, where $\Omega_0^2 = (3\beta\Psi_{max}^2/4)^2$. We are interested in the solution of Eq. (24) with the initial conditions $\delta(0) = 0$ and $\dot{\delta}(0) = \frac{3}{2}\beta\Psi_{max}^2$. The corresponding initial conditions for Ξ in Eq. (25) are $\Xi(0) = 0$ and $\dot{\Xi}(0) = C$.

The important property of the solution of the pendulum equation, (24) or (25), which has exact analytical solution, see, e.g., [46], is the existence of two qualitatively different dynamical regimes of excitation and energy exchange, which have a separatrix corresponding to the condition $|\ S\ | = 1$, where $S = 3\beta\Psi_{max}^2/(2C)$ is the nonlinearity-over-coupling parameter.

For $|\ S\ | \ll 1$ or $|\ \beta\ |\Psi_{max}^2 \ll 2C/3$, the phase Θ linearly grows with the "running" time $\tilde{t} \equiv t - kx/\omega$:

$$\begin{aligned} \Theta &\approx \tilde{C}\frac{\tilde{t}}{4} + \frac{9\beta^2\Psi_{max}^4}{64\tilde{C}^2}\sin(\tilde{C}\tilde{t}), \\ \Delta &\approx \frac{\pi}{2} + \frac{3\beta\Psi_{max}^2}{2\tilde{C}}\sin(\tilde{C}\frac{\tilde{t}}{2}), \\ z &\approx \cos(\tilde{C}\frac{\tilde{t}}{2}), \\ \tilde{C} &= C - \frac{\Omega_0^2}{C} = C - \frac{9\beta^2\Psi_{max}^4}{16C}. \end{aligned} \tag{26}$$

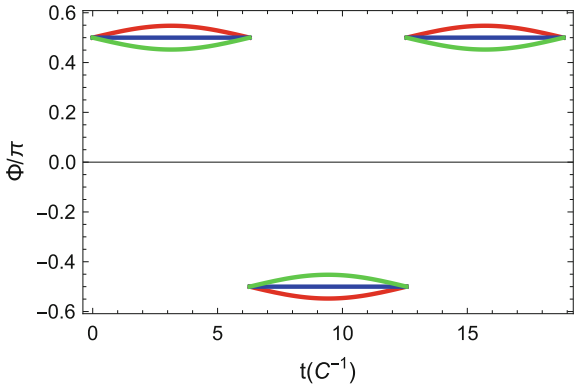

Fig. 1 Time evolution of relative phase Φ in the $\pi/2$ tunneling mode between two weakly coupled nonlinear chains, for $S \equiv 3\beta\Psi_{max}^2/(2C) = 0$ (blue straight lines), $S = 0.15$ (red curved lines) and $S = -0.15$ (green curved lines). Dynamics of the relative phase is described by Eqs. (12) and (26), time is measured in C^{-1}

In this regime, Θ spans the full range from 0 to 2π, which corresponds to the *total* energy exchange between the nonlinear chains and therefore to the ILM, periodically tunneling between the two chains, when the reduced phase Δ is close to $\pi/2$. We call the excitation exchange in this regime as the $\pi/2$ tunneling mode of ILM. According to Eq. (11), the inter-chain flux of excitations and energy in this mode is $\propto C\Psi_{max} \sin 2\Theta \sin\Delta \approx C\Psi_{max} \sin(C\tilde{t}/2)$.

The relative phase Φ is defined by Eq. (12) and its time evolution in the $\pi/2$ tunneling mode, described by Eq. (26), is presented in Fig. 1 for different values of the parameter S in the weakly-nonlinear limit. [Negative parameter S, caused by negative nonlinear force constant β, corresponds to the *tunneling dark soliton* in the vibrational pattern of the confined lattice mode with eigenfrequency slightly below ω_m in the system of two weakly coupled identical nonlinear chains with equal finite lengths, when the factors $\Psi_{max} \exp[i(kx - \Omega t)]/\cosh[\kappa_i(x - Vt)]$ with $\Omega > 0$ in the complex fields (9) and (10), are replaced by the factors $\Psi_{max} \exp(i(kx - \Omega t) \tanh[\kappa_i(x - Vt)]$ with $\Omega < 0$, $i = 1, 2$, see e.g., [15].]

Figure 1 clearly shows that there are abrupt changes (jumps) of the relative phase Φ by π, between $\pi/2$ and -$\pi/2$, at each instant when the ILM is located completely in one of the coupled chains and the relative population is equal to unit in modulus, $|z| = 1$. According to Eq. (26), the interval between such instants in the weakly-nonlinear limit is given by $2\pi/C$. In the case of vanishing nonlinearity, the time evolution of the relative phase Φ coincides exactly with the experimentally observed dynamics of the relative phase of the tunneling quantum particles in a double-well potential [9]. The jumps of the relative phase at the instants of $|z| = 1$ are related with the uncertainty of the phase when the particle wave function is exactly zero in one of the coupled potential wells or chains, $\Psi_i = 0$ either for $i = 1$ or $i = 2$, see Eqs. (9) and (10). On the other hand, the abrupt change of the relative phase can be related with the non-quantum *uncertainty principle*: the variables z and Φ are canonically conjugate, see Eqs. (17) and (18), and therefore cannot be measured simultaneously because the

product of their uncertainties Δz and $\Delta\Phi$ is bounded from below by the inequality $\Delta z \cdot \Delta\Phi \geq 1/2$. At the instants of $|z| = 1$, the inter-chain tunneling current is zero, $\dot{z} = 0$, see (11), and therefore the relative population z and correspondingly the location of the ILM or quantum particle is well defined, which makes the value of Φ be uncertain at these instants. On the other hand, the reduced phase Δ is a single-valued function and the wave functions (9) and (10) of the displacement fields, which are determined by this phase, are the single-valued functions as it is required by quantum mechanics [47] and the jumps by π of the relative phase Φ, which is determined by (12), do not make the wave functions ambiguous functions. The continuity of the Δ and Θ functions is also confirmed by the existence of the second-order pendulum Eqs. (24) and (25) for these functions, which provide description of the tunneling dynamics, equivalent to that given by Eq. (23). Since both the classical ILM in a system of two weakly coupled nonlinear chains and the quantum particle, tunneling in a double-well potential, can be described with the use of the canonically conjugate relative population z and relative phase Φ, there is clear coincidence of the phase dynamics and the correspondence between periodic tunneling of classical and quantum objects.

The phase dynamics in the $\pi/2$ tunneling mode can also be compared with the phase dynamics in the quantum Rabi oscillations, see, e.g., [48]. Here, for the superposition of two states

$$\Psi(t) = a_1(t) \mid 1 > + a_2(t) \mid 2 > \tag{27}$$

with equal on-site energies $E_1 = E_2 \equiv E$, Schrödinger equations for the complex amplitudes a_1 and a_2 are the following:

$$\begin{aligned} i\dot{a}_1 &= Ea_1 + \gamma a_2, \\ i\dot{a}_2 &= Ea_2 + \gamma a_1, \end{aligned} \tag{28}$$

where parameter γ is the coupling matrix element between the states, and $\hbar = 1$. For the initial conditions $a_1(0) = 1$ and $a_2(0) = 0$ and the value of the coupling parameter $\gamma = -C/4$, which corresponds to Eqs. (4) and (28) have the solution,

$$\begin{aligned} a_1 &= \cos(\gamma t)\exp(-iEt) = \cos(Ct/4)\exp(-iEt), \\ a_2 &= -i\sin(\gamma t)\exp(-iEt) = i\sin(Ct/4)\exp(-iEt), \end{aligned} \tag{29}$$

which exactly corresponds to the $\pi/2$ tunneling mode, described by Eq. (26) in the linear case $S = 0$ for the ansatz given by Eqs. (9) and (10) with $\Theta = Ct/4$ and $\Delta = \pi/2$. [In the system of two weakly coupled atomic chains, the linear case $S = 0$ corresponds to two weakly coupled identical harmonic chains with equal finite lengths when the $\pi/2$ tunneling mode describes the periodic inter-chain tunneling of the confined harmonic vibrational mode with eigenfrequency $\omega = \omega_m$ at the top of acoustic band of the chains.] Therefore the $\pi/2$ tunneling mode for $0 <| S |< 1$ can be considered as the *nonlinear Rabi-like* oscillations of excitation population

in two coupled anharmonic chains, in which the wave functions Ψ_1 and Ψ_2 in (9) and (10) play role of the complex amplitudes a_1 and a_2 in the superposition of two states (27). The $\pi/2$ tunneling mode, which is described by the single-valued wave function in accordance with the requirement of quantum mechanics [47], can also be realized in two weakly linked Bose–Einstein condensates.

The separatrix, realized for $\mid S \mid = 1$ and $H_{eff} = C/\omega_m$, is characterized by infinite oscillation period of the physical pendulum (24) or (25), which corresponds to the infinite period of the inter-chain energy exchange. For the considered initial conditions, the separatrix is described by the following solution of Eq. (23):

$$\Theta = \arctan[\exp(\frac{C}{2}t)] - \frac{\pi}{4}, \quad \Delta = 2\arctan[\exp(\frac{C}{2}t)], \tag{30}$$

$$z(0) = 1, \quad z(\infty) = 0, \quad \Delta(0) = \frac{\pi}{2}, \quad \Delta(\infty) = \pi. \tag{31}$$

There is no difference between the reduced Δ and relative Φ phases in the separatrix mode, see the aforementioned arguments in connection with Eq. (12) for the coincidence of the two phases. The flux of the inter-chain excitation exchange is zero at the separatrix for $t \to \infty$: $J_i = 0$ since $\sin\Delta = 0$, see Eq. (11).

Beyond the separatrix, in the limit of $\mid S \mid \gg 1$ or $\mid \beta \mid \Psi_{max}^2 \gg 2C/3$, one has

$$\Theta \approx \frac{C}{3\beta\Psi_{max}^2}\sin(\frac{3}{4}\beta\Psi_{max}^2\tilde{t}), \quad \Delta \approx \frac{\pi}{2} + \frac{3}{4}\beta\Psi_{max}^2\tilde{t}. \tag{32}$$

This dynamical regime corresponds to the asymmetric nonlinear mode (known, e.g., for two coupled nonlinear waveguides [49–51]), in which one system, here is chain 1, carries almost all vibrational energy while the other is almost at rest. This excitation-exchange regime can be called as the *winding* tunneling mode because of linear increase in time of the reduced phase Δ. The relative phase Φ experiences periodic jumps by π, with the period of $2\pi/\mid S \mid$, see Fig. 2. The time instants of the relative-phase jumps coincide with the instants of $|z| = 1$, similar to the case of the phase jumps by π in the $\pi/2$ tunneling mode shown in Fig. 1. In the winding tunneling mode, the energy exchange between the coupled chains is relatively weak and gradually decreases with the increase of the parameter $\mid S \mid$ beyond the separatrix value of $\mid S \mid = 1$. The inter-chain flux of excitations and energy in this mode is $\propto C\Psi_{max}\sin 2\Theta \sin\Delta \propto (C^2/\Psi_{max})\sin(3\beta\Psi_{max}^2\tilde{t}/2)$.

The two dynamical regimes of energy and excitation exchange between ILMs in two weakly coupled nonlinear chains, given by Eqs. (26) and (32), are analogous, respectively, to anharmonic Josephson-like oscillations or nonlinear self-trapping, which were detected in a single bosonic Josephson junction [4].

It is worth mentioning that the form and frequency of a stationary or slowly-moving ILM in an *isolated* chain can be obtained only in the winding tunneling (self-trapping) mode, in which one can consider the limit of $C \to 0$ (for positive β). Indeed, according to Eq. (32), in this limit one has $\Theta = 0$ in Eqs. (9) and (10) and ILM frequency is obtained from Eqs. (13), (22) and (32), and is equal to

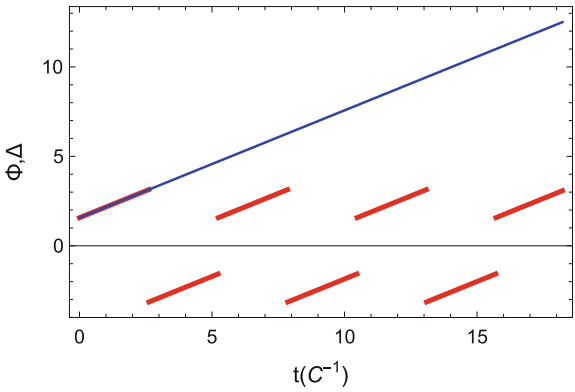

Fig. 2 Time evolution of relative Φ (red lines) and reduced Δ (blue line) phases of two ILMs in the winding tunneling mode between two weakly coupled nonlinear chains, for $S \equiv 3\beta\Psi_{max}^2/(2C) = 1.2$. Dynamics of the relative and reduced phases is described by Eqs. (12) and (32), time is measured in C^{-1}

$$\omega = 2 + \Omega + \frac{3}{8}\beta\Psi_{max}^2 = 2 + \frac{3}{2}\beta\Psi_{max}^2 - \frac{k^2}{4}. \tag{33}$$

This expression for the ILM frequency fully coincides with the known expressions for a single stationary or slowly-moving ILM in the small-amplitude limit, see, e.g., Refs. [5–7, 11, 44]. This coincidence confirms the correct choice of the distribution of the reduced phase Δ between the tunneling objects, given by $-i\Delta/2$ and $i\Delta/2$ in the exponents in Eqs. (9) and (10), similar to that in the superposition of two states in quantum mechanics [48]. It is important to underline that to get this expression for ω, one has to take explicitly into account in Eq. (9) the linear increase in time (winding up) of the reduced relative phase Δ in the self-trapping mode, given by Eq. (32). The winding up of the relative phase of two weakly coupled macroscopic BECs in the nonlinear self-trapping mode has been directly measured in a single bosonic Josephson junction [4]. This finding gives us an additional argument in favour of the profound similarity between macroscopic tunneling quantum dynamics and phase-coherent dynamics of weakly coupled intrinsic localized modes.

4 Conclusions

In conclusion, we have discussed analytical description of two qualitatively different regimes of energy exchange between phase-coherent intrinsic localized modes in two weakly linked nonlinear chains. These regimes have a profound analogy, and are described by a similar pair of equations, to the anharmonic Josephson-like oscillations and nonlinear self-trapping, which were observed in a single bosonic Josephson junction. We show that the dynamics of the relative phase in the $\pi/2$ tunneling mode exactly coincides with the experimentally observed dynamics of the relative phase of a quantum particle, periodically tunneling in a double-well potential. The $\pi/2$ tunneling mode can also be observed in two weakly linked Bose–Einstein condensates. The observed coincidence demonstrates the correspondence between the dynamics of

classical localized excitations in two weakly coupled nonlinear chains and tunneling dynamics of quantum particles in a double-well potential. In both $\pi/2$ and winding tunneling modes, the relative phase Φ experiences periodic jumps by π in the instants of complete depopulation of one of the two weakly coupled chains or potential wells, when $|z| = 1$. The connection of the observed phase dynamics with the non-quantum uncertainty principle is discussed. The obtained dispersion and evolution equations, together with the wave functions of the coupled nonlinear excitations, can be applied to the tunneling macroscopic Bose–Einstein condensate, moving along two weakly linked bosonic waveguides, to classically-tunneling phase-coherent intrinsic localized modes (discrete breathers) in two weakly linked macromolecules, α-helices or DNA, and to electron-phonon and exciton-phonon polarons in two weakly coupled polymer molecules or semiconductor waveguides.

Acknowledgement The author is grateful to L.I. Manevitch for interesting and helpful discussions of many aspects of nonlinear dynamics in anharmonic chains, especially for the long-lasting and fruitful discussions of the analogy between classical and quantum dynamics.

This work was supported by the Program of Fundamental Researchers of the Russian State Academies of Sciences 2013-2020 (project No. 0082-2014-0013).

References

1. Josephson, B.D.: Possible new effects in superconductive tunnelling. Phys. Lett. **1**, 251–253 (1962)
2. Pereverzev, S.V., Loshak, A., Backhaus, S., Davis, J.C., Packard, R.E.: Quantum oscillations between two weakly coupled reservoirs of superfluid ^{3}He. Nature (London) **388**, 449–451 (1997)
3. Sukhatme, K., Mukharsky, Y., Chui, T., Pearson, D.: Observation of the ideal Josephson effect in superfluid ^{4}He. Nature (London) **411**, 280–283 (2001)
4. Albiez, M., Gati, R., Fölling, J., Hunsmann, S., Cristiani, M., Oberthaler, M.K.: Direct observation of tunneling and nonlinear self-trapping in a single bosonic Josephson junction. Phys. Rev. Lett. **95**, 010402-1–010402-4 (2005)
5. Kosevich, Yu.A, Manevitch, L.I., Savin, A.V.: Energy transfer in coupled nonlinear phononic waveguides: transition from wandering breather to nonlinear self-trapping. J. Phys. Conf. Ser. **92**, 012093-1–012093-5 (2007)
6. Kosevich, Yu.A., Manevitch, L.I., Savin, A.V.: Wandering breathers and self-trapping in weakly coupled nonlinear chains: classical counterpart of macroscopic tunneling quantum dynamics. Phys. Rev. E **77**, 046603-1–046603-20 (2008)
7. Kosevich, Yu.A, Manevitch, L.I., Savin, A.V.: Energy transfer in weakly coupled nonlinear oscillator chains: transition from a wandering breather to nonlinear self-trapping. J. Sound Vib. **322**, 524–531 (2009)
8. Manevitch, L.I., Kovaleva, A., Smirnov, V., Starosvetsky, Y.: Nonstationary Resonant Dynamics of Oscillatory Chains and Nanostructures. Springer, Singapore (2018)
9. Fölling, S., Trotzky, S., Cheinet, P., Feld, M., Saers, R., Widera, A., Müller, T., Bloch, I.: Direct observation of second-order atom tunnelling. Nature (London) **448**, 1029–1033 (2007)
10. Zabusky, N.J., Kruskal, M.D.: Interaction of solitons in a collisionless plasma and the recurrence of initial states. Phys. Rev. Lett. **15**, 240–243 (1965)
11. Kosevich, A.M., Kovalev, A.S.: Self-localization of oscillations in a one-dimensional anharmonic chain. Sov. Phys. JETP **40**, 891–898 (1974)

12. Dolgov, A.S.: On localization of oscillations in nonlinear crystal structure. Sov. Phys. Solid State **28**, 907–909 (1986)
13. Sievers, A.J., Takeno, S.: Intrinsic localized modes in anharmonic crystals. Phys. Rev. Lett. **61**, 970–973 (1988)
14. Page, J.B.: Asymptotic solutions for localized vibrational modes in strongly anharmonic periodic systems. Phys. Rev. B **41**, 7835–7838 (1990)
15. Kosevich, Yu.A: Nonlinear envelope-function equation and strongly localized vibrational modes in anharmonic lattices. Phys. Rev. B **47**, 3138–3152 (1993)
16. Kosevich, Yu.A: Erratum: nonlinear envelope-function equation and strongly localized vibrational modes in anharmonic lattices. Phys. Rev. B **48**, 3580 (1993)
17. Kosevich, Yu.A: Nonlinear sinusoidal waves and their superposition in anharmonic lattices. Phys. Rev. Lett. **71**, 2058–2061 (1993)
18. Aubry, S.: Breathers in nonlinear lattices: existence, linear stability and quantization. Physica D **103**, 201–250 (1997)
19. Flach, S., Willis, C.R.: Discrete breathers. Phys. Rep. **295**, 181–264 (1998)
20. Flach, S., Gorbach, A.V.: Discrete breathers - advances in theory and applications. Phys. Rep. **467**, 1–116 (2008)
21. Eisenberg, H.S., Silberberg, Y., Morandotti, R., Boyd, A.R., Aitchison, J.S.: Discrete spatial optical solitons in waveguide arrays. Phys. Rev. Lett. **81**, 3383–3386 (1998)
22. Swanson, B.I., Brozik, J.A., Love, S.P., Strouse, G.F., Shreve, A.P., Bishop, A.R., Wang, W.-Z., Salkola, M.I.: Observation of intrinsically localized modes in a discrete low-dimensional material. Phys. Rev. Lett. **82**, 3288–3293 (1999)
23. Sato, M., Sievers, A.J.: Direct observation of the discrete character of intrinsic localized modes in an antiferromagnet. Nature (London) **432**, 486–488 (2004)
24. Sato, M., Hubbard, B.E., Sievers, A.J., Ilic, B., Czaplewski, D.A., Craighead, H.G.: Observation of locked intrinsic localized vibrational modes in a micromechanical oscillator array. Phys. Rev. Lett. **90**, 044102-1–044102-4 (2003)
25. Sato, M., Hubbard, B.E., Sievers, A.J.: Colloquium: nonlinear energy localization and its manipulation in micromechanical oscillator arrays. Rev. Mod. Phys. **78**, 137–157 (2006)
26. Trias, E., Mazo, J.J., Orlando, T.P.: Discrete breathers in nonlinear lattices: experimental detection in a Josephson array. Phys. Rev. Lett. **84**, 741–744 (2000)
27. Binder, P., Abraimov, D., Ustinov, A.V., Flach, S., Zolotaryuk, Y.: Observation of breathers in Josephson ladders. Phys. Rev. Lett. **84**, 745–748 (2000)
28. Campbell, D.K., Flach, S., Kivshar, Y.S.: Localizing energy through nonlinearity and discreteness. Phys. Today **57**, 43–49 (2004)
29. Edler, J., Pfister, R., Pouthier, V., Falvo, C., Hamm, P.: Direct observation of self-trapped vibrational states in α-helices. Phys. Rev. Lett. **93**, 106405-1–106405-4 (2004)
30. Juanico, B., Sanejouand, Y.-H., Piazza, F., De Los Rios, P.: Discrete breathers in nonlinear network models of proteins. Phys. Rev. Lett. **99**, 238104-1–238104-4 (2007)
31. Manley, M.E., Yethiraj, M., Sinn, H., Volz, H.M., Alatas, A., Lashley, J.C., Hults, W.L., Lander, G.H., Smith, J.L.: Formation of a new dynamical mode in α-Uranium observed by inelastic X-ray and neutron scattering. Phys. Rev. Lett. **96**, 125501-1–125501-4 (2006)
32. Chen, D., Aubry, S., Tsironis, G.P.: Breather mobility in discrete ϕ^4 nonlinear lattices. Phys. Rev. Lett. **77**, 4776–4779 (1996)
33. Kosevich, Yu.A, Corso, G.: Temporal Fourier spectra of stationary and slowly moving breathers in Fermi-Pasta-Ulam anharmonic lattice. Physica D **170**, 1–12 (2002)
34. Kosevich, Yu.A, Khomeriki, R., Ruffo, S.: Supersonic discrete kink-solitons and sinusoidal patterns with "magic" wavenumber in anharmonic lattices. Europhys. Lett. **66**, 21–27 (2004)
35. Archilla, J.F.R., Kosevich, Yu.A, Jiménez, N., García-Raffi, L.M.: Ultradiscrete kinks with supersonic speed in a layered crystal with realistic potentials. Phys. Rev. E **91**, 022912-1–022912-12 (2015)
36. Kosevich, Yu.A: Charged ultradiscrete supersonic kinks and discrete breathers in nonlinear molecular chains with realistic interatomic potentials and electron-phonon interactions. J. Phys. Conf. Ser. **833**, 012021-1–012021-6 (2017)

37. Mehrem, A., Salmerón-Contreras, L.J., Jiménez, N., Sánchez-Morcillo, V.J., Picó, R., García-Raffi, L.M., Archilla, J.F.R., Kosevich, Yu.A: Kinks in a lattice of repelling particles. Experimental study with a chain of coupled pendulums. In: Archilla, J.F.R., Palmero, F., Lemos, M.C., Sánchez-Rey, B., Casado-Pascual, J. (eds.) Nonlinear Systems, Vol. 2. Nonlinear Phenomena in Biology, Optics and Condensed Matter, pp. 261–282. Springer, Cham (2018)
38. Savin, A.V., Manevitch, L.I.: Discrete breathers in a polyethylene chain. Phys. Rev. B **67**, 144302-1–144302-5 (2003)
39. Anderson, B.P., Kasevich, M.A.: Macroscopic quantum interference from atomic tunnel arrays. Science **282**, 1686–1689 (1998)
40. Kinoshita, T., Wenger, T., Weiss, D.S.: A quantum Newton's cradle. Nature (London) **440**, 900–903 (2006)
41. Smerzi, A., Fantoni, S., Giovanazzi, S., Shenoy, S.R.: Quantum coherent atomic tunneling between two trapped Bose-Einstein condensates. Phys. Rev. Lett. **79**, 4950–4953 (1997)
42. Raghavan, S., Smerzi, A., Fantoni, S., Shenoy, S.R.: Coherent oscillations between two weakly coupled Bose-Einstein condensates: Josephson effects, π oscillations, and macroscopic quantum self-trapping. Phys. Rev. A **59**, 620–632 (1999)
43. Greiner, M., Mandel, O., Esslinger, T., Hänsch, T.W., Bloch, I.: Quantum phase transition from a superfluid to a Mott insulator in a gas of ultracold atoms. Nature (London) **415**, 39–44 (2002)
44. Kosevich, Yu.A, Lepri, S.: Modulational instability and energy localization in anharmonic lattices at finite energy density. Phys. Rev. B **61**, 299–307 (2000)
45. Kosevich, Yu.A, Manevitch, L.I., Manevitch, E.L.: Vibrational analogue of nonadiabatic Landau-Zener tunneling and a possibility for the creation of a new type of energy traps. Phys. Uspekhi **53**, 1281–1286 (2010)
46. Sagdeev, R.Z., Usikov, D.A., Zaslavsky, G.M.: Nonlinear Physics: From the Pendulum to Turbulence and Chaos. Harwood Academic Publishers, New York (1988)
47. Landau, L.D., Lifshitz, E.M.: Quantum Mechanics. Non-relativistic Theory. Pergamon Press, Oxford (1977)
48. Cohen-Tannoudji, C., Diu, B., Laloë, F.: Quantum Mechanics, Vol. 1, Ch. IV. Hermann, Paris (1977)
49. Jensen, S.M.: The nonlinear coherent coupler. IEEE J. Quantum Electron. **QE–18**, 1580–1583 (1982)
50. Akhmediev, N., Ankiewicz, A.: Novel soliton states and bifurcation phenomena in nonlinear fiber couplers. Phys. Rev. Lett. **70**, 2395–2398 (1993)
51. Uzunov, I.M., Muschall, R., Gölles, M., Kivshar, Y.S., Malomed, B.A., Lederer, F.: Pulse switching in nonlinear fiber directional couplers. Phys. Rev. E **51**, 2527–2537 (1995)

Non-linear Beatings as Non-stationary Synchronization of Weakly Coupled Autogenerators

Margarita A. Kovaleva, Leonid I. Manevitch and Valery N. Pilipchuk

Abstract The present work represents a selective overview of recent advances in the area dealing with a new type of synchronization in systems of weakly coupled active oscillators. The description is focused on the evolution of non-stationary beat wise self-sustained oscillations developed as attractors and repellers when the system non-linearity and dissipation is varied.

1 Introduction

Systems of weakly coupled oscillators are often used as simple models of various non-linear oscillatory processes in different fields of Science. For instance, coupled Van der Pol or Van der Pol–Duffing oscillators is one of the fundamental models in nonlinear dynamics [1, 2], and many other fields of physics, biophysics, and interdisciplinary areas of research [1, 3–6]. In the continuum limit, the description of such system can be reduced to the complex Ginzburg–Landau equation [6–9], which may have both periodic and localized solutions [1, 7–9]. The simplest discrete model of this type, which consists of two nonlinear dissipative oscillators, was considered in a number of publications [3, 4, 6]. The main attention was usually paid to synchronization of oscillators in dynamics close to nonlinear normal modes (NNMs) [1, 3, 4, 6, 10]. Specifically, this is a 1:1 resonance characterized by conservation of the energy initially imparted to oscillators [11, 12]. It has been shown recently that beats with complete energy exchange between oscillators in the conservative case are, in fact, a fundamental type of motions alternative to NNMs [12], which is referred to as the limiting phase trajectory (LPT) [13, 14]. The LPT is defined as the phase trajectory which corresponds to the most intensive resonant energy exchange

M. A. Kovaleva (✉) · L. I. Manevitch
Semenov Institute of Chemical Physics, Russian Academy of Sciences, Kosygin St.4, 119991 Moscow, Russia
e-mail: margo.kovaleva@gmail.com

V. N. Pilipchuk
Wayne State University, 1200 Holden Street, Detroit, MI 48202, USA

I. V. Andrianov et al. (eds.), *Problems of Nonlinear Mechanics and Physics of Materials*, Advanced Structured Materials 94,
https://doi.org/10.1007/978-3-319-92234-8_5

between the two coupled oscillatory subsystems. These can be individual oscillators of the two-oscillator model or different groups of oscillators in a certain oscillatory chain [12]. Along LPT, the energy is recurrently passing through the unique state of complete localization on one of the sub-systems; see e.g. [12–14]. In terms of the LPT, a transition from the intense recurrent energy exchange to energy localization can also be described [13, 14]. Clearly, in conservative systems, neither the LPT nor NNM can be an attractor. In contrast, active dissipative systems can possess NNM attractors corresponding to synchronization of oscillators [1, 3, 4, 6, 10].

In the present work we review the recent results concerning the intensive LPT beating as phase attractors or repellers in weakly coupled generators including different dynamic transitions due to system parameter variations [15–18]. In particular, synchronous oscillations developed as intensive beatings are found to exist in the system of two coupled generators with hard excitation and a relatively weak coupling. This new type of synchronization can also be observed in the system of generators when the coupling is imposed via linear oscillator. The analogy to the quantum 2-level system interacting with the external field was analyzed in [19, 20].

2 Empirical Model of Self-localization with Dissipative Coupling

A dissipative chain of coupled oscillators, which is described in this section, was suggested in somewhat empirical way to illustrate the possibility of energy self-localization [21]. However, some dynamic behaviors of this model appeared to be quite similar to those found later in different models eventually leading to new physical interpretations, in particular, such as non-stationary synchronization; see the next section. The term 'auto-localization' means that the system itself may come into the nonlinear local mode vibration and stay there regardless initial energy distribution among its particles. As follows from the Poincare's recurrence theorem, such phenomena are rather impossible within the class of conservative systems. However, interactions between the system particles can be designed in specific ways in order to achieve desired phenomena. It is assumed that such a design can be implemented practically within the class of electromechanical devices, which may help to optimize vibration suppression. Let us consider an array of N harmonic oscillators such that each of the oscillators interacts with only the nearest neighbors. The corresponding differential equations of motion are of the form

$$\ddot{x}_j + \Omega^2 x_j = \beta(x_{j-1} - 2x_j + x_{j+1}) + \alpha[(E_j - E_{j-1})E_{j-1} - (E_{j+1} - E_j)E_{j+1}]\dot{x}_j$$

where $j = 1, \ldots, N$, $E_j = (\dot{x}_j^2 + \Omega^2 x_j^2)/2$ is the total energy of the jth oscillator, the boundary conditions of fixed ends are imposed on the chain, Ω, β, and α are constant parameters of the model. On the right-hand side of this equation, two groups of terms describe coupling between the oscillators. If $\alpha = 0$ then the only linear coupling

remains, and the chain becomes perfectly conservative. In this case, under special initial conditions, N different linear normal modes, can take place. It is well known that any other motion is combined of the linear normal mode motions, whereas the energy is conserved on each of the modes the way it was initially distributed between the modes. In other words, if $\alpha = 0$, no energy localization is possible on individual particles. However, another group of terms with the common factor α, has the opposite to linear elastic interaction effect. These nonlinear terms simulate possible 'competition' between the oscillators, in other words, a one-way energy flow to the neighbor whose energy is lager.

The model was considered in terms of complex amplitudes introduced as $x_j = [A_j(t)\exp(i\Omega t) + \bar{A}_j(t)\exp(-i\Omega t)]/2$. In the particular case of two-degrees-of freedom, $N = 2$, the transformed system admits first integral $K = |A_1|^2 + |A_2|^2 = const.$, which allows for the system reduction through transition to phase variables as $A_1 = \sqrt{K}\ \cos\psi\ \exp(i\varphi_1)$ and $A_2 = \sqrt{K}\ \sin\psi\ \exp(i\varphi_2)$. Finally, the reduced system takes the form

$$\frac{d\Delta}{dp} = -\cot 2\psi\ \cos\Delta, \quad \frac{d\psi}{dp} = -\frac{1}{2}(\sin\Delta + \lambda\ \sin 4\psi)$$

where $\Delta = \varphi_2 - \varphi_1$ is phase difference, $p = \Omega t/\beta$ is a new time scale, and $\lambda = \alpha K^2\Omega^5/(16\beta)$ is a parameter of both non-linear non-conservative effects.

Figure 1 illustrates a typical behavior of the phase states on the phase plane (a) and in time histories (b) and (c). It is seen that the phase cell boundary is a periodic attractor (limit cycle) whose period admits exact analytical expression in the form $T = 2\pi/\sqrt{1-\lambda^2}$. It is seen that $T \to \infty$ as $\lambda \to 1$, which actually points to the energy localization effects since the energy exchange between the two oscillators takes the infinitely long time. In addition, the temporal behavior of the phase difference between the oscillators becomes almost constant except for very narrow time intervals. Physical interpretation of this effect was suggested later, however, based on different type of models, as described below.

3 The Model of Non-stationary Synchronization and Its Reduction

The essence of the non-stationary synchronization phenomenon can be illustrated in all the details based on the model of two weakly coupled generators with hard excitation. We consider the evolution of the system in the vicinity of the primary 1:1 resonance. However, for generality reason, the oscillators can be slightly detuned:

$$\begin{aligned}
&\frac{d^2u_1}{dt^2} + u_1 + 8\alpha\varepsilon u_1^3 + 2\beta\varepsilon(u_1 - u_2) + 2\varepsilon(\gamma - 4bu_1^2 + 8du_1^4)\frac{du_1}{dt} = 0;\\
&\frac{d^2u_2}{dt^2} + u_2 + 4\varepsilon\kappa u_2 + 8\alpha\varepsilon u_2^3 + 2\beta\varepsilon(u_2 - u_1) + 2\varepsilon(\gamma - 4bu_2^2 + 8du_2^4)\frac{du_2}{dt} = 0. \quad (1)
\end{aligned}$$

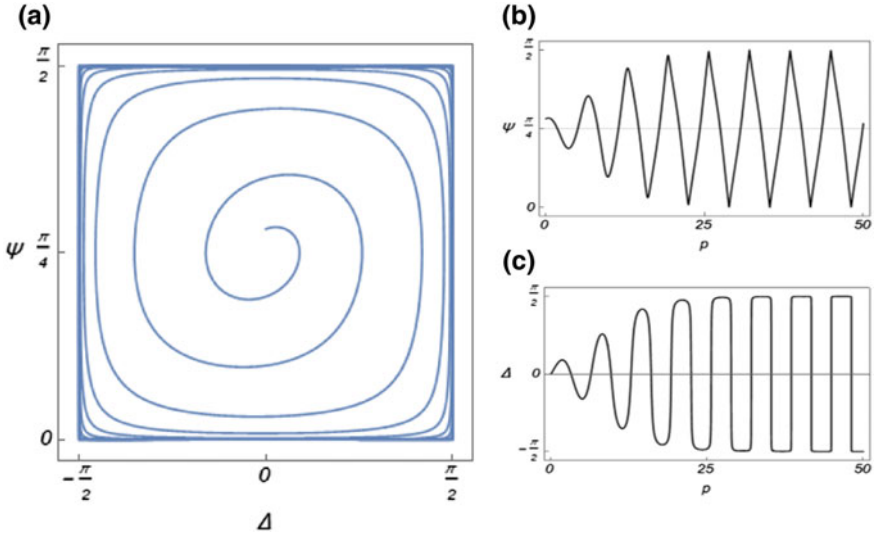

Fig. 1 Dynamic transition to the periodic attractor of phase system: **a** phase portrait showing the cell boundary as a periodic limit cycle [21]; **b** and **c** transition to 'non-smooth' temporal shapes corresponding to the attractor; $\lambda = 0.2$, $\Delta(0) = 0$, $\psi(0) = \pi/4 + 0.1$

Introducing complex variables $\psi_j = v_j + iu_j$, $v_j = du_j/dt\,(j = 1, 2)$, or inversely, $v_j = \left(\psi_j + \psi_j^*\right)/2$ and $u_j = -i\left(\psi_j - \psi_j^*\right)/2$, where the asterisk indicates complex conjugate, brings system (1) to the complex form

$$\frac{d\psi_1}{dt} + i\psi_1 - \varepsilon\Big(i\alpha\big(\psi_1 - \psi_1^*\big)^3 + i\beta\big(\big(\psi_1 - \psi_1^*\big) - \big(\psi_2 - \psi_2^*\big)\big) + \Big(\gamma + b\big(\psi_1 - \psi_1^*\big)^2 + d\big(\psi_1 - \psi_1^*\big)^4\Big)\big(\psi_1 + \psi_1^*\big)\Big) = 0,$$

$$\frac{d\psi_2}{dt} + i\psi_2 - \varepsilon\Big(2i\kappa\psi_2 + i\alpha\big(\psi_2 - \psi_2^*\big)^3 + i\beta\big(\big(\psi_2 - \psi_2^*\big) - \big(\psi_3 - \psi_3^*\big)\big) + \Big(\gamma + b\big(\psi_2 - \psi_2^*\big)^2 + d\big(\psi_2 - \psi_2^*\big)^4\Big)\big(\psi_2 + \psi_2^*\big)\Big) = 0.$$

Following the idea of two variable expansions, we separate the "fast" $\tau_0 = t$ and "slow" $\tau_1 = \varepsilon t$ time scales, taking into account that $\frac{d}{dt} = \frac{\partial}{\partial\tau_0} + \varepsilon\frac{\partial}{\partial\tau_1}$. Then, representing solutions in the form $\psi_j = \left[\phi_{j,0}(\tau_0, \tau_1) + \varepsilon\phi_{j,1}(\tau_0, \tau_1) + O(\varepsilon^2)\right]e^{i\tau_0}$, $(j = 1, 2)$ and applying the two-scale method, gives the leading-order approximation [17]

$$\begin{aligned}
&\frac{df_1}{d\tau_1} - 3i\alpha|f_1|^2 f_1 + \left(\gamma - b|f_1|^2 + d|f_1|^4\right)f_1 + i\beta f_2 = 0,\\
&\frac{df_2}{d\tau_1} - 3i\alpha|f_2|^2 f_2 - 2i\kappa f_2 + \left(\gamma - b|f_2|^2 + d|f_2|^4\right)f_2 + i\beta f_1 = 0,
\end{aligned} \tag{2}$$

where new complex coordinates f_j are given by $\varphi_{j,0} = f_j e^{i\beta\tau_1}$. Equations (2) represent a generalization of equations derived in the references [15, 16], which accounts for the detuning effect described by the term $2i\kappa f_2$ in the second equation.

Representing the complex coordinates in the form $f_1 = R_1 e^{i\delta_1}$, $f_2 = R_2 e^{i\delta_2}$, we obtain a system of three real-valued equations

$$\frac{dR_1}{d\tau_1} + \gamma R_1 - bR_1^3 + dR_1^5 + \beta R_2 \sin\Delta = 0,$$
$$\frac{dR_2}{d\tau_1} + \gamma R_2 - bR_2^3 + dR_2^5 - \beta R_1 \sin\Delta = 0,$$
$$R_1 R_2 \frac{d\Delta}{d\tau_1} - 2\kappa R_1 R_2 + 3\alpha R_1 R_2 (R_2^2 - R_1^2) + \beta (R_2^2 - R_1^2)\cos\Delta = 0, \quad (3)$$

where $\Delta = \delta_2 - \delta_1$. The principal idea of the above transition from system (1) to system (3) is that system (3) possesses an additional symmetry, as compared to system (1), and therefore it reveals both types of the dynamic synchronization NNMs and LPTs from the unified standpoint of symmetries as discussed below.

4 The NNM and LPT Symmetries

First, let us consider the system (3) without detuning, $\kappa = 0$. While being non-integrable, system (3), possesses, nevertheless, the discrete symmetry, namely it preserves its form under the coordinate replacements:

$$R_1 \to R_2,\ R_2 \to R_1,\ \Delta \to -\Delta$$
$$R_1 \to -R_2,\ R_2 \to -R_1,\ \Delta \to \Delta \quad (4)$$

Symmetries (4) provide the existence of in-phase ($R_1 = R_2$, $\Delta = 0$) and out-of-phase ($R_1 = R_2$, $\Delta = \pi$) NNMs, respectively. In the general case, the form of Eq. (4) does not explicitly reveal any other symmetries, discrete or continuous, except of temporal translation. However, if any non-trivial continuous symmetry does exist under certain conditions, it can be found in the framework of the Lie group theory [22] by manipulating the infinitesimal differential operator of the dynamical system (3), $X = X_0 + X_1$, where $X_0 = \xi(R_1, R_2, \Delta)\frac{\partial}{\partial\tau_1} + \eta(R_1, R_2, \Delta)\frac{\partial}{\partial R_1} + \zeta(R_1, R_2, \Delta)\frac{\partial}{\partial R_2} + \varsigma(R_1, R_2, \Delta)\frac{\partial}{\partial\Delta}$, X_1—is the first continuation of the operator X_0 whose components are given by time derivatives in system (3). Following the technique [22] and considering the partial differential equations for the components of operator X, reveals under special conditions the existence of rotation group in the plane $(R_1 R_2)$ with the invariant $I \equiv N = R_1^2 + R_2^2$. For the rotational symmetry to take place, the parameters of system (4) must satisfy the relation

$$b^2 = 9\gamma d/2 \quad (5)$$

under the excitation level determined by the number

$$N = 2b/3d. \quad (6)$$

In this case, introducing the coordinate transformation $R_1 = \sqrt{N}\,\sin\theta$, $R_2 = \sqrt{N}\,\cos\theta$ finally gives the reduced system

$$\begin{aligned} \frac{d\theta}{d\tau_2} &= \frac{1}{2}(\sin\Delta - \lambda\,\sin 4\theta), \\ \sin 2\theta\frac{d\Delta}{d\tau_2} &= \cos 2\theta\,\cos\Delta + 2k\,\sin 4\theta, \end{aligned} \tag{7}$$

where $\tau_2 = 2\beta\tau_1$ is a new temporal scale, and parameters $k = \frac{3\alpha N}{2\beta}$ and $\lambda = \frac{N^2 d}{8\beta}$ characterize the nonlinearity and dissipation, relative to the coupling of the generators, respectively.

5 Phase Plane Analysis and Effect of Dissipation

We start from the particular case $\lambda = 0$ when system (7) represents the conservative case and the NNMs are stable (Fig. 2a). Two branches of LPT associate with the complete energy exchange between the generators. We choose the parameter of nonlinearity between 0 and 1/4 to avoid the conservative-type bifurcation of the NNMs which occurs at $k = 1/4$ and will be considered below. Note that transition to the non-conservative case makes the notion of energy somewhat vague. Nevertheless, the energy term of the corresponding conservative oscillator still can be viewed as a Lyapunov's function describing the excitation level in the non-conservative case.

At first, we vary the dissipative parameter. When λ is relatively small, the system has two unstable focuses corresponding to the NNMs of the original system (1) (Fig. 2b). The focuses transform into unstable nodes when $\lambda^2 > 1 - 2k$ (Fig. 2, panels (b) and (c)). If the dissipative parameter λ does not exceed the value $\frac{1}{2}\left(1 + \sqrt{1 - 4k^2}\right)$, the only attractor of the system is the LPT with the intensive energy exchange between the oscillators. The phase shift between the oscillators on the LPT remains near $\pm\,\pi/2$ almost all the time (Fig. 3d) while sign switches of the phase shift take negligibly short time as the system approaches the LTP attractor.

Therefore, the oscillators become synchronized in a nonconventional way that can be qualified as the 'LPT-type synchronization'. We underline that the attracting behavior of LPTs presented in Fig. 1 means that LPT attracts all phase trajectories corresponding to the arbitrary energy distribution between the oscillators. However, the attractor itself still represents a particular solution which takes place under certain initial conditions similarly to the conventional limit cycles. Moreover, we can show numerically that, by changing the magnitude of N within a wide range while preserving the dissipative parameters, we obtain the similar attracting behavior of LPT. Therefore, the perfectly symmetric case can serve as a generating model for description of the LPT synchronization in a more general situation.

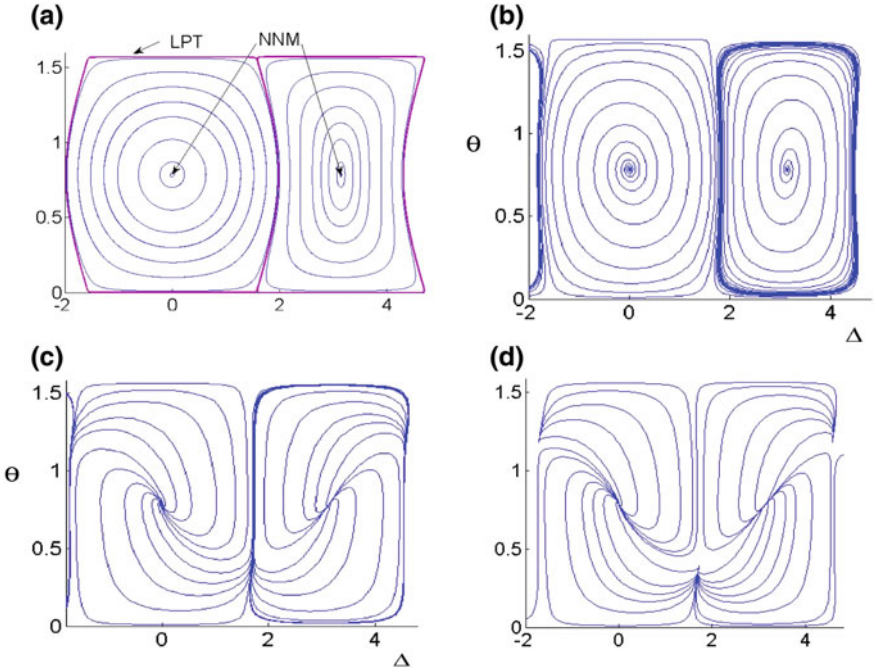

Fig. 2 Phase planes of the system (7) in terms of the variables θ and Δ characterizing the relationship between the generators' amplitudes, R_1 and R_2, and phases, δ_1 and δ_2, as $R_1 = \sqrt{N}\sin\theta$, $R_2 = \sqrt{N}\cos\theta$ and $\Delta = \delta_2 - \delta_1$: **a** nonlinearity parameter $k = 0.2$, dissipative parameter, $\lambda = 0$ (conservative system), the stationary points $(0, \pi/4)$ and $(\pi, \pi/4)$ correspond to stable in-phase and out-of-phase NNMs, respectively; the two branches of LPT (solid pink lines) associate with the complete energy exchange between the generators, namely when $\theta = 0$ or $\theta = \pi/2$, the energy is concentrated on one of the oscillators; **b** $k = 0.2$, $\lambda = 0.1$ —the stationary points transform into unstable focuses, the left branch of the LPT becomes unclosed, and the right branch transforms into the attractor; **c** $k = 0.1$, $\lambda = 0.9$ —the further increase of the dissipative parameter results in the transformation of the unstable focuses into the unstable nodes, however the LPT-like attractor still survives; **d** $k = 0.1$, $\lambda = 0.99$—the LPT-like attractor corresponding to the intensive energy exchange between the generators is destroyed and the localized nonlinear normal mode (LNNM) becomes a new attractor; all the results are in a good agreement with simulations of the original system (1) (see Fig. 4) [15]

Further, if $\lambda \geq \frac{1}{2}\left(1 + \sqrt{1 - 4k^2}\right)$, the LPT becomes unstable, and the attractor is a stationary point corresponding to the localized NNM with the energy predominantly trapped on one of the two oscillators (Fig. 2d). Such a transition to localized mode was described earlier for somewhat artificially designed model in [21].

It is important to note that the evolution of the LPT leading to the transition from the energy exchange to the energy localization, turns out to be independent of the evolution of the stationary points and occurs "later" than the transformation from unstable focus to unstable node (Fig. 3e) In the range of intensive energy exchange,

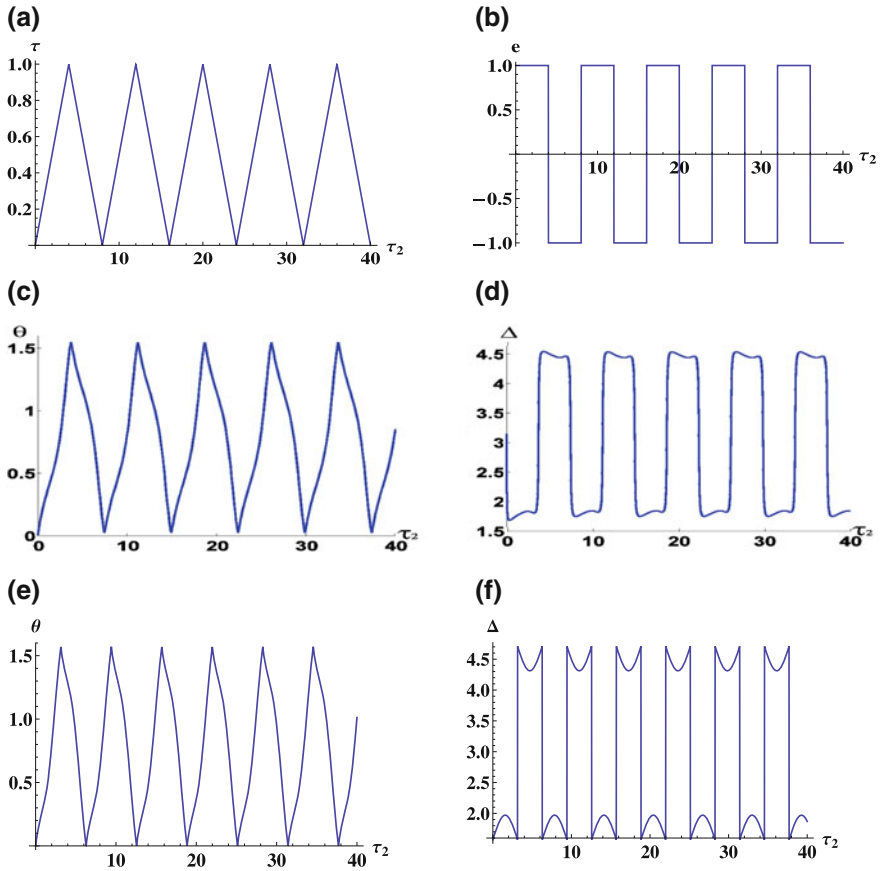

Fig. 3 The basic functions $\tau(\xi)$ (**a**) and $e(\xi)$ (**b**), and the time histories of the phases θ (**c**) and Δ (**d**) obtained from system (7) for the set of parameters corresponding to Fig. 2b; transition to non-smooth variables allows finding the appropriate analytical representation (8) for θ (**e**) and Δ (**f**) of the functions characterizing the relationship between the excitations of two oscillators and the relative phase shift [15]

one can obtain the analytical solution of system (7) by adapting the analytical tool of nonsmooth temporal substitutions [26]:

$$\theta = A\tau + \frac{\lambda}{4}[\cos(4A\tau) - 1]e + \ldots,$$

$$\Delta = \pi - \left[\frac{\pi}{2} - 2k\ \sin(2A\tau)\right]e + \ldots, \tag{8}$$

where the basis functions $\tau = \tau(\tau_2/(2A))$ and $e = e(\tau_2/(2A))$ are illustrated by Fig. 3, panels (a), (b); the period of solution (8) $T = 4A = 2\pi$ is found from the

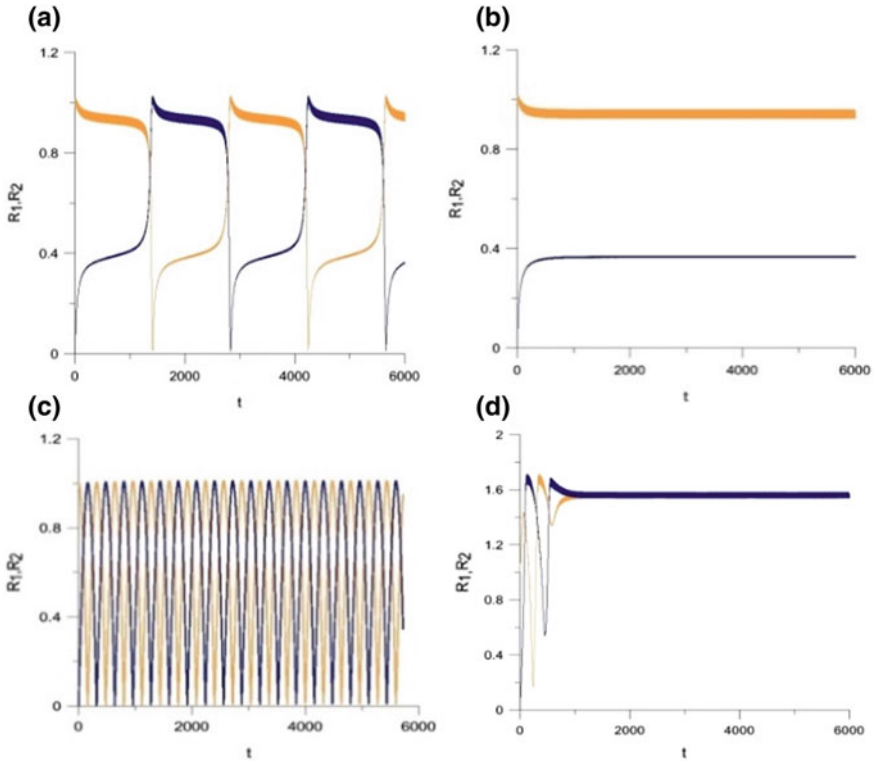

Fig. 4 The transition from the energy exchange to the energy localization in the system (3) of two coupled generators. We show the temporal behavior of the amplitudes $R_i = |\psi_i| = u_i^2 + v_i^2$ ($i = 1, 2$) obtained by numerical integration of the original system (1) to verify the existence of a new type of synchronization: R_1—orange line, R_2—blue line; **a** $k = 0.1$, $\lambda = 0.98$—the energy exchange just before the transition to localization; **b** $k = 0.1$, $\lambda = 0.99$—the behavior just over the localization threshold, most of the energy is localized on one of the oscillators; **c** the non-conventional synchronization corresponding to the parameters set of Fig. 2b, far from the localization threshold; and **d** the conventional synchronization on out-of-phase NNM when the parameters of generators do not satisfy the accepted symmetry conditions [15]

full energy exchange condition, which is equivalent to the smoothness condition, $\theta(1) = \pi/2$, of the function; and temporal shapes of the solution are shown in Fig. 3c–f, respectively. The numerical solution, which is illustrated by Fig. 3c, d, appears to be in good compliance with the analytical solution (8) shown in Fig. 3e, f.

The behavior of the system before and after the transition from non-conventional synchronization on the LPT to the synchronization on the localized NNM is illustrated in Fig. 4a, b, in terms of the original variables. The non-conventional synchronization on the LPT far from the localization threshold is shown in Fig. 4c.

We presented also for comparison the plot demonstrating well-studied conventional synchronization in Fig. 4d, which is realized on the out-of-phase NNM. The set of parameters in the latter case was taken "far enough" from the accepted symmetry conditions.

6 The Role of Nonlinearity

As noticed in Introduction, the LPT associates with the complete energy transfer between the oscillators, and thus it can play the role of a 'nonstationary alternative' to stationary NNM dynamic regimes. There are two subsequent topological transitions that can be observed in the phase plane. The first one occurs when the nonlinearity parameter k exceeds the value 1/4. At this nonlinearity level, the anti-phase NNM becomes unstable and two new stationary points are born as a result of supercritical pitchfork bifurcation. From the physical standpoint, such a bifurcation points to the onset of energy localization on individual oscillators, which is the so-called nonlinear local modes (NLMs). This happens due to the fact that high nonlinearity levels make the oscillators effectively stiffer or, in other words, the coupling between them weaker.

Following [18], Fig. 5 presents phase portraits of system (7) under a gradually increasing nonlinearity level while the dissipation parameter is fixed, $\lambda > 0$. As seen from Fig. 5, all the topological transformations happen inside the cell of anti-phase mode. Due to the presence of non-conservative term, the NNM stationary point becomes unstable focus while the nonlinearity level is low enough. In this case, a limit cycle, which is very close to the cell boundary, becomes the only attractor of the system representing the non-stationary LPT-type synchronization. Note that the term 'limit cycle' relates to the reduced system (3) describing the slow-time modulation dynamics of the original system (1). During this type of synchronization, the "energy" is periodically transferred from one oscillator to another while the phase shift between the oscillators Δ remains almost constant all the time except for very narrow time intervals. During such interval the phase shift Δ jumps along the horizontal pieces of limit cycle while the "energy" distribution, described by the angle\theta is almost fixed. As mentioned previous section such temporal behaviors admit approximations with the non-smooth periodic basis [16] analogously to solution (8). Note that the limit cycle can be attractor provided that the nonlinear dissipation parameters satisfies the relationship $b^2 = 9\gamma d/2$.

Now we focus on the evolution of the phase plane assuming the nonlinearity parameter can vary within a relatively large range. We showed that the evolution of the phase flow inside the cell of anti-phase mode develops in several stages as follows; see Fig. 5. In particular, increasing the non-linearity parameter k above the anti-phase NNM's stability threshold still keeps the limit cycle corresponding to nonconventional synchronization stable, although the two new NNMs are seen bifurcated from the antiphase mode; Fig. 5b. When the newborn normal modes become stable focuses, two unstable limit cycles (repellers) encircling each of the newborn modes develop demonstrating Hopf bifurcation of each focus; see the red curves in

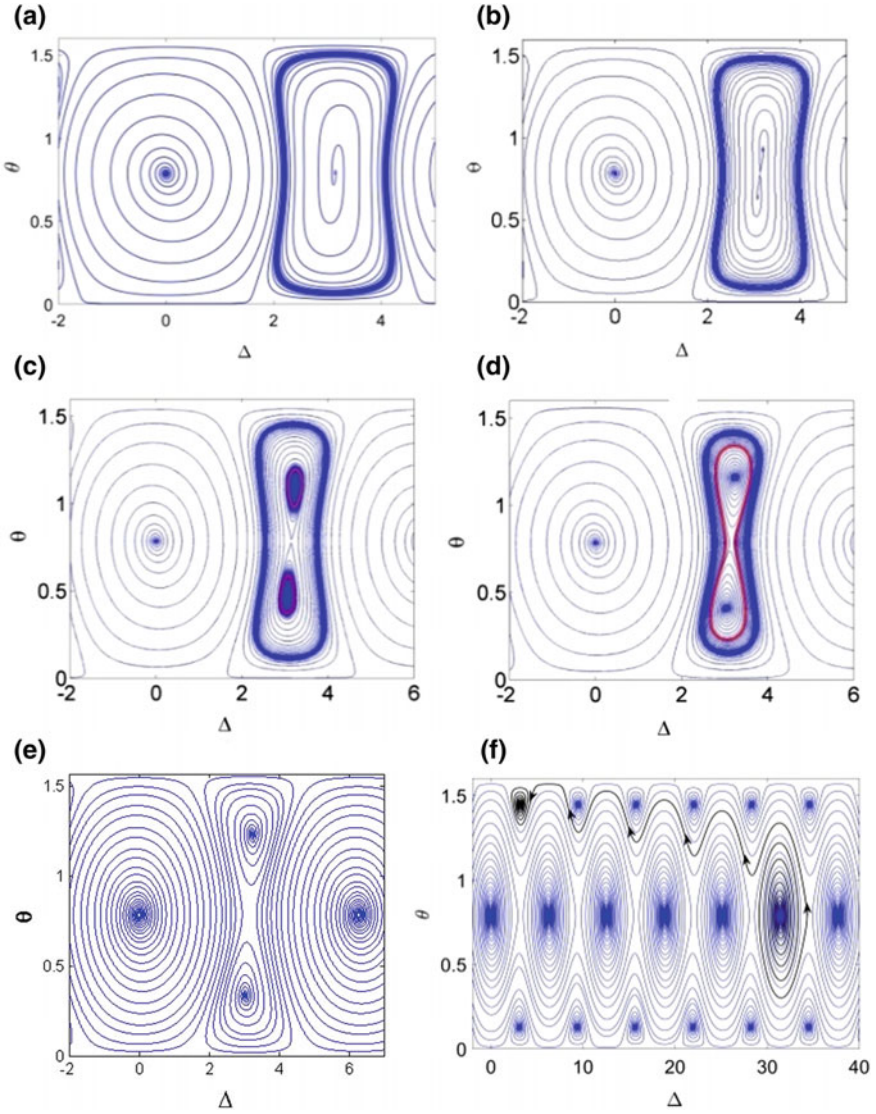

Fig. 5 Evolution of the phase plane of system (7) in the 'weakly nonlinear' case, due to a gradual nonlinearity increase, where the variables θ and Δ characterize the relation between the two amplitudes and the phase shift, respectively, $\lambda = 0.1$—weak dissipation, **a** $k = 0.23$ and the stationary points are unstable focuses, the limit cycle corresponding to LPT becomes attractor; **b** $k = 0.26$ the out-of-phase NNM becomes unstable, two new unstable stationary points are born separated by a saddle point, the limit cycle is still stable; **c** $k = 0.31$—further increase of the nonlinearity does not affect the topology of phase portrait, however, the limit cycles encircling the newborn stationary points can be observed; **d** $k = 0.34$—two unstable limit cycles collide by forming one unstable limit cycle, attractors of the system remain same; **e** $k = 0.4$—stable and unstable limit cycles collided, the two stable focuses on the right hand side become the only attractors of the system; **f** $k = 1$—rotating phase trajectory appears, which is eventually captured by a stable focus [18]

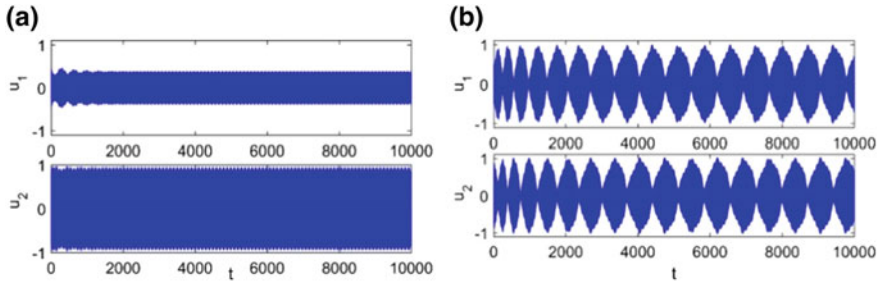

Fig. 6 Numerical solutions of Eq. (1): **a** inside of the repeller: $u_1(0) = 0.4794$; $v_1(0) = 0$; $u_2(0) = -0.8776$; $v_2(0) = 0$; **b** outside of the repeller: $u_1(0) = 0.4794$; $v_1(0) = 0$; $u_2(0) = 0.8776$; $v_2(0) = 0$ the parameter values are: $\varepsilon = 0.01$; $\alpha = 0.9071$; $\beta = 1.0$; $b = 2.4$; $d = 0.8$; $k = 0.34$; $\lambda = 0.1$ [18]

Fig. 5c. Since the both repellers occur from the separatrix loops, the dynamics in their vicinities are extremely slow compared to those close to the larger (stable) limit cycle.

If we further increase the nonlinearity parameter the repellers collide with each other to form a new (unstable) limit cycle that separates two areas of attraction; see the red curve in Fig. 5d. Outside the repeller loop, the non-conventional synchronization is possible, while inside the repeller synchronization on one of the two localized NNMs is developed. In Fig. 6, we illustrate the behavior of system (1) using the set of parameters, corresponding to Fig. 5d. In particular, Fig. 6a shows the dynamics under the initial conditions inside the repeller. It is seen that most of the energy/excitation becomes localized on the second oscillator. When the initial conditions are taken outside the repeller, the system becomes attracted to the beat-wise dynamics with the intensive energy exchange; see Fig. 6b. Therefore, the repellers separate domains of attraction of different types of synchronization.

Eventually the stable and unstable limiting cycles collide and the newborn focuses become the only attractors of the system; see Fig. 5e. These attractors correspond to a synchronization with predominantly one of the two oscillators excited.

To predict the parameter range for the existence of repellers we study the stability of the stationary points in the neighborhood of anti-phase mode. Such stationary points can be interpreted as additional nonlinear normal modes with partial localization of excitation on one of the two oscillators. Figure 7b presents the bifurcation diagram of stationary points in the phase plane $(\theta; \Delta)$. We see that the stability of newborn stationary points is associated with the appearance of the repellers surrounding them. Note that the coordinates of both points admit exact analytical solutions [18]

$$\begin{aligned} \theta_1 &= \frac{1}{2}\arcsin(A), \\ \Delta_1 &= \pi - \arccos(4kA) \end{aligned} \tag{9}$$

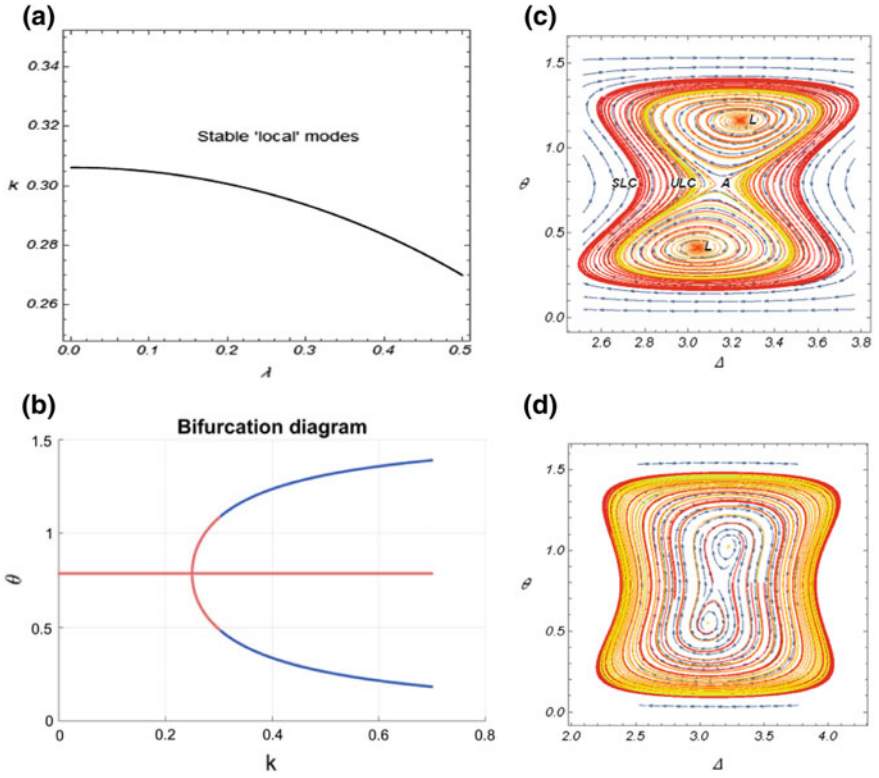

Fig. 7 Left panel: The boundary of stable quasi local modes in the non-linearity (k)—dissipation (λ) plane and bifurcation diagram showing the amplitude of the stationary points (9), for different values of the parameter k and for $\lambda = 0.1$; blue color denotes stable solutions, red color denotes unstable ones. Right panel: Phase portraits of system (7) above (**a**) and below (**b**) the boundary, which is shown in the left panel: **a** $k = 0.34$, $\lambda = 0.1$; **b** $k = 0.28$, $\lambda = 0.1$; in particular, the fragment (**b**) shows the saddle point A, corresponding to the unstable antiphase mode, two stable spiral points L, corresponding to stable 'quasi' local modes, the unstable ULC and stable SLC limit cycles [18]

and

$$\theta_2 = \frac{\pi}{2} - \frac{1}{2}\arcsin(A)\,,$$
$$\Delta_2 = \pi + \arccos(4kA)\,, \tag{10}$$

where $A = \sqrt{\frac{1}{2}\left(1 + \frac{4k^2}{\lambda^2} - \sqrt{\left(1 + \frac{4k^2}{\lambda^2}\right)^2 - \frac{1}{\lambda^2}}\right)}$. The presence of solutions (9) and (10) enables us to linearize system (7) near the stationary points and thus conduct their local stability analysis. Note that eigen values of the corresponding Jacobian matrixes appear to be the same for both points due to the symmetry. In other words,

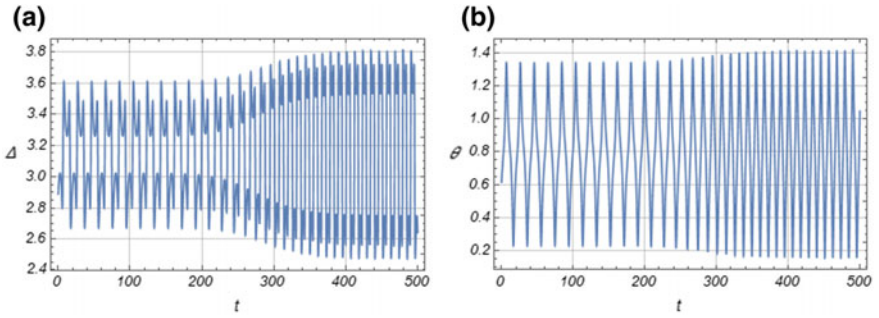

Fig. 8 Time history of the transition from the unstable ULC to stable SLC limit cycles; see the phase portrait in Fig. 7b, c

points (9) and (10) possess the same stability properties as soon as nonlinearity and dissipation parameters of system (7) remain fixed. The result of such analysis is summarized in Fig. 7, where the curve represents a manifold of parameters that separates the areas of positive and negative Lyapunov's exponents in such a way that they are positive below the curve. Therefore, points (9) and (10) are stable above while unstable below the curve in Fig. 7. Direct numerical integrations of Eq. (7) on both sides of the boundary are illustrated in Fig. 8 to confirm our conclusion.

Remark In the vicinity of the antiphase mode the system (7) can be represented in the form:

$$\begin{aligned} \frac{dx}{d\tau_2} &= 2(1-4k)y + \frac{8}{3}(1+2k)y^3 - x^2 y \\ \frac{dy}{d\tau_2} &= -\frac{1}{2}x + 2\lambda y + \frac{1}{12}x^3 - \frac{16}{3}\lambda y^3 \end{aligned} \tag{11}$$

where $\Delta = \pi + x$, and $\theta = \pi/4 + y$. As is seen from the Fig. 7 the system (11) represents evolution of all the (stable and unstable) limit cycles of the system (7). When the unstable limit are born, the stationary points inside each of them become stable focuses.

7 The Effect of Soft and Stiff Nonlinearities

In the previous sections we studied the case of the 'hard' nonlinearity. If the sign of the parameter is changed to negative, the effect of the conservative nonlinearity is changed quite drastically from the standpoint of its effect on the evolution of the phase planes. Let us note that all the analysis provided for the case of 'stiff nonlinearity can be completed for the 'soft' one as well. The new asymptotic system will coincide with the system (3). Only the sign of the parameter k must be changed. Therefore,

the phase plane analysis remains applicable to the case of soft nonlinearity leading however to quite different outcome. For instance, the anti-phase NNM will remain stable in all the range of parameters considered, while the in-phase NNM becomes unstable if the threshold value $k = 1/4$ is exceeded. In the non-conservative case, the stable limit cycle with the intensive energy exchange occurs around the in-phase mode. All the phase plane analysis can be conducted similarly to the 'stiff case. The only difference is that the in-phase and anti-phase mode cells will replace each other on the phase plane.

8 Synchronization in the Presence of Detuning

If we repeat the asymptotic procedure respecting the weak detuning of the two generator we obtain a similar to (7) system:

$$\begin{aligned} \frac{d\theta}{d\tau_2} &= \frac{1}{2}(\sin\Delta - \lambda\ \sin 4\theta), \\ \sin 2\theta \frac{d\Delta}{d\tau_2} &= \cos 2\theta\ \cos\Delta + 2k\ \sin 4\theta + g\ \sin 2\theta, \end{aligned} \tag{12}$$

where parameters $k = \frac{3\alpha N}{2\beta}$, $\lambda = \frac{N^2 d}{8\beta}$, and $g = \frac{\kappa}{\beta}$ characterize the nonlinearity, dissipation and detuning, respectively. In the Fig. 9 we show that the non-stationary synchronization is preserved in some range of the weak detuning.

Remembering that if the detuning is zero, $g = 0$, and the dissipation parameter is small enough, then, within the interval $0 < k < 1/4$, the system has two unstable focuses $(\theta, \Delta) = (\pi/4, 0)$ and $(\theta, \Delta) = (\pi/4, \pi)$. They become unstable nodes if $\lambda^2 > 1 - 2k$. When $0 < \lambda < \left(1 + \sqrt{1 - 4k^2}\right)/2$ the intensive energy exchange between the two oscillators is observed along the boundary between phase cells in the phase plane (LPT). If the detuning is gradually increased starting from zero, then we see first a slight deformation of the LPT-attractor. Then the nonlinear local mode (NLM), which corresponds to the energy localization on mostly one of the two generators, becomes the only attractor of the system (Fig. 9).

Now, if we increase the nonlinearity parameter, $k > 1/4$, then the phase diagram of conservative system changes its structure. Namely, the stationary point corresponding to the out-of-phase NNM transforms from center to saddle so that out-of-phase mode loses its stability. As a result, new stationary points corresponding to NLMs occur as shown in Fig. 5b. For dissipative case and large enough values of nonlinearity parameter k these two stationary points become stable focuses so that the NLMs become attractors. Depending on the initial conditions the phase trajectories are attracted by one of the two focuses; see Fig. 5e. Adding some detuning leads to no significant change of the phase plane picture, except one of the two NLMs becomes dominating as an attractor on the phase plane (Fig. 10). The area of attraction of the

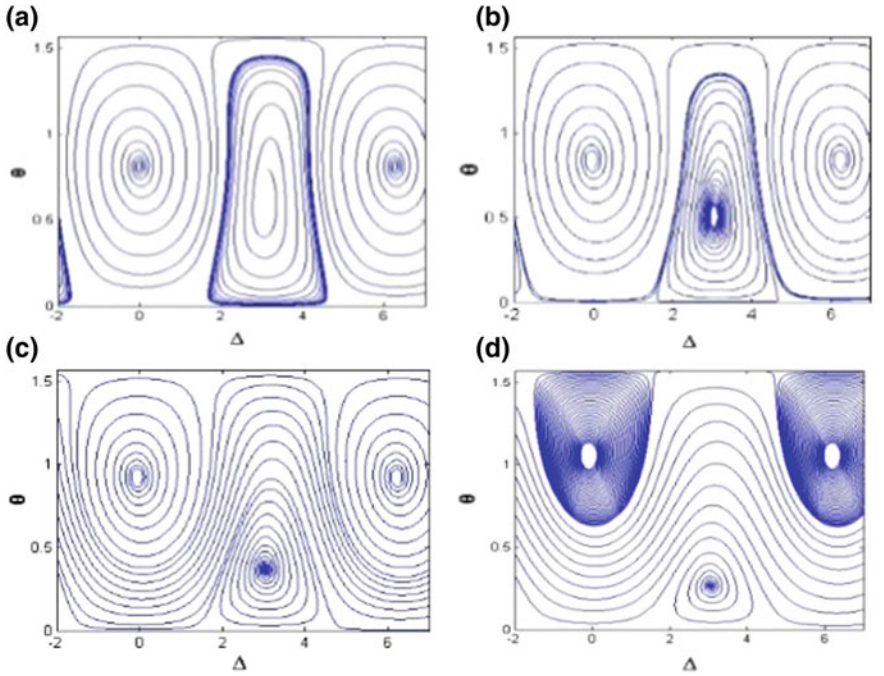

Fig. 9 Evolution of the phase plane of system (12) in the 'weakly nonlinear' case, $k = 0.2$, due to a gradual increase of the frequency detuning parameter **c** $\lambda = 0.1$ and $g = 0.1$ the limit cycle is slightly deformed but still remains attractor; **d** $\lambda = 0.1$ and $g = 0.2$—the limit cycle disappears by giving rise to the 'running phase' trajectory, which becomes attractor; **e** $\lambda = 0.1$ and $g = 0.5$—the NLM becomes the only attractor of the system with energy localization on the generator with lower frequency; **f** $\lambda = 0.1$ and $g = 1$.- further increase of the detuning does not affect the topology of phase portrait, however, the energy localization effect becomes stronger [17]

mode with the higher frequency decreases with the increase of the detuning, and it disappears completely at some threshold value of the detuning; see Fig. 10d.

Further, Fig. 11 illustrates the evolution of phase portrait due to detuning increase under a stronger influence of dissipative terms. The result of strong dissipation is that the limit cycles along the cell boundaries (LPTs), corresponding to the most intensive energy exchange between generators, become broken apart by new stationary points associated with NLMs. Compared to Fig. 7, these NLMs are born on the limit cycle, at the cell boundary, not inside the cell; compare, for instance, Figs. 9b and 11a. This enables us to bridge the gap between nonstationary synchronization and NLMs. In the case when detuning is present disappearance of LPT synchronization is also accompanied by the birth of two stable and two unstable stationary points (stable focuses and saddles can be seen at the phase plane Fig. 11c) exactly as in the case when the detuning is absent (Fig. 2d). Note that those correspond to limiting cycles in the initial system. If now we increase significantly the dissipation parameter of the system while the nonlinearity term is relatively small and detuning is absent,

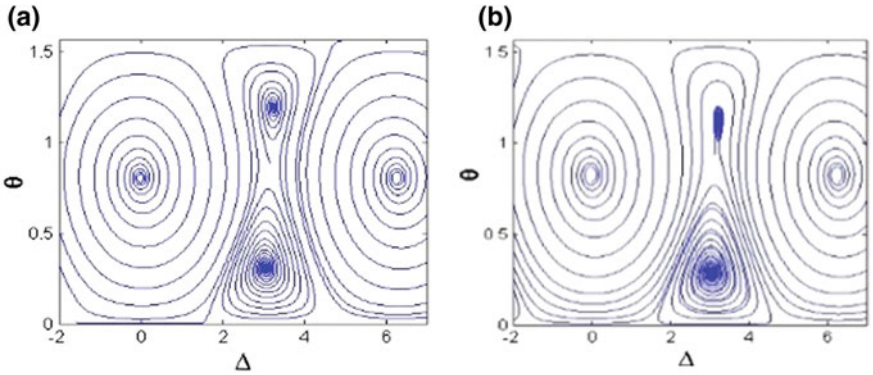

Fig. 10 Evolution of the phase diagrams of system (12) due to the detuning increase under the greater nonlinearity level, $k = 0.4$: **a** $\lambda = 0.1$ and $g = 0.1$—the attraction area of one of the two NLMs is shrinking; **d** $\lambda = 0.1$ and $g = 0.2$ most of the energy localizes on the active oscillator with lower frequency [17]

the limiting cycle corresponding to intensive energy exchange becomes unstable as two new stationary points are born (Fig. 4). Note that the presence of NLMs is not affected by the detuning increase in some range, as clearly seen from Fig. 9 fragments (b), (c), and (d), where the corresponding stationary points are just slightly shifted in both horizontal and vertical directions. However, detuning breaks the symmetry, that manifests in the shift of the left saddle and its annihilation with the unstable node, corresponding to the out-of-phase NNM (see Fig. 11c). Final stage of the evolution (with increase of detuning) consists in annihilation of the right stable focus and saddle point. It leads to qualitative change of the phase plane and as a result only one attractor (stable stationary point), corresponding to limiting cycle (of the full system) on the LNM remains.

9 Non-symmetric Case

Figure 12 shows the results of numerical integration of system (7) for the initial conditions or the parameters of the system that do not match symmetry conditions. Thus, in this case we analyze the stability regions for the regimes determined for a system with symmetry. In the case of symmetry breaking, the representation on the R_1, R_2 plane is more informative than the graph in the θ, Δ plane; this is illustrated in Fig. 13a, b. The set of parameters corresponds to that in Fig. 13b; the initial energy of excitation of the oscillators is $I \equiv N = R_1^2 + R_2^2$ (which is essential for satisfying the symmetry conditions). If the initial conditions correspond to the initial energy of the oscillators determined by symmetry condition (5), (6) (see Fig. 13b) (e.g., the amplitude of one of the oscillators decreases; see Fig. 13c), the LPT attractor attracts all phase trajectories as before. Upon a further decrease in the initial energy, the system

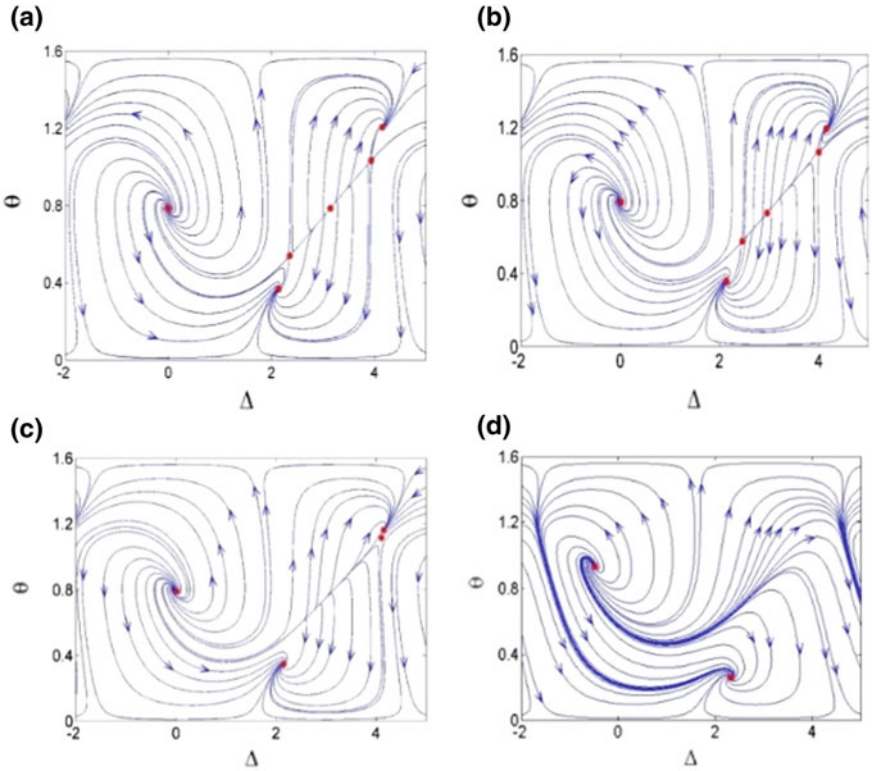

Fig. 11 Evolution of the phase diagrams of system (12) due to the detuning increase under the greater dissipation parameter value $\lambda = 0.85$, $k = 0.2$: **a** detuning $g = 0$—system of identical oscillators; **b** $g = 0.02$ system with a weak detuning, red dots mark stationary point obtained analytically; **c** $g = 0.1$; **d** $g = 0.5$ [17]

tends to a stable equilibrium position (Fig. 13d). Conversely, if the initial energy of the oscillators exceeds the value required for fulfillment of the symmetry conditions, the regime of steady-state energy transfer (LPT—synchronization) sets in a wide range of initial conditions (Fig. 13e). When symmetry is broken due to a change in one of parameters (e.g., parameter b) in both directions, the LPT—synchronization limit is attained (Fig. 13f). Thus, we have shown that the found regime of LPT synchronization in which the LPT is an attractor can be implemented in a certain range of initial conditions and for values of parameters that do not correspond to symmetry. It should also be noted that the regime illustrated in Fig. 13d is the so-called case of oscillation death, which was considered earlier for dissipatively coupled oscillators [6].

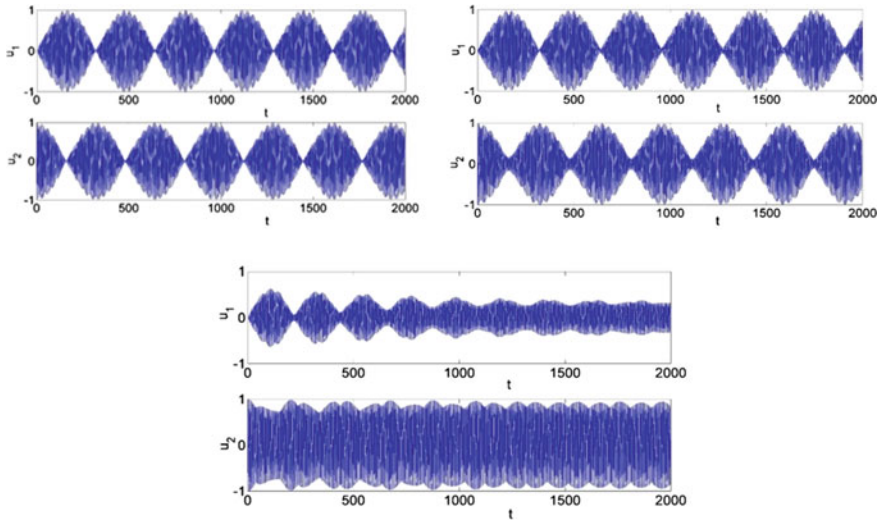

Fig. 12 $\varepsilon = 0.01$; $\alpha = 0.268$; $\beta = 1.0$; b = 1.2; d = 0.8; $k = 0.2$; $\lambda = 0.1$; $E_0(0) = 0.5$; $u_1(0) = 0$; $v_1(0) = 0.0001$; $u_2(0) = 0$; $v_2(0) = 1$; numerical solutions of Eqs. (1) [17]

10 Energy Balance Approach

Recall that the limit cycle can exist if the balance between the energy inflow and outflow during one period of the oscillation holds. Let us consider first van der Pol's oscillator:

$$\frac{d^2u}{dt^2} + u + \varepsilon(bu^2 - \gamma)\frac{du}{dt} = 0, \tag{13}$$

where ε—is small parameter.

Assuming $0 < \varepsilon \ll 1$ and thus harmonic temporal shape of the oscillation, $u = A\cos t$, gives the work of dissipative force done over one period

$$I = \int_0^{2\pi} (bu^2 - \gamma)\left(\frac{du}{dt}\right)^2 dt = A^2\pi\left(\frac{bA^2}{4} - \gamma\right)$$

If $I = 0$, then there is a balance between the energy inflow and outflow, which gives the amplitude of limit cycle $A = 2\sqrt{\gamma/b}$.

Now let us apply similar approach to the dissipative terms of the equations in the slow time-scale (2). For simplicity reason we integrate along one period of the linear beating as

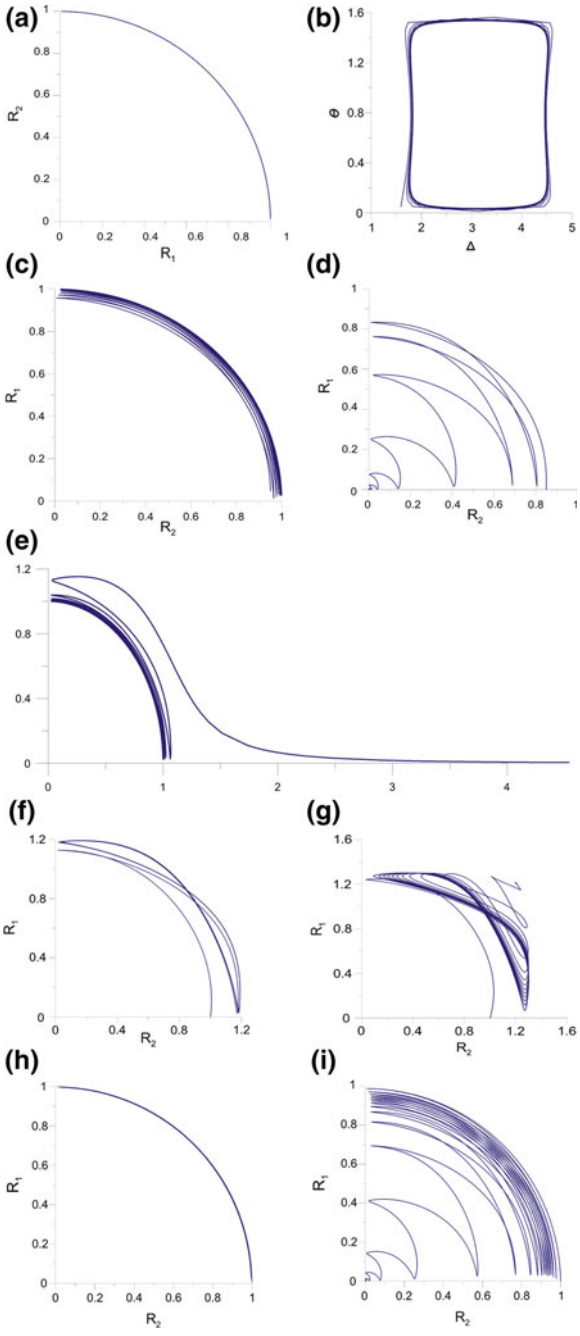

Fig. 13 Numerical study of the ranges of parameters and initial conditions in which the regime of the LPT synchronization in the system (3) can be realized: **a** representation on the plane (R_1, R_2), the parameters set corresponds to Fig. 2b, initial excitation level is $I = N = R_1^2 + R_2^2$, which is necessary for the symmetry conditions to hold; **b** same regime on the (θ,Δ) plane; the symmetry break is made with initial excitation level not equal to 1, **c** $R_1 = 0.95$, $R_2 = 0$: non-conventional synchronization attracts the phase trajectories; **d** $R_1 = 0.85$, $R_2 = 0$: system comes to equilibrium; **e** $R_1 = 10$, $R_2 = 0$: LPT synchronization attracts the phase trajectories; the parameters of the system differ from those under symmetry conditions: $b = \sqrt{\frac{9\gamma d}{2}}(1 + \delta)$ **f** LPT synchronization, δ = 0.1 **b** in-phase mode (NNM synchronization), δ = 0.2; (c) LPT synchronization, δ = –0.001; **d** the system evolves to the equilibrium position, δ = –0.005 [16]

$$I = \int_0^{2\pi/\beta} \left(\gamma - b|f_i|^2 + d|f_i|^4\right) f_i^2 d\tau_1, i = 1, 2, \tag{14}$$

where, due to the assumption of small nonlinearity, the envelope-functions are supposed to have the harmonic temporal shape

$$f_1 = iC\ \sin(\beta\tau_1), \quad f_2 = iC\ \cos(\beta\tau_1). \tag{15}$$

Substituting (15) in (14) gives

$$I = \frac{C^2}{2}\frac{2\pi}{\beta}\left(-\gamma + b\frac{3}{4}C^2 - \frac{5}{8}C^4\right) \tag{16}$$

The condition $I = 0$ gives $C^2 = \left(\frac{3}{4}b \pm \sqrt{\frac{9}{16}b^2 - \frac{5}{2}d\gamma}\right)/\left(\frac{5}{4}d\right)$ under condition

$$b^2 \geq \frac{40}{9}d\gamma \tag{17}$$

and

$$C^2 = N = \frac{3}{5}\frac{b}{d} \tag{18}$$

Estimates (17)–(18) is fairly close to that obtained by symmetry analysis:

$$b^2 = \frac{9}{2}d\gamma, \quad N = \frac{2}{3}\frac{b}{d} \tag{19}$$

In Fig. 14 we illustrate the evolution of the non-linear beating for different initial conditions and parameter sets. The border condition obtained by integration criterion is too rough and the nonlinear beating realized for the set (18) is unstable, while the prediction of the area, given by the inequality (17) holds, as for broad area 'above' the border the nonlinear beating regime is stable.

11 Model with Coupling via Linear Oscillator

This section deals with a two-level quantum model [23], according to which the interaction of a material system with a electromagnetic field can cause the loss of stability of the lower level. As a result of this instability, the role of the ground state is played by a periodic process generating superradiance. A classical analogue of a super radiant quantum transition is given by two generators weakly coupled through a linear oscillator. The reason for the transition to intensive energy exchange is the

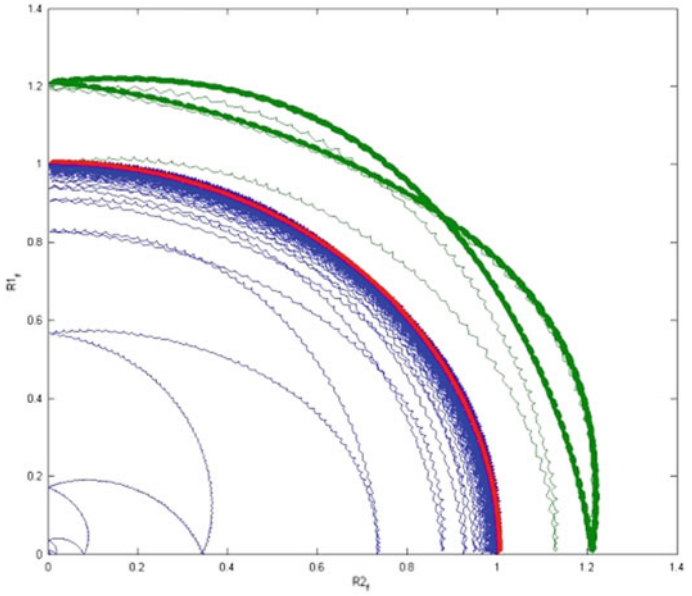

Fig. 14 Comparison of the nonlinear beating realization for different parameter sets: energy estimate—blue line; symmetry analysis—red line; condition (17) with a slight overshoot—green line

instability of the nonlinear normal mode (NNM) in the classical system similar to instability of the ground state in the quantum system.

$$\begin{aligned}
&\frac{d^2u_1}{dt^2} + u_1 + 8\alpha\varepsilon u_1^3 + 2\beta\varepsilon(u_1 - u_2) + 2\varepsilon(4bu_1^2 - \gamma)\frac{du_1}{dt} = 0;\\
&\frac{d^2u_2}{dt^2} + (1 - 2\varepsilon\kappa)u_2 + 2\beta\varepsilon(u_2 - u_1) + 2\beta\varepsilon(u_2 - u_3) + 2\varepsilon\eta\frac{du_2}{dt} = 0;\\
&\frac{d^2u_3}{dt^2} + u_3 + 8\alpha\varepsilon u_3^3 + 2\beta_2\varepsilon(u_3 - u_2) + 2\varepsilon(4bu_3^2 - \gamma)\frac{du_3}{dt} = 0.
\end{aligned} \tag{20}$$

where $0<\varepsilon \ll 1$, and therefore nonlinearity, damping, and coupling are small; η- parameter of damping on the linear oscillator, α β, κ as in previous sections characterize nonlinearity, coupling and detuning correspondingly, b and γ are nonlinear and linear dissipative terms of the generator; in addition, it is assumed that $\alpha = b = 1$, $\beta = 1.2$, and $\kappa = 1$.

There are three NNMs in the system with amplitudes $\left\{1, -(\beta-\kappa) - \sqrt{(\beta-\kappa)^2 + 8\beta^2}, 1\right\}$, $\{1, 0, -1\}$ and $\left\{1, -(\beta-\kappa) + \sqrt{(\beta-\kappa)^2 + 8\beta^2}, 1\right\}$ [24] and frequencies $\Omega_I = 1 + \varepsilon\left(3\beta - \Delta - \sqrt{(\beta-\Delta)^2 + 8\beta^2}\right)$, $\Omega_{II} = 1 + 2\beta\varepsilon$, $\Omega_{III} = 1 +$

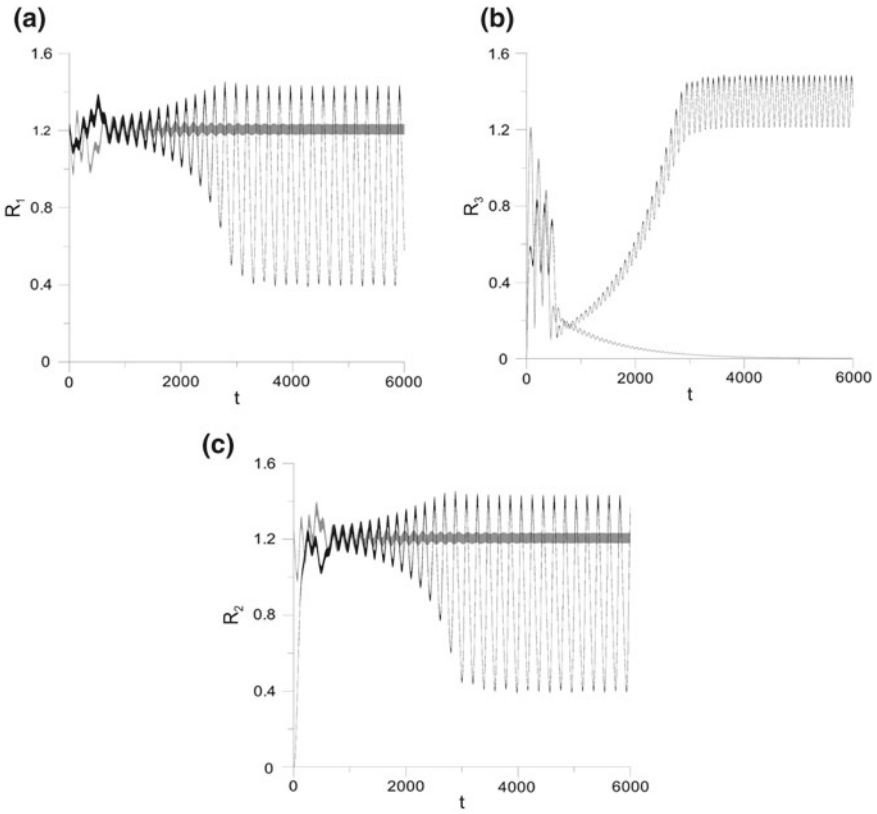

Fig. 15 Numerical realization of NNM II at $\eta = 0.3$ at initial conditions similar to those corresponding to mode II (grey lines) and of intense energy exchange at $\eta = 0.11$ (black lines); the quantities $R_i = |\psi_i| = u_i^2 + v_i^2$ (i = 1, 2, 3) characterize the intensity of excitation of the oscillators described by system (17); **a** first generator, **b** linear oscillator, and **c** second generator [20]

$\varepsilon\left(3\beta - \Delta + \sqrt{(\beta - \Delta)^2 + 8\beta^2}\right)$ correspondingly. Mode I is stable over the entire η range; mode III is unstable throughout the η range; mode II becomes unstable at a certain value of the dissipation parameter η, for given set of the parameters $\eta = \eta_{cr} \sim 0.21$. This means that the system is moved away from normal mode II, and it appears that the disturbance is directed along the vector corresponding to mode I. Figure 15 shows the numerical results characterizing the time evolution of the amplitude of each oscillator at $\eta = 0.3$ (gray lines) and initial conditions similar to those corresponding to mode II. Since the pattern of mode I is similar (with the exception of the linear oscillator, the amplitude of which goes to zero), it is not shown in the Fig. 15.

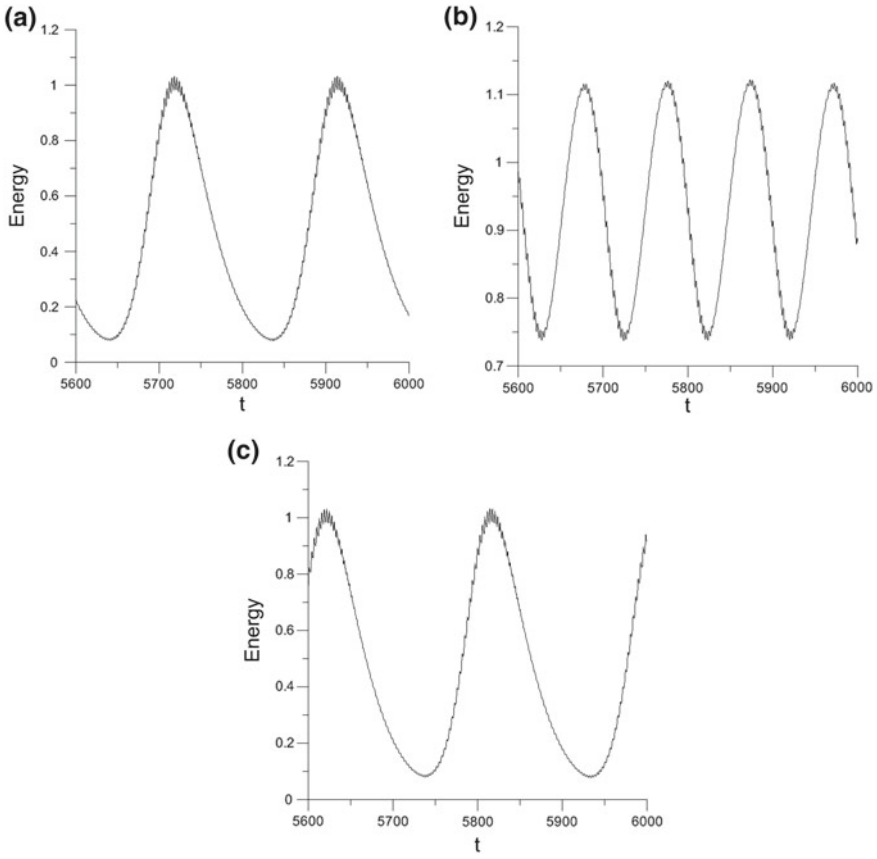

Fig. 16 Illustration of energy exchange mechanism; see Fig. 15a–c [20]

The instability of mode II leads to a regime of intensive stationary energy exchange between the two generators; fraction of energy transferred depends on the parameter η, reaching more than 90%. Energy exchange process is shown in Fig. 15 (black lines) for $\eta = 0.11$; the initial conditions are essentially asymmetrical. It should be noted that a similar process occurs under a wide range of initial conditions, including those corresponding to the unstable mode II. Such behavior is typical to that for the attractor vicinity; i.e., a wide range of initial conditions leads to this trajectory. The evolution of the system cannot be adequately described in terms of NNM, since they correspond to a fixed energy of each oscillator. Obviously, the motion of the system is similar to that takes place for LPT. Note that the vibrational frequency of the energy evolution of the linear oscillator in Fig. 16 is twice of those of each generator.

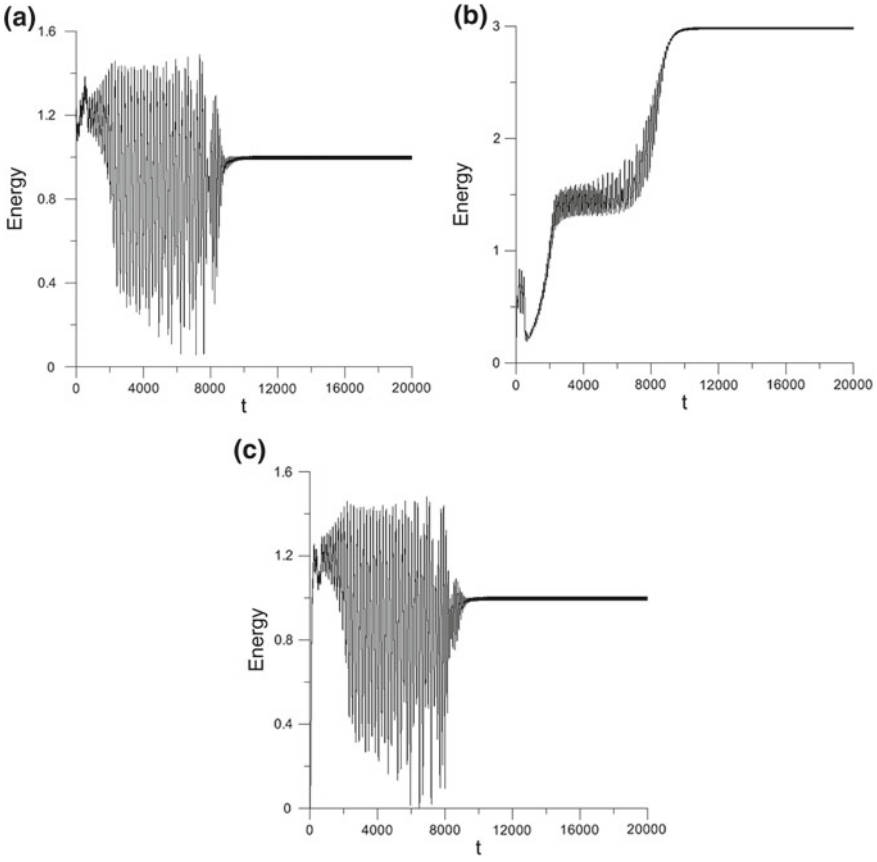

Fig. 17 Stability loss of the energy exchange process: $\eta = 0.09$ at initial conditions similar to those corresponding to mode II: **a** first generator, **b** linear oscillator, and **c** second generator [19]

If the value of controlling parameter η is below second threshold value ($\eta < 0.1$), the energy exchange regime loses its stability and after some acts of energy exchange the system is attracted by a stable NNM. The energy evolution for $\eta = 0.09$ is presented in the Fig. 17.

12 Quantum Analogy

Superradiant quantum transition (SQT) is one of the most important quantum phenomena having numerous physical applications. Although its first model was proposed as long ago as 1954, the discussion of the SQT mechanisms, as well as search for possible classical analogues of this phenomenon is still ongoing. Some of the

proposed models involve thermodynamic analyses of an ensemble of dipoles, while others deal with the interaction of dipoles with a resonant field. A number of models describe SQT type processes as a formation of unstable pulse.

However, there is a fundamental model, based on quantum electrodynamics, which takes into account the dynamic factors that lead to the instability of the ground state of a two-level system in the presence of resonant electromagnetic radiation [6]. This model, a further development of the Dicke model, describes the mechanism of the formation of a new ground state, far from the original. At a relatively low density of resonant radiation, the traditional two-level system demonstrates the normal behavior: the lower level is stable, whereas the upper is unstable. If the upper level of the system is overpopulated, classical laser radiation arises with spontaneous transition to the lower level. However, at certain threshold values of the coupling parameter and field frequency, the lower level becomes unstable. This gives rise to steady oscillations between the two levels, a process corresponding to SQT.

The starting system reads as [23]

$$\dot{\chi}_1 = -igA^*\chi_2;$$
$$\dot{\chi}_2 = -igA\chi_1;$$

$$\frac{i}{2}\ddot{A} + \dot{A} + i\mu A = -g\chi_1^*\chi_2. \tag{21}$$

where χ_1, and χ_2 are the wave functions of the lower and upper levels of the material system and A is a characteristic of the electromagnetic field. System (21) has integrals

$$\chi_1^*\chi_1 + \chi_2^*\chi_2 = 1$$

$$Q = A^*A + \frac{i}{2}(A^*\dot{A} + \dot{A}^*A) + \chi_2^*\chi_2 \tag{22}$$

$$H = Q + \frac{1}{2}A^*\dot{A} + \mu A^*A + g(A\chi_2^*\chi_1 + A^*\chi_1^*\chi_2)$$

The system possesses three stationary states: I.$\chi_1 = 0; \chi_2 \neq 0; A = 0, A^* = 0$;—the lower level in the absence of the field, the ground state in the domain of its stability; II. $\chi_1 \neq 0; \chi_2 = 0; A = 0, A^* = 0$;—the upper unsustainable level; III.$\chi_1 = 0; \chi_2 = 0; A \neq 0$;—the field does not interact with the two-level system.

Change of variables, $\chi_1 = \cos\theta\ e^{i\delta_1}$, $\chi_2 = \sin\theta\ e^{i\delta_2}$, $\Delta = \delta_1 - \delta_2$ and differentiation with respect to the time transforms original equation (19) for the field to the form

$$\dddot{A} - 2i\ddot{A} + 2\mu\dot{A} - 2ig^2A\cos 2\theta = 0 \tag{23}$$

or for $A = a + ib$; and using the integrals of the system

$$Q = a^2 + b^2 + (\dot{a}b - \dot{b}a) + \sin^2\theta; H = Q + \frac{1}{2}(\dot{a}^2 + \dot{b}^2) + \mu(a^2 + b^2) + g\ \sin 2\theta(a\ \cos\Delta - b\ \sin\Delta)$$

we obtain a system:

$$\ddot{a} + 2\ddot{b} + 2\mu\dot{a} + 2g^2 b(1 - 2(Q - (a^2 + b^2) - (\dot{a}b - a\dot{b}))) = 0$$

$$\ddot{b} + 2\ddot{a} + 2\mu\dot{b} + 2g^2 a(1 - 2(Q - (a^2 + b^2) - (\dot{a}b - a\dot{b}))) = 0$$

These two equations describe the dynamics of the field for a given value of the integral Q. The values of θ and Δ, describing the behavior of the levels, can be determined by using the integrals ($0 < \theta < \pi/2, \pi/2 < \Delta < \pi/2$):

$$\theta = \arcsin\left(Q - \sqrt{(a^2 + b^2) - (\dot{a}b - \dot{b}a)}\right) \quad \Delta = \arcsin\left(a/\sqrt{a^2 + b^2}\right) - \arcsin\left[\left(H - Q - \tfrac{1}{2}(\dot{a}^2 + \dot{b}^2) - \mu(a^2 + b^2)\right)/g\ \sin 2\theta\right] \tag{24}$$

In order to investigate the stability of the ground state, we linearize Eq. (23) in the vicinity of state I and obtain a condition on the instability of the ground state [23]:

$$g^2 > g_C^2 = \frac{8}{27} + \frac{2}{3}\mu + \left[\frac{4}{9} + \frac{2}{3}\mu^2\right]^{3/2} \quad (\text{for } \mu = 0,\ g_C = 0.769).$$

For the initial conditions corresponding to oscillations, namely: $\omega = 1.2$; $a = 0.01$; $b = 10^{-8}$; $\dot{a} = 1 * 10^{-10}$; $\dot{b} = \omega a$; $\ddot{a} = -\omega^2 a$; $\ddot{b} = 10^{-10}$ the system behavior changes sharply after passing through the point of stability loss of the ground state (Fig. 17). The time scale of the process of superradiance becomes comparable with the field oscillation period, as values of g far from the critical one (Fig. 18). As seen from Fig. 18, both the field envelope-function and amplitude of the wave functions of the levels with the same period (Fig. 19) also show periodic variations, which correspond to the process of superradiance.

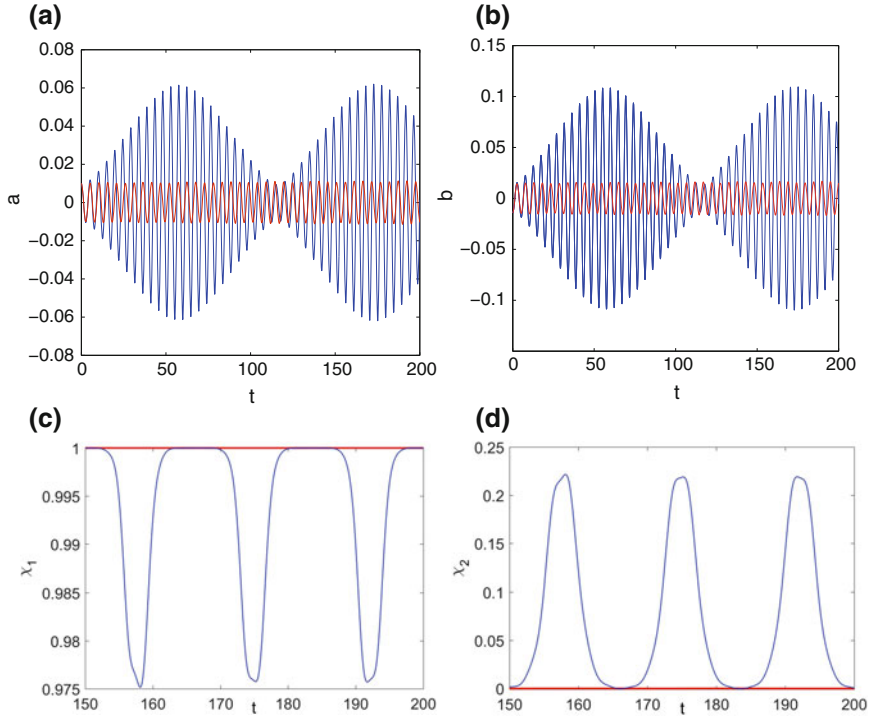

Fig. 18 Upper panel: evolution of the field components a and b at g = 0.76 (blue line) and g = 0.77 (red line); lower panel: evolution of the wave-functions at g = 0.76 (blue line) and g = 0.77 (red line) [20]

13 Conclusions

It should be emphasized that the scenario of the nonstationary LPT-type synchronization seems to be universal in the range of parameters in which NNM synchronization is rather impossible, as confirmed by the presented results. The importance of the "symmetric" case considered in forth section is that it provides a detailed analytical investigation revealing the new type of synchronization. In addition, such investigations make it possible to establish the conditions for a transition to energy localization. After the prediction of the range of dissipative parameters in which the nonstationary synchronization exists, it can be observed experimentally in physical, chemical, and biological systems simulated with two coupled oscillators.

Acknowledgements This work was supported by the Program of Fundamental Researches of the Russian Academy of Sciences (project No. 0082-2014-0013, state registration number AAAA-A17-117042510268-5)

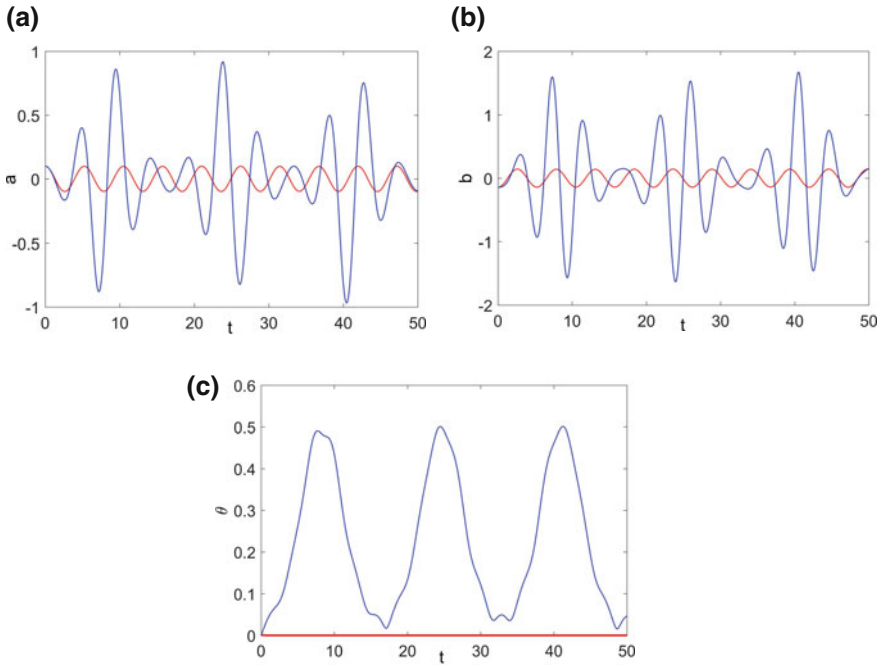

Fig. 19 Evolution of the field components **a** and **b** and the ratio of the amplitudes of the wavefunctions of the levels θ at g = 0.76 (**red** line) and g = 0.9 (**blue** line) [20]

Appendix: Symmetry Analysis

The conditions of the system invariance leads to partial differential equations for the constituents of operator (3) as follows

$$\begin{aligned}&\eta_\tau + p_1\eta_{R_1} + p_2\eta_{R_2} + p_3\eta_\Delta - p_1\xi_\tau - p_1^2\xi_{R_1} - p_1p_2\xi_{R_2} - p_1p_3\xi_\Delta\\&= \xi\left[-\gamma p_1 + 3bR_1^2p_1 - 10dR_1^4p_1 + \beta p_2\sin\Delta + p_3\beta R_2\cos\Delta\right]\\&+ \eta\left[-\gamma + 3bR_1^2 - 10dR_1^4\right] + \zeta[\beta\ \sin\Delta] + \varsigma[\beta R_2\cos\Delta]\end{aligned}$$

$$\begin{aligned}&\zeta_\tau + p_1\zeta_{R_1} + p_2\zeta_{R_2} + p_3\zeta_\Delta - p_2\xi_\tau - p_1p_2\xi_{R_1} - p_2^2\xi_{R_2} - p_2p_3\xi_\Delta\\&= \xi\left[-\gamma p_2 + 3bR_2^2p_2 - 10dR_2^4p_2 + \beta p_1 sin\Delta - p_3\beta R_1 cos\Delta\right]\\&+ \eta[\beta\, sin\Delta] + \zeta\left[-\gamma + 3bR_2^2 - 10dR_2^4\right] + \varsigma[-\beta R_1 cos\Delta]\end{aligned} \tag{1A}$$

$$\begin{aligned}&\varsigma_\tau + p_1\varsigma_{R_1} + p_2\varsigma_{R_2} + p_3\varsigma_\Delta - p_3\xi_\tau - p_1p_3\xi_{R_1} - p_1p_2\xi_{R_2} - p_3^2\xi_\Delta\\&= \xi\left[-3\alpha(2R_2p_2 - 2R_1p_1) - \beta\left(\cos\Delta(R_1p_2 - R_2p_1)\frac{\left(R_1^2 + R_2^2\right)}{R_1^2R_2^2} + \beta\ \sin\Delta\frac{\left(R_2^2 - R_1^2\right)}{R_1R_2}p_3\right)\right]\end{aligned}$$

$$+\eta\left(6\alpha R_1^2+\beta\,\cos\Delta\frac{\left(R_1^2+R_2^2\right)}{R_1^2R_2}\right)-\zeta\left(6\alpha R_2^2+\beta\,\cos\Delta\frac{\left(R_1^2+R_2^2\right)}{R_1R_2^2}\right)+\varsigma\left(\beta\,\sin\Delta\frac{\left(R_2^2-R_1^2\right)}{R_1R_2}\right)$$

Solving Eq. (1A), gives the Lie group operator

$$X=\frac{\partial}{\partial\tau_1}+(-\gamma R_1+bR_1^3-2dR_1^5+\beta R_2\sin\Delta)\frac{\partial}{\partial R_1}+(-\gamma R_2+bR_2^3-2dR_2^5-\beta R_1\sin\Delta)\frac{\partial}{\partial R_2}$$
$$+\left(-3\alpha(R_2^2-R_1^2)-\beta\frac{(R_2^2-R_1^2)}{R_1R_2}\cos\Delta\right)\frac{\partial}{\partial\Delta}+X_1$$

If exists, the corresponding invariant, say I, must satisfy the condition

$$XI\equiv\frac{\partial I}{\partial\tau_1}+(-\gamma R_1+bR_1^3-2dR_1^5+\beta R_2\sin\Delta)\frac{\partial I}{\partial R_1}$$
$$+(-\gamma R_2+bR_2^3-2dR_2^5-\beta R_1\sin\Delta)\frac{\partial}{\partial R_2}$$
$$+\left(-3\alpha(R_2^2-R_1^2)-\beta\frac{(R_2^2-R_1^2)}{R_1R_2}\cos\Delta\right)\frac{\partial I}{\partial\Delta}+X_1I=0$$

As mentioned in the main text, it is assumed that $I=I(R_1,R_2)$. In this case, the variables R_1, R_2 satisfy the following ordinary differential equation, which can be also directly obtained from first two Eqs. (3),

$$\frac{dR_1}{(-\gamma R_1+bR_1^3-2dR_1^5+\beta R_2\sin\Delta)}=\frac{dR_2}{(-\gamma R_2+bR_2^3-2dR_2^5-\beta R_1\sin\Delta)}\tag{2A}$$

The group operator becomes a rotation operator with the invariant $I\equiv N=R_1^2+R_2^2$ if the parameters of the system (3) satisfy the relation $b^2=9\gamma d/2$ while the initial conditions provide the excitation level $N=2b/3d$. This can be easily proved using the combination of 1st equation of (3) multiplied by R_1 minus 2nd equation of (3) multiplied by R_2.

References

1. Pikovsky, A., Rosenblum, M.J., Kurths, A.: Synchronization. A Universal Concept in Nonlinear Sciences. Cambridge University Press, Cambridge (2001)
2. Verhulst, F.: Invariant Manifolds in Dissipative Dynamical Systems. Acta Appl. Math. **87**, 229–244 (2005)
3. Rand, R.H., Holmes, P.J.: Bifurcation of periodic motions in two weakly coupled van der Pol oscillators. Int. J. Nonlinear Mech. **15**, 387–399 (1980)
4. Chakraborty, T., Rand, R.H.: The transition from phase locking to drift in a system of two weakly coupled van der Pol oscillators. Int. J. Nonlinear Mech. **23**, 369–376 (1988)
5. Rompala, K., Rand, R.: Howland, H: Dynamics of three coupled Van der Pol oscillators, with application to circadian rhythms. Commun. Nonlinear Sci. **12**, 794–803 (2007)
6. Kuznetsov, A.P., Stankevich, N.V., Turukina, L.V.: Coupled van der Pol–Duffing oscillators: Phase dynamics and structure of synchronization tongues. Physica. D **238**, 1203–1215 (2009)

7. Mihalache, D., Mazilu, D., Lederer, F., Kivshar, YuS: Collisions between discrete spatiotemporal dissipative Ginzburg-Landau solitons in two-dimensional photonic lattices Phys. Rev. A **77**, 043828 (2008)
8. Malomed, B.A.: Waves and solitary pulses in a weakly inhomogeneous Ginzburg-Landau equations. Phys. Rev. E **50**, 4249–4252 (1994)
9. Akhmediev, N.N., Ankiewicz, A.: Solitons: Nonlinear Pulses and Beams, vol. 9. Chapman and Hall, London (1992)
10. Blekhman, I.I.: Vibrational Mechanics: Nonlinear Dynamic Effects, General Approach, Applications. World Scientific, London (2000)
11. Manevitch, L.I., Smirnov, V.V.: Resonant energy exchange in nonlinear oscillatory chains and Limiting Phase Trajectories: from small to large systems. In: Vakakis A.F (ed.) Advanced Nonlinear Strategies for Vibration Mitigation and System Identification, CISM Courses and Lectures, vol 518. Springer, New York (2010)
12. Vakakis, A.F., Manevitch, L.I., Mikhlin, YuV, Pilipchuk, V.N., Zevin, A.A.: Normal Modes and Localization in Nonlinear Systems. Wiley, New York (1996)
13. Manevitch, L.I.: New approach to beating phenomenon in coupled nonlinear oscillatory chains. Arch. Appl. Mech. **77**, 301–312 (2007)
14. Manevitch, L.I., Smirnov, V.V.: Limiting phase trajectories and the origin of energy localization in nonlinear oscillatory chains. Phys. Rev. E **82**, 036602 (2010)
15. Manevitch, L.I., Kovaleva, M.A., Pilipchuk, V.N.: Non-conventional synchronization of weakly coupled active oscillators. EPL—Europhys. Lett. **101**, 50002 (2013)
16. Kovaleva, M.A., Manevich, L.I., Pilipchuk, V.N.: New Type of Synchronization of Oscillators with Hard Excitation. J. Exp. Theor. Phys. **117**(2), 369–377 (2013)
17. Kovaleva, M.A., Pilipchuk, V., Manevich, L.I.: Nonconventional synchronization and energy localization in weakly coupled autogenerators. Phys. Rev. E **94**, 032223 (2016)
18. Kovaleva, M., Manevitch, L.I., Pilipchuk, V.: Non-conventional phase attractors and repellers in weakly coupled autogenerators with hard excitation. EPL—Europhys. Lett EPL **120**, 30007 (2017)
19. Manevitch, L.I., Kovaleva, M.A.: Vibration Analog of a Superradiant Quantum Transition Dokl. Phys. **58**(10), 428–432 (2013)
20. Kovaleva, M.A., Manevich, L.: I: Superradiant Transition and Its Classical Analogue Russian. J. Phys. Chem. B **7**(5), 534–539 (2013)
21. Pilipchuk, V.N.: Autolocalized modes in array of nonlinear coupled oscillators. In: Manevich A.I., Manevitch, L.I. (eds.) Problems of Nonlinear Mechanics and Physics of Materials. RIK NGA, Dnepropetrovsk (1999)
22. Ovsyannikov, L.V.: Group Analysis of Differential Equations. Academic Press, New York (1982)
23. Preparata, G.: QED Coherence in Matter. World Scientific, Singapore (1995)
24. Kovaleva, M.A., Manevitch, L.I.: Nonlinear normal modes in the system of weakly coupled Van-derPol-Duffing oscillators. In: Awrejcewicz, J., Kazmierczak, M., Olejnik, P., Mrozowski, J. (eds.) Dynamical Systems. Analytical/Numerical Methods, Stability, Bifurcation and Chaos, pp. 85–90. Lódz, December 5-8, 2011, Poland (2011)
25. Manevitch, L.I., Gendelman, O.V.: Tractable Models of Solid Mechanics: Formulation. Springer, New York (2011)
26. Pilipchuk, V.N.: Nonlinear Dynamics: Between Linear and Impact Limits. Springer, New York (2010)

Normal Modes of Chaotic Vibrations and Transient Normal Modes in Nonlinear Systems

Yuri V. Mikhlin, Katarina Yu. Plaksiy, Tatyana V. Shmatko and Gayane V. Rudneva

Abstract Nonlinear normal modes of forced chaotic vibrations can be found in models which are obtained by discretization of some elastic systems that have lost stability under external compressive force. Transient nonlinear normal modes, which exist only for some specific values of the system energy, appear in nonlinear dissipative systems in vicinity of external or internal resonance. These dissipative systems under resonance conditions are analyzed by transformation to *reduced systems* stated with respect to the parameter which characterizes the system energy, the arctangent of the amplitudes ratio and the phase difference.

1 Introduction

Concept of nonlinear normal modes (NNMs), first proposed by Kauderer and Rosenberg [1, 2], is an important step of investigation of the nonlinear systems behavior. Principal fundamentals of the NNMs theory and different applications of the theory are presented in [3–5].

The NNMs concept can be used not only for periodic vibrations. In particular, the NNMs having smooth trajectories in configuration space and chaotic in time behavior can be found in some non-conservative systems. Such vibration modes are observed in post-buckling dynamics of elastic systems that have lost stability under external compressive force.

In vicinity of the internal resonance the transfer of energy from unstable NNMs to stable ones is noted. This phenomenon is discussed in various publications. A description of the energy transfer was presented in the pioneering publication [6], where it was showed that in spring pendulum a transfer of angular oscillation mode to vertical oscillation one, and back, takes place near the fundamental frequencies ratio of 2:1. The transfer of energy caused by internal resonance was also investigated

Y. V. Mikhlin (✉) · K. Yu. Plaksiy · T. V. Shmatko · G. V. Rudneva
Kharkiv Polytechnic Institute, National Technical University, Kyrpychev str. 2, Kharkiv 61002, Ukraine
e-mail: Yuri_Mikhlin@mail.ru

I. V. Andrianov et al. (eds.), *Problems of Nonlinear Mechanics and Physics of Materials*, Advanced Structured Materials 94,
https://doi.org/10.1007/978-3-319-92234-8_6

in [7–9]. Some principal results in problems of the energy transfer are summarized in the book [10]. The book [11] is devoted to complex behavior of autonomous and non-autonomous nonlinear systems under the internal resonance conditions. Here an interaction of nonlinear vibration modes in neighborhood of external and internal resonances in nonlinear dissipative systems is analyzed by the multiple scales method [12] and a transformation to so-called *reduced system.* The reduced system is written with respect to some variable which characterizes the system energy, arctangent of ratio of amplitudes and difference of phases. Earlier the reduced system was used for conservative systems in [13, 14] and for dissipative systems in [15]. The new phenomenon in analysis of transient of the dissipative system near resonance is an appearance of so-called *transient nonlinear normal vibration modes* (TNNMs) [15] which are realized only for some levels of the systems energy that is, for some specific values of time, corresponding to these energy levels. It is important that near these values of time motions of the dissipative systems are close to the modes, that is the TNNMs are attractive.

An appearance of TNNMs in the system with a limited power-supply (or non-ideal system) having nonlinear absorber and in the spring-pendulum system (oscillator-rotator) is considered. The systems with a limited power-supply are characterized by interaction of source of energy and elastic sub-system which is under action of the source. The most important effect observed in such systems is the Sommerfeld effect [16], when the stable resonance regime with large amplitudes is appeared in the elastic sub-system. Resonance dynamics of such systems was first described by V.O. Kononenko [17]. Then investigations on the subject were continued in numerous publications, in particular, in [18–20]. Some surveys on studies of the non-ideal systems dynamics are made in [12, 21]. Transfer of energy from some unstable mode to other stable one, that is the so-called "saturation phenomenon", in such systems under the internal resonance condition, is described in [22]. Reduction of the vibration amplitudes in the non-ideal systems coupled with different type nonlinear absorbers and dampers, is studied in [23, 24]. Forced synchronic regimes of the oscillator-rotator system are analyzed in [25]. Free stationary and non-stationary regimes, as well localization of energy in such system are considered in [26].

The paper is organized as follow. Forced NNMs in models which are obtained by discretization of some elastic systems are examined in Sect. 2. These NNMs with chaotic in time behavior, are obtained in post-buckling dynamics of such systems. In Sect. 3, external resonances on the first fundamental frequency and both external and internal resonances in the dissipative system with a limited power supply coupled with nonlinear absorber are considered. Resonance behavior in the dissipative spring-pendulum system for a case of simultaneous external and internal resonances is considered in Sect. 4. Modes of coupled vibrations and localized modes, including TNNMs are obtained; their influence to transient process in these systems is shown.

2 Forced Nonlinear Normal Modes of Chaotic Vibrations

Consider the following system that can be obtained by discretization of equations of nonlinear dynamics of some elastic systems:

$$\begin{aligned} &\ddot{y}_1 + \delta\dot{y}_1 - \alpha y_1 + \beta y_1^3 + c y_1 y_2^2 = f\ \cos\omega t, \\ &\ddot{y}_2 + \delta\dot{y}_2\ + a y_2 + b y_2^3 + c y_2\, y_1^2 = 0, \end{aligned} \tag{1}$$

where $y_1(t)$ and $y_2(t)$ are unknown functions; δ is the coefficient determining friction; all coefficients are positive, excepting the coefficient α which can have any sign. In the case $\alpha > 0$ the Eq. (1) describe post-critical dynamics of the corresponding elastic systems.

The system (1) can be obtained, in particular, in the following problems: the beam bending vibrations within framework of the Kirchhoff beam theory and the dynamics of cylindrical shells described by the Donnell equations can be considered. Then a discretization by the Bubnov–Galerkin procedure is used. If displacements of the nonlinear elastic system are approximated by a single harmonic of the Fourier series expansion for spatial coordinates, a system having a single degree of freedom is obtained. Behavior of the model described by the non-autonomous Duffing equation was examined in numerous publications. Chaotic motions begin when the force amplitudes are slowly increased [27]. If two harmonics of the Fourier series for spatial coordinates are used, one obtains a set of two second order ODEs, coupled in nonlinear terms only. Two NNMs, which are determined by smooth trajectories in the system configuration place, exist here. One of these modes can be chaotic in time in some domain of the system parameters. Boundaries of the domain are determined as some combination of the external amplitude and parameters of nonlinearity and dissipation. The energy transfer from some vibration mode to another one is possible. Thus one can formulate a problem of the stability of periodic or chaotic vibration mode in the higher-dimensional spaces. The orbital stability of trajectories of the regular or chaotic modes is determined by the numerical-analytical approach which is based on the known Lyapunov definition of stability [28].

In Figs. 1 and 2 phase places of the variables $y_1(t)$ and $y_2(t)$ show orbital stability/instability of the NNM trajectory $y_2 = 0$ for some parameters of the system (1). The variable y_2 is considered here as variation of the NNM trajectory in orthogonal direction. Note that these results are obtained for the problem of the post-buckling nonlinear beam dynamics.

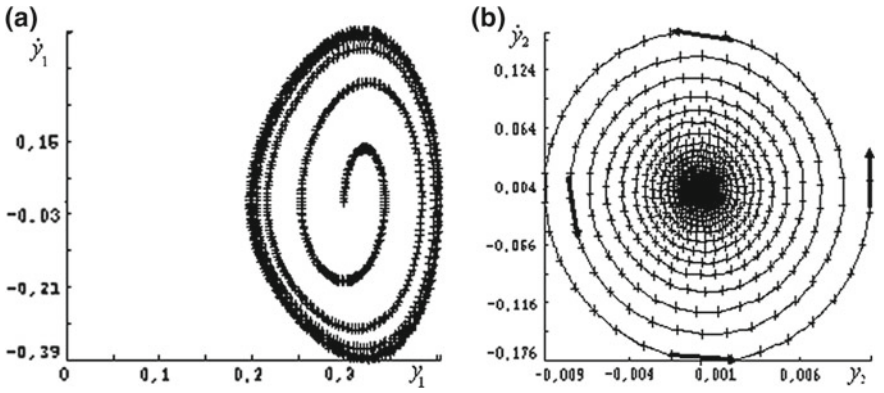

Fig. 1 The unstable mode of regular vibrations

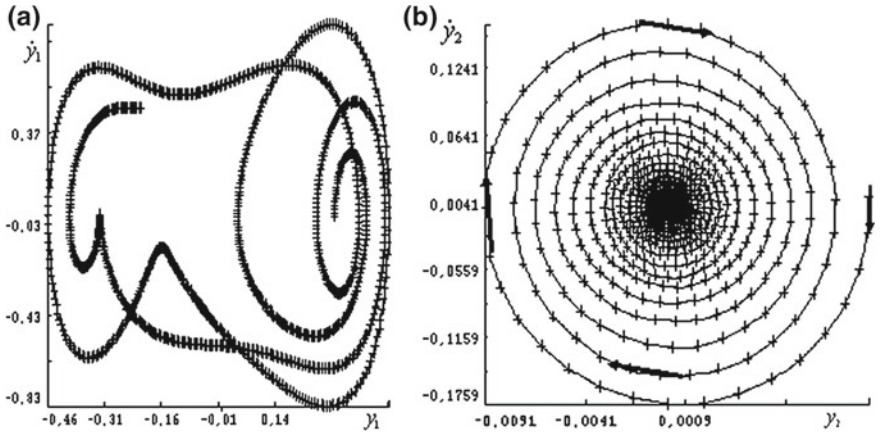

Fig. 2 The stable mode of chaotic vibrations

3 Transient Nonlinear Normal Modes in Dissipative System with a Limited Power-Supply Coupled with Nonlinear Absorber

One considers the resonance behavior of the dissipative non-ideal system which contains the nonlinear absorber with cubic type nonlinearity. Model under consideration is shown in Fig. 3. The motor D acts to the elastic sub-system by the crank shaft. The nonlinear oscillator is attached to the elastic sub-system of the mass M.

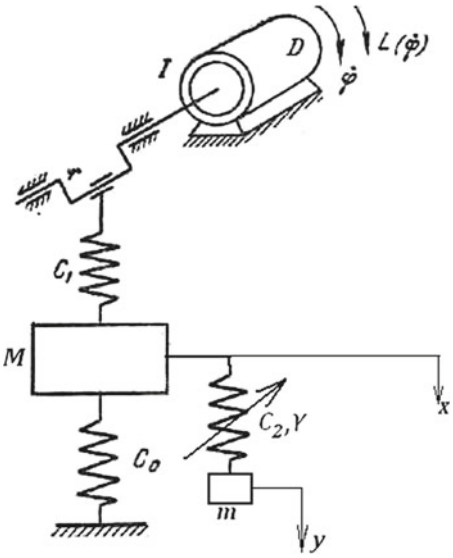

Fig. 3 System with a limited power-supply coupled with non-linear absorber

Equations describing motion of the system are the following:

$$\begin{aligned} &I\ddot{\varphi} = \varepsilon(L(\dot{\varphi}) - H(\dot{\varphi}) + c_1 r(x - r\,\sin\varphi)\cos\varphi), \\ &M\ddot{x} + \varepsilon\eta\dot{x} + cx + c_2(x - y) + \gamma(x - y)^3 = \varepsilon c_1 r\,\sin\varphi, \\ &\varepsilon m\ddot{y} + \varepsilon\eta\dot{y} - c_2(x - y) - \gamma(x - y)^3 = 0. \end{aligned} \tag{2}$$

Here the following notation is used: M is a mass of the elastic sub-system; r is a radius of the crank shaft; coefficients $c = c_0 + c_1$ and c_2 characterize stiffness of springs in the system; m is a mass of the nonlinear absorber; I is a moment of inertia of rotating masses; $H(\dot{\varphi}) = d\dot{\varphi}$ is the moment of resistance to rotation; $L = a + b\dot{\varphi}$ is a driving moment of the motor. The small parameter ε characterizes a smallness of mass of absorber with respect to the mass of elastic sub-system, of dissipation in the system and of the vibration components in variability in time of the angle φ velocity with respect to the constant component of the velocity.

Equations of motion (2) are transformed and presented of the next form:

$$\begin{aligned} &\ddot{\varphi} = \varepsilon(\bar{A} + \dot{\varphi} + \bar{C}x\,\cos\varphi - \bar{D}\,\sin 2\varphi), \\ &\ddot{x} + \omega_x^2 x - qy + 2\varepsilon\eta_x\dot{x} + \varepsilon\gamma_x(x - y)^3 = \varepsilon k\,\sin\varphi, \\ &\ddot{y} + \omega_y^2 y - \omega_y^2 x + 2\varepsilon\eta_y\dot{y} - \varepsilon\gamma_y(x - y)^3 = 0, \end{aligned} \tag{3}$$

where $\bar{A} = \frac{a}{I}$, $\bar{B} = \frac{b-d}{I}$, $\bar{C} = \frac{c_1 r}{I}$, $\bar{D} = \frac{c_1 r^2}{2I}$, $\omega_x^2 = \frac{c+c_2}{M}$, $2\eta_x = \frac{\eta}{M}$, $\gamma_x = \frac{\gamma}{M}$, $q = \frac{c_2}{M}$, $k = \frac{c_1 r}{M}$, $\omega_y^2 = \frac{c_2}{m}$, $2\eta_y = \frac{\eta}{m}$, $\gamma_y = \frac{\gamma}{m}$.

One transforms the system (3) to principal coordinates, solving corresponding eigenvalue problem of the linearized system. Fundamental frequencies and coordinates of eigenvectors $\chi_{1,2} = (\alpha_{1,2}, \beta_{1,2})$ are the following:

$$\omega_{1,2}^2 = \frac{(\omega_x^2 + \omega_y^2) \mp \sqrt{(\omega_x^2 - \omega_y^2)^2 + 4\omega_y^2 q}}{2}, \tag{4}$$

$$\alpha_{1,2} = 1, \beta_{1,2} = \frac{2\omega_y^2}{(\omega_y^2 - \omega_x^2) \pm \sqrt{(\omega_x^2 - \omega_y^2)^2 + 4\omega_y^2 q}}. \tag{5}$$

In the principal coordinates the system under consideration can be written of the form:

$$\begin{aligned}
&\ddot{\varphi} = \varepsilon(\bar{A} + \bar{B}\dot{\varphi} + \bar{C}(z_1 + z_2)\cos\varphi - \bar{D}\ \sin 2\varphi),\\
&\ddot{z}_1 + \omega_1^2 z_1 = \tfrac{\varepsilon\beta_2}{\beta_2-\beta_1}(-2\eta_x(\dot{z}_1 + \dot{z}_2) - \gamma_x(z_1 + z_2 - \beta_1 z_1 - \beta_2 z_2)^3 + k\ \sin\varphi)\\
&-\tfrac{\varepsilon}{\beta_2-\beta_1}(-2\eta_y(\beta_1\dot{z}_1 + \beta_2\dot{z}_2) + \gamma_y(z_1 + z_2 - \beta_1 z_1 - \beta_2 z_2)^3),\\
&\ddot{z}_2 + \omega_2^2 z_2 = \tfrac{\varepsilon}{\beta_2-\beta_1}(-2\eta_y(\beta_1\dot{z}_1 + \beta_2\dot{z}_2) + \gamma_y(z_1 + z_2 - \beta_1 z_1 - \beta_2 z_2)^3)\\
&-\tfrac{\varepsilon\beta_1}{\beta_2-\beta_1}(-2\eta_x(\dot{z}_1 + \dot{z}_2) - \gamma_x(z_1 + z_2 - \beta_1 z_1 - \beta_2 z_2)^3 + k\ \sin\varphi).
\end{aligned} \tag{6}$$

To analyze the external resonance on the fundamental frequency corresponding to the coordinate z_1, one introduces the detuning parameter Δ by the relation $\Omega^2 = \omega_1^2 + \varepsilon\Delta$. The multiple scale method [12] is used here. So, the following scales of time as new independent variables are introduced: $T_0 = t; T_1 = \varepsilon t$, etc. All generalized coordinates of the system (6) are presented as functions of these variables. The next standard transformations are used:

$$\frac{d}{d\tau} = \frac{\partial}{\partial T_0} + \varepsilon\frac{\partial}{\partial T_1} + \cdots, \quad \frac{d^2}{d\tau^2} = \frac{\partial^2}{\partial T_0^2} + 2\varepsilon\frac{\partial^2}{\partial T_1 \partial T_0} + \cdots \tag{7}$$

The variables φ, z_1 and z_2 are presented also as power series by the small parameter. Saving only the zero and first approximations by the small parameter, $\varphi = \varphi_0 + \varepsilon\varphi_1$, $z_1 = z_{10} + \varepsilon z_{11}$, $z_2 = z_{20} + \varepsilon z_{21}$, one obtains the following PDE systems:

$$\frac{\partial^2\varphi_0}{\partial T_0^2} = 0, \quad \frac{\partial^2 z_{10}}{\partial T_0^2} + \Omega^2 z_{10} = 0, \quad \frac{\partial^2 z_{20}}{\partial T_0^2} + \omega_2^2 z_{20} = 0, \tag{8}$$

$$\frac{\partial^2\varphi_1}{\partial T_0^2} = -2\frac{\partial^2\varphi_0}{\partial T_0\partial T_1} + \bar{A} + \bar{B}\left(\frac{\partial\varphi_0}{\partial T_0}\right) + \bar{C}(z_{10}+z_{20})\cos\varphi_0 - \bar{D}\,\sin 2\varphi_0,$$

$$\frac{\partial^2 z_{11}}{\partial T_0^2} + \Omega^2 z_{11} = -2\frac{\partial^2 z_{10}}{\partial T_0\partial T_1} + \Delta z_{10} + \frac{1}{\beta_2-\beta_1}\Big[\beta_2\Big(-2\eta_x\frac{\partial(z_{10}+z_{20})}{\partial T_0} - \gamma_x\,(z_{10}+z_{20}$$

$$-\beta_1 z_{10} - \beta_2 z_{20})^3 + k\,\sin\varphi_0\Big) + 2\eta_y\frac{\partial(\beta_1 z_{10}+\beta_2 z_{20})}{\partial T_0} - \gamma_y(z_{10}+z_{20}-\beta_1 z_{10}-\beta_2 z_{20})^3\Big], \qquad (9)$$

$$\frac{\partial^2 z_{20}}{\partial T_0^2} + \omega_2^2 z_{20} = -2\frac{\partial^2 z_{20}}{\partial T_0\partial T_1} + \frac{1}{\beta_2-\beta_1}\Big[-2\eta_y\frac{\partial(\beta_1 z_{10}+\beta_2 z_{20})}{\partial T_0} + \gamma_y(z_{10}+z_{20}$$

$$-\beta_1 z_{10} - \beta_2 z_{20})^3 - \beta_1\Big(-2\eta_x\frac{\partial(z_{10}+z_{20})}{\partial T_0} - \gamma_x(z_{10}+z_{20}-\beta_1 z_{10}-\beta_2 z_{20})^3 + k\,\sin\varphi_0\Big)\Big].$$

Solution of the Eq. (8) is presented as

$$\varphi_0 = \Omega t,\; z_{10} = C_1 e^{i\Omega T_0} + \bar{C}_1 e^{-i\Omega T_0},\; z_{20} = C_2 e^{i\omega_2 T_0} + \bar{C}_2 e^{-i\omega_2 T_0}, \qquad (10)$$

where Ω is the constant by the time scale T_0, but this is a function by the scale T_1.

Introducing relations (10) to the system (9), it is possible to write the following conditions of the secular terms elimination:

$$\frac{\partial\Omega}{\partial T_1} = \frac{1}{2}(\bar{A}+\bar{B}\Omega) + \frac{1}{4}\bar{C}(C_1+\bar{C}_1),$$

$$-2i\Omega\frac{\partial C_1}{\partial T_1} + (\Delta + iL\Omega)C_1 + 2C_1(\Omega T_0 - i)\frac{\partial\Omega}{\partial T_1} - MC_1^2\bar{C}_1 - PC_1C_2\bar{C}_2 - iN = 0,$$

$$-2i\omega_2\frac{\partial C_2}{\partial T_1} + iSC_2 + RC_2^2\bar{C}_2 + TC_2C_1\bar{C}_1 = 0, \qquad (11)$$

where $L = \frac{2}{\beta_2-\beta_1}(\beta_1\eta_y - \beta_2\eta_x)$, $P = \frac{6(1-\beta_1)(1-\beta_2)^2}{\beta_2-\beta_1}(\beta_2\gamma_x + \gamma_y)$, $N = \frac{k\beta_2}{2(\beta_2-\beta_1)}$, $M = \frac{3(1-\beta_1)^3}{\beta_2-\beta_1}(\beta_2\gamma_x+\gamma_y)$, $S = \frac{2\omega_2}{\beta_2-\beta_1}(\beta_1\eta_x - \beta_2\eta_y)$, $T = \frac{6(1-\beta_2)(1-\beta_1)^2}{\beta_2-\beta_1}(\beta_1\gamma_x+\gamma_y)$, $R = \frac{3(1-\beta_2)^3}{\beta_2-\beta_1}(\beta_1\gamma_x+\gamma_y)$.

By the change of variables, $C_1 = a_1 e^{ib_1}$, $C_2 = a_2 e^{ib_2}$ one has from the system (11) the following equations with respect to amplitudes and phases of the unknown solutions in the resonance domain, and the equation with respect to the variables Ω:

$$\frac{\partial\Omega}{\partial T_1} = \frac{1}{2}(\bar{A}+\bar{B}\Omega + \bar{C}a_1\cos b_1),$$

$$\frac{\partial a_1}{\partial T_1} = \frac{L}{2}a_1 - \frac{a_1}{\Omega}\frac{\partial\Omega}{\partial T_1} - \frac{N}{2\Omega}\cos b_1,$$

$$\frac{\partial b_1}{\partial T_1} = -\frac{\Delta}{2\Omega} + \frac{M}{2\Omega}a_1^2 + \frac{P}{2\Omega}a_2^2 + T_0\frac{\partial\Omega}{\partial T_1} + \frac{N}{2\Omega a_1}\sin b_1,$$

$$\frac{\partial a_2}{\partial T_1} = \frac{S}{2\omega_2}a_2,$$

$$\frac{\partial b_2}{\partial T_1} = -\frac{R}{2\omega_2}a_2^2 - \frac{T}{2\omega_2}a_1^2. \qquad (12)$$

Note that the first equation of the system (12) corresponds to unsteady regime when the variable Ω changes in time. If $\Omega = const$, one obtains the well-known relation

[17, 19, 20] connecting the rotor constant and amplitude of the elastic vibration as $L(\Omega) - H(\Omega) - 0,5\Omega\eta A_1^2 = 0$, where $A_1 = 2a_1$ is the vibration amplitude, and η is a coefficient of dissipation. Here the unsteady behavior of the non-ideal system under consideration is investigated. The change of variables, $a_1 = K \sin\psi, a_2 = K \cos\psi$, is introduced, and the following reduced system [13–15] is obtained:

$$\begin{aligned}
\frac{\partial\Omega}{\partial T_1} &= \frac{1}{2}(\bar{A} + \bar{B}\Omega + \bar{C}K \sin\psi \cos b_1),\\
\frac{\partial K}{\partial T_1} &= \frac{L\Omega - \bar{A} - \bar{B}\Omega}{2\Omega} K \sin^2\psi + \frac{S}{2\omega_2} K \cos^2\psi - \left(\frac{\bar{C}}{2\Omega} K^2 \sin^2\psi + \frac{N}{2\Omega}\right)\cos b_1 \sin\psi,\\
\frac{\partial\psi}{\partial T_1} &= \left(\frac{L\Omega - \bar{A} - \bar{B}\Omega}{2\Omega} - \frac{S}{2\omega_2}\right)\sin\psi \cos\psi - \left(\frac{\bar{C}}{2\Omega} K \sin^2\psi + \frac{N}{2\Omega K}\right)\cos\psi \cos b_1,\\
\frac{\partial b_1}{\partial T_1} &= -\frac{\Delta + \Omega T_0(\bar{A} + \bar{B}\Omega)}{2\Omega} - \frac{T_0\bar{C}}{2} K \sin\psi \cos b_1 + \frac{M}{2\Omega} K^2 \sin^2\psi + \frac{P}{2\Omega} K^2 \cos^2\psi + \frac{N}{2\Omega K \sin\psi} \sin b_1,\\
\frac{\partial b_2}{\partial T_1} &= -\frac{R}{2\omega_2} K^2 \cos^2\psi - \frac{T}{2\omega_2} K^2 \sin^2\psi,
\end{aligned} \tag{13}$$

where the variable parameter K characterizes the reduced system energy; ψ is an arctangent of ratio of amplitudes. Equation with respect to difference of phases, $\varphi = b_1 - b_2$ can be written as

$$\begin{aligned}
\frac{\partial\varphi}{\partial T_1} = &-\frac{\Delta + \Omega T_0(\bar{A} + \bar{B}\Omega)}{2\Omega} - \frac{T_0\bar{C}}{2} K \sin\psi \cos b_1 + \frac{M}{2\Omega} K^2 \sin^2\psi + \frac{P}{2\Omega} K^2 \cos^2\psi\\
&+ \frac{N}{2\Omega K \sin\psi} \sin b_1 + \frac{R}{2\omega_2} K^2 \cos^2\psi + \frac{T}{2\omega_2} K^2 \sin^2\psi.
\end{aligned} \tag{14}$$

One analyzes the equilibriums in the Eqs. (13), (14). The relation $\sin\psi = 0$ corresponds to energy localization on the coordinate z_2, and the relation $\cos\psi = 0$ corresponds to energy localization on the coordinate z_1.

Under the relation $\sin\psi = 0$ a condition of existence of the equilibrium in the third equation of the system (13) gives us the equation $\cos b_1 = 0$. This equilibrium corresponds to the following relation for the energy: $\frac{\partial K}{\partial T_1} = \frac{S}{2\omega_2} K$. Taking into account that the parameter S is negative for any system parameters, we can conclude that the energy of this equilibrium position decreases; so, the localized vibrations are unstable. If $\cos\psi = 0$, the third equation of the system (13) is an identity. So, this equilibrium position of the reduced system is situated at the straight line $\psi = \frac{\pi}{2}$. In this case a conclusion about change of energy and stability of the equilibrium position can be made by analysis of trajectories in the place (φ, ψ).

For a case when both $\sin\psi \neq 0$ and $\cos\psi \neq 0$, an existence of the equilibrium position of the third equation of the system (13) is possible if $\cos b_1 = \frac{(L\Omega - \bar{A} - \bar{B}\Omega - S\Omega/\omega_2)K \sin\psi}{N + \bar{C}K^2 \sin^2\psi}$. One has from here the inequality $\left|\frac{(L\Omega - \bar{A} - \bar{B}\Omega - S\Omega/\omega_2)K \sin\psi}{N + \bar{C}K^2 \sin^2\psi}\right| \leq 1$. On the other hand, the function $\sin\psi$ can be found from the equation

$$\bar{C}K^2 \cos b_1 \sin^2\psi - (L\Omega - \bar{A} - \bar{B}\Omega - S\Omega/\omega_2)K \sin\psi + N \cos b_1 = 0,$$

that is, $\sin\psi = \frac{(L\Omega - \bar{A} - \bar{B}\Omega - S\Omega/\omega_2) \pm \sqrt{(L - \bar{A} - \bar{B}\Omega - S\Omega/\omega_2)^2 - 4\bar{C}N \cos b_1^2}}{2\bar{C}K \cos b_1}$.

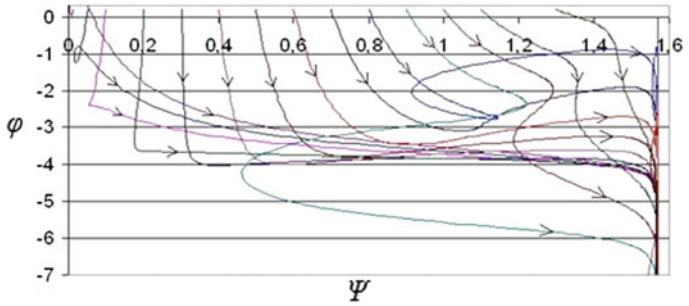

Fig. 4 Dependence $\varphi(\psi)$ for the external resonance on the first fundamental frequency

One has from here an inequality, $\left|\frac{(L\Omega-\bar{A}-\bar{B}\Omega-S\Omega/\omega_2)\pm\sqrt{(L-\bar{A}-\bar{B}\Omega-S\Omega/\omega_2)^2-4\bar{C}N\ \cos b_1^2}}{2\bar{C}K\ \cos b_1}\right| \leq 1$, and a condition of the discriminant positiveness as $(L\Omega - \bar{A} - \bar{B}\Omega - S\Omega/\omega_2)^2 - 4\bar{C}N\ \cos b_1^2 \geq 0$.

We can see from the Eq. (13) that in this case ψ and φ are functions of K, so, this equilibrium position is not stationary. This position corresponds to vibrations which are equivalent to NNMs of coupled vibrations of the conservative sub-system of the system (6). This mode of coupled vibrations is realized only for some specific value of time, corresponding to conditions presented above, so, it can be called as t*ransient nonlinear vibration mode* (TNNM). It is interesting that near this value of time motions of the system are close to the mode, that is, the TNNM is attractive.

The system (13) is integrated by the Runge–Kutta method; initial conditions take values on the interval $0 \leq \psi(0) \leq \pi/2$, and the following system parameters are chosen: $K(0) = 0.1$, $c_0 = 1$ N/m, $c_1 = 1$ N/m, $c_2 = 0.2$ N/m, $M = 1$ kg, $m = 0.05$ kg, $\beta = 0.05$, $\gamma = 0.3$ N/m, $r = 0.05$ m, $\bar{A} = 0.115$, $\bar{B} = -0.08$, $\bar{C} = 0.01$ and $\Delta(0) = -0.5$. A dependence $\varphi(\psi)$ is shown in Fig. 4 where trajectories do not remain near the straight line $\psi = 0$, and tend in time to the line $\psi = \frac{\pi}{2}$, that is, localized on z_1 vibrations are stable near resonance, and localized on z_2 vibrations lose stability. Some trajectories approach the equilibrium position corresponding to the TNNM of coupled vibrations, and remain near this state while one exists. When the time increases the coupled vibrations disappear, and motions of the system tend to the stable localized mode.

The transfer from the localization on z_1 to the stable vibration mode of localization on z_2 is shown in Fig. 5. We can see that for some values of time trajectories in Fig. 5 are close to two TNNMs of the coupled vibrations which appear here.

Similar results can be obtained for a case of external resonance on the second fundamental frequency. For a case of both external and internal resonances after the transformation to reduced system and analysis of the system the following conclusions can be made (corresponding relations are not presented here): two localized vibration modes are TNNMs existing only for some values of time when the specific

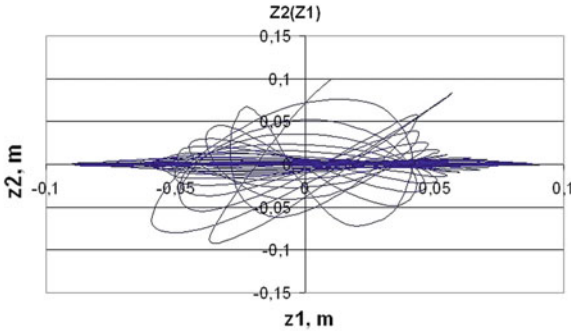

Fig. 5 Dependences z_2 (z_1) for the external resonance on the first fundamental frequency

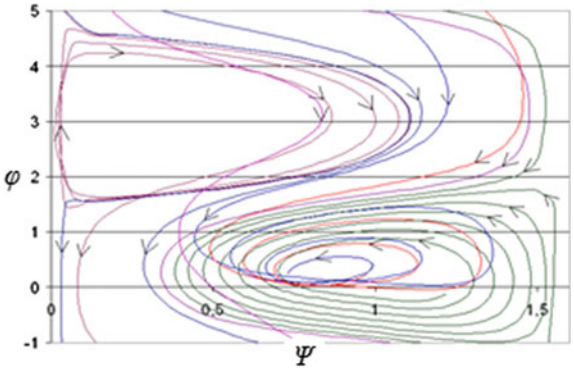

Fig. 6 Dependence $\varphi(\psi)$ for the both external and internal resonances

values of energy are reached. Any time only coupled vibrations exist in the system. The reduced system is integrated by the Runge–Kutta method. Initial conditions are changed on the interval $0 \le \psi(0) \le \pi/2$, and the next system parameters are chosen: $K(0) = 0.1$, $c_0 = 0.1$ N/m, $c_1 = 0.14$ N/m, $c_2 = 0.01$ N/m, $M = 1$ kg, $m = 0.1$ kg, $\beta = 0.2$, $\gamma = 1.5$ N/m, $r = 2.1$ m, $\bar{A} = 0.02$, $\bar{B} = -0.009$, $\bar{C} = 0.005$ and $\Delta(0) = 0.04$. Dependence $\varphi(\psi)$ is shown in Fig. 6 where we can see two equilibrium positions corresponding to coupled vibrations of the elastic subsystem and absorber. TNNMs correspond to $\psi = 0$ and $\pi/2$. All trajectories pass from the equilibrium position at the top of the figure to the equilibrium position in the bottom of the figure, the last one corresponds to the stable mode of coupled vibrations. The obtained results are confirmed by direct numerical simulation of the initial nonlinear system.

4 Transient Nonlinear Normal Modes in Dissipative Spring-Pendulum System Under Resonance Conditions

The spring-pendulum system with small dissipation under external periodic excitation is considered (Fig. 7).

Equations of motion of the system are the following:

$$\begin{aligned} &\ddot{u} + \omega_u^2 x + \varepsilon \eta_u \dot{u} - \mu(\ddot{\theta} \sin\theta + \dot{\theta}^2 \cos\theta) = \varepsilon^2 f \cos\tau, \\ &\ddot{\theta} + \varepsilon \eta_\theta \dot{\theta} + p^2 \sin\theta - \ddot{u} \sin\theta = 0, \end{aligned} \tag{15}$$

where $u = \frac{y}{R}$, $\tau = \Omega t$, $\omega = \sqrt{\frac{k}{M+m}}$, $p^2 = \frac{g}{R\Omega}$, $\mu = m/(m+M)$, $\omega_u^2 = 1/\Omega^2$, $f = \frac{F_0}{(M+m)R\omega^2\Omega^2}$, $\eta_u = \frac{\beta_u}{(M+m)\Omega}$, $\eta_\theta = \frac{\beta_\theta}{m\Omega}$; β_u and β_θ are coefficients of dissipation; ε is the small parameter.

There are two Kauderer–Rosenberg NNMs in the system (15) without dissipation and external excitation: the localized $u-$ mode of vertical vibrations ($u = u(\tau)$, $\theta = 0$) and the non-localized mode, when vibration amplitudes for vertical and angle coordinates are comparable. When dissipation exists, vibration modes are not the Kauderer–Rosenberg NNMs, because they are not periodic.

To consider motions of the system under consideration in the vicinity of both external and internal resonances one introduces to equations of motion (15) two detuning parameters Δ_1 and Δ_2 by two relations. First relation, $\omega_u^2 = 1 + \varepsilon\Delta_1$ corresponds to the vicinity of external resonance, and the second one, $p^2 = 0.25 + \varepsilon\Delta_2$ corresponds to the vicinity of the main parametrical resonance of the system (15). Using these resonance relations and expansions in power series for sinθ and cosθ, one has the following equations of the first and second approximations by the small parameter ε:

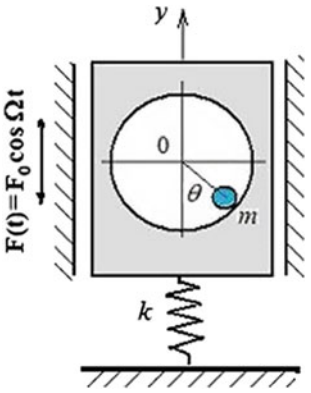

Fig. 7 Spring-pendulum system

$$\frac{\partial^2 u_0}{\partial T_0^2} + u_0 = 0,$$
$$\frac{\partial^2 \theta_0}{\partial T_0^2} + \frac{1}{4}\theta_0 = 0, \tag{16}$$

$$\frac{\partial^2 u_1}{\partial T_0^2} + u_1 = -\Delta_1 u_0 - 2\frac{\partial^2 u_0}{\partial T_1 \partial T_0} + \mu\left(\frac{\partial^2 \theta_0}{\partial T_0^2}\right)\theta_0 + \mu\left(\frac{\partial \theta_0}{\partial T_0}\right)^2 - \eta_u \frac{\partial u_0}{\partial T_0} + \frac{f}{2}(e^{iT_0} + e^{-iT_0}),$$
$$\frac{\partial^2 \theta_1}{\partial T_0^2} + \theta_1 = -\Delta_2 \theta_0 - 2\frac{\partial^2 \theta_0}{\partial T_1 \partial T_0} + \left(\frac{\partial^2 u_0}{\partial T_0^2}\right)\theta_0 - \eta_\theta \frac{\partial \theta_0}{\partial T_0}. \tag{17}$$

Solution of the system (16),

$$u_0 = C_u(T_1)e^{iT_0} + \bar{C}_u(T_1)e^{-iT_0},$$
$$\theta_0 = C_\theta(T_1)e^{\frac{1}{2}iT_0} + \bar{C}_\theta(T_1)e^{-\frac{1}{2}iT_0}, \tag{18}$$

is substituted to Eq. (17). Then secular terms are eliminated; as a result, one has the following nonlinear equations:

$$2i\frac{\partial C_u}{\partial T_1} + \frac{\mu}{2}C_\theta^2 + C_u\Delta_1 + i\eta_u C_u - \frac{f}{2} = 0,$$
$$i\frac{\partial C_\theta}{\partial T_1} + C_u\bar{C}_\theta + C_\theta\Delta_2 + \frac{1}{2}i\eta_\theta C_\theta = 0. \tag{19}$$

Change of variables, $C_u = a_u e^{i\beta_u}$, $C_\theta = a_\theta e^{i\beta_\theta}$ gives the system of modulation equations written with respect to amplitudes a_u, a_θ and phases β_u, β_θ. Next change of variables, $a_u = \frac{\sqrt{\mu}}{2}K\cos\psi$, $a_\theta = K\sin\psi$, gives the *reduced system,* written with respect to the energy K, the arctangent of the amplitudes ratio ψ and the phases β_u, β_θ:

$$K' = -K\left(\frac{\eta_u}{2}\cos^2\psi + \frac{\eta_\theta}{2}\sin^2\psi\right) - \frac{f}{2\sqrt{\mu}}\sin\beta_u\cos\psi,$$
$$\psi' = \sin\psi\left(\frac{\sqrt{\mu}}{2}K\sin(2\beta_\theta - \beta_u) + \frac{\eta_u - \eta_\theta}{2}\cos\psi + \frac{f}{2\sqrt{\mu}K}\sin\beta_u\right),$$
$$\beta_u' = \frac{\Delta_1}{2} + \frac{\sqrt{\mu}}{2}\frac{K\sin^2\psi}{\cos\psi}\cos(2\beta_\theta - \beta_u) - \frac{f}{2\sqrt{\mu}K\cos\psi}\cos\beta_u,$$
$$\beta_\theta' = \Delta_2 + \frac{\sqrt{\mu}}{2}K\cos\psi\cos(2\beta_\theta - \beta_u). \tag{20}$$

Equilibrium positions for the second equation of the system (20) are considered. Condition $\sin\psi \equiv 0$ corresponds to the localized mode of the spring vibrations. This mode exists for all values of the energy K; it is described by the straight line $\psi = 0$ in the plane (ψ, φ). For the case, when both $\cos\psi \neq 0$, and $\sin\psi \neq 0$, it is possible to observe mode of coupled vibrations of the system (15). Condition of the mode existence can be obtained from the second equation of the reduced system (20)

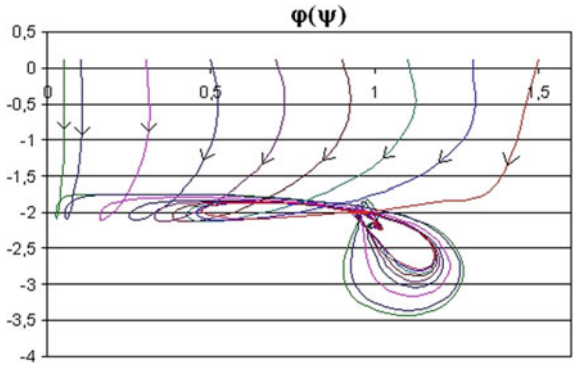

Fig. 8 Trajectories in the place (ψ, φ)

as $\cos\psi = \frac{\sqrt{\mu}}{\eta_\theta - \eta_u} K \sin(2\beta_\theta - \beta_u) + \frac{f}{2\sqrt{\mu}K(\eta_\theta - \eta_u)} \sin\beta_u$. This condition corresponds to two modes of coupled vibrations. The further examination shows that one of them is stable and another one is the transient mode of coupled vibrations.

To construct trajectories in the place (ψ, φ) the system (20) is integrated numerically, when the initial value of arctangent of the amplitudes ratio changes on the interval $0 \le \psi(0) \le \frac{\pi}{2}$, $K(0) = 0.5$ and system parameters are the following: $\eta_u = 0.3$, $\eta_\theta = 0.2$, $\mu = 0.4$, $\Delta_1 = 0.2$, $\Delta_2 = 0.1$, $f = 0.35$. Trajectories in the place (ψ, φ) for the case of simultaneous external and internal resonances are shown in Fig. 8. Each trajectory has a loop near some quasi-equilibrium state of the reduced system. This state moves in the space (ψ, φ) and corresponds to TNNM of coupled vibrations existing only for specific values of the system energy, that is, the TNNM exist in some moments of time corresponding to these energy levels. This transient mode is attractive and other motions are close to this TNNM near the mentioned moment of time. We can see in the Fig. 8, that later, when the TNNM disappears, trajectories in the plane (ψ, φ) approach the equilibrium position which corresponds to the stable mode of coupled vibrations. Note that this equilibrium position is closer to the straight line $\psi = \frac{\pi}{2}$, which corresponds to localized on pendulum vibrations, than to the straight line $\psi = 0$, which corresponds to localized vibrations of spring. We can see that the mode of the localized vibrations of spring is not stable.

To illustrate behavior of the spring-pendulum system in vicinity of the resonance the initial system is integrated numerically on the interval $\tau \in [0, 5000]$ for the following initial values $a_u(0) = 0.05$, $a_\theta(0) = 0.01$, $\beta_u(0) = 0.1$, $\beta_\theta(0) = 0.2$ and system parameters $\eta_u = 0.3$, $\eta_\theta = 0.2$, $f = 0.35$, $\Delta_1 = 0.2$, $\Delta_2 = 0.1$. The first approximation of the solution can be written as $u_0 = 2a_u \cos(\tau + \beta_u)$, $\theta_0 = 2a_\theta \cos(\frac{1}{2}\tau + \beta_\theta)$. Trajectories in the system configuration plane are shown in Fig. 9 for the following intervals of time: $\tau \in [0, 100]$ (Fig. 8a), $\tau \in [4800, 5000]$ (Fig. 8b) and $\tau \in [0, 5000]$ (Fig. 8c). Here the transient nonlinear normal mode of coupled vibrations appears. At the beginning of the process motions of the system are close to this TNNM which is determined by parabolic trajectory (Fig. 8a). Then, due to instability of this mode, motions of the system tend to the stable mode of coupled vibrations. Trajectory of this stable mode can be observed in Fig. 8b where vibrations

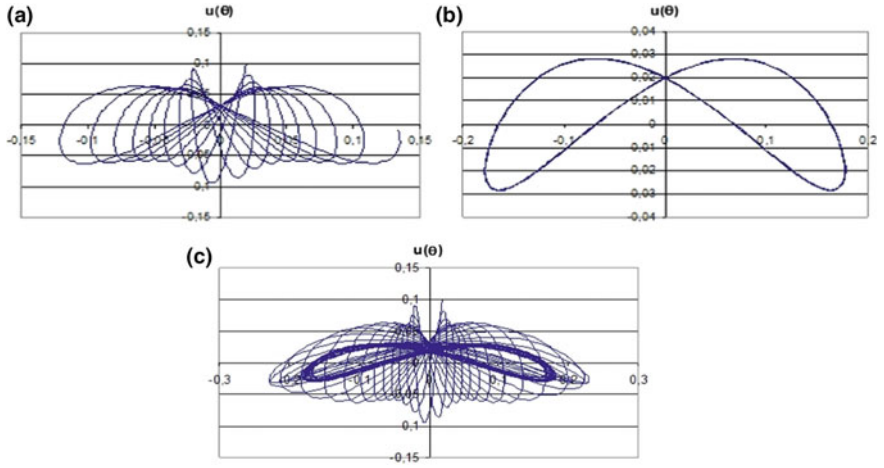

Fig. 9 Trajectories $u(\theta)$ in configuration space for $t \in [0, 100]$ (**a**); $t \in [4800, 5000]$ (**b**); $t \in [0, 5000]$ (**c**)

for large values of time are shown. The stable mode is close to the localized mode of the pendulum vibrations, and this fact can be used in the problem of vibration absorption. Namely, it is possible to guarantee the energy transfer from vibrations of spring to vibrations of pendulum, where the vibration energy can be dissipated. It is clear that the numerical simulation fully confirms results obtained by analysis of the reduced system.

5 Conclusion

The NNMs which are different from the NNMs proposed by Kauderer–Rosenberg are obtained in some non-conservative systems. Namely, NNMs having smooth trajectories in configuration space and chaotic in time behavior can be found in analysis of some of elastic systems. It seems that this is typical situation in post-buckling dynamics of shells, arches etc.

Resonance dynamics of the dissipative limited power-supply system with a nonlinear vibration absorber and the dissipative spring-pendulum system is investigated by the multiple-scale method and transformation to the reduced system. In the nonideal system, in the case of external resonance on the first fundamental frequency, except the localized vibration modes, the TNNM of coupled vibrations appears. This mode exists only for some value of energy, that is, for a single moment of time. This mode is attractive near the mentioned moment of time. In the case of simultaneous external and internal resonances two modes of coupled vibrations appear; one of them is unstable, and motions of the system come close to the stable NNMs of the coupled vibrations. Two localized modes are TNNMs in this case. Existence of the

localized modes depends on the energy levels and the system parameters; they are attractive near moments of their existence. For the dissipative spring-pendulum system in the case of simultaneous external and internal resonances the mode of coupled vibrations is stable, and the localized mode loses stability. The TNNM also exists here for some level of the system energy. Reliability of obtained analytical results is verified by numerical simulation. We can conclude that such transient normal modes essentially affects to transient process of the nonlinear dissipative system.

References

1. Kauderer, H.: Nichtlineare Mechanik. Springer, Berlin (1958)
2. Rosenberg, R.M.: Nonlinear vibrations of systems with many degrees of freedom. Adv. Appl. Mech. **9**, 156–243 (1966)
3. Vakakis, A.F., Manevitch, L.I., Mikhlin, Yu.V., Pilipchuk, V.N., Zevin, A.A.: Normal Modes and Localization in Nonlinear Systems. Wiley, New York (1996)
4. Mikhlin, Yu.V., Avramov, K.V.: Nonlinear normal modes for vibrating mechanical systems. Review of theoretical developments. Appl. Mech. Rev. **63**(6), 060802 (2010)
5. Avramov, K.V., Mikhlin, Yu.V.: Review of applications of nonlinear normal modes for vibrating mechanical systems. Appl. Mech. Rev. **65**(2), 020801 (2013)
6. Witt, A.A., Gorelik, G.S.: Oscillations of an elastic pendulum as an example of the oscillations of two parametrically coupled linear systems. J. Tech. Phys. **3**(2–3), 294–307 (1933)
7. Struble, R.A., Heinbockel, J.H.: Energy transfer in a beam–pendulum system. Trans. ASME. J. Appl. Mech. **29**, 590–592 (1963)
8. Tsel'man, F.Kh.: On pumping transfer of energy between nonlinearly coupled oscillators in third-order resonance. J. Appl. Math. Mech. (PMM USSR) **34**(5), 957–962 (1970)
9. Mercer, C.A., Rees, P.L., Fahy, V.J.: Energy flow between two weakly coupled oscillators subject to transient excitation. J. Sound Vib. **15**(3), 373–379 (1971)
10. Vakakis, A.F., Gendelman, O.V., Bergman, J.A., McFarland, D.M., Kerschen, G., Lee, Y.S.: Nonlinear Targeted Energy Transfer in Mechanical and Structural Systems. Springer Science, Berlin (2008)
11. Manevich, A.I., Manevitch, L.I.: The Mechanics of Nonlinear Systems with Internal Resonances. Imperial College Press, London (2005)
12. Nayfeh, A.H., Mook, D.T.: Nonlinear Oscillations. Wiley, New York (1979)
13. Pilipchuk, V.N.: Nonlinear Dynamics: Between Linear and Impact Limits. Springer, Berlin (2010)
14. Wang, F., Bajaj, A., Kamiya, K.: Nonlinear Normal Modes and Their Bifurcations for an Inertially-Coupled Nonlinear Conservative System. Purdue University (2005)
15. Plaksiy, K.Yu., Mikhlin Yu.V.: Dynamics of nonlinear dissipative systems in the vicinity of resonance. J. Sound Vib. **334**, 319–337 (2015)
16. Sommerfeld, A.: Beitraege zum dynamischen Ausbau der Festigkeitslehe. Phys. Zeitschr **3**, 266–286 (1902)
17. Kononenko, V.O.: Vibrating Systems with Limited Power Supply. Illife Books, London (1969)
18. Goloskokov, E.G., Filippov, A.P.: Nonstationary Vibrations of Mechanical Systems. Naukova Dumka, Kiev (1966) (in Russian) (Goloskokov, E.G., Filippov, A.P.: Einstationäre Schwingungen Mechanischer Systeme. Academie-Verlag, Berlin (1971))
19. Alifov, A.A., Frolov, K.V.: Interaction of Nonlinear Oscillatory Systems with Energy Sources. Taylor & Francis Inc., London (1990)
20. Eckert, M.: The Sommerfeld effect: theory and history of a remarkable resonance phenomenon. Eur. J. Phys. **17**(5), 285–289 (1996)

21. Balthazar, J.M., Mook, D.T., Weber, H.I., Brasil, R.M.L.R.F., Fenili, A., Belato, D., Felix, J.L.P.: An overview on non-ideal vibrations. Meccanica **38**(6), 613–621 (2003)
22. Felix, J.L.P., Balthazar, J.M., Dantas, M.J.H.: On energy pumping, synchronization and beat phenomenon in a non-ideal structure coupled to an essentially nonlinear oscillator. Nonlinear Dyn. **56**(1–2), 1–11 (2009)
23. de Godoy, W.R.A., Balthazar, J.M., Pontes Jr., B.R., Felix, J.L.P., Tusset, A.M.: A note on nonlinear phenomena in a non-ideal oscillator, with a snap-through truss absorber, including parameter uncertainties. Proc. Inst. Mech. Eng. Part K. J. Multi-Body Dyn. **227**(1), 76–86 (2013)
24. Tusset, A.M., Balthazar, J.M., Felix, J.L.P.: On elimination of chaotic behavior in a non-ideal portal frame structural system, using both passive and active controls. J. Vib. Control **19**(6), 803–813 (2013)
25. Manevich, A., Saiko, C.: Synchronic regimes in oscillator-rotator system (Rotation in vertical plane). In: Proceedings of the 4th International Conference on Nonlinear Dynamics "ND-KhPI 2013", 19–22 June 2013, Sevastopol, Ukraine, pp. 118–124 (2016)
26. Vorotnikov, K., Starosvetsky, Y.: Nonlinear energy channeling in the two-dimensional, locally resonant, unit-cell model. I. High energy pulsations and routes to energy localization. Chaos **25**, 073106 (2015)
27. Guckenheimer, J., Holmes, P.: Nonlinear Oscillations, Dynamical Systems, and Bifurcations of Vector Fields. Springer, New York (1993)
28. Mikhlin, Yu.V., Shmatko, T.V., Manucharyan, G.V.: Lyapunov definition and stability of regular or chaotic vibration modes in systems with several equilibrium positions. Comput. Struct. **82**, 2733–2742 (2004)

Advanced Nonlinear System Identification for Modal Interactions in Nonlinear Structures: A Review

K. J. Moore, A. Mojahed, M. Kurt, M. Eriten, D. M. McFarland, L. A. Bergman and A. F. Vakakis

Abstract In this work, we review a recently developed method for the characterization and identification of strongly nonlinear dynamical systems, including the detection of strongly nonlinear modal interactions, directly from transient response data. The method synergistically combines the proper orthogonal decomposition and the Rayleigh quotient to create estimated frequency-energy plots (FEPs) that capture the rich and interesting nonlinear dynamical interactions. The method is first applied to the experimentally measured response of a cantilever beam with a local, smooth nonlinearity. In this application, the estimated FEP reveals the presence of nonsmooth perturbations that connect different nonlinear normal modes (NNMs) of the system. The wavelet-bounded empirical mode decomposition and slow-flow analysis are used to demonstrate that the nonsmooth perturbations correspond to strongly nonlinear internal resonances between two NNMs. In the second example, the method is applied to the experimentally measured response of a cantilever beam

K. J. Moore (✉) · A. Mojahed · D. M. McFarland · L. A. Bergman · A. F. Vakakis
University of Illinois, Urbana, IL 61801, USA
e-mail: kmoore14@illinois.edu

A. Mojahed
e-mail: mojahed2@illinois.edu

D. M. McFarland
e-mail: dmmcf@illinois.edu

L. A. Bergman
e-mail: lbergman@illinois.edu

A. F. Vakakis
e-mail: avakakis@illinois.edu

M. Kurt
Stevens Institute of Technology, Hoboken, NJ 07030, USA
e-mail: mkurt@stevens.edu

M. Eriten
University of Wisconsin-Madison, Madison, WI 53706, USA
e-mail: eriten@engr.wisc.edu

D. M. McFarland
Zhejiang University of Technology, Hangzhou 310014, Zheijiang, China

I. V. Andrianov et al. (eds.), *Problems of Nonlinear Mechanics and Physics of Materials*, Advanced Structured Materials 94,
https://doi.org/10.1007/978-3-319-92234-8_7

with a local, nonlinear attachment in the form of a nonlinear energy sink (NES). An estimated frequency-displacement plot for the NES is created, and an optimization routine is then used to identify the unknown parameters for a given model of the nonlinearity. Ultimately, the method is conceptually and computationally simple compared to traditional methods while providing significant insight into the nonlinear physics governing dynamical systems with strong, local nonlinearity directly from measured time series data.

1 Introduction

Modal analysis, system identification and reduced-order modeling have been thoroughly studied in [5, 8, 28]. Nonlinear system identification (NSI) methods for nonlinear dynamical systems [15, 26], including the method of proper orthogonal decomposition (POD), [6, 13, 14, 16, 22] and a new promising technique for nonlinear system identification [31], which involves employing empirical mode decomposition (EMD) [7, 10, 11, 33], that operates under the assumption that measured time series can be decomposed into a finite set of harmonic components in the form of fast, nearly monochromatic oscillations that are modulated by slowly varying amplitudes. Using these NSI techniques, [17] showed that strong nonlinearities can lead to strongly nonlinear beat phenomena, which are the result of strongly nonlinear modal interactions, i.e. internal resonances (IRs) which occur between the nonlinear normal modes of the system.

Nonlinear normal modes (NNMs) are defined to be time-periodic oscillations, which one may regard as the nonlinear extensions of the linear vibrational normal modes [30]. While there are no modal interactions, the NNMs are synchronous, time-periodic oscillations; in contrast, in the case that IRs happen (which results in nonlinear energy exchange between modes), mode mixing is realized. In this case, non-synchronous oscillations with more than one participating NNM occur which cause scale mixing in the nonlinear dynamics that makes scale separation impossible. IRs depend highly on the total energy of the system and the necessary condition for them to occur is that the frequency ratio of the NNMs is a rational number. Also, IRs take place at different energy levels due to the fact that lower NNMs are affected at lower energy levels while higher NNMs are not affected as much. IRs have been shown to cause energy localization as in targeted energy transfer [29, 30], which lead to significantly altered stress distributions that can result in component failures [4], along with triggering bifurcations in the dynamics that change the stability of NNMs [1].

Utilizing POD to extract proper orthogonal modes (POMs), which represent the participating NNMs, and computing the Rayleigh quotient (RQ) using the POMs as trial vectors, [9] generalized the results described in [17]. By plotting the resulting RQs as functions of energy in the form of a frequency-energy plot (FEP) [29], it was revealed that the dynamics of the nonlinear system can be divided into three distinctive regimes. Of these, two are linear–in the low and high energy limits–

and are connected by the third regime,a strongly nonlinear transition regime. The duration of this nonlinear transition regime has been found to increase with increasing frequency. These regimes are different for each NNM because each modal response depends on the system energy. Additionally, by looking at the the RQ-FEP curves, one can see that there exist a number of non-smooth perturbations (spikes) which appeared to be the result of NNMs mixing due to occurrence of IRs.

The study performed by [23] on two comparable cantilever beams, each with strong, local nonlinearity led, to a physical interpretation of these spikes and substantiated the claim that these spikes represent modal interactions in the dynamics of stronlgy nonlinear systems. In order to investigate the physics of the spikes, POMs corresponding to RQs off and on the spikes were examined. The POMs computed off the spikes were found to correspond to periodic solutions of the non-interacting NNMs, while on the spikes the POMs of interacting NNMs were found to be similar and corresponded to the mixed periodic solutions of the NNMs during an IR. Furthermore, in the displacement responses for points on and off the spikes the presence of slow-flow dynamics [18, 20, 21, 31], which occurs as result of IRs, was investigated by means of the wavelet-bounded empirical mode decomposition [25]. The aforementioned analysis showed that only the responses corresponding to points on the spikes contained internal resonances. This demonstrated that the spikes in RQ-FEP are the result of IRs in the dynamics. In short, the appearance of spikes in the RQ-FEP or similar POMs mean the presence of IRs, while the absence of spikes and dissimilar POMs corresponds to the absence of such IRs.

2 Preliminary Concepts and the Proposed Method

2.1 Proper Orthogonal Decomposition

Proper orthogonal decomposition (POD) [6, 13, 14, 16, 22] is a system identification and model reduction tool that extracts an orthonormal basis of modes, termed the proper orthogonal modes (POMs), that represent a large set of interdependent variables in a least-squares sense. For linear response data, the POMs have been proven to be the minimum number of mutually orthogonal modes necessary to reconstruct that linear response data. Moreover, the POMs converge to the linear normal modes of vibration for classically damped, linear, discrete systems with mass matrices proportional to the identity matrix and in the limit of infinite measurement points [6]. In this work, we consider spatially discretized models of continuous systems obtained using the finite element (FE) method and, accordingly, employ the singular value decomposition (SVD), which is equivalent to POD for discrete systems [6]. The response data matrix X of dimensions $m \times n$ is factored as,

$$X = USV^T, \tag{1}$$

where U is an $m \times m$ orthonormal matrix containing the left singular vectors, S is an $m \times n$ pseudo-diagonal and positive semi-definite matrix containing the singular values, and V is an $n \times n$ orthonormal matrix composed of the right singular vectors. The left singular vectors, which are equivalent to the POMs, and the POVs are computed as the eigenvectors and eigenvalues of the matrix XX^T respectively. The singular values are equal to the POVs squared and divided by the number of samples m. The right singular vectors, V contain the time modulation of the corresponding POMs, normalized by the singular values, and are computed as the eigenvectors of the matrix $X^T X$.

2.2 Rayleigh Quotient

The Rayleigh quotient is a classical operator that uses a trial vector (discrete systems) or function (continuous systems) to estimate the fundamental natural frequency of a linear system. The frequencies of higher vibration modes can be estimated provided that the new trial vector or function is mass-orthogonal to the trial vectors used to estimate the lower modes. Since the FE method is used to discretize the continuous structures in this work, we employ the discrete version of the RQ:

$$R(v) = \frac{v^T K v}{v^T M v}, \tag{2}$$

where v is the trial vector, K is the stiffness matrix, and M is the mass matrix. A celebrated property of the RQ is its relative insensitivity to the trial vector, which permits the use of a large range of trial vectors, provided that the trial vectors satisfy the relevant boundary conditions. Moreover, the RQ has a minimum value equal to the fundamental eigenvalue of the linear mass and stiffness matrices. In this study, the frequencies of each system are estimated using the POMs extracted from the translational degrees of freedom (DOFs) of continuous structures in bending. Although the POMs are not mass-orthogonal (they are mutually orthogonal), we use them independently to estimate the frequencies of their respective modes as

$$f_i = \frac{1}{2\pi}\sqrt{R(v_i)}. \tag{3}$$

Consequently, the procedure is ad hoc and there is no guarantee that the estimated frequencies will correspond to the natural frequencies of the nonlinear systems under study. Nevertheless, it will be shown that the RQ-based procedure will lead to physically meaningful results, indicating that the computed POMs are close to the linear modes of the systems considered.

2.3 The Wavelet-Bounded Empirical Mode Decomposition

The empirical mode decomposition (EMD) proposed by [11] decomposes an oscillatory signal into a finite basis of nearly orthogonal, monochromatic intrinsic mode functions (IMFs). By using a sifting algorithm, EMD decomposes an oscillatory signal, $x(t)$, into N nearly orthogonal IMFs that satisfy

$$x(t) = \sum_{i=1}^{N} c_i(t) + R_{N+1}(t), \qquad \max\left(R_{N+1}(t)\right) < \tau, \tag{4}$$

where $c_i(t)$ is the ith IMF and $R_{N+1}(t)$ is the remainder signal with an amplitude less than the tolerance τ. In theory, each IMF possesses a single characteristic time scale such that the IMF is physically and mathematically representative of a single time scale contained in the original signal [19, 27, 32]. However, in practice, applying EMD often results in more IMFs than the number of characteristic time scales present in the original signal (i.e., the method yields spurious, non-physically meaningful IMFs which need to be eliminated before the dynamical analysis can commence), and care must be taken to select only the physically meaningful IMFs from the extracted ones [10–12].

Another pitfall of EMD is the issue of mode mixing, where a single IMF contains multiple components at different frequencies and, therefore, is not representative of any single time scale contained in the original signal. The wavelet-bounded EMD (WBEMD) [25] solves the issue of mode mixing by isolating each IMF around the frequency of a particular component (NNM). This is accomplished by first applying EMD to the signal combined with a masking signal [3],

$$s(t) = \alpha \max\left[z_i(t)\right] \sin(\beta \omega_i t), \tag{5}$$

where α and β are free parameters used by the optimization routine, ω_i is the frequency of the component being extracted, and

$$z_i(t) = x(t) - \sum_{q=1}^{i-1} c_q(t). \tag{6}$$

Following the application of EMD, the IMF is transformed to the maximum wavelet domain [25], where a bounding function is fitted over the IMF. Finally, the isolation of the IMF is measured by computing the area under the bounding function. It follows that well-separated IMFs result in a bounding-function area that is smaller than that of poorly separated IMFs. Thus, WBEMD minimizes the bounding-function area by adjusting the masking-signal parameters, α and β such that a well-separated IMF is extracted. The use of WBEMD will be critical in the next section, where we will use the IMFs to demonstrate that the proposed method captures these strongly nonlinear interactions while relying only on the systems known linear properties.

2.4 The Proposed Method

The proposed method requires that the system be naturally described by evolving time scales and a characteristic, time-varying energy quantity, that the formulation of the RQ operator be permitted, and that non-mixed response data is available, which reflects the fact that the method is data-driven. By "non-mixed," we mean that all variables or measurements in the response data must possess the same units of measure (i.e., all displacements or accelerations) to ensure that the results from POD are meaningful [2]. Further assumptions are provided in [23]. If the RQ operator cannot be formulated for the system, the method can still be applied using the POMs and their time-varying shapes instead of estimated frequency-energy plots. For mechanical structures undergoing linear and nonlinear vibrations, the modal characteristics of the system and mechanical energy serve as the evolving time scales and characteristic, time-varying energy quantity, respectively. For such systems, the RQ operator is formulated using linear models (FE models in this work) updated to capture the relevant modal properties of the experimental systems. We refer the reader to [5, 8, 28] for discussions of linear model updating. The response data in this work takes the form of displacement response data, which is obtained by numerical integration and filtering of measured acceleration responses.

The proposed method is divided into two processes: first, the nonlinearity is characterized and the accompanying strongly nonlinear modal interactions are identified using the RQ-FEP created using the POMS extracted from the displacement response. Second, the user computes the characteristic displacement (defined below), creates a RQ frequency-displacement plot (RQ-FDP) and identifies the nonlinearity by fitting a model to the RQ-FDP. The method is summarized by the following steps:

1. For n measurement coordinates, extract n POMs using SVD from windowed segments of a single time record.
2. Using the POMs, compute the estimated RQs for the NNMs within the frequency range of interest and plot these as functions of energy or time.
3. Characterize the nonlinearity and identify the modal interactions present in the measured response using the RQ-FEP.
4. Compute the characteristic displacement as defined for the system and plot the RQ estimates as functions of that characteristic displacement to form the RQ-FDP.
5. Based on the previous characterization, propose a model for the nonlinearity and derive the frequency-displacement relationship.
6. dentify the unknown parameters explicitly or using an optimization routine.

The characteristic displacement for the window defined by the interval $[T_1, T_2]$ is

$$\delta_c = \frac{1}{T_2 - T_1} \int_{T_1}^{T_2} |\delta| dt, \tag{7}$$

where δ is the relative displacement between the attachment and the point of attachment on the structure. For discrete signals, the characteristic displacement is defined

as

$$\delta_c = \frac{1}{N}\sum_{n=1}^{N} |\delta_n|, \tag{8}$$

for N points in the interval $[T_1, T_2]$. The resulting characteristic displacement enables us to plot the estimated frequencies as functions of displacement. In this work, we consider a local nonlinear attachment in the form of an NES and model the nonlinearity as $\alpha|\delta|^{\beta}\delta$ where δ is the relative displacement between the NES and its attachment points. For this nonlinearity, the equation of motion for the NES is

$$\ddot{u}_{NES} + \frac{d}{m}\dot{\delta} + \left(\omega_n^2 + \frac{\alpha}{m}|\delta|^{\beta}\right)\delta = 0, \tag{9}$$

and, replacing the relative displacement with the characteristic displacement, the displacement-dependent frequency equation is

$$f(\delta_c) = \frac{1}{2\pi}\sqrt{\omega_n^2 + \frac{\alpha}{m}\delta_c^{\beta}}. \tag{10}$$

As will be seen in Sect. 4, if the estimated frequency of the NES intersects the ith NNM with frequency f_i at the characteristic displacement δ_i, then we can relate α to β by requiring that $f(\delta_i) = f_i$. Thus,

$$\alpha = \frac{m}{\delta_i^{\beta}}\left((2\pi f_i)^2 - \omega_n^2\right), \tag{11}$$

and substituting (11) into (10) results in

$$f(\delta_c) = \frac{1}{2\pi}\sqrt{\omega_n^2 + \left((2\pi f_i)^2 - \omega_n^2\right)\left(\frac{\delta_c}{\delta_i}\right)^{\beta}}. \tag{12}$$

The remaining parameter is identified using an optimization routine (described in [24]) that maximizes the R-squared value between the RQ-FDP for the NES and the model in (12).

3 Detection of Strongly Nonlinear Modal Interactions

The described methodology is validated by being applied to the experimentally measured response of the cantilever shown in Fig. 1a. The beam is low-carbon steel, 0.749 m long with a 0.045×0.008 m^2 cross section and was connected at 0.7 m from its fixed end to two 0.0762 m long steel wires with of diameter 0.0012 m. The wires were attached to a steel shaft extended from the beam via two shaft collars. In

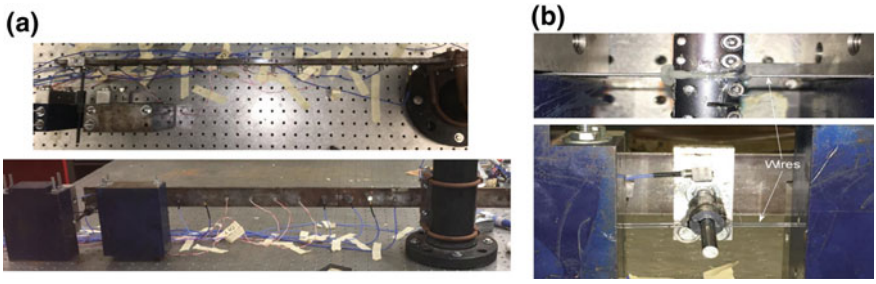

Fig. 1 **a** Top and front view of beam used in experiments. **b** Top and front view of nonlinear attachment. Reprinted with permission from [23]

order to achieve a 3:1 IR with a low-amplitude excitation, the length of the beam and the attachment shown in Fig. 1b were tuned in such a way that the frequency ratio of the two first NNMs was close to 3:1. The beam was excited at the position of the attachment by an impulse from a PCB Piezotronics modal impact hammer (model 086C01). Using PCB accelerometers (models U356A11 and Y353B17) with nominal sensitivities of 1 mV/(m/s2) along with VibPilot hardware (m+p International, Hannover, Germany) and m+p analyzer software, the acceleration responses of 14 locations along the beem were recorded for a duration of 2 s with 16384 Hz sampling rate. Measurements showed that the 9th accelerometer was saturated, and therefore the corresponding data was removed from the data set before analysis. To compute the velocities, the accelerations were numerically integrated and filtered, using a third-order Butterworth high-pass filter with a cutoff frequency of 18 Hz. Numerically integrating the velocities and then high-pass filtering the resulting signal with a cutoff frequency of 10 Hz, the displacements were computed. Additionally, before and after each integration the temporal means of the signals were subtracted so that the accelerations, velocities and displacements had zero mean.

The proposed method is used to study the displacement response of the beam subjected to the large amplitude impact shown in Fig. 2a. The nonstationary nature of the displacement can be seen in both the wavelet and Fourier spectra shown in Fig. 2b. The FFT shows that the first and the second NNMs cover frequency ranges from 21.6 to 31.5 Hz and 68.8 to 73 Hz, respectively, while the third NNM contains only a single peak at 186.6 Hz. Looking at the wavelet spectra of the displacement, the hardening nature of the nonlinearity can be seen; for instance, the first NNM frequency decreases from 31 to 21.5 Hz as the total energy of the system decreases due to dissipation.

Since the method does not require a priori knowledge of the nonlinearity, the nonlinearity was not identified in this work, and the attachment was modeled as a point mass and a discrete linear spring from the beam to ground. For this model, the mass of the attachment was measured to be 0.171 kg and the density of the beam was chosen to be 7800 kg/m3. By matching the first six bending eigenfrequencies of the beam, found from the low-amplitude impact experiment, with those obtained

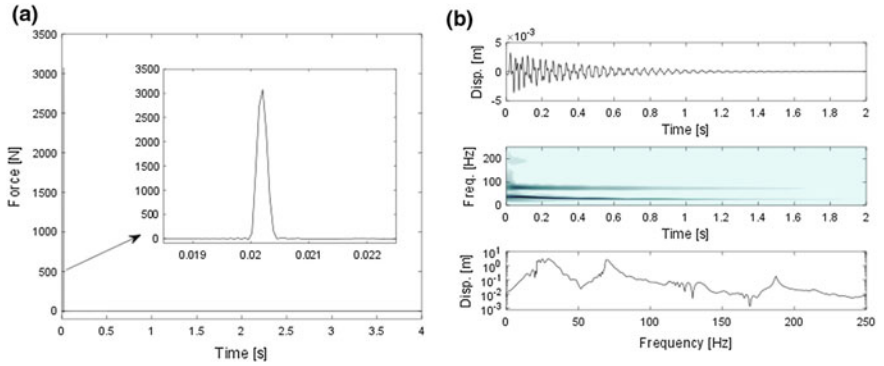

Fig. 2 **a** High-amplitude, impulsive load applied at nonlinearity location, **b** Time series, wavelet transform, and FFT of the displacement at the nonlinearity location (integrated from accelerometer measurements). Reprinted with permission from [23]

from an FE model of the beam using Euler–Bernoulli beam elements, the elastic modulus of the beam and the linear stiffness of the attachment were identified. The GlobalSearch function of MATLAB was used to perform a global minimization of the error norm

$$\varepsilon_k = \sum_{n=1}^{6} \frac{\left|\omega_n^{Exp} - \omega_n^{FE}\right|}{n\omega_n^{Exp}}, \tag{13}$$

where $|\cdot|$ denotes absolute value. The contribution of each mode is weighted by its modal number. Note that by using Guyan reduction method, the rotational DOFs were condensed out of the FE matrices. After performing the global search, the identified values for elastic modulus and linear stiffness turned out to be 1.90×10^{11} N/m^2 and 10854 N/m, respectively, and the average error for the first six bending modes between the experimental and FE model eigenfrequencies was 2.73%.

According to the data presented in Fig. 2b, the energy of the experimental system dissipates quickly within the recorded time window. Thus, in order to capture and analyze the transient response of the experimental system, the 2 s time window needs to be divided into sufficiently small segments to capture at least a half cycle of the first NNM as well as the transient response of the system. Consequently, for the experimental system under study, the 2 s time window is divided into 92 nonoverlapping time segments, each with 0.0216 s duration. Notice that the first 0.0251 s portion of the recorded response is excluded from the data set because this portion was recorded before the impact was applied. Thirteen POMs are extracted out of each time segment. Because of the damping effects, internal resonances are more likely to happen between the first two NNMs than between the higher NNMs, so only the POMs corresponding to the first and second NNMs are taken into consideration. To obtain the final POMs with least effects of measurement noise, a sixth-order polynomial with zero constant, linear and quadratic terms is fitted to each POM at

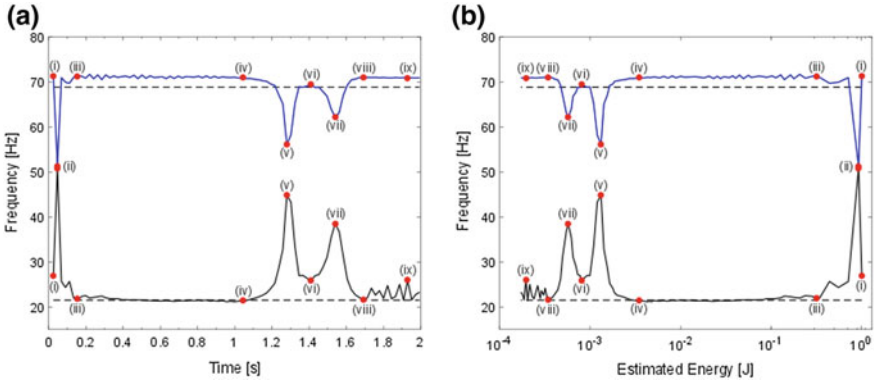

Fig. 3 RQ frequency computed using the POMs corresponding to the first two NNMs plotted as a function of **a** time and **b** estimated energy. The black dashed lines represent the experimental frequencies at low energies. Reprinted with permission from [23]

each accelerometer location. Note that data from the 9th accelerometer was not used because of the reason explained before.

That the first capture happens in such a short period of time implies that a great amount of energy is dissipated quickly, which is not caused only by the viscous damping in the system. The other factor that causes this rapid dissipation of energy is the IR that is indicated by the first spike in Fig. 3a, b. During this modal interaction, the energy in the first NNM is irreversibly transferred to the second NNM, and there it gets dissipated at a higher rate. Looking at the wavelet spectrum of the system during the first spike, i.e. Fig. 3b, one can see that the frequency ratio of the second and first NNMs is 72 to 28.6 Hz, which is approximately a 5:2 ratio. This ratio indicates that first spike is the result of a 5:2 IR.

While the first spike in the RQ happens in a short period of time, the second and third spikes occur for a longer period of time and almost right after each other. These two spikes being close to each other indicates that the third IR happens almost immediately after the second IR, which corresponds to the second spike. According to the wavelet spectrum shown in Fig. 2b, the frequencies of the first and second NNMs during these IRs are 23 and 68.8 Hz, respectively, which indicate 3:1 IRs during the second and third spikes. It should be mentioned that the system was tuned so that a 3:1 IR can be achieved at low energy levels, which explains why the last two IRs remain active for a longer period of time compared to the first spike. Moreover, because of this tuning, for a certain change in the energy level of the system, the frequency change around the 3:1 IR is much lower than that around the 5:2 IR. For this reason, it can be concluded that the energy threshold for 3:1 IR to happen is much larger than the threshold for a 5:2 IR to happen. Several spikes with small amplitude on the curve for the first spike can be seen from 1.7 to 2 s, which one may consider as modal interactions. Because the first POM corresponding to these spikes corresponds to only the first NNM (specifically, the only node is at the

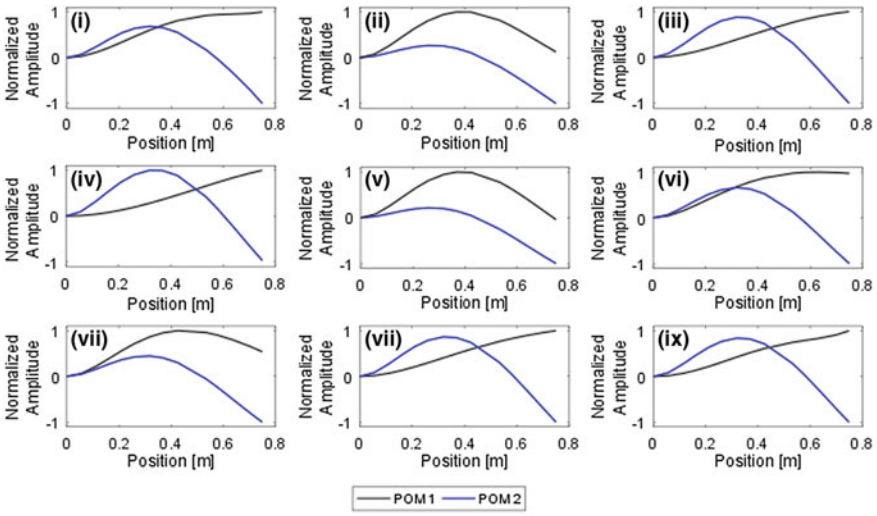

Fig. 4 POMs 1 and 2 for each of the nine red dots in Fig. 3. Reprinted with permission from [23]

fixed boundary), we can conclude that these spikes are results of signal decay, small measurement and numerical errors.

The POMs corresponding to the nine red dots in Fig. 3 are shown in Fig. 4. While away from the spikes, i.e. at points i, iii, iv, vi, viii, and ix, the POMs represent the periodic solutions of their corresponding NNMs. However, on the spikes, i.e. at points ii, v, and vii, the POMs become similar to the periodic solution of the second NNM, in which both POMs have one anti-node near the center and one at the free end. These results are very similar to those obtained for the computational system, which is further evidence that the previous theoretical results represent physical phenomena. Also, in accordance to what was explained before, one can clearly see that the POMs corresponding to the first and second NNMs are not similar on spike ix. This means that even though there is a spike on point ix, but this spike does not represent any modal interactions between the first and second NNMs. Additionally, the slight oscillation that has appeared in the first POM is caused by small measurement and numerical errors that result in deviation from the linear, experimental natural frequency.

The existence of IRs is demonstrated by computing the slow phases of the NNMs. Up to this point, WBEMD is applied to the response presented in Fig. 2b, four well-separated IMFs which represent four individual NNMs are extracted and their corresponding phase trajectories are computed. Since it was predicted that the first modal interaction corresponds to a 5:2 IR, the corresponding phase trajectory, along with a zoomed-in view of its initial portion, is plotted in Fig. 5a. The single loop in the zoomed-in view occurs between 0.02 and 0.13 s, which is the duration of the first spike shown in Fig. 3. The presence of this loop and its correspondence with the first spike is a further proof that the first spike is indeed the result of a 5:2 IR and not a

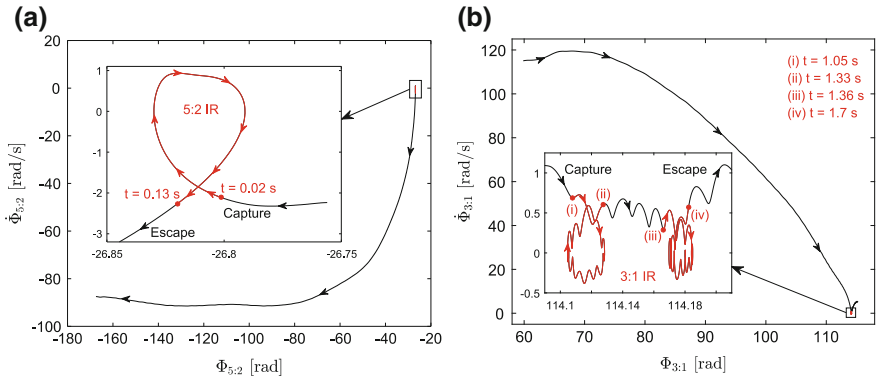

Fig. 5 **a** Phase trajectory for $\Phi_{5:2}(t) = 5\theta_1(t) - 2\theta_2(t)$, which corresponds to the second and third spikes in Fig. 3. **b** Phase trajectory for $\Phi_{3:1}(t) = 3\theta_1(t) - 1\theta_2(t)$, which corresponds to the first spike in Fig. 3. Reprinted with permission from [23]

numerical artifact. Figure 5b and its zommed-in views depict 3:1 trajectories and the two loops corresponding to the second and third spikes, respectively. These loops are non-time-like and indicate that 3:1 IRs occur between the first and second NNMs. As before, the interval in which each loop occurs corresponds to the duration of the loops corresponding spikes. Moreover, the fact that there are two loops in the 3:1 trajectory plot confirms the modal interactions represented as spikes in Fig. 3.

According to the presented and discussed results, the current method proves to be a valuable and powerful tool for detecting strongly nonlinear modal interactions directly from measured data. By means of this method one can get significant insight into the governing nonlinear physics of the response of dynamical systems with smooth and local nonlinearities. Hence, this method is a valuable tool to gain a thorough understanding of the transient responses of strongly nonlinear dynamical systems, including nonlinear modal interactions caused by IRs.

4 Nonlinear System Identification of a Strongly Nonlinear Attachment

To demonstrate the NSI procedure presented in Sect. 2.4, we apply it to the experimentally measured response of the cantilevered wing in Fig. 6a. The wing is aluminum and detailed dimensions can be found in [24]. A local NES is attached to the free end of the wing. The nonlinearity is realized through transverse displacements of thin steel wires, which are fixed at both ends and each have a diameter of 0.00036 m and a length of 0.0552 m. The attachment, depicted in Fig. 6b, results in a hardening-type, ideally essential nonlinearity; however, the resulting force-displacement relationship is not purely nonlinear. Instead, a small linear stiffness is introduced by pretension in

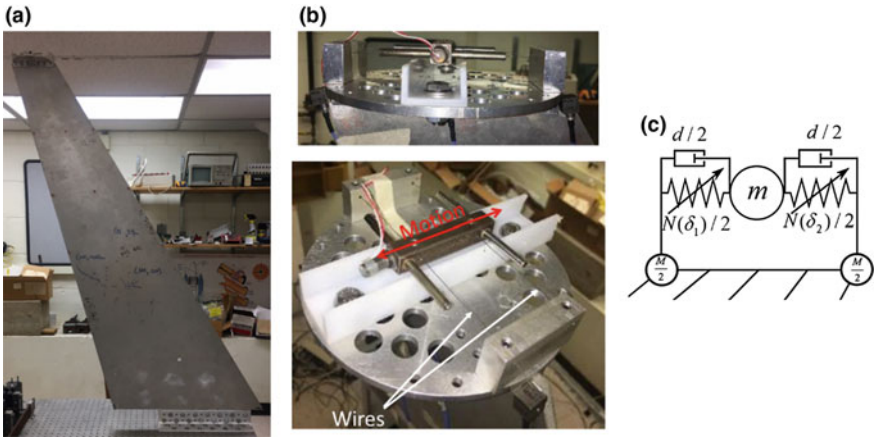

Fig. 6 **a** Front view of wing used in experiments. **b** Front and top view of the nonlinear attachment. **c** Model used for the nonlinear attachment and baseplate. Modified and reprinted from [24]

the wires due to the boundary conditions, resulting in a natural frequency associated with the motion of the NES. The diameter of the wires was tuned such that a 1:1 IR between the NES and the second NNM is realizable using a standard modal hammer. The acceleration responses of the wing and the NES were measured using PCB Piezotronics accelerometers (models U356A11 and Y353B17) for an impact applied using a PCB Piezotronics modal impact hammer (model 086C01). The acceleration response of the wing was measured at 14 location along the leading and trailing edges. Using VibPilot hardware (m+p International, Hannover, Germany) and m+p analyzer software, the responses were measured for a duration of 8 s at a sampling rate of 4096 Hz. The displacement and velocity responses of the wing and NES were obtained using the same numerical integration scheme used in the prior experiments with the cantilever beam, except that the cut-off frequency was set to 2 Hz.

To demonstrate the proposed NSI method, we study the response of the wing to the impact depicted in Fig. 7a. The corresponding velocity response of the NES and the corresponding wavelet transform and frequency response function (FRF) are depicted in Fig. 7b. Both the wavelet and FRF reveal the nonstationary nature of the response. Full details of the model for the wing and NES are provided in [24]; we present a summary of the modeling procedure here. The wing is modeled using the FE mesh described in [24] using an elastic modulus of N/m2 and a density of 2700 kg/m^3. The added mass of the base plate is modeled as two lumped masses at the leading and trailing edges of the free end of the wing, which allows the added mass to affect both the bending and torsional NNMs. The mass of the base plate was measured to be 0.408 kg. The attachment is modeled as a discrete mass with linear and nonlinear springs coupling it to the leading and trailing edges. The mass of the attachment is found to be 0.908 kg, and the frequency of the NES at small energy is 8.36 Hz. The linear stiffness coupling the NES to the wing was computed to be 241.5

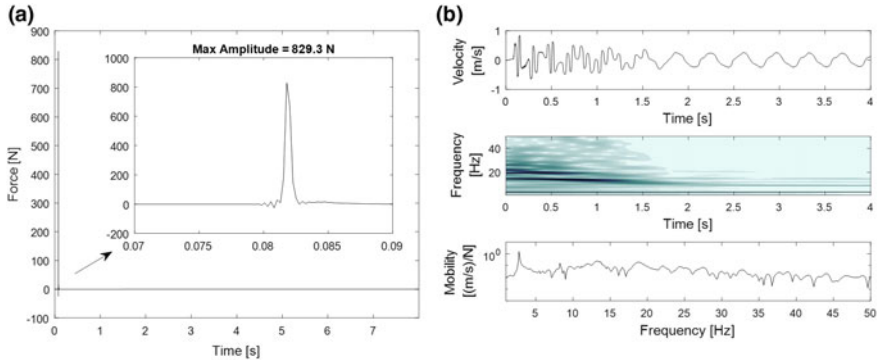

Fig. 7 **a** High-amplitude, impulsive load applied at nonlinearity location, **b** Time series, wavelet transform, and FRF of the velocity of the NES (integrated from accelerometer measurements). Reprinted from [24]

N/m using an optimization routine that minimized the error between the frequency of the NES NNM in the FE model and that of experimental system.

As in Sect. 3, the time window is divided into segments that are sufficiently small to capture the transient nature of the response, but large enough to capture at least one-half cycle of the first NNM. For this system, we use a segment length of 0.173 s and consider the response in the window defined by [0.09,7.5], which results in a total of 42 nonoverlapping time segments. The first 0.09 s of the measurement is excluded from the analysis because it contained the response of the wing to ambient vibration before the impact. For each time segment, we extract 15 POMs; however, only those corresponding to the first four NNMs are analyzed. A fourth-order polynomial with no constant or linear terms is fitted to each POM, which reduces the effect of measurement noise. The final POMs are created by evaluating the polynomials at each accelerometer location.

Using the POMs, we compute the RQ for the first four NNMs for each time segment and plot them as functions of time in Fig. 8a. In this plot, there are two periods of IR between the NES and the second NNM. The first occurs from an energy of 0.363–0.103 J and the second corresponds to the spike that occurs at 0.0880 J. For this system, the relative displacement is defined as the difference between the displacement of the NES and the average of the displacement of the leading and trailing edges at the tip of the wing. Following the procedure presented in Sect. 2.4, we compute the characteristic displacement defined by (8) for each segment and plot the RQ in Fig. 8b, where the frequency-displacement pairs have been sorted in ascending order based on the displacements. Using the low-energy frequency of the second NNM, $f_2 = 14.34$ Hz, the corresponding characteristic displacement is found to be $\delta_2 = 0.00150$ m using linear interpolation. Using the optimization routine described in [24], the parameters $\alpha = 3.4887 \times 10^8$ N/m$^{3.0714}$ and $\beta = 2.0714$ are found. The resulting frequency-displacement curve for the identified parameters is depicted as the red line in Fig. 8b.

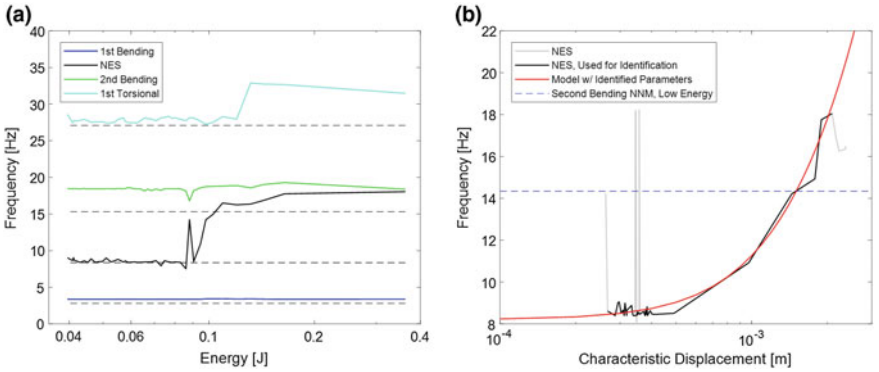

Fig. 8 **a** The RQ-FEP for the response depicted in Fig. 7. **b** Comparison of the RQ FDP for the NES and the identified model. Modified and reprinted from [24]

The identified model is validated by comparing its response to that of the exact system for multiple forcing values. Although the nonlinearity is identified using displacements, the displacement response is dominated by the first bending mode (which is why this NNM was filtered out from the characteristic displacement), and effects from higher NNMs are difficult to ascertain. Instead, we present the velocity responses of the measured and identified systems in Fig. 9a for the impact depicted in Fig. 7a, which corresponds to the response used to perform the identification. The velocity responses for impacts of 264.8, 504.4 and 1158.6 N are shown in Fig. 9b–d, respectively, and correspond to measurements that were not used to perform the identification. The match between the velocity responses, the wavelets and the FRFs confirm that the identified system accurately models the measured system for multiple forcing impacts. These results validate the proposed method for nonlinear system identification of strongly nonlinear attachments in both theoretical and experimental frameworks.

5 Concluding Remarks

We studied the experimental responses of two mechanical systems with smooth, local nonlinearities. The first system was a cantilever beam with a smooth, nonlinear spring attached near its free end and the second system was a model airplane wing with a local NES connected to the tip. Using POD, energy-dependent POMs were extracted from the displacement responses of each system, and were representative of the NNMs governing each system. For both systems, the frequencies of the NNMs were estimated using the discrete RQ with the POMs as trial vectors. The estimated frequencies were plotted as functions of time and energy, which revealed the presence of non-smooth perturbations (spikes), which appeared to indicate strongly nonlinear

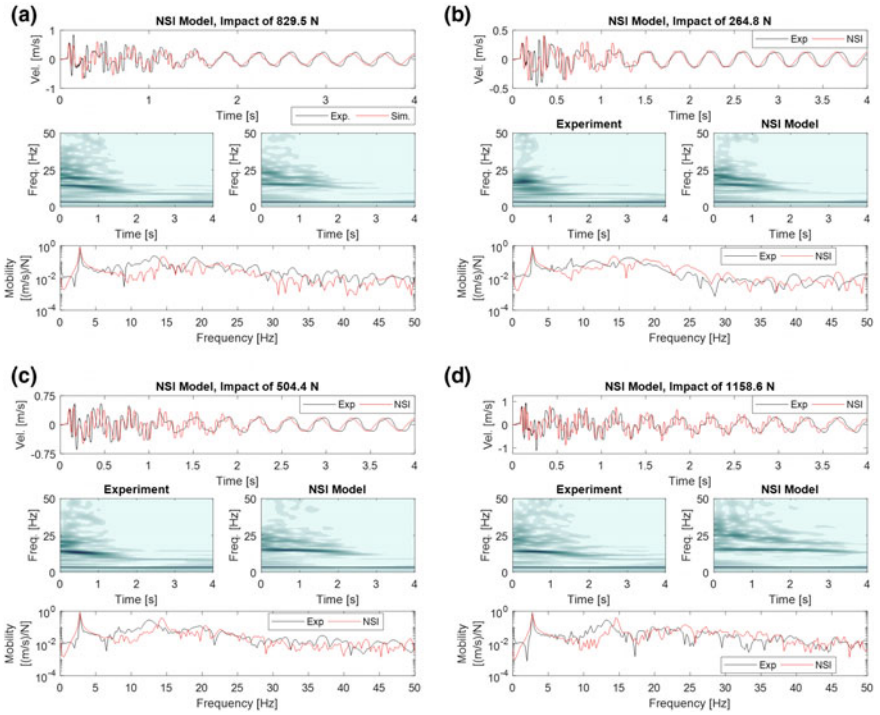

Fig. 9 The measured and predicted response for impacts of **a** 829 N, **b** 265 N, **c** 504 N and **d** 1158 N. Modified and reprinted from [24]

modal interactions. The POMs corresponding to the points off and on the spikes were found to be similar to the periodic solutions of non-interacting and interacting NNMs, respectively.

The displacement response of the beam was decomposed into well-separated IMFs using WBEMD, and using the Hilbert transform a phase variable for each spike was defined and the corresponding phase trajectories examined. The spikes were found to correspond to periods of non-time-like behavior (loops), which indicated the presence of strongly nonlinear IRs. The estimated frequencies of the model wing were also plotted as functions of characteristic displacement, which was used to identify the nonlinear stiffness coupling the NES to the wing. The resulting model accurately reproduced the relevant nonlinear dynamics for all four loading cases investigated.

Funding. This material is based upon work supported in part by the National Science Foundation Graduate Research Fellowship under Grant No. DGE-1144245.

Disclaimer. Any opinion, findings, and conclusions or recommendations expressed in this material are those of the authors(s) and do not necessarily reflect the views of the National Science Foundation.

References

1. Attar, M., Karrech, A., Regenauer-Lieb, K.: Non-linear modal analysis of structural components subjected to unilateral constraints. J. Sound Vib. **389**, 380–410 (2017). https://doi.org/10.1016/j.jsv.2016.11.012
2. Chatterjee, A.: An introduction to the proper orthogonal decomposition. Curr. Sci. **78**(7), 808–817 (2000)
3. Deering, R., Kaiser, J.: The use of a masking signal to improve empirical mode decomposition. In: IEEE International Conference on Acoustics, Speech, and Signal Processing (ICASSP '05), vol. 4, pp. 485–488. (2005). https://doi.org/10.1109/ICASSP.2005.1416051
4. Ehrhardt, D.A., Allen, M.S., Beberniss, T.J., Neild, S.A.: Finite element model calibration of a nonlinear perforated plate. J. Sound Vib. **392**, 280–294 (2017). https://doi.org/10.1016/j.jsv.2016.12.037
5. Ewins, D.J.: Modal Testing: Theory, Practice, and Application. Research Studies Press, Philadelphia (2000)
6. Feeny, B.F., Kappagantu, R.: On the physical interpretation of proper orthogonal modes in vibrations. J. Sound Vib. **211**(4), 607–616 (1998). https://doi.org/10.1006/jsvi.1997.1386
7. Flandrin, P., Rilling, G., Goncalves, P.: Empirical mode decomposition as a filter bank. IEEE Signal Process. Lett. **11**(2), 112–114 (2004). https://doi.org/10.1109/LSP.2003.821662
8. Friswell, M.I., Mottershead, J.E.: Finite Element Model Updating in Structural Dynamics. Springer Science and Business Media, Berlin (1995)
9. Herrera, C.A., McFarland, D.M., Bergman, L.A., Vakakis, A.F.: Methodology for nonlinear quantification of a flexible beam with a local, strong nonlinearity. J. Sound Vib. **388**, 298–314 (2017). https://doi.org/10.1016/j.jsv.2016.10.037
10. Huang, N., Wu, M.L., Long, S., Shen, S., Qu, W., Gloersen, P., Fan, K.: A confidence limit for the empirical mode decomposition and Hilbert spectral analysis. Proc. Royal Soc. A: Math. Phys. Eng. Sci. **459**(2037), 2317–2345 (2003). https://doi.org/10.1098/rspa.2003.1123
11. Huang, N.E., Shen, Z., Long, S.R., Wu, M.C., Shih, H.H., Zheng, Q., Yen, N.C., Tung, C.C., Liu, H.H.: The empirical mode decomposition and the Hilbert spectrum for nonlinear and non-stationary time series analysis. Proc. Royal Soc. A: Math. Phys. Eng. Sci. **454**(1971), 903–995 (1998)
12. Huang, N.E., Shen, Z., Long, S.R.: A new view of nonlinear water waves: the Hilbert spectrum 1. Annu. Rev. Fluid Mech. **31**(1), 417–457 (1999). https://doi.org/10.1146/annurev.fluid.31.1.417
13. Karhunen, K.: Uber lineare methoden in der wahrscheinlichkeitsrechnung, (1947)
14. Kerschen, G., Golinval, J.C., Vakakis, A., Bergman, L.: The method of proper orthogonal decomposition for dynamical characterization and order reduction of mechanical systems: an overview. Nonlinear Dyn. **41**(1–3), 147–169 (2005). https://doi.org/10.1007/s11071-005-2803-2
15. Kerschen, G., Worden, K., Vakakis, A.F., Golinval, J.C.: Past, present and future of nonlinear system identification in structural dynamics. Mech. Syst. Signal Process. **20**(3), 505–592 (2006). https://doi.org/10.1016/j.ymssp.2005.04.008
16. Kosambi, D.: Statistics in function space. J. Indian Math. Soc. **7**(1), 76–88 (1943)
17. Kurt, M., Eriten, M., McFarland, D.M., Bergman, L.A., Vakakis, A.F.: Strongly nonlinear beats in the dynamics of an elastic system with a strong local stiffness nonlinearity: analysis and identification. J. Sound Vib. **333**(7), 2054–2072 (2014). https://doi.org/10.1016/j.jsv.2013.11.021
18. Lee, Y., Nucera, F., Vakakis, A., McFarland, D., Bergman, L.: Periodic orbits, damped transitions and targeted energy transfers in oscillators with vibro-impact attachments. Phys. D: Nonlinear Phenom. **238**(18), 1868–1896 (2009). https://doi.org/10.1016/j.physd.2009.06.013
19. Lee, Y.S., Tsakirtzis, S., Vakakis, A.F., Bergman, L.A., McFarland, D.M.: Physics-based foundation for empirical mode decomposition. AIAA J. **47**(12), 2938–2963 (2009). https://doi.org/10.2514/1.43207

20. Lee, Y.S., Vakakis, A.F., McFarland, D.M., Bergman, L.A.: A global-local approach to nonlinear system identification: a review. Struct. Control Health Monit. **17**(7), 742–760 (2010). https://doi.org/10.1002/stc.414
21. Lee, Y.S., Tsakirtzis, S., Vakakis, A.F., Bergman, L.A., McFarland, D.M.: A time-domain nonlinear system identification method based on multiscale dynamic partitions. Meccanica **46**(4), 625–649 (2011). https://doi.org/10.1007/s11012-010-9327-7
22. Lévy, P., Loève, M.: Processus stochastiques et mouvement brownien. Gauthier-Villars, Paris (1948)
23. Moore, K.J., Kurt, M., Eriten, M., McFarland, D.M., Bergman, L.A., Vakakis, A.F.: Direct detection of nonlinear modal interactions from time series measurements. Mech. Syst. Signal Process. (2018). https://doi.org/10.1016/j.ymssp.2017.09.010. (in press)
24. Moore, K.J., Kurt, M., Eriten, M., McFarland, D.M., Bergman, L.A., Vakakis, A.F.: Data-driven system identification of strongly nonlinear attachments, (2018). (in preparation)
25. Moore, K.J., Kurt, M., Eriten, M., McFarland, D.M., Bergman, L.A., Vakakis, A.F.: Wavelet-bounded empirical mode decomposition for measured time series analysis. Mech. Syst. Signal Process. **99**, 14–29 (2018)
26. Noël, J.P., Kerschen, G.: Nonlinear system identification in structural dynamics: 10 more years of progress. Mech. Syst. Signal Process. **83**, 2–35 (2017). https://doi.org/10.1016/j.ymssp.2016.07.020
27. Sharpley, R.C., Vatchev, V.: Analysis of the intrinsic mode functions. Constr. Approx. **24**(1), 17–47 (2005). https://doi.org/10.1007/s00365-005-0603-z
28. Silva, J.M.M.: Modal Analysis and Testing. Springer, Netherlands, Dordrecht (1999)
29. Vakakis, A., Gendelman, O., Bergman, L., McFarland, D., Kerschen, G., Lee, Y.: Nonlinear targeted energy transfer in mechanical and structural systems I. Solid Mech. Appl. **156**, 1–1033 (2008)
30. Vakakis, A.F., Manevitch, L.I., Mikhlin, Y.V., Pilipchuk, V.N., Zevin, A.: Normal Modes and Localization of Nonlinear Systems. Wiley, New York (1996)
31. Vakakis, A.F., Bergman, L.A., McFarland, D.M., Lee, Y.S., Kurt, M.: Current efforts towards a non-linear system identification methodology of broad applicability. Proc. Inst. Mech. Eng. Part C: J. Mech. Eng. Sci. **225**(11), 2497–2515 (2011). https://doi.org/10.1177/0954406211417217
32. Vatchev, V., Sharpley, R.: Decomposition of functions into pairs of intrinsic mode functions. Proc. R. Soc. A: Math. Phys. Eng. Sci. **464**(2097), 2265–2280 (2008)
33. Wu, Z., Huang, N.E.: Ensemble empirical mode decomposition: a noise-assisted data analysis method. Adv. Adapt. Data Anal. **01**(01), 1–41 (2009). https://doi.org/10.1142/S1793536909000047

Non-smooth Spatial and Temporal Substitutions in Impact Dynamics

Valery N. Pilipchuk

Abstract This paper presents an overview of physical ideas and mathematical methods for implementing non-smooth and discontinuous substitutions in dynamical systems. A general purpose of such substitutions is to bring the differential equations of motion to the form, which is convenient for further use of analytical and numerical methods of analyses. Three different approaches are discussed as follows: positional coordinate transformation, state variables transformation, and temporal transformations. Also a new type of substitutions eliminating both infinite and step-wise discontinuities and thus completely smoothing the system is suggested. Different illustrating examples are introduced.

1 Introduction

Discontinuities of states in physical models often represent the result of intentional idealization of abrupt but still smooth changes in dynamical characteristics. Such idealizations help to skip complicated details of modeling on relatively narrow intervals of impact interactions by considering their integral effects. However, every discontinuity of states actually breaks the system into two systems, and thus increases the system dimension as many as twice even though the equations may remain the same before and after the collision. This work will outline and illustrate different ideas of preventing the dimension increase when dealing with discontinuities of dynamic states. Note that many analytical methods dealing with dynamical systems preliminarily adapt the equations of motions through different substitutions and transformations in order to ease further steps of analyses. Although a universal recipe for such substitutions is rather difficult to suggest, there are some general principles to follow. For instance, classes of transformations should comply with classes of systems considered. The term *classes* remains intentionally unspecified here since it may indicate any generic feature of the model, such as linearity or nonlinearity, a class

V. N. Pilipchuk (✉)
Wayne State University, Detroit, MI 48202, USA
e-mail: pilipchuk@wayne.edu

I. V. Andrianov et al. (eds.), *Problems of Nonlinear Mechanics and Physics of Materials*, Advanced Structured Materials 94,
https://doi.org/10.1007/978-3-319-92234-8_8

of smoothness, or other mathematical properties. In particular, this work focuses on substitutions including nonsmooth or discontinuous functions.

Generally speaking, differential operations with nonsmooth functions require generalized interpretations of equalities as integral identities, in other words, in terms of distributions [39]. In linear cases, such interpretations are usually quite straightforward since distributions represent linear functionals [50]. Nonlinear models however impose certain structural constraints on the presence of non-smooth or discontinuous functions in differential equations [5, 6]. Moreover, whether or not some combinations of discontinuous functions are meaningful may depend upon physical contents of variables participating in such combinations [23]. From the mathematical standpoint, physical interpretations allow for narrowing families of smooth functions that have discontinuities in their asymptotic limits. As a result, some combinations of discontinuous functions may acquire certain meanings of distributions.

To conclude this, as follows from the above remarks, despite of the universal notations, discontinuous functions may still inherit some features of the corresponding generating families of smooth functions. *Therefore, analytical manipulations with discontinuous and delta-functions must account for both physical content of the problem and mathematical structure of equations*. Unfortunately, intuitive use of delta-functions may lead to mathematical ambiguities and logical missteps; explanations and illustrations of the related issues from different standpoints can be found in [5, 54]. This happens by two main reasons. First, according to the so-called sequential approach, the delta-function is actually not a function but the limit of very different sequences of functions or a linear integral operator in the theory of distributions. Second, the symbol of delta function is used sometimes just as a logical operator formalizing specifics of transitions through discontinuities, for instance, $\delta_-(t)$ or $\delta_+(t)$. In Sect. 2.2 below, the issue is illustrated on example discussed earlier in [5]. In the most direct way, such complications can be avoided by considering models on different time intervals and introducing appropriate matching conditions for the corresponding pieces of solutions. In many cases, however, the matching times are a priory unknown and must also be determined from the same matching conditions. As mentioned at the beginning, this work gives an overview of another approaches satisfying the matching conditions automatically through specific non-smooth transformations of variables. Briefly, topics of this paper are as follows: (1) Caratheodori equations and discontinuous substitutions [5] for systems under external pulses and wave propagation problems, (2) non-smooth positional coordinate transformations for impact systems with elastic perfectly stiff constraints and possible extensions on non-elastic constraints [52–54], (3) non-smooth state (phase) space transformation [11, 12, 14] and applications to modeling the impact dynamics with an arbitrary coefficient of restitution, and (4) generalizations of non-smooth temporal transformations [28, 29] for impact systems with one-sided barriers, periodic and modulated motions.

2 Nonsmooth Coordinates and Velocities

2.1 Systems with Delta-Pulses Included as Summands

Different types of differential equations with distributions were considered by Filippov [5]. In particular, it was shown that the effect of discontinuous singular terms can be included separately into specific discontinuous substitutions for unknown functions in such a way that new equations are free of singular terms. As a result, it becomes possible to prove the existence and investigate different properties of solutions with conventional qualitative tools. Note that the differential equations including distributions must be interpreted in a generalized way in terms of integral identities. In many cases, the corresponding generalization is based on the integral form of the differential equation $\dot{x} = f(t, x)$:

$$x(t) = x(t_0) + \int_0^t f(s, x(s))ds. \tag{1}$$

If the function $f(t, x)$ is discontinuous in t, but still continuous in x, then the functions satisfying (1) can be viewed as solutions of the equation $\dot{x} = f(t, x)$. Generally, integration in (1) should comply with the concept of Lebesgue integral. In this case, the function $f(t, x)$ does not have to be point-wise defined.[1] If $f(t, x)$ includes δ-functions as summands then some preliminary transformation may help to justify further manipulations. As a simple illustration, let us consider a single degree-of-freedom system whose velocity, $v = v(t)$, is described by the differential equation

$$\dot{v} + kv^3 = q\delta\,(t - t_1)\,, \tag{2}$$

where k, q and t_1 are constant parameters, and δ is the Dirac'delta function.

Equation (2) describes a unit-mass particle in a nonlinearly viscous media with the cubic dissipation law. In this case, the δ-input generates a step-wise discontinuity of the response $v(t)$ at $t = t_1$, nevertheless the nonlinear operation in (2) remains meaningful. Moreover, the δ-pulse can be eliminated from Eq. (2) by means of the following substitution

$$v = u + q\theta\,(t - t_1)\,, \tag{3}$$

where $u = u\,(t)$ is a new unknown function, and $\theta\,(t - t_1)$ is the Heaviside unit-step at $t = t_1$.

Substituting (3) in (2), and taking into account that $\dot{\theta}(t - t_1) = \delta\,(t - t_1)$ and $\theta^2\,(t - t_1) = \theta\,(t - t_1)$, gives equation

[1] Practically, such an extension almost never contradicts to physical contents of modeling; recall that the differential equations of motion are derived from variational principles formulated in the integral form.

$$\dot{u} + ku^3 = Q(u, q)\theta\,(t - t_1)\,, \tag{4}$$

where $Q = -(q^3 + 3uq^2 + 3u^2q)$.

In contrast to (2), Eq. (4) includes no δ -function and thus admits a visualization of its phase flow on the (t, v) -plane. Note that substitution (3) is easy to generalize on equation

$$\dot{v} = f(v, t) + \sum_{i=1}^{\infty} q_i \delta\,(t - t_i)\,, \tag{5}$$

where $f(v, t)$ is assumed to have no singularities within some domain of the (v, t)-plane, $\{q_i\}$ and $\{t_i\}$ are sets of constants.

In this case, the following substitution eliminates all the δ -functions from Eq. (5)

$$v = u(t) + \sum_{i=1}^{\infty} q_i \theta\,(t - t_i)\,. \tag{6}$$

Further generalization on the vector-form equations is quite obvious. Complications may occur however when the structure of original equations is changed as described in the Sect. 2.3. Finally, note that substitutions of type (3) and (6) as well as its different variations are widely used in the literature to describe moving discontinuity waves [8, 23, 51].

2.2 *Distributions as Parametric Inputs*

As mentioned in Sect. 1, using the delta-function intuitively may face some logical problems. The related example is considered below in this section based on the linear initial value problem [5]

$$\begin{aligned} \dot{v} + k\delta\,(t - t_1)\,v &= 0; \\ v(0) &= v_0, \end{aligned} \tag{7}$$

where k and $t_1 > 0$ are constant.

On first look, Eq. (7) may serve as an adequate model for a 1D motion of free particle striking a very narrow super-viscous layer at the neighborhood of time $t = t_1$. Since $\delta\,(t - t_1) = 0$ everywhere except for $t = t_1$ then, according to Eq. (7), $\dot{v} = 0$ in both subintervals $t < t_1$ and $t > t_1$. As a result, the velocity v is constant but may be different before and after the point $t = t_1$. Therefore, taking into account the initial condition suggests solution

$$v = v_0[1 - \lambda\theta\,(t - t_1)], \tag{8}$$

where λ is an unknown constant parameter quantifying the discontinuity of function $v(t)$, such that $v = v_0$ for $t < t_1$ and $v = -\lambda v_0$ for $t > t_1$.

However, Eq. (7) shows that the jump of the solution depends on the behavior of solution itself near the point $t = t_1$. Namely, integrating both sides of the equations over the interval $(t_1 - \varepsilon, t_1 + \varepsilon)$ and taking into account the basic property of δ-function gives $v(t_1 + 0) - v(t_1 - 0) = -kv(t_1)$, as $\varepsilon \to 0$. In this case, there is no certain choice for $v(t_1)$, or λ, and thus additional assumptions regarding the model are required to uniquely determine the velocity jump. This becomes even more clear after substitution (8) in (7) with the intent to find λ. After simple manipulations, such substitution gives

$$\theta(t - t_1)\delta(t - t_1) = \alpha\delta(t - t_1), \tag{9}$$

where $\alpha = \lambda^{-1} - k^{-1}$, or $\lambda = k/(1 + \alpha k)$.

Now, following the idea of distribution theory and taking into account the property of delta function brings (9) to the form

$$\int_{-\infty}^{\infty} \theta(t - t_1)\delta(t - t_1)dt = \alpha. \tag{10}$$

According to the property of delta-function, Eq. (10) formally gives $\theta(0) = \alpha$, which means that α can be any number from the interval $0 \le \alpha \le 1$, because zero is the point of step-wise discontinuity of the function θ. This just reminds the well known fact that the combination $\theta(t - t_1)\delta(t - t_1)$ has no certain meaning in the distribution theory, and therefore the number α on the right remains uncertain. Trying to resolve this uncertainty, let assume that $\theta_\varepsilon(t)$ is a sequence of differentiable functions such that $\theta_\varepsilon(t) \to \theta(t)$ and thus $d\theta_\varepsilon(t)/dt \to \delta(t)$ as $\varepsilon \to 0$ in the sense of so-called *weak limit,* for instance,

$$\begin{aligned} \theta_\varepsilon(t) &= \frac{1}{2}\left(1 + \tanh\frac{t}{\varepsilon^2}\right) \to \theta(t); \\ \delta_\varepsilon(t) &= \frac{d\theta_\varepsilon(t)}{dt} = \frac{1}{2\varepsilon^2}\cosh^{-2}\frac{t}{\varepsilon^2} \to \delta(t). \end{aligned} \tag{11}$$

Therefore, we assume that both functions $\theta(t)$ and $\delta(t)$ are generated by the same family of smooth functions $\theta_\varepsilon(t)$. Then the integral in Eq. (10) is calculated explicitly as

$$\lim_{\varepsilon\to 0}\int_{-\infty}^{\infty} \theta_\varepsilon(t)\frac{d\theta_\varepsilon(t)}{dt}dt = \frac{1}{2} = \alpha. \tag{12}$$

However, in our case, we cannot use the number $\alpha = 1/2$ for determining the discontinuity parameter λ in (8) as soon as there is no reason to believe that functions θ and δ, in (8) and (7), respectively, are generated by the same family of smooth functions. Moreover, it is rather not the case at all [34]. This can be illustrated with

replacing the function δ in Eq. (7) with its smooth pre-limit δ_ε defined in (11). The corresponding regular separable equation has the solution,

$$v = v_0 \exp\left[-\frac{1}{2}k\left(\tanh\frac{1}{\varepsilon^2} + \tanh\frac{t-t_1}{\varepsilon^2}\right)\right]$$

such that

$$v = v_0\{1 - [1 - \exp(-k)]\theta(t - t_1)\} \quad \text{as} \quad \varepsilon \to 0. \tag{13}$$

Comparing (13) to (8) gives $\lambda = 1 - \exp(-k)$ and therefore

$$\alpha = \lambda^{-1} - k^{-1} = \frac{1}{1 - \exp(-k)} - \frac{1}{k}. \tag{14}$$

However, expression (14) shows that the number $\alpha = 1/2$ (12) is reached only as $k \to 0$, when *the model* (7) *makes no sense*.

Remark 1 A formal asymptotic approach can provide some justification for model (7) at least in the leading-order approximation as follows. Let us assume that $0 < k \ll 1$, and $v = v_0 + kv_1 + k^2v_2 + O(k^3)$. Then Eq. (7) gives $\dot{v}_0 = 0$, $\dot{v}_1 + v_0\delta(t - t_1) = 0$, $\dot{v}_2 + v_1\delta(t - t_1) = 0, \ldots$. Since v_0 is continuous (constant) then the equation for v_1 is meaningful and gives solution with a step-wise discontinuity at $t = t_1$. However, the equation for v_2 has a discontinuous factor with the delta-pulse and thus is questionable.

Remark 2 The second-order equation $\ddot{x} + k\delta(t - t_1)x = 0$ is replaced with the system, $\dot{x} = v$ and $\dot{v} = -k\delta(t - t_1)x$, which does not lead to any contradiction, since the coordinate x appears to be non-smooth but continuous.

As follows from this section, using the generalized δ-function for physical modeling requires proper justifications. Due to the fact that models are different, justifications must be different as well, which is an obvious inconvenience. This is why the idea of so-called non-smooth transformations is being developed with the purpose of incorporating singularities of models into the corresponding transformations in a more or less universal way, and then deal with classical problem formulations for the resultant systems. Simple examples of nonsmooth transformations of unknown functions were given already in Sect. 2.1 following the Ref. [5]. Below in this work we introduce some generalization, and discuss other non-smooth transformations developed earlier.

2.3 Continualization of Impulsively Loaded Systems

Note that substitution (6) eliminates δ-impulses from system (5) and thus significantly improves the system smoothness, however, the resultant system still has step-wise

discontinuities due to the presence of Heaviside unit-step function. In the present section, we propose a generalization of substitution (6) such that the new equation includes no discontinuities at all. Consider the multidimensional linear system with variable coefficients

$$\dot{\boldsymbol{v}} = \boldsymbol{A}(t)\boldsymbol{v} + \sum_{i=1}^{\infty} \boldsymbol{q}_i \delta\left(t - t_i\right), \tag{15}$$

where $\boldsymbol{v}(t) \in R^n$, and $\boldsymbol{A}(t)$ is at least one time continuously differentiable $n \times n$-matrix-function.

Let us introduce the so-called ramp function as $R(t) = (t + |t|)/2$, such that $\dot{R}(t) = \theta(t)$ is Heaviside's unit-step function, and $\ddot{R}(t) = \delta(t)$.

Proposition 1 *Substitution*

$$\boldsymbol{v} = \boldsymbol{u}(t) + \sum_{i=1}^{\infty} [\boldsymbol{p}_i(t) R\left(t - t_i\right) + \boldsymbol{q}_i \theta\left(t - t_i\right)], \tag{16}$$

where $\boldsymbol{p}_i(t) = \boldsymbol{A}(t)\boldsymbol{q}_i$*, brings impulsively loaded system (15) to the class of continuous systems of the form*

$$\dot{\boldsymbol{u}} = \boldsymbol{A}(t)\boldsymbol{u} + \sum_{i=1}^{\infty} [\boldsymbol{A}^2(t) - \dot{\boldsymbol{A}}(t)]\boldsymbol{q}_i R\left(t - t_i\right). \tag{17}$$

Proof Substituting (16) in Eq. (15) gives

$$\dot{\boldsymbol{u}} + \sum_{i=1}^{\infty} [\boldsymbol{p}_i(t) - \boldsymbol{A}(t)\boldsymbol{q}_i]\theta\left(t - t_i\right)$$
$$= \boldsymbol{A}(t)\boldsymbol{u} + \sum_{i=1}^{\infty} [\boldsymbol{A}(t)\boldsymbol{p}_i(t) - \dot{\boldsymbol{p}}_i(t)] R\left(t - t_i\right).$$

Choosing $\boldsymbol{p}_i(t) = \boldsymbol{A}(t)\boldsymbol{q}_i$ gives (17). ■

2.4 Nonsmooth Positional Coordinates

The idea of nonsmooth coordinates deals with elastic but perfectly stiff barriers reflecting moving particles in a mirror-wise manner. Since outcome of such reflections is predictable then it can be built into the mechanical model in advance by means of the corresponding nonsmooth coordinates. It was shown in Refs. [52, 53] that introducing nonsmooth coordinates effectively eliminates barriers by unfolding the configuration space. As a result, the differential equations of motion are derived on the entire time interval with no impact conditions. For illustrating purposes, con-

sider the following N-degree-of-freedom Lagrangian system

$$L = \frac{1}{2}\sum_{i=1}^{N}\dot{q}_i^2 - \frac{1}{2}\sum_{i=0}^{N}k_i(q_{i+1}-q_i)^2; \tag{18}$$

$$|q_i(t)| \le 1; \tag{19}$$

$$q_0(t) \equiv q_{N+1}(t) \equiv 0. \tag{20}$$

This is a chain of unit-mass particles connected by linearly elastic springs of stiffness k_i. Perfectly stiff elastic constraints are imposed on each of the coordinates according to (19). Although Lagrangian (18) generates linear differential equations, these equations alone do not completely describe the system. Due to the presence of constraints (19), the system is actually strongly nonlinear, and this becomes obvious in adequately chosen coordinates. Transition to such coordinates is described by

$$q_i = \tau(x_i), \tag{21}$$

where τ is the triangular wave

$$\tau(x) = \begin{cases} x & \text{for } -1 \le x \le 1 \\ -x+2 & \text{for } 1 \le x \le 3 \end{cases} \tag{22}$$

$$\tau(x) \overset{\forall x}{=} \tau(4+x)$$

Note that notation (22) and normalization of the period differ from those introduced in original works [52, 53]. The only reason for such modification is to deal with the triangular wave of unit slope[2]

$$[\tau'(x)]^2 = 1 \tag{23}$$

for almost all x.

The coordinate transformation (21) brings system (18) through (20) to the form

$$L = \frac{1}{2}\sum_{i=1}^{N}\dot{x}_i^2 - \frac{1}{2}\sum_{i=0}^{N}k_i[\tau(x_{i+1})-\tau(x_i)]^2; \tag{24}$$

$$x_0(t) \equiv x_{N+1}(t) \equiv 0. \tag{25}$$

It is seen from (24) that transformation (22) preserves the quadratic form of kinetic energy while the constraint conditions (19) are satisfied automatically due to the property $|\tau(x)| \le 1$. In contrast to (18), Lagrangian (24) completely describes the model on the entire time interval $0 \le t < \infty$. However, in terms of the new coordinates, the potential energy acquired a non-local cell-wise structure so that the

[2] Although this condition does no matter for the method introduced in Refs. [52–54], Sect. 3 of the present paper describes another method for which property (23) is essential.

corresponding differential equations of motion are essentially nonlinear; for example, see (26) below. Now every impact interaction with constraints is interpreted as a transition from one cell to another as illustrated below on the two degrees-of-freedom model, $N = 2$. In this case, Lagrangian (24) gives the differential equations of motion on the infinite plane $-\infty < x_i < \infty$ $(i = 1, 2)$ with no constraints

$$\begin{aligned} \ddot{x}_1 + [(k_0 + k_1)\tau(x_1) - k_1\tau(x_2)]\tau'(x_1) = 0; \\ \ddot{x}_2 + [(k_1 + k_2)\tau(x_2) - k_1\tau(x_1)]\tau'(x_2) = 0. \end{aligned} \tag{26}$$

Figure 1a shows the corresponding equipotential energy levels and a sample trajectory of beat-wise dynamics. It is seen, for instance, that the system is trapped in some cells sometimes for the energy exchange process. After one of the two masses accumulated the energy, which is sufficient to reach the barrier, the impact event happens accompanied by the transition to another cell. The fact of energy exchange inside a trapping cell is confirmed by the transversality of incoming and outcoming pieces of the trajectory. As long as the mass remains in impact regime, its trajectory is passing through one cell to another until the system is trapped again in another cell for a new energy exchange process. A similar geometrical interpretation but for *impact normal mode* dynamics was introduced earlier in [49], where the impact modes were associated with 'hidden geometrical symmetries' revealed by periodic patterns of equipotential lines as shown in Fig. 1b.

In particular, closed form analytical solutions for different impact modes were obtained by means of the averaging procedure. Note that, according to the original works [52, 53], applicability of the averaging procedure constitutes the major advan-

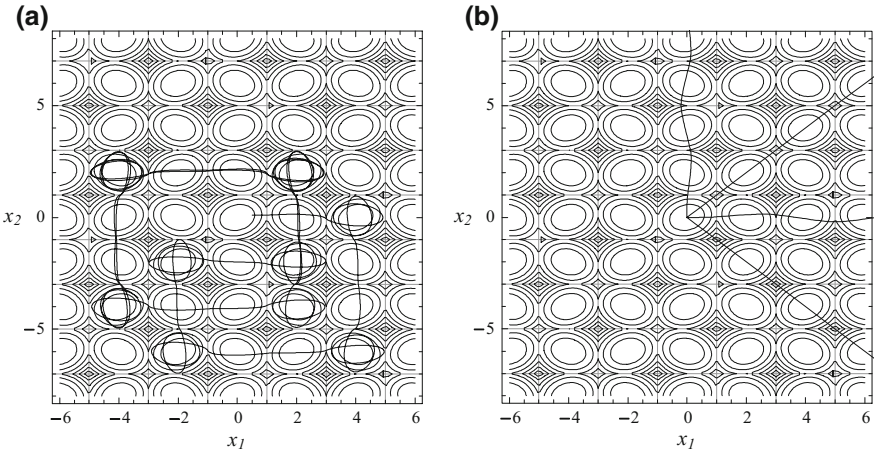

Fig. 1 **a** Equipotential energy levels in the unfolded configuration plane and a sample dynamic trajectory obtained under the initial conditions at $t = 0$: $x_1 = 0.5, x_2 = 0.0, \dot{x}_1 = 1.0$, and $\dot{x}_2 = 0.0$; **b** The impact mode trajectories in the unfolded configuration plane: in-phase and out-of-phase modes (the diagonal lines), and local modes (the horizontal and vertical lines.)

tage given by transformation (21) since the infinite impact forces are effectively eliminated from the system. Similar kind of visualization for a two-degree-of-freedom vibrating system with only one mass under two-sided constraint condition was used in [36].

Although original works [52, 53], deal with illustrating models of deterministic dynamics, further applications were shifted mostly into the area of random vibrations [4, 26, 40]. From the standpoint of practical applications, inelastic effects of interactions with stiff constraints become essential. Generally, impact dissipation effects can be modeled by the dissipative term [1, 4] $(1-\kappa)\dot{x}|\dot{x}|\delta_-(x)$, where $\delta_-(x)$ is a specific rule rather than the conventional Dirac's function. According to this rule, the impulsive damping acts right before the result of such damping namely velocity jump occurs. Such damping model is justified if the restitution coefficient κ is close to unity so that the factor $1-\kappa$ is small. In this case, the integral effect of the impulsive damping can play the role perturbation within asymptotic procedures, in which the velocity $\dot{x}$ is given by an unperturbed system and therefore remains continuous. Non-elastic impact interactions with constraints can be modeled also in a purely geometrical way however under some conditions on the type of motions [54].

2.5 *Nonsmooth Transformation of Dynamic States*

Transformations eliminating non-elastic constraints should obviously involve both types of the state variables - coordinates and velocities. Let us consider the case of harmonic oscillator under the constraint condition

$$\dot{\mathbf{x}} = \mathbf{A}\mathbf{x}; \tag{27}$$

$$x_1 > 0, \tag{28}$$

where $\mathbf{x} = [x_1(t), x_2(t)]^T$ is the state vector such that $x_2 = \dot{x}_1$, and

$$\mathbf{A} = \begin{bmatrix} 0 & 1 \\ -\omega^2 & 0 \end{bmatrix}. \tag{29}$$

It is also assumed that every collision with the barrier $x_1 = 0$ at some time t^* happens with a momentary energy loss characterized by the coefficient of restitution κ:

$$x_1(t^*) = 0: \quad x_2(t^* + 0) = -\kappa x_2(t^* - 0). \tag{30}$$

The idea is to unfold the phase space in such way that the energy loss occurs automatically whenever the system crosses preimage of the line $x_1 = 0$. The corresponding non-conservative transformation was introduced in [11, 12] as a transformation of state vector, $\mathbf{x} \longrightarrow \mathbf{y}$, of the form

$$\mathbf{x} = \mathbf{S}\mathbf{y}, \tag{31}$$

where $\mathbf{y} = [s(t), v(t)]^T$ is a new state vector, and the transition matrix is given by

$$\mathbf{S} = \begin{bmatrix} 1 & 0 \\ 0 & 1 - k\text{sgn}(sv) \end{bmatrix} \text{sgn}(s), \tag{32}$$

where $k = (1 - \kappa)/(1 + \kappa)$.

Note that transformation (31) is strongly nonlinear due to the dependence $\mathbf{S} = \mathbf{S}(\mathbf{y}, k)$. Nevertheless, substitution (31), gives equation

$$\dot{\mathbf{y}} = (S^{-1}\mathbf{A}\mathbf{S})\mathbf{y}. \tag{33}$$

It is seen that the transformed equation (33) has the same form as it would have in the case of constant matrix $\mathbf{S}$. However, the matrix $\mathbf{S}$ is constant *almost* everywhere except for discontinuity lines in the plane sv. A formal substitution of (31) in (27) would eventually impose specific conditions on distributions similar to those described in Sect. 2.2. In the component-wise form, expressions (31) and (33) are written as, respectively,

$$\begin{aligned} x_1 &= x_1(s, v) \equiv s\text{sgn}(s); \\ x_2 &= x_2(s, v) \equiv \text{sgn}(s)[1 - k\text{sgn}(sv)]v \end{aligned} \tag{34}$$

and

$$\begin{aligned} \dot{s} &= [1 - k\text{sgn}(sv)]v; \\ \dot{v} &= -\omega^2 s[1 + k\text{sgn}(sv)]/(1 - k^2). \end{aligned} \tag{35}$$

Figure 2a and b illustrates a sample trajectory of the harmonic oscillator in its original transformed phase planes, respectively. Now both unknown components of the state vector are continuous, whereas effects of non-elastic collisions (30) are captured by transformation (34). Further, consider the general case of one-degree-of-freedom nonlinear oscillator

$$\begin{aligned} \dot{x}_1 &= x_2; \\ \dot{x}_2 &= -f(x_1, x_2, t), \end{aligned} \tag{36}$$

whose motion is restricted to the positive half plane $x_1 > 0$ by a non-elastic barrier at $x_1 = 0$ of the restitution coefficient κ.

Applying transformation (34) to system (36), gives

$$\begin{aligned} \dot{s} &= [1 - k\text{sgn}(sv)]v; \\ \dot{v} &= -f(x_1(s, v), x_2(s, v), t)\text{sgn}(s)[1 + k\text{sgn}(sv)]/(1 - k^2). \end{aligned} \tag{37}$$

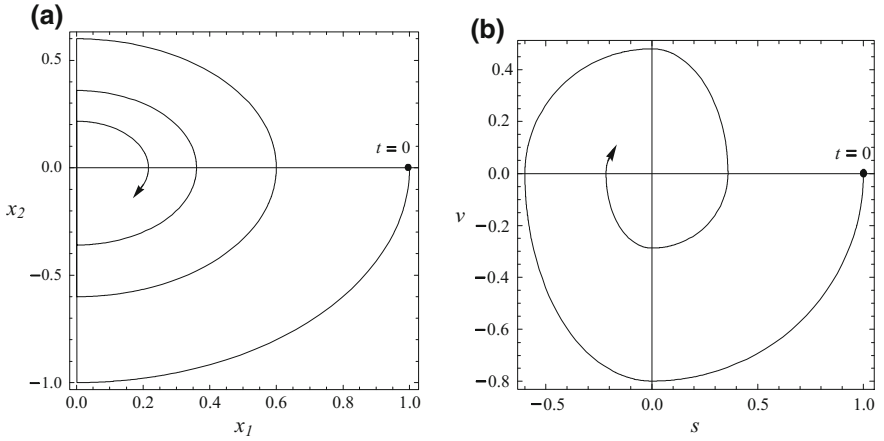

Fig. 2 **a** The original phase plane of the harmonic oscillator with a perfectly stiff but inelastic one-sided barrier; **b** The phase trajectory of inelastic impact oscillator in the auxiliary coordinates

Although the technique is illustrated on a one-degree-of-freedom model, similar coordinate transformations apply to multiple degree-of-freedom systems by choosing one of the coordinates perpendicular to the constraint. For that reason, it is convenient to use the descriptive Routh function whose normal to the constraint coordinate is Lagrangian whereas other coordinates and associated momenta are Hamiltonian [12]. As mentioned in Sect. 1, improving the class of smoothness of dynamical systems extends applicability of different analytical tools, such as, for instance, bifurcation analyses [12]. In fact, before the transformation, discontinuities of phase trajectories as those shown in Fig. 2a would complicate any local analyses. However, the transformation improves the class of smoothness which is needed to build major objects of local analyses and averaging tools. A regular approach to stability and bifurcation analysis in impact systems was proposed in [13]. In particular, it was shown that the discontinuous bifurcation of grazing impact can be regularized. This may lead to a new interpretation of grazing bifurcations. Namely, after such bifurcation, some periodic motion might survive and even preserve stability.

3 Nonsmooth Temporal Arguments

In this section, we describe nonsmooth substitutions of the independent variables, which is the temporal argument in the present context. It is shown below that such nonsmooth substitutions associate with common temporal symmetries of motions regardless of types of systems. This approach was originally developed for the class of strongly non-linear but smooth oscillators [28, 29]. However, its main specifics are clearly seen even in the case of non-oscillatory motion of a classic unit-mass

particle under returning potential force. *The idea is to employ the most 'elementary' strongly nonlinear dynamics as a basis for observing strongly nonlinear dynamic effects in general case* [33]. Examples of such 'elementary' nonlinear processes are found among the rigid-body motions [27]. However, the key question is how to bridge the gap between the classes of smooth and nonsmooth motions within the same mathematical formalism. It will be shown below on simple examples that nonsmooth substitutions of temporal argument may play the role of such a bridge.

3.1 Positive Time

Let us consider the motion of a unit-mass particle under the restoring monotonically increasing force $f(x)$

$$\ddot{x} + f(x) = 0. \tag{38}$$

The initial conditions are $x = x_0 > 0$ and $\dot{x} = v_0 < 0$ at $t = t_0 < 0$. As the particle reaches a turning point at some time $t = a$ it makes a U-turn. Since Eq. (38) admits the group $t \longrightarrow -t$, the reverse motion will be symmetric with respect to the time point $t = a$. Such a prediction incorporates into the differential equation of motion (38) through the new temporal argument, $x = x(s)$ [33],

$$t \longrightarrow s: \quad s = |t - a|. \tag{39}$$

Note that the function $s(t)$ describes the coordinate of a free particle striking a perfectly stiff obstacle with no energy loss at some time $t = a$. Although the temporal shape of the dynamics of system (38) is different, the function $s(t)$ captures its symmetry with respect to the turning point $t = a$. Therefore, the substitution of argument (39) includes important information into the differential equation of motion before any solution procedure is applied. Obviously, $\dot{s} = \text{sgn}(t - a)$ and $\ddot{s} = 2\delta(t - a)$, therefore, except possibly for a single point $t = a$, the following relationship holds

$$\dot{s}^2 = 1 \tag{40}$$

then, substituting (39) in (38), gives

$$\frac{d^2x}{ds^2} + f(x) = 0, \quad s > 0; \tag{41}$$

$$\frac{dx}{ds} = 0, \quad s = 0, \tag{42}$$

where condition condition (42) eliminates the singularity caused by the derivative $\ddot{s}$, which formally occurs due to the non-smoothness of substitution (39).

From geometrical standpoint, substitution (39) reverses the time direction exactly when the particle makes the U-turn. Although the form of the equation remains the

same, certain advantages are achieved [27]. For instance, even a drastically simplified equation, say $d^2x/ds^2 = 0$, still preserves the main dynamical event, which is the U-turn of the particle. Such a simplification effectively replaces the smooth potential barrier with a perfectly stiff one, as follows from the general solution, $x = As(t) + B$, where A and B are arbitrary constants of integration. Now, if some perturbation series converges for $s \geq 0$, then it is automatically converges for the entire interval of the original time, $-\infty < t < \infty$.

As another example, let us consider the case of impulsively loaded single degree-of-freedom system,

$$\ddot{x} + f(x) = 2p\delta(t-a) = p\ddot{s}, \tag{43}$$

where $p = const$.

Substituting (39) in (43) and taking into account (40), gives[3]

$$\frac{d^2x}{ds^2} + f(x) = \left(p - \frac{dx}{ds}\right)\ddot{s}. \tag{44}$$

Eliminating the singularity $p\ddot{s}$ in (44), gives the same Eq. (41) however under non-homogeneous boundary condition

$$\frac{dx}{ds} = p \quad \text{if} \quad s = 0. \tag{45}$$

Since substitution (39) is non-invertible on the entire time interval, then using the argument s in a general case of dynamical systems appears to be less straightforward but nonetheless possible based on the following identity

$$t = a + s\dot{s}. \tag{46}$$

Due to relationship (40), the combination (46) represents a specific complex number with the basis $\{1, \dot{s}\}$ [33]. In contrast to the conventional elliptic complex algebra, the operation $1/t$ with (46) may not hold. Interestingly enough, such algebraic structures has been known for quite a long time [3, 47] with no relation to nonsmooth functions or any dynamical systems. In the modern mathematical literature, it is usually introduced just as a set of abstract elements and referred to as a simple example of the so-called Clifford's algebras. We prefer the term 'hyperbolic algebra' although many synonyms do exist [15]. Some areas of physics are linked to this algebra quite closely [9], however constructive applications are rather limited. The hyperbolic numbers are isomorphic to symmetric 2×2-matrixes as for instance,

$$t^2 = (a + s\dot{s})^2 \longleftrightarrow \begin{pmatrix} a & s \\ s & a \end{pmatrix}^2. \tag{47}$$

[3] It is worth to compare this technique with that described in Sect. 2.1 based on the first-order equation.

We emphasize that, in our case, the hyperbolic structure is generated naturally rather than imposed by abstract mathematical assumptions. Since the components of our hyperbolic numbers are functions of time then differential and integral operations can be introduced. Briefly, for practically any function $x(t)$, it can be shown that [32]

$$\begin{aligned} x(t) &= x(a + s\dot{s}) = X(s) + Y(s)\dot{s}; \\ X(s) &= \frac{1}{2}\left[x(a+s) + x(a-s)\right]; \\ Y(s) &= \frac{1}{2}\left[x(a+s) - x(a-s)\right]. \end{aligned} \tag{48}$$

Obviously, algebraic manipulations with the element $X + Y\dot{s}$ can be conducted in the same way as manipulations with the element $t = a + s\dot{s}$ since both belong to the same algebra. Then, taking into account (40) gives first time derivative

$$\dot{x}(t) = Y'(s) + X'(s)\dot{s} + p\ddot{s}, \tag{49}$$

where, $p = Y(0)$.

According to (48), the number p must be zero, if the function $x(t)$ is continuous. In this case, the derivative $\dot{x}(t)$ belongs to the same hyperbolic algebra as the function $x(t)$ does. High-order derivatives can be considered in the same as soon as the result of differentiation remains continuous. At some stage of differentiation, the singular term $\ddot{s} = 2\delta(t-a)$ can be preserved in order to eliminate a similar type of singularity from the differential equation of motion, if needed; regarding second-order equations, see (44) and (45) for illustration. In case of Eq. (38), it was possible to set $Y(s) \equiv 0$ in representation (48) due to the specific temporal symmetry of the process dictated by the differential equation of motion. Generally speaking, however, both 'real' X and 'imaginary' Y components must be considered in (48). For instance, using representation (48) and considering the functions $X(s)$ and $Y(s)$ as new unknowns, solution of the initial value problem $\dot{x} + \lambda x = 2p\delta(t-a) = p\ddot{s}$ and $x(0) = 0$ can be found in the form $x = p\exp(-\lambda s)(1+\dot{s})$ [27].

Remark 3 In addition to the original basis $\{1, \dot{s}\}$, the so-called 'idempotent' orthogonal basis can be introduced as [33] $i_\pm = (1 \pm \dot{s})/2$, such that $t = (a+s)i_+ + (a-s)i_-$. Since $i_\pm^2 = i_\pm$ and $i_+ i_- = 0$, then $t^\alpha = (a+s)^\alpha i_+ + (a-s)^\alpha i_-$ for any real number α.

The advantage of the idempotent basis is that the differential equations of motion with respect to the two components become decoupled. However, the boundary conditions become more complicated. Representations of solutions in the idempotent basis were used recently to describe acoustic wave propagation in periodic composite media [38]. Note that, from the mathematical point of view, the term *time* simply means argument of the unknown function. This is the main distinctive feature of the present methodology, in which nonsmooth transformations are applied to *arguments*. Typically, the unknown functions are modified as well. However, such

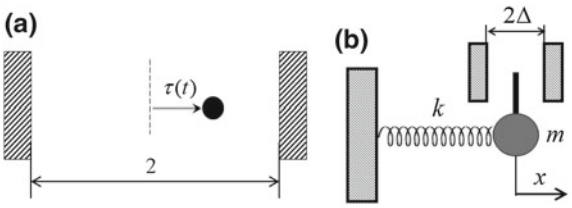

Fig. 3 **a** Standard impact oscillator; **b** harmonic oscillator between perfectly stiff two-sided constraints

modifications are imposed due to the irreversibility of the argument substitutions and lead to hyperbolic elements.

3.2 Triangular Wave Time Substitution

Since any vibrating process is a sequence of U-turns then the corresponding nonsmooth time substitution can be combined of functions given by (39) with different signs and temporal shifts. In periodic case of the period $T = 4$, such combination is given by the triangular wave function (22), whose argument is replaced by time, $\tau = (2/\pi)\arcsin\sin(\pi t/2)$. A mechanical model generating such time substitution is a free particle moving in between to perfectly stiff barriers with no energy loss; see Fig. 3a. The direct verification shows that, during one period of vibrations, the time variable admits representation in the form of hyperbolic element as

$$t = 1 + (\tau - 1)\,\dot{\tau} \qquad \text{if } -1 < t < 3, \tag{50}$$

where the derivative $\dot{\tau}$ is the rectangular wave, such that $\dot{\tau}^2 = 1$, and therefore (50) is a periodic version of (46) with the basis $\{1, \dot{\tau}\}$.

In physical terms, it follows from (50) that *any periodic process, whose period is normalized to $T = 4$, is uniquely expressed through the dynamic states of standard impact oscillator in the form* [29]

$$\begin{aligned} x\,(t) &= X\,(\tau) + Y\,(\tau)\,\dot{\tau}; \\ X\,(\tau) &= \frac{1}{2}\,[x\,(\tau) + x\,(2-\tau)]\,; \\ Y\,(\tau) &= \frac{1}{2}\,[x\,(\tau) - x\,(2-\tau)]\,. \end{aligned} \tag{51}$$

Identity (51) means that the triangular and rectangular waves capture temporal symmetries of periodic processes regardless specifics of individual vibrating systems. Different applications of nonsmooth argument substitutions with the related techniques to problems of theoretical and applied mechanics can be found in [7, 10, 16–19, 24, 25, 37, 41–43, 45]. The methodology was adapted also to the nonlinear normal mode analyses and included in monograph [48]. Another important

area of application deserves rather special consideration. While the idea of NNMs is effective in case of weak or no energy exchange, the concept of the limiting phase trajectories [18] considers the opposite situation namely intense energy exchanges between weakly coupled oscillators or modes [20–22]. In this case, nonsmooth time substitutions are invoked by the temporal behavior of phase angle, which is responsible for energy distribution. This resembles the triangular wave as the energy swing reaches its asymptotic limit.

A class of strongly nonlinear traveling waves and localized modes in one-dimensional homogeneous granular chains with no precompression were considered in [44]. As a result, the authors developed a systematic semianalytical approaches for computing different families of nonlinear traveling waves parametrized by spatial wave number and energy.

3.3 Modeling Energy Losses at Perfectly Stiff Barriers

Let us consider a free vibro-impact model as shown in Fig. 3b. Introducing the notation $\Omega^2 = \mathrm{k}/\mathrm{m}$ brings the differential equation of motion between the barriers to the form

$$\ddot{x} + \Omega^2 x = 0, \, |x| \leq \Delta \tag{52}$$

under the impact conditions at $x = \pm\Delta$:

$$\begin{gathered} \dot{x}(t_i + 0) = -k\dot{x}(t_i - 0); \\ 0 \leq k \leq 1. \end{gathered} \tag{53}$$

Here t_i is the collision time, and k is the so-called coefficient of restitution, which is convenient to represent in the form

$$k = 1 - \varepsilon \tag{54}$$

such that $\varepsilon = 0$ means a perfectly 'elastic' collision with no energy loss, whereas $\varepsilon = 1$ is a perfectly 'plastic' limit, when all the kinetic energy momentarily dissipates at the collision time. In the present work, the energy loss due to collisions is assumed to be small so that

$$0 < \varepsilon \ll 1. \tag{55}$$

Assuming that the oscillator strikes each of the amplitude limiters ones per one cycle of oscillations, we replace (52) with the effective model with no constraints however under the "external" pulses [31]

$$\ddot{x} + \Omega^2 x = p\tau''(\varphi), \tag{56}$$

where $p = p(\varphi)$ is a phase dependent quantity associated with the impact impulses, and $\varphi = \varphi(t)$ is the phase such that the period of effective impulsive forcing function is normalized to $T = 4$; both functions p and φ are unknown at this stage.

Further, solution is represented in the form (51), where the original time argument t is replaced by the phase φ

$$x(t) = X(\tau) + Y(\tau)\tau', \quad \tau = \tau(\varphi), \quad \varphi = \varphi(t). \tag{57}$$

Substituting (57) in (56) and (53), and introducing notation for the phase time rate, $\omega(t) = \dot{\varphi}(t)$, gives the boundary value problem [35]

$$\begin{aligned} \omega^2 X'' + \Omega^2 X + Y'\dot{\omega} = 0; \\ \omega^2 Y'' + \Omega^2 Y + X'\dot{\omega} = 0; \end{aligned} \tag{58}$$

$$\tau = \pm 1: \quad Y = 0, \quad X'\omega^2 = p; \tag{59}$$

$$\tau = \pm 1: \quad X = \pm\Delta; \tag{60}$$

$$\tau = \pm 1: \quad Y' \mp X' = -(1-\varepsilon)\left(Y' \pm X'\right). \tag{61}$$

The second equation in (59) serves for determining the unknown parameter p, and dictates the symmetry condition $X'|_{\tau=1} = X'|_{\tau=-1}$. Note that, the derivation of inelastic impact condition (61) in terms of the triangular wave temporal argument was obtained very recently and appears to be not straightforward. This allowed us to apply the asymptotic averaging approach based on the assumption (55). In particular, solution of the boundary value problem (58) through (61) is found the form of asymptotic expansions

$$\begin{aligned} X(\tau) &= X_0(\tau) + X_1(\tau)\varepsilon + X_2(\tau)\varepsilon^2 + O\left(\varepsilon^3\right); \\ Y(\tau) &= Y_0(\tau) + Y_1(\tau)\varepsilon + Y_2(\tau)\varepsilon^2 + O\left(\varepsilon^3\right); \\ \omega &= \omega_0(\eta) + \omega_1(\eta)\varepsilon + \omega_2(\eta)\varepsilon^2 + O\left(\varepsilon^3\right); \\ p &= p_0(\eta) + p_1(\eta)\varepsilon + p_2(\eta)\varepsilon^2 + O\left(\varepsilon^3\right), \end{aligned} \tag{62}$$

where $\eta = \varepsilon t$ is a slow temporal scale dictated by the rate of energy loss.

In particular, the leading order asymptotic solution is [35]

$$x(t) = \Delta\left[\frac{\sin\lambda\tau}{\sin\lambda} - \frac{\varepsilon}{2\Omega}\frac{d\lambda}{d\eta}\left(\frac{\cos\lambda\tau}{\cos\lambda} - \tau\frac{\sin\lambda\tau}{\sin\lambda}\right)\frac{d\tau}{d\varphi}\right] + O(\varepsilon^2); \tag{63}$$

$$p = \frac{\Omega^2\Delta}{\lambda\tan\lambda} + O(\varepsilon), \tag{64}$$

where $\tau = \tau(\varphi)$, $\dot{\varphi} = \omega = \lambda^{-1}\Omega$, and the auxiliary slowly varying 'frequency ratio' obeys the first-order differential equation

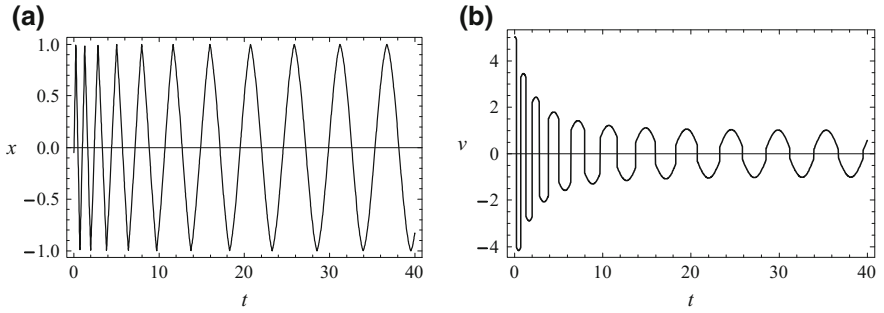

Fig. 4 **a** Temporal shape of impact oscillations under the following parameters: $\Omega = 1.0$, $\Delta = 1.0$, $\varepsilon = 0.2$, and $\omega(0) = 5.0$; **b** velocity

$$\dot{\lambda} = \varepsilon \frac{\Omega}{2}(1 + \cos 2\lambda)\left(1 + \frac{\sin 2\lambda}{2\lambda}\right)^{-1}. \tag{65}$$

A sample case of solution (63) is illustrated in Fig. 4. Note that, within the present modeling, the amplitude of vibration cannot change even though the intensity of impact interaction with constraints is diminishing with time. The reason is that no energy loss is assumed in between the limiters, and the system should eventually reach some 'grazing' regime with near zero impact pulses but still the same amplitude [2].

4 Concluding Remarks

In this work, we outlined very different ways to modeling dynamical systems with discontinuities by choosing proper spatial coordinates or temporal arguments within the class of nonsmooth functions. In particular, we described three groups of methods using non-smooth functions for modeling mechanical systems under either *external* impulsive loads or *internal* impact interactions. Physical basis and mathematical implementations of these methods are quite different. However, the purpose of use seems to be the same, namely - eliminating singularities from the corresponding differential equations of motions in order to consider the problem within the classical theory of differential equations with the set of well developed analytical tools. Section 2.1 describes simple and effective way eliminating delta-impulses from the system by splitting the unknown solution into smooth and step-wise discontinuous subcomponents, if the impulse times are known. Then, it is shown in Sects. 2.4 and 2.5 that impact singularities can be incorporated into appropriate non-smooth space-unfolding generalized coordinates in such a way that the dynamics in the new state space is continuous. Due to the fact that the corresponding coordinate transformations are strongly nonlinear, the resultant system is typically strongly nonlinear as well, regardless the type of dynamics between collision times. It must be noticed that

the independent argument (time) is not affected by any of the above substitutions. However, as described in Sect. 3, the singularities due external impulses or internal interactions can be eliminated by means of nonsmooth substitutions for the temporal argument without any drastic changes of the differential equations. For instance, if the equations are linear between collisions, then the linearity is preserved after the nonsmooth temporal substitution has been applied. Another specific feature of the nonsmooth time substitutions is the induced hyperbolic structure of spatial coordinates. Keeping in mind that the conventional complex numbers create the so-called elliptic algebra, we can conclude that the tool of nonsmooth temporal substitutions may generate a reasonable alternative to quasi harmonic analyses. Finally note that it is possible to combine different transformations described in the present survey whenever technical reasons for such combinations are present; some examples can be found in [30, 46].

References

1. Babitsky, V.I.: Theory of Vibroimpact Systems and Applications. Springer, Berlin (1998)
2. Chin, W., Ott, E., Nusse, H.E., Grebogi, C.: Grazing bifurcations in impact oscillators. Phys. Rev. E **50**, 4427–4444 (1994)
3. Cockle, J.: On certain functions resembling quaternions, and on a new imaginary in algebra. Lond. Edinb. Dublin Philos. Mag. **33**, 345–349 (1848)
4. Dimentberg, M.F., Gaidai, O., Naess, A.: Random vibrations with strongly inelastic impacts: response PDF by the path integration method. Int. J. Non-Linear Mech. **44**(7), 791–796 (2009)
5. Filippov, A.F.: Differential Equations with Discontinuous Righthand Sides. Kluwer Academic Publishers Group, Dordrecht (1988)
6. Fucik, S., Kufner, A.: Nonlinear Differential Equations. Studies in Applied Mechanics, vol. 2. Elsevier Scientific Publishing Company, Amsterdam (1980)
7. Gendelman, O., Manevitch, L.I., Vakakis, A.F., M'Closkey, R.: Energy pumping in nonlinear mechanical oscillators. I. Dynamics of the underlying Hamiltonian systems. Trans. ASME J. Appl. Mech. **68**(1), 34–41 (2001)
8. Haller, S., Hormann, G.: Comparison of some solution concepts for linear first-order hyperbolic differential equations with non-smooth coefficients. Publications De Linstitut Mathematique, Nouvelle serie **84**(98), 123–157 (2008)
9. Hucks, J.: Hyperbolic complex structures in physics. J. Math. Phys. **34**, 5986 (1993)
10. Ibrahim, R.A.: Vibro-Impact Dynamics: Modeling, Mapping and Applications. LNACM, vol. 43. Springer, Berlin (2009)
11. Ivanov, A.P.: Analytical methods in the theory of vibro-impact systems. J. Appl. Math. Mech. **57**(2), 221–236 (1993)
12. Ivanov, A.P.: Impact oscillations: linear theory of stability and bifurcations. J. Sound Vib. **178**(3), 361–378 (1994)
13. Ivanov, A.P.: Bifurcations in impact systems. Chaos, Solitons Fractals **7**(10), 1615–1634 (1996)
14. Ivanov, A.P.: Dynamics of systems with mechanical collisions. International Program of Education, Moscow (1997). in Russian
15. Kisil, V.V.: Induced representations and hypercomplex numbers. Adv. Appl. Clifford Algebr. **23**(2), 417–440 (2013)
16. Lee, Y.S., Kerschen, G., Vakakis, A.F., Panagopoulos, P., Bergman, L., McFarland, D.M.: Complicated dynamics of a linear oscillator with a light, essentially nonlinear attachment. Phys. D **204**, 41–69 (2005)

17. Lee, Y.S., Nucera, F., Vakakis, A.F., McFarland, D.M., Bergman, L.A.: Periodic orbits, damped transitions and targeted energy transfers in oscillators with vibro-impact attachments. Phys. D **238**(18), 1868–1896 (2009)
18. Manevitch, L.I.: New approach to beating phenomenon in coupled nonlinear oscillatory chains. Arch. Appl. Mech. **77**, 301–312 (2007)
19. Manevitch, L.I., Gendelman, O.V.: Oscillatory models of vibro-impact type for essentially non-linear systems. Proc. Inst. Mech. Eng. Part C J. Mech. Eng. Sci. **222**(10), 2007–2043 (2008)
20. Manevitch, L.I., Musienko, A.I.: Limiting phase trajectory and beating phenomena in systems of coupled nonlinear oscillators. In: 2nd International Conference on Nonlinear Normal Modes and Localization in Vibrating Systems, Samos, Greece, 19-23 June, pp. 25–26 (2006)
21. Manevitch, L.I., Smirnov, V.V.: Resonant energy exchange in nonlinear oscillatory chains and limiting phase trajectories: from small to large systems (2009). arXiv:0903.5455v1
22. Manevitch, L.I., Kovaleva, A.S., Shepelev, D.S.: Non-smooth approximations of the limiting phase trajectories for the duffing oscillator near 1:1 resonance. Phys. D Nonlinear Phenom. **240**(1), 1–12 (2011)
23. Maslov, V.P., Omel′janov, G.A.: Asymptotic soliton-form solutions of equations with small dispersion. Russ. Math. Surv. **36**(3), 73–149 (1981)
24. Mikhlin, Yu.V., Reshetnikova, S.N.: Dynamical interaction of an elastic system and a vibro-impact absorber. Math. Probl. Eng. (Article ID 37980):15 pp. (2006)
25. Mikhlin, Yu.V., Volok, A.M.: Solitary transversal waves and vibro-impact motions in infinite chains and rods. Int. J. Solids Struct. **37**, 3403–3420 (2000)
26. Namachchivaya, N.S., Park, J.H.: Stochastic dynamics of impact oscillators. J. Appl. Mech. **72**(6), 862–870 (2005)
27. Pilipchuk, V.: Asymptotic of rigid-body motions for nonlinear dynamics: physical insight and methodologies. In: Awrejcewicz, J. (ed.) Applied Non-Linear Dynamical Systems. Springer Proceedings in Mathematics and Statistics, vol. 93, pp. 11–22. Springer International Publishing (2014)
28. Pilipchuk, V.N.: The calculation of strongly nonlinear systems close to vibroimpact systems. J. Appl. Math. Mech. **49**(5), 572–578 (1985)
29. Pilipchuk, V.N.: Transformation of oscillating systems by means of a pair of nonsmooth periodic functions. Dokl. Akad. Nauk Ukrain. SSR Ser. A (4), 37–40 (1988). (in Russian)
30. Pilipchuk, V.N.: Non-smooth spatio-temporal transformation for impulsively forced oscillators with rigid barriers. J. Sound Vib. **237**(5), 915–919 (2000)
31. Pilipchuk, V.N.: Impact modes in discrete vibrating systems with bilateral barriers. Int. J. Non-liinear Mech. **36**(6), 999–1012 (2001)
32. Pilipchuk, V.N.: Temporal transformations and visualization diagrams for nonsmooth periodic motions. Int. J. Bifurc. Chaos **15**(6), 1879–1899 (2005)
33. Pilipchuk, V.N.: Nonlinear Dynamics: Between Linear and Impact Limits. Lecture Notes in Applied and Computational Mechanics. Springer, Berlin (2010)
34. Pilipchuk, V.N.: Non-smooth spatio-temporal coordinates in nonlinear dynamics (2011). arXiv:1101.4597
35. Pilipchuk, V.N.: Closed-form solutions for oscillators with inelastic impacts. J. Sound Vib. **359**, 154–167 (2015)
36. Pilipchuk, V.N., Ibrahim, R.A.: Dynamics of a two-pendulum model with impact interaction and an elastic support. Nonlinear Dyn. **21**(3), 221–247 (2000)
37. Pilipchuk, V.N., Starushenko, G.A.: A version of non-smooth transformations for one-dimensional elastic systems with a periodic structure. J. Appl. Math. Mech. **61**(2), 265–274 (1997)
38. Pilipchuk, V.N., Andrianov, I.V., Markert, B.: Analysis of micro-structural effects on phononic waves in layered elastic media with periodic nonsmooth coordinates. Wave Motion **63**, 149–169 (2016)
39. Richtmyer, R.D.: Principles of Advanced Mathematical Physics. Springer, Berlin (1985)

40. Rong, H., Wang, W., Xu, X., Fang, T.: Subharmonic response of a single-degree-of-freedom nonlinear vibroimpact system to a randomly disordered periodic excitation. J. Sound Vib. **327**(1–2), 173–182 (2009)
41. Salenger, G., Vakakis, A.F., Gendelman, O., Manevitch, L., Andrianov, I.: Transitions from strongly to weakly nonlinear motions of damped nonlinear oscillators. Nonlinear Dyn. **20**(2), 99–114 (1999)
42. Sheng, G., Dukkipati, R., Pang, J.: Nonlinear dynamics of sub-10 nm flying height air bearing slider in modern hard disk recording system. Mech. Mach. Theory **41**, 1230–1242 (2006)
43. Sophianopoulos, D.S., Kounadis, A.N., Vakakis, A.F.: Complex dynamics of perfect discrete systems under partial follower forces. Int. J. Non-Linear Mech. **37**(6), 1121–1138 (2002)
44. Starosvetsky, Yu., Vakakis, A.F.: Traveling waves and localized modes in one-dimensional homogeneous granular chains with no precompression. Phys. Rev. E **82**(2, Part 2), 026603 (2010)
45. Starushenko, G., Krulik, N., Tokarzewski, S.: Employment of non-symmetrical saw-tooth argument transformation method in the elasticity theory for layered composites. Int. J. Heat Mass Trans. **45**, 3055–3060 (2002)
46. Thomsen, J.J., Fidlin, A.: Near-elastic vibro-impact analysis by discontinuous transformations and averaging. J. Sound Vib. **311**, 386–407 (2008)
47. Tucker, R.: Mathematical Papers by William Kingdon Clifford. AMS Chelsea Publishing, Providence (2007)
48. Vakakis, A.F., Manevitch, L.I., Mikhlin, YuV, Pilipchuk, V.N., Zevin, A.A.: Normal Modes and Localization in Nonlinear Systems. Wiley, New York (1996). A Wiley-Interscience Publication
49. Vedenova, E.G., Manevich, L.I., Pilipchuk, V.N.: Normal oscillations of a string with concentrated masses on non-linearly elastic supports. 1. J. Appl. Math. Mech. **49**(2), 153–159 (1985)
50. Vladimirov, V.S.: Equations of Mathematical Physics. Monographs and Textbooks in Pure and Applied Mathematics, vol. 3. M. Dekker (1971)
51. Whitham, G.B.: Linear and Nonlinear Waves. Wiley, New York (1999). Reprint of the 1974 original, A Wiley-Interscience Publication
52. Zhuravlev, V.F.: A method for analyzing vibration-impact systems by means of special functions. Izvestiya AN SSSR Mekhanika Tverdogo Tela (Mech. Solids) **11**(2), 30–34 (1976)
53. Zhuravlev, V.F.: Equations of motion of mechanical systems with ideal one-sided links. J. Appl. Math. Mech. **42**(5), 839–847 (1978)
54. Zhuravlev, V.F., Klimov, D.M.: Prikladnye metody v teorii kolebanii. Nauka, Moscow (1988). (in Russian)

Revolution of Pendula: Rotational Dynamics of the Coupled Pendula

Valeri V. Smirnov

Abstract The analysis of the rotational dynamics of two coupled pendula is presented. The description of the oscillations of the pendulum on the background of the rotation with the average velocity was performed by the asymptotic method for the single pendulum. The source and the significance of the formation of the Limiting Phase Trajectory is clarified. The stability analysis of the rotation of two coupled pendula shows a qualitative difference between in-phase and out-of-phase rotational modes. It is shown that the origin of the in-phase rotation instability is its parametric excitation by the out-of-phase perturbations. The domain of in-phase rotation instability has been determined in the space of the system parameters. The analytic results are confirmed by the numerical simulation data.

1 Introduction

The pendulum is one of most famous objects in the history of the science. All people learning the natural sciences start their studying the periodic motion from the small-amplitude oscillations of the pendulum [1]. However, the significance of the pendulum not specialized as the teaching aids. Many models in the modern physics from the classical mechanics up to the quantum field theory, in the chemistry, biology, etc. are based on the dynamical equations of pendulum's motion [2–5]. The dynamics of the pendula coupled by the nonlinear periodic potential (both the oscillatory and the rotational regimes) is essential for the problems of the thermoconductivity of quasi-one-dimesional lattices [6, 7], the rotational mobility in the flexible polymeric chains [8, 9], including DNA [10, 11], the existence and interactions of the intrinsic localized modes in the Heisenberg ferromagnetics [8, 12] and the Josephson junction ladders [13]. The non-stationary dynamics of the weakly coupled pendula and the forced pendulum were studied in [14, 15], respectively. The effect of the dissipation and the external force on the rotational of the coupled pendula was considered in

V. V. Smirnov (✉)
Semenov Institute of Chemical Physics RAS, 119991, 4 Kosygin street, Moscow, Russia
e-mail: vvs@polymer.chph.ras.ru

I. V. Andrianov et al. (eds.), *Problems of Nonlinear Mechanics and Physics of Materials*, Advanced Structured Materials 94,
https://doi.org/10.1007/978-3-319-92234-8_9

[16, 17]. The pendulum's motion demonstrates the diversity of the dynamical behaviours that allows us to understand the transitions between regular and chaotic motions [18, 19]. In spite of the enormous volume of the studies, the problem of pendulum motion remains very exciting for the researches. It is of interest from the viewpoint of the applied as well as the fundamental sciences. The latter needs in understanding the basic principles of the dynamics of the essentially nonlinear system. Due to the strong nonlinearity of the pendulum's motion with the large amplitudes including the rotations, the majority of the problems are studied in the quasi-linear approximation or by the numerical methods. However, the analytic studies are very important for the progress of the nonlinear dynamics.

The aim of this paper is the description of the pendulum rotation as the process of the small amplitude oscillations on the background of the rotation with the average angle velocity. Introducing the complex variables we obtain the equations, the stationary solution of which describes these oscillations, while the non-stationary solutions correspond to the nearby trajectories in the phase space of the system. The rotation of the coupled pendula is considered from the viewpoint of the stability the in-phase and out-of-phase rotational modes. It is shown that the problem of the stability is reduced to the study of the parametric resonance, which can be solved analytically.

2 Rotation of Single Pendulum

We begin from the reformulation of the dynamical problem for the single pendulum. The pendulum energy is determined as follows:

$$H = \frac{1}{2}\left(\frac{d\varphi}{dt}\right)^2 + \sigma(1 - \cos\varphi), \tag{1}$$

where the dimensionless variables have been introduced: $t = \sqrt{g/l}t'$ with t' is the real time; l and g are the pendulum length and the acceleration due to gravity. φ is the deviation the pendulum from the origin. The "gravity" constant σ is kept for the generality and for the real pendulum $\sigma = 1$. Corresponding equation of motion has the form

$$\frac{d^2\varphi}{dt^2} + \sigma \sin\varphi = 0. \tag{2}$$

If the energy is smaller than 2σ, the pendulum undergoes a periodic oscillations with an amplitude $Q < \pi$ and the frequency

$$\omega = \sqrt{\frac{2J_1(Q)}{Q}}, \tag{3}$$

where J_1 is the Bessel function of the first order and the amplitude $Q = \arccos\left(1 - \frac{E_0}{\sigma}\right)$.

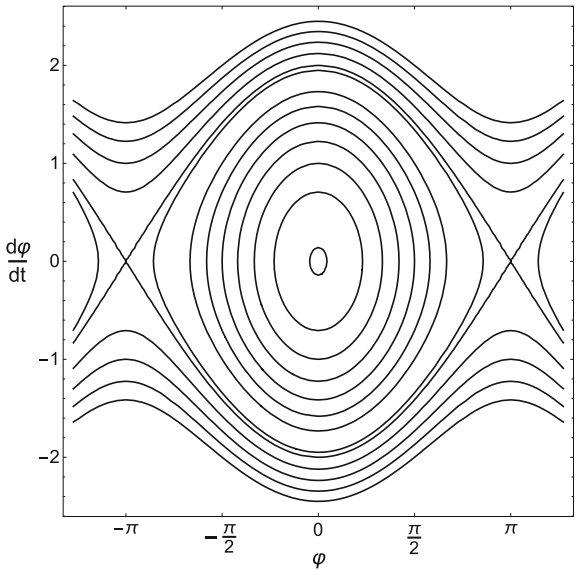

Fig. 1 The phase plane of the single pendulum. $\sigma = 1$

The periodic oscillations correspond to the close trajectories surrounding equilibrium point on the phase plane of the system. The rotation of the pendulum with energy $E_0 > 2\sigma$ corresponds to the transit-time trajectories on the phase plane (see Fig. 1). The rotation period is equal to

$$T = \oint dt = 2\int_0^{\pi} \frac{d\varphi}{\sqrt{2\left(E_0 - \sigma(1-\cos\varphi)\right)}} = \frac{2\sqrt{2}K\left(2\sigma/E_0\right)}{\sqrt{E_0}}, \tag{4}$$

where K is the complete elliptic integral of the first kind.

The average angle velocity is

$$\omega = \frac{2\pi}{T} = \frac{\pi\sqrt{E_0}}{\sqrt{2}K\left(2\sigma/E_0\right)}. \tag{5}$$

The instant velocity differs from the average one and it is undergoes a periodic oscillations with the period T and the amplitude, which depends on the rotation energy. It is clear that if the energy of the rotation is large enough, these oscillations are small and $\varphi \approx \omega t$. In such a case the equation of motion is

$$\frac{d^2\varphi}{dt^2} + \sigma \sin\omega t = 0. \tag{6}$$

It has the obvious solution

$$\varphi = \omega t + \lambda \sin\omega t, \tag{7}$$

where $\lambda = \frac{\sigma}{\omega^2} \ll 1$ and $\frac{d\varphi}{dt} = \omega + \frac{\sigma}{\omega}\cos\omega t$. Let' s try to define the oscillation amplitude. First, we need in the separation of the rotation and oscillation constituents. We assume that the instant angle φ is the sum of the rotation with the average angle velocity ω and oscillation ϕ:

$$\varphi = \omega t + \phi(t). \tag{8}$$

So, the equation of motion is transformed into following form:

$$\frac{d^2\phi}{dt^2} + \sigma(\cos\phi\sin\omega t + \sin\phi\cos\omega t) = 0. \tag{9}$$

This is the time to introduce the complex variable:

$$\begin{gathered} \Psi = \frac{1}{\sqrt{2}}\left(\frac{i}{\sqrt{\omega}}\frac{d\phi}{dt} + \sqrt{\omega}\phi\right); \\ \phi = \frac{1}{\sqrt{2\omega}}\left(\Psi + \Psi^*\right); \quad \frac{d\phi}{dt} = \sqrt{\frac{\omega}{2}}\left(\Psi - \Psi^*\right); \\ \frac{d^2\phi}{dt^2} = -i\sqrt{2\omega}\frac{d\Psi}{dt} + \frac{\omega^{3/2}}{\sqrt{2}}\left(\Psi - \Psi^*\right). \end{gathered} \tag{10}$$

Substituting expressions (10) into Eq. (9) and expanding the trigonometric functions into Taylor series, we can write

$$\begin{aligned} i\frac{d\Psi}{dt} - \frac{\omega}{2}\left(\Psi - \Psi^*\right) - \frac{\sigma}{2\sqrt{2\omega}}\Bigg(-i\left(e^{it\omega} - e^{-it\omega}\right)\sum_k \frac{(-1)^k}{(2k)!}\left(\frac{\Psi + \Psi^*}{\sqrt{2\omega}}\right)^{2k} \\ + \left(e^{-it\omega} + e^{it\omega}\right)\sum_k \frac{(-1)^k}{(2k+1)!}\left(\frac{\Psi + \Psi^*}{\sqrt{2\omega}}\right)^{2k+1}\Bigg) = 0. \end{aligned} \tag{11}$$

Because the frequency of oscillations coincides with the average velocity of the rotation, we should extract the rotation frequency as follows:

$$\Psi = \chi e^{-i\omega t}. \tag{12}$$

Substituting this expression into above equation we get the equation for unknown complex function χ. However, taking into account solution (7) one should assume that this variable is a constant. So, multiplying the equation by $e^{i\omega t}$ and integrating for the period T, we obtain

$$\frac{\omega}{2}\chi + \frac{i\sigma}{2\sqrt{2\omega}}\sum_{k=0}^{\infty}\frac{(-1)^k}{(2\omega)^k}\left(\frac{\chi^{k+1}\chi^{*k-1}}{(k-1)!(k+1)!} - \frac{\chi^k\chi^{*k}}{(k!)^2}\right) = 0. \tag{13}$$

The sums in Eq. (13) can be calculated, and the final equation is written as follows:

$$\frac{\omega}{2}\chi + \frac{i\sigma}{2\sqrt{2\omega}}\left(\frac{\chi-\chi^*}{\chi^*}J_0\left(\sqrt{\frac{2}{\omega}}|\chi|\right) - \sqrt{2\omega}\frac{|\chi|}{\chi^{*2}}J_1\left(\sqrt{\frac{2}{\omega}}|\chi|\right)\right) = 0, \quad (14)$$

where J_0 and J_1 are the Bessel functions of zero and first order.

Equation (14) allows us to define the amplitude of the oscillations around the average angle velocity (5) during the period. Representing the value χ as $ae^{i\delta}$, we obtain two equations:

$$\left(\sqrt{\frac{2}{\omega}}\sigma \sin\delta\, J_2\left(\sqrt{\frac{2}{\omega}}a\right) + a\omega\right)\cos\delta = 0. \quad (15)$$

$$\sqrt{\frac{2}{\omega}}\sigma \sin^2\delta\, J_0\left(\sqrt{\frac{2}{\omega}}a\right) + \frac{\sigma\left(1-2\sin^2(\delta)\right)}{a}J_1\left(\sqrt{\frac{2}{\omega}}a\right) - a\omega\sin\delta = 0. \quad (16)$$

Equation (15) has two solutions but only one of them is physically sensible. It is $\delta = \pi/2$. It correlates with approximating solution (7) obtained above. Taking into account the value of δ after some simple reductions, we obtain the transcendental equation for variable a, which can be solved numerically for a fixed value of the average angle velocity ω.

$$\frac{\sigma}{a}J_1\left(\sqrt{\frac{2}{\omega}}a\right) - \omega a = 0. \quad (17)$$

The comparison of the value $\sqrt{\frac{2}{\omega}}a$, which is the amplitude of the oscillating function ϕ, with the asymptotic value λ (see Eq. (7)) is shown in Fig. 2. It is clear that the compliance between these values is excellent for the energies $E_0 > 3.0$. One should note, that, in spite of the analysis has been performed under the assumption that the oscillatory component is small enough (the high-energy rotations), its expansion into the range of the low-energy rotations demonstrates the same behaviour as the expansion of the value $\lambda(\omega)$.

Now it is important to compare the value of the rotation velocity defined by Eq. (17) with the exact solution. Such comparison is represented in Fig. 3. One can see that the compliance between values is good enough for the rotation energy $E_0 > 2.75$, but the plots show different behaviour near the start point of the rotation $E_0 = 2$. It is very expected behaviour because of the essential anharmonicity (and the retardation) of the oscillations in the vicinity of the separatrix.

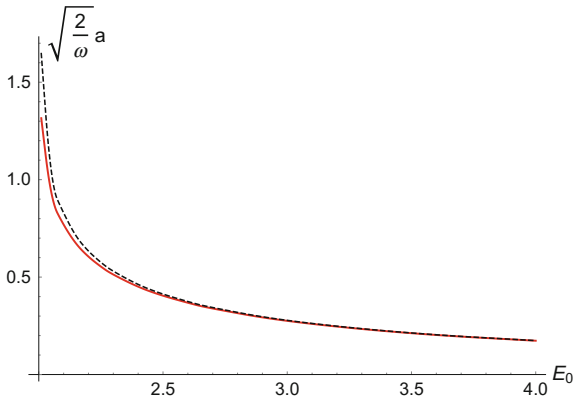

Fig. 2 Comparison of the solutions of Eq. (17) (solid red curve) with the asymptotic value λ (dashed black curve) at the different values of the rotation energy E_0. The parameter $\sigma = 1$

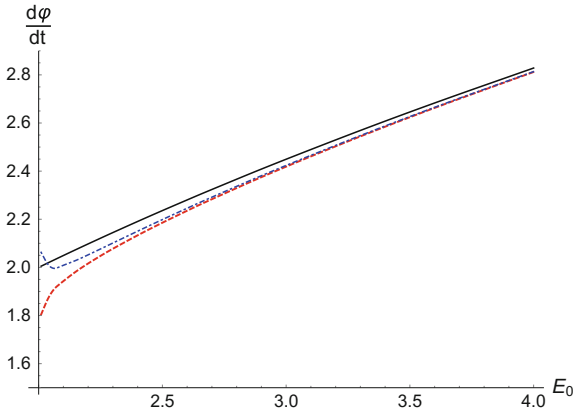

Fig. 3 Comparison of the exact value of the rotation velocity (solid black curve) with the solutions of Eq. (17) (dashed red curve) and the asymptotic value (dot-dashed blue curve) at the different values of the rotation energy E_0. The parameter $\sigma = 1$

Equations (15) and (16) are the equations of the equilibrium for the system with energy

$$H_1 = \frac{\omega}{2}a^2 - \sigma J_1\left(\sqrt{\frac{2}{\omega}}a\right)\sin\delta \tag{18}$$

or

$$H_1 = \frac{\omega}{2}|\chi|^2 - i\frac{\sigma}{2}J_1\left(\sqrt{\frac{2}{\omega}}|\chi|\right)\frac{\chi - \chi^*}{|\chi|}. \tag{19}$$

Considering expression (18) as the Hamilton function, one can obtain the non-stationary equation for the variables a, δ. The set of the canonical variables of the Hamilton function (18) is formed by the values a^2 and δ. In such a case, the dynamical equations can be written as follows:

$$\frac{da^2}{dt} = 2a\frac{da}{dt} = -\frac{\partial H_1}{\partial \delta}, \qquad \frac{d\delta}{dt} = \frac{\partial H_1}{\partial a^2} = \frac{1}{2a}\frac{\partial H_1}{\partial a}. \tag{20}$$

A non-stationary dynamics of the system with Hamilton function (18) occurs when the initial conditions do not correspond to the stationary point which are determined by Eqs. (15) and (16) at the fixed value of parameter ω. In such a case the imaginary point moves along the one of the trajectories surrounding the stationary state (see Fig. 4). One should note that there are two kinds of the trajectories. The trajectories of the first kind encircle the stationary point and the trajectories of second type are the transit-time ones, along of which the variable δ increases indefinitely. These classes of the trajectories are separated by the Limiting Phase Trajectory (LPT) which is shown in Fig. 4 by red dashed line.

What is the non-stationary dynamics from the viewpoint of original system (1)? Coming back to the variable φ (see Eqs. (8) and (10)), one can write follows:

$$\varphi(t) = \omega t + \sqrt{\frac{2}{\omega}}\, a \sin(\omega t + \delta). \tag{21}$$

If a and δ are the constant values, which are determined by Eqs. (15) and (16), the functions φ, $d\varphi/dt$ describe the trajectory on phase portrait in Fig. 1, which is specified by the parameter ω. If it is wrong, φ is the slowly changed function, its slowness is determined by the time of the single pass of the representing point along some trajectory in phase portrait on Fig. 4.

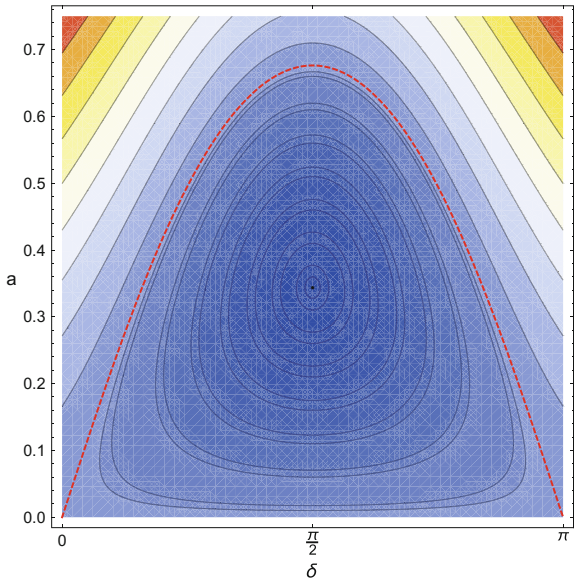

Fig. 4 Phase portrait of system (18) in the variables (δ, a). The Limiting Phase Trajectory is shown by the red dashed curve

However, because of the trajectory set in Fig. 1 is dense everywhere, there is no non-stationary regimes in the single pendulum rotation. Therefore, one should conclude that the non-stationary trajectories on the phase portrait on Fig. 4 describe the neighbourhood of the chosen trajectory on Fig. 1. So, the non-stationary dynamics of the single pendulum rotation is sensible if we need in accounting the external perturbations, but the non-stationary approach is very effective for the dynamical analysis of more complicated systems, where the processes of the energy exchange and localization are important.

In the next section we will consider two weakly coupled pendulums under rotation and will use the above procedure for the study of non-stationary dynamics.

3 Rotation of Two Weakly Coupled Pendulums

The energy of two pendulums is determined as follows:

$$H = \sum_{j=1,2} \left(\frac{1}{2} \left(\frac{d\varphi_j}{dt} \right)^2 + \sigma (1 - \cos \varphi_j) + \frac{\beta}{2} \left(1 - \cos \left(\varphi_j - \varphi_{3-j} \right) \right) \right). \tag{22}$$

The equation of motion has the form

$$\frac{d^2 \varphi_j}{dt^2} - \beta \sin \left(\varphi_{3-j} - \varphi_j \right) + \sigma \sin \varphi_j = 0; \quad j = 1, 2. \tag{23}$$

It can be checked immediately that the in-phase mode $\psi_1 = (\varphi_1 + \varphi_2)/2$ as well as the out-of phase mode $\psi_2 = (\varphi_1 - \varphi_2)/2$ are the exact solutions of the equations:

$$\begin{aligned} \frac{d^2 \psi_1}{dt^2} + \sigma \cos \psi_2 \sin \psi_1 = 0, \\ \frac{d^2 \psi_2}{dt^2} + \beta \sin 2\psi_2 + \sigma \cos \psi_1 \sin \psi_2 = 0. \end{aligned} \tag{24}$$

Continuing the oscillatory terminology, we call the uni-directional and contra-directional rotations as the in-phase and out-of-phase modes, respectively. The problem of the description of the coupled pendula rotations is that we can not construct any unified set of the asymptotic equations for the different kinds of rotations, because the sign of the rotation velocity is essential for the asymptotic procedure. Therefore we need in a separated description of the each mode.

3.1 In-Phase Rotation of Coupled Pendula

We start from the analysis of more simple in-phase mode. The first of Eq. (24) shows that if the out-of-phase component is negligible, the system is the analogue of the single pendulum and the results of the previous section can be used immediately.

However, if we take an interest in the stability of the in-phase rotation of the coupled pendula, one should consider the interaction of the modes. The numerical simulation shows that the instability of in-phase rotation of coupled pendula can be manifested as a short-time modulation of the rotation frequency of the both pendula (Fig. 5). Figure 5 shows a manifestation of the instability near its low boundary in the plane $\{\omega,\ \beta\}$. The unstable in-phase rotation far from the low boundary is specified by abrupt acceleration and retardation of the pendula up to transition of one of them into the oscillatory movement.

Now we try to find the source of the instability and to define the crucial parameters. Let us assume that the rotation frequency is large enough and the variable $\psi_1 \approx \omega t$ (see previous section), while the energy of out-of-phase mode ψ_2 is small. In such a case we propose that the first of Eq. (24) is satisfied and we write the second of these equations as follows:

$$\frac{d^2\psi_2}{dt^2} + (2\beta\cos\psi_2 + \sigma\cos\omega t)\sin\psi_2 = 0. \tag{25}$$

Accounting that ψ_2 takes a small value, we assume $\cos\psi_2 \approx 1$. (Generally speaking this assumptions is not required, but it makes the follows calculations more transparent.) So, Eq. (25) becomes

$$\frac{d^2\psi_2}{dt^2} + (2\beta + \sigma\cos\omega t)\sin\psi_2 = 0. \tag{26}$$

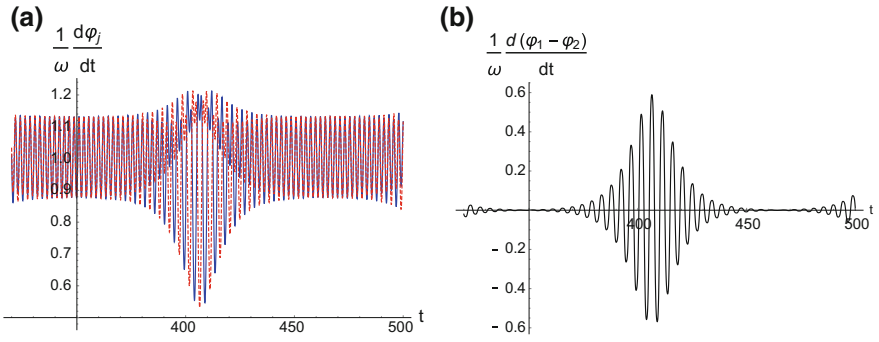

Fig. 5 Instability of the in-phase rotation of two coupled pendula. **a** The rotation velocities $\varphi_j{}'$ of the first and second pendula (blue and red dashed curves, respectively) versus time t. **b** The difference of rotation velocities of the pendula for the time range, which corresponds to the panel **a**. The parameters are $\sigma = 1, \beta = 0.8, \omega = 2.7945$

Equation (26) is the well-known equation of the parametrically excited pendulum. Therefore, the parametric resonance should occur for the some combinations of the parameters $\{\beta,\ \sigma,\ \omega\}$. Because we assume that the "gravity" force (σ) is constant, we can vary the rotation frequency ω and the coupling parameter β. In order to find the boundaries of the parametric resonance, we will use the approach, which is an analogue of used above. It is known [20] that the first parametric resonance occurs at the frequency, which is equal to the half of the own frequency of the system. So, we introduce the complex variables similar to presented above Eq. (10), changing the frequency ω by the value $\Omega = \omega/2$. The method of the extraction of the secular terms has been already described in detail above, therefore we write the stationary equations for the amplitude a and the phase δ immediately:

$$\begin{gathered} \frac{\sigma}{a} J_2\left(\sqrt{\frac{2}{\Omega}}a\right)\sin 2\delta = 0 \\ \frac{\Omega}{2}a - \frac{1}{\sqrt{2\Omega}}2\beta J_1\left(\sqrt{\frac{2}{\Omega}}a\right) - \frac{\sigma}{\sqrt{2\Omega}}\left[J_1\left(\sqrt{\frac{2}{\Omega}}a\right) - \frac{\sqrt{2\Omega}}{a}J_2\left(\sqrt{\frac{2}{\Omega}}a\right)\right]\cos 2\delta = 0. \end{gathered} \tag{27}$$

Equations (27) describe the stationary oscillations with the frequency Ω for the system, which is defined by Eq. (26). One can show that the value $a = 0$ satisfies Eq. (27) at various values of δ.

The energy corresponding to Eq. (27) is written as follows:

$$H_2 = \frac{\Omega}{2}a^2 - 2\beta\left(1 - J_0\left(\sqrt{\frac{2}{\Omega}}a\right)\right) - \sigma J_2\left(\sqrt{\frac{2}{\Omega}}a\right)cos2\delta. \tag{28}$$

Considering this value as the Hamilton function of reduced system, one can obtain the equations of motion according to rules (20). Let us consider the phase plane of the system with Hamilton function (28). Some examples of it are shown in Fig. 6.

If the coupling parameter β is small enough, there is no stationary solutions, which are differed from the $a = 0$. Therefore, no parametric instability exists due to that any excitation in the vicinity the line $a = 0$ can not grow. The phase plane which is specific for small values of coupling parameter β is shown in panel (a) of Fig. 6.

Figure 6b shows the phase plane of system (28) after the first bifurcation resulting in the generation of new stationary state with $a \neq 0$ at the line $\delta = 0$. The stationary value of the amplitude a can be found as the solution of Eq. (27). This stationary state is surrounded by the set of the close trajectories, the most remote of which passes through zero state ($a = 0$). It is the LPT (see previous section). This trajectory separates two different sets of the trajectories - the periodic and transit-time ones. It is important to emphasize that the parametric instability starting from zero state (with an arbitrary value of the phase δ) is realized via the LPT.

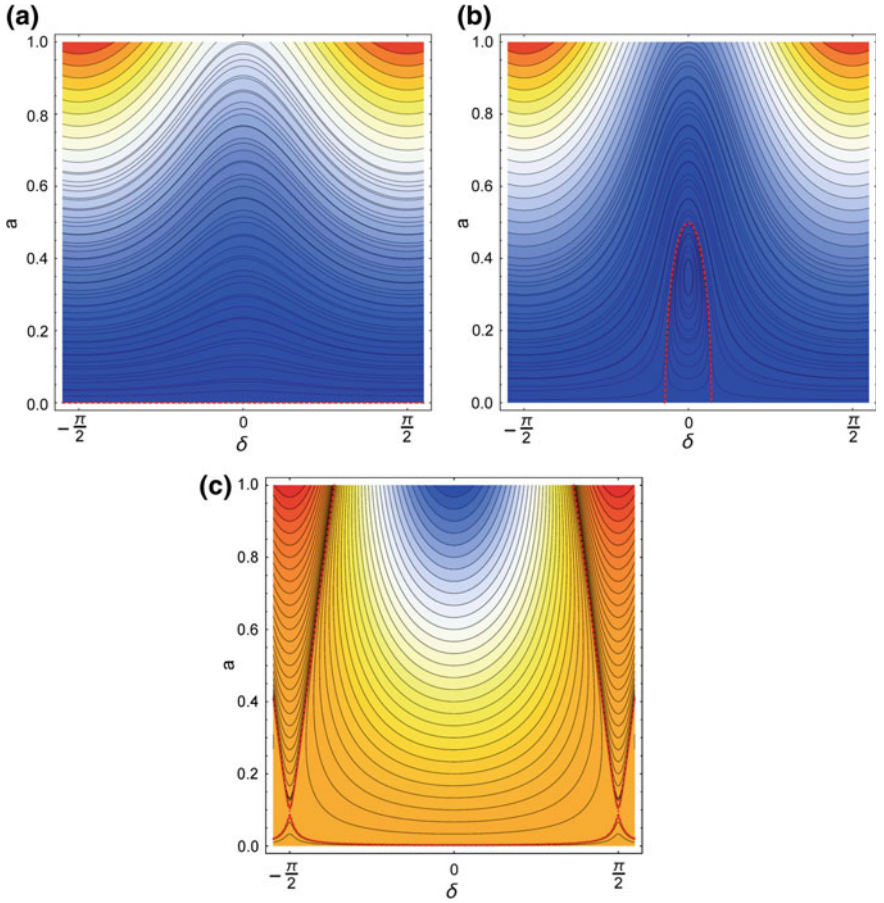

Fig. 6 The phase plane of system (28) at three values of the coupling β **a** $\beta = 0.5$, **b** $\beta = 0.7228$, **c** $\beta = 1.2275$. $\omega = 2.7945$, $\sigma = 1$

One can calculate the threshold value of the coupling parameter β, taking into account that the creation of stationary state in Fig. 6 needs in the condition $\partial^2 H_2/\partial a^2 < 0$ for the variables' values $a = 0$ and $\delta = 0$. So, one can formulate the criterion for the bifurcation threshold:

$$\frac{\partial^2 H_2}{\partial a^2}_{|a=0,\delta=0} = 0. \tag{29}$$

This condition leads to next value of the instability threshold:

$$\beta_{bottom} = \frac{1}{4}\left(2\Omega^2 - \sigma\right). \tag{30}$$

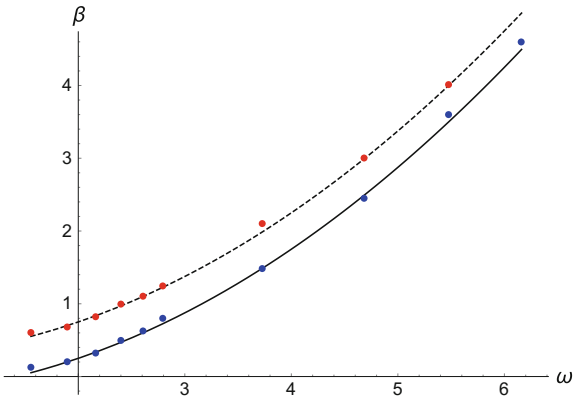

Fig. 7 The domain of instability of the in-phase rotation on the plane $(\omega,\ \beta)$. The solid and dashed curves correspond to instability thresholds (30) and (31), respectively. The color points show the numerically measured values (blue and red points correspond to low and high boundaries of instability, respectively)

Figure 6c shows the phase plane after second bifurcation resulting in the creation of stationary points at the phase $\delta = \pm\pi/2$. It is important that every stationary point is the saddle, i.e., corresponds to unstable state. The latter means that the trajectories passing through this point are the separatrixes (they are shown by the red dashed curves in Fig. 6c). Therefore, they distinctly separate the space below and above of them and none trajectories starting below the separatrix can not grow. So, the creation of these stationary states leads to the inhibition of the parametric instability. One can estimate the threshold of this process using the criterion (29) for the $\delta = \pi/2$. The crucial value of the coupling parameter β turns out to be:

$$\beta_{top} = \frac{1}{4}\left(2\Omega^2 + \sigma\right). \tag{31}$$

One can compare the threshold values (30) and (31) with the data of the numerical simulation of original system (23). Figure 7 shows the domain of instability in the plane $(\omega,\ \beta)$ as it is calculated by criteria (30) and (31). The red and blue points represent the instability thresholds measured in the numerical simulation. One can say that the agreement is excellent.

3.2 Out-of-Phase Rotation of Coupled Pendula

The out-of-phase mode ψ_2 is described by second of Eq. (23). Under assumption $\psi_1 = 0$ it has the form:

$$\frac{d^2\psi_2}{dt^2} + \beta \sin 2\psi_2 + \sigma \sin \psi_2 = 0. \tag{32}$$

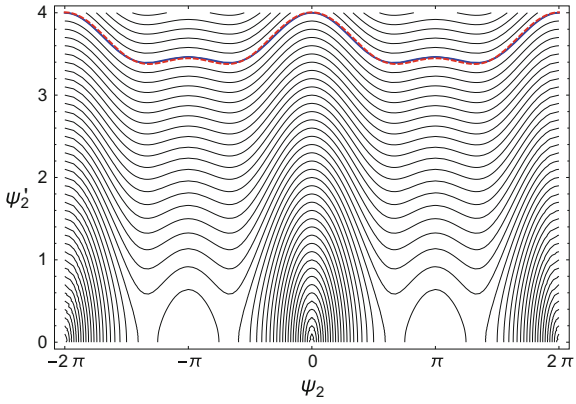

Fig. 8 The part of the phase plane of the system (32) for the parameters $\sigma = 1,\ \beta = 1$. The approximate solution (35) is shown by the red dashed line. The respective exact trajectory is marked by blue line. The total energy $E_0 = 8$ and the rotation frequency $\omega = 3.5868$

This equation is essentially differed from the first of Eq. (23) because of the presence of $\sin 2\psi_2$. If the coupling constant $\beta > \sigma/2$ the additional stationary point occurs (see Fig. 8). Therefore, there is no single-frequency solution for Eq. (32). Naturally, one can find the exact solution of this equation in the quadrature. However, such a representation does not allow us to analyse the stability of the out-of-phase rotation mode. In order to perform the stability analysis we use the approximate solution, which can be found by analogy with Eq. (7). We can assume that the oscillatory part of the solution is small enough and rewrite Eq. (32) as follows:

$$\frac{d^2\psi_2}{dt^2} + \beta \sin 2\omega t + \sigma \sin \omega t = 0, \tag{33}$$

where the rotation frequency

$$\omega = \pi \left(\int_0^{\pi} \frac{d\psi}{\sqrt{2\left(E_0 - \beta\left(1 - \cos 2\psi\right) - \sigma\left(1 - \cos\psi\right)\right)}} \right)^{-1}. \tag{34}$$

In such a case we can write the solution of Eq. (33) as follows:

$$\psi_2 = \omega t + \frac{\sigma}{\omega^2} \sin \omega t + \frac{\beta}{4\omega^2} \sin 2\omega t. \tag{35}$$

The comparison of solution (35) with the exact trajectories in the phase plane is represented in Fig. 8

In order to analyse the stability of the out-of-phase rotation one should use the first of Eq. (24) in the form:

$$\frac{d^2\psi_1}{dt^2} + \sigma \cos\psi_2 \sin\psi_1 \approx \frac{d^2\psi_1}{dt^2} + \sigma \cos\omega t \sin\psi_1 = 0. \tag{36}$$

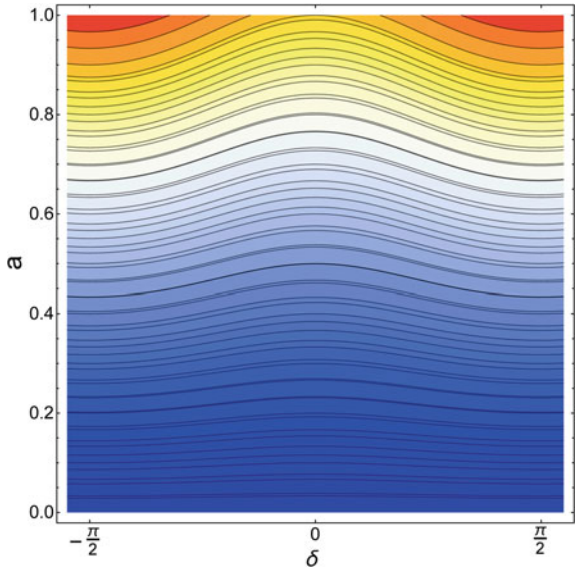

Fig. 9 The phase plane of system (37) for the parameters: $\sigma = 1, \omega = 3.5868$

One can see that this equation is similar to Eq. (27) under assumption $\beta = 0$. So, we can use the results of the previous section and write the respective Hamilton function for the disturbance:

$$H = \frac{\Omega}{2}a^2 - \sigma J_2\left(\sqrt{\frac{2}{\Omega}}a\right)cos2\delta, \tag{37}$$

where $\Omega = \omega/2$.

The topology of the phase plane of system (37) is shown in Fig. 9 and it is similar to the one in Fig. 6a. There is no stationary states in this phase portrait and all of the trajectories are the transit-time ones. It is important that the phase portrait preserves the same structure for any values of rotation frequency. This fact allows us to conclude that the out-of-phase rotations of coupled pendula is the stable process.

4 Conclusion

We considered the rotational motion of both the single and the coupled pendula in the different regimes. The asymptotic analysis of the oscillation of the pendulum's velocity during the rotation has been preliminary performed for the single pendulum. It shows the efficiency of the method for the description of the rotation. The analysis of the stability of the both in-phase and out-of-phase rotations of two coupled pendula shows the qualitative difference between these modes. If the out-of-phase

rotation shows the stability for all values of the parameters (the "gravity" force σ, coupling parameter β and rotation frequency ω), the in-phase mode demonstrates some range of instability for these parameters. We have found the origin of instability in the parametric excitation of the out-of-phase mode by the in-phase rotation. (It is interesting to note that in spite of difference between the conservative (this work) and the dissipative forced dynamics [17] of the coupled pendula the conditions and scenario of the in-phase rotation instability turn out to be actually the same.) The analysis performed in the framework of the asymptotic approach allows us to find both the sources of instability and their boundaries. All the trajectories of the out-of-phase perturbations, which can lead to destruction of the in-phase rotation, are the transit-time ones for the small values of the coupling β and an arbitrary values of the rotation frequencies. The low boundary of the parameter corresponds to the formation of the center-type stationary point. Its generation is accompanied by the creation of the LTP, which separates the transit-time and closed trajectories and passes through zero value of the perturbation's amplitude. Therefore any small out-of-phase perturbations are forced along the LPT that leads to the instability of the in-phase rotation. This situation occurs while the coupling β grows up to the value at which the second bifurcation happens. As the result of this bifurcation new saddle-type stationary states arise. However, the separatrix crossing this stationary point does not forbids only small amplitude perturbations. Therefore, at this point the instability of in-phase rotation becomes to be impossible. The method used for the analysis permits to find the analytic dependences of the instability boundaries on the system parameters. The estimations made in the framework of the method, are in excellent agreement with the numerical simulation data.

Acknowledgements Author is grateful to Prof. L.I. Manevitch for his attention to the work and fruitful discussion.

This work was supported by the Program of Fundamental Researchers of the Russian State Academies of Sciences 2013–2020 (project No. 0082-2014-0013)

References

1. Baker, G.L., Blackburn, J.A.: The Pendulum. A Case Study in Physics. Oxford University Press, New York (2005)
2. Braun, O.M., Kivshar, Yu.S.: The Frenkel–Kontorova Model. Idea. Concept. Methods. Springer, Berlin (2004)
3. Cuevas-Maraver, J., Kevrekidis, P.G., Williams, G. (eds.): The Sine-Gordon Model and its Applications. From Pendula and Josephson Junctions to Gravity and High-Energy Physics. Springer, Heidelberg (2014)
4. Scott, A.: Nonlinear Science. Emergence and Dynamics of Coherent Structures. Oxford University Press, New York (2003)
5. Yakushevich, L.V.: Nonlinear Physics of DNA. Wiley VCH, Weinheim (2004)
6. Gendelman, O.V., Savin, A.V.: Normal heat conductivity of the one-dimensional lattice with periodic potential of nearest-neighbor interaction. Phys. Rev. Lett. **84**, 2381 (2000)
7. Lepri, S., Livi, R., Politi, A.: Thermal conduction in classical low-dimensional lattices. Phys. Rep. **377**, 1 (2003)

8. Takeno, S., Homma, S.: A sine-lattice (sine-form discrete sine-gordon) equation. J. Phys. Soc. Jpn. **55**, 65 (1986)
9. Cadoni, M., et al.: Twist solitons in complex macromolecules: from DNA to polyethylene. Int. J. Nonlinear Mech. **43**, 1094 (2008)
10. Homma, S.: Thermodynamic properties of coupled sine-lattice. Phys. D **113**, 202 (1998)
11. Homma, S.: Statistical mechanical theory of DNA denaturation. J. Biol. Phys. **24**, 115 (1999)
12. Takeno, S., Peyrard, M.: Nonlinear rotating modes: green's-function solution. Phys. Rev. E **55**, 1922 (1997)
13. Mazo, J., Orlando, T.P.: Discrete breathers in Josephson arrays. Chaos **13**, 733 (2003)
14. Manevitch, L.I., Romeo, F.: Non-stationary resonance dynamics of weakly coupled pendula. EPL **112**, 30005 (2015)
15. Manevitch, L.I., Smirnov, V.V., Romeo, F.: Non-stationary resonant dynamics of the harmonically forced pendulum. Cybern. Phys. **5**, 91 (2016)
16. Qian, M., Wang, J.-Z.: Transitions in two sinusoidally coupled Josephson junction rotators. Ann. Phys. **323**, 1956 (2008)
17. Smirnov, L.A., et al.: Bistability of rotational modes in a system of coupled pendulums. Regul. Chaotic Dyn. **21**, 849 (2016)
18. Sagdeev, R.Z., Usikov, D.A., Zaslavsky, G.M.: Nonlinear Physics: From the Pendulum to Turbulence and Chaos. Harwood Academic Publishers, New York (1988)
19. Zaslavsky, G.M.: Hamiltonian Chaos and Fractional Dynamics. Oxford University Press, New York (2005)
20. Butikov, E.I.: Parametric excitation of a linear oscillator. Eur. J. Phys. **25**, 535 (2004)

Plane Motion of a Rigid Body Suspended on Nonlinear Spring-Damper

Roman Starosta, Grażyna Sypniewska-Kamińska and Jan Awrejcewicz

Abstract The paper deals with the analytical investigation of the behaviour of the harmonically excited physical pendulum suspended on the nonlinear spring. The asymptotic method of multiple scales (MS) has been used to derive approximate solutions in the analytical form. The applied approach allows one to perform a qualitative analysis of the behaviour of the system. MS method gives possibility, among others, to recognize resonance conditions which can appear in the system.

1 Introduction

Although pendulums are relatively simple systems, they can be used to simulate the dynamics of a variety of engineering devices and machine parts. The behaviour of pendulum-type mechanical systems with nonlinear and parametric interactions is complicated, and hence its understanding and prediction are important from a point of view of both the theory and application. The coupling of the equations of motion results in a possibility of autoparametric excitation and is connected to the energy exchange between vibration modes [6]. Various kinds of pendulums are widely discussed in numerous references and analytical investigations are recently of great interest of many researchers. Main and parametric resonances of the kinematically driven spring pendulum are studied in the paper [2]. The nonlinear response of a system including a double pendulum and having three degrees of freedom (DOFs) is analytically investigated in the paper [5]. Stationary and non-stationary resonant

R. Starosta (✉) · G. Sypniewska-Kamińska
Poznan University of Technology, Institute of Applied Mechanics, Poznań, Poland
e-mail: Roman.starosta@put.poznan.pl

G. Sypniewska-Kamińska
e-mail: Grazyna.Sypniewska-Kaminska@put.poznan.pl

J. Awrejcewicz
Department of Automatics, Biomechanics and Mechatronics, Łódź University of Technology, Łódź, Poland
e-mail: jan.awrejcewicz@p.lodz.pl

I. V. Andrianov et al. (eds.), *Problems of Nonlinear Mechanics and Physics of Materials*, Advanced Structured Materials 94,
https://doi.org/10.1007/978-3-319-92234-8_10

dynamics of the harmonically forced pendulum is the subject of the paper [4]. The physical pendulum suspended on the spring-damper which has linear features has been modelled and discussed in the article [1]. The present paper extends these investigations and presents further development of the model and results of asymptotic analysis.

2 Problem Formulation and Equations of Motion

Plane motion of a rigid body mounted on a spring-damper suspension is analyzed in the paper. The scheme of the system is presented in Fig. 1. The spring is assumed to be massless and nonlinear. The non-linearity is of the cubic type, and k_1 and k_2 are constant elastic coefficients. L_0 denotes the spring length in the non-stretched state. There is a purely viscous damper having a damping coefficient C_1, and the damper and the spring are arranged in parallel. The rigid body of mass m is connected to this system via a pin joint A. The distance between the point A and the mass centre C of the body is denoted by S and called further the eccentricity. The body moment of inertia relative to the axis passing through the centre of mass C and perpendicular to the plane of motion is equal to I_C. In the direction compatible with the main axis of the suspension system acts the known force $\mathbf{F}$ the magnitude of which changes harmonically $F(t) = F_0 \cos(\Omega_1 t)$. Besides, the system is loaded by two known harmonically changing torques $M_1(t) = M_{01} \cos(\Omega_2 t)$ and $M_2(t) = M_{02} \cos(\Omega_3 t)$ shown in Fig. 1. There are also assumed two torques of the viscous nature attenuate the swing vibration related to the angles Φ and Ψ, where C_2 and C_3 are their viscous coefficients. The body is free in its plane motion, so it has three degrees of freedom. The time functions $X(t)$, $\Phi(t)$ and $\Psi(t)$ are assumed as the generalized coordinates. The coordinate $X(t)$ is understood as the total elongation of the spring involving also the static elongation X_r that satisfies the equilibrium condition

$$k_2 X_r^3 + k_1 X_r = mg. \tag{1}$$

The kinetic and potential energy of the system are

$$\mathrm{T} = m\,S\,\dot{X}\,\dot{\Psi}\,\sin(\Phi - \Psi) + S\,m\,\dot{\Phi}\,\dot{\Psi}(L_0 + X)\cos(\Phi - \Psi) + \frac{1}{2}R_A^2 m\dot{\Psi}^2 + \frac{m}{2}(L_0 + X)^2\dot{\Phi}^2 + \frac{m}{2}\dot{X}^2, \tag{2}$$

$$\mathrm{V} = \frac{1}{2}k_1 X^2 + \frac{1}{4}k_2 X^4 - mg((L_0 + X)\cos(\Phi) + S\,\cos(\Psi)). \tag{3}$$

In Eq. (2) occurs the quantity denoted by R_A which is a radius of gyration of the body with respect to the axis passing through the joint A and perpendicular to the plane of motion. The radius R_A is related to the inertia moment I_C by commonly known parallel axis theorem

$$mR_A^2 = I_C + mS^2. \tag{4}$$

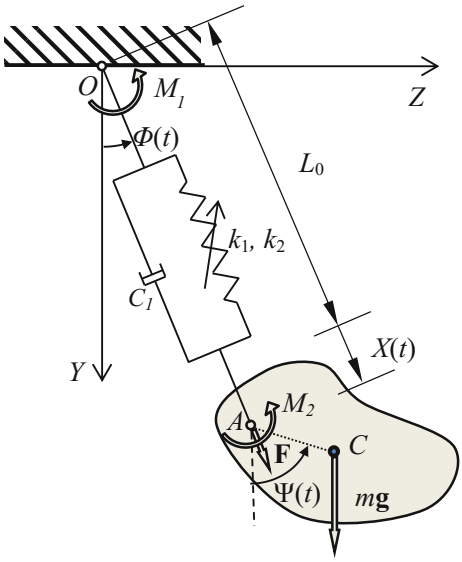

Fig. 1 Mass-spring-damper system

In order to obtain the equations of motion we write the equations Lagrange equations of the second kind

$$\frac{d}{dt}\left(\frac{\partial \mathrm{L}}{\partial \dot{X}}\right) - \left(\frac{\partial \mathrm{L}}{\partial X}\right) = Q_X,\ \frac{d}{dt}\left(\frac{\partial \mathrm{L}}{\partial \dot{\Phi}}\right) - \left(\frac{\partial \mathrm{L}}{\partial \Phi}\right) = Q_\Phi,\ \frac{d}{dt}\left(\frac{\partial \mathrm{L}}{\partial \dot{\Psi}}\right) - \left(\frac{\partial \mathrm{L}}{\partial \Psi}\right) = Q_\Psi, \tag{5}$$

where $\mathrm{L} = T - V$ is the Lagrange function, and the general forces are given by

$$\begin{aligned} Q_X &= F_0 \cos(\Omega_1 t) - C_1 \dot{X}, \\ Q_\Phi &= M_{02} \cos(\Omega_2 t) - C_2 \dot{\Phi}, \\ Q_\Psi &= M_{03} \cos(\Omega_3 t) - C_3 \dot{\Psi}. \end{aligned} \tag{6}$$

The dimensionless form of the equations of motion derived from (5) is as follow

$$\begin{aligned} &\ddot{\xi} + c_1\dot{\xi} + \xi + \alpha\,\xi^3 + 3\xi_r\alpha\,\xi^2 + 3\xi_r^2\alpha\,\xi - w_2^2(\cos\varphi - 1) - (1+\xi)\dot{\varphi}^2 \\ &\quad - s\,\cos(\varphi - \gamma)\dot{\gamma}^2 + s\,\sin(\varphi - \gamma)\ddot{\gamma} = f_1\cos(p_1\tau), \end{aligned} \tag{7}$$

$$\begin{aligned} &\ddot{\varphi}\left(1 + 2\xi + \xi^2\right) + w_2^2 \sin\varphi(1+\xi) + c_2\dot{\varphi} + 2\dot{\xi}\,\dot{\varphi} + 2\xi\,\dot{\xi}\dot{\varphi} \\ &\quad + s\,\sin(\varphi - \gamma)(1+\xi)\dot{\gamma}^2 + s\,\cos(\varphi - \gamma)(1+\xi)\ddot{\gamma} = f_2\cos(p_2\tau), \end{aligned} \tag{8}$$

$$\begin{aligned} &\ddot{\gamma} + w_3^2 \sin\gamma + c_3\dot{\gamma} + 2\frac{w_3^2}{w_2^2}\cos(\varphi - \gamma)\dot{x}\dot{\varphi} - \frac{w_3^2}{w_2^2}(1+\xi)\sin(\varphi - \gamma)\dot{\varphi}^2 \\ &\quad + \frac{w_3^2}{w_2^2}\sin(\varphi - \gamma)\ddot{\xi} + \frac{w_3^2}{w_2^2}(1+\xi)\cos(\varphi - \gamma)\ddot{\varphi} = f_3\cos(p_3\tau). \end{aligned} \tag{9}$$

The frequency $\omega_1 = \sqrt{\frac{k_1}{m}}$ and the spring length $L = L_0 + X_r$ in the static equilibrium position are assumed as the reference quantities. The functions $\varphi(\tau)$ and $\gamma(\tau)$ of the dimensionless time $\tau = \omega_1 t$ are generalized coordinates related to $\Phi(t)$ and $\Psi(t)$, respectively, whereas $\xi(t)$ is associated with $X(t)$ by the relation $\xi(t) = X(t)/L$. The others dimensionless quantities are defined as follows:

$$s = S/L, \xi = X/L, \xi_r = X_r/L,$$

$c_1 = \frac{C_1}{m\omega_1}$, $c_2 = \frac{C_2}{mL^2\omega_1}$, $c_3 = \frac{C_3}{\omega_1 m\, r_A^2 L^2}$, $f_1 = \frac{F_0}{mL\omega_1^2}$, $f_2 = \frac{M_{01}}{mL^2\omega_1^2}$, $f_3 = \frac{M_{02}}{\omega_1^2 m\, R_A^2 L^2}$, $\alpha = \frac{k_2 L^2}{\omega_1^2 m}$, $w_2 = \frac{\omega_2}{\omega_1}$, $w_3 = \frac{\omega_3}{\omega_1}$, $p_1 = \frac{\Omega_1}{\omega_1}$, $p_2 = \frac{\Omega_2}{\omega_1}$, $p_3 = \frac{\Omega_3}{\omega_1}$, where $\omega_2^2 = \frac{g}{L}$ and $\omega_3^2 = \frac{S\,g}{R_A}$. Dimensionless counterpart of condition (1) is

$$\alpha\, \xi_r^3 + \xi_r = w_2^2. \tag{10}$$

Equations (7)–(9) are supplemented by the initial conditions related the generalized coordinates and their first derivatives

$$\xi(0) = u_{01}, \dot{\xi}(0) = u_{02}, \varphi(0) = u_{03}, \dot{\varphi}(0) = u_{04}, \gamma(0) = u_{05}, \dot{\gamma}(0) = u_{06}, \tag{11}$$

where dimensionless quantities $u_{01}, \ldots, u_{06}$ are known.

3 Multiple Scales Method

The oscillations of the system are investigated in the neighborhood of the equilibrium position, hence the trigonometric functions of the generalized coordinates can be substituted by their power series approximations

$$\sin\varphi \approx \varphi - \varphi^3/6, \cos\varphi \approx 1 - \phi^2/2, \sin\gamma \approx \gamma - \gamma^3/6, \cos\gamma \approx 1 - \gamma^2/2. \tag{12}$$

The method of multiple scales (MSM) is used to solve the initial value problem described by (7)–(9) and (11). According to this method, we introduce two scales related to the dimensionless time as follows: the fast scale $\tau_0 = \tau$ and the slow scale $\tau_1 = \varepsilon\tau$, where ε is the small parameter. Then, taking into account the existence of three scales we assume the following expansion of the functions ξ, φ, and γ in the power series of the small parameter

$$\xi = \sum_{k=1}^{2} \varepsilon^k x_k(\tau_0, \tau_1) + O\left(\varepsilon^3\right),\ \varphi = \sum_{k=1}^{2} \varepsilon^k \phi_k(\tau_0, \tau_1) + O\left(\varepsilon^3\right),\ \gamma = \sum_{k=1}^{2} \varepsilon^k \chi_k(\tau_0, \tau_1) + O\left(\varepsilon^3\right). \tag{13}$$

The ordinary derivatives with respect to time τ are equivalent to the following differential operators for the two introduced time scales

$$\begin{aligned} \frac{d}{d\tau} &= \frac{\partial}{\partial \tau_0} + \varepsilon \frac{\partial}{\partial \tau_1}, \\ \frac{d^2}{d\tau^2} &= \frac{\partial^2}{\partial \tau_0^2} + 2\varepsilon \frac{\partial^2}{\partial \tau_0 \partial \tau_1} + \varepsilon^2 \frac{\partial^2}{\partial \tau_1^2} + O(\varepsilon^3). \end{aligned} \tag{14}$$

Moreover, the amplitudes of generalized forces, all damping coefficients, and the eccentricity are assumed to be small, therefore they are expressed in the form [3]

$$c_i = \varepsilon \tilde{c}_i, \; f_i = \varepsilon^2 \tilde{f}_i, \; i = 1, 2, 3, \; s = \varepsilon \tilde{s}, \alpha = \varepsilon \tilde{\alpha}, \tag{15}$$

where each of the quantities $\tilde{c}_i, \; \tilde{f}_i, \; \tilde{s}, \; \tilde{\alpha}$ can be understood as $O(1)$ as $\varepsilon \to 0$.

Substituting, in sequence (12), (13) and (15) into the original Eqs. (7)–(9) and replacing the ordinary derivatives by the differential operators (14) we obtain the equations in which the small parameter ε appears in the first, second, and higher powers. These equations should be satisfied for any value of the small parameter. So, after ordering each of these equations according to the powers of small parameter we require that the coefficients of each order of ε equal to zero. Omitting the coefficients of order higher than two, we obtain a sequence of six equations that should be satisfied instead of the original equations. We can organize them into two groups:

- equations of the first order approximation

$$\frac{\partial^2 x_1}{\partial \tau_0^2} + x_1 = 0, \tag{16}$$

$$\frac{\partial^2 \phi_1}{\partial \tau_0^2} + w_2^2 \phi_1 = 0, \tag{17}$$

$$\frac{\partial^2 \chi_1}{\partial \tau_0^2} + w_3^2 \chi_1 + \frac{w_3^2}{w_2^2} \frac{\partial^2 \phi_1}{\partial \tau_0^2} = 0, \tag{18}$$

- equations of the second order approximation

$$\frac{\partial^2 x_2}{\partial \tau_0^2} + x_2 = \tilde{f}_1 \cos(\tau_0 p_1) - 3\xi_r^2 \tilde{\alpha} x_1 - \frac{1}{2} w_2^2 \phi_1^2 - \tilde{c}_1 \frac{\partial x_1}{\partial \tau_0} - 2\frac{\partial^2 x_1}{\partial \tau_0 \partial \tau_1} + \left(\frac{\partial \phi_1}{\partial \tau_0}\right)^2, \tag{19}$$

$$\frac{\partial^2 \phi_2}{\partial \tau_0^2} + w_2^2 \phi_2 = \tilde{f}_2 \cos(\tau_0 p_2) - \tilde{s} \frac{\partial^2 \chi_1}{\partial \tau_0^2} - w_2^2 x_1 \phi_1 - \tilde{c}_2 \frac{\partial \phi_1}{\partial \tau_0} - 2 x_1 \frac{\partial^2 \phi_1}{\partial \tau_0^2} - 2\frac{\partial x_1}{\partial \tau_0} \frac{\partial \phi_1}{\partial \tau_0} - 2\frac{\partial^2 \phi_1}{\partial \tau_0 \partial \tau_1}, \tag{20}$$

$$\begin{aligned} &\frac{\partial^2 \chi_2}{\partial \tau_0^2} + w_3^2 \chi_2 + \frac{w_3^2}{w_2^2} \frac{\partial^2 \phi_2}{\partial \tau_0^2} = \tilde{f}_3 \cos(\tau_0 p_3) - \tilde{c}_3 \frac{\partial \chi_1}{\partial \tau_0} - \frac{w_3^2}{w_2^2} \left((\phi_1 - \chi_1) \frac{\partial^2 x_1}{\partial \tau_0^2} + x_1 \frac{\partial^2 \phi_1}{\partial \tau_0^2} \right) - \\ &2\frac{\partial^2 \chi_1}{\partial \tau_0 \partial \tau_1} - 2\frac{w_3^2}{w_2^2} \left(\frac{\partial^2 \phi_1}{\partial \tau_0 \partial \tau_1} + \frac{\partial x_1}{\partial \tau_0} \frac{\partial \phi_1}{\partial \tau_0} \right), \end{aligned} \tag{21}$$

The applied procedure replace, in the approximate meaning, the original equations of motion (7)–(9) with the system of six partial differential Eqs. (16)–(21). This system is solved recursively i.e. solutions of the equations of the lower order are introduced into the equations of higher order approximation. It is worth to notice that differential operators are the same for each step of approximation. The operators of two first equations in every group are mutually independent what significantly simplifies the solving. In every group, the third equation is coupled with the second one. This dependence demands solving at first the first two equations at every step of approximation procedure. Next these solutions are introduced into Eqs. (18) and (21). The general solution of Eqs. (16)–(17) can be presented in the form

$$x_1 = B_1 e^{\mathrm{i}\,\tau_0} + \bar{B}_1 e^{-\mathrm{i}\,\tau_0}, \tag{22}$$

$$\phi_1 = B_2 e^{\mathrm{i}\,w_2\tau_0} + \bar{B}_2 e^{-\mathrm{i}\,w_2\tau_0}, \tag{23}$$

where i denotes the imaginary unit.

The solution (23) is then introduced into Eq. (18) what allows to obtain its solution

$$\chi_1 = B_3 e^{\mathrm{i}\tau_0 w_3} + \bar{B}_3 e^{-\mathrm{i}\tau_0 w_3} + \frac{w_3^2}{w_2^2 - w_3^2}\left(B_2 e^{\mathrm{i}\,w_2\tau_0} + \bar{B}_2 e^{-\mathrm{i}\,w_2\tau_0}\right). \tag{24}$$

The symbol B_i for $i = 1, 2, 3$ in (22)–(24) denotes the unknown complex-valued functions of time scale τ_1, whereas the bar over the symbol denotes its complex conjugate function.

After introducing solutions (22)–(23) into equations of the second order (19)–(20), the secular terms appear. Elimination of them leads to the solvability conditions

$$2\mathrm{i}\frac{dB_1}{d\tau_1} + 3B_1\tilde{\alpha}\, z_r^2 + \mathrm{i}\tilde{c}_1 B_1 = 0, \tag{25}$$

$$2\mathrm{i}w_2\frac{dB_2}{d\tau_1} + \mathrm{i}\tilde{c}_2 w_2 B_2 + \frac{w_2^2 w_3^2}{w_2^2 - w_3^2}\tilde{s}\,B_2 = 0. \tag{26}$$

There exist also two equations that are conjugate to Eqs. (25)–(26).

Taking advantage of solutions (22)–(24) and conditions (25)–(26), the solutions to Eqs. (19)–(20) are as follows

$$x_2 = \frac{3e^{2\mathrm{i}\,w_2\,\tau_0} w_2^2 B_2^2}{2\left(-1+4w_2^2\right)} + w_2^2 B_2\bar{B}_2 + \frac{e^{\mathrm{i}\,p_1\tau_0}\,\tilde{f}_1}{2\left(1-p_1^2\right)} + CC, \tag{27}$$

$$\phi_2 = -\frac{e^{\mathrm{i}(1+w_2)\tau_0} w_2(2+w_2)}{1+2w_2} B_1 B_2 + \frac{e^{\mathrm{i}(-1+w_2)\tau_0} w_2(-2+w_2)}{-1+2w_2}\bar{B}_1 B_2 + \frac{e^{\mathrm{i}\,w_3\tau_0} w_3^2\tilde{s}}{w_2^2 - w_3^2} B_3 + \frac{e^{\mathrm{i}\,p_2\tau_0}\,\tilde{f}_2}{2(w_2^2 - p_2^2)} + CC. \tag{28}$$

Substituting all the previously obtained solutions i.e. (22)–(24), (27)–(28) and conditions (25)–(26) into Eq. (21), and then demanding of elimination of secular terms lead to the following solvability condition

$$-\mathrm{i}w_3 B_3 \tilde{c}_3 + \frac{w_3^6 \tilde{s}}{w_2^2\left(w_2^2 - w_3^2\right)} - 2\mathrm{i}w_3 \frac{\partial B_3}{\partial \tau_1} = 0. \tag{29}$$

Beside, we obtain also the condition which is conjugate to (29).

The solution to the Eq. (21) in the following general form

$$\begin{aligned}
\chi_2 = {} & \frac{e^{\mathrm{i}(1+w_2)\tau_0} w_3^2\left(-1+2w_2^3+w_2^4-w_2^2w_3^2-2w_2\left(1+w_3^2\right)\right)B_1B_2}{(1+2w_2)(w_2-w_3)(1+w_2-w_3)(w_2+w_3)(1+w_2+w_3)} + \frac{e^{\mathrm{i}(1+w_3)\tau_0} w_3^2 B_1 B_3}{w_2^2(1+2w_3)} \\
& + \frac{e^{\mathrm{i}(-1+w_2)\tau_0} w_3^2\left(1+2w_2^3-w_2^4+w_2^2w_3^2-2w_2\left(1+w_3^2\right)\right)\bar{B}_1B_2}{(-1+2w_2)(w_2-w_3)(-1+w_2-w_3)(w_2+w_3)(-1+w_2+w_3)} + \frac{e^{\mathrm{i}(-1+w_3)\tau_0} w_3^2 \bar{B}_1 B_3}{w_2^2(-1+2w_3)} \\
& - \frac{\mathrm{i}\,e^{i\,w_2\tau_0} w_3^2\left(\left(w_3^4-w_2^2w_3^2\right)\tilde{c}_2 + w_2\left(w_2^3-w_2w_3^2\right)\tilde{c}_3 + \mathrm{i}\,w_2w_3^4\tilde{s}\right)B_2}{(-1+2w_2)\left(w_2^2-w_3^2\right)(-1+w_2-w_3)(-1+w_2+w_3)} + \frac{e^{\mathrm{i}\,p_2\tau_0} p_2^2 w_3^2 \tilde{f}_2}{2w_2^2\left(p_2^2-w_2^2\right)\left(p_2^2-w_3^2\right)} \\
& - \frac{e^{\mathrm{i}\,p_3\tau_0}\tilde{f}_3}{2\left(p_3^2-w_3^2\right)}
\end{aligned} \tag{30}$$

has been obtained analytically.

The solution of the considered problem, given by (22)–(24), (27)–(28) and (30), is valid when the oscillations take place away from any resonance. However, the analytical form of the approximate solution of the problem allows to recognize the parameters of the system for which the resonances occur. The resonance case appears when any of the polynomials that stand in the denominators of the solutions (27)–(28) and (30) tends to zero. The resonances detected in this way can be selected as:

(i) primary external resonance, when $p_1 = 1$, $p_2 = w_2$, $p_3 = w_3$;
(ii) internal resonance, when $w_2 = 1/2$, $w_2 = w_3$, $w_3 = 1/2$, $p_2 = w_3$, $w_2 + w_3 = 1$, $w_2 - w_3 = 1$.

Satisfying of one or more of the conditions listed above, implies the need to modify the method of solution, what is described in Sect. 5.

4 Non-resonant Vibration

The solvability conditions (25), (26) and (29) (together with their complex conjugated forms) constitute a set of constraints with respect to unknown functions $B_1(\tau_1)$, $\bar{B}_1(\tau_1)$, $B_2(\tau_1)$, $\bar{B}_2(\tau_1)$, $B_3(\tau_1)$, $\bar{B}_3(\tau_1)$. They have form of the ordinary differential equations with respect to these functions. Let us postulate that the unknown complex-valued functions $B_i(\tau_1)$ are of the following exponential form

$$B_i = \frac{\tilde{a}_i(\tau_1)}{2} e^{\mathrm{i}\,\psi_i(\tau_1)}, \quad \text{and } a_i = \varepsilon\tilde{a}_i,\ i = 1, 2, 3, \tag{31}$$

where $a_i(\tau_1)$, $\psi_i(\tau_1)$ are real-valued functions and have the meaning of the vibration amplitudes and the phases, respectively.

Substituting relationships (31) into solvability conditions (25), (26) and (29), and then separating real and imaginary parts leads to the modulation equations of amplitudes and phases

$$\frac{da_1}{d\tau} = -\frac{1}{2}c_1 a_1, \quad \frac{d\psi_1}{d\tau} = \frac{3}{2}\xi_r^2 \alpha, \tag{32}$$

$$\frac{da_2}{d\tau} = -\frac{1}{2}c_2 a_2, \quad \frac{d\psi_2}{d\tau} = \frac{s\, w_2 w_3^2}{2\left(w_2^2 - w_3^2\right)}, \tag{33}$$

$$\frac{da_3}{d\tau} = -\frac{1}{2}c_3 a_3, \quad \frac{d\psi_3}{d\tau} = \frac{s w_3^5}{2w_2^2\left(w_2^2 - w_3^2\right)}. \tag{34}$$

Equations (32)–(34) are written after returning to the original denotations according to (15) and (31). The initial conditions supplementing the set (32)–(34) are

$$a_1(0) = a_{10},\ \psi_1(0) = \psi_{10},\ a_2(0) = a_{20},\ \psi_2(0) = \psi_{20},\ a_3(0) = a_{30},\ \psi_3(0) = \psi_{30}. \tag{35}$$

The sets of initial conditions (11) and (35) must be agreed one to another using the final analytical form of the solution.

Solution to the modulation Eqs. (32)–(34) follows

$$a_1 = a_{10} e^{-c_1 \tau/2}, \quad \psi_1 = \frac{3}{2}\xi_r^2 \alpha \tau + \psi_{10} \tag{36}$$

$$a_2 = a_{20} e^{-c_2 \tau/2}, \quad \psi_2 = \frac{s\, w_2 w_3^2 \tau}{2\left(w_2^2 - w_3^2\right)} + \psi_{20}, \tag{37}$$

$$a_3 = a_{30} e^{-c_3 \tau/2}, \quad \psi_3 = -\frac{s\, w_3^5 \tau}{2w_2^2\left(w_2^2 - w_3^2\right)} + \psi_{30}. \tag{38}$$

Finally, expressing the complex-valued functions $B_i(\tau_1)$ by the real-valued functions $a_i(\tau_1)$, $\psi_i(\tau_1)$ according to (31) and then substituting (36)–(38) into solutions (22)–(24), (27), (28) and (30), one can obtain the approximate solution to the original problem (7)–(9) with (11). The solution has the following analytical form

$$\xi = a_1 \cos(\tau + \psi_1) - \frac{f_1 \cos(p_1 \tau)}{p_1^2 - 1} + \frac{1}{4} w_2^2 a_2^2 + \frac{3 w_2^2 a_2^2 \cos(2w_2\tau + 2\psi_2)}{4(2w_2 - 1)(2w_2 + 1)} \tag{39}$$

$$\varphi = a_2 \cos(w_2 \tau + \psi_2) - \frac{f_2 \cos(p_2 \tau)}{p_2^2 - w_2^2} + \frac{s w_3^2 a_3 \cos(w_3 \tau + \psi_3)}{w_2^2 - w_3^2} - \frac{w_2 a_1 a_2 \left((3w_2 + 2 - 2w_2^2)\cos(\tau - w_2\tau + \psi_1 - \psi_2) + (3w_2 - 2 + 2w_2^2)\cos(\tau + w_2\tau + \psi_1 + \psi_2)\right)}{2(4w_2^2 - 1)} \tag{40}$$

$$\gamma = a_3\cos(w_2\tau+\psi_2) - \frac{f_3\cos(p_3\tau)}{p_3^2-w_3^2} + \frac{p_2^2w_3^2f_2\cos(p_2\tau)}{w_2^2\left(p_2^2-w_2^2\right)\left(p_2^2-w_3^2\right)} + \frac{s\,w_3^6a_2\cos(w_2\tau+\psi_2)}{(w_2-w_3)^3(w_2+w_3)^3}$$
$$+ \frac{w_3^2\left(-1+2w_2^3+w_2^4-w_2^2w_3^2-2w_2\left(1+w_3^2\right)\right)a_1a_2\cos(\tau+w_2\tau+\psi_1+\psi_2)}{2(1+2w_2)(w_2-w_3)(1+w_2-w_3)(w_2+w_3)(1+w_2+w_3)}$$
$$- \frac{w_3^2\left(-1+2w_2-2w_2^3+w_2^4-w_2^2w_3^2+2w_2w_3^2\right)a_1a_2\cos(\tau-w_2\tau+\psi_1-\psi_2)}{2(1+2w_2)(w_2-w_3)(1+w_2-w_3)(w_2+w_3)(1+w_2+w_3)}$$
$$- \frac{w_3^2a_1a_3\cos(\tau-w_3\tau+\psi_1-\psi_3)}{2w_2^2(1-2w_3)} + \frac{w_3^2a_1a_3\cos(\tau+w_3\tau+\psi_1+\psi_3)}{2w_2^2(1+2w_3)} - \frac{w_3^2a_2\cos(w_2\tau+\psi_2)}{(w_2-w_3)(w_2+w_3)} \tag{41}$$

As is earlier mentioned, the solutions (39)–(41) are valid only for non-resonant vibration. If the system is close to any of resonance cases then singularities appear in the analytical solution since some of the denominators in (39)–(41) tend to zero.

The correctness of the solution (39)–(41) is confirmed by numerical solution of the original problem (7)–(9) and (11) obtained using the functions of Mathematica software. The example of time histories of the system oscillations involving the strong influence of the initial conditions are presented in Fig. 2. Parameters fixed in calculations are as follows:

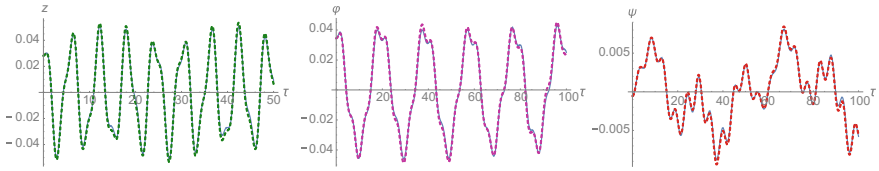

Fig. 2 Time history of vibration; solid curve—analytical solution, dashed curve—numerical solution

$\alpha = 2.25$, $f_2 = 0.01$, $f_3 = 0.002$, $f_1 = 0.05$, $c_1 = 0.001$, $c_2 = 0.001$, $c_3 = 0.001$, $w_2 = 0.32$, $w_3 = 0.09$, $p_1 = 2.3$, $p_2 = 1.28$, $p_3 = 1.18$, $e = 0.3$, $a_{10} = 0.04$, $a_{20} = 0.04$, $a_{30} = 0.004$, $\psi_{10} = 0.0$, $\psi_{20} = 0.0$, $\psi_{30} = 0.0$.

Figure 2 consists of three parts. Each of them present two solutions related to general coordinate $z(\tau)$, $\varphi(\tau)$ and $\gamma(\tau)$, (from left to right, respectively). These solutions are obtained in two ways as analytical solutions (39)–(41) using MSM and by numerical integration of the original equations.

5 Resonant Vibration

Let us consider the case of the three primary main resonances, induced by the triple external loading, occurring simultaneously i.e. $1 \approx p_1$, $w_2 \approx p_2$, and $w_3 \approx p_3$. The resonance effects are reflected in the secular generating terms. In order to deal with the resonance, the detuning parameters, as a measure of the distance of the system vibration from the strict resonance conditions, are introduced in the following way

$$p_1 = 1 + \sigma_1,\ p_2 = w_2 + \sigma_2, p_3 = w_3 + \sigma_3. \tag{42}$$

We assume the detuning parameters are of the order of small parameter, i.e. we take

$$\sigma_i = \varepsilon\tilde{\sigma}_i \quad i = 1, 2, 3. \tag{43}$$

The conditions (42)–(43) are introduced into Eqs. (7)–(9). Further procedure is analogous to this one described in the two previous sections. Therefore, we focus mainly on the secular terms generated by the resonance conditions (42). As a result of elimination of these secular terms we get the solvability conditions of the problem. They may be written as follows

$$2\mathrm{i}\frac{dB_1}{d\tau_1} + 3B_1\tilde{\alpha}\,\xi_r^2 + \mathrm{i}\tilde{c}_1 B_1 - \frac{1}{2}e^{\mathrm{i}\,\tau_1\sigma_1}\tilde{f}_1 = 0, \tag{44}$$

$$2\mathrm{i}w_2\frac{dB_2}{d\tau_1} + \mathrm{i}\tilde{c}_2 w_2 B_2 + \frac{w_2^2 w_3^2}{w_2^2 - w_3^2}\tilde{s}B_2 - \frac{1}{2}e^{\mathrm{i}\,\tau_1\sigma_2}\tilde{f}_2 = 0, \tag{45}$$

$$-\mathrm{i}w_3 B_3\tilde{c}_3 + \frac{w_3^6\tilde{s}B_3}{w_2^2\left(w_2^2 - w_3^2\right)} - 2\mathrm{i}w_3\frac{dB_3}{d\tau_1} + \frac{1}{2}e^{\mathrm{i}\,\tau_1\sigma_3}\tilde{f}_3 = 0. \tag{46}$$

5.1 Modulation Problem Near Resonances

The solvability conditions (44)–(46) create a system of the ordinary differential equations with respect to unknown functions $B_1(\tau_1)$, $\bar{B}_1(\tau_1)$, $B_2(\tau_1)$, $\bar{B}_2(\tau_1)$, $B_3(\tau_1)$, $\bar{B}_3(\tau_1)$. After introducing the exponential form (31) for the complex-valued functions $B_i(\tau_1)$, it is convenient to define the modified phases in the following way

$$\begin{aligned}\theta_1(\tau_1) &= \tau_1\tilde{\sigma}_1 - \psi_1(\tau_1),\\ \theta_2(\tau_1) &= \tau_1\tilde{\sigma}_2 - \psi_2(\tau_1),\\ \theta_3(\tau_1) &= \tau_1\tilde{\sigma}_3 - \psi_3(\tau_1).\end{aligned} \tag{47}$$

After substitution the modified phases (47) into solvability conditions (44)–(46) and having returned to the original denotations according to (14)–(15), (31) and (43), the obtained modulation equations become autonomous of the following form

$$\frac{da_1}{d\tau} = -\frac{1}{2}a_1 c_1 + \frac{f_1}{2}\sin(\theta_1), \tag{48}$$

$$\frac{d\theta_1}{d\tau}a_1 = a_1\sigma_1 - \frac{3}{2}\xi_r^2\alpha a_1 + \frac{f_1}{2}\cos(\theta_1), \tag{49}$$

$$\frac{da_2}{d\tau} = -\frac{1}{2}c_2 a_2 + \frac{f_2}{2\mathrm{w}_2}\sin(\theta_2), \tag{50}$$

$$\frac{d\theta_2}{d\tau}a_2 = \sigma_2 a_2 - \frac{s\,w_2 w_3^2 a_2}{2\left(w_2^2 - w_3^2\right)} + \frac{f_2}{w_2}\cos(\theta_2), \tag{51}$$

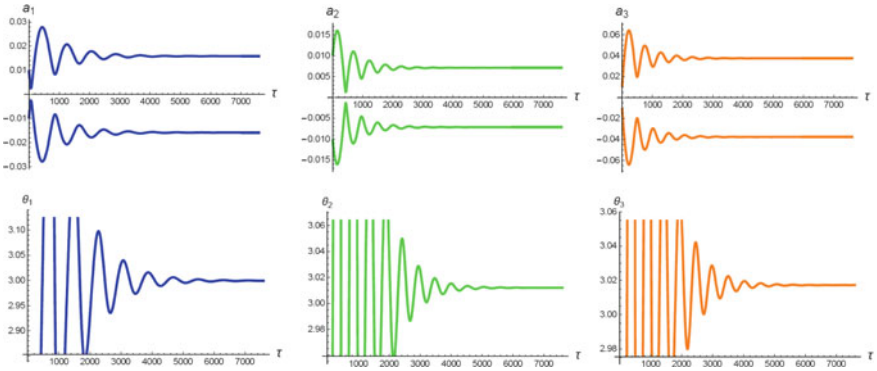

Fig. 3 Temporal behaviour of amplitudes and modified phases which tend to steady point

$$\frac{da_3}{d\tau} = -\frac{1}{2}c_3 a_3 + \frac{f_3}{2w_3}\sin(\theta_3), \tag{52}$$

$$\frac{d\theta_3}{d\tau}a_3 = \sigma_3 a_3 + \frac{s\, w_3^5 a_3}{2w_2^2\left(w_2^2 - w_3^2\right)} + \frac{f_3}{w_3}\cos(\theta_3). \tag{53}$$

In contrary to the previously discussed case of the non-resonant vibration, the modulation Eqs. (48)–(53) cannot be solved in the analytical manner.

The initial conditions supplementing the set (48)–(53) are as follows

$$a_1(0) = a_{10},\ \psi_1(0) = \psi_{10},\ a_2(0) = a_{20},\ \psi_2(0) = \psi_{20},\ a_3(0) = a_{30},\ \psi_3(0) = \psi_{30}, \tag{54}$$

and must be compatible with the initial conditions (11).

The modulation curves describe the slow time changes in the motion. For some conditions vibration tends to the steady values of the amplitudes and phases. This case is presented in Fig. 3. The assumed parameters are:

$\sigma_1 = 0.01$, $\sigma_2 = 0.01$, $\sigma_3 = 0.01$, $w_2 = 0.293$, $w_3 = 0.055$, $s = 0.02$, $f_1 = 0.00025$, $f_2 = 0.00005$, $f_3 = 0.00005$, $c_1 = 0.00223$, $c_2 = 0.0031$, $c_3 = 0.003$, $\alpha = 0.2$, $a_{10} = 0.01$, $a_{20} = 0.01$, $a_{30} = 0.01$, $\psi_{10} = 0$, $\psi_{20} = 0$, $\psi_{30} = 0$.

Equations (48)–(53) describe effects related to the slow time scale. They allow to observe and follow non-steady oscillations, and to recognize and follow qualitative transitions in the character of motion. A good way of illustration of the dynamical behaviour of the system are trajectories depicted in a space the points of which are amplitudes and modified phases, and so the functions connected to the modulation equations. The projections of the trajectories onto the chosen planes of this space are shown in Fig. 4. The simulations are carried out for the same data as previously.

After the transient state, all trajectories achieve the stable steady state, although the duration of the transient vibration is various for the particular general coordinates. The steady state conditions correspond to the demand of vanish of time derivatives

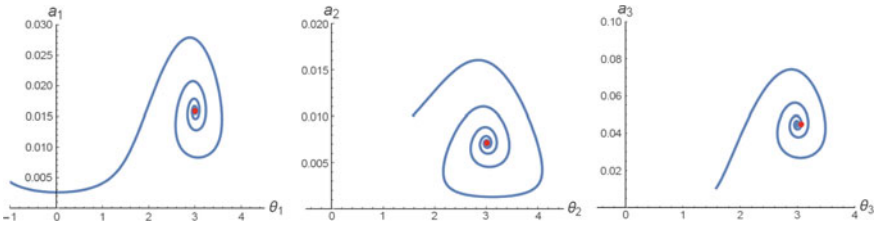

Fig. 4 Trajectories of motion in the amplitude-modified plane; red points indicate stable state

of amplitudes and modified phases in modulation Eqs. (48)–(53). They are governed by the following equations

$$-\frac{1}{2}a_1c_1 + \frac{f_1}{2}\sin(\theta_1) = 0, \tag{55}$$

$$a_1\sigma_1 - \frac{3}{2}\xi_r^2\alpha a_1 + \frac{f_1}{2}\cos(\theta_1) = 0, \tag{56}$$

$$-\frac{1}{2}c_2a_2 + \frac{f_2}{2w_2}\sin(\theta_2) = 0, \tag{57}$$

$$\sigma_2a_2 - \frac{s\,w_2w_3^2a_2}{2\left(w_2^2 - w_3^2\right)} + \frac{f_2}{w_2}\cos(\theta_2) = 0, \tag{58}$$

$$-\frac{1}{2}c_3a_3 + \frac{f_3}{2w_3}\sin(\theta_3) = 0, \tag{59}$$

$$\sigma_3a_3 + \frac{s\,w_3^5a_3}{2w_2^2\left(w_2^2 - w_3^2\right)} + \frac{f_3}{w_3}\cos(\theta_3) = 0. \tag{60}$$

Equations (55)–(60) stand for algebraic system with unknown values of amplitudes and modified phases a_1, a_2, a_3, θ_1, θ_2 and θ_3 in steady-state motion.

The fully explicit form of the approximate solution of the original problem in case of the resonance is usually impossible to achieve. The modulation equations due to their complexity are solved in numerical manner. Having however the solutions of the governing equations in the analytic form of functions of amplitudes and phases (or modified phases), we can substitute the numerical solutions into this analytical form. Time histories obtained in this way with comparison to the numerically obtained solutions are presented in Fig. 5. The results presented in Fig. 5 are obtained for the same values of system parameters as the ones listed above and demonstrated in Figs. 3 and 4.

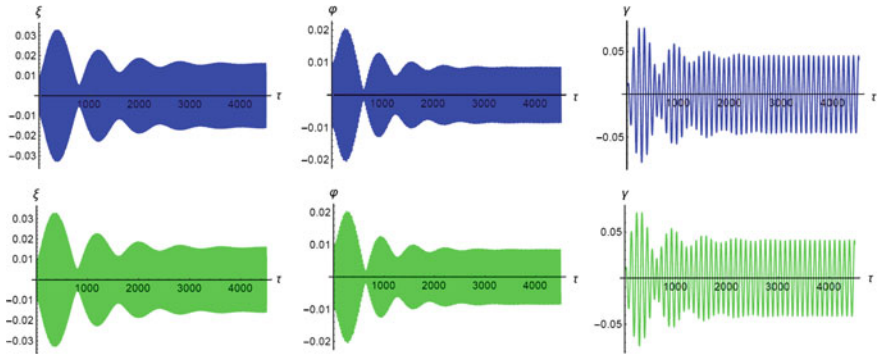

Fig. 5 Time histories; upper graphs are obtained analytically while the lower ones numerically

6 Conclusions

The approximate solution to the governing equations has been obtained using the multi scales method with two time scales. The analytical form of this solution is the main advantage of the applied approach, giving the possibility to the qualitative and quantitative study of the system dynamics in a wide range of the frequency spectrum. The approximate solution for non-resonant vibration has been obtained in fully analytical form because the modulation equations governing the evolution of amplitudes and phases in the slow time scale were solved analytically. Admittedly an approximate but however analytical form of this solution create, among others, the possibility to determine the conditions at which the resonances occur. The adequate conditions for possible resonances have been detected. The case of three primary main resonances occurring simultaneously has been considered.

Acknowledgements This paper was financially supported by the grant of the Ministry of Science and Higher Education in Poland realized in Institute of Applied Mechanics of Poznan University of Technology (DS-PB: 02/21/DSPB/3493).

References

1. Awrejcewicz, J., Starosta, R., Sypniewska-Kamińska, G.: Asymptotic analysis of resonances in nonlinear vibrations of the 3-dof pendulum. Differ. Equ. Dyn. Syst. **21**(1&2), 123–140 (2013)
2. Awrejcewicz, J., Starosta, R., Sypniewska-Kamińska, G.: Resonances in kinematically driven nonlinear spring pendulum. In: DSTA 11th Conference, 103-108
3. Menevitch, E.L., Manevitch L.I.: Limiting phase trajectories (LPT) in 1 dof asymmetric system with damping and 1:1 resonance. In: 10th Conference on Dynamical Systems Theory and Applications, Łódź, Poland, pp. 559–668 (2009)
4. Manevitch, L.I., Smirnov, V.V., Romeo, F.: Non-stationary resonance dynamics of the harmonically forced pendulum. Cyber. Phys. **5**(3), 91–95 (2016)

5. Sado, D., Gajos, K.: Analysis of vibrations of three-degree-of-freedom dynamical system with double pendulum. J. Theor. Appl. Mech. **46**(1), 141–156 (2008)
6. Starosvetsky, Y., Gendelman, O.V.: Dynamics of a Strongly Nonlinear Vibration Absorber Coupled to a Harmonically Excited Two-Degree-of-Freedom System. J. Sound Vib. **312**, 234–256 (2008)

Part II
Molecular Dynamics of Polymer Crystals and Nanostructures

Supermolecular Structure Formation During Electrospinning, and Its Effect on Electrospun Polymer Nanofiber Unique Features

Arkadii Arinstein

Abstract Electrospun polymer nanofibers demonstrate outstanding mechanical and unusual thermodynamic properties as compared to macroscopic-scale structures. Now-a-days is wide accepted that these features are attributed to nanofiber microstructure (Arinstein et al. Nat Nanotechnol 2:59–62, 2007, [1]). It is clear that this microstructure is formed during the electrospinning process characterized by a high stretching rate and rapid evaporation. The first circumstance (high stretching rate) results in formation of non-equilibrium supermolecular structure; whereas the second one (rapid evaporation) provides the fixing of the formed internal non-equilibrium structure of electrospun polymer nanofibers. Thus, when studying microstructure formation, its fast evolution must be taken into account.

1 Introduction

The phenomenon of size-dependent behavior of objects having nano-scale size, is now well known and observed in different nano-objects, such as polymer nanofibers [1, 2], metallic nanowires [3], and thin polymer films [4]. Many experimental studies have demonstrated the effect of size on the mechanical, thermomechanical, and thermodynamic properties of the above nano-objects. For example, the elastic modulus of nanowires [3], polypyrrole nanotubes [5], and electrospun polystyrene and nylon-6.6 nanofibers [1, 2] sharply increases when their diameter becomes sufficiently small. Also, a shift in the glass transition and melting temperatures was observed in polymer nano-objects [6]. At first the explanations of the above size-dependent behavior were attributing to surface tension [5] or near-surface layers [7, 8]. Unfortunately, all these proposed mechanisms cannot satisfactorily describe the above phenomena quantitatively. As an alternative, we suggested that the dominant role in

A. Arinstein (✉)
Department of Mechanical Engineering, Technion, Israel Institute of Technology, 32000 Haifa, Israel
e-mail: mearin@technion.ac.il

I. V. Andrianov et al. (eds.), *Problems of Nonlinear Mechanics and Physics of Materials*, Advanced Structured Materials 94,
https://doi.org/10.1007/978-3-319-92234-8_11

size-dependent behavior of polymer nanofibers (in particular, in their reinforcement) belongs to confinement-induced phenomena [1].

Further progress in understanding of the features of electrospun polymer nanofibers influencing their behavior requires examination of their internal structure, more specifically, the supermolecular structures in the amorphous regions of the polymer matrix, as well as crystallite ordering. At the initial stages of such analyses, the impact of fabrication conditions upon the final state of the polymer matrix of as-spun nanofibers must be determined. In doing so, the high strain rate (on the order 10^3 s^{-1}) acting during electrospinning [10–16], must be taken into account. This dominant factor is believed to cause stretching and orientation of polymer chains, as indicated by in-process measurements of jets, using birefringence [17] and Raman [18] techniques.

In parallel, extremely rapid solvent evaporation adversely affects the polymer matrix macrostructure of as-spun nanofibers. Rapid evaporation first leads to formation of a solid skin, followed by further evaporation from the liquid core, leaving voids previously occupied by solvents and allowing partial relaxation of the matrix. This frequently induces generation of a heterogeneous and porous fiber structure [19, 20]. Theoretical analysis [21, 22], confirmed by experimental observations [19] and computer simulation [23], demonstrated that a sharp increase in polymer density at the fiber-vapor interface is induced upon rapid solvent evaporation, consequently increasing heterogeneity and porosity of a solidificating polymer matrix.

Thus, heterogeneous, high-porosity fiber structures should be formed under certain electrospinning conditions (see Fig. 1a). At the same time, skin formation prevents further stretching and orientation of polymer chains within the semiliquid fiber core. Relaxation of the non-equilibrium state of the stretched macromolecules consequentially occurs, with no detectable influence of the fabrication conditions on the final state of the polymer matrix of as-spun nanofibers. On the other hand, there exist spinning conditions resulting in homogeneous as-spun fiber structures (see Fig. 1b). In such cases, relaxation of stretched polymer chains is suppressed, and the effect of fabrication conditions on the final state of the nanofiber polymer matrix should be noticeable.

If the mechanisms resulting in formation of the porous structure of as-spun polymer nanofibers are well understood [19, 21, 22], the physical principals providing generation of the nanofibers with homogeneous structure, require clarification. The required mechanism can be proposed based on the assumption that the polymer system, which is an interconnected network of subchains, undergoes substantial stretching during electrospinning. It's clear that under high rapid stretching, the initial equilibrium state of this polymer network transforms to an almost fully stretched state along the jet; in doing so, this stretching should be accompanied by radial contraction of the network.

This stretching hypothesis was developed in [25], where a theoretical model describing the polymer system as an entangled network and its evolution in the initial stage of electrospinning was proposed. It was shown that the initial equilibrium state of the polymer network can transform to an almost fully stretched state along the jet. The observed stretching is accompanied by network contraction across the

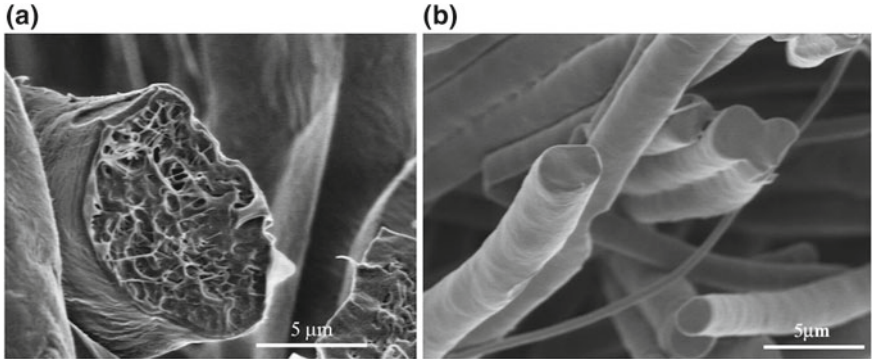

Fig. 1 SEM images of electrospun nanofibers fabricated from 10 wt.% PCL (Mw 80 kDa) in DCM/DMF (75:25 wt.%), in an electric field of 0.63 kV/cm [24]. **a** Heterogeneous fibers fabricated at a flow rate of 20 ml/h and **b** homogeneous fibers fabricated at a flow rate of 3 ml/h [25]

jet. These theoretical results were experimentally confirmed by X-ray phase-contrast imaging of electrospinning jets of PEO (polyethylene oxide) and PMMA (polymethyl methacrylate) semidilute solutions. The similar ideas were also discussed in [26], where instability development in a jet of a viscoelastic polymer solution under high stretching was examined. It turned out that above some threshold value of deformation degree corresponding to almost maximum possible stretching (about of 90% of the maximum), the volume content of residual solvent in the system sharply decreases and tends to zero. By the other words, under very high draw ratio, the solvent is "wringing out" of the polymer network, resulting in oriented filament formation and polymer solidification.

2 Theoretical Modelling of Polymer Dynamics During Electrospinning

2.1 Velocity and Radius of an Electrospinning Jet

Under an electric field, the moving solution jet accelerates, so that its local velocity contains both longitudinal and radial components. Hydrodynamic analysis demonstrates that in the jet beginning the longitudinal velocity can be approximated by a parabolic profile, whereas the radial velocity component increases linearly along the jet [27]:

$$v_z \approx v_0\left(1+\frac{z}{z_0}\right)^2+\cdots, \quad v_r \approx -v_0\left(1+\frac{z}{z_0}\right)\frac{r}{z_0}+\cdots \tag{1}$$

Therefore, the jet takes on a hyperbolic form:

$$r_J(z) \approx \frac{r_0}{1 + /z_0}, \tag{2}$$

here v_0 is the jet initial velocity, and r_0 is the jet initial radius. The characteristic length z_0 determines the scale of velocity increase, and depends on the flow rate, viscosity, electric field and electric conductivity of the solution [27].

Typical values of these parameters, measured by optical microscopy of the jet [15, 16], and substantiated by our experimental observations are $v_0 \propto (1 \div 5) \times 10^{-2}$ m/s and $z_0 \propto (0.5 \div 1) \times 10^{-3}$ m. Such hydrodynamic flux with increasing longitudinal velocity influences on the polymer macromolecules results in their nonequilibrium conformation state and heterogeneous distribution inside the jet.

It is clear that this regularity is applicable only on the initial stage of jet spinning, since the velocity increase of the liquid jet is limited, due to viscosity increase as a result of solvent evaporation and final solidification of the jet.

2.2 Polymer System Structure

It is well known that viscoelasticity is a prerequisite for polymer solution spinnability, meaning that spinnable solutions are semidilute, highly entangled. Therefore, the polymer system is assumed to be a network, whose connectivity is provided by topological knots [11] (see Fig. 2a). The sections of macromolecules between two adjacent topological knots are called subchains, which feature a conformation at equilibrium that corresponds to their nonzero end-to-end distance, even in the absence of external force. This end-to-end distance is equal to the distance between two topological knots or to an average mesh size ξ_0 of the network in a semidilute solution

$$\xi_0 \propto R_g \left(c/c^*\right)^{\nu/(1-3\nu)} \tag{3}$$

where $R_g \propto aN^{\nu}$ is the end-to-end distance of a polymer coil, c is the mass concentration of the polymer solution, c^* is the crossover concentration of macromolecules overlap, N is the number of monomers in a polymer chain, and a is the monomer scale.

Solvents usually used in such systems vary between good and moderately poor solvents; so the conformation of a polymer chain should be a Gaussian or swelled coil ($1/2 < \nu < 3/5$). On the other hand, the polymer concentration in spinnable solutions is relatively high [$(5 \div 10) \times c^*$], and this prevents a coil swelling. Therefore, for simplicity, we can assume that $\nu = 1/2$. Assuming Gaussian statistics of subchains, one can estimate the number of monomers, N_S, in a subchain as follows:

$$N_S = (\xi_0/a)^2 = N\left(c/c^*\right)^{-2} \tag{4}$$

Thus, the elements of the system which undergo noticeable stretching are the above-defined subchains which form the polymeric physical network with topological links arising as a result of a chain entanglement. This topological network provides the required viscoelasticity of the polymer solution. Moreover, under rapid deformation this physical network can be regarded as a gel (the high-elastic state) and this fact is of high importance for further analysis. The evolution of subchain conformation under stretching of the polymer network will now be examined.

2.3 *Axial Stretching of an Entangled Polymer Network During Electrospinning*

The polymer network in question can be approximated by a lattice model of "beads" and linear "springs," similar to the Rouse model. Each bead represents a topological knot and is connected to six adjacent beads by springs, or polymer subchains which demonstrate Gaussian statistics leading to a linear force-elongation relationship. In spite of the fact that the above polymeric network is a random one, the system in question can be approximated by a regular cubic lattice with elementary cell having the scale of the above mesh size, ξ_0 (see Fig. 2a, and also Fig. 5a). The averaging of the system over the jet cross-section results in a one-dimensional chain of springs interconnecting the beads, each bead having an effective subchain mass,

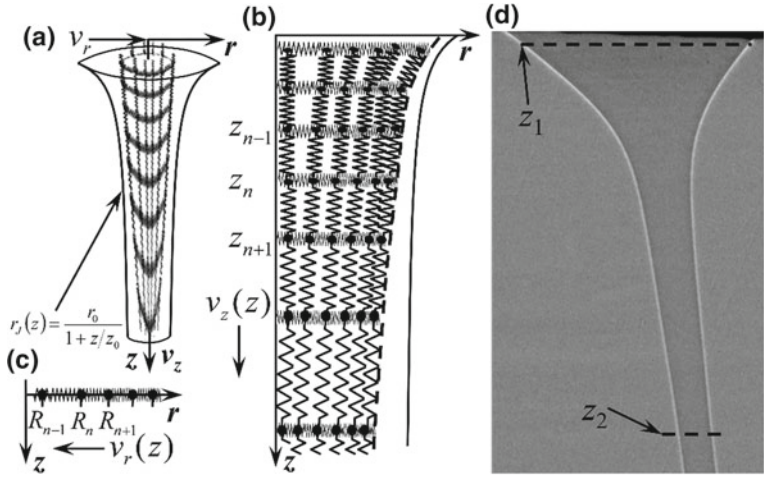

Fig. 2 **a** Illustration of polymer network stretching in an electrospinning jet. **b** and **c** Definition of the polymer network parameters: **b** in z-direction, **c** in radial direction r. **d** On-line fast X-ray phase-contrast image of spinning jet: zooming on the Taylor cone. The lines at $z_1 = 0.02$ mm and $z_2 = 0.5$ mm indicate the cross sections of the absorption measurements across the electrospinning jet [25]

m. The beads are influenced by an effective hydrodynamic force proportional to the effective subchain size, as well as entropic elastic forces from its two neighbors (see Fig. 2b). The dynamics of this chain of springs can be described by the following difference-differential equation:

$$m\frac{d^2z_n}{dt^2} = a_{eff}\eta\left[v_z(z_n) - \frac{dz_n}{dt}\right] + \frac{k_BT}{\xi_0^2}\left\{[z_{n+1} - z_n - \xi_0] - [z_n - z_{n-1} - \xi_0]\right\}, \quad (5)$$

here η is the effective viscosity of the dilute solution surrounding the polymer network, v_z is the jet velocity from Eq. (1), and k_BT/ξ_0^2 is the linear entropic elasticity of a polymer sub-chain, k_B is Boltzmann constant. According to Eq. (4), the average mesh size, ξ_0, is assumed as $\xi_0 = aN_s^{1/2}$.

This difference equation can be approximated by a differential equation relative to the space argument, $l \equiv \xi_0 n$, and then reduced to the following form by introducing the dimensionless argument, $\zeta \equiv (l + v_0 t)/z_0$, and function, $\hat{z}(\zeta) \equiv z(l,\ t)/z_0$:

$$\frac{d^2\hat{z}(\zeta)}{d\zeta^2} = \alpha\left[\hat{v}_z(\hat{z}) - \frac{d\hat{z}(\zeta)}{d\zeta}\right], \quad (6)$$

here $\hat{v}_z(\hat{z}) \equiv v_z(z)/v_0$, and $\alpha = z_0 v_0 a_{eff}\eta/[m(v_0^2 - c_{net}^2)] \propto 10^3 \div 10^4 >> 1$ is a dimensionless parameter. The parameter $c_{net} = \sqrt{T/m}$ is the "sound" velocity in the polymer network (as the polymer network demonstrates only entropic elasticity of a semidilute solution, it is much lower than the sound velocity in solid polymer systems). The polymer is at equilibrium at the cross-section $z = -z_0$, so the boundary conditions at the point $\hat{z} = -1$ correspond to zero-acceleration and zero-velocity, while at $\hat{z} = +\infty$ free boundary conditions are assumed.

Using the substitution $d\hat{z}(\zeta)/d\zeta = P(\hat{z})$, the second-order differential equation (6) can be reduced to a first-order equation:

$$\frac{dP(\hat{z})}{d\hat{z}} = \alpha\left[\frac{\hat{v}_z(\hat{z})}{P(\hat{z})} - 1\right], \quad (7)$$

The solution of Eq. (7) can be obtained, using a $1/\alpha$-approximation. Assuming that

$$\frac{\hat{v}_z(\hat{z})}{P(\hat{z})} - 1 = \frac{1}{\alpha}P_1(\hat{z}) + \ldots, \quad (8)$$

we obtain $P_1(\hat{z}) = d\,v(\hat{z})/d\hat{z}$, so within accuracy of $(1/\alpha)^2$, the function $P(\hat{z})$ is

$$P(\hat{z}) = \frac{d\hat{z}(\zeta)}{d\zeta} = \frac{dz(l,t)}{dl} = \frac{\xi_{||}(\hat{z})}{\xi_0} \approx \frac{\hat{v}_z(\hat{z})}{1 + \frac{1}{\alpha}d\hat{v}_z(\hat{z})/d\hat{z}}, \quad (9)$$

and the function $\hat{z}(\zeta)$ can be obtained as an inverse function:

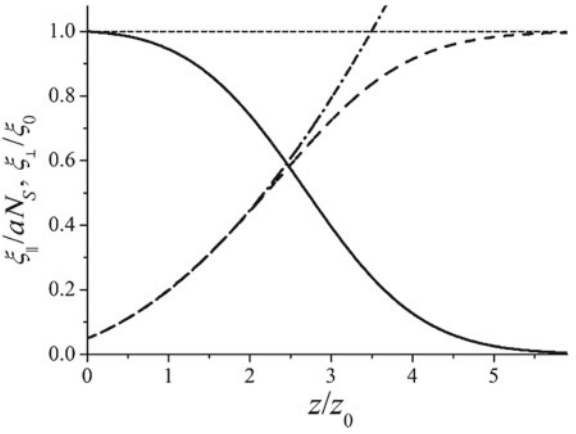

Fig. 3 **a** Polymer network conformation. Relative radial contraction, $\xi_{\perp}/\xi_0$, (solid line), and relative axial stretching, $\xi_{\parallel}/aN_s$, (dashed and dot-dashed lines), versus relative axial position, z/z_0. The results were obtained by the simulation (dashed and solid lines) and theoretical model (dot-dashed line). The system parameters were: N_S = 400, and α = 1000 [25]

$$\zeta(\hat{z}) = \int_0^{\hat{z}} \frac{dx}{\hat{v}_z(x)} - \frac{1}{\alpha} \ln\left[\hat{v}_z(\hat{z})\right] \tag{10}$$

The stretching of the polymer network, $\xi_{||}(\hat{z})$, introduced in Eq. (9), allows one to determine the stretching level of a mesh size in the direction of the jet, as a function of the position $\hat{z}$ along the jet.

$$\xi_{||}(\hat{z}) = \xi_0 \frac{dz(l,\, t)}{dl} \approx \frac{\xi_0 \hat{v}_z(\hat{z})}{1 + \frac{1}{\alpha} d\hat{v}_z(\hat{z})/d\hat{z}}, \tag{11}$$

The sign of the parameter α which depends on the sign of the term $v_0^2 - c_{net}^2$, and its magnitude determine the behavior of the system: for $\alpha > 0$ the jet local velocity is faster than the polymer network local velocity, and the effect of the hydrodynamic force is dominant; for $\alpha < 0$ the polymer network local velocity is faster than the jet local velocity, and the effect of network connectivity is dominant (i.e. stretching is caused by a pull at the far end of the jet). For $\alpha >> 1$ the derivative in Eq. (9) vanishes, and the polymer network local velocity coincides with the jet local velocity. At large z, where the jet velocity v_z saturates to v_∞, the stretching ratio converges to $\xi_{||}/\xi_0 \approx v_\infty/v_0$, confirming that the stretched conformation of the polymer network remains even after velocity saturation.

The obtained dependence $\xi_{||}/aN_s$ is shown in Fig. 3 (dot-dashed lines) with respect to the position z/z_0 along the jet, for unsaturated longitudinal velocity, v_z, from the first equation of the Eq. (1). The theoretical calculations were supported by numerical simulations basing on the 3*D* random walk model under external field (see Fig. 3, dashed lines). The difference between analytical calculations and numerical simulations is observed for the highly stretched state of polymer subchains, when the stretching of the polymer subchains according to Eq. (9) exceeds the maximal possible elongation corresponding to fully-stretched state, whereas the stretching, calculated on the base of the 3*D* random walk simulations, tends to saturation.

A term preventing the unlimited stretching of subchains, can be introduced into Eq. (5) by replacing the linear elasticity of polymer subchains, k_BT/ξ_0^2, with the nonlinear $k_BT/\left\{\xi_0^2[1-(z_{n+1}-z_n)/aN_s]\right\}$. However, such a modification cannot correctly describe the real system behavior due to the additional processes, associated with high level of polymer subchain stretching. For example, almost fully-stretched subchains begin to disentangle, thereby raising the subchain length, ξ_0.

This disentanglement process was discussed in our review paper [28] on the base of experimental observations [29–34]. It turns out that the simple estimation of a shrinking of the radius of a spinning jet caused only by solvent evaporation and stretching of the topological network without its reorganization, shows that the final diameter of as-spun fibers cannot be less than 10 μm, whereas in real electrospinning process, the fibers with diameters of diameters of 100 nm and even less can be obtained. Indeed, the typical polymer concentrations (c_p) of a polymer solution are amounting of about 10–15%. Therefore, as a result of only solvent evaporation, the fiber radius can be reduced down to $r_{J0}\sqrt{c_P}$ (here r_{J0} is the initial jet radius). The discussed above stretching of the topological network without its reorganization results in elongation and shrinking of a polymer slug in $\sqrt{N_s}$ times, so the final fiber radius, R_F, can be

$$R_F \propto r_{J0}\sqrt{c_P/N_s} \approx 10-30\ \mu\text{m}, \tag{12}$$

here the initial jet radius, r_{J0}, is assumed of about 1 mm, and the polymer subchains of the topological network corresponding to average mesh size $\xi_0 = a\sqrt{N_s}$, consist of 100–1000 monomers.

In addition, the highly stretched polymer network begins to affect the effective viscosity of the solution, influencing the jet velocity. Furthermore, slipping of the solvent surface layer relative to the polymer network is also possible.

Therefore, it is reasonable to restrict ourselves to the simplest model describing only the initial stage of polymer network evolution inside the electrospinning jet. Although the proposed model does not describe the final state of the polymer matrix in electrospun nanofibers, and is applicable only to the initial part of the jet where the stretching of a polymer system is not too high, it allows to understand the tendency in the evolution of the polymer during the electrospinning process.

Note that the transformation of subchains from a coil-like equilibrium state into a stretched state occurs as a continuous crossover, and no phase transition is observed, in contrast to the well-known coil-stretch transition, described by de Gennes [35]. Unlike stretching of an individual chain, during network stretching locally the dominant force that provides this transformation is the elastic force, whereas the hydrodynamic forces give rise to the global stretching of the network. As a result, the network subchains are subjected to the action of the network portion situated farther along the jet, a force independent of local stretching. In contrast, the force acting on an individual polymer chain under an ultrahigh velocity gradient increases with macromolecule stretching. Similar behavior (continuous crossover from a coil-like

state into a stretched one) was observed by Balabaev et al. upon examination of the state of an individual macromolecule under an external force acting on its ends [36].

2.4 Radial Contraction

When analyzing the compression of the polymer network in a plane perpendicular to the jet, the process becomes stationary quite rapidly and can be presented as a one-dimensional (1D) chain of springs (see Fig. 2c) in a steady state, described by the following differential equation:

$$\frac{k_B T}{\xi_0^2}\left\{[R_{n+1} - R_n - \xi_\perp] - \left[R_n - R_{n-1} - \xi_\perp\right]\right\} + a_{eff}\,\eta v_r(R_n) = 0, \tag{13}$$

here the transversal mesh size $\xi_\perp = \xi_\perp(z)$ describes the radial contraction due to stretching, parametrically dependent on z. At the cross-section $z = -z_0$ the parameter $\xi_\perp$ is assumed to be the initial network mesh size, ξ_0.

This difference equation can be also approximated by a differential equation:

$$\frac{d^2R(\rho, z)}{d^2\rho} - \kappa^2(z)R(\rho, z) = 0, \tag{14}$$

here $\rho = r/z_0$, $\kappa(z) = \kappa_0[\xi_0/\xi_\perp(z)]\sqrt{1 + z/z_0}$, $\kappa_0^2 = z_0 v_0 a_{eff}\,\eta/mc_{net}^2 = (v_0^2/c_{net}^2 - 1)\alpha$, ($\kappa_0 \propto 10 \div 10^2$), and the velocity v_r from Eq. (1) is used.

Taking into account that the outermost nodes of the polymer network have only one neighbor generating an elastic force acting inward, the boundary conditions for Eq. (14) are

$$\left.\frac{dR(\rho)}{d\rho}\right|_{\rho=\rho_0} - z_0 + \frac{\xi_\perp(z)}{z_0}\kappa^2(z)R(\rho_0) = 0, \quad R(0) = 0 \tag{15}$$

here $\rho_0 \equiv \rho_0(z) = r_J(z)/z_0$ corresponds to the jet radius in the cross section z (see Eq. (2)), and $\xi_\perp$ is the lateral contraction of the mesh size due to the axial stretching $\xi_{||}$:

$$\xi_\perp \cong \frac{3\xi_0}{2 + \left[1 - (a\xi_{||}/\xi_0^2)^2\right]^{-2}} \tag{16}$$

The solution of Eq. (14) with boundary conditions (15) is:

$$r(\rho, z) = \frac{z_0\,\sinh[\kappa(z)\rho]/\cosh[\kappa(z)\rho_0]}{\kappa(z)\left\{1 + \left[\xi_\perp(z)/z_0\right]\kappa(z)\,\tanh[\kappa(z)\rho_0]\right\}} \tag{17}$$

The polymer network radius is given at $\rho = \rho_0$ by the following form

$$r_P(z) = \frac{z_0 \tanh[\kappa(z)\rho_0]}{\kappa(z)\left\{1 + \left[\xi_\perp(z)\Big/ z_0\right]\kappa(z)\tanh[\kappa(z)\rho_0]\right\}} \tag{18}$$

For small values of argument of hyperbolic tangent, $\kappa(z)\rho_0 << 1$, and $\kappa(z)\xi_\perp(z)\Big/ z_0 << 1$, Eq. (18) demonstrates no radial contraction of the polymer network, yielding

$$r_P(z) = z_0\rho_0 = r_J(z) \tag{19}$$

For large values of the argument of hyperbolic tangent, $(\kappa(z)\rho_0 >> 1)$, one can assume that $\tanh[\kappa(z)\rho_0] \approx 1$, so that Eq. (18) can be simplified. Taking into account the fact that $\kappa(z)\xi_\perp(z)\Big/ z_0 << 1$, in case of finite $z\Big/ z_0$ one can write

$$r_P(z) \cong \frac{\xi_\perp(z)}{\xi_0}\frac{z_0}{\kappa_0\sqrt{1 + z\Big/ z_0}}, \tag{20}$$

and in the case of large $z\,(z\Big/ z_0 >> 1)$, the polymer network has the following form

$$r_P(z) \cong \frac{z_0}{\kappa_0^2\left(\xi_0\Big/ z_0\right)\left(1 + z\Big/ z_0\right)}, \tag{21}$$

indicating a constant ratio between the jet and polymer radii. However, the last asymptote lacks physical significance, as the effects dominant at this stage of the processes are not accounted for, thereby making the model inappropriate far from the jet start.

An approximate dependence of the polymer network radius on the jet radius, $r_J(z)$, is given by

$$r_P(z) \approx \frac{\xi_\perp(z)}{\xi_0}\frac{r_0}{1 + z\Big/ z_0} = \frac{\xi_\perp(z)}{\xi_0}r_J(z), \tag{22}$$

showing that the axial stretching is the dominant factor determining the network radius, while the radial hydrodynamic compression has a negligible effect. When presenting this relationship as a function of position z along the jet and comparing it to Eq. (20), a rapid narrowing of the network radius is observed with respect to the jet radius (see Fig. 4). The expected outcome is a substantial rise in polymer concentration towards the jet center.

Summarizing the above results, one can conclude that no contraction of the polymer network occurs at the initial region of the jet. The intermediate asymptote demonstrates that the radial hydrodynamic effect is negligible, and that longitudinal stretching acts as the dominant factor affecting polymer network contraction, resulting in shortened distances between adjacent topological knots in the transversal direction. In the case of very large $z\,(z\Big/ z_0 >> 1)$, the form of the polymer network conforms

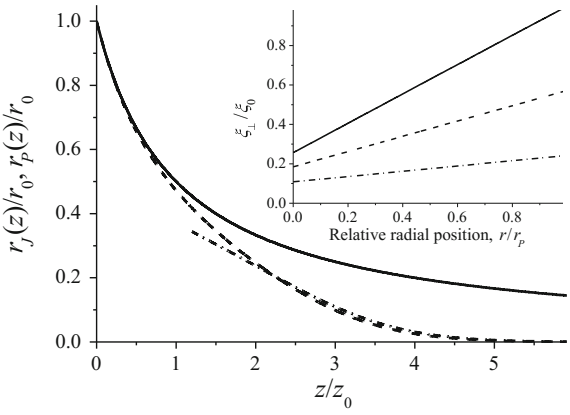

Fig. 4 Polymer network contraction. Relative jet radius, r_J/r_0 (solid line), and polymer network radius, r_P/r_0 (dashed line—Eq. (22) and dot-dashed line—Eq. (20)), as a function of the relative axial position, z/z_0. The inset displays radial contraction, $\xi_\perp/\xi_0$, obtained by simulations, as a function of the relative radial position, r/r_P, at three axial positions, $z = 0$ (solid line), $z/z_0 = 2.5$ (dashed line), and $z/z_0 = 3.5$ (dot-dashed line). Parameters are the same as in Fig. 3 [25]

to that of the jet. Note that the last asymptote is barely discernable in a real system, due to rapid solvent evaporation in this region, which acts as the dominant factor determining the state of the polymer system.

2.5 System State Depending on Network Strain

Let us consider the deformation of elementary cell of the polymer network in question under system stretching. Introducing the network strain as $\lambda = \xi_{||}/\xi_0$, we get that the relative contraction, $\xi_\perp/\xi_0$, of elementary cell versus strain is

$$\frac{\xi_\perp(\lambda)}{\xi_0} = \frac{3}{2 + \left\{1 - \left[\left(a/\xi_0\right)(\lambda - 1)\right]^2\right\}^{-1/2}} = \frac{3}{2 + \left\{1 - \left[c_0(\lambda - 1)\right]^2\right\}^{-1/2}}, \tag{23}$$

here $c_0 = V_P/V_{Cell}^{(0)} = a^3 N_S/\xi_0^3 \propto (a/\xi_0)^{3-1/\nu}$ is the initial local volumetric concentration of the polymer (if $\nu = 1/2$, the concentration is $c_0 = a/\xi_0$); and it is taken into account that at low strain ($\lambda \to 1$), the relative contraction also is small ($\xi_\perp/\xi_0 \to 1$).

This cell contraction results in the contraction of the polymer network as a whole in the same proportion, so the effective radius of the polymer network, $r_P(\lambda)$, reduces with stretching as

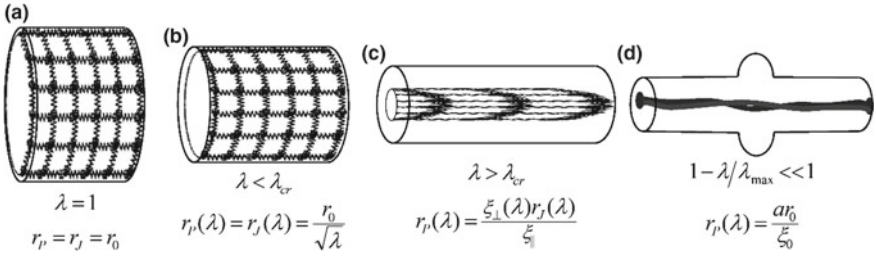

Fig. 5 Schematic illustration of polymer network structure and its stretching. An initial jet state (**a**); low stretching of the jet (**b**); high stretching of the jet (**c**); a formed filament and arising of capillary instability (**d**). The explanation of the equations and inequalities are given in the text [26]

$$r_P(\lambda) = \frac{3r_{P,0}}{2 + \left\{1 - [c_0(\lambda - 1)]^2\right\}^{-1/2}}, \tag{24}$$

here $r_{P,0}(\lambda)$ is the initial radius of the unstretched polymer network.

Note that the jet stretching results in its contraction in accordance to volume conservation law of incompressible liquid:

$$r_J(\lambda) = r_0 \Big/ \sqrt{\lambda}, \tag{25}$$

here r_0 and $r_J(\lambda)$ are the radii of initial and stretched jets, respectively.

This jet contraction does not affect the polymer network state, if $r_P(\lambda) < r_J(\lambda)$, whereas in opposite case, if $r_P(\lambda) > r_J(\lambda)$, an additional hydrodynamic forces are acting on the polymer network, generating its additional contraction. In the first case the polymer network contraction is being described by the Eq. (24); whereas in the latter case this Eq. (24) is to be modified by the following way [26]

$$\tilde{r}_P(\lambda) = \frac{3r_J(\lambda)}{2 + \left\{1 - [c_0(\lambda - 1)]^2\right\}^{-1/2}} = \frac{3}{2 + \left\{1 - [c_0(\lambda - 1)]^2\right\}^{-1/2}} \cdot \frac{r_0}{\sqrt{\lambda}} \tag{26}$$

The lateral contraction, $\xi_\perp$, of the mesh size also is to be renormalized in the same way:

$$\tilde{\xi}_\perp(\lambda) = \frac{3}{2 + \left\{1 - [c_0(\lambda - 1)]^2\right\}^{-1/2}} \cdot \frac{\xi_0}{\sqrt{\lambda}} \tag{27}$$

It turns out that the hydrodynamic contraction of the polymer network is dominant if the jet stretching is not too high (see Fig. 5b); whereas the polymer network contraction due to its stretching is dominant only in case of very high (see Fig. 5c), almost maximum-possible stretching (see Fig. 6a). Note that the last case corresponds to the situation when the polymer contraction results in a filament formation in the center of the stretching jet (see Fig. 5d).

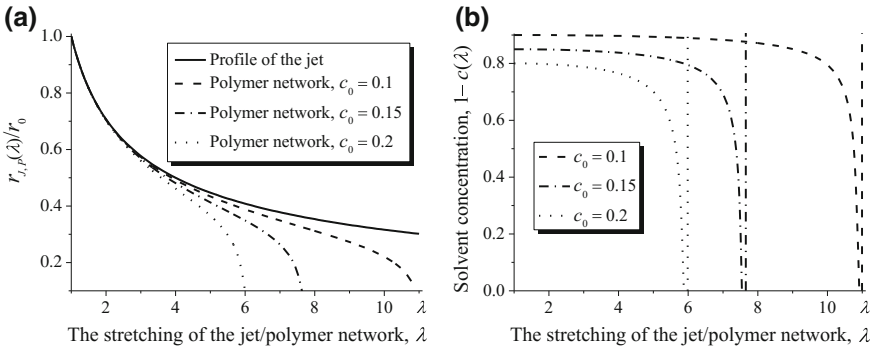

Fig. 6 **a** The polymer network contraction versus polymer network stretching: with additional contraction due to hydrodynamic forces. **b** The volumetric solvent concentration versus polymer network stretching (the vertical dashed lines show the maximum possible stretching) [26]

The effective radius of the zone containing almost the entire polymer, is shown in the Fig. 6a. A zone outside of this radius (between solid and dashed lines in Fig. 6a) contains almost pure solvent. So, we have a situation of phase separation: oriented polymer in the center of a jet surrounded by a solvent (maybe by a dilute solution).

A non-linear response of the polymer network under stretching results in changes in its volume that, in turn, results in changes in local polymer concentration. Indeed, the volumetric polymer concentration in stretched system is

$$c(\lambda) = \frac{V_P}{V_{Cell}(\lambda)} = \frac{V_P}{V_{Cell}^{(0)}} \cdot \frac{V_{Cell}^{(0)}}{V_{Cell}(\lambda)}, \tag{28}$$

here the initial cell volume is $V_{Cell}^{(0)} = \xi_0^3$, and the volume of the stretched cell is $V_{Cell}(\lambda) = \tilde{\xi}_\perp^2(\lambda)\,\xi_{||}$. The first factor in the Eq. (28) corresponds to initial polymer concentration, c_0; and the second one can be calculated with the help of the Eq. (27):

$$c(\lambda) = c_0 \frac{\xi_0^2}{\lambda \tilde{\xi}_\perp^2(\lambda)} = \left[2 + \left\{1 - [c_0(\lambda - 1)]^2\right\}^{-1/2}\right]^2 \frac{c_0}{9} \tag{29}$$

Using the obtained dependence (29), the volumetric portion of residual solvent, $1 - c(\lambda)$, remaining in the stretched network, is depicted the Fig. 6b. The vertical dashed lines indicate the maximum-possible stretching of the system in question (for given initial polymer concentrations) with no disentanglement of the topological network. In case of relative low deformations, the solvent content is decreasing slowly, but beyond some threshold, corresponding to almost maximum possible stretching (about of 90% of the maximum), the volume content of residual solvent sharply decreases and tends to zero. By the other words, under very high draw ratio, the solvent is "wringing out" of the polymer network, resulting in oriented filament

formation and polymer solidification. So, this model can be called the model of "wringing out a wet rag".

Note that the filament formation under high draw ratio seems similar to a phase separation process. Nevertheless, in our opinion, the polymer densification due to a lateral contraction of the polymer network being accompanied by the solvent replacement, is dominant, and the phase separation (if this term can be used) occurs only in the last stage of the process (see Fig. 5d) that corresponds to results of [37, 38] where the "blistering" effect described.

3 Experimental

The above theoretical analysis demonstrating a possibility for polymer redistribution, got the validation on the base of some experimental observations, such as fast X-ray imaging [39, 40] of electrospinning jets, as well as analysis of "bead-on-a-string structure" evolution [26].

3.1 Fast X-Ray Phase-Contrast Imaging

On the base of on-line fast X-ray phase-contrast imaging [39, 40], the radiation absorption of Poly(ethylene oxide) and Poly(methyl methacrylate) semi-dilute solutions was measured in the straight regions of electrospinning jets [25].

The idea of this experimental examination was to compare profiles of the radiation transmission, measured across the jet close to the jet start as well as farther along the jet, with those obtained by the wave propagation simulation for homogeneous polymer solution. The agreement between the experimental profiles and the simulation data indicates that the polymer distribution across the spinning jet is homogeneous. And in the case of variation of the experimental profile relative to simulation, the heterogeneous distribution of polymer across the spinning jet is observed.

Realizing this idea, profiles of the radiation transmission, T_{exp}, were measured across the jet close to the jet start as well as farther along the jet, for PEO as well as for PMMA. The results of this measurement and simulations for the spinning homogeneous solution of 3 wt.% PEO in water at two z-positions ($z_1 = 0.02$ mm and $z_2 = 0.02$ mm), are presented in the Fig. 7. In these figures the measured transmission, T_{exp}, (thin solid line) and its smoothing (thick solid line) compared to simulated transmission, T_{sim}, (dashed line) are shown. The inset displays calculated variations in X-ray absorption coefficient, $\Delta\alpha(r, z)$, (dashed line), and resulting variations in the local polymer mass concentration, $\Delta c_P(r, z)$, (solid line).

Close to the jet start, the radiation transmissions T_{exp} and T_{sim} almost coincide, as expected for homogeneous polymer solution (see Fig. 7a), whereas farther along the jet, T_{exp} rises above T_{sim} at the jet center (see Fig. 7b). Since in the used solution, the polymer has a lower absorption coefficient compared to the solvent, the decrease

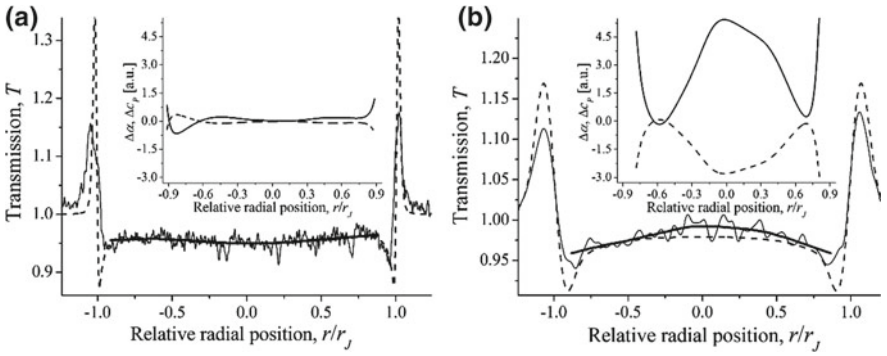

Fig. 7 Typical absorption measurements across the spinning jet of a solution of 3 wt.% PEO in water at two z-positions indicated in Fig. 2*d*. **a** z = 0.02 mm; **b** z = 0.5 mm. The inset displays calculated variations in X-ray absorption coefficient, and resulting variations in the local polymer concentration [26]. Detailed explanation see in the text

(increase) in absorption reflects a polymer concentration increase (decrease). Based on the above experimental observations one can conclude that while almost no change in absorption coefficient, and hence in polymer concentration, was observed across the jet close to the jet start (see inset in Fig. 7a), the absorption coefficient varied across the jet with respect to its initial value, when measured at points farther along the jet, indicating a non-uniform polymer concentration distribution with increased concentration in the jet center (see inset in Fig. 7b). Indeed, a decrease in absorption coefficient which corresponds to a rise in the polymer concentration, was observed namely close to the jet center, while absorption coefficient increased, when measured at greater distances from the center and this increase corresponds to the polymer concentration decrease, as expected from the redistribution of the polymer across the jet.

3.2 "Bead-on-a-String Structure"

The analysis of instability development in a jet of a viscoelastic polymer solution under high stretching [26] allows one to observe some phenomenon being of high interest for our discussion. The point is that the stability of the jet form is being determined by the relationship between the solution elasticity and the surface tension. A jet stretching results in a sharp radial gradient in the polymer distribution: the polymer concentration is sharply increasing in the jet center, whereas a low-viscous fluid is remaining in near-surface layer. As a result, the central oriented polymer filament surrounded by the shell layer consisting mainly of a solvent, is being formed.

Although, such a polymer state looks like a phase separation, one can accept also an alternative point of view that the phenomenon can be explained in the framework

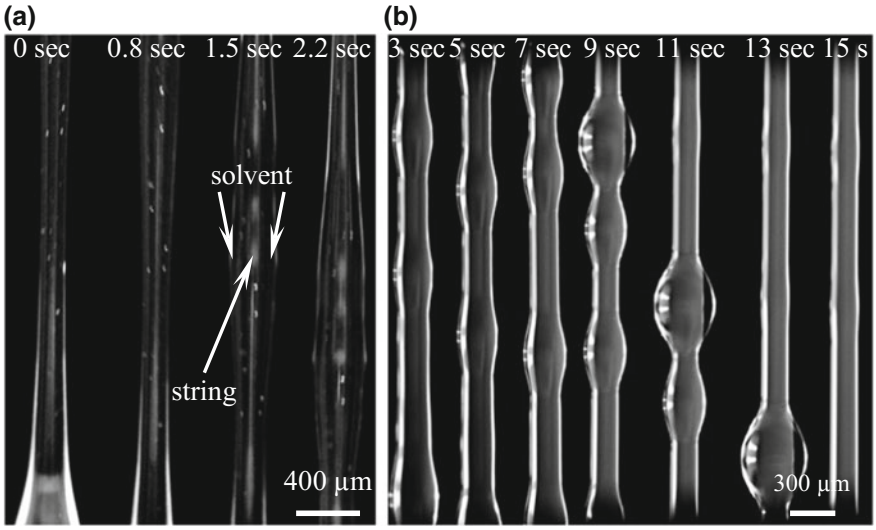

Fig. 8 **a** Consecutive stages of "phase separation", accompanied by formation of a near-surface solvent layer. **b** Appearance of separate droplets. The full observation time was 16 s. Noticeable waves appeared in the third second; droplets united with their neighbors and formed larger droplets in the seventh second; the large droplet descended along a string, collecting all solvent in the fifteenth second [26]

of "wringing out wet rag" mechanism proposed in [26]. This mechanism is based on the same or similar ideas proposed in [25] and discussed above.

The main portion of experiments was carried out according to the following scheme. A drop of the volume of about 1 mm^3 of polymer solution was pressed out from a syringe on a glass plate and then the syringe moved up with constant velocity ($\approx$ 10 mm/s). The process was filmed for the further analysis. The experiments were performed with entangled concentrated (18–22%) solutions of *polyacrylonitrile* (PAN) with M_W = 94.6 kDa in *dimethyl sulfoxide* (DMSO), at temperature of 20 °C. The crossover concentration, c^*, for this system equals about of 0.5%.

A snapshot demonstrating the solvent wringing out of a fiber and the formation of a surface layer of the solvent around of an oriented polymer filament, is depicted in the Fig. 8a. The more prolonged evolution of the surface instability is shown in Fig. 8b. The observed process stages are: the formation of a layer of a liquid with low viscosity on a cylindrical surface, the transformation of this layer into an unduloid structures, and finally, this structure transforms of into individual droplets.

The kinetics of droplet formation is presented in Fig. 9. In this series of experiments, a light beam was directed along the fiber axis from the bottom of a syringe. The jet works as a light guide, and the optical heterogeneity (local change in the refraction index) allows us to visualise the boundary between regions with high and low polymer concentration (polymeric core and solvent).

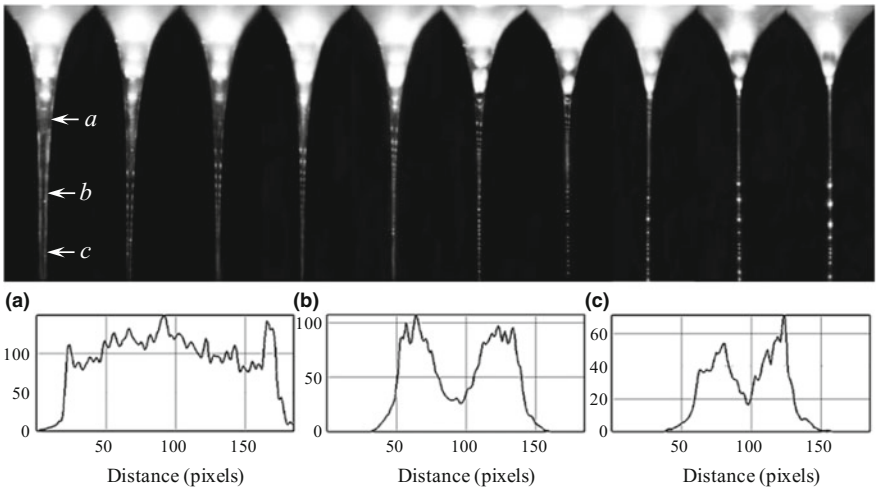

Fig. 9 Consequent stages of the phase separation in stretching of an entangled polymer solution, accompanied by formation of near-surface solvent layer and by appearance of separate drops. (PAN/DMSO 20% solution). Time step equals 0.5 s. The light intensities showing the polymer distribution across the jet in three cross-sections of the left snapshot are depicted in the three bottom plots [26]

Analysing these images, one can conclude that a shrinkage of a polymer core occurs with stretching. The solvent release begins in the form of a liquid cylinder at some distance from the Taylor cone vertex which corresponds to the definite extension ratio where critical conditions for "phase separation" have been reached. As can see on the snapshot 1, the jet diameter is ~90 μm at the distance equal to 2/3 of the full length and decreases along the jet up to 20 μm. This shrinkage is accompanied by polymeric core formation (see Fig. 9, plots *a*, *b*, and *c*). Two next snapshots demonstrate the further reducing of the jet diameter. This decrease in the jet diameter is accompanied by droplet initiation. Separate droplets are distinguishable and can be seen by the naked eye. These droplets can be simply collected and taken off with blotter paper. The chemical analysis of the collected droplets shows that usually they contain no more than 0.5% of a residual polymer in comparison to 18–22% in the initial solution.

In addition, the droplets, formed close to the cone vertex, started to move back towards the cone against gravity and were dissolved in the unstretched part of the jet. This observation has the simple explanation: the droplet motion is caused by capillary forces. Indeed, the Laplace pressure increases with a decrease in the jet diameter, and this pressure gradient results in the above movement of the droplets in the direction of an increase in the jet diameter. At the same time, in the central part of the jet where the jet diameter does not vary, the droplets do not move and remain on a core surface until they will evaporate without dissolving the oriented polymer filament.

The described phenomenon is rather similar to the mentioned above "blistering" effect described in [37, 38], but actually these two processes (blistering and considered above) are similar only in the final stage of macromolecule stretching. However, the initial stage of appearance of the solvent shell as well, when the solvent is being pressed out to the jet surface, and the polymer filament is forming in the jet center, is governed by different physical mechanism related to high stretching level of a polymer network accompanying by its radial contraction. By the other words, the formation of a polymer filament, surrounded by a liquid shell, is not related to the equilibrium thermodynamics of the system. The point is that under very high stretching of a polymer solution the solvent is "wringing out" of the polymer network due to effects of excluded volume, resulting in the formation of an oriented filament and polymer solidification.

4 Size-Dependent Behaviour of Electrospun Polymer Nanofibers and Their Internal Structure

The next step in our examinations is related to understanding of a physical mechanisms resulting in the confinement-induced size-dependent behavior of polymer nanofibers. Below, a theoretical model for require physical mechanism proposed in our work [41], is being discussed. Taking into account the fact that the size-dependent behavior was demonstrated both by amorphous and by semi-crystalline polymer nanofibers, we can conclude that the amorphous portion of the polymer matrix of as-spun nanofibers plays a dominant role in the phenomenon in question. Therefore, we can restrict our consideration only by amorphous polymer nanofibers, more specifically, we focus on examination of their internal structure formed during nanofiber fabrication.

4.1 The Structure of an Amorphous Polymer Matrix of Electrospun Nanofibers

As a result of discussed above evolution of polymer solution during a spinning, the final state of polymer matrix of electrospun fiber is non-equilibrium one, demonstrating some level of frozen supermolecular ordering. The high strain rate (of the order 10^3 s^{-1}) acting during electrospinning [14–16], results in stretching and orientation of the polymer chains in the solution [25, 42]. Unfortunately, up to now there is no detailed information regarding the structure of polymer matrix inside of electrospun nanofibers. We know only that after solidification of the spinning jet the amorphous portion of polymer inside of electrospun fibers is partially oriented along the fiber axis.

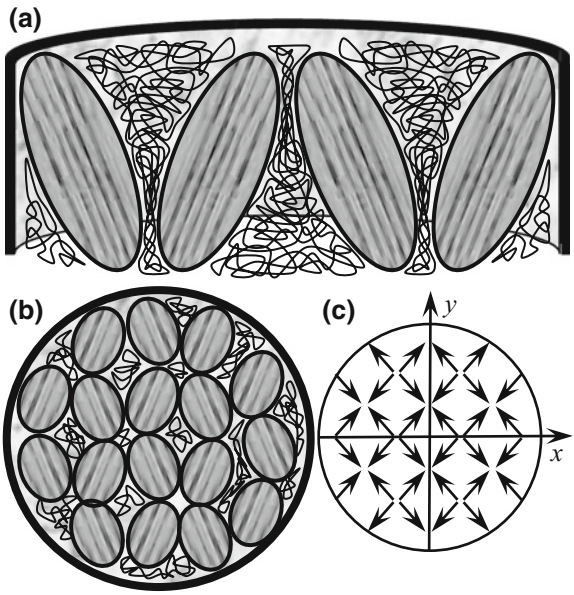

Fig. 10 Schematic internal structure of as-spun polymer nanofiber. **a** A cross-section along a fiber. **b** A cross-section across a fiber. **c** The effective regular lattice of effective "anisotropic particles" across a fiber [41]

Let us assume that the above amorphous portion of the nanofiber polymer matrix contains anisotropic regions consisting of directional-correlated worm-like subchains, partially oriented along the fiber. These ordered regions have no clearly delineated boundaries and smoothly transfer one into another. Nevertheless, in order to introduce an effective internal structure of electrospun polymer nanofibers, these ordered regions can be assumed as ellipsoid-like "anisotropic particles" with one long, $l_{||}$, and two short, d_f, axes; in doing so, the long axis of these "anisotropic particles" is tilted relative to the fiber axis. The tilt angle, θ, is a random parameter being described by a distribution function. The mean-value of the tilt angle, Θ, corresponds to the degree of orientational ordering in amorphous polymer matrix. The orientational ordering is characterized by the order parameter, $\eta = 0.5\left(3\left\langle\cos^2\theta\right\rangle - 1\right)$, so $\cos\,\Theta = \sqrt{\left\langle\cos^2\theta\right\rangle} = \sqrt{(2\eta+1)/3}$. The typical values of the order parameter for polymer electrospun nanofibers is not too high. For example, the order parameter, η, for *Nylon*-6,6 electrospun nanofibers was about of 0.2 [1] and $\Theta \approx \pi/4$, whereas for a completely disordered polymer matrix ($\eta = 0$) the mean-value of the tilt angle is $\Theta \approx \pi/3$. Below we will use the mean-value of the tilt angle, Θ, and such approximation sufficiently simplifies the mathematical calculations. Note that even if two neighbor "particles" have the same tilt angle, these "particles" can be nonparallel due to possibility of free rotations in the plane perpendicular to the fiber axis (see Fig. 10a, b).

The above anisotropic ordered regions, separated by thin amorphous layers, play the role of structural elements reflecting the supermolecular structure of polymer matrix of electrospun nanofibers. Note that the mechanical properties of the intro-

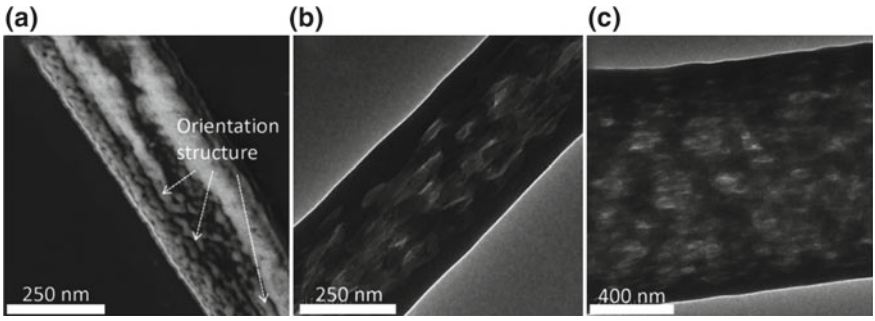

Fig. 11 Morphologies of molecular chain orientation of PC nanofibers: **a** AFM image, **b** and **c** TEM images [47]

duced "particles" are also anisotropic: in direction of the long axis the elastic modulus, $E_{||}$, is much higher than in perpendicular directions, $E_{\perp}$, and this fact is of great importance for our concept. It is reasonable to assume that $E_{\perp}$ is approximately equal to the Young's modulus of bulk polymer: $E_{\perp} \approx E_{bulk}$ ($E_{||} >> E_{bulk}$).

The key point of the proposed model of the internal structure of electrospun nanofibers is: the nanofiber can be considered as a "composite" consisting of effective "anisotropic particles" (the ellipsoid-like regions), surrounded by a binder (thin amorphous polymer layers). This idea is based on the following experimental observations and theoretical analysis. Recently Malkin et al. have shown that high rate deformation of the macromolecular network results in the formation of large inhomogeneous structures—grains or bundles [43]. Note that this phenomenon is in line with the well-known phenomenon called "shear-induced concentration fluctuations and/or phase separation" which has been examined both theoretically [44, 45] and experimentally [46]. Taking into account the fact that the electrospinning process is accompanied by high strain rate, it is reasonable to assume that the similar structures can be forming also in electrospun polymer nanofibers.

In addition, recently Xu et al. analyzing the phase contrast and transmission electron microscopy images, have shown that the electrospun polycarbonate nanofibers exhibit a cylinder-like structure composed of molecular chains that are highly oriented along the fiber axis [47]; and such a structure seems very similar to described above (see Fig. 11).

The similar structure of electrospun polystyrene-block-polyisoprene nanofibers was observed also by Kalra et al. [48].

The simplest scale estimation of the introduced above structural elements inside of electrospun polymer nanofibers can be obtained, examining of the network structure evolution of polymer solution in the stretching jet during the spinning (see Sect. 4.2).

The polymer subchains between two nearest (along the chain) topological knots are stretching due to hydrodynamic flux with an increasing velocity; and this stretching of subchains in the direction along the fiber axis results in their compression in

perpendicular directions. This compression is related to the stretching of a subchain by Eq. (16) which can be modified into following form:

$$\frac{\xi_{\perp}}{\xi_0} \cong \frac{3}{2 + \left[1 - (\xi_{||}/an)^2\right]^{-2}} \tag{30}$$

here $n = (\xi_0/a)^2 = N(c/c^*)^{-2}$ is the monomer number in above subchains, a is the scale of one monomer, c is solution polymer concentration; c^* is the crossover concentration of macromolecules overlap; N is the number of monomers of polymer chain (polymerization degree). Assuming, $N = 10^3$, $c/c^* = 4$, we get that $n \approx 50$, the ratios $\xi_{||}/\xi_0$ and $\xi_{\perp}/\xi_0$ can amount 10–15 and 0.5 respectively, so the aspect ratio $\xi_{||}/\xi_{\perp}$ can amount 20–30.

Such the aspect ratio allows one to consider the stretched subchains as worm-like objects and to apply the concept of orientational self-ordering to the system in question. The self-ordering of worm-like subchains which is caused by effects of excluded volume, in contrast to the hydrodynamic stretching, is not dominant, but this mechanism controls the ordering kinetics, determining the local scale of ordered regions within electrospun polymer nanofibers after solidification. The thickness of a bundle consisting of directional-correlated worm-like subchains inside of a polymer solution jet can be estimated with the help of the following equation, obtained in [49] on the base of the modified Onsager model [50, 51]:

$$d_s = \frac{\xi_{||}^2}{\xi_{\perp}\sqrt{c_V}}[\ln(1 - c_V)]^2, \tag{31}$$

here c_V is volumetric polymer concentration in the solution (the free volume in polymer solution, $\vartheta = 1 - c_V$, amounts about 0.9). After fiber solidification the bundle thickness reduces up to value:

$$d_f = \frac{a}{\sqrt{c_V}}\left[\frac{\xi_{||}}{\xi_{\perp}}\ln(1 - c_V)\right]^2 \approx 3\,\text{nm} \tag{32}$$

Note that the estimation of the correlation length, obtained in [1], exceeds the above bundle thickness, d_f, by two orders of magnitude. This difference is caused by the fact that the bundle thickness (32) corresponds to a polymer solution correlations, frozen due to rapid solvent evaporation whereas the correlation length, obtained in [1], corresponds to condensed state of semi-flexible polymer chain. Nevertheless, assuming the stretched subchain as a Kuhn segment, in condensed state the bundle thickness (32) has the same order of magnitude like the correlation length, obtained in [1].

The length of the above bundle can be estimated, assuming the random shift of neighboring worm-like subchains relative to each other in the fiber direction resulting in the diffusive law of the bundle length depending on the chain number in the bundle:

$$l_{||} \propto \frac{\xi_{||}}{2}\sqrt{\frac{d_f}{a}} = \frac{\xi_{||}^2 |\ln(1-c_V)|}{2\xi_\perp c_V^{1/4}} \approx 10\,\text{nm} \tag{33}$$

Last two Eqs. (32) and (33) allow one to calculate the aspect ratio of the ordered anisotropic regions

$$\varepsilon = \frac{d_f}{l_{||}} = \frac{2|\ln(1-c_V)|}{(\xi_\perp / a)\, c_V^{1/4}} \approx \frac{1}{3} \tag{34}$$

Thus, according our assumption, the nanofiber polymer matrix contains anisotropic regions consisting of directional-correlated worm-like subchains, partially orientated along the fiber; and the geometrical parameters of these ordered regions ("anisotropic particles") are described by Eqs. (32) and (33).

At first glance, the system of such type can be analyzed on the base of the theories of composite elasticity. However, in the framework of these theories the accounting of the boundary conditions which are the key point of the problem in question, is very hard (may be, unsolvable) problem. In addition, this analogy with a composite material is hardly applicable due to the extreme high concentration of the "anisotropic particles". Another analogy with granular materials or cellular solids seems more suitable. The main distinction of granular materials from the system in question is weak linking between grains. Nevertheless, in case of deformation mode at which this distinction is of no importance the behavior of granular material and as-spun polymer nanofibers can be similar. Indeed, C. Tekoğlut et al. showed with the help of the two-dimensional numerical simulations that granular solid demonstrates the size-dependent behavior: in case of shear and indentation deformations, the stiffness and the strength of granular sample are increasing with decrease of its thickness [52].

Summing this section, one can conclude that the introduced micro-structure of electrospun polymer nanofiber is suitable and can be a base for further analysis of the problem in question.

4.2 The Mathematical Model for Polymer Nanofiber Elongation

Unfortunately, no suitable theory describing the above phenomenon in granular materials, is known, so a novel mathematical model should be considered.

Let us to examine a monolayer (in a cross-section of the fiber) of the introduced "anisotropic particles". This monolayer having thickness $l_0 = l_{||} \cos\,\Theta$, lies in the xy-plane (the z-axis is oriented along the fiber). In spite of the fact that these "anisotropic particles" are located randomly, in order to simplify the mathematical description of the system a regular square lattice with period d_f can be introduced (see Fig. 10c). The "particles" are situated in the lattice nodes numbered by number pairs (i, j).

In case of need, the irregular character of the system in question can be taken into account by introducing of random fluctuation of system parameters.

Under external stretching force the considered monolayer undergoes an elongation, Δl, which is accompanied by relative rotations of the above "anisotropic particles". The "particle" rotation occurs because of a torque arising due to local stress. This torque strives to decrease the angle between "particle" long axis, $l_{||}$, and fiber axis. At the same time, the relative displacement of neighbor "particles" gives rise to a torque having the opposite sign, so the rotation angle corresponds to the equality of these two torques. Confinement effect is that the above rotations are hindered by the fiber surface layer in which no rotations occur; and this fact is to be taken into account by boundary conditions. As a result, the elastic modulus depends on the diameter of the deformed fiber. In case of small fiber diameters this restriction is dominant while the effect decreases with increase of fiber diameter, and tends to zero for large fiber diameters.

The elongation of the considered monolayer, Δl, is caused by two reasons: due to longitudinal elongation of the "anisotropic particles", and due to its rotations (an impact of a transversal deformation of the "particles" with low elastic constant, E_{bulk}, into fiber elongation is not taken into account due to the fact that this deformation type is repressed due to counteraction of neighbor "particles"). Thus, the fiber strain is

$$\varepsilon = \frac{\Delta l}{l_{||}\cos\,\Theta} = \frac{\sigma_{i,j}\cos\,\Theta}{E_{||}} + \delta\theta_{i,j}\tan\,\Theta, \tag{35}$$

here $\delta\theta_{i,j}$ is the rotation angle of the "particle" located in the point $(x_i,\ y_j)$.

The Eq. (35) can be rewritten as the relationship between the local stress, $\sigma_{i,j}$, and the local rotation angle, $\delta\theta_{i,j}$

$$\sigma_{i,j} = E_{||}\varepsilon\frac{1 - (\delta\theta_{i,j}\big/\varepsilon)\tan\,\Theta}{\cos\,\Theta}, \tag{36}$$

here the strain, ε, does not vary in fiber cross-section.

The mean-stress, $\bar{\sigma}$, is to be defined as

$$\bar{\sigma} = \frac{1}{S}\sum_{i,j}\sigma_{i,j} = \frac{E_{||}\varepsilon}{\cos\,\Theta}\left[1 - \frac{\tan\,\Theta}{S}\sum_{i,j}\frac{\delta\theta_{i,j}}{\varepsilon}\right] \tag{37}$$

And, with accordance to the definition $E_{eff} = \bar{\sigma}\big/\varepsilon$, the required effective elastic modulus of our system is calculated as following

$$E_{eff} = \frac{E_{||}}{\cos\,\Theta}\left[1 - \frac{2\tan\,\Theta}{R^2}\int_0^R\frac{\delta\theta(r)}{\varepsilon}rdr\right], \tag{38}$$

here the radial symmetry of the system in question is taken into account.

Let us estimate the local torques acting on a trial "particle". The first torque, M_+, which strives to decrease the angle between long ellipse axis, $l_{||}$, and fiber axis, is proportional to the local stress, $\sigma_{i,j}$, to the square of the long axis of the ellipsoid, $l_{||}$, as well as to the first-degree of the short one, d_f. In addition, this torque is equal to zero for the isotropic sphere-like particle or if the angle, Θ, between long ellipsoid axis, $l_{||}$, and the fiber axis is equal to 0 or $\pi \big/ 2$. So, the torque M_+ can be approximated by the following equation

$$M_+ \propto \sigma_{i,j} l_{||}^2 d_f \sin\,\Theta \cos\,\Theta(1-\varepsilon) \tag{39}$$

There are two torques caused by elastic deformation and shear stress arising as a result of relative rotation of two neighbor ellipsoids, and acting in opposite direction. The first one, M_{el}, is proportional to the third power of the ellipsoid long axis, $l_{||}$, to $\cos^2\theta$, and to the rotation angle, $\delta\theta_{i,j}$; in so doing the elastic constant is approximately equal to the Yang's modulus of amorphous polymer corresponding to bulk modulus, E_{bulk}. So, the torque M_{el} can be approximated as

$$M_{el} \propto E_{am} l_{||}^3 \cos^2\Theta \cdot \delta\theta_{i,j} \tag{40}$$

The second torque, M_{sh}, is proportional to the first-degree of the ellipsoid long axis, $l_{||}$, to the third power of the short one, d_f, and to the differences in the rotation angles of the neighbor ellipsoids, $\delta\theta_{i,j}$. In addition, this torque is inversely proportional to the thickness of a layer between two neighbor "particles" consisting of one or two polymer chains, so the thickness of this inter-layer can be taken as the scale of one monomer, a. In this case the elastic constant, $E_{||}$, is related to the chain stretching due to presence of tie molecules, so $E_{||} >> E_{bulk}$. Thus, the torque M_{sh} can be approximated as

$$M_{sh} \propto E_{||} \frac{l_{||} d_f^3}{a} \left[\left(\delta\theta_{i,j} - \delta\theta_{i-1,j}\right) + \left(\delta\theta_{i,j} - \delta\theta_{i+1,j}\right) + \left(\delta\theta_{i,j} - \delta\theta_{i,j-1}\right) + \left(\delta\theta_{i,j} - \delta\theta_{i,j+1}\right) \right] \tag{41}$$

In equilibrium the torques acting in opposite direction, are to compensate each other, and this condition allows one to write the following equation determining the internal state of deformed fiber

$$\sigma_{i,j} l_{||}^2 d_f \sin\,\Theta \cos\,\Theta(1-\varepsilon) =$$
$$E_{am} l_{||}^3 \delta\theta_{i,j} \cos\,\Theta - E_{||} \frac{l_{||} d_f^3}{a} \left[\left(\delta\theta_{i+1,j} + \delta\theta_{i-1,j} - 2\delta\theta_{i,j}\right) + \left(\delta\theta_{i,j+1} + \delta\theta_{i,j-1} - 2\delta\theta_{i,j}\right) \right] \tag{42}$$

This difference Eq. (42) can be approximated by the differential one:

$$\frac{1}{\xi} \frac{d}{d\xi} \xi \frac{d}{d\xi} \Phi(\xi) = \Phi(\xi) - \Phi_0 \tag{43}$$

here $\xi \equiv \xi_i = id_f / r_0 \equiv r / r_0$, $r_0 = d_f^2 \Big/ \sqrt{al_{||}\left[(1-\varepsilon)\tan\Theta\sin\Theta + \left(E_{am}/E_{||}\varepsilon\cos\Theta\right)\right]}$ ($r_0 \approx 10 \div 20$ nm) and $\Phi_0 = \left[\tan\Theta + \left(E_{am}/E_{||}\varepsilon(1-\varepsilon)\tan\Theta\right)\right]^{-1}$.

The boundary conditions for the Eq. (43) are

$$\frac{d}{d\xi}\Phi(\xi)\Big|_{\xi=0} = 0, \quad \Phi(R/r_0) = 0 \tag{44}$$

The solution of the Eq. (43) satisfying the boundary conditions (44), is

$$\Phi(\xi) = \Phi_0\left[1 - \frac{I_0(\xi)}{I_0(R/r_0)}\right], \tag{45}$$

here $I_0(\xi) = J_0(i\xi)$ is the Bessel function.

Multiplying the Eq. (43) by ξ and integrating it over ξ, we find that

$$\frac{2}{R^2}\int_0^R \frac{\delta\theta(r)}{\varepsilon} r dr = \frac{2r_0^2}{R^2}\int_0^{R/r_0} \Phi(\xi)\,\xi d\xi = \Phi_0\left[1 - \frac{2r_0}{R}\frac{d}{d\xi}\ln\left[I_0((\xi))\right]\Big|_{\xi=R/r_0}\right], \tag{46}$$

and the effective modulus, E_{eff}, is

$$E_{eff} = E_{bulk} + \Delta E \frac{r_0}{R}\frac{d\,\ln\left[I_0(\xi)\right]}{d\xi}\Big|_{\xi=R/r_0}, \tag{47}$$

here $E_{bulk} = E_{am}\cos\Theta/\left[\varepsilon(1-\varepsilon)\sin^2\Theta\right]$, $\Delta E = 2E_{||}/\cos\Theta$, and the strong inequality $E_{bulk} << E_{||}$ is taken into account.

Using the asymptotic behavior of Bessel function $I_0(\xi)$ for small and large arguments, one can find that for large fiber diameters, the effective modulus, E_{eff}, increases with diameter decreases:

$$E_{eff} \approx E_{bulk} + \frac{2E_{||}}{\cos\Theta}\frac{r_0}{R}, \quad R > r_0 \tag{48}$$

However, for small fiber diameters ($R < r_0$) the increase of the effective modulus, E_{eff}, stops, and it tends to a certain finite value:

$$E_{eff} \approx \frac{E_{||}}{\cos\Theta}\left[1 - \frac{1}{8}\left(R/r_0\right)^2\right], \quad R < r_0 \tag{49}$$

Unfortunately, the obtained Eq. (47) describes the elastic modulus of electrospun nanofibers depending on their diameter not so well. Although this dependence demonstrates, as expected, an increase in the elastic modulus of nanofibers with decrease of their diameters, the calculated increase turns out to be much weaker

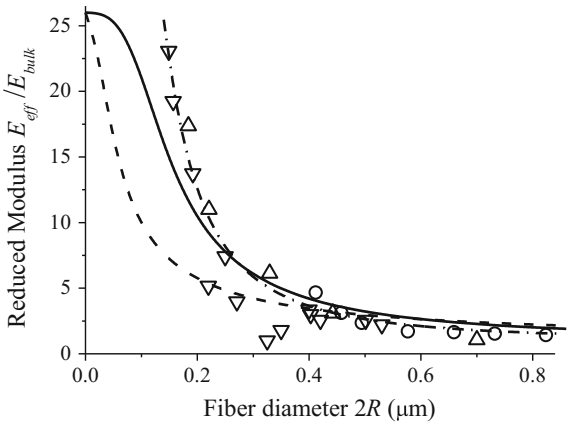

Fig. 12 Dependence of relative Young's modulus, E_{eff}/E_{bulk}, versus nanofiber diameter, D. The dashed line corresponds to the Eq. (47) describing the Young's modulus, E_{eff}, at $r_0 = 10$ nm. The solid line demonstrates the modified dependence, $\hat{E}_{eff}$ (56) corresponding to the renormalization of the ratio R/r_0 (55) with $\bar{a}N^{\gamma} = 40$. The dashed-dot line corresponds to the asymptote (57). The ratio $\Delta E/E_{bulk} = 25$. The circles and triangles show the experimental values of relative Young's modulus, E_{eff}/E_{bulk}, for electrospun Nylon-6,6 nanofibers, obtained by the tensile test (O) [1], by the resonant vibration method (∇) [53], and by the 3-point bending method (Δ) [9, 41]

compare to the one, observed experimentally (see Fig. 12, dashed line). Such disagreement is related to the fact that the scale of the introduced above ordered regions, $l_{\|}$ and d_f do not vary with variation of fiber diameters, whereas from the physical point of view such a dependence should take place, and it is to be taken into account.

4.3 Scaling of the Size-Dependent Elastic Modulus of Electrospun Polymer Nanofibers

Up to now the normalization parameter, r_0, which depends, in particular, on the sizes of ordered regions (the thickness, d_f, and the length, $l_{\|}$) assumed to be independent on the fiber diameter. But both these parameters, both the thickness, d_f, and the length, $l_{|}$, depend on the volumetric polymer concentration in the solution, c_V. In turn, the concentration of the spinning solution, c_V, affects the radius of electrospun nanofibers. Thus, the parameters d_f, and $l_{|}$, should vary with variation of the fiber diameter, and therefore, the normalization parameter, r_0, depends on the radius of electrospun nanofibers, R. This dependence will be defined below with the help of well-known scaling equations.

First of all, taking into account the fact that concentrations which are usually using in electrospinning, are relatively low ($c_V \leq 0.15$), and assuming that $\ln(1-x) \approx x$, the Eqs. (32) and (33) can be rewritten as the following scaling dependences

$$d_f \propto an^2 c_V^{3/2}, \quad l_{||} \propto an^2 c_V^{3/4}, \tag{50}$$

where $n = (\xi_0 / a)^{\nu} = N(c_V / c_V^*)^{1/(1-3\nu)}$ is the monomer number in the subchains of the topological polymer network, $c_V^* = N^{1-3\nu}$ is the volumetric crossover concentration of macromolecules overlap. Therefore, the normalization parameter, r_0, depends on the volumetric polymer concentration, c_V, as well as on the polymerization degree, N, and this dependence also can be approximated by a scaling equation

$$r_0 \propto d_f^2 \Big/ \sqrt{al_{||}} \propto a\left(nc_V^{7/8}\right)^3 = aN^{\alpha}\left(c_V / c_V^*\right)^{-\alpha/(3\nu-1)} \tag{51}$$

where $\alpha = 3[1 - 7(3\nu - 1)/8]$.

It is well known that the radius of electrospun nanofibers depends on concentration of spinning solution. Thus, Gupta et al. [13] showed that the relative concentration of spinning solution, c_V / c_V^*, and the final radius of electrospun nanofibers, R, also are related by the scaling equation

$$\frac{R}{R_0} \propto \left(c_V / c_V^*\right)^{\beta} \tag{52}$$

here R_0 is the normalization parameter $R_0 \approx 10^{-3} - 10^{-2}$ μm. The index β equals to about 3. According the data, presented by Gupta et al. $\beta \approx 3.1$; [13] the other measurements using a different types of polymer, have shown the following values: $\beta \approx 3.0$ [14] or $\beta \approx 2.9$ [14].

As a result, the normalization parameter, r_0, increases with the fiber radius decrease

$$r_0 \propto aN^{\alpha}\left(R / R_0\right)^{-\alpha/\beta(3\nu-1)} \tag{53}$$

Let us present the normalization parameter, r_0, in the following form

$$r_0 \propto aN^{\gamma}\left(R / R_0 N^{\gamma}\right)^{-\alpha/\beta(3\nu-1)} \tag{54}$$

here $\gamma = \alpha\beta(3\nu - 1)/[\alpha + \beta(3\nu - 1)]$.

The last Eq. (54) for the normalization parameter, r_0, allows to present the ratio R / r_0 in the form of a power function of the fiber radius, R,

$$\frac{R}{r_0} = \left(R / \tilde{a}N^{\gamma}\right)^{\delta} \tag{55}$$

here $\tilde{a} = (R_0 / a)^{\gamma/\beta(3\nu-1)} a$ and $\delta = 1 + \alpha / \beta(3\nu - 1)$.

Substituting the ratio (55) into Eq. (47), we receive the modified equation for the effective module, $\hat{E}_{eff}$ (see Fig. 12, solid line)

$$\hat{E}_{eff} = E_{bulk} + \Delta E \frac{1}{\xi} \frac{d \ln [I_0(\xi)]}{d\xi}\Big|_{\xi=(R/\tilde{a}N^{\gamma})^{\delta}} \tag{56}$$

In case of large fiber diameters ($R >> \tilde{a}N^{\gamma}$) the effective modulus, $\hat{E}_{eff}$, increases with fiber diameter decrease according the power law

$$\hat{E}_{eff} \approx E_{bulk} + \Delta E\left(\tilde{a}N^{\gamma}/R\right)^{\delta}, \tag{57}$$

whereas for small fiber diameters ($R << \tilde{a}N^{\gamma}$) the effective modulus, $\hat{E}_{eff}$, tends to a certain finite value also according the power law with the doubled index

$$\hat{E}_{eff} \approx \Delta E\left[1 - \frac{1}{8}\left(R/\tilde{a}N^{\gamma}\right)^{2\delta}\right] \tag{58}$$

Note that though the behavior of the asymptote for small fiber diameters (58) seems reasonable, its accuracy is not too high due to the fact that the continuous approximation (43) of the difference Eq. (42) in this case is too rough. Therefore, for the comparison to the experimental data we should restrict ourselves by asymptote for large fiber diameters ($R >> \tilde{a}N^{\gamma}$). And indeed, the Eq. (57) agree well to the experimental data for electrospun *Nylon*-6,6 nanofibers [1, 9, 52] (see Fig. 12, dashed-dot line).

The values of the indexes γ and δ in the above Eqs. (55)–(58) cannot be considered as a free model parameters and are to be calculated. As the solvents which are usually used in electrospinning, are a good ones, the index ν can be estimated as $\nu \approx 0.55$. Assuming $\beta \approx 2.9$, we receive that $\gamma \approx 0.75$ and $\delta \approx 1.6$.

The dependence (56), $\hat{E}_{eff}/E_{bulk}$, with $\tilde{a}N^{\gamma} = 40$ nm is depicted on the Fig. 12 (solid line). In order to compare the dependence (47) and its modification (56), the values of the parameter $\Delta E/E_{bulk}$ were chosen the same in both cases: $\Delta E/E_{bulk} = 25$. One can see that the modified dependence (56) demonstrates the better agreement with the experimental data compared with dependence (47), particularly for thin fibers, in region of small fiber diameters where the noticeable discrepancy between Eq. (47) and experimental data is being observed.

The obtained dependence can be verified on the base of experimental observations of Ji et al. [2] that the molecular weight affects the elastic modulus of electrospun nanofibers; and the relative elastic moduli of electrospun nanofibers of various molecular weights can be described by one master curve as a function of fiber radius, scaled by R_g, i.e., according to power law. And in the Eq. (55), the argument, R, is scaled by the factor $\tilde{a}N^{\gamma}$ having the same form as the radius of gyration, $R_g \propto aN^{\nu}$.

However, in spite of such a similarity, the index $\gamma \approx 0.75$ is too high in order to consider the scaling factor $\tilde{a}N^{\gamma}$ as an approximation for the radius of gyration, $R_g \propto aN^{\nu}$ (for the system in question the maximum possible value of index ν is 0.6). Therefore, the scaling property of the Eq. (56) seems non-applicable for the explanation of the effect of the molecular weight on the elastic modulus of electrospun nanofibers.

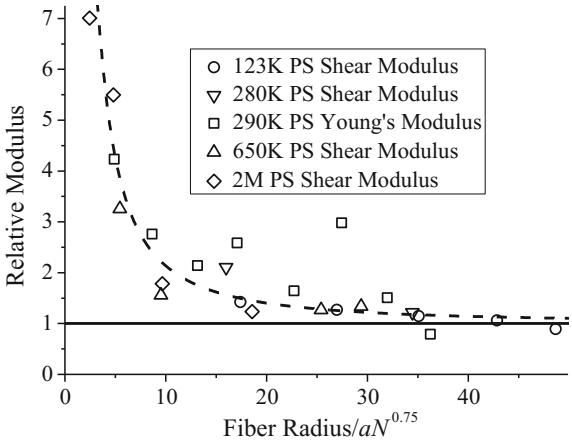

Fig. 13 Relative moduli of fibers, fabricated of the polymers of various molecular weights, as a function of their radius, rescaled by $\tilde{a}N^{\gamma}$ (the used data is taken from [2]). The fitting of the experimental data results in the function $1 + 35x^{1.5}$, depictured by the dashed line [41]

Nevertheless, this contradiction can be resolved by alternative interpretation of the experimental data. The point is that the index ν in the scaling factor $R_g \propto aN^{\nu}$ can be modified within the accuracy of the experimental data. By the other words, the values of fiber radius in the experimental data can be rescaled by the factor, $N^{\tilde{\nu}}$, with another index, $\tilde{\nu}$, being higher than ν. Indeed, such a rescaling by the factor N^{γ} with $\gamma \approx 0.75$ results in the fact that all experimental points collapse on one curve (see Fig. 13).

Moreover, the linear fitting of the rescaled experimental data in the double-log coordinates results in the following equation for the approximating curve

$$E_{rel} \approx 1 + 35\left(R \Big/ aN^{0.75}\right)^{1.5} \tag{59}$$

The index value in the Eq. (59) is $\delta = 1.5$, i.e., slightly less than the calculated index value $\delta \approx 1.6$ in the Eq. (55). Such a small difference is in this case negligible, showing a good agreement of the theoretical model to the experimental data.

5 Conclusions

The theoretical modelling of dynamics of the polymer network structure within the electrospinning jet of highly entangled, semidilute polymer solutions demonstrates that the polymer network can transform from a free state to an almost fully stretched state under extreme longitudinal acceleration. The stretching of the network is accompanied by substantial lateral contraction that leads to a rise in polymer concentration at the jet center. This outcome was confirmed experimentally by X-ray absorption measurements of the jet [25], as well as by analysis of the redistribution in the intensity of the visible light in a stretched semidilute entangled polymer solution [26].

As a result of the above evolution, the non-equilibrium state of polymer matrix inside of electrospun nanofibers is being formed. This supermolecular structure, formed as a result of electrospinning of semidilute entangled polymer solution, consists of anisotropic regions containing directional-correlated well packed worm-like subchains, partially oriented along the fiber. In reality, these ordered regions have no clearly delineated boundaries and smoothly transfer one into another. At the same time, the ordered regions are separated each from other by amorphous polymer layers.

In our opinion, just such an internal non-equilibrium structure of electrospun polymer nanofibers provides their unique features, in particular, the size-dependent behaviour which is caused by confinement of the supermolecular structures, formed as a result of electrospinning process. Moreover, the proposed model [41] describes the mechanism realizing the above confinement effect: due to interaction between ordered regions, the mobility suppression in near-surface layers hampers deformation of polymer matrix inside of electrospun fibers. If the scale of such surface influence on the deformability of electrospun fibers is comparable to their radius, the effective modulus start to depend on the fiber diameter, i.e., the size-dependent behaviour will be observed. However, in the case of thick fibers, when their radii are much larger of the interaction scale of ordered regions, the fibers demonstrate the properties of regular bulk specimens.

References

1. Arinstein, A., Burman, M., Gendelman, O., Zussman, E.: Effect of supramolecular structure on polymer nanofibre elasticity. Nat. Nanotechnol. **2**, 59–62 (2007)
2. Ji, Y., Li, C., Wang, G., et al.: Confinement-induced super strong PS/MWNT composite nanofibers. Europhys. Lett. **84**, 56002 (2008)
3. Cuenot, S., Frétigny, C., Demoustier-Champagne, S., Nysten, B.: Surface tension effect on the mechanical properties of nanomaterials measured by atomic force microscopy. Phys. Rev. B **69**, 165410 (2004)
4. Schonherr, H., Frank, C.W.: Ultrathin films of poly(ethylene oxides) on oxidized silicon. 1. Spectroscopic characterization of film structure and crystallization kinetics. Macromolecules **36**, 1188–1198 (2003)
5. Cuenot, S., Demoustier-Champagne, S., Nysten, B.: Elastic modulus of polypyrrole nanotubes. Phys. Rev. Lett. **85**, 1690 (2000)
6. Summary and perspectives on dynamics in confinement: McKenna GB Confit III. Eur. Phys. J. Spec. Topics **141**, 291–301 (2007)
7. Brown, H.R., Russell, T.P.: Entanglements at polymer surfaces and interfaces. Macromolecules **29**, 798–800 (1996)
8. de Gennes, P.G.: Glass transitions in thin polymer films. Eur. Phys. J. E **2**, 201–205 (2000)
9. Burman, M., Arinstein, A., Zussman, E.: Do surface effects explain the unique elasticity of polymer nanofibers? Europhys. Lett. **96**, 16006 (2011)
10. Reneker, D.H., Yarin, A.L., Fong, H., Koombhongse, S.: Bending instability of electrically charged liquid jets of polymer solutions in electrospinning. J. Appl. Phys. **87**, 4531–4547 (2000)
11. Hohman, M.M., Shin, M., Rutledge, G., Brenner, M.P.: Electrospinning and electrically forced jets. I. Stability theory. Phys. Fluids **13**, 2201–2220 (2001)

12. Shin, Y.M., Hohman, M.M., Brenner, M.P., Rutledge, G.C.: Temperature dependence of polymer crystalline morphology in nylon 6/montmorillonite nanocomposites. Polymer **42**, 09955–09967 (2001)
13. Gupta, P., Elkins, C., Long, T.E., Wilkes, G.L.: Electrospinning of linear homopolymers of poly(methyl methacrylate): exploring relationships between fiber formation, viscosity, molecular weight and concentration in a good solvent. Polymer **46**, 4799–4810 (2005)
14. Reneker, D.H., Yarin, A.L., Zussman, E., Xu, H.: Electrospinning of nanofibers from polymer solutions and melts. Adv. Appl. Mech. **41**, 43–195 (2007)
15. Bellan, L.M., Craighead, H.G., Hinestroza, J.P.: Direct measurement of fluid velocity in an electrospinning jet using particle image velocimetry. J. Appl. Phys. **102**, 094308 (2007)
16. Han, T., Yarin, A.L., Reneker, D.H.: Viscoelastic electrospun jets: Initial stresses and elongational rheometry. Polymer **49**(6), 1651–1658 (2008)
17. Larrondo, L., Manley, R.S.J.: Electrostatic fiber spinning from polymer melts. II. Examination of the flow field in an electrically driven jet. J. Polym. Sci. Polym. Phys. **19**, 921–932 (1981)
18. Stephens, J.S., Frisk, S., Megelski, S., et al.: "Real time" Raman studies of electrospun fibers. Appl. Spectrosc. **55**, 1287–1290 (2001)
19. Dayal, P., Liu, J., Kumar, S., Kyu, T.: Experimental and theoretical investigations of porous structure formation in electrospun fibers. Macromolecules **40**, 7689–7694 (2007)
20. Casper, C.L., Stephens, J.S., Tassi, N.G., Chase, D.B., Rabolt, J.F.: Controlling Surface Morphology of Electrospun Polystyrene Fibers: Effect of humidity and molecular weight in the electrospinning process. Macromolecules **37**, 573–578 (2004)
21. Guenthner, A.J., Khombhongse, S., Liu, W., Dayal, P., Reneker, D.H., Kyu, T.: Solvent evaporation in flexible and semiflexible polymer solutions. Macromol. Theor. Simul. **15**, 87–93 (2006)
22. Dayal, P., Kyu, T.: Dynamics and morphology development in electrospun fibers driven by concentration sweeps. Phys. Fluids **19**, 107106 (2007)
23. Koombhongse, S., Liu, W.X., Reneker, D.H.: Flat polymer ribbons and other shapes by electrospinning. J. Polym. Sci. Polym. Phys. **39**, 2598–2606 (2001)
24. Arinstein, A., Zussman, E.: Electrospun polymer nanofibers: mechanical and thermodynamic perspectives. J. Polym. Sci. Polym. Phys. **49**, 691–707 (2011)
25. Greenfeld, I., Arinstein, A., Fezzaa, K., Rafailovich, M.H., Zussman, E.: Polymer dynamics in semidilute solution during electrospinning: A simple model and experimental observations. Phys. Rev. E **84**, 041806 (2011)
26. Kulichikhin, V.G., Malkin, A.Ya., Arinstein, A. et al.: Liquid filament instability due to stretch-induced phase separation in polymer solutions. Eur. Phys. J. **E37**, 10 (2014)
27. Reznik, S.N., Zussman, E.: Capillary-dominated electrified jets of a viscous leaky dielectric liquid. Phys. Rev. E **81**, 026313 (2010)
28. Arinstein, A.: The evolution of polymer systems during electrospinning: from a semi-dilute polymer solution to a non-equilibrium state. In: Uvarova, L.A., Nadykto, A.B., Latyshev, A.V. (eds.) Nonlinearity: Problems, Solutions and Applications, pp. 203–232. Nova Science Publishers, US p (2017)
29. Odell, J.A., Keller, A., Miles, M.J.: Assessment of molecular connectedness in semi-dilute polymer solutions by elongational flow. Polymer **26**(8), 1219–1226 (1985)
30. Archer, L.A.: Polymer disentanglement in steady-shear flow. J. Rheol. **43**(6), 1617–1633 (1999)
31. Haward, R.N., Young, R.J. (ed.): The Physics of Glassy Polymers, 2nd edn. Chapman & Hall, London (1997)
32. Reneker, D.H., Chun, I.: Nanometre diameter fibres of polymer, produced by electrospinning. Nanotechnology **7**(3), 216–223 (1996)
33. Zussman, E., Rittel, D., Yarin, A.L.: Failure modes of electrospun nanofibers. Appl. Phys. Let. **82**(22), 3958–3960 (2003)
34. Yoshioka, T., Dersch, R., Greiner, A., Tsuji, M., Schaper, A.K.: Highly oriented crystalline pe nanofibrils produced by electric-field-induced stretching of electrospun wet fibers. Macromol. Mat. Eng. **295**(12), 1082–1089 (2010)

35. de Gennes, P.G.: Coil-stretch transition of dilute flexible polymers under ultrahigh velocity gradients. J. Chem. Phys. **60**, 5030–5042 (1974)
36. Balabaev, N.K., Borodin, I.P., Borodina, T.I., Khazanovich, T.N.: Stretching of a semiflexible chain composed of elastic bonds. Polym. Sci. A **52**, 655–661 (2010)
37. Sattler, R., Wagner, C., Eggers, J.: Blistering pattern and formation of nanofibers in capillary thinning of polymer solutions. Phys. Rev. Let. **100**, 164502 (2008)
38. Sattler, R., Gier, S., Eggers, J., Wagner, C.: The final stages of capillary break-up of polymer solutions. Phys. Fluids **24**, 023101 (2012)
39. Wang, Y., Liu, X., Im, K.-S., Lee, W.-K., et al.: Ultrafast X-ray study of dense-liquid-jet flow dynamics using structure-tracking velocimetry. Nat. Phys. **4**, 305–309 (2008)
40. Im, K.S., Fezzaa, K., Wang, Y.J., et al.: Particle tracking velocimetry using fast x-ray phase-contrast imaging. Appl. Phys. Lett. **90**, 09191 (2007)
41. Arinstein, A.: Confinement mechanism of electrospun polymer nanofiber reinforcement. J. Polym. Sci. Polym. Phys. **51**, 756–763 (2013)
42. Richard-Lacroix, M., Pellerin, Ch.: Orientation and partial disentanglement in individual electrospun fibers: diameter dependence and correlation with mechanical properties. Macromolecules **48**, 4511–4519 (2015)
43. AlYa, Malkin, AV, Semakov, Kulichikhin, V.G.: Modeling macromolecular movement in polymer melts and its relation to nonlinear rheology. Rheol. Acta **50**, 485–489 (2011)
44. Helfand, E., Fredrickson, G.H.: Large fluctuations in polymer solutions under shear. Phys. Rev. Let. **62**, 2468–2471 (1989)
45. Saito, Sh, Matsuzaka, K., Hashimoto, T.: Structures of a semidilute polymer solution under oscillatory shear flow. Macromolecules **32**, 4879–4888 (1999)
46. Morfin, I., Lindner, P., Boué, F.: Shear-induced concentration fluctuations and form factor changes in polymer solution in the good-solvent regime. Eur. Phys. J. E **15**, 41–45 (2004)
47. Xu, Y., Gao, Y., Wang, X., Jiang, J., Hou, J., Li, Q.: Internal structure of amorphous electrospun nanofiber: oriented molecular chains. Macromol. Mat. Eng. **302**, 1700054 (2017)
48. Kalra, V., Mendez, S., Lee, Ju.H. et al.: Confined assembly in coaxially electrospun block-copolymer fibers. Adv. Mater. **18**, 3299–3303 (2006)
49. Mezikovskii, S.M., Arinstein, A.E., Deberdeev, R.Ja.: Oligomeric State of Substances. Series: Polymer Science and Technology. Nova Publishers p 56–60 (2009)
50. Onsager, L.: The effects of shape on the interaction of colloidal particles. Ann. N.-Y. Acad. Sci. **51**, 627–659 (1949)
51. Khokhlov, A.R., Semenov, A.N.: On the theory of liquid-crystalline ordering of polymer chains with limited flexibility. J. Stat. Phys. **38**, 161–182 (1985)
52. Tekoğlu, C., Gibson, L.J., Pardoen, T., Onck, P.R.: Size effects in foams: experiments and modeling. Prog. Mat. Sci. **56**, 109–138 (2001)
53. Burman, M., Arinstein, A., Zussman, E.: Free flight of an oscillated string pendulum as a tool for the mechanical characterization of an individual polymer nanofiber. Appl. Phys. Let. **93**, 193118 (2008)

Recent Developments in Theory and Modeling of Polymer-Based Nanocomposites

Valeriy V. Ginzburg

Abstract Polymer-based nanocomposites represent relatively new class of materials, often with unique synergy of polymer ("matrix") and inorganic ("filler") properties. In recent years, the industry developed new techniques to reduce the size of the fillers (from 10–100 microns in conventional composites to <100 nm in nanocomposites), and to functionalize their surfaces, thus enabling better control over the spatial distribution of the particles in the matrix. The structure of resulting materials is thus a complex product of particle/polymer interactions, particle size and shape, and processing history. In turn, the properties of the composite material are a function of its microstructure (e.g., particle aggregation or dispersion), as well as the properties of the matrix, filler, and interfacial regions. Today, theory and modeling of nanocomposites is one of the most rapidly developing areas in Polymer Science. In this review, I discuss theoretical and computational work related to the prediction of the nanocomposite structure and morphology.

1 Introduction

In July of 2000, I was finishing my postdoctoral fellowship at the University of Pittsburgh. Prof. Manevitch ("L. I.", as he is called by his colleagues and former students) was visiting the U.S. at the time and was in Pittsburgh as part of that trip. We spent several days walking around the historic Oakland area near the University, discussing each other's research. At that time, my postdoc advisor was Prof. Anna Balazs, and her most recent emphasis was on polymer-clay nanocomposites (PNC). In the late 1980s and early 1990s, Toyota researchers demonstrated that the addition of montmorillonite clay to Nylon-6 polymer matrix can lead to a ~2X increase in modulus even at 2–4 wt.% filler levels [76, 117]. Extensive experimental studies demonstrated that depending on the polymer/clay surface interaction, the clay fillers can remain aggregated ("immiscible morphology"), allow some degree of polymer

V. V. Ginzburg (✉)
Dow Chemical Company, Midland, MI, USA
e-mail: vvginzburg@dow.com

I. V. Andrianov et al. (eds.), *Problems of Nonlinear Mechanics and Physics of Materials*, Advanced Structured Materials 94,
https://doi.org/10.1007/978-3-319-92234-8_12

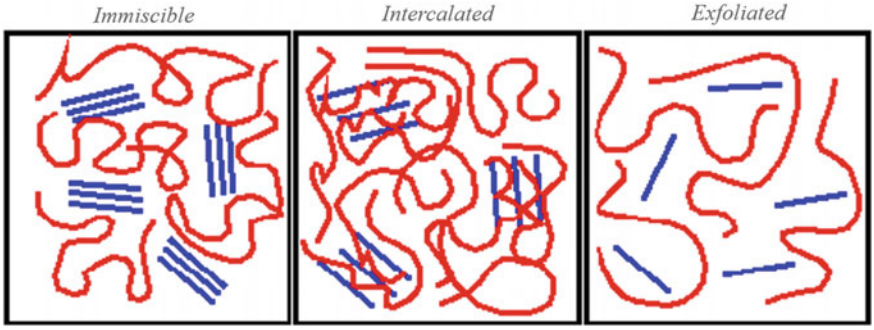

Fig. 1 Morphologies of polymer-clay nanocomposites (idealized schematic representation)

penetration between the adjacent platelets ("intercalated morphology"), or separate completely and mix with the polymer as single sheets ("exfoliated morphology"), as shown in Fig. 1 [36, 79, 157, 158]. Dr. Richard Vaia and Prof. Emmanuel Giannelis proposed that the polymer-clay nanocomposite morphology is mainly influenced by the interplay between the polymer entropy losses due to confinement between the two adjacent plates and the potential enthalpy gains due to any favorable interaction between the polymer and surface. They concluded that polar polymers like Nylon-6 have favorable interactions with the clay surfaces and thus could form intercalated hybrids with clays more easily than, say, polyethylene or polypropylene [155, 156]. To counter this effect, one could make the clay surface more polymer-like by covalently grafting short-chain nonpolar oligomers. Such organically-modified clays were indeed synthesized (e.g., Cloisite® organoclay by Southern Clay Co.) and used in industry, often with mixed results. Prof. Balazs and her collaborators (Drs. Ekaterina Zhulina, Chandralekha Singh, Yulia Lyatskaya, June Huh, Dmitri Kuznetsov, and the author of this review) developed theoretical approaches to explain how the interaction between the polymer matrix, organic ligands, and clay surfaces can determine the phase behavior of the polymer-clay nanocomposite [7–9, 37, 38, 43, 45, 65, 83, 84, 95].

The question that L. I. and I discussed in Pittsburgh was this—if thermodynamics of polymer/clay interactions favor intercalation or exfoliation, how does this process take place? Profs. A. Baljon, R. Loring, and co-workers considered the case where the clay platelets were relatively small and rigid and modeled the scenario where they remained parallel while the intercalating polymer was pushing them apart [10, 86–88]. However, for larger clay platelets, it was more likely that intercalation would occur only in a small area, where the two surfaces would be pried apart (perhaps due to hydrodynamic stresses). Then, as the polymer penetrates into the space between the platelets, a "kink" can move along to push the transition from "closed" to "intercalated" state (Fig. 2). As a result of this discussion (later joined remotely by Prof. Oleg Gendelman), we proposed a model for the "kink" or "solitonic" mechanism of exfoliation [35, 44]. This model also helped us estimate the hydrodynamic stresses needed to exfoliate or intercalate clays in polymers such as

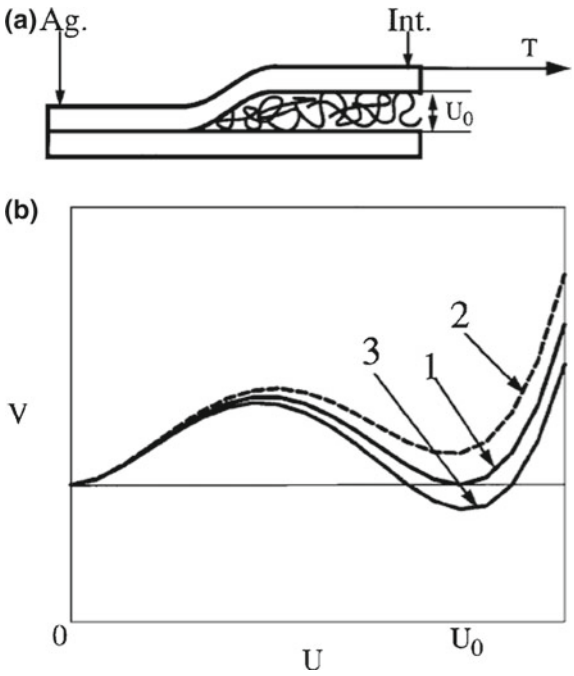

Fig. 2 Kink model of polymer intercalation between clay platelets (**a**) and effective double-well potential used to model the kink. Reproduced with permission from Ref. [44]. Copyright 2001 American Physical Society

typical commercial polyethylene or polypropylene [6]. Thus, it is easy to realize that even when polymer and organoclay are favored to mix, the resulting morphology depends strongly on the processing history (e.g., the design of the extruder used, etc.), and the ultimate properties could be very different from the "ideal" scenario.

Several months later, I joined The Dow Chemical Company in Midland, Michigan. One of Dow's scientists at the time, Dr. Jozef Bicerano, was interested in understanding how the arrangement of clay particles impacts the nanocomposite properties such as viscosity [12], modulus [17] and gas permeability [31]. The appeal of clay particles as fillers was often tied to their anisotropy—property changes were strongly tied to the filler aspect ratio. We used and developed various micromechanical models to relate structure to properties, initially for polymer-clay nanocomposites, and subsequently for other systems [11].

Over the past two decades, the nanocomposite field broadened substantially to include many new types of fillers (carbon nanotubes, graphene, metal nanoparticles, SiO2 nanoparticles, etc.) and many new applications (electrically conducting coatings, photonic materials, etc.) [80]. In this chapter, I attempt to describe some recent developments in theory and modeling of polymer-based nanocomposite materials. (While there is some overlap with an earlier review [40] published in 2010, I have added discussion of many new developments that took place subsequently.) Note that this review is limited to the nanocomposite structure and phase behavior prediction, with emphasis on the mesoscale, field-theoretical and hybrid approaches; a more comprehensive review will be published elsewhere.

2 Polymer-Based Nanocomposites: Morphology and Structure Prediction

Predicting morphologies of nanocomposite materials usually requires understanding events occurring on several length scales. The smallest lengthscale (0.1–1 nm) involves interactions between individual atoms. At the next scale (1–10 nm), one considers interactions between repeat units of the polymer matrix and grafted ligands, as well as individual nanoparticles. Finally, at the next level (10–100 nm), one can resolve the large-scale morphology, such as crystalline arrangement of particles, aggregate size, etc. Moving from one level to another involves a process known as coarse-graining, where one can derive interaction potentials between larger-scale "objects" (e.g., repeat units) on the basis of simulations on the smaller scale [24, 115, 116]. While some studies include rigorous coarse-graining, many others concentrate primarily on modeling a specific length scale and undertaking parametric explorations in which the interactions between various objects are characterized by, say, Flory-Huggins interaction parameters. In this section, I start from molecular-level simulations (atomistic Molecular Dynamics) and then proceed to discuss coarse-grained or "mesoscale" models.

2.1 Molecular-Level Simulations

Molecular-level simulations (e.g., Molecular Dynamics, MD) are a necessary first step to investigate the intrinsic properties of the fillers, the polymers, the organic ligands grafted onto the fillers, as well as the properties of both polymers and ligands confined in the spaces between adjacent filler particles. In some instances, MD simulations can be used even to directly predict macroscale properties. Those studies can help elucidate the impact of the surface functionalization of the filler on the thermal conductivity of composites, as well as predict the relationship between the thermal conductivity and the minimum distance between the nanofillers.

For polymer-nanoclay hybrids, atomistic MD simulations were used to compute the intrinsic properties of the clay platelets themselves, as well as the configurations of the grafted organic ligands, and the potential of mean force (PMF) between the clay platelets as function of their separation. In a series of papers, Mazo et al. [106–109] modeled the elastic properties of pure montmorillonite (MMT) clay platelets, as well as hydrated MMT, MMT with grafted poly(ethylene oxide) (PEO) oligomers, and pyrophillite platelets. Heinz et al. used MD simulations to investigate elastic properties of nanoclays, adsorption of various polymers onto the nanoclay surfaces, and the PMF between those organoclays as a function of the ligand chemistry and grafting density [26, 57–59, 167]. Other examples of the use of MD for pure silicate and polymer-silicate materials have been described by Coveney and co-workers in a number of recent papers [22, 145, 146]. They also propose approaches on integrating MD simulations into a multi-scale framework.

2.2 Mesoscale Modeling Approaches

Even as atomistic MD simulations are necessary to capture the details of the short-range interactions between various atoms and molecules present in the system, they can usually address only relatively small ensembles, not enough to predict mesoscale structures. Thus, the majority of nanocomposite simulations today are coarse-grained. Usually in coarse-grained (CG) simulations, several atoms are combined to form a single "bead", and the interactions between the beads are re-parameterized [115, 116]. Polymer chains are then represented as "strings" comprised of such mesoscale or coarse-grained beads. One can then simulate the behavior of such systems directly, using Molecular Dynamics (or, as alternatives, Brownian Dynamics or Dissipative Particle Dynamics) and compute thermodynamic variables for the system as time averages from the simulation runs. Alternatively, one can re-write the thermodynamic partition function of the same system in terms of local densities of individual monomer types and/or correlation functions. The former approach is often termed "particle-based" models, and the second "field-based" models or theories. In nanocomposite literature, there are also "hybrid" models where the fillers are treated as "particles" while the polymers are described by the density "fields" contributing to the forces acting on the particles.

2.2.1 Particle-Based Models

Coarse-grained particle-based models are widely used today in predicting structure and mechanical properties of nanocomposites. Typical strategies for coarse-grained Molecular Dynamics or Monte Carlo simulations in nanocomposites are described by various authors, [2, 164, 168] Some examples are given below.

Nanocomposites with Plate-like Fillers. The most typical examples of plate-like fillers are nanoclays (montmorillonite, bentonite, and others). Thermodynamics of exfoliation and intercalation in mixtures of bare and organically modified clays with polymers have been studied by multiple authors. Vaia and co-workers [3, 141] used coarse-grained Molecular Dynamics (CG-MD) to investigate how the exfoliation and intercalation of organoclays in polymer matrices depended on the structure and grafting density of the grafted surfactants. Farmer and co-workers expanded this work to include factors like added solvent, clay sheet flexibility, and others [56–59, 119, 120]. Scocchi et al. [137–139] developed Dissipative Particle Dynamics (DPD) based approach to study the structure of polymer (such as Nylon 6) layers in the vicinity of the clay particles. All these studies provided important guidance in designing organoclays for improved dispersion and exfoliation.

Nanocomposites with Rod-like Nanofillers. The examples of rod-like nanofillers include carbon nanotubes (single-wall and multi-wall), as well as metal (gold and silver) nanorods with various aspect ratios. The dispersion of nanorods in the polymer depends strongly on the balance between the repulsive and attractive forces, as discussed, e.g., in a recent review [63]. Hore and co-workers used Dissipative Par-

ticle Dynamics (DPD) to determine the aggregation/dispersion phase diagram for a simple case of a brushed nanorod in a matrix chemically identical to its brush [71]. Karatrantos et al. [70] utilized DPD simulations to investigate how the dynamics of polymer changes in the presence of nanorods, showing that the effective density of entanglements can change substantially in the vicinity of the fillers.

Modeling the behavior of nanorods in a block copolymer or polymer blend represents a further challenge. Hore and Laradji [62] used DPD to describe how the nanorods can potentially compatibilize immiscible polymer blends by going to the interfaces and reducing the interfacial tension. Balazs and co-workers [121, 163] developed a hybrid field-particle approach to model the dynamics of A-preferential nanorods in phase-separating AB-binary blends. Given the multidimensional parameter space and the multitude of possible morphologies (typically, non-equilibrium), understanding of these systems will remain an area of interest for polymer science in the near future.

Nanocomposites with Spherical Nanofillers. The literature on polymer-dispersed nanospheres (such as silica or metal nanoparticles) is probably the most immense, going back to classical research on colloid-polymer interactions [4, 5]. For the case of nanocolloids dispersed in the melt, Smith and co-workers performed CG-MD simulations showing that for the case where polymer matrix does not have a preferential attraction to the particle and the particle volume fraction is not too low, depletion attraction causes the nanoparticles to aggregate, the effect depending strongly on the nanoparticle size [142, 143]. Most of the studies confirmed that nanoparticles placed in a polymer melt tend to aggregate, unless there was a preferential attraction between them and the polymer matrix. Interestingly, though, Mackay et al. [96] found that highly-crosslinked PS nanoparticles can be dispersed in a linear PS, provided that the nanoparticle radius was smaller than the matrix polymer radius of gyration, $R_P/R_g < 1$. While this scaling seems reasonable for purely entropic systems (nanoparticles with $R_P/R_g << 1$ represent a relatively small obstacle to the polymer chains and thus the conformational entropy loss by the polymers cannot overcome the translational entropy loss by the particles if one compares dispersed state to the aggregated state; the opposite would be true when $R_P/R_g >> 1$), there is, to my knowledge, no rigorous theory to describe this transition (see Ganesan and Jayaraman [34] and Kumar, Ganesan, and Riggleman [81]). One additional complication could be whether the cross-linked polymer nanoparticle can be considered a "hard" or "bare" sphere, or is it perhaps closer to the case of "hairy" or organically-modified nanoparticles. This is the case we consider next.

Grafting of organic ligands onto the particle surface is widely used to promote the particle dispersion in the matrix. The dispersion of nanoparticles with ligands of length N in a matrix having length P, in the simplest possible scenario, depends on the P/N ratio—if P/N >> 1, the ligands are usually unable to separate the particles and the nanocomposite is in the aggregated state; if, on the other hand, P/N << 1, the steric repulsion overcomes the depletion attraction, and particles become well-dispersed. This picture generally holds for all particle shapes (platelets, rods, or spheres), with only some quantitative changes, [34, 55, 61, 69, 153] in the limit of very large particle curvatures. For nanoscale particles, especially spheres, one expects that the

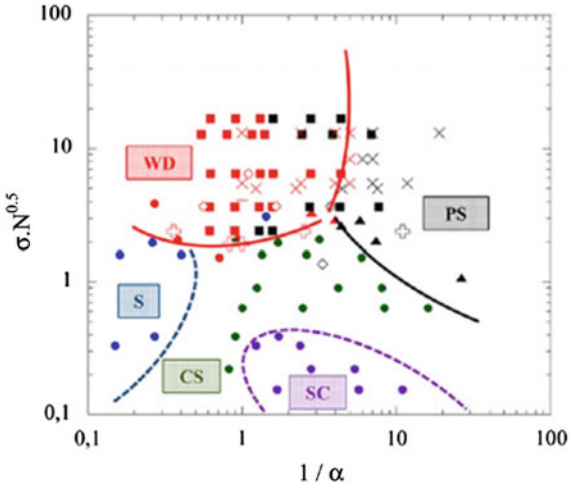

Fig. 3 Phase diagram for "hairy" spherical nanoparticles in polymer matrix. Here, σ is the grafting density, N is the ligand length, P is the matrix length, and α = N/P. Labeling of morphologies: WD—widely dispersed; PS—phase-separated (aggregates); S—strings; CS—connected sheets; SC—small clusters. Various symbols correspond to experimental data from various research groups and studies. Reproduced with permission from [82]. Copyright 2013 American Chemical Society

boundary between aggregation and dispersion shifts towards smaller ligand lengths, all other things being equal [55, 153] Furthermore, dispersion of nanospheres in a polymer melt can be improved by using bidisperse or polydisperse ligands, as shown by Jayaraman and Martin in their Monte Carlo simulations [102, 104].

Intriguingly, Akcora and co-workers [1] demonstrated that grafted nanoparticles in a polymer melt display a variety of morphologies. In addition to the expected aggregated and dispersed states, the authors also found nanoparticle "sheets" and "strings". The morphology was found to be a function of the same P/N ratio, as well as the ligand grafting density (Fig. 3). Kumar and co-workers [16, 51, 82, 125] used experiments and Monte Carlo simulations to elucidate the origins of this behavior. They found that even though the ligand density is isotropic in the limit of a single particle in a polymer matrix, the presence of other particles in the vicinity breaks the symmetry. Thus, it is not appropriate to replace the effect of the ligand shell with a simple pairwise interparticle potential (as is often done in colloidal dispersion analysis). More appropriate is to compare the "hairy" nanoparticles to soft spheres, having hard core and deformable shell; simulations by Glaser et al. [46] showed that such core-shell particles had richer phase behavior than either pure hard spheres or spheres with pairwise interaction potentials. It is now fully accepted and confirmed in multiple experiments that "hairy" nanoparticles in polymer matrices form various anisotropic structures even as the building blocks themselves are perfectly isotropic [113].

One can dispose of the matrix altogether, creating "one-component nanocomposites", also referred to as "nanoparticle organic hybrid materials" (NOHM) [14, 15, 23, 27, 28, 50, 74, 75]. Since these materials are one-component, they—like block copolymers—should generally exhibit microphase separation, not macroscopic aggregation. Changing the ligand characteristics (e.g., using block copolymer ligands or a mixture of ligands of various molecular weights and chemical compositions) could expand the complexity of possible morphologies, while changing the particle nature (metal, semiconductor, or polymeric) could determine for which application the composite would be best suited. Thus, HNPs could become ideal "building blocks" for versatile nanostructure engineering, as envisioned, e.g., by Cheng et al. [144, 165, 166, 169] and Glotzer et al. [19, 47–49, 123, 170]

2.2.2 Field-Based and Theoretical Models

In this section, I describe three methods that have been successfully used to describe thermodynamics and phase behavior of nanocomposites: [1] Integral equation theories and specifically Polymer Reference Interaction Site Model (PRISM); [2] Density Functional Theory (DFT), and [3] Self-Consistent Field Theory (SCFT). In the SCFT sub-section, I will also include the SCF-DFT formalism originally proposed by Thompson, Ginzburg, Matsen, and Balazs [148] for the case of bare spherical nanoparticles in block copolymer melts, and extended [41, 42] to describe the "hairy" nanoparticles. Theoretical approaches also include Strong Segregation Theory (SST), which has been successfully applied to describe the phases of block copolymer/nanoparticle mixtures [66, 124] and single-component hairy nanoparticles [125]. For more details, see recent reviews [33, 34].

Integral Equation Theories. Integral equation theories aim to describe the structure of a complex fluid by computing the interparticle pair correlation function, $g(r)$, and using it to draw conclusions about the short-range ordering (if any); in multicomponent mixtures, the pair correlation functions can be computed between various species present in the system. For simple liquids, this approach goes back to the work of Ornstein and Zernike (OZ) (Ornstein and Zernike [118]. To solve the OZ equations and compute the correlation function, one needs to introduce additional conditions such as closure approximation (usually based on molecular theory, simulations, or experiments). Some of the most well-known closure approximations are Percus-Yevick (PY) [122] and hypernetted chain (HNC) [114, 159].

This approach can be generalized to describe single and multicomponent polymer melts, as discussed, e.g., by Schweizer and Curro [136]. The method developed by Schweizer and Curro—Polymer Reference Interaction Site Model or PRISM [134, 135]—has by now become one of the most widely used in describing the structure of polymers melts, solutions, colloid-polymer dispersions, and nanocomposites. Recently, Jayaraman and co-workers developed the so-called PRISM-MC approach in which the intramolecular contribution to the correlation function is determined based on single-chain Monte Carlo simulations (see [34] for a succinct yet detailed description of this technique); they then applied it to compute the polymer-mediated

potential of mean force (PMF) between organically-modified nanospheres in polymer melt [68, 99–101, 103, 112]. Among interesting findings from those studies was that the ligand polydispersity improves the dispersion of the nanoparticles in the melt, all other things being equal [99, 101, 103].

Density Functional Theory (DFT). One significant drawback of the liquid state theories is that they are, well, ***liquid state*** theories. In many cases, one needs to explore the structure of not just the liquid (disordered) state, but also various crystalline and possibly liquid crystalline states. For example, in the case of hard spheres [53, 130] or Lennard-Jones spheres, [52–54] the fluid is known to organize into face-centered-cubic (FCC) crystalline morphology at high sphere volume fraction due to entropic and/or enthalpic considerations. The liquid-state theory is able to describe the liquid branch of the pressure-density phase diagram but not the solid branch or the coexistence of the two branches; to do this, one needs to use DFT-type approaches.

Classical (fluids) DFT originates from the same Hohenberg-Kohn theorem [60] that gave rise to the quantum DFT, namely that the overall free energy F is a unique functional of the single-particle density, $\rho(\mathbf{r})$ [162]. The free energy functional consists of the ideal-gas contribution, f_{id}, and the excess free energy, f_{ex}. The latter is constructed so that the equation of state for the liquid branch (below the liquid-solid transition) is satisfied, and that the liquid-solid transition itself is also captured correctly. For various ways of constructing f_{ex}, see [126, 131, 147]. For the case of polymeric liquids, one needs to include the influence of intramolecular (bonded) interactions, as well as enthalpic (Flory-Huggins) interactions between different monomer types. Those effects are treated as perturbations, [151, 152, 160, 161] resulting in a complex non-local free energy functional such as iSAFT (interfacial Statistical Associating Fluid Theory) [67, 97]. Frischknecht et al. [110, 111] applied a modified DFT formalism to describe the behavior of polymer-nanoparticle mixture near a hard wall. According to the simulations, the particles stay away from the hard wall at low volume fractions, but prefer to segregate to the wall and form a monolayer there as their volume fraction is increased. Overall, DFT showed excellent promise for describing polymer nanocomposites; I note, however, that so far, most DFT analyses were performed for quasi-one-dimensional systems (most likely, due to computational resource limitations).

Self-Consistent Field Theory (SCFT) and SCFT-DFT Approaches. Polymer SCFT is a widely used approach that is based on the Edwards' description of flexible Gaussian polymer chains with excluded volume, [25] combined with the Flory-Huggins [29, 64] lattice description of non-bonded interactions (for more details, see Fredrickson et al. [30, 32, 39]. Schmid [132, 133] and many other authors). Within SCFT, one minimizes the free energy functional with respect to the monomer densities and conjugate chemical potentials, to obtain self-consistency equations which are then solved iteratively. Those equations could, in principle, have multiple solutions corresponding to various morphologies (disordered, FCC, BCC, lamellar, hexagonal, etc.). It is then possible to calculate free energies of individual structures, and, for each point in parameter space, select the morphology with the lowest free energy. However, in its simplest form, SCFT is not suited to describe nanoparticles or other three-dimensional objects. To use the SCFT mechanism for investigating

nanocomposites, Balazs and co-workers proposed combining it with the DFT-like description of the nanoparticles [18, 85, 89–94, 148, 149, 150, 154]. The SCFT-DFT formalism turned out to be computationally less expensive than a pure DFT approach, and provided good insights into the nanoparticle ordering in bulk block copolymers and in polymer thin films [90, 91]. Another example where SCFT-DFT provided interesting new results was the case of a "tadpole" copolymer where a single A-ligand was grafted onto a B-nanosphere; the calculations of Lee, Balazs, Thompson, and Hill [85] showed the formation of a hexagonal phase. For the case of AB-diblocks, mixed with the A-preferential nanospheres, [148] the distribution of nanoparticles within the A-domains showed a good qualitative agreement with experimental results [13].

The above investigations (except for the "tadpole" study) considered only "bald" nanoparticles. Recently, Ginzburg [41, 42] proposed a modification of the SCFT-DFT approach that allows for explicit accounting for multiple grafting ligands, provided the ligands are "weakly grafted" and thus able to move around the nanoparticle surface. For the case of single-component nanocomposites ("hairy" nanoparticles without matrix polymer), he predicted [42] several soft-crystalline morphologies similar to those of block copolymers (lamellar, hexagonal cylinders, FCC spherical, and "sheets", see Fig. 4). The morphologies are similar to earlier predictions [47, 48, 98, 170] and support potential use of "hairy" or "tethered" nanoparticles as "design materials" able to form various anisotropic structures. The SCFT-DFT formalism is able to account for the main driving force in this anisotropic self-assembly—the re-arrangement of ligands so that the effective interaction between the particles becomes anisotropic and "polarized".

While SCFT-DFT is a fast and straightforward technique, questions remain about some of its major assumptions. The description of nanoparticles using density fields implies that there is some degree of "smearing" and overlap between the particles and polymers, which is not quite physical (same criticism can be applied to the pure DFT approach as well). Increasing the enthalpic incompatibility (large Flory-Huggins parameter) between the particles and all polymer species can help solve this problem, however, this can be at a cost of slowing down the calculation and potentially even causing numerical divergences. More studies are needed to determine the "sweet spot" for both SCFT-DFT and other field-based approaches.

Another SCFT-based field theory of nanocomposites was recently proposed by Riggleman and co-workers [20, 21, 77, 78]. Their model uses a SCFT-like description for the polymers, while for the nanoparticles, they utilize the effective "cavity function" (mathematically describing the shape of the particle), which must be convoluted with the particle center probability to yield the effective particle density. Riggleman's approach allows for a straightforward generalization to the case of non-spherical fillers, as well as fillers in confined geometries, and fillers with various grafting ligands. Recently, Riggleman and co-workers investigated the dispersion of nanorods in thin films, and compared their results with experiments and other theoretical approaches [127].

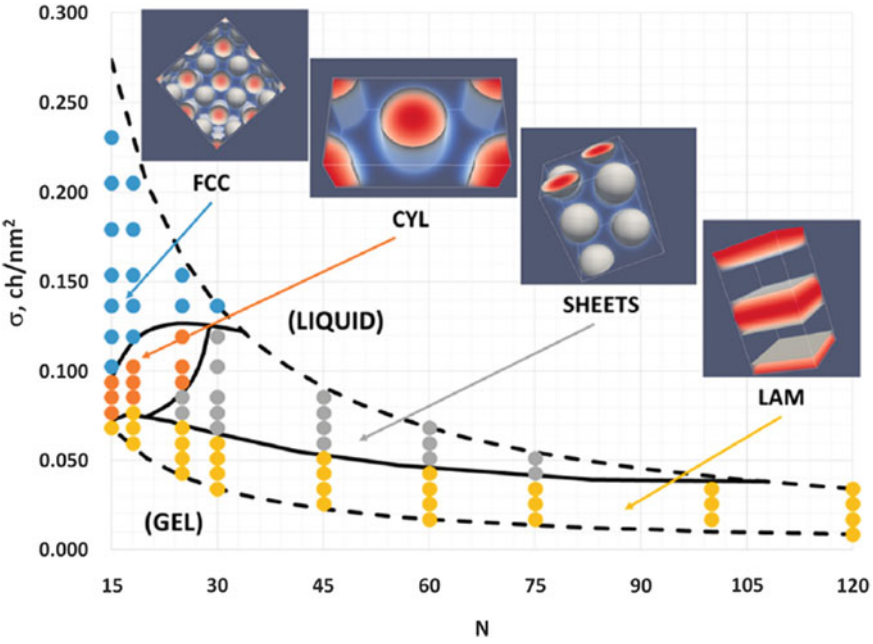

Fig. 4 SCFT-DFT phase map for single-component "hairy nanoparticle" (HNP) melts. Here, N is the ligand length, and σ is the grafting density. Nanoparticle radius R = 3.05 nm. Reproduced with permission from [42]. Copyright 2017 American Chemical Society

2.2.3 Hybrid Models

Finally, we briefly mention the so-called hybrid models where particles and polymers are described in different ways. Usually, in these studies, the polymers are represented using a density field or an order parameter, while the particles are modeled as solid objects, either fixed in place or able to jump from one position to the next. For example, Reister and Fredrickson [128, 129] considered the case of "bare" and "hairy" spherical nanoparticles immersed in a lamella-forming diblock copolymer, and calculated the effective potential of mean force between the particles as function of their separation and positions relative to the block copolymer lamellae. This approach was subsequently expanded by Matsen and co-workers [72, 73, 105]. They developed an elegant multi-coordinate system (MCS) approach to solving SCFT equations in the presence of one or two spherical particles, and, in one example, computed the positional distribution function of Janus nanoparticles in a lamellar diblock copolymer.

Today, probably the most successful hybrid approach is the so-called Hybrid Particle Field (HPF) approach developed by Sides and Fredrickson [140]. Within the HPF approach, the particles are represented as "cavity functions", and the polymer is forced to avoid the particle-occupied space due to the incompressibility constraint.

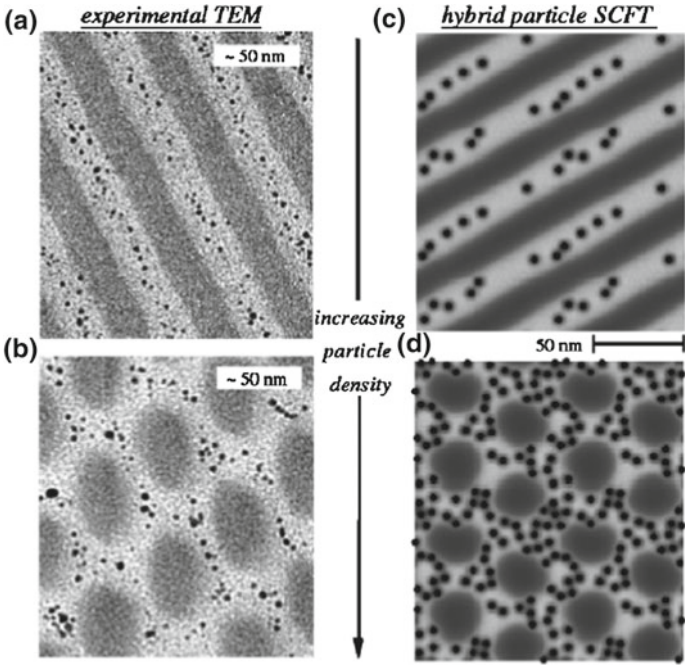

Fig. 5 Experimental TEM images (**a**, **b**) and HPF simulations (**c**, **d**) of nanoparticles in symmetric (f = 0.5) diblock copolymers. The nanoparticles favor one of the blocks. As the nanoparticle volume fraction is increased, the morphology is changed from lamellar to distorted hexagonal, as observed in both experiment and simulation. Reproduced with permission from [140]. Copyright 2006 American Physical Society

This is not dissimilar from the SCF-DFT approach of Balazs et al. [85, 92–94, 148, 149, 150] or from the field theory of Riggleman et al. [20, 77, 78] (which itself was highly influenced by the HPF method). However, unlike in the field theories, within HPF, the coordinates of the particle centers, $\mathbf{r}_i$, are explicitly retained as degrees of freedom. Thus, the free energy is a "mixed" functional of densities (for polymers) and center coordinates (for nanoparticles); the minimization procedure then includes self-consistency equations for the polymeric species and Langevin or Brownian dynamics for the particles. The method was successful in describing the distribution of "bare" nanoparticles in lamellae- and cylinder-forming diblocks, and agreed reasonably well with experimental results (Fig. 5). However, collecting sufficient statistics on the particles requires a very long time, making the HPF approach computationally expensive.

3 Summary and Outlook

Today, polymer-based nanocomposites are widely utilized in a number of technological applications, yet their adoption is not as ubiquitous as was originally hoped. In a recent Perspective in Macromolecules, Kumar, Benicewicz, Vaia, and Winey [80] discussed why nanocomposites have taken foothold in some industries (filler rubber in tire industry; membranes for gas separations; continuous fiber-reinforced thermoset composites; dielectric materials for capacitors and insulation) but not in others. Many of the bottlenecks are related to engineering concerns (filler availability and cost; environmental impact; difficulties in processing, especially for high filler loading; overall need to balance cost and performance of the final material). Others, however, are critically linked to the topics discussed in this paper—how one can control the dispersion of the nanoparticles, and how one can then optimize the dispersion to improve the overall material properties. Certainly, the answer to both of these questions can be often found through theory and modeling.

As discussed above, theory and modeling of polymer nanocomposites is still developing rapidly, and will remain one of the most active fields in applied polymer science for years to come. In a recent Perspective in the Journal of Chemical Physics, Kumar, Ganesan, and Riggleman formulated several specific challenges that nanocomposite theory and modeling will need to tackle in the near future [81]. Those challenges vary from predicting the structure (how does the nanofiller size, the ligand length, architecture, and grafting density impact the nanocomposite morphology) to dynamics (how do the nanofillers influence the melt viscosity and other rheological characteristics) to properties in the solid state. Ultimately, as those individual models are developed, it would be necessary to combine them together in a combined framework. Examples of such multi-scale combinations are still very few and far between, and their development will be one of the most exciting and challenging tasks in the coming years.

Acknowledgements I am greatly indebted to Drs. Robbyn Prange and Cathy Tway for critical reading of this manuscript and many helpful suggestions.

References

1. Akcora, P. et al.: Anisotropic self-assembly of spherical polymer-grafted nanoparticles Nat Mater 8:354–359 (2009)
2. Allegra, G., Raos, G., Vacatello, M.: Theories and simulations of polymer-based nanocomposites: from chain statistics to reinforcement. Prog. Polym. Sci. **33**, 683–731 (2008)
3. Anderson, K.L., Sinsawat, A., Vaia, R.A., Farmer, B.: Control of silicate nanocomposite morphology in binary fluids: Coarse-grained molecular dynamics simulations. J. Polym. Sci., Part B: Polym. Phys. **43**, 1014–1024 (2005)
4. Asakura, S., Oosawa, F.: On interaction between two bodies immersed in a solution of macromolecules. J. Chem. Phys. **22**, 1255–1256 (1954)
5. Asakura, S., Oosawa, F.: Interaction between particles suspended in solutions of macromolecules. J. Polym. Sci., Part A: Polym. Chem. **33**, 183–192 (1958)

6. Balazs, A.C., Bicerano, J., Ginzburg, V.V.: Polyolefin/clay nanocomposites: theory and simulation. In: Polyolefin Composites. Wiley, pp. 415–448 (2007)
7. Balazs, A.C., Ginzburg, V.V., Lyatskaya, Y., Singh, C., Zhulina, E.: Modeling the phase behavior of polymer-clay nanocomposites. In: Pinnavaia, T., Beall, G.W. (eds.) Polymer-Clay Nanocomposites, pp. 281–314. Wiley, New York (2000)
8. Balazs, A.C., Singh, C., Zhulina, E.: Modeling the interactions between polymers and clay surfaces through self-consistent field theory. Macromolecules **31**, 8370–8381 (1998)
9. Balazs, A.C., Singh, C., Zhulina, E., Lyatskaya, Y.: Modeling the phase behavior of polymer/clay nanocomposites. Accounts Chem Res **32**, 651–657 (1999)
10. Baljon, A.R.C., Lee, J.Y., Loring, R.F.: Molecular view of polymer flow into a strongly attractive slit. J Chem Phys **111**, 9068–9072 (1999)
11. Bicerano, J., et al.: Polymer modeling at the Dow Chemical Company. J. Macromol. Sci.-Polymer Rev. **C44**, 53–85 (2004)
12. Bicerano, J., Douglas, J.F., Brune, D.A.: Model for the viscosity of particle dispersions. J. Macromol. Sci. R M C **C39**, 561–642 (1999)
13. Bockstaller, M.R., Lapetnikov, Y., Margel, S., Thomas, E.L.: Size-selective organization of enthalpic compatibilized nanocrystals in ternary block copolymer/particle mixtures. J. Am. Chem. Soc. **125**, 5276–5277 (2003)
14. Bourlinos, A.B., Herrera, R., Chalkias, N., Jiang, D.D., Zhang, Q., Archer, L.A., Giannelis, E.P.: Surface-functionalized nanoparticles with liquid-like behavior. Adv. Mater. **17**, 234–237 (2005)
15. Bourlinos, A.B., Ray Chowdhury, S., Herrera, R., Jiang, D.D., Zhang, Q., Archer, L.A., Giannelis, E.P.: Functionalized nanostructures with liquid-like behavior: expanding the gallery of available nanostructures. Adv. Funct. Mater. **15**, 1285–1290 (2005)
16. Bozorgui, B., Meng, D., Kumar, S.K., Chakravarty, C., Cacciuto, A.: Fluctuation-driven anisotropic assembly in nanoscale systems. Nano Lett. **13**, 2732–2737 (2013)
17. Brune, D.A., Bicerano, J.: Micromechanics of nanocomposites: comparison of tensile and compressive elastic moduli, and prediction of effects of incomplete exfoliation and imperfect alignment on modulus. Polymer **43**, 369–387 (2002)
18. Buxton, G.A., Lee, J.Y., Balazs, A.C.: Computer simulation of morphologies and optical properties of filled diblock copolymers. Macromolecules **36**, 9631–9637 (2003)
19. Chan, E.R., Ho, L.C., Glotzer, S.C.: Computer simulations of block copolymer tethered nanoparticle self-assembly. J. Chem. Phys. **125**, 064905 (2006)
20. Chao, H., Hagberg, B.A., Riggleman, R.A.: The distribution of homogeneously grafted nanoparticles in polymer thin films and blends. Soft Matter **10**, 8083–8094 (2014)
21. Chao, H.K., Lindsay, B.J., Riggleman, R.A.: Field-Theoretic Simulations of the Distribution of Nanorods in Diblock Copolymer Thin Films. J. Phys. Chem. B **121**, 11198–11209 (2017)
22. Chen, B., Evans, J.R., Greenwell, H.C., Boulet, P., Coveney, P.V., Bowden, A.A., Whiting, A.: A critical appraisal of polymer–clay nanocomposites. Chem. Soc. Rev. **37**, 568–594 (2008)
23. Choi, J., Hui, C.M., Schmitt, M., Pietrasik, J., Margel, S., Matyjazsewski, K., Bockstaller, M.R.: Effect of polymer-graft modification on the order formation in particle assembly structures. Langmuir **29**, 6452–6459 (2013)
24. de Pablo, J.J.: Coarse-grained simulations of macromolecules: from DNA to nanocomposites. Annu. Rev. Phys. Chem. **62**, 555–574 (2011)
25. Edwards, S.F.: The statistical mechanics of polymers with excluded volume. Proc. Phys. Soc. **85**, 613 (1965)
26. Feng, J., Heinz, H.: Modification of Inorganic Fillers and Interfacial Properties in Polyolefin Nanocomposites: Theory versus Experiment. In: Advances in Polyolefin Nanocomposites, pp. 205–224. CRC Press (2010)
27. Fernandes, N.J., Koerner, H., Giannelis, E.P., Vaia, R.A.: Hairy nanoparticle assemblies as one-component functional polymer nanocomposites: opportunities and challenges. MRS Commun. **3**, 13–29 (2013)
28. Fernandes, N.J., Wallin, T.J., Vaia, R.A., Koerner, H., Giannelis, E.P.: Nanoscale Ionic Mater. Chem. Mater. **26**, 84–96 (2013)

29. Flory, P.J.: Thermodynamics of high polymer solutions. J. Chem. Phys. **10**, 51–61 (1942)
30. Fredrickson, G.: The Equilibrium Theory of Inhomogeneous Polymers, vol. 134. Oxford University Press on Demand (2006)
31. Fredrickson, G.H., Bicerano, J.: Barrier properties of oriented disk composites. J. Chem. Phys. **110**, 2181–2188 (1999)
32. Fredrickson, G.H., Ganesan, V., Drolet, F.: Field-theoretic computer simulation methods for polymers and complex fluids. Macromolecules **35**, 16–39 (2002)
33. Ganesan, V., Ellison, C.J., Pryamitsyn, V.: Mean-field models of structure and dispersion of polymer-nanoparticle mixtures. Soft. Matter. **6**, 4010–4025 (2010)
34. Ganesan, V., Jayaraman, A.: Theory and simulation studies of effective interactions, phase behavior and morphology in polymer nanocomposites. Soft. Matter. **10**, 13–38 (2014)
35. Gendelman, O.V., Manevitch, L.I., Manevitch, O.L.: Solitonic mechanism of structural transition in polymer-clay nanocomposites. J Chem Phys **119**, 1066–1069 (2003)
36. Giannelis, E.P.: Polymer layered silicate nanocomposites. Adv. Mater. 8:29 (1996)
37. Ginzburg, V., Balazs, A.: Calculating phase diagrams for nanocomposites: the effect of adding end-functionalized chains to polymer/clay mixtures. Adv. Mater. **12**, 1805–1809 (2000)
38. Ginzburg, V., Singh, C., Balazs, A.: Predicting phase diagrams of polymer/clay composites: the role of grafted organic modifiers. Polymeric Mater. Sci. Eng. (USA) 82:217 (2000)
39. Ginzburg, V,, Weinhold, J., Hustad, P., Trefonas, P., Kim, B., Laachi, N., Fredrickson, G.: Field-theoretic simulations and self-consistent field theory for studying block copolymer directed self-assembly. In: Directed Self-assembly of Block Co-polymers for Nano-manufacturing, pp. 67–95. Elsevier (2015)
40. Ginzburg, V.V.: Nanoparticle/Polymer Blends: Theory and Modeling. In: Encyclopedia of Polymer Blends, pp. 233–268. Wiley-VCH Verlag GmbH & Co. KGaA (2010)
41. Ginzburg, V.V.: Polymer-grafted nanoparticles in polymer melts: Modeling using the combined SCFT–DFT approach. Macromolecules **46**, 9798–9805 (2013)
42. Ginzburg, V.V.: Modeling the morphology and phase behavior of one-component polymer-grafted nanoparticle systems. Macromolecules **50**, 9445–9455 (2017)
43. Ginzburg, V.V., Balazs, A.C.: Calculating phase diagrams of polymer – platelet mixtures using density functional theory: implications for polymer/clay composites. Macromolecules **32**, 5681–5688 (1999)
44. Ginzburg, V.V., Gendelman, O.V., Manevitch, L.I.: Simple "kink" model of melt intercalation in polymer-clay nanocomposites. Phys. Rev. Lett. **86**, 5073–5075 (2001)
45. Ginzburg, V.V., Singh, C., Balazs, A.C.: Theoretical phase diagrams of polymer/clay composites: The role of grafted organic modifiers. Macromolecules **33**, 1089–1099 (2000)
46. Glaser, M.A., Grason, G.M., Kamien, R.D., Košmrlj, A., Santangelo, C.D., Ziherl, P.: Soft spheres make more mesophases. EPL (Europhys. Lett.) **78**, 46004 (2007)
47. Glotzer, S.C., Anderson, J.A.: Nanoparticle assembly: made to order. Nat. Mater. **9**, 885–887 (2010)
48. Glotzer, S.C., Horsch, M.A., Iacovella, C.R., Zhang, Z.L., Chan, E.R., Zhang, X.: Self-assembly of anisotropic tethered nanoparticle shape amphiphiles. Curr. Opin. Colloid Interface Sci. **10**, 287–295 (2005)
49. Glotzer, S.C., Solomon, M.J.: Anisotropy of building blocks and their assembly into complex structures. Nat. Mater. **6**, 557–562 (2007)
50. Goel, V., Pietrasik, J., Dong, H.C., Sharma, J., Matyjaszewski, K., Krishnamoorti, R.: Structure of polymer tethered highly grafted nanoparticles. Macromolecules **44**, 8129–8135 (2011)
51. Green, P.F., Oh, H., Akcora, P., Kumar, S.K.: Structure and dynamics of polymer nanocomposites involving chain-grafted spherical nanoparticles. In: Dynamics of Soft Matter, pp 349–366. Springer (2012)
52. Hansen, J.-P.: Phase transition of the Lennard-Jones system II. High-temperature limit. Phys. Rev. A **2**, 221 (1970)
53. Hansen J.-P., McDonald, I.R.: Theory of Simple Liquids. Elsevier (1990)
54. Hansen, J.-P., Verlet, L.: Phase transitions of the Lennard-Jones system. Phys. Rev. **184**, 151 (1969)

55. Harton, S.E., Kumar, S.K.: Mean-field theoretical analysis of brush-coated nanoparticle dispersion in polymer matrices. J. Polym. Sci., Part B: Polym. Phys. **46**, 351–358 (2008)
56. Heinz, H., Patnaik, S.S., Pandey, R.B., Farmer, B.L.: Modeling of Polymer Matrix Nanocomposites. In: Modeling and Simulation in Polymers, pp. 37–92 Wiley (2010)
57. Heinz, H., Vaia, R., Farmer, B.: Interaction energy and surface reconstruction between sheets of layered silicates. J. Chem. Phys. **124**, 224713 (2006)
58. Heinz, H., Vaia, R., Krishnamoorti, R., Farmer, B.: Self-assembly of alkylammonium chains on montmorillonite: effect of chain length, head group structure, and cation exchange capacity. Chem. Mater. **19**, 59–68 (2007)
59. Heinz, H., Vaia, R.A., Farmer, B.L.: Relation between packing density and thermal transitions of alkyl chains on layered silicate and metal surfaces. Langmuir **24**, 3727–3733 (2008)
60. Hohenberg, P., Kohn, W.: Inhomogeneous electron gas. Phys. Rev. **136**, B864 (1964)
61. Hooper, J.B., Schweizer, K.S.: Contact aggregation, bridging, and steric stabilization in dense polymer-particle mixtures. Macromolecules **38**, 8858–8869 (2005)
62. Hore, M.J., Laradji, M.: Prospects of nanorods as an emulsifying agent of immiscible blends. J. Chem. Phys. **128**, 054901 (2008)
63. Hore, M.J.A., Composto, R.J.: Functional polymer nanocomposites enhanced by nanorods. Macromolecules **47**, 875–887 (2014)
64. Huggins ML (1941) Solutions of long chain compounds. J. Chem. Phys. **9**, 440–440 (1941)
65. Huh, J., Balazs, A.C.: Behavior of confined telechelic chains under shear. J. Chem. Phys. **113**, 2025–2031 (2000)
66. Huh, J., Ginzburg, V.V., Balazs, A.C.: Thermodynamic behavior of particle/Diblock copolymer mixtures: simulation and theory. Macromolecules **33**, 8085–8096 (2000)
67. Jain, S., Dominik, A., Chapman, W.G.: Modified interfacial statistical associating fluid theory: a perturbation density functional theory for inhomogeneous complex fluids. J. Chem. Phys. **127**, 244904 (2007)
68. Jayaraman, A.: Polymer grafted nanoparticles: Effect of chemical and physical heterogeneity in polymer grafts on particle assembly and dispersion. J. Polym. Sci., Part B: Polym. Phys. **51**, 524–534 (2013)
69. Jog, P.K., Ginzburg, V.V., Srivastava, R., Weinhold, J.D., Jain, S., Chapman, W.G.: Application of mesoscale field-based models to predict stability of particle dispersions in polymer melts. In: Advances in Chemical Engineering, vol. 39, pp. 131–164. Elsevier (2010)
70. Karatrantos, A., Clarke, N., Kröger, M.: Modeling of polymer structure and conformations in polymer nanocomposites from atomistic to mesoscale: a review. Polym. Rev. **56**, 385–428 (2016)
71. Khani, S., Jamali, S., Boromand, A., Hore, M.J., Maia, J.: Polymer-mediated nanorod self-assembly predicted by dissipative particle dynamics simulations. Soft Mater. **11**, 6881–6892 (2015)
72. Kim, J.U., Matsen, M.W.: Interaction between polymer-grafted particles. Macromolecules **41**, 4435–4443 (2008)
73. Kim, J.U., Matsen, M.W.: Positioning Janus nanoparticles in block copolymer scaffolds. Phys. Rev. Lett. **102**, 078303 (2009)
74. Koerner, H., Drummy, L., Benicewicz, B., Yu, L., Vaia, R.: Nonisotropic Self-Organization of Single-Component Hairy Nanoparticle Assemblies. ACS Macro Lett. **2**, 670–676 (2013)
75. Koerner, H., et al.: Physical aging and glass transition of hairy nanoparticle assemblies. J. Polym. Sci., Part B: Polym. Phys. **54**, 319–330 (2016)
76. Kojima, Y., Usuki, A., Kawasumi, M., Okada, A., Fukushima, Y., Kurauchi, T., Kamigaito, O.: Mechanical-properties of Nylon 6-clay hybrid. J. Mater. Res. **8**, 1185–1189 (1993)
77. Koski, J., Chao, H., Riggleman, R.A.: Predicting the structure and interfacial activity of diblock brush, mixed brush, and Janus-grafted nanoparticles. Chem. Commun. **51**, 5440–5443 (2015)
78. Koski, J., Chao, H., Riggleman, R.A.: Field theoretic simulations of polymer nanocomposites J. Chem. Phys. 139, 244911 (2013)

79. Krishnamoorti, R., Vaia, R.A., Giannelis, E.P.: Structure and dynamics of polymer-layered silicate nanocomposites. Chem. Mater. **8**, 1728–1734 (1996)
80. Kumar, S.K., Benicewicz, B.C., Vaia, R.A., Winey, K.I.: 50th anniversary perspective: are polymer nanocomposites practical for applications? Macromolecules **50**, 714–731 (2017)
81. Kumar, S.K., Ganesan, V., Riggleman, R.A.: Perspective: outstanding theoretical questions in polymer-nanoparticle hybrids. J. Chem. Phys. **147**, 020901 (2017)
82. Kumar, S.K., Jouault, N., Benicewicz, B., Neely, T.: Nanocomposites with polymer grafted nanoparticles. Macromolecules **46**, 3199–3214 (2013)
83. Kuznetsov, D.V., Balazs, A.C.: Phase behavior of end-functionalized polymers confined between two surfaces. J. Chem. Phys. **113**, 2479–2483 (2000)
84. Kuznetsov, D.V., Balazs, A.C.: Scaling theory for end-functionalized polymers confined between two surfaces: Predictions for fabricating polymer/clay nanocomposites. J. Chem. Phys. **112**, 4365–4375 (2000)
85. Lee, J.Y., Balazs, A.C., Thompson, R.B., Hill, R.M.: Self-assembly of amphiphilic nanoparticle-coil "tadpole" macromolecules. Macromolecules **37**, 3536–3539 (2004)
86. Lee, J.Y., Baljon, A.R.C., Loring, R.F.: Spontaneous swelling of layered nanostructures by a polymer melt. J. Chem. Phys. **111**, 9754–9760 (1999)
87. Lee, J.Y., Baljon, A.R.C., Loring, R.F., Panagiotopoulos, A.Z.: Simulation of polymer melt intercalation in layered nanocomposites. J. Chem. Phys. **109**, 10321–10330 (1998)
88. Lee, J.Y., Baljon, A.R.C., Sogah, D.Y., Loring, R.F.: Molecular dynamics study of the intercalation of diblock copolymers into layered silicates. J. Chem. Phys. **112**, 9112–9119 (2000)
89. Lee, J.Y., Buxton, G.A., Balazs, A.C.: Using nanoparticles to create self-healing composites. J. Chem. Phys. **121**, 5531–5540 (2004)
90. Lee, J.Y., Shou, Z., Balazs, A.C.: Modeling the self-assembly of copolymer-nanoparticle mixtures confined between solid surfaces. Phys. Rev. Lett. **91**, 136103 (2003)
91. Lee, J.Y., Shou, Z.Y., Balazs, A.C.: Predicting the morphologies of confined copolymer/nanoparticle mixtures. Macromolecules **36**, 7730–7739 (2003)
92. Lee, J.Y., Thompson, R.B., Jasnow, D., Balazs, A.C.: Effect of nanoscopic particles on the mesophase structure of diblock copolymers. Macromolecules **35**, 4855–4858 (2002)
93. Lee, J.Y., Thompson, R.B., Jasnow, D., Balazs, A.C.: Entropically driven formation of hierarchically ordered nanocomposites. Phys. Rev. Lett. **89**, 155503 (2003)
94. Lee, J.Y., Thompson, R.B., Jasnow, D., Balazs, A.C.: Self-assembly of a binary mixture of particles and diblock copolymers. Faraday Discuss. **123**, 121–131 (2003)
95. Lyatskaya, Y., Balazs, A.C.: Modeling the phase behavior of polymer-clay composites. Macromolecules **31**, 6676–6680 (1998)
96. Mackay, M.E., et al.: General strategies for nanoparticle dispersion. Science **311**, 1740–1743 (2006)
97. Marshall, B.D., Chapman, W.G.: Thermodynamic perturbation theory for associating molecules. Adv. Chem. Phys. **160**, 1 (2016)
98. Marson, R.L., Nguyen, T.D., Glotzer, S.C.: Rational design of nanomaterials from assembly and reconfigurability of polymer-tethered nanoparticles. MRS Commun. **5**, 397–406 (2015)
99. Martin, T.B., Dodd, P.M., Jayaraman, A.: Polydispersity for tuning the potential of mean force between polymer grafted nanoparticles in a polymer matrix. Phys. Rev. Lett. **110**, 018301 (2013)
100. Martin, T.B., Jayaraman, A.: Identifying the ideal characteristics of the grafted polymer chain length distribution for maximizing dispersion of polymer grafted nanoparticles in a polymer matrix. Macromolecules **46**, 9144–9150 (2013)
101. Martin, T.B., Jayaraman, A.: Polydisperse homopolymer grafts stabilize dispersions of nanoparticles in a chemically identical homopolymer matrix: an integrated theory and simulation study. Soft Matter **9**, 6876–6889 (2013)
102. Martin, T.B., Jayaraman, A.: Effect of matrix bidispersity on the morphology of polymer-grafted nanoparticle-filled polymer nanocomposites. J. Polym. Sci. Pol. Phys. **52**, 1661–1668 (2014)

103. Martin, T.B., Jayaraman, A.: Effect of matrix bidispersity on the morphology of polymer-grafted nanoparticle-filled polymer nanocomposites. J. Polym. Sci., Part B: Polym. Phys. **52**, 1661–1668 (2014)
104. Martin, T.B., Jayaraman, A.: Using Theory and Simulations To Calculate Effective Interactions in Polymer Nanocomposites with Polymer-Grafted Nanoparticles. Macromolecules **49**, 9684–9692 (2016)
105. Matsen, M., Thompson, R.: Particle distributions in a block copolymer nanocomposite. Macromolecules **41**, 1853–1860 (2008)
106. Mazo, M., Manevitch, L., Balabaev, N., Berlin, A., Gusarova, E., Rutledge, G.: temperature dependence of elastic properties of a pyrophyllite plate by molecular dynamics simulation. J. Phys. Chem. B **112**, 2964–2969 (2008)
107. Mazo, M.A., Manevitch, L.I., Gusarova, E.B., Berlin, A.A., Balabaev, N.K., Rutledge, G.C.: Molecular dynamics simulation of thermomechanical properties of montmorillonite crystal. II Hydrated montmorillonite crystal. J. Phys. Chem. C **112**, 17056–17062 (2008)
108. Mazo, M.A., Manevitch, L.I., Gusarova, E.B., Shamaev, M.Y., Berlin, A.A., Balabaev, N.K., Rutledge, G.C.: Molecular dynamics simulation of thermomechanical properties of montmorillonite crystal. 1 Isolated clay nanoplate. J. Phys. Chem. B **112**, 2964–2969 (2008)
109. Mazo, M.A., Manevitch, L.I., Gusarova, E.B., Shamaev, M.Y., Berlin, A.A., Balabaev, N.K., Rutledge, G.C.: Molecular dynamics simulation of thermomechanical properties of Montmorillonite crystal. 3 Montmorillonite crystals with PEO oligomer intercalates. J. Phys. Chem. B **112**, 3597–3604 (2008)
110. McGarrity, E., Frischknecht, A., Frink, L., Mackay, M.: Surface-induced first-order transition in athermal polymer-nanoparticle blends. Phys. Rev. Lett. **99**, 238302 (2007)
111. McGarrity, E., Frischknecht, A., Mackay, M.: Phase behavior of polymer/nanoparticle blends near a substrate. J. Chem. Phys. **128**, 154904 (2008)
112. Modica, K.J., Martin, T.B., Jayaraman, A.: Effect of polymer architecture on the structure and interactions of polymer grafted particles: theory and simulations. Macromolecules **50**, 4854–4866 (2017)
113. Moffitt, M.G.: Self-assembly of polymer brush-functionalized inorganic nanoparticles: from hairy balls to smart molecular mimics. J. Phys. Chem. Lett. **4**, 3654–3666 (2013)
114. Morita, T.: Theory of Classical Fluids: Hyper-Netted Chain Approximation, Formulation for a One-Component System. Progr. Theoret. Phys. **20**, 920–938 (1958)
115. Müller-Plathe, F.: Coarse-graining in polymer simulation: from the atomistic to the mesoscopic scale and back. ChemPhysChem **3**, 754–769 (2002)
116. Nielsen, S.O., Lopez, C.F., Srinivas, G., Klein, M.L.: Coarse grain models and the computer simulation of soft materials. J. Phys.: Condens. Matter **16**, R481 (2004)
117. Okada, A., Usuki, A., Kurauchi, T., Kamigaito, O.: Polymer-Clay hybrids. ACS Sym. Ser. **585**, 55–65 (1995)
118. Ornstein, L.S., Zernike, F.: Integral equation in liquid state theory. In: Proc. Acad. Sci. Amsterdam, p. 793 (1914)
119. Pandey, R.B., Anderson, K., Farmer, B.: Exfoliation of stacked sheets: effects of temperature, platelet size, and quality of solvent by a Monte Carlo simulation. J. Polym. Sci., Part B: Polym. Phys. **44**, 3580–3589 (2006)
120. Pandey, R.B., Farmer, B.: Exfoliation of a stack of platelets and intercalation of polymer chains: effects of molecular weight, entanglement, and interaction with the polymer matrix. J. Polym. Sci., Part B: Polym. Phys. **46**, 2696–2710 (2008)
121. Peng, G., Qiu, F., Ginzburg, V.V., Jasnow, D., Balazs, A.C.: Forming supramolecular networks from nanoscale rods in binary phase-separating mixtures. Science **288**, 1802–1804 (2000)
122. Percus, J.K., Yevick, G.J.: Analysis of classical statistical mechanics by means of collective coordinates. Phys. Rev. **110**, 1 (1958)
123. Phillips, C.L., Iacovella, C.R., Glotzer, S.C.: Stability of the double gyroid phase to nanoparticle polydispersity in polymer-tethered nanosphere systems. Soft Mater. **6**, 1693–1703 (2010)
124. Pryamitsyn, V., Ganesan, V.: Strong segregation theory of block copolymer-nanoparticle composites. Macromolecules **39**, 8499–8510 (2006)

125. Pryamtisyn, V., Ganesan, V., Panagiotopoulos, A.Z., Liu, H., Kumar, S.K.: Modeling the anisotropic self-assembly of spherical polymer-grafted nanoparticles. J. Chem. Phys. **131**, 221102 (2009)
126. Ramakrishnan, T., Yussouff, M.: First-principles order-parameter theory of freezing. Phys. Rev. B **19**, 2775 (1979)
127. Rasin, B., Chao, H.K., Jiang, G.Q., Wang, D.L., Riggleman, R.A., Composto, R.J.: Dispersion and alignment of nanorods in cylindrical block copolymer thin films. Soft Matter. **12**, 2177–2185 (2016)
128. Reister, E., Fredrickson, G.H.: Nanoparticles in a diblock copolymer background: The potential of mean force. Macromolecules **37**, 4718–4730 (2004)
129. Reister, E., Fredrickson, G.H.: Phase behavior of a blend of polymer-tethered nanoparticles with diblock copolymers. J. Chem. Phys. **123**, 214903 (2005)
130. Rintoul, M., Torquato, S.: Metastability and crystallization in hard-sphere systems. Phys. Rev. Lett. **77**, 4198 (1996)
131. Rosenfeld, Y., Tarazona, P.: Density functional theory and the asymptotic high density expansion of the free energy of classical solids and fluids. Mol. Phys. **95**, 141–150 (1998)
132. Schmid, F.: Self-consistent-field theories for complex fluids. J Phys-Condens Mat **10**, 8105–8138 (1998)
133. Schmid, F., Muller, M.: Quantitative comparison of self-consistent-field theories for polymers near interfaces with Monte-Carlo simulations. Macromolecules **28**, 8639–8645 (1995)
134. Schweizer, K., Curro, J.: PRISM theory of the structure, thermodynamics, and phase transitions of polymer liquids and alloys. In: Atomistic Modeling of Physical Properties, pp 319–377. Springer (1994)
135. Schweizer, K.S., Curro, J.G.: Integral-equation theory of the structure of polymer melts. Phys. Rev. Lett. **58**, 246 (1987)
136. Schweizer, K.S., Curro, J.G.: Integral equation theories of the structure, thermodynamics, and phase transitions of polymer fluids. Adv. Chem. Phys. **98**:1–142 (1997)
137. Scocchi, G., Posocco, P., Danani, A., Pricl, S., Fermeglia, M.: To the nanoscale, and beyond!: multiscale molecular modeling of polymer-clay nanocomposites. Fluid Phase Equilib. **261**, 366–374 (2007)
138. Scocchi, G., Posocco, P., Fermeglia, M., Pricl, S.: Polymer − clay nanocomposites: a multiscale molecular modeling approach. J. Phys. Chem. B **111**, 2143–2151 (2007)
139. Scocchi, G., Posocco, P., Handgraaf, J.W., Fraaije, J.G., Fermeglia, M., Pricl, S.: A complete multiscale modelling approach for polymer–clay nanocomposites Chemistry-A. Eur. J. **15**, 7586–7592 (2009)
140. Sides, S.W., Kim, B.J., Kramer, E.J., Fredrickson, G.H.: Hybrid particle-field simulations of polymer nanocomposites. Phys. Rev. Lett. **96**, 250601 (2006)
141. Sinsawat, A., Anderson, K.L., Vaia, R.A., Farmer, B.: Influence of polymer matrix composition and architecture on polymer nanocomposite formation: Coarse-grained molecular dynamics simulation. J. Polym. Sci., Part B: Polym. Phys. **41**, 3272–3284 (2003)
142. Smith, G.D., Bedrov, D.: Dispersing nanoparticles in a polymer matrix: are long, dense polymer tethers really necessary? Langmuir **25**, 11239–11243 (2009)
143. Smith, J.S., Bedrov, D., Smith, G.D.: A molecular dynamics simulation study of nanoparticle interactions in a model polymer-nanoparticle composite. Composites Science and Technology **63**, 1599–1605 (2003)
144. Su, H., et al.: Sequential Triple "Click" approach toward polyhedral oligomeric silsesquioxane-based multiheaded and multitailed giant surfactants. ACS Macro Letters **2**, 645–650 (2013)
145. Suter, J.L., Coveney, P.V.: Computer simulation study of the materials properties of intercalated and exfoliated poly (ethylene) glycol clay nanocomposites. Soft Matter. **5**, 2239–2251 (2009)
146. Suter, J.L., Groen, D., Coveney, P.V.: Mechanism of exfoliation and prediction of materials properties of clay-polymer nanocomposites from multiscale modeling. Nano Lett. **15**, 8108–8113 (2015)

147. Tarazona, P.: Free-energy density functional for hard spheres. Phys. Rev. A **31**, 2672 (1985)
148. Thompson, R.B., Ginzburg, V.V., Matsen, M.W., Balazs, A.C.: Predicting the mesophases of copolymer-nanoparticle composites. Science **292**, 2469–2472 (2001)
149. Thompson, R.B., Ginzburg, V.V., Matsen, M.W., Balazs, A.C.: Block copolymer-directed assembly of nanoparticles: Forming mesoscopically ordered hybrid materials. Macromolecules **35**, 1060–1071 (2002)
150. Thompson, R.B., Lee, J.Y., Jasnow, D., Balazs, A.C.: Binary hard sphere mixtures in block copolymer melts Phys. Rev. E **66**, 031801 (2002)
151. Tripathi, S., Chapman, W.G.: Microstructure and thermodynamics of inhomogeneous polymer blends and solutions. Phys. Rev. Lett. **94**, 087801 (2005)
152. Tripathi, S., Chapman, W.G.: Microstructure of inhomogeneous polyatomic mixtures from a density functional formalism for atomic mixtures. J. Chem. Phys. **122**, 094506 (2005)
153. Trombly, D.M., Ganesan, V.: Curvature effects upon interactions of polymer-grafted nanoparticles in chemically identical polymer matrices. J. Chem. Phys. **133**, 154904 (2010)
154. Tyagi, S., Lee, J.Y., Buxton, G.A., Balazs, A.C.: Using nanocomposite coatings to heal surface defects. Macromolecules **37**, 9160–9168 (2004)
155. Vaia, R.A., Giannelis, E.P.: Lattice model of polymer melt intercalation in organically-modified layered silicates. Macromolecules **30**, 7990–7999 (1997)
156. Vaia, R.A., Giannelis, E.P.: Polymer melt intercalation in organically-modified layered silicates: Model predictions and experiment. Macromolecules **30**, 8000–8009 (1997)
157. Vaia, R.A., Jandt, K.D., Kramer, E.J., Giannelis, E.P.: Microstructural evolution of melt intercalated polymer-organically modified layered silicates nanocomposites. Chem. Mater. **8**, 2628–2635 (1996)
158. Vaia, R.A., Teukolsky, R.K., Giannelis, E.P.: Interlayer structure and molecular environment of alkylammonium layered silicates. Chem. Mater. **6**, 1017–1022 (1994)
159. van Leeuwen, J.M.J., Groeneveld, J., de Boer, J.: New method for the calculation of the pair correlation function. Physica **25**, 792–808 (1959)
160. Wertheim, M.: Fluids with highly directional attractive forces. I. Statistical thermodynamics. J. Stat. Phys. **35**, 19–34 (1984)
161. Wertheim, M.: Fluids with highly directional attractive forces. II. Thermodynamic perturbation theory and integral equations. J. Stat. Phys. **35**, 35–47 (1984)
162. Wu, J.: Density functional theory for chemical engineering: From capillarity to soft materials. AIChE J. **52**, 1169–1193 (2006)
163. Yan, L.-T., Maresov, E., Buxton, G.A., Balazs, A.C.: Self-assembly of mixtures of nanorods in binary, phase-separating blends. Soft Matter **7**, 595–607 (2011)
164. Yan, L.-T., Xie, X.-M.: Computational modeling and simulation of nanoparticle self-assembly in polymeric systems: Structures, properties and external field effects. Prog. Polym. Sci. **38**, 369–405 (2013)
165. Yu, X., et al.: Giant surfactants provide a versatile platform for sub-10-nm nanostructure engineering. Proc. Natl. Acad. Sci. **110**, 10078–10083 (2013)
166. Yue, K., et al.: Sequential "click" approach to polyhedral oligomeric silsesquioxane-based shape amphiphiles. Macromolecules **45**, 8126–8134 (2012)
167. Zartman, G.D., Liu, H., Akdim, B., Pachter, R., Heinz, H.: Nanoscale tensile shear, and failure properties of layered silicates as a function of cation density and stress. J. Phys. Chem. C **114**, 1763–1772 (2010)
168. Zeng, Q., Yu, A., Lu, G.: Multiscale modeling and simulation of polymer nanocomposites. Prog. Polym. Sci. **33**, 191–269 (2008)
169. Zhang, W.-B., et al.: Molecular nanoparticles are unique elements for macromolecular science: From "nanoatoms" to giant molecules. Macromolecules **47**, 1221–1239 (2014)
170. Zhang, Z.L., Horsch, M.A., Lamm, M.H., Glotzer, S.C.: Tethered nano building blocks: Toward a conceptual framework for nanoparticle self-assembly. Nano Lett. **3**, 1341–1346 (2003)

B↔A Transition in a Short DNA Molecule

Natalya A. Kovaleva and Elena A. Zubova

Abstract In the framework of the 'sugar' coarse-grained DNA model [N.A. Kovaleva, I.P. Koroleva (Kikot), M.A. Mazo, Journal of Molecular Modeling 23(2):66 (2017), https://doi.org/10.1007/s00894-017-3209-z], we study the transition between B and A forms of a short DNA molecule (12 base pairs) when the concentration of salt changes. The model exploits the explicit ions and implicit water representation and allows to separately change the friction of the ions and of the DNA molecule. We compare the behavior of the system for different values of friction which proved to not affect the order of the transition, but allowed to determine the roles of the DNA and the ions in the behavior of the conglomerate. We find the order (the first) and the point of the transition (0.316 M) in the case of 'inviscid' water (zero friction for both the ions and the DNA, the NVE ensemble). The helix consisting of 12 bp (more than thousand atoms) proved to exhibit the features of small systems. Namely, even at low salt concentrations, one can observe the jumps from B-DNA to A-DNA and back. We analyse the structure of the A-DNA and find the reasons for such a behavior.

1 Introduction

DNA is being actively studied experimentally and theoretically because of its extraordinary biological role. The basic objects of theoretical interest are (in addition to the principles of protein-DNA recognition) protein binding to DNA, transcription, and replication. In these processes, both chains of the DNA double helix are strongly distorted, including the changes in the conformation of the ribose rings. Their conformational mobility is one of the main sources of flexibility of the double helix. The

N. A. Kovaleva (✉) · E. A. Zubova
N. N. Semenov Institute of Chemical Physics, Kosygina St. 4, Moscow, Russia
e-mail: natykov@gmail.com

E. A. Zubova
e-mail: zubova@chph.ras.ru

I. V. Andrianov et al. (eds.), *Problems of Nonlinear Mechanics and Physics of Materials*, Advanced Structured Materials 94,
https://doi.org/10.1007/978-3-319-92234-8_13

change in the conformation of sugars from C2'-endo (C1'-exo) to C3'-endo causes the transition from one geometric form of the double helix (B) to the other (A).

A local transition to A-DNA often occurs in physiological saline, and is also observed when DNA interacts with minor groove binding proteins (TBP, SRY, LEF-1, PurR). The necessary local increase in the minor groove width is achieved through the switching of several ribose rings to the A-DNA conformation [1]. In DNA–protein complexes, many other biologically determined local transitions from B- to A-DNA have been found [2]. In particular, this transition is observed when DNA binds to enzymes which interact with the atoms located inside the molecule in the B form. In addition, there is evidence of the possible role of local transitions to the A form during replication [3]. It is believed that such transitions are caused by the effect on DNA of partial charges on the surface of proteins. DNA can also adopt the A-form conformation when the properties of the solution or the number or type of ions around the molecule change, for example, when ethanol is added to the water and the salt concentration (NaCl) is increased [4, 5].

An adequate theoretical (molecular dynamics) study of the B-A conformational transition is difficult for two reasons. The first reason is the well-known imbalance of the AMBER and CHARMM all-atom force fields usually used for DNA modeling. The AMBER force field is "B-philic", while the CHARMM force field is "A-philic" [6, 7]. Correction of the dihedral angle potentials in the CHARMM force field in 2012 [8] led [9] to some improvement in the modeling by this field of the A to B transition problematic for this field. Appropriate changes have also been made to the AMBER force field [10]. As a result, the minima of the potential of mean force at the pseudo-rotational angle corresponding to the A-form decreased. The new AMBER force field parmbsc1 has not yet been tested for the B to A transition.

The second reason for the difficulties in studying the A-B transitions is their duration (a few nanoseconds together with the waiting time). With such times, it is difficult to collect the necessary statistics within the framework of an all-atom model, especially with explicit water. We first proposed [11, 12] a coarse-grained DNA model capable of reproducing both forms under appropriate conditions - B-DNA at low and A-DNA at high NaCl concentration - and both the transitions between them. In this model, both the ions in solution and the charges on the DNA surface (negative on phosphates and partial positive and negative on bases) are explicitly included. Their solvation is taken into account by the form of interaction potentials between them, which ensures the adequacy of the representation of the balance of interactions in the complex of the DNA molecule with the neighboring ions. Both for the DNA beads and for the ions, a Langevin thermostat is used, which also introduces friction against water molecules. Unlike all-atom models, our model allows for the variation of water viscosity. When the thermostat is switched off (NVE ensemble), the effective friction is zero, both for the DNA beads and for the ions. This provides a unique opportunity to investigate the behavior of DNA in both the cases of experimental water viscosity and under "ideal" conditions, when the dynamics of the molecule is dominated by its inertial properties. The proposed CG DNA model allows the full investigation of the transition between A and B forms of the DNA, both the structure

of the DNA-ions conglomerate and collecting the statistics needed for the analysis of the order of the transition.

The article is organized as follows. In the second chapter, we shortly describe the sugar CG DNA model. The formulas and the constants of the force field are listed in the Appendix. In the third chapter, we investigate the influence of the friction on the character of the A-B transition, and determine the order and the point (the salt concentration) of the transition. More detailed analysis of the structure of the system is carried out in the fourth chapter.

2 Description of the Sugar CG DNA Model

We use the 'sugar' CG model proposed in [11]. The way of combining the atoms into grains is shown in Fig. 1. Every one of the two DNA strands is modeled by a zigzag of alternating grains P and C3': ...-P-C3'-P-C3'-... (see Fig. 2). These grains are connected by CG bonds. A grain C1' is linked to each C3' grain by another CG bond. This "comb" is a skeleton of the strand. The grain C1'and grains on the base B1, B2, B3 are connected by very rigid CG bonds C1'-B1, C1'-B3, B1-B2, B2-B3, B2-B3. We keep grains C1', B1, B2 and B3 in one plane by means of rigid dihedral angle C1'-B1-B3-B2. The three rigidly bound grains (B1, B2, B3) almost freely rotate around glycosidic bond C1'-N(1,9) (position of atom N(1,9) is calculated on each step from coordinates of grains B1, B2, B3).

To maintain the shape of the helix ...-P-C3'-P-C3'-..., we introduce, besides the CG bonds, the CG angle C3'-P-C3' and two dihedral angles C3'-P-C3'-P and P-C3'-P-C3'. The position of the glycosidic bond C1'-N(1,9) relative to the "skeleton" helix is supported by two CG angles P-C1'-N(1,9) and C3'-C1'-N(1,9). Another dihedral angle C1'-C3'-P-C3' provides base pair opening.

Ribose flexibility is modeled by the deformation of the pyramid {P(1)P(2)C1'C3'}. The possibility of sugar repuckering is provided by a double-well potential for the CG bond C1'-P. The length of the edge P(1)-P(2) correlates with length of the double-well bond:

$$U = \frac{1}{2} k_P (|P(1)P(2)| + t_P \left|C1'P(2)\right| - l_{P0})^2, \tag{1}$$

where $t_P > 0$. The grains P(1) and C1' are connected by a soft CG bond.

The model system consist of a DNA double helix and explicit sodium and chlorine ions. The potential energy of the system includes ten distinct contributions:

$$\begin{aligned} H = \; & E_{base} + E_{hydr-bonds} + E_{stacking} + \\ & + E_{val-bonds} + E_{val-angles} + E_{tors-angles} + \\ & + E_{el} + E_{vdW} + E_{ion-DNA} + E_{ion-ion} \end{aligned} \tag{2}$$

Potential functions and the used parameters are collected in Table 1 in Appendix. The term E_{base} describes the energy of deformation of rigid bases. The terms $E_{hydr-bonds}$

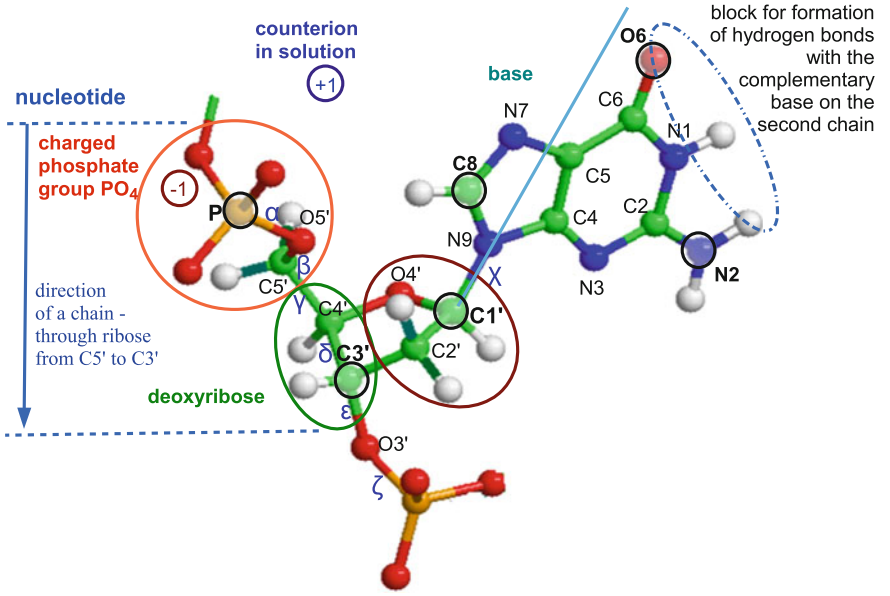

Fig. 1 Coarse-graining of nucleotide backbone in a DNA strand. We show locations of grains in the sugar CG DNA model and (for the backbone) - groups of atoms united into the grains. A nucleobase rotates about the glycosidic bond χ

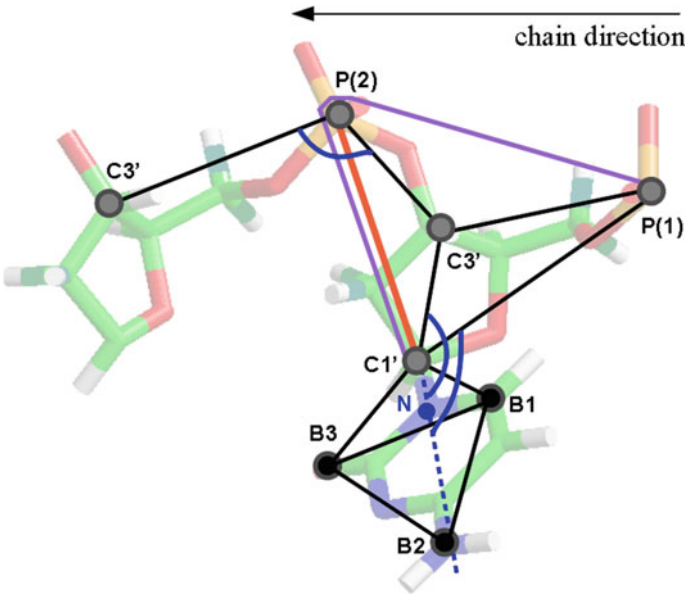

Fig. 2 CG bonds and angles of the sugar CG model. The double-well bond C1'-P(2) models ribose flexibility, the length |P(1)P(2)| correlates with the length |C1'P(2)| (potential (1) is symbolically depicted as the polyline P(1)-P(2)-C1')

Table 1 A summary of potential functions and parameters of the sugar CG DNA model. The order of grains in the notation of bonds and angles is their order along the chain direction (see Fig. 2). The letter N stands for atom $N1$ (or $N9$), and C - for atom $C6$ (or $C8$) on bases

Interaction	**Potential**	**Constants**		
	CG bonds	r_0 , Å	k_r, kcal/(mol ·Å^2)	
P-C3'		4.52	35	
C3'-C1'	$\frac{1}{2}k_r(r-r_0)^2$	2.4	192	
C3'-P		2.645	201	
P-C1'		5.4	28	
double-well CG bond (imitating ribose flexibility)		parameter	value	dimension
		r_A	4.8	Å
	$U(r) =$	r_B	4.2	Å
	$= U_B(r-r_B)f(r)+$	r_C	4.584	Å
C1'-P	$+[U_A(r-r_A)+\epsilon_0][1-f(r)]+$	ϵ_0	0	kcal/mol
	$+\epsilon_{barrier}e^{-\mu_0(r-r_C)^2}$	$\epsilon_{barrier}$	-0.46	kcal/mol
	$U_j(r) =$	K_A	63	kcal/(mol · Å^2)
	$= \frac{1}{2}K_j r^2$, $j = A, B$	K_B	25	kcal/(mol · Å^2)
	$f(r) = \frac{1}{1+e^{2\mu(r-r_C)}}$	μ	20	Å^{-1}
		μ_0	300	Å^{-1}
CG bond correlated with ribose conformation		parameter	value	dimension
	$U(r_{C1'P}, r_{P(1)P(2)}) =$	k_P	39	kcal/mol
P(1)-P(2)	$\frac{1}{2}k_P(r_{P(1)P(2)}$	l_{P0}	12.235	Å
	$+t_P r_{C1'P} - l_{P0})^2$	t_P	1.27	
	CG angles	θ_0, deg	k_θ, kcal/(mol · deg^2)	
C3'-P-C3'		110	0.017	
P-C1'-N	$k_\theta(\theta-\theta_0)^2$	84	0.026	
C3'-C1'-N		112	0.032	
	"torsion" angles	δ_0, deg	ϵ_δ, kcal/mol	comment
C3'-P-C3'-P		188	4.6	long P-C3' bond
P-C3'-P-C3'	$\epsilon_\delta(1-\cos(\delta-\delta_0))$	194	4.6	short C3'-P bond
C1'-C3'-P-C3'		13	3.0	base-pair opening
C3'-C1'-N-C		-32	0.03	glycosidic bond
	interactions in rigid bases			
bonds	$\frac{1}{2}k_r(r-r_0)^2$	see formula (B4)		
torsion angle	$\epsilon(1+\cos\delta)$	and table III in [13]		
hydrogen bonds and stacking interactions		from AMBER		
electrostatic interactions between phosphate grains		parameter	value	dimension
		ε_0	58	
$P-P$	$\frac{q_i q_j}{4\pi\varepsilon_0\varepsilon(r)r_{ij}}$	ε_1	22	
	$\varepsilon(r) = \varepsilon_0+$	α	12	Å^{-1}
	$+\varepsilon_1\tanh[\exp\left(\frac{\alpha}{2}(r-r_0)\right)]$	r_0	8.5	Å
van der Waals interactions between skeleton grains		σ_i, Å	ϵ_i , kcal/mol	
P	$4\epsilon_{ij}\left[\left(\frac{\sigma_{ij}}{r}\right)^{12}-\left(\frac{\sigma_{ij}}{r}\right)^{6}\right]$	2.18	0.23	
$C3'$	$\sigma_{ij} = (\sigma_i+\sigma_j)/2$, $\epsilon_{ij} = \sqrt{\epsilon_i\epsilon_j}$	2.0	0.115	
interaction of Na^+ and Cl^- ions with charged grains of DNA and one with another				
$\frac{A}{r_{ij}^{12}} + \sum_{k=1}^{5} D_k \exp^{-C_k[r_{ij}-R_k]^2} + \frac{q_i q_j}{4\pi\varepsilon_0\varepsilon r_{ij}}$		q_{Na^+}=+e, q_{Cl^-}=-e, q_P=-e, charges of grains of bases see in Table 6; A, D_k, C_k, R_k, ε are in Tables 2, 3, 4		
interaction of ions with uncharged grains		σ, Å	ϵ , kcal/mol	
Na^+ with C1'	$\epsilon(\sigma/r)^{16}$	3.5	0.369	
Na^+ with C3'	$\epsilon(\sigma/r)^{12}$	3.2	0.369	
Cl^- with C1'	$\epsilon(\sigma/r)^{16}$	3.3	0.369	
Cl^- with C3'	$\epsilon(\sigma/r)^{12}$	3.3	0.369	

Table 2 Parameters A, D_k, C_k, R_k for potentials of interaction between a sodium ion and a phosphate grain Na^+-P^-, between a chlorine ion and a phosphate grain Cl^--P^- between two sodium ions Na^+-Na^+ and between a sodium ion and a chlorine ion Na^+-Cl^- and between two chlorine ions Cl^--Cl^- in the sugar CG DNA model

Parameter	Dimension	Na^+-P^-	Cl^--P^-	Na^+-Na^+	Na^+-Cl^-	Cl^--Cl^-
A	kcal/mol·Å^{12}	$8.50 \cdot 10^5$	$10.2 \cdot 10^7$	$15.0 \cdot 10^5$	$2.2 \cdot 10^5$	$4.0 \cdot 10^7$
D_1	kcal/mol	−1.25	−0.05	−0.62	−1.36	−0.52
D_2	kcal/mol	1.54	0.54	0.29	1.87	0.29
D_3	kcal/mol	−0.73	−0.02	−0.55	−0.27	−0.07
D_4	kcal/mol	0.53	0.25	0.16	0.276	0.06
D_5	kcal/mol	−0.38	0	−0.25	−0.073	−0.022
C_1	Å^{-2}	0.92	2.9	1.4	5.0	3.0
C_2	Å^{-2}	5.00	2.0	4.0	2.0	4.0
C_3	Å^{-2}	0.75	0.5	0.7	1.5	3.5
C_4	Å^{-2}	5.50	0.7	5.5	5.5	3.0
C_5	Å^{-2}	0.90	0	1.5	5.0	3.0
R_1	Å	3.65	5.4	3.40	2.80	5.00
R_2	Å	4.18	6.7	4.75	3.62	6.35
R_3	Å	5.86	8.6	6.20	5.20	7.60
R_4	Å	6.70	8.9	7.15	6.00	8.50
R_5	Å	7.97	0	8.47	6.80	9.70
ε		80	80	80	80	80

and $E_{stacking}$ stand for energy of hydrogen bonds between complementary bases and for base pairs stacking, correspondingly. We recalculate the coordinates of all nucleobase atoms on each step and compute these terms using the all atom force field AMBER. The terms $E_{val-bonds}$, $E_{val-angles}$, $E_{tors-angles}$ describe energy of deformation of the CG bonds, CG angles and dihedral angles on the strands of the CG DNA. Equilibrium values of the angles and the bonds, not pertaining to the ribose flexibility, were chosen equal to the values in A-DNA. For the rigidities, we chose the maximal values. Two wells in the double-well potential of the bond C1'-P(2) were made of equal depth. Coulombic interactions E_{el} between charged phosphate beads have distance dependent permittivity. We introduce van der Waals interactions E_{vdW} for the beads P and $C3'$ not connected through CG bonds, CG angles or dihedral angles.

Interaction of ions with DNA $E_{ion-DNA}$ includes interactions with charged phosphate beads P and beads on bases and with uncharged beads (C1', C3'). In the present realization of the model, we introduce sequence dependence: the charges on beads of a base depend on the type of this base. Interactions of ions one with another $E_{ion-ion}$ and with charges on DNA (phosphate beads and beads on bases) $E_{ion-DNA}$ take into account solvation effects (besides direct Coulomb force). The detailed description and the constants of all the potentials are collected in Appendix. The description of the resulting force field is given in Tables 1, 2, 3, 4, 5 and 6.

Table 3 Parameters A, D_k, C_k, R_k for potentials of interaction between a sodium ion and a base grain Na^+-B_j in the sugar CG DNA model

Parameter	Dimension	Na^+-B_1	Na^+-B_2	Na^+-B_3	Na^+-B_1	Na^+-B_2	Na^+-B_3
		Adenine			Guanine		
A	$\sqrt[12]{\text{kcal/mol}}$Å	2.43	4.0	3.256	1.78	2.187	3.97
D_1	kcal/mol	−1.0	−1.237	−1.11	−0.85	−0.75	−1.18
D_2	kcal/mol	1.6	0.307	2.1	2.149	1.5	0.304
D_3	kcal/mol	−0.4	−0.3	−0.298	−0.55	−0.298	−0.243
D_4	kcal/mol	0.2	0.115	0.13	0.2	0.132	0.114
D_5	kcal/mol	−0.1	−0.08	−0.0895	−0.3	−0.22	−0.073
C_1	$Å^{-2}$	2	2	2.8	4.5	4.5	4.5
C_2	$Å^{-2}$	4	4.5	4	3	3.4	3.6
C_3	$Å^{-2}$	2	2	2	2	2	2
C_4	$Å^{-2}$	7	7	7	7	7	5
C_5	$Å^{-2}$	2	2	2	2	2	3
R_1	Å	2.52	4.05	3.5	2.4	2.5	4.06
R_2	Å	3.6	5.27	4.7	3.29	3.29	5.27
R_3	Å	4.9	6.53	5.8	4.8	4.6	6.53
R_4	Å	6.2	7.53	6.9	5.94	5.94	7.53
R_5	Å	7.4	8.53	7.8	6.9	6.8	8.53
		Thymine			Cytosine		
A	$\sqrt[12]{\text{kcal/mol}}$Å	3.86	2.366	2.366	4.92	4.0	2.366
D_1	kcal/mol	−1.4	−1.0	−1.0	−1.7	−1.4	−0.6
D_2	kcal/mol	0.483	2.19	2.19	0.283	0.31	2.147
D_3	kcal/mol	-0.5	−0.298	−0.298	−0.5	−0.41	−0.298
D_4	kcal/mol	0.104	0.132	0.132	0.104	0.104	0.132
D_5	kcal/mol	−0.073	−0.0895	−0.0895	−0.21	−0.17	−0.0895
C_1	$Å^{-2}$	3	3.42	3.42	1.5	1.5	3.42
C_2	$Å^{-2}$	5	4.5	4.5	5.5	4.5	4.5
C_3	$Å^{-2}$	1.5	2.0	2.0	2.0	1.6	2.0
C_4	$Å^{-2}$	5	7	7	5.0	5.0	7.0
C_5	$Å^{-2}$	3	2	2	3.0	3.0	2.0
R_1	Å	3.9	2.66	2.66	4.94	4.03	2.66
R_2	Å	4.8	3.45	3.45	6.2	5.07	3.45
R_3	Å	5.2	4.96	4.96	7.4	6.23	4.96
R_4	Å	6.46	6.1	6.1	8.46	7.53	6.1
R_5	Å	7.4	6.96	6.96	9.4	8.53	6.96
ε		80	80	80	80	80	80

Table 4 Parameters A, D_k, C_k, R_k for potentials of interaction between a chlorine ion and a base grain Cl^--B_j in the sugar CG DNA model

Parameter	Dimension	Cl^--B_1	Cl^--B_2	Cl^--B_3	Cl^--B_1	Cl^--B_2	Cl^--B_3
		Adenine			Guanine		
A	$\sqrt[12]{\text{kcal/mol}}$Å	5.7	3.2	5.7	4.6	3.2	3.2
D_1	kcal/mol	−1.5	−1.11	−1.5	−1.36	−1.11	−1.11
D_2	kcal/mol	0.29	2.1	0.29	0.317	2.1	2.10
D_3	kcal/mol	−0.245	−0.298	−0.245	−0.245	−0.298	−0.298
D_4	kcal/mol	0.105	0.13	0.105	0.105	0.13	0.130
D_5	kcal/mol	−0.07	−0.0895	−0.073	−0.070	−0.0895	−0.0895
C_1	$Å^{-2}$	3	2.8	3	3	2.8	2.8
C_2	$Å^{-2}$	4	4	4	4	4	4
C_3	$Å^{-2}$	2	2	2	2	2	2
C_4	$Å^{-2}$	4	7	4	4	7	7
C_5	$Å^{-2}$	3	2	3	3	2	2
R_1	Å	5.65	3.3	5.81	4.6	3.3	3.3
R_2	Å	6.96	4.59	6.96	5.96	4.62	4.59
R_3	Å	8.11	5.74	8.11	7.11	5.77	5.74
R_4	Å	9.11	6.74	9.11	8.11	6.9	6.74
R_5	Å	10.11	7.74	10.11	9.11	7.77	7.74
		Thymine		Cytosine			
A	$\sqrt[12]{\text{kcal/mol}}$Å	4.1	4.79	4.79	4.1	3.2	4.79
D_1	kcal/mol	−1.3	−1.39	−1.39	−1.3	−1.11	−1.39
D_2	kcal/mol	2.1	0.317	0.317	2.1	2.1	0.317
D_3	kcal/mol	−0.298	−0.245	−0.245	−0.298	−0.298	−0.245
D_4	kcal/mol	0.13	0.105	0.105	0.13	0.13	0.105
D_5	kcal/mol	−0.0895	−0.070	−0.070	−0.0895	−0.0895	−0.070
C_1	$Å^{-2}$	2.8	3	3	2.8	2.8	3
C_2	$Å^{-2}$.	4	4	4	4	4	4
C_3	$Å^{-2}$	2	2	2	2	2	2
C_4	$Å^{-2}$	7	4	4	7	7	4
C_5	$Å^{-2}$	2	3	3	2	2	3
R_1	Å	4.12	4.76	4.76	4.12	3.3	4.76
R_2	Å	5.46	6.12	6.12	5.46	4.59	6.12
R_3	Å	6.61	7.27	7.27	6.61	5.74	7.27
R_4	Å	7.61	8.27	8.27	7.61	6.74	8.27
R_5	Å	8.61	9.27	9.27	8.61	7.74	9.27
ε		80	80	80	80	80	80

Table 5 Masses of grains m_1, m_2, m_3 and moments of inertia of real i_{xx} and i_{yy} and CG I_{xx} and I_{yy} bases A, T, G, C. Masses of grains are given in a.e.m., moments of inertia - in a.e.m.·Å^2

X	m_1	m_2	m_3	i_{xx}	I_{xx}	i_{yy}	I_{yy}
A	52.230	28.139	53.632	690	475	1704	1712
T	51.822	16.204	56.974	584	256	1636	1543
G	61.731	34.357	53.912	1302	800	1885	1858
C	39.254	35.492	35.254	233	164	1344	1231

Table 6 Charges (in units of the elementary charge e) of base grains interacting with ions in solution

Type of base	B_1	B_2	B_3
Adenine	−0.048	0.109	−0.061
Thymine	0.390	−0.240	−0.150
Guanine	−0.496	0.134	0.362
Cytosine	0.433	0.061	−0.494

The influence of water on DNA and on ions is described implicitly, by Langevin equation. Experimental damping constant (friction) is equal to $\gamma_1 = 50\text{ps}^{-1}$ for the DNA beads and $\gamma_2 = 70\text{ps}^{-1}$ for the ions.

The energy minimization (near different initial states at corresponding boundary and initial conditions) confirms the existence of two equilibrium states of the system: A-DNA and B-DNA. In a large reservoir: a cube 60 × 60 × 60 Å, DNA takes B form. In this volume, the additional 32 salt ions (16 Na^+ and 16 Cl^-) give the molar concentration 0.12 M, very close to the one of physiological saline. In a small volume: a cylinder with diameter 18.5 Åand height 30 Å(salt concentration with the same number of additional ions is 0.8 M), DNA molecule takes A form. The obtained stable configurations at temperature 300 K are shown in Fig. 3.

3 The Influence of Water Viscosity, the Order and the Location of the A-B Transition

In our CG model, in contrast to the all atom models, the viscosity of water - friction coefficients for ions and for DNA grains - may be selected separately and arbitrarily. It gives the unique opportunity to investigate the influence of friction against water molecules on the A-B transition. We compared the case without friction with the cases of low friction for both the DNA and the ions; low friction for the DNA and high friction (corresponding to the experiment) for the ions; high friction for the DNA (corresponding to the experiment) and low friction for the ions; and, finally, experimental case of the high friction for both the DNA and the ions (see Fig. 4).

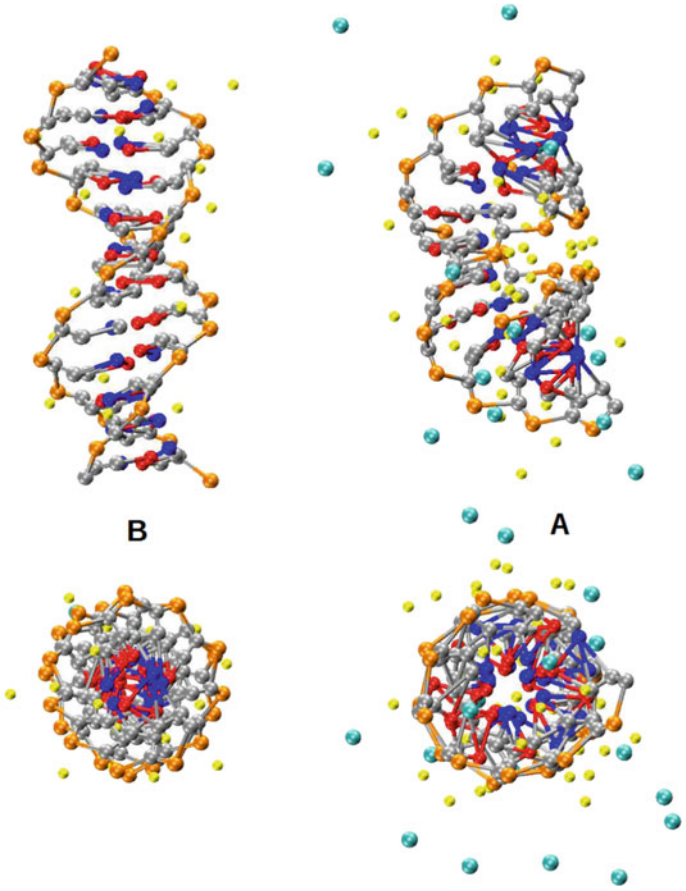

Fig. 3 Frames from the trajectories of sugar CG A-DNA (on the right) and B-DNA (on the left). Temperature is 300 K. Sodium ions are yellow, chlorine - blue

We obtained the trajectories with a duration of 360 ns for a series of concentrations. It turned out that the introduction of realistic friction into the model reduces the frequency of transitions by two orders, but the order of the transition does not change. Namely, since the system is very small, even quite far from the transition point, the molecule can make transitions to the second state, not characteristic for the given concentration, due to thermal fluctuations. The maximum number of such jumps is present for the low friction of the DNA. Thus, it is the DNA, and not ions, which initiates the transitions - due to the presence of two locally stable configurations (first of all, for the bases). The high ion friction leads to a delay in the configuration with a higher minimum, while fast ions quickly return the system to the ground state at the given concentration.

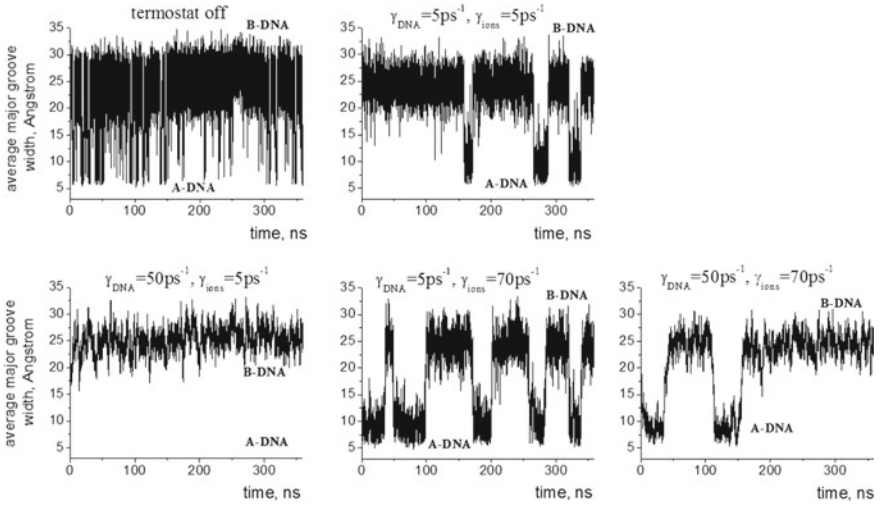

Fig. 4 Examples of calculated trajectories for the concentration of additional salt 0.19 M. The average width of the major groove along the molecule (which is about 25 Å in the B-DNA, and about 10 Å in the A-DNA) is plotted against time (in ns)

In the B to A transition, the distance between the bases starts to change first, then the major groove begins to narrow, and only at the end of the transition the sugars are repuckered (the double-well bonds move from one well to another) and the helix abruptly changes its geometry (the slide parameter adjusts much later than the parameters shift and twist). The number of ions near the axis of the molecule begins to grow immediately after the beginning of the change in the magnitude of the major groove. In the B to A transition, the groove begins to narrow from one end, while in the A to B transition, it widens from both the ends.

As the type of the transition for the small molecule does not seem to be affected by friction, one may determine the type in the case of 'inviscid' water (zero friction for both the ions and the DNA, the NVE ensemble). For this purpose, we obtained the trajectories for a large series of concentrations of additional salt, the only control parameter we used. We considered two order parameters: the average major groove width and the interaction energy between phosphate grains and sodium ions. We calculated autocorrelation functions of the order parameters, and chose the time between the counts for histograms to be 10 ns. The collected statistics was 750–1850 points. The histograms of the order parameters turned out to be double-peaked (also for the concentrations near the transition point), which signals a first order transition (see Fig. 5). For both the parameters, the area under the peaks turned out to be equal at the concentration of the additional salt 0.316 M, which we regarded as the transition point. Figure 6 shows the salt concentration dependence of the (time-averaged) major groove width (the average distance between the nearest phosphate beads located on different DNA strands) and frequency of the jumps between the forms. The large dispersion of the groove width over a wide range of concentrations from 0.15 to

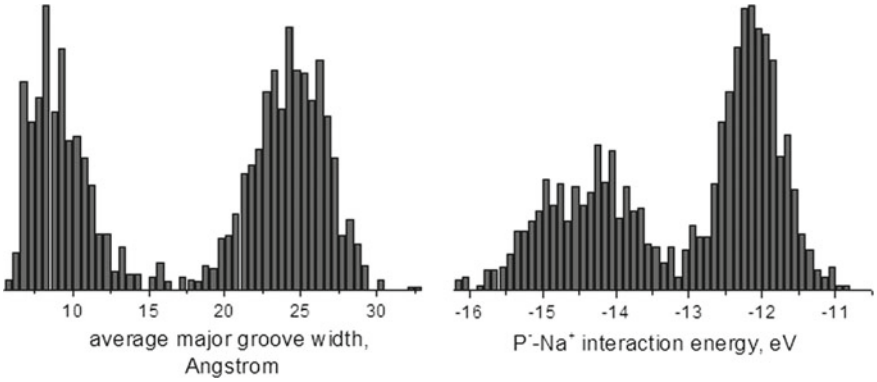

Fig. 5 Histograms of the order parameters at a point near the transition (NVE ensemble). The values of the parameters (the average major groove width (in angstroms) and the interaction energy between the DNA phosphate grains and the sodium ions (in eV)) are plotted against the number of points on the trajectory with such parameters. The total number of points is 1845. The time between counts is 10 ns. The salt concentration is 0.31 M

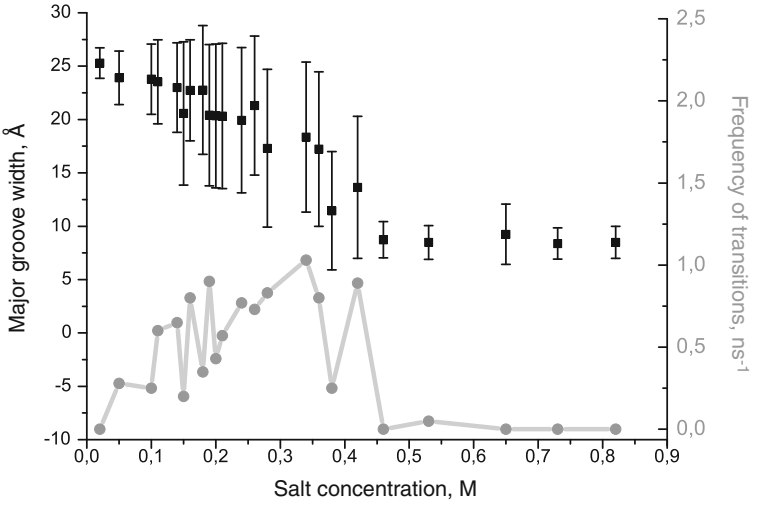

Fig. 6 Frequency of jumps between the B- and A- forms and the average width of the major groove (the value was measured every picosecond along a 30 ns trajectory) as a function of salt concentration

0.45 M reflects global B to A transitions (jumps). There is no intermediate shape between A and B forms, neither a configuration partly in B and partly in A form. The DNA molecule consisting of 12 base pairs (more than 1000 atoms) behaves like a small atom cluster near the transition between two configurations. To understand this behavior, in the next chapter we will consider the structure of the DNA-ions system more closely.

4 The Structure of the DNA-Ions Conglomerate in the 'Inviscid' Water

For a DNA molecule, it is natural to characterize the ion cloud around this molecules by a cylindrical distribution function. Figure 7 shows the functions for the A- and B-forms. The most noticeable difference between them is observed at distances less than 5 angstroms from the axis of the molecule. In the A-form, these distances correspond to the location of ions in the deep major groove (Fig. 3). In the B-form, this space is occupied by the atoms of the molecule itself, and the ions are unable to be there. Interestingly, the ions, including those located deep inside the major groove, migrate throughout the available volume of the solution not only in the B- but also in the A-form. Figure 8 shows the dynamics of all sodium ions relative to the surface of the major groove of A-DNA. One can see that each ion enters the major groove and leaves it to occur in the solution several times during one nanosecond. Because of the lack of water viscosity, many ions go into the groove just for a few picoseconds, which is impossible in real DNA. However, for the real DNA as well, the conglomerate of the molecule and the ions is dynamic, with a constant replacement of ions within the groove. This is the mechanism how the molecule is aware of changes

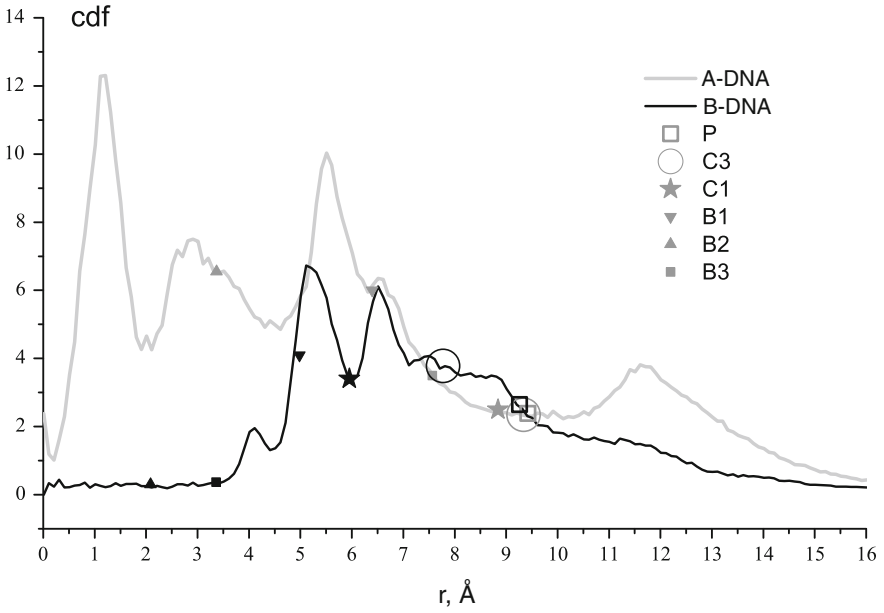

Fig. 7 Cylindrical distribution function (Cdf) of ions as a function of the distance r from the axis of the DNA molecule in A- and B-forms. For each form, the distances from the axis (r) are marked at which the beads of the molecule itself are located: phosphorus (P), two beads belonging to ribose (C1' and C3'), and three beads on the bases (B1, B2, and B3). For the clarity of the picture, we kept the grains of the DNA molecule immobile

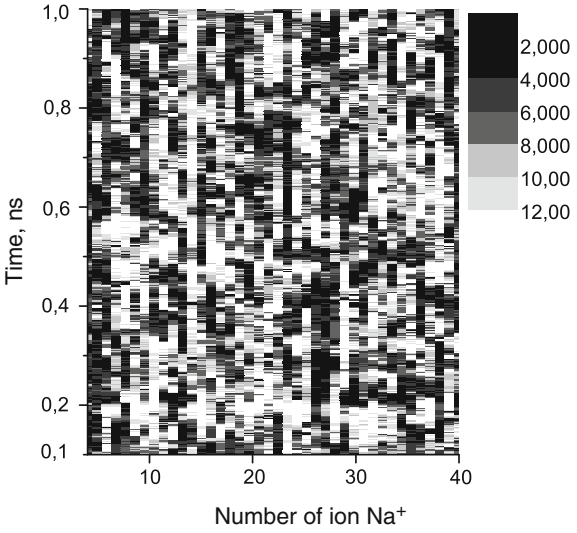

Fig. 8 Distance between sodium ions and the nearest beads of the major groove surface of A-DNA (beads P, B1, and B2) as a function of time. For distances smaller than 4 angstroms, the ions are located inside the major groove; for distances larger than 8 angstroms, the ions are in the solution outside the DNA helix

in the ion concentration in the external solution, and correspondingly responds to them by changing its geometrical shape. In the model without water viscosity, the ions forming this conglomerate spend 100–200 ps in the major groove. There are, on average, only eight or nine ions inside the A-form, but they are the critical part of this conglomerate. This is the reason why the DNA molecule made of more than a thousand atoms (12 bp), behaves as a small system.

5 Discussion and Conclusions

We saw that the introduction of the sugar CG model allowed to fully study the B-A transition in a DNA molecule. We were able to easily collect the needed statistics to determine the order of the transition, which required the calculation of many trajectories of hundreds of microseconds long. On the other hand, the model is detailed enough to catch the local structure of the double helix during the transition.

We studied a short DNA molecule, 12 base pairs long. As the control parameter for the transition we chose the salt concentration because the dependence of the effective ions potentials proved to be not sufficient for the transition [13], and we used identical potentials for all the concentrations. The natural order parameter of the system is the average major groove width. We obtained the dependence of the order parameter on the concentrations, and the histogram of the parameter for a series of concentrations. The histogram proved to be double-peaked, and we never found the molecule in a shape intermediate between A and B forms, or in a configuration partly in B and partly in A form during an appreciable time interval. So, the DNA molecule consisting of 12 base pairs (more than 1000 atoms) behaves like a small atom cluster near the

transition between two conformations. Namely, the molecule jumps between B and A form even at low concentrations, where the B-DNA corresponds to the global minimum of the thermodynamic potential. The reason for it is that there are, on average, only eight or nine ions inside the A-DNA, but they are the critical part of this conglomerate. From the shape of the histogram, we also concluded that the transition has to be of the first order (as it should be from the symmetry considerations). The frequency of jumps between the A and B forms reaches 1 per nanosecond and is the highest in the vicinity of the transition. The friction of the DNA grains and the ions does not affect the type of the transition.

We also investigated the structure and behavior of the DNA-ions conglomerate. The A-DNA proved to be a dynamical ensemble, with the ions entering the deep major groove from the solution and then leaving. The possibility to independently vary the friction of the DNA and the ions allowed to easily determine the roles of the molecule and the ions in the conglomerate. The DNA molecule initiates the jumps between the A and B forms, as it has two local energy minima, because of both the base pairs interactions and the sugar conformations (which we model by the double-well bond C1'-P). The ions turned out to be responsible for keeping the geometrical shape of the molecule corresponding to the concentration. The high ion friction leads to a delay in the configuration with a higher minimum, while fast ions quickly return the system to the ground state at the given concentration.

Acknowledgements We thank Dr. I.A. Strelnikov for pointing out some errata in numerical values and in one formula in the tables in [11]. We appreciate financial support of the Russian Science Foundation (grant 16-13-10302). The simulations were carried out in the Joint Supercomputer Center of Russian Academy of Sciences.

Appendix: The Sugar DNA CG Force Field: Potential Functions and Parameters

In the Tables 1, 2, 3, 4, 5 and 6, we list the current potentials of interactions between the grains of the sugar GC DNA model, and the corresponding constants of the model.

References

1. Lebrun, A., Lavery, R.: Modeling DNA deformations induced by minor groove binding proteins. Biopolymers **49**(5), 341–353 (1999). https://doi.org/10.1002/(sici)1097-0282(19990415)49:5%3C341::aid-bip1%3E3.0.co;2-c
2. Lu, X.J., Shakked, Z., Olson, W.: A-form conformational motifs in ligand-bound DNA structures. J. Mol. Biol. **300**(4), 819–840 (2000). https://doi.org/10.1006/jmbi.2000.3690
3. Timsit, Y.: DNA structure and polymerase fidelity. J. Mol. Biol. **293**(4), 835–853 (1999). https://doi.org/10.1006/jmbi.1999.3199
4. Ivanov, V., Minchenkova, L., Schyolkina, A., Poletayev, A.: Different conformations of double-stranded nucleic acid in solution as revealed by circular dichroism. Biopolymers **12**(1), 89–110 (1973). https://doi.org/10.1002/bip.1973.360120109

5. Nishimura, Y., Torigoe, C., Tsuboi, M.: Salt induced B - A transition of poly(dG).poly(dC) and the stabilization of A form by its methylation. Nucl. Acids Res. **14**, 2737–2748 (1986)
6. Feig, M., Pettitt, B.M.: Experiment versus force fields: DNA conformation from molecular dynamics simulations. J. Phys. Chem. B **101**(38), 7361–7363 (1997). https://doi.org/10.1021/jp971180a
7. Pastor, N.: The B- to A-DNA transition and the reorganization of solvent at the DNA surface. Biophys. J. **88**(5), 3262 (2005). https://doi.org/10.1529/biophysj.104.058339
8. Hart, K., Foloppe, N., Baker, C.M., Denning, E.J., Nilsson, L., MacKerell, A.D.: Optimization of the charmm additive force field for DNA: improved treatment of the BI/BII conformational equilibrium. J. Chem. Theory Comput. **8**(1), 348–362 (2012). https://doi.org/10.1021/ct200723y
9. Waters, J.T., Lu, X.J., Galindo-Murillo, R., Gumbart, J.C., Kim, H.D., Cheatham, T.E., Harvey, S.C.: Transitions of double-stranded DNA between the A- and B-forms. J. Phys. Chem. B **120**(33), 8449–8456 (2016). https://doi.org/10.1021/acs.jpcb.6b02155
10. Ivani, I., Dans, P.D., Noy, A., Pérez, A., Faustino, I., Hospital, A., Walther, J., Andrio, P., Goñi, R., Balaceanu, A., Portella, G., Battistini, F., Gelpí, J.L., González, C., Vendruscolo, M., Laughton, C.A., Harris, S.A., Case, D.A., Orozco, M.: Parmbsc1: a refined force field for DNA simulations. Nat. Methods **13**(1), 55–58 (2015). https://doi.org/10.1038/nmeth.3658
11. Kovaleva, N., Koroleva (Kikot), I., Mazo, M., Zubova, E.: The sugar coarse-grained DNA model. J. Mol. Model. **23**(2), 66 (2017). https://doi.org/10.1007/s00894-017-3209-z
12. Savin, A., Mazo, M., Kikot, I., Manevitch, L., Onufriev, A.: Heat conductivity of the DNA double helix. Phys. Rev. B **83**(24), 245,406 (2011). https://doi.org/10.1103/physrevb.83.245406
13. Klinov, A.P., Zubova, E.A., Mazo, M.A.: Temperature and concentration dependence of effective potentials of Na+ and Cl-ions in aqueous solution. Phys. Chem. Asp. Study Clust. Nanostruct. Nanomater. (9), 230–235 (2017). https://doi.org/10.26456/pcascnn/2017.9.230

2D Chain Models of Nanoribbon Scrolls

Alexander V. Savin and Mikhail A. Mazo

Abstract We propose a simplified 2D model of the molecular chain that allows to describe molecular nanoribbon's scrolled packings of various structures as spiral packaging chain. The model allows to obtain the possible stationary states of single-layer nanoribbons scrolls of graphene, graphane, fluorographene, fluorographane, graphone C_4H and fluorographone C_4F. We show the stability of scrolled packings and calculate the dependence of energy, the number of coils, inner and outer radius of the scrolled packing on the nanoribbon length. It is shown that a scrolled packing is the most energetically favorable conformation for nanoribbons of graphene, graphane, fluorographene, and fluorographane at large lengths. A double-scrolled packing when the nanoribbon is symmetrically rolled into a scroll from opposite ends is more advantageous for longer lengths nanoribbons of graphone and fluorographone. We show the possibility of existence of scrolled packings for nanoribbons of fluorographene and existence of two different types of scrolls for nanoribbons of fluorographane. The simplicity of the proposed model allows to consider the dynamics of molecular nanoribbon scrolls of sufficiently large lengths and at sufficiently large time intervals.

1 Introduction

Due to its unique electrical and mechanical properties, graphene in various conformations is of great interest [1–5]. Graphene is a two-dimensional structure with a peak rigidity and tensile strength, but easily flexing in space. Secondary structures of graphene (folds, scrolls) can be attributed to a special class of carbon nanomaterials, the stability of which is provided by weak non-valent (van der Waals) interactions of carbon atoms. In 1960 it was found that use of graphite lubricant from flat pieces of graphite causes the forming of microscopic scrolls that play the role of roller

A. V. Savin (✉) · M. A. Mazo
Semenov Institute of Chemical Physics, Russian Academy of Sciences,
Moscow 119991, Russia
e-mail: asavin@center.chph.ras.ru

I. V. Andrianov et al. (eds.), *Problems of Nonlinear Mechanics and Physics of Materials*, Advanced Structured Materials 94,
https://doi.org/10.1007/978-3-319-92234-8_14

bearings and provide a low value of the coefficient of friction [6]. Graphene nanoribbon, folding into a scroll, forms a new quasi-one-dimensional structure, which has a cross-section in the form of truncated Archimedean spiral. The geometric shape of the scroll is determined by the energy balance between the increasing van der Waals energy of the contacting areas of the graphene sheet and the energy lost due to the nanoribbon's bending.

There are several experimental technologies for obtaining scrolls of graphene nanoribbon and studying their structure and properties [7–12]. The properties of the scrolled packing of carbon nanoribbons were studied in a series of theoretical researches. Electrical, optical and mechanical properties of short nanoribbons scrolls were modeled from the first principles [13–15]. The mechanical properties of longer nanoribbons scrolls and different scenarios of their self-assembly were described using the molecular dynamics method in numerous articles [16–26]. The mechanical properties of long nanoribbons scrolls were described in the context of the continuum model of an elastic coiled rod [16, 21, 27, 28], in which the flexural energy of the rod is compensated by the energy from the interaction of the contacting surfaces.

All-atom models have always been used for modeling the dynamics of folds and scrolls of nanoribbons. Such models require considerable computer resources and do not allow to consider the dynamics of long nanoribbons over significant time intervals. Therefore, only scrolls having two or three coils are usually considered. The complexity of the all-atomic models also makes it difficult to carry out a full analysis of possible stationary packings of long nanoribbons. To overcome these difficulties, we proposed a 2D model of the molecular chain [29, 30] that allows to describe with high accuracy the possible stationary states of graphene nanoribbons scrolled packings.

Here, we propose a more simplified model of a 2D chain that allows to describe the stationary states of scrolled packings of molecular nanoribbons with different chemical structures. Using the model, we obtained possible stationary states of single-layer nanoribbons scrolls of graphene, graphane, fluorographene, fluorographane, graphone C_4H and fluorographone C_4F. The model can be used both for the description of scrolled packings of molecular nanoribbons with the same surfaces (nanoribbons of boron nitride, silicene, phosphorene, carbon nitride, etc.), and for the nanoribbons which sides have different chemical modification (nanoribbons of graphone and their analogs).

2 Chain Model of Molecular Nanoribbon

Molecular nanoribbon is a narrow, straight-edged strip, cut from a single-layered molecular plane. The simplest example of such molecular plane is a graphene sheet (isolated monolayer of carbon atoms of crystalline graphite) and its various chemical modifications: graphane (fully hydrogenated on both sides graphene sheet), fluorographene (fluorinated graphene), fluorographane (hydrogenated on one side and fluorinated on the other side graphene sheet), graphone C_4H (hydrogenated

on one side with a density of 0.25 graphene sheet) and fluorographone C_4F – see Fig. 1a–f.

As is known, graphene and its modifications are elastically isotropic materials, the longitudinal and flexural rigidity of which is weakly dependent on chirality of the structure. Therefore, for definiteness, we will consider nanoribbons with the zigzag structure shown in Figs. 1 and 2a.

Suppose that in the ground state the nanoribbon lies in the plane xz of the three-dimensional space along the axis x - see Fig. 2a. Such nanoribbon is a periodic structure with a constant step. Translational cells of this structure form atoms located along lines parallel to the z axis (along transverse lines). We consider such motions of the nanoribbon, when its atoms located on lines parallel to the z axis move as a rigid whole in the xy plane, keeping its coordinates along the z axis. Then these atomic lines can be considered as effective particles moving in the xy plane, and the movement of the nanoribbon is reduced to the motion of a chain of these particles – see Fig. 2b, c.

Thus, the longitudinal and flexural movements of the nanoribbon can be described as the motion of a chain of pointwise particles in the xy plane. The simplest model of a molecular chain in two-dimensional space is shown in Fig. 2c. The Hamiltonian of the chain has the following form

$$H = \sum_{n=1}^{N} \frac{1}{2} M(\dot{x}_n^2 + \dot{y}_n^2) + \sum_{n=1}^{N-1} V(R_n) + \sum_{n=2}^{N-1} U(\theta_n) + \sum_{n=1}^{N-3} \sum_{m=n+3}^{N} W(r_{nm}), \qquad (1)$$

where N – number of particles in the chain, M – particle mass, and the vector $\mathbf{u}_n = (x_n, y_n)$ defines the position of the nth particle.

The potential

$$V(R) = K(R - a)^2/2, \qquad (2)$$

is responsible for the longitudinal rigidness of the chain, K – interaction rigidness, a – equilibrium bond length (chain step), $R_n = |\mathbf{u}_{n+1} - \mathbf{u}_n|$ – distance between neighbor particles n and $n + 1$.

The potential

$$U(\theta) = \varepsilon[1 - \cos(\theta - \theta_0)] \approx \varepsilon(\theta - \theta_0)^2/2, \qquad (3)$$

describes the flexural chain mobility, θ – the valence angle formed by two neighbor bonds, θ_0 – equilibrium angle, the parameter $\varepsilon > 0$ specifies the flexural rigidity of the chain. For the n-th valent angle $\cos(\theta_n) = -(\mathbf{u}_{n-1}, \mathbf{u}_n)/|\mathbf{u}_{n-1}| \cdot |\mathbf{u}_n|$.

The Lennard-Jones (l, k) potential

$$W(r) = \varepsilon[l(r_0/r)^k - k(r_0/r)^l]/(k - l), \qquad (4)$$

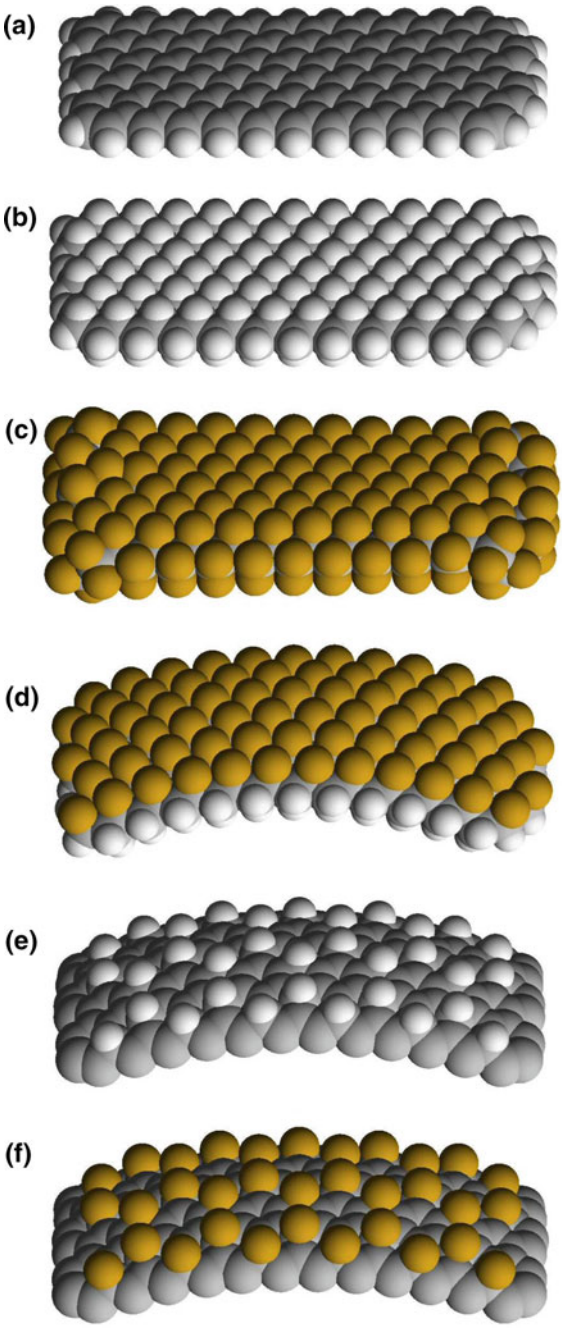

Fig. 1 Structures of nanoribbons **a** graphene $(C_{12}H_2)_{11}C_{10}H_{12}$ (of size $29.85 \times 13.44 Å^2$); **b** graphane $(C_{12}H_{14})_{11}C_{10}H_{22}$; **c** fluorographene $(C_{12}F_{14})_{11}C_{10}F_{22}$; **d** fluorographane $(C_{12}H_8F_6)_{11}C_{10}H_{15}F_5$; **e** graphone $(C_{12}H_3)_{11}C_{18}$ **f** fluorographone $(C_{12}F_3)_{11}C_{18}$

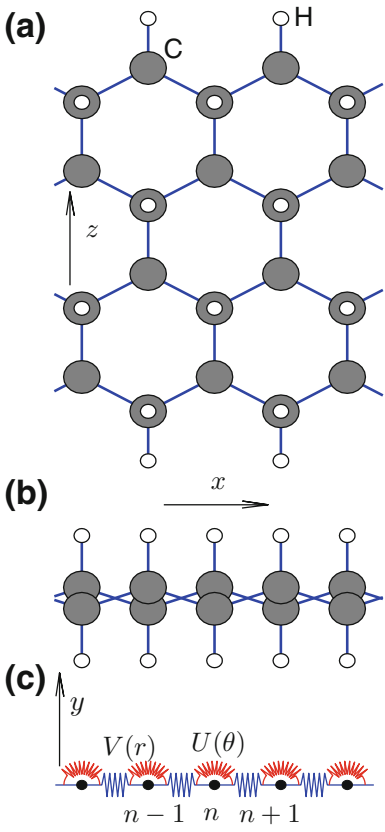

Fig. 2 View **a** from the top and **b** from the side of the graphane nanoribbon $(C_8H_{10})_\infty$ with a zigzag structure (the nanoribbon lies in the plane xz), **c** a mechanical model of a chain of particles in the plane xy in which the particle defines the position of the corresponding transverse line of nanoribbon atoms (n is the line number). The potential $V(r)$ describes the longitudinal rigidity, and the angular potential $U(\theta)$ – the flexural rigidity of the chain

describes a weak non-valent interaction between remote chain particles, ε – bond energy, r_0 – equilibrium bond length, $k > l$ (degree of repulsion k is always greater than the degree of attraction l), $r_{nm} = |\mathbf{u}_n - \mathbf{u}_m|$ – distance between particles n and m.

The step of the chain a is found as half of the period of the ground state of a flat zigzag nanoribbon. The parameter K, which determines the longitudinal rigidness, and the parameter ε, which determines the flexural rigidness of the chain, can be obtained from the analysis of the dispersion curves of the nanoribbon. The parameters of the Lennard-Jones potential (4) can either be directly calculated as sums of the non-valent interactions of one atom with the transverse line of nanoribbon atoms, or estimated from the analysis of the structure of nanoribbon scroll obtained using a full-atomic model. Values of the parameters of the chain model for the nanoribbons of graphene CC, graphane HCCH, fluorographene FCCF, fluorographane HCCF, graphone C_4H and fluorographone C_4F are presented in the Table 1.

While constructing the model, wide nanoribbons are considered, so the chemical modification of its edges can be ignored, and all parameters of the nanoribbon

Table 1 Values of the parameters of the two-dimensional chain model for the nanoribbon of graphene CC, graphane HCCH, fluorographene FCCF and fluorographane HCCF, graphone C_4H and fluorographone C_4F

Nanoribbon	M (m_p)	a(Å)	K (N/m)	ε (eV)	θ_0 (deg)	ε_0 (eV)	r_0 (Å)	k	l
CC	24	1.228	910.0	7.00	180	0.01970	3.68	8	5
HCCH	26	1.261	607.2	3.38	180	0.00984	5.01	16	6
FCCF	62	1.285	606.6	4.00	180	0.00304	5.75	20	9
HCCF	44	1.285	607.0	3.70	177	0.00325	5.06	16	3
C_4H	24.5	1.250	800.0	5.00	171	0.01430	4.30	20	5
C_4F	32.5	1.260	800.0	6.00	173	0.01900	4.60	24	7

should be normalized on its width. In this case, the particle mass M for graphene nanoribbon will be equal to the mass of two carbon atoms ($M = 2M_C = 24m_p$), for nanoribbon of graphane $M = 2(M_C + M_H) = 26m_p$, fluorographene $M = 2(M_C + M_F) = 62m_p$, fluorographane $M = 2M_C + M_H + M_F = 44m_p$, graphone $M = 2M_C + 0.5M_H = 24.5m_p$ and fluorographone $M = 2M_C + 0.5M_F = 32.5m_p$, where m_p – proton mass.

The longitudinal and flexural rigidness parameters of the chain K and ε for graphene are obtained in [29, 30]. For values of $K = 910$ N/m and $\varepsilon = 7$ eV, the dispersion curves of the chain most exactly coincide with the dispersion curves of a flat graphene nanoribbon corresponding to its longitudinal and flexural vibrations. The values of K and ε for other nanostructures can also be obtained from the analysis of the dispersion curves of nanoribbons obtained using a full-atomic model. The force fields COMPASS [31] and CFF91 were used for the analysis of the structure and dynamics of nanoribbons of graphane, fluorographene, and fluorographane.

Van der Waals interactions of atoms in the COMPASS force field are described by the Lennard-Jones potential (4) with parameters $l = 6$, $k = 9$. We consider nanoribbon of graphene and using this potential calculate the interaction energy of two bound carbon atoms located on one transverse line with all carbon atoms located on the other transverse line of the nanoribbon. The calculations show that the dependence of this interaction energy of two different transverse lines of atoms on the distance between the lines is well described by the Lennard-Jones potential (4) with parameters $l = 5$, $k = 8$ – see Fig. 3. Similar calculations of the transverse lines of atoms interaction energy can also be made for graphane nanoribbons (here it will be necessary to calculate the interaction energy of a group of bound atoms H–C–C–H of one transverse line with all atoms of another transverse line). The calculations show that the energy of the interaction of transverse lines for graphane can also be described with good accuracy by a potential (4) with parameters $l = 6$, $k = 16$.

For nanoribbons of fluorographene, fluorographane, graphone and fluorographone parameters of the interaction potential (4) can be more conveniently estimated from the analysis of stationary states of nanoribbons scrolls obtained with help of the

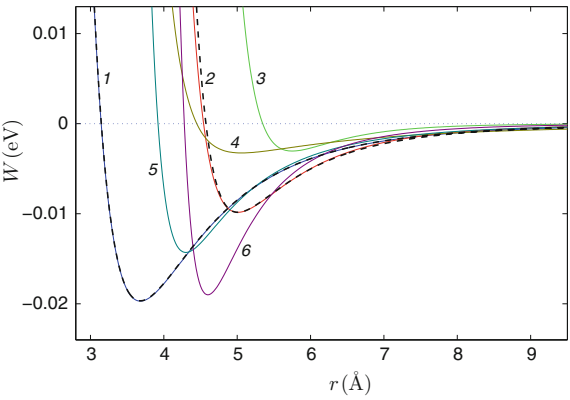

Fig. 3 Paired potentials of the non-valent interaction of the chain nodes $W(r)$ for the nanoribbons of graphene CC, graphane HCCH, fluorographene FCCF, fluorographane HCCF, graphone C_4H and fluorographone C_4F (curves 1, 2, 3, 4, 5 and 6). Dotted curves give the dependencies calculated using a full-atomic model of a wide nanoribbon

full-atomic models. The analysis shows that the fluorographene nanoribbon has the weakest nonvalent interaction (this is due to Coulomb repulsion of fluorine atoms).

3 Stationary States of Nanoribbon Scrolls

To find the stationary state of nanoribbon scrolls, it is necessary to solve the minimum problem

$$E_{total} \to \min, \tag{5}$$

i.e. to minimize the potential energy of a full-atom model of the nanoribbon along all coordinates of its atoms, starting from the initial scroll-like configuration.

Using a chain model to find a scroll structure, it is necessary to solve the minimum problem

$$E = \sum_{n=1}^{N-1} V(R_n) + \sum_{n=2}^{N-1} U(\theta_n) + \sum_{n=1}^{N-3} \sum_{m=n+3}^{N} W(r_{nm}) \to \min : \{\mathbf{u}_n\}_{n=1}^{N}, \tag{6}$$

where N – the number of particles in the chain [nanoribbon length $L = (N-1)a$].

The problem (6) was solved numerically using the conjugate gradient method. To verify stability of the obtained stationary configuration $\{\mathbf{u}_n^0\}_{n=1}^N$ we found the eigenvalues of the matrix of second derivatives of dimension $2N \times 2N$

$$B = \left(\frac{\partial E}{\partial \mathbf{u_n} \partial \mathbf{u}_m} \bigg|_{\{\mathbf{u}_l^0\}_{l=1}^N} \right)_{n=1,m=1}^{N,\ N}. \tag{7}$$

The stationary configuration of the chain will be stable only if all eigenvalues of the symmetric matrix B are nonnegative: $\lambda_i \geq 0, i = 1, 2, \ldots, 2N$. Note that for the

stable configuration first three eigenvalues are always zero: $\lambda_1 = \lambda_2 = \lambda_3 = 0$. These eigenvalues correspond to the motion of chain in the plane as rigid body (shift in two coordinates and rotation). The remaining positive eigenvalues $\lambda_i > 0$ correspond to the natural oscillations of the structure with frequencies $\omega_i = \sqrt{\lambda_{3+i}/M}$, $i = 1, \ldots, 2N - 3$.

The structure of the stationary state of the chain is determined by its initial configuration used in solving the minimum problem (6). Varying the initial configuration, it is possible to obtain various stable chain packages. The linear configuration of the chain (flat nanoribbon) is stable if the angle $\theta_0 = 180°$. The presence of non-valent interactions of chain particles leads to the existence on the plane other, more energy-efficient stationary packings of the chain. The spiral packing (scrolled packing of nanoribbons) will be more energetically advantageous for long chain.

Typical view of the scrolled packing nanoribbon and the corresponding two-dimensional spiral packing is shown in Fig. 4. As can be seen from the figure, the spiral packing of the chain practically coincides with the cross-section of the nanoribbon scroll. The geometry of a scroll (spiral) is given by the number of its coils N_c and its internal and external radii R_1 and R_2.

Scrolled packing of nanoribbon corresponds to the chain arrangement in the shape of an Archimedean spiral with an inner cavity. The center of the spiral is conveniently defined as the center of its mass

$$\mathbf{u}_0 = (x_0, y_0) = \frac{1}{N} \sum_{n=1}^{N} \mathbf{u}_n^0,$$

where $\mathbf{u}_n^0 = (x_n^0, y_n^0)$ is the two-dimensional radius vectors of the nth chain node of the stationary spiral. In the polar coordinate system it can be written as

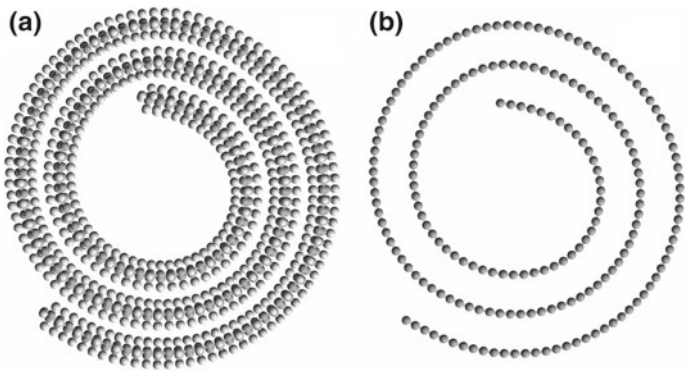

Fig. 4 Scrolled packing **a** of graphane nanoribbons $(C_{12}H_{14})_{99}C_{10}H_{22}$ of size 252×13.7Å^2 and its **b** two-dimensional chain model (number of chain links $N = 200$, number of coil $N_c = 2.67$, scroll inner radius $R_1 = 11.7$Å, scroll outer radius $R_2 = 19.0$Å)

$$x_n^0 = x_0 + r_n \cos(\phi_n), \quad y_n^0 = y_0 + r_n \sin(\phi_n),$$

where the radius $r_n = |\mathbf{u_n^0} - \mathbf{u_0}|$ and the angle ϕ_n increase monotonically with increasing node number $n = 1, 2, \ldots, N$. The spiral can be characterized by the number of coils

$$N_c = (\phi_n - \phi_1)/2\pi.$$

It is also convenient to define the integer number of coils $n_c = [N_c] + 1$, where $[x]$ is the integer part of x. Let us define the inner radius of the scroll by its first coil:

$$R_1 = \frac{1}{n_1} \sum_{n=1}^{n_1} r_n,$$

where n_1 is the number of chain nodes involved in formation of the spiral first coil (maximal value of index n wherein $\phi_n < \phi_1 + 2\pi$). The outer radius of the scroll can be defined by its last coil as

$$R_2 = \frac{1}{n_2} \sum_{n=N-n_2+1}^{N} r_n,$$

where n_2 is the number of chain nodes involved in the formation of the spiral last coil ($N - n_2 + 1$ is the minimal value of n wherein $\phi_n > \phi_N - 2\pi$).

The twisting rigidity of the spiral is characterized by the lowest natural frequency $\omega_1 = \sqrt{\lambda_4/M}$. This frequency corresponds to the periodic twisting/untwisting oscillations of the spiral. In the approximation of a continuous elastic rod this oscillation motion has been studied in [16, 27].

4 Scrolled Packing of Graphane Nanoribbons

The structure of scrolled packing of graphene nanoribbons was considered in the articles [29, 30]. The simpler model proposed here leads to the same results, so we consider the scroll packings of the other five types of nanoribbons.

Let us first describe the possible stationary structures of graphane nanoribbons. To do this, we consider the dependence of the number of coils N_c, inner R_1 and outer radius R_2 and the smallest natural frequency ω_1 on the number of chain nodes N [on the chain length $L = (N - 1)a$] – see Fig. 5.

A typical form of packages for nanoribbons of different lengths is shown in Fig. 6. Single-coil configuration (the number of coils $n_c = 1$) of the scroll (a) can exist only for nanoribbons of length $L \in [50.4, 76.6]$Å (for $41 \leq N \leq 62$). Double-coil configuration ($n_c = 2$) of the scroll (b) is stable at lengths $L \in [60.5, 187.9]$Å ($49 \leq N \leq 150$), (c) three-coil ($n_c = 3$) – at $L \in [167.7, 339.2]$Å ($134 \leq N \leq 270$), (d)

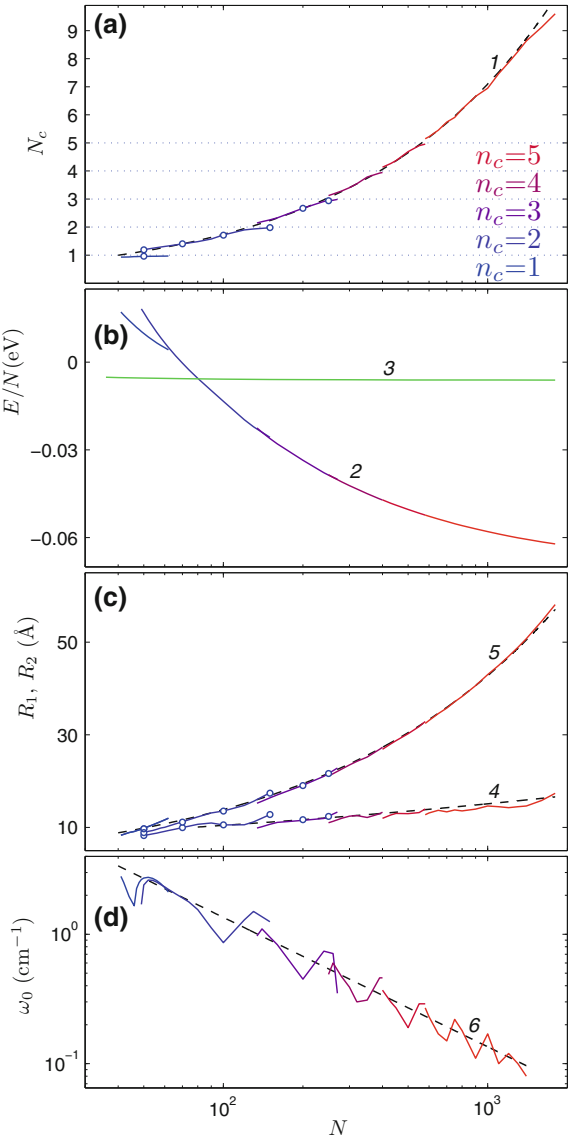

Fig. 5 Dependencies of **a** number of scroll coils N_c of graphane nanoribbon, **b** the specific energy of the structure E/N for the scroll and the flat nanoribbon (curves 2 and 3), **c** inner R_1 and outer radius R_2 of the scroll (curves 4 and 5), **d** the lowest frequency of the scroll's natural oscillations ω_1 (curve 6) on the number of chain particles N. Markers give values obtained using a full-atomic model of a nanoribbon $(C_{12}H_{14})_{N/2-1}C_{10}H_{22}$ with width $D = 13.7$Å. Dashed lines give power-law dependencies $N_c = 0.105N^{0.61}$, $R_1 = 5N^{0.16}$Å, $R_2 = 01.45N^{0.49}$Å, $\omega_1 = 135/N\,\mathrm{cm}^{-1}$

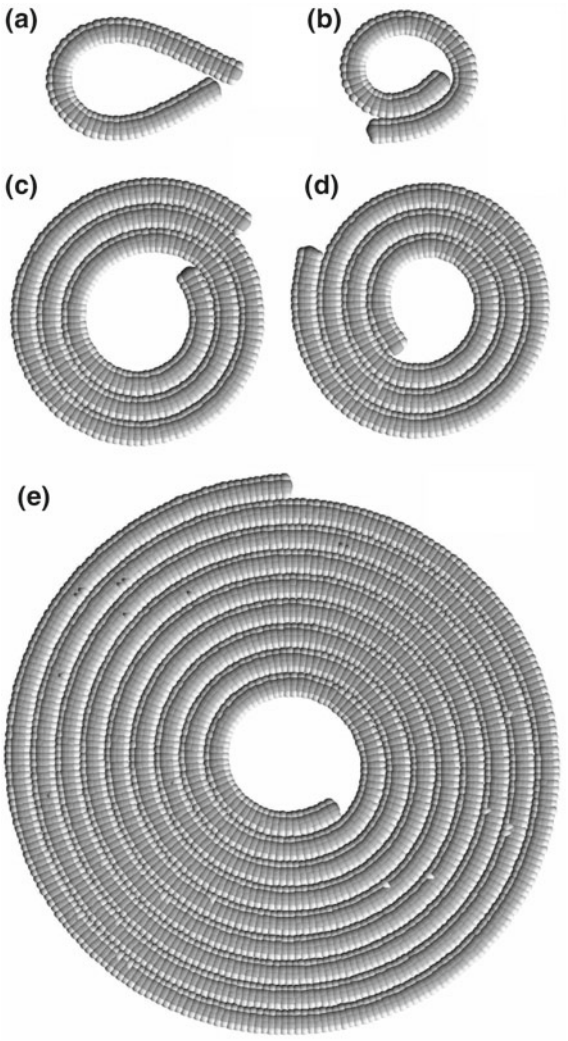

Fig. 6 Scrolled packing of graphane nanoribbons for chain with number particles: **a** $N = 62$ (number of the scroll coils $N_c = 0.97$, inner and outer radius of the scroll $R_1 = R_2 = 11.98$Å); **b** $N = 62$ ($N_c = 1.33$, $R_1 = 9.33$Å, $R_2 = 10.29$Å); **c** $N = 270$ ($N_c = 2.99$, $R_1 = 13.31$Å, $R_2 = 22.82$Å); **d** $N = 270$ ($N_c = 3.23$, $R_1 = 11.68$Å, $R_2 = 22.10$Å); **e** $N = 1400$ ($N_c = 8.6$, $R_1 = 14.64$Å, $R_2 = 50.74$Å)

four-coil ($n_c = 4$) – at $L \in [314.0, 503.1]$Å ($250 \leq N \leq 400$), and (e) structures with five or more coils ($n_c \geq 5$) are stable for $L \geq 503.1$Å ($N \geq 400$).

At certain lengths, there may be two stable configurations of the scroll packing – see Fig. 6c and d. This bistability is due to the non-valent interaction of the nanoribbon ends. In one configuration, the ends interact more strongly (are closer to each other), in the other – weaker (the ends are more distant from each other). Such bistability also exists for scrolls of graphene nanoribbons [30]. Therefore, the dependence of N_c, R_1, R_2, ω_1 on the length (on the number of particles in the chain N) is divided into branches corresponding to the configurations of the scrolled packing with the same number of coils n_c – see Fig. 5.

As can be seen from Fig. 5 increasing the nanoribbon length leads to a monotonic increase of the coils of its scrolled packing according to the power law $N_c \approx 0.105N^{0.61}$ for $N \to \infty$. With increasing length the radius of inner cavity $R_1 \approx 5N^{0.16}$Å and the outer scroll radius $R_2 \approx 1.45N^{0.49}$Å also increase. The specific energy of the spiral (scroll) E/N decreases monotonically with increasing number of particles (the longer is the nanoribbon, the greater is the energy gain from its assembly into a scroll). At small lengths $L < 101$Å $(N < 81)$ the flat form of the nanoribbon is most advantageous in energy, and at lengths $L \geq 101$Å $(N \geq 81)$ the scrolled packing becomes more profitable.

The eigenmode of the lowest positive frequency ω_1 is the twisting-untwisting mode when all nodes of the model chain move along the Archimedes spiral. The increase in the scroll length leads to a decrease in the frequency of this oscillation $\omega_1 \approx 135/N\,\mathrm{cm}^{-1}$ for $N \to \infty$ – see Fig. 5d. By the similar law, the smallest natural frequency of the scrolled packing of graphene nanoribbon decreases [16, 27, 30].

To verify the results obtained via the chain model, stationary scrolled packings of graphane nanoribbons of various lengths were also found using a full-atomic model. The graphane nanoribbon of width $D = 13.7$Å corresponding to a chain of N links can be described by formula $(C_{12}H_{14})_{N/2-1}C_{10}H_{22}$ – see Figs. 1b and 2b. As can be seen from Fig. 5, the full-atomic model leads to the same values of the number of coils N_c and the radii of the scroll R_1, R_2, as the two-dimensional chain model. Thus, the chain model for graphane nanoribbon makes it possible to find their scrolled packings with good accuracy.

5 Scrolled Packing of Fluorographene Nanoribbons

The fluorographene nanoribbon differs from the graphane nanoribbon in such a way that its carbon atoms are joined by fluorine atoms instead of hydrogen atoms. The fluorine atom is much larger than the hydrogen atom, and the C–F valence bond is more strongly polarized than the C–H bond (in the COMPASS force field [31] it is assumed that on the C–F bond atoms there are charges $q_C = 0.25e, q_F = -0.25e$, and on the C–H bond atoms – charges $q_C = -0.053e$, $q_H = 0.053e$, where e – electron charge). Coulomb repulsion of negatively charged fluorine atoms leads to a significant weakening of the interaction between the contacting sections of the nanoribbon. The analysis of the full-atom model of nanoribbon shows that the contacting regions of the nanoribbon continue to be attracted to each other, and the nanoribbons can form stable scrolled structures – see Fig. 7.

The large size of the fluorine atoms and the strong polarization of the valence bonds C–F make it difficult to directly calculate the nonvalent interaction potential $W(r)$ for the chain model. The parameters k and l of the potential (4) can be estimated from the asymptotics of the interaction energy of the nanoribbon sections as they approach and distance from each other. The parameters r_0 and ε here were chosen so that the structure of the scrolls obtained using a full-atomic model would best coincide with

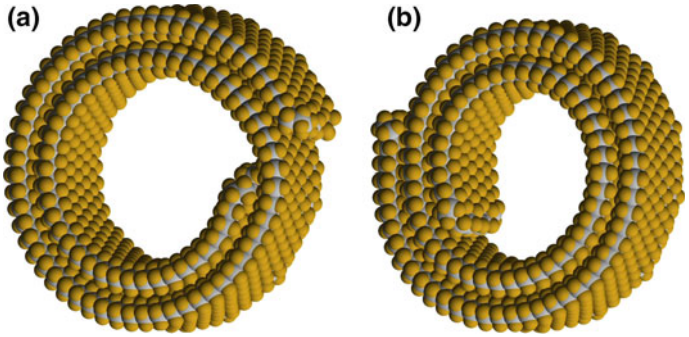

Fig. 7 Scrolled packing of fluorographene nanoribbons $(C_{12}F_{14})_{99}C_{10}F_{22}$ of size 256.3×14.2Å^2 (number of particles $N = 200$) with **a** number of coils $N_c = 1.94$ (inner radius $R_1 = 18.2$Å, outer radius of the scroll $R_2 = 23.5$Å) and **b** $N_c = 2.16$ ($R_1 = 15.7$Å, $R_2 = 22.1$Å)

the structure of the spiral chain packages obtained using the chain model. The best match is achieved when using the values of the parameters presented in the Table 1.

The dependence of the number of coils N_c, inner R_1 and outer radius R_2 of the scroll on the number of chain nodes N for fluorographene nanoribbon is given in Fig. 8. There are only two or more coils scrolled packings for fluorographene nanoribbons (number of coils $N_c > 1$). Double-coil configuration ($n_c = 2$) can exist only for nanoribbons of length $L \in [86, 294]$Å (for $68 \leq N \leq 230$). Three-coil configuration ($n_c = 3$) of the scroll is stable at lengths $L \in [256, 513]$Å ($200 \leq N \leq 400$), four-coil ($n_c = 4$) – at $L \in [513, 641]$Å ($400 \leq N \leq 600$), five-coil ($n_c = 5$) – at $L \in [641, 1078]$Å ($600 \leq N \leq 840$), and structures with five or more coils ($n_c \geq 5$) are stable for $L \geq 1078$Å ($N \geq 840$).

At certain lengths, there can be simultaneously two stable configurations of the scrolled packing of the nanoribbon (see Fig. 7). This bistability as well as for graphane nanoribbons is due to the non-covalent interaction of the nanoribbon ends. Because of this, the dependencies N_c, R_1 and R_2 on N are divided into branches corresponding to the configurations of a scrolled packing with the same number of coils n_c – see Fig. 8.

As can be seen from Fig. 8 increasing the nanoribbon length leads to a monotonic increase in the number of coils of its scrolled packing according to the power law $N_c \approx 0.083N^{0.61}$ for $N \to \infty$. With increasing length, the radius of the inner cavity also grows according to the power law $R_1 \approx 7N^{0.18}$Å and the outer radius of the scroll $R_2 \approx 1.8N^{0.48}$Å. The specific energy of the spiral (scroll) E/N decreases monotonically with the number of particles – the longer the nanoribbon, the greater the energy gain from its assembly into a scroll. The flat form of the nanoribbon is most advantageous in energy at small lengths $L < 154$Å ($N < 121$), and the scrolled packing becomes more profitable at lengths $L \geq 154$Å ($N \geq 121$).

Stationary scrolled packing of fluorographene nanoribbons of various lengths was also found using a all-atomic model to verify the results obtained via the chain model. The fluorographene nanoribbon of width $D = 14.2$Å corresponding to a chain of

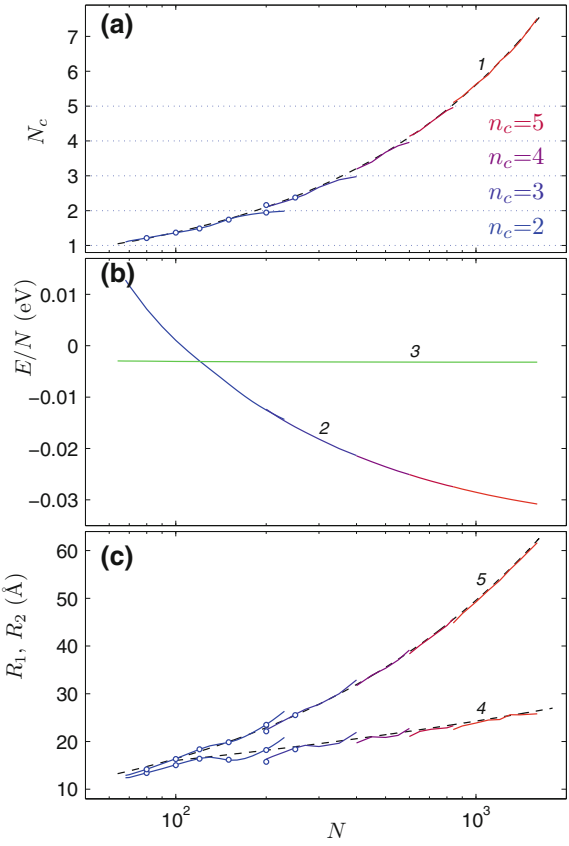

Fig. 8 Dependencies of **a** number of scroll coils N_c of fluorographene nanoribbons, **b** the specific energy of the structure E/N for the scroll and the flat nanoribbon (curves 2 and 3), **c** inner R_1 and outer radius R_2 of the scroll (curves 4 and 5) on the number of chain particles N. Markers give values obtained using a full-atomic model of a nanoribbon $(C_{12}F_{14})_{N/2-1}C_{10}F_{22}$ with width $D = 14.2$Å. Dashed lines give power-law dependencies $N_c = 0.083N^{0.61}$ (curve 1), $R_1 = 7N^{0.18}$Å, $R_2 = 1.8N^{0.48}$Å (curves 4 and 5)

N links can be described by formula $(C_{12}F_{14})_{N/2-1}C_{10}F_{22}$ – see Fig. 1c. As can be seen from Fig. 8 a full-atomic model gives a good coincidence of the number of coils N_c and scroll radii R_1, R_2 with the values obtained via the chain model. Thus, the chain model for fluorographene nanoribbons also makes it possible to find with good accuracy their scrolled packings.

6 Scrolled Packing of Fluorographane Nanoribbons

Let us consider the fluorographane nanoribbon shown in Fig. 1d. The main feature of this nanoribbon is the non-equivalence of its sides. One side of it is hydrogenated (hydrogen atoms are attached to carbon atoms), and the other is fluorinated (fluorine atoms are attached to carbon atoms). Since fluorine atoms are larger than hydrogen atoms and have a much greater electrical charge, they are more repulsive from each other. Therefore, the flat form of such nanoribbon is not a stable state. Nanoribbon

always bends and forms a convex surface the outer side of which contains fluorine atoms, and the inside contains hydrogen atoms. If nanoribbon length considerably exceeds its width, in the ground state it takes the form of a circular arc – see Fig. 9a. Formation of the arc leads to the convergence of the nanoribbon ends, which can lead to the self-assembly of the nanoribbon into a scroll structure [32].

In the chain model the non equivalence of nanoribbon sides is reflected in difference of the equilibrium value of the bond angle θ_0 from 180°. For a fluorographane nanoribbon angle $\theta_0 = 177°$. Convex nanoribbon can be rolled into a scroll by two ways - to the scroll in which its outer side contains fluorine atoms and to the scroll in which its outer side contains hydrogen atoms – see Fig. 9b and c. The most advantageous in energy is always the first form of the scroll, since in it the convexity of the nanoribbon coincides with its bend in the scroll. In the chain model these forms of the scroll correspond to the chain packings in a spiral with different chirality (right and left spiral).

The dependence of the number of coils N_c, the specific energy E/N, inner R_1 and outer radius R_2 of the scroll on the number of particles N is given in Fig. 10. As can be seen from the figure, a scroll of nanoribbon with a fluorinated outer surface is always more energy efficient and has a more compact shape than a scroll with a hydrogenated outer surface. The number of coils $N_c \approx 0.165N^{0.56}$ for the first form and $N_c \approx 0.135N^{0.56}$ for the second form of the scroll. The inner cavity radius of the first form scroll is practically independent of its length $R_1 \approx 8.4$Å, and the outer radius $R_2 \approx 1.1N^{0.53}$Å. For the second form scroll $R_1 \approx 3.8N^{0.23}$Å, $R_2 \approx 1.35N^{0.51}$Å for $N \to \infty$.

It is necessary to note that both forms of scroll having different twist are stable configurations. The most energetically advantageous first form of a scroll can be formed by nanoribbons of length $L > 45.0$Å ($N > 35$), and the second – only by nanoribbons of length $L > 70.7$Å ($N > 55$).

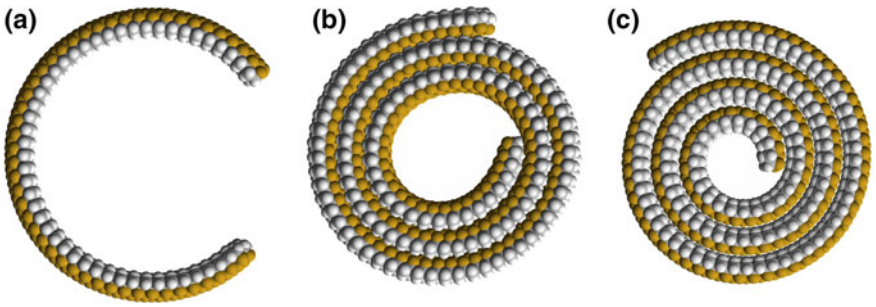

Fig. 9 The ground state **a** of fluorographene nanoribbons $(C_{12}H_8F_6)_{47}C_{10}H_{17}F_5$ (ribbon width $D = 13.9$Å, number of particles $N = 96$). The most **b** and the least **c** energetically favorable scrolled packings of nanoribbon $(C_{12}H_8F_6)_{127}C_{10}H_{17}F_5$ ($N = 256$): packing with fluorinated outer surface (number of scroll coils $N_c = 3.43$, scroll radii $R_1 = 9.1$Å, $R_2 = 21.8$Å) and packing with fluorinated inner surface ($N_c = 2.8$, $R_1 = 14.4$Å, $R_2 = 23.4$Å). The energy difference between conformations **b** and **c** $\Delta E = 29.7$ eV

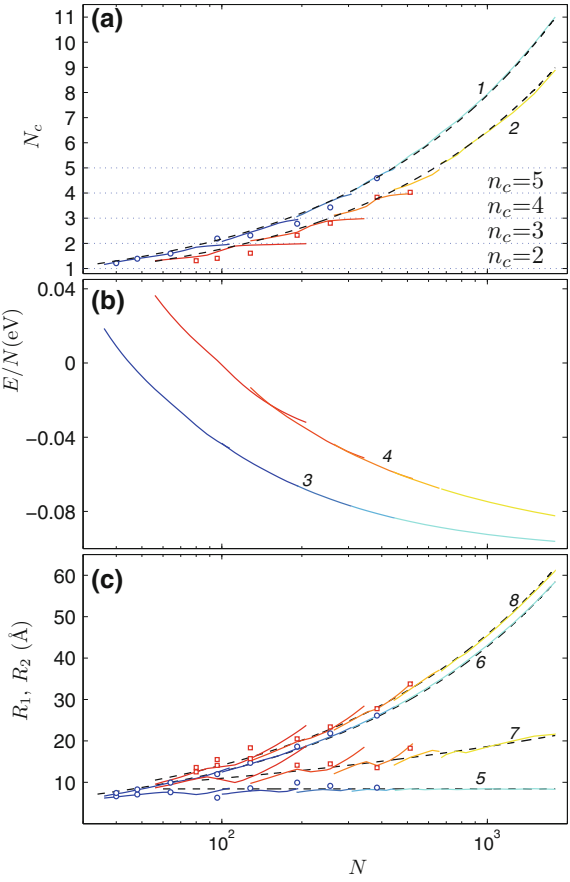

Fig. 10 Dependencies of **a** the number of scroll coils N_c, **b** the specific energy E/N, **c** inner R_1 and outer radius R_2 of the scrolled packing of fluorographene nanoribbons on the number of chain particles N. Curves 1, 3, 5 and 6 give dependencies for scroll with fluorinated outer surface, curves 2, 4, 7 and 8 - for scroll with fluorinated inner surface. Markers give values obtained using the full-atomic model of nanoribbon $(C_{12}H_8F_6)_{N/2-1}C_{10}H_{17}F_5$ of width $D = 13.9$Å. Dashed lines give power-law dependencies $N_c = 0.165N^{0.56}$ and $N_c = 0.135N^{0.56}$ (curves 1 and 2), $R_1 = 8.4$Å, $R_2 = 1.1N^{0.53}$Å (curves 5 and 6) and $R_1 = 3.8N^{0.23}$Å, $R_2 = 1.35N^{0.51}$Å (curves 7 and 8)

To verify the results obtained via the chain model, stationary scrolled packing of fluorographane nanoribbons of various lengths was also found using a full-atomic model. The fluorographane nanoribbon width $D = 13.9$Å corresponding to the chain of N links can be described by the formula $(C_{12}H_8F_6)_{N/2-1}C_{10}H_{17}F_5$ – see Fig. 1d. As can be seen from Fig. 10 the 2D chain model gives a good coincidence of the number of coils N_c and the radii of the scroll R_1, R_2 with the values obtained via the full-atomic model. Thus, the chain model for fluorographane nanoribbons also allows to find their scrolled packings.

7 Scrolled Packing of Graphone Nanoribbons

Graphone C_4H (25% one-side hydrogenated graphene sheet) is the most stable structure formed by hydrogenation on one side of a graphene sheet [33]. Attaching a

hydrogen (fluorine) atom leads to a local change in the valence bonds with sp^2 hybridization by sp^3, which entails to the appearance of local convexity in the sheet. The addition of hydrogen atoms along a single line leads to a break in the flat sheet of graphene along this line to the formation of a dihedral angle [34, 35].

One-side hydrogenation (fluorination) of graphene nanoribbon entails to non equivalence of its sides. The flat form of the nanoribbon becomes unstable, it bends and forms a convex surface on the outside with attached atoms. Strong bending of the nanoribbon leads to its folding into scroll structures [36, 37].

In the chain model the non equivalence of nanoribbon sides is reflected in a difference of the equilibrium value of the bond angle θ_0 from 180°. The non equivalence of graphone nanoribbon sides is more revealed than that of the fluorographane nanoribbons, here the angle $\theta = 171°$ for C_4H and $\theta = 173°$ for C_4F. Graphone nanoribbons are always rolled up so that its convex side is the outer side of the scroll – see Fig. 11. As can be seen from the figure, it is possible to fold the nanoribbon into a single-scrolled (a), (d) and a double-scrolled (b), (c) packing. The double-scrolled packing becomes more energy efficient for graphone C_4H with the number of particles $N > 700$ ($L > 874$Å), and for C_4F - with $N > 1400$ ($L > 1763$Å) – see Figs. 12b and 13b.

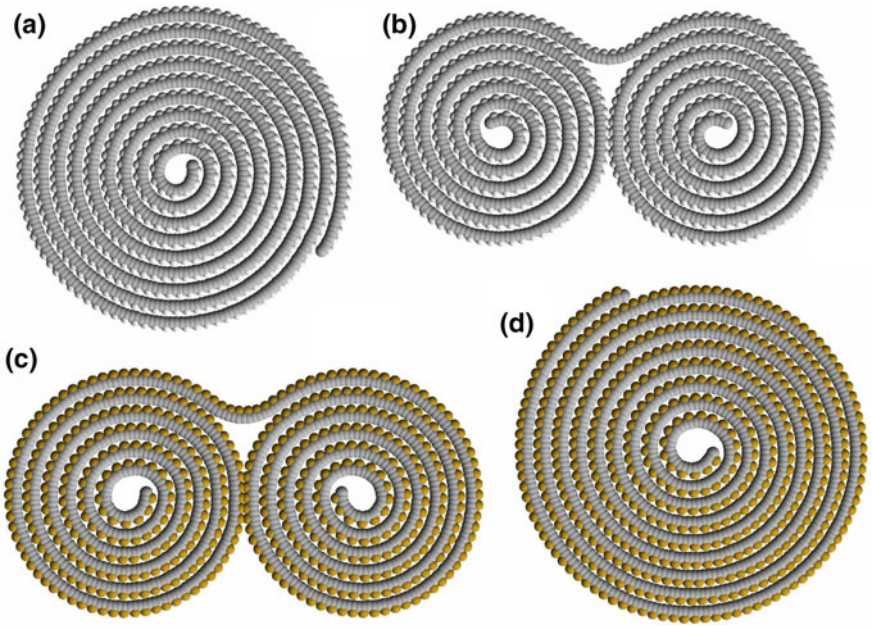

Fig. 11 Single-scrolled **a**, **d** and double-scrolled **b**, **c** packings of graphone nanoribbons C_4H, C_4F with number of chain particles $N = 1001$. For packing **a** number of coils $N_c = 9.12$, inner and outer radii of the scroll $R_1 = 5.29$Å, $R_2 = 38.40$Å; **b** $N_c = 6.21$, $R_1 = 5.26$Å, $R_2 = 26.41$Å; **c** $N_c = 8.68$, $R_1 = 6.54$Å, $R_2 = 40.14$Å; **d** $N_c = 5.95$, $R_1 = 6.24$Å, $R_2 = 27.56$Å

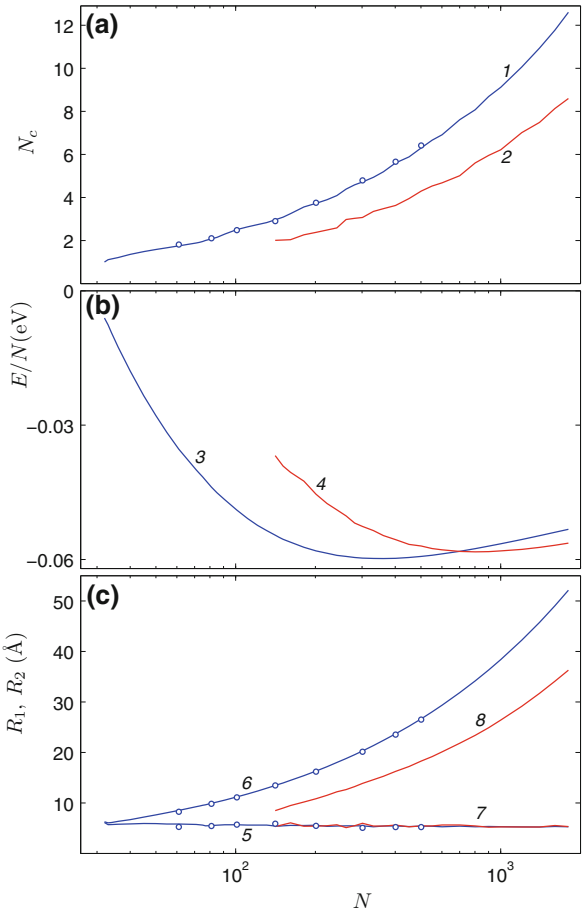

Fig. 12 Dependencies of **a** number of scroll coils N_c; **b** specific energy E/N; **c** inner R_1 and outer R_2 of single-scrolled (curves 1, 3, 5 and 6) and double-scrolled (curves 2, 4, 7 and 8) packings of graphone nanoribbons C_4H on the number of chain particles N. Markers give values obtained using the full-atomic model of nanoribbon $(C_{12}H_3)_{N/2-1}C_{18}$ of width $D = 11.4$Å

Dependence of the number of coils N_c, the specific energy E/N, inner R_1 and outer radius R_2 of single-scrolled and double-scrolled nanoribbon packings on its length (on the number of chain particles N) for C_4H and C_4F are shown in Figs. 12 and 13. A feature of graphone scrolls is a decrease in the inner radius R_1 with an increase in the nanoribbon length. The inner cavity decreases monotonically, and the number of coils and the outer diameter of the scroll increase monotonically with increasing nanoribbon length.

For graphone C_4H specific energy E/N decreases monotonically at $N < 361$ ($L < 450$Å) and increases monotonically at $N > 361$ for single-scrolled (double-scrolled) packing of nanoribbon – see Fig. 12b. For double-scroll specific energy decreases monotonically at $N < 801$ ($L > 1000$Å) and increases monotonically at $N > 801$. For fluorographone C_4F switching from decrease to increase in the specific energy takes place with the number of chain particles $N = 701$ ($L = 882$Å) for single-scrolled packing of nanoribbon – see Fig. 13b. For double-scroll this switching

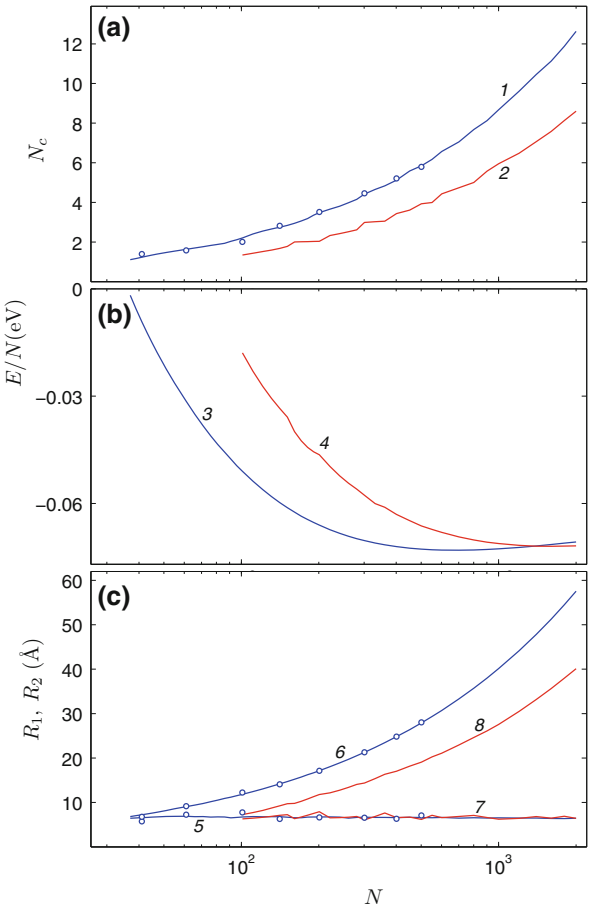

Fig. 13 Dependencies of **a** number of scroll coils N_c; **b** specific energy E/N; **c** inner R_1 and outer R_2 of single-scrolled (curves 1, 3, 5 and 6) and double-scrolled (curves 2, 4, 7 and 8) packings of fluorographone nanoribbon C_4F on the number of chain particles N. Markers give values obtained using the full-atomic model of nanoribbon $(C_{12}F_3)_{N/2-1}C_{18}$ of width $D = 11.5$Å

take place at $N = 1601$ ($L = 2016$Å). The increase in the energy of the scrolled packing for large nanoribbon lengths is due to the fact that for larger scroll diameters, it's further winding of the nanoribbon becomes less energetically favorable (the small curvature of the outer layers does not allow to realize the natural curvature of the layer with nonequivalent sides). Therefore, for the length $L > 100$ nm ($L > 202$ nm) graphone nanoribbons C_4H (C_4F) will forms not the scrolls having a cross-sectional shape of a flat spiral, but more complex 3D spiral structures.

To verify the results obtained via the chain model, stationary scrolled packing of graphone nanoribbons C_4H (C_4F) of different lengths was also found using the full-atomic model. The graphone nanoribbon of width $D = 11.4$Å [$D = 11.5$Å] corresponding to a chain of N particles can be described by formula $(C_{12}H_3)_{N/2-1}C_{18}$ [$(C_{12}F_3)_{N/2-1}C_{18}$] – see Fig. 1e, f. As can be seen from Figs. 12 and 13 the two-dimensional chain model for graphone nanoribbons also gives a good coincidence

of the number of coils N_c and the radii of the scroll R_1, R_2 with the values obtained via the full-atomic model.

8 Conclusions

All-atomic modeling of long nanoribbon dynamics requires considerable computing resources and to solve this problem we propose a simple 2D model of a molecular chain that allows to describe folded and scrolled packages of nanoribbons. Here, we propose the most simplified 2D model of a two-dimensional chain, allowing to describe the scroll conformations of graphene-like single-layer nanoribbons of graphene, graphane, fluorographene, fluorographane (hydrogenated on one side and fluorinated on the other side graphene), graphone C_4H (partially hydrogenated on one side graphene) and fluorographone C_4F.

The Hamiltonian of the chain model (1) takes into account the longitudinal and flexural nanoribbon rigidness, as well as non-valent interactions between the transverse layers of nanoribbon atoms. Using the model, possible stationary states of the scrolls were obtained. The dependencies of energy, the number of coils, the inner and outer radii of the scrolled packing on the nanoribbon length was analyzed and it was shown that a scrolled packing is the most energetically favorable conformation for nanoribbons depicted above. The longer nanoribbons of graphone and fluorographone, a double-scrolled packing is more advantageous when the nanoribbon is symmetrically rolled into scrolls from opposite ends. The possibility of the existence of rolled packing for nanoribbon of fluorographene was shown and two different types of fluorographane rolls that in the chain model correspond to the left and right spirals of Archimedes were discovered. To verify the results obtained via the chain model we also used the full-atom model and found scrolled packings of graphene, graphane, fluorographene, fluorographane, graphone C_4H and fluorographone C_4F nanoribbons of different lengths. The chain model allows to find the scrolled packings for these nanoribbons with good accuracy.

The simplicity of the proposed model allows to consider the dynamics of molecular nanoribbon scrolls of sufficiently large lengths and at sufficiently large time intervals. The model can be used for the description of scrolled packings of molecular nanoribbons with the same surfaces (nanoribbons of boron nitride, silicene, phosphorene, carbon nitride, etc.), of the nanoribbons which sides have different chemical modification (nanoribbons of graphone and their analogs) and for describing the dynamics of multi-layered nanoribbons.

Acknowledgements This work is supported by the Russian Science Foundation under grant 16-13-10302. The research was carried out using supercomputers at Joint Supercomputer Center of the Russian Academy of Sciences (JSCC RAS).

References

1. Novoselov, K.S., Geim, A.K., Morozov, S.V., Jiang, D., Zhang, Y., Dubonos, S.V., Grigorieva, I.V., Firsov, A.A.: Electric field effect in atomically thin carbon films. Science **306**, 666 (2004)
2. Geim, A.K., Novoselov, K.S.: The rise of graphene. Nat. Mater. **6**, 183 (2007)
3. Soldano, C., Mahmood, A., Dujardin, E.: Production, properties and potential of graphene. Carbon **48**, 2127 (2010)
4. Baimova, J.A., Liu, B., Dmitriev, S.V., Srikanth, N., Zhou, K.: Mechanical properties of bulk carbon nanostructures: effect of loading and temperature. Phys. Chem. Chem. Phys. **16**, 19505 (2014)
5. Baimova, J.A., Korznikova, E.A., Dmitriev, S.V., Liu, B., Zhou, K.: Review on crumpled graphene: unique mechanical properties. Rev. Adv. Mater. Sci. **39**, 69 (2014)
6. Bollmann, W., Spreadborough, J.: Action of graphite as a lubricant. Nature **186**, 29 (1960)
7. Cheng, G., Calizo, I., Liang, X., Sperling, B.A., Johnston-Peck, A.C., Li, W., Maslar, J.E., Richtera, C.A., Walker, A.R.H.: Carbon scrolls from chemical vapor deposition grown graphene. Carbon **76**, 257 (2014)
8. Zhou, H.Q., Qiu, C.Y., Yang, H.C., Yu, F., Chen, M.J., Hu, L.J., Guo, Y.J., Sun, L.F.: Raman spectra and temperature-dependent Raman scattering of carbon nanoscrolls. Chem. Phys. Lett. **501**, 475 (2011)
9. Chen, X., Boulos, R.A., Dobson, J.F., Raston, C.L.: Shear induced formation of carbon and boron nitride nano-scrolls. Nanoscale **5**, 498 (2013)
10. Savoskin, M.V., Mochalin, V.N., Yaroshenko, A.P., Lazareva, N.I., Konstantinova, T.E., Barsukov, I.V., Prokofiev, I.G.: Carbon nanoscrolls produced from acceptor-type graphite intercalation compounds. Carbon **45**, 2797 (2007)
11. Xie, X., Ju, L., Feng, X., Sun, Y., Zhou, R., Liu, K., Fan, S., Li, Q., Jiang, K.: Controlled fabrication of high-quality carbon nanoscrolls from monolayer graphene. Nano Lett. **9**, 2565 (2009)
12. Chuvilin, A.L., Kuznetsov, V.L., Obraztsov, A.N.: Chiral carbon nanoscrolls with a polygonal cross-section. Carbon **47**, 3099 (2009)
13. Pan, H., Feng, Y., Lin, J.: Ab initio study of electronic and optical properties of multiwall carbon nanotube structures made up of a single rolled-up graphite sheet. Phys. Rev. B **72**, 085415 (2005)
14. Rurali, R., Coluci, V.R., Galvao, D.S.: Prediction of giant electroactuation for papyruslike carbon nanoscroll structures: first-principles calculations. Phys. Rev. B **74**, 085414 (2006)
15. Chen, Y., Lu, J., Gao, Z.: Structural and electronic study of nanoscrolls rolled up by a single graphene sheet. J. Phys. Chem. C **111**, 1625 (2007)
16. Shi, X., Pugno, N.M., Cheng, Y., Gao, H.: Gigahertz breathing oscillators based on carbon nanoscrolls. Appl. Phys. Lett. **95**, 163113 (2009)
17. Martins, B.V.C., Galvao, D.S.: Curved graphene nanoribbons: structure and dynamics of carbon nanobelts. Nanotechnology **21**, 075710 (2010)
18. Huang, S., Wang, B., Feng, M., Xu, X., Cao, X., Wang, Y.: Carbon nanoscrolls fabricated from graphene nanoribbons using Ni nanowire templates: a molecular dynamics simulation. Surf. Sci. **634**, 3 (2015)
19. Perim, E., Paupitz, R., Galvao, D.S.: Controlled route to the fabrication of carbon and boron nitride nanoscrolls: a molecular dynamics investigation. J. Appl. Phys. **113**, 054306 (2013)
20. Wang, Y., Zhan, H.F., Yang, C., Xiang, Y., Zhang, Y.Y.: Formation of carbon nanoscrolls from graphene nanoribbons: a molecular dynamics study. Comput. Mater. Sci. **96**, 300 (2015)
21. Shi, X., Cheng, Y., Pugno, N.M., Gao, H.: A translational nanoactuator based on carbon nanoscrolls on substrates. J. Appl. Phys. **96**, 053115 (2010)
22. Zhang, Z., Li, T.: Carbon nanotube initiated formation of carbon nanoscrolls. Appl. Phys. Lett. **97**, 081909 (2010)
23. Chu, L., Xue, Q., Zhang, T., Ling, C.: Fabrication of carbon nanoscrolls from monolayer graphene controlled by p-doped silicon nanowires: a MD simulation study. J. Phys. Chem. C **115**, 15217 (2011)

24. Patra, N., Song, Y., Kral, P.: Self-assembly of graphene nanostructures on nanotubes. ACS Nano **5**, 1798 (2011)
25. Song, H.Y., Geng, S.F., An, M.R., Zha, X.W.: Temperature-induced unfolding of scrolled graphene and folded graphene. J. Appl. Phys. **113**, 164305 (2013)
26. Yin, Q., Shi, X.: Mechanics of rolling of nanoribbon on tube and sphere. Nanoscale **5**, 5450 (2013)
27. Shi, X., Pugno, N.M., Gao, H.: Mechanics of carbon nanoscrolls: a review. Acta Mech. Solida Sin. **23**, 484 (2010)
28. Shi, X., Pugno, N.M., Gao, H.: Constitutive behavior of pressurized carbon nanoscrolls. Int. J. Fract. **171**, 163 (2011)
29. Savin, A.V., Korznikova, E.A., Dmitriev, S.V.: Scroll configurations of carbon nanoribbons. PRB **92**, 035412 (2015)
30. Savin, A.V., Korznikova, E.A., Dmitriev, S.V.: Simulation of folded and scrolled packings of carbon nanoribbons. Fiz. Tver. Tela **57**(11), 2278–2285 (2015). [Phys. Solid State **57** (11) 2348-2355 (2015)]
31. Sun, H.: Compass: an Ab initio force-field optimized for condensed-phase applications – overview with details on alkane and benzene compounds. J. Phys. Chem. B **102**, 7338 (1998)
32. Jin, Y., Xue, Q., Zhu, L., Li, X., Pan, X., Zhang, J., Xing, W., Wu, T., Liu, Z.: Self-assembly of hydrofluorinated Janus graphene monolayer: a versatile route for designing novel Janus nanoscrolls. Sci. Rep. **6**, 26914 (2016). https://doi.org/10.1038/srep26914
33. Boukhvalov, D.W., Katsnelson, M.I.: Chemical functionalization of graphene. J. Phys. Condens. Matter **21**, 344205 (2009)
34. Reddy, C.D., Zhang, Y.-W.: Structure manipulation of graphene by hydrogenation. Carbon **69**, 86–91 (2014)
35. Zhu, S., Li, T.: Hydrogenation enabled scrolling of graphene. J. Phys. D Appl. Phys. **46**, 075301 (2013)
36. Liu, Z., Xue, Q., Tao, Y., Li, X., Wu, T., Jinb, Y., Zhang, Z.: Carbon nanoscroll from C4H/C4F-type graphene superlattice: MD and MM simulation insights. Phys. Chem. Chem. Phys. **17**(5), 3441–3450 (2015)
37. Zhang, L., Zeng, X., Wang, X.: Programmable hydrogenation of graphene for novel nanocages. Sci. Rep. **3**(3162) (2013). https://doi.org/10.1038/srep03162

Interaction Between DNA Molecule and Nanosize Pore

Robert A. Turusov

The author thanks his colleague, anniversary celebrant L.I. Manevich for the idea of this work.

Abstract We present a new approach in studying the interaction between DNA macromolecule and nanopore. This approach is based on the "method of contact layer" which is elaborated by the author in application to description of adhesive interaction in the frameworks of "Adhesive mechanics". We suggest now to extend the method onto nanomechanics.

1 Introduction

This publication [1] describes direct experimental measurement (carried out for the first time ever) of electrophoretic force that occurs while pulling a single DNA molecule through a nanopore in a solid body as a function of the pore size. Theory of this method, which has already been offered in publications [2–5] regards the force in electrophoresis as a result of interaction between ionic screening and hydrodynamics. Authors [1] simulate this process with Poisson–Boltzmann and Stokes equations and receive a good agreement with experimental data. This method is meant for DNA sequencing, i.e. to define the sequences of nucleotides forming the molecule, by observing the change of the electrophoretic force in the process of DNA pulling through a nanopore. It is likely that the hydrodynamic approach applied there allows to evaluate the force integrally, i.e. as an average value throughout the nanopore length. But this length is likely to be significantly longer than one DNA molecular

R. A. Turusov (✉)
Semenov Institute of Chemical Physics, Russian Academy of Sciences, Moscow, Russia
e-mail: rob-turusov@yandex.ru

I. V. Andrianov et al. (eds.), *Problems of Nonlinear Mechanics and Physics of Materials*, Advanced Structured Materials 94,
https://doi.org/10.1007/978-3-319-92234-8_15

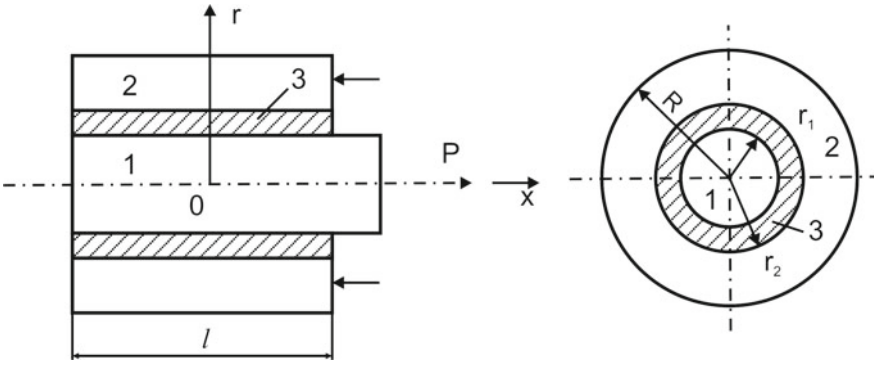

Fig. 1 DNA molecule in a nanopore model. 1—DNA molecule, 2—solid elastic body with a nanopore, 3—electric field between DNA and nanopore (contact layer)

fragment. That's why the electrophoretic force will be a result of interaction of the pore 'walls' with several DNA molecular groups. In this article its authors basing on a mechanical model that describes adhesive interaction between reinforcing fiber and polymer matrix, and on the strength of this model in trials, when the fiber was pulled out of the matrix, offer an 'incremental' way of estimation, based on investigation of the narrow zone of tangential stress concentration, the tangential stress being applied along the fiber on the 'fiber-polymer adhesive' boundary. The incremental characteristic here is represented by adhesive strength τ_{ad}, which presumably reflects the charge nature of the DNA fragment with the length approximately equal to the width of the stress concentration zone. The problem of stress distribution in such adhesive model can be solved by the contact layer method [6–9] and is represented in an attachment below. The results of the solution and its analysis is used in the text itself. Authors presume that this approach may also be applied to estimate the interaction between an enzyme and DNA.

2 Interaction Simulation

A DNA molecule is being pulled through a nanosize pore in a solid body. Let us presume that the DNA molecule and the walls of the nanopore represent an electrostatic cylindrical condenser. Let's name linear density of the charge as $\sigma = q/l\ \left(Kl/m\right)$, where q—total charge of the DNA piece limited by a nanopore, L—length of the nanopore, r_1—radius of the inner cylinder (core), simulating the DNA, r_2—nanopore radius—here it's the outer radius of the condensor (Fig. 1).

Then, according to the Gauss theorem for electrostatics, the interaction force of the core surface length unit with the nanopore walls is:

$$F_r(r_1) = E(r_1)\sigma = \frac{\sigma^2}{2\pi\varepsilon_0\varepsilon r_1} \tag{1}$$

Here *E(r)*—is the electrostatic field intensity. Let us assume that the solid body with the nanopore is immobilized (settled fixed), and a certain pulling force F is applied to one of the ends of the central core (i.e. to the DNA along its axis). Let us also assume that the core has also changed its position against the nanopore elastically without breaking any links on relatively small length *dl*. As a result the radiuses, being elongated, form a small displacement angle γ with the previous position. As a result, shear force per unit length occurs

$$dF_{fr} = F_r\gamma dl = \frac{\sigma^2}{2\pi\varepsilon_0\varepsilon r_1}\gamma dl \tag{2}$$

Dividing (2) by $\gamma\ dl$ we receive average (by nanopore length) shear modulus G^*:

$$G^* = \frac{dF_{fr}}{\gamma dl} = F_r = \frac{1}{2\pi\varepsilon\varepsilon_0}\frac{\sigma^2}{r_1} \tag{3}$$

It is well known that potential difference between the core and the nanopore wall is

$$\varphi(r_1) - \varphi(r_2) = \frac{\sigma}{2\pi\varepsilon\varepsilon_0}\ln\frac{r_1}{r_2} \tag{4}$$

Therefore the average density of charge is:

$$\sigma = \frac{2\pi\varepsilon\varepsilon_0[\varphi(r_1) - \varphi(r_2)]}{\ln\left(r_2/r_1\right)} \tag{5}$$

From (5) and (3) we receive an average shear modulus

$$G^* = \frac{2\pi\varepsilon\varepsilon_0[\varphi(r_1) - \varphi(r_2)]^2}{r_1\left[\ln\left(r_2/r_1\right)\right]^2} \tag{6}$$

Dimension of shear modulus is N/m^2. Let us call the cylindrical layer between the matrix r_2 and the fiber (i.e. DNA molecule) r_1—a contact layer. There are no normal stresses σ_x, perpendicular to any cross section $x = const$. I.e. this layer is anisotropic. In such a continuous medium Young's modulus in radial direction is identically linked to shear modulus with this simple equation $E^* = 2G^*$.

Thus, pulling a DNA molecule through a nanopore we are measuring a certain force, destructing the settled interaction between the molecule and the pore. Although the distribution of the tangential stress remains unrevealed.

To find the relation $\tau_p(x,\ r_1)$ let us regard the DNA molecule as a thin cylindrical solid core (fiber) and the matrix 2 with nanopore—as a hollow cylinder of finite size with inner radius r_2, outer radius R and length l (Fig. 1). We consider the problem as

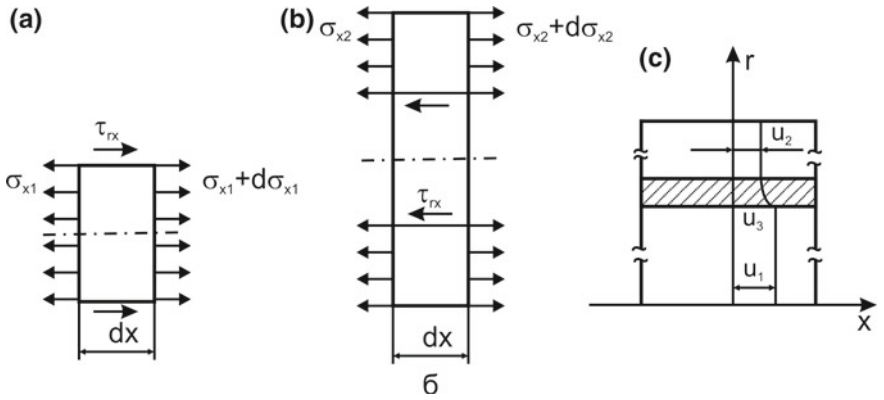

Fig. 2 Stresses in the elements of central (**a**) and outer (**b**) cylindrical cores; **c**—displacements «*u*» in axial direction in the cores and the contact layer

generally axisymmetric. In addition let's not take into consideration a small possible shrinkage of the diameter during elongation of the fiber along the axis. It's highly possible that the electric field in the pore being significant, the molecule can change its size while getting into it. This possible fact is neglected in our approach.

I.e., let us presume that there exists a certain anisotropic layer of small thickness δ (of the electric nature—in our case) between the polymer matrix and the fiber, and this layer can transfer normal stresses σ_r and tangential ones—τ_{rx} [1–3]. Let's write down the balance equations for the elements of the above mentioned cores 1 and 2 of dx length (Fig. 2c):

for the central core element (DNA molecule) 1:

$$(d\sigma_{x1}/dx)dx\pi r_1^2 + \tau_{rx}(r_1)dx\,2\pi r_1 = 0; \tag{7}$$

for cylindrical element 2 of the matrix r_2, separating the matrix from the contact layer:

$$(d\sigma_{x2}/dx)dx\,\pi(R^2 - r_2^2) - \tau_{rx}(r_2)dx\,2\pi r_2 = 0 \tag{8}$$

after reduction:

$$\begin{aligned}\tau_{rx}(x, r_1) &= -(r_1/2)(d\sigma_{x1}/dx);\\ \tau_{rx}(x, r_2) &= \frac{R^2 - r_2^2}{2r_2}\frac{d\sigma_{x2}}{dx}.\end{aligned} \tag{9}$$

Let us mark normal forces in cores as $N_1 = \pi r_1^2\sigma_{x1}$ and $N_2 = \pi(R^2 - r_2^2)\sigma_{x2}$, and rewrite the Eq. (9) in a more convenient way:

$$dN_1/dx = -2\pi r_1\tau_{rx}(x, r_1); \quad dN_1/dx = 2\pi r_2\tau_{rx}(x, r_2) \tag{10}$$

One of these equations can be substituted by a balance equation of a part of the model in any cross section x:

$$N_1 + N_2 = 0 \tag{11}$$

After reduction

$$\partial\tau(x,r)\big/\partial r + \tau(xr)\big/r = 0 \tag{12}$$

Integrating (12):

$$\tau(x,r) = -f(x)/r, \quad (r_1 \le r \le r_2) \tag{13}$$

Let's mark the displacement along the x axis according to the layers u_1, u_2 and in the contact layer u_3 (see Fig. 2c). To keep the continuity (solidness) of the model on the boundaries r_1 and r_2 the following criteria should take place:

$$u_3(x,r_1) = u_1(x);\ u_3(x,r_2) = u_2(x). \tag{14}$$

Deformations in layers 1 and 2 can be described with the help of Cauchy relations

$$\varepsilon_{x1} = du_1\big/dx;\ \varepsilon_{x2} = du_2\big/dx \tag{15}$$

For contact layer 3, the change of radial displacement along x being neglected, we receive the following equation for shear deformations:

$$\varepsilon_{rx} = \partial u_3(x,r)\big/\partial r, \quad (r_1 \le r \le r_2) \tag{16}$$

Presuming the deformations in cylinders 1 and 2 are elastic and linked with the stresses by Hooke law:

$$e_{xi} = \sigma_{xi}\big/E_i = N_i\big/S_iE_i, \quad i = 1,2. \tag{17}$$

In contact layer 3 only shear deformations occur, also linked with tangential stresses by Hooke law:

$$\varepsilon_{rx} = e_{rx} = \tau(x,r)\big/G^*. \tag{18}$$

From (15)–(18):

$$u_3(x,r) = \int \varepsilon_{rx}dx + \varphi(x) = -\frac{f(x)}{G*}\ln r + \varphi(x). \tag{19}$$

From boundary conditions (14):

$$r = r_1 : \; u_1 = -\frac{f(x)}{G^*} \ln r_1 + \varphi(x); \quad r = r_2 : \; u_2 = -\frac{f(x)}{G^*} \ln r_2 + \varphi(x). \tag{20}$$

Subtracting the first equation from the second in (20) and differentiating with respect to x:

$$\frac{d}{dx}(u_1 - u_2) = \frac{1}{G^*} \ln \frac{r_2}{r_1} \left[\frac{df(x)}{dx} \right] \tag{21}$$

Substituting Eqs. (15), (17), (10) and (17) in (21), we receive an equation for the required functional relation N_1:

$$\frac{d^2 N_1}{dx^2} = \frac{2\pi G^*}{\ln(r_2 / r_1)} \left[\left(\frac{1}{E_1 S_1} + \frac{1}{E_2 S_2} \right) \right] N_1 \tag{22}$$

Let us mark

$$\omega^2 = \frac{2\pi G^*}{\beta \ln(r_2 / r_1)}, \quad \beta = \frac{\pi}{1 / (E_1 r_1^2) + 1 / [E_2 (R^2 - r_2^2)]} \tag{23}$$

And rewrite Eq. (22) as:

$$d^2 N_1 / dx^2 - \omega^2 N_1 = 0 \tag{24}$$

Solution of (24):

$$N_1(x) = A \, ch\omega x + B \, sh\omega x \tag{25}$$

Boundary conditions here are the following:

$$x = 0 \quad N_1 = 0; \quad x = l : \quad N_1 = P. \tag{26}$$

From (25) and (26):

$$A = 0; \quad B = \frac{P}{sh\, \nu}; \quad \nu = \omega l.$$

Finally:

$$N_1(x) = -N_2(x) = P \left(\frac{sh\,(\omega x)}{sh\, \nu} \right) \tag{27}$$

$$\tau_{rx}(x, r) = -\frac{f(x)}{r} = -\frac{1}{r} \left(\frac{1}{2\pi} \frac{dN_1}{dx} \right) = -\frac{\omega}{2\pi r} \left[P \frac{ch\,(\omega x)}{sh\, \nu} \right],$$
$$\nu = \omega l \tag{28}$$

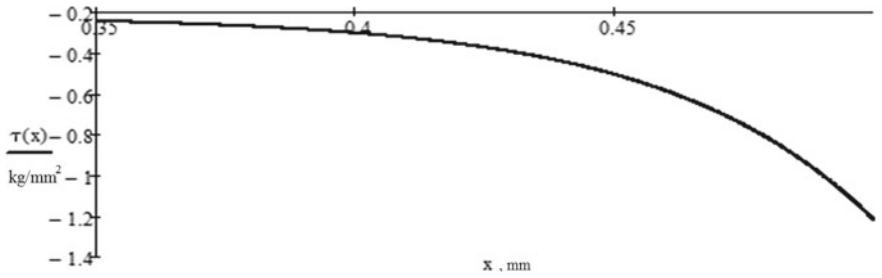

Fig. 3 Distribution of tangential stresses in a cylindrical 'fiber-polymer' sample near the 'fiber-polymer' boundary

Let us presume that R is large in comparison with the nanopore radius. That's why the parameter of tensile stiffness still stays in Eq. (23): $\beta = E\pi r_1^2$. Then the parameter ω:

$$\omega = \sqrt{\frac{2G^*}{E_1 r_1^2 \ln \frac{r_2}{r_1}}} \tag{29}$$

If $r_2 - r_1 = \delta << r_1$, after expanding the logarithm:

$$\omega = \sqrt{2G^* / E_1 \delta r_1} \tag{30}$$

I.e. the main difference between this model and the model 'fiber-polymer' [6–9] is in ability to control the shear modulus G* of the contact layer (in our case it's electric layer, and the modulus is the difference of potentials), or, in other words, stiffness of the contact layer G*/δ. Its value defines the width of the zone of tangential stresses concentration near the point of DNA exit from the pore (or near the fiber exit from the matrix [7, 9]) and the maximum of these stresses. Keeping under control the value of G*, we can control the length of the fragments being torn at the output. Other sequencing methods are also possible with the above-mentioned approach.

Figure 3 represents an example of distribution of the tangential stresses on the 'fiber-polymer' boundary, thermal stresses taken into account. The calculations were made with the following parameters of the model:

$$\begin{aligned} r_1 &= 4 \circ 10^{-3} \text{ mm},\ R = 1 \text{ mm},\ l = 1 \text{ mm},\ \alpha_1 = 10^{-5} \text{ K}^{-1}, \\ \alpha_2 &= 8 \circ 10^{-5} \text{ K}^{-1},\ E_1 = 2 \circ 10^5 \text{ MPa},\ E_2 = 4 \circ 10^3 \text{ MPa}, \\ G^* / \delta &= 25 \circ 10^4 \text{ MPa/mm},\ \mu_1 = 0,3, \\ \mu_2 &= 0,35,\ (\alpha_2 - \alpha_1)\,\Delta T = -0,5 \circ 10^{-2},\ P = 10^{-2} \text{ N}. \end{aligned}$$

As it can be seen from the Fig. 3 the tangential stress are centered near the exit of the fiber from the polymer matrix while $x = l/2$. The statement that the action takes

place in the zone of stresses concentration and the fiber/molecule piece which is torn, has the length roughly equal to the width of the zone of the stresses concentration, is based on trials and one-dimensional solution. It's partially verified by the solution for two-dimensional problem. Strict demonstration is to be received.

References

1. van Dorp, S., Keyser, U.F., Dekker, N.H., Dekker, C., Lemay, G.: Origin of the electrophoretic force on DNA in solid-state nanopores. Nat. Phys. **5**, 347–351 (2009)
2. Long, D., Viovy, J.L., Ajdari, A.: Stretching DNA with electric fields revisited. Biopolymers **39**, 755–759 (1996)
3. Viovy, J.L.: Electrophoresis of DNA and other polyelectrolytes: physical mechanisms. Rev. Mod. Phys. **72**, 813–822 (2000)
4. Luan, B., Aksimentiev, A.: Electro-osmotic screening of the DNA charge in nanopore. Phys. Rev. E **78**, 021912-1– 021912-4 (2008)
5. Luan, B., Aksimentiev, A.: Strain softening in stretched DNA. Phys. Rev. Lett. **101**, 118101-1–118101-4 (2008)
6. Turusov, R.A., Manevich, L.I.: Introduction to adhesion mechanics. Polymer Sci. Ser. D. Glues Seal. Mater. **2**(4), 209–213 (2009)
7. Turusov, R.A., Manevich, L.I.: Contact - layer method in adhesion mechanics: picking fiber from matrix. Polymer Sci. Ser. D, Glues Seal. Mater. **3**(2), 75–86 (2010)
8. Freidin, A.S., Turusov, R.A.: Properties and calculations of adhesion joints. Chemistry, Moscow (1990) (in Russian)
9. Turusov, R.A.: Adhesion mechanics. NIU MGSU, Moscow (2016) (in Russian)

Part III
Condensed Matter Mechanics and Physics

Wave-Particle Duality and Quantum-Classical Analogy

Leonid I. Manevitch

Abstract Mathematical analogy between the systems of weakly coupled oscillators and multi-level quantum system allows considering them in the framework of a unified approach. In particular, an asymptotic interpretation of wave-particle duality provides an efficient analytical tool for solving both linear and nonlinear non-stationary dynamical problems of classical and quantum mechanics.

1 Introduction

1.1 Genesis of Wave-Particle Duality

It is well-known that the alternative versions regarding the light nature were proposed at dawn of theoretical physics. Newton's corpuscular model could easily explain a rectilinear propagation of light. However, it was not so successful when dealing with a superposition of the beams going by different ways through a clearance between lens and underlying glass. On the contrary, the appearance of the ring fringes in this case was easily explained by alternative theory of the wave perturbations in the hypothetic elastic ether. In spite of the fact that the wave theory did not describe simply the rectilinear light propagation, its explanation became possible due formulation by Huygens of his name principle.

Huygens's principle opened the possibility to understand different wave manifestations of the light. However, the most significant of them, i.e. interference and diffraction were not initially recognized as its consequences. The complete understanding had been attained after the decisive experiments of T. Young and A. Fresnel. They led to common conclusion: Huygens was right. As F. Arago claimed: "who might think that the light merging with the light can induce the gloom!" When Maxwell discovered electromagnetic nature of the light, the conclusion concerning

L. I. Manevitch (✉)
Department Polymer and Composite Materials, Semenov Institute of Chemical Physics RAS, Moscow 119991, Russia
e-mail: manevitchleonid3@gmail.com

I. V. Andrianov et al. (eds.), *Problems of Nonlinear Mechanics and Physics of Materials*, Advanced Structured Materials 94,
https://doi.org/10.1007/978-3-319-92234-8_16

its wave nature was extended to any electromagnetic radiation. It was a second great synthesis in the physics after world-wide Newton's gravitation law.

The wave electromagnetic theory remained to be indisputable advancement even after the demonstration of its contradiction to thermodynamics laws. Let us remind the essence of this contradiction. As classical thermodynamics claims the energy of the radiation in the box with non-transparent heated walls has to be uniformly distributed between the normal waves of all possible lengths (frequencies). The lengths of electromagnetic waves in the cavity (inside the box) can be infinitely small (then the frequencies are infinitely large). Therefore, their number as well as the general energy becomes infinite ("ultraviolet catastrophe"). This contradiction is removed by M. Planck's hypothesis supposing that the absolutely black body irradiates by the discrete energy portions only. Then the contribution of the high frequencies sharply decreases and turns out to be finite. Several years later A. Einstein supposed that the carriers of Planck's discrete portions are the particles, i.e., he returned to Newton's corpuscles and explained on this base the phenomenon of photoelectric effect. The reasons of Planck and Einstein were strongly different. The former one wanted to theoretically describe the frequency and temperature dependences of the radiation density with preservation of the wave paradigm. However, while solving brilliantly the first problem, he could preserve the wave picture only due to incorrectness in his arguments, which was recognized later. As for Einstein, he paid the main attention to the "ultraviolet catastrophe" considering it as inevitable consequence of the classical wave paradigm which remained nevertheless necessary as an explanation of the interference and diffraction [10].

This contradiction seemed to be insuperable and therefore the notion of photon was not accepted by the physical community over almost two decades. "A. Einstein did not even attempt to remove the internal contradictions of his interpretation. He accepted the contradictions as something that, probably, can be understood much later due to entirely new thinking" [8]. The hypothesis of light quanta was considered, in particular, by M. Planck as a misconception, although deserving the forgiveness because of Einstein's other scientific achievements.

However, A. Kompton's experiment revealed that the radiation scattering on electrons is similar to that of a collection of particles having the mass and momentum. Two years later, S. Bose showed that Planck's formula can be obtained without any reference to waves. It is sufficient to suppose that the radiation is a gas of *non-interacting but undistinguished* particles which is not subordinated to the classical statistics of independent events. In other words, the particles, being non-interacting, are *nevertheless statistically dependent.* Then P. Dirac and P. Jordan concluded that it is possible, similarly, if to restrict the consideration with the wave description without the notion "corpuscule", but performing the wave quantization [17]. Finally, it became clear that even the explanation of photoelectric effect does not require the consideration of the radiation as a collection of particles. Thus, it seems that both interpretations are admissible in the radiation theory. However, we have to keep in mind that, contrary to the classical theory, the non-interacting waves as well as non-interacting particles are statistically dependent.

1.2 Duality and Statistical Dependence

It is clear that statistical dependence of two throwing indistinguishing coins means decreasing the probability of failing out of heads (or tails) from 3/4 to 2/3, but what does it mean in the case of the quantized waves or particles? To answer this question, it is convenient to use R. Feynman's formulation of the quantum mechanics via the path integrals [4]. Let us imagine that the particle is in a point A (or the wave amplitude has a value a) at the initial moment, and comes finally into a point B (the wave amplitude accepts a value b). We consider all possible paths connecting the points A and B. In the classical physics, only one trajectory can be realized. If the actual trajectory is spreading, we would no longer be able to talk about the particle. In the quantum mechanics, all geometrically possible trajectories contribute into the path integral. This means that the notion of particle ceases to be definite. However, the notion of the stationary state corresponding to certain energy and obtained by quantization of normal modes of radiation remains definite. In the classical limit, when the energy is high enough, one can connect the stationary states only with *a statistical description* of the normal modes. A stationary state itself is so far from the classical wave, as the Feynman particle is far from the intuitive notion of a particle. In both cases, we have to deal, generally speaking, with a probabilistic description. Feynman's formulation of the quantum mechanics allows explaining the wave properties of the radiation by considering an ideal gas of dynamically independent, but statistically dependent particles. Their dependence, which is taken into account by the Bose-Einstein statistics, reflects the possibility of Feynman's particle "to pass simultaneously" all possible trajectories.

1.3 On the Asymptotic Interpretation of Duality

Then, what is the role of the "wave—particle" duality? Does the discussion relating to this phenomenon should be left only to the historians of science? Such a radical position is not justified, at least because of the phenomenon of the wave packet reduction in the measurement, a meaningful discussion of which continues to this day [39]. But in the context of this article, it is useful to refer also to Einstein's presentation of the mean square fluctuations of the energy and momentum of the radiation [10]. The formulas for these quantities contain the additive contributions, which correspond to the ensemble of the classical waves and the classical ideal gas of particles with energy $h\nu$:

$$(\varepsilon^2) = (Vd\nu)[h\nu\rho + (c/8\pi\nu^2)\rho^2];\ \overline{\Delta^2/\tau} = (1/c)[h\nu\rho + (c^2/8\pi\nu^2)\rho^2]Ad\nu, \quad (1)$$

where

$$\rho(\nu, T) = (8\pi\nu^2/c^2)(h\nu)[\exp(h\nu/kT) - 1]^{-1} \quad (2)$$

is the Planck energy distribution of the thermal radiation over the frequencies at a temperature T per unit volume and unit frequency interval, $\nu-$ the frequency of the radiation, V—the volume of the vessel containing the radiation, c—speed of light, k and h—Boltzmann and Planck constants, respectively, τ- relaxation time, A—the area of the flat, ideally reflecting plate located in the vessel with the radiation at a temperature determined by its walls, and able to move freely in a direction perpendicular to its plane.

It is known that the limit of Planck's formula for the high frequencies and the low temperatures is the Wien distribution:

$$\rho(\nu, T) = a \exp(-b/kT), \tag{3}$$

where

$$a = (8\pi\nu^2/c^2)b; b = h\nu, \tag{4}$$

and at low frequencies and high temperatures—the Rayleigh–Jeans distribution

$$\rho(\nu, T) = (8\pi\nu^2/c^2)(kT). \tag{5}$$

Einstein showed that the wave theory can give only the second terms in the above formulas (1) for the fluctuations of the energy and the momentum. On the other hand, if the radiation consists of an ideal gas of the classical particles with energy $h\nu$, the classical statistics would lead to the appearance of the only first terms in (1). Moreover, each of two first terms can be interpreted as resulting from limiting Wien's expression (3) (classical corpuscular approach) and each of the second terms—from the Rayleigh–Jeans limiting expression (5) (classical wave approximation) [10].

The fact that the relative weights of the two contributions are determined by the frequency of radiation and temperature indicates the asymptotic nature of the particle and wave representations of the radiation, which are subordinated to the classical statistics. Of course, in the high-frequency (low temperature) limit a "quantum trace" remains, but actually only in the magnitude of the particle energy. It is noteworthy that the transition to the Bose-Einstein statistics for the purely corpuscular or pure wave approach is asymptotically equivalent to the integration of the two contributions.

1.4 Coherence and Quantum-Classical Analogy

The quantum-classical analogy, which is discussed below, shows that the problem of the wave-particle duality also manifests in an important class of the classical systems. This allows considering the quantum and classical problems in parallel, and to clarify the asymptotic interpretation of the wave-particle dualism, both qualitatively and quantitatively. Keeping in mind this analogy, let us discuss the limiting transition to the classical particles and waves. The key concept here is coherence. Usually,

the limiting transition from quantum to classical mechanics, according to Bohr's correspondence principle, is due to the presence of a multi-photon excitation, when the transition between the discrete energy levels can be considered as continuous. However, by staying in the framework of the quantum mechanics, we must still keep the appropriate probabilistic estimations corresponding to the multi-photon levels. In other words, the limiting case is not the Newtonian mechanics but the classical statistical mechanics [3]. This is easily seen when dealing with the quantum oscillator. Its multi-photon levels reflect the predominant presence of the oscillator in the region of maximum deviation from the equilibrium. This is valid also for the ensemble of classical oscillators because the maximum deviation corresponds to the minimum velocity.

As for the coherent state which was first constructed by E. Schrödinger for the quantum oscillator in the form of the wave packet, it does not spread because includes all the energy levels which are equidistant [20, 48].The coherent state is close to the classical description of the oscillator as possible. This provides the existence of a limiting transition from quantum mechanics to Newtonian mechanics. The *phase* of the wave function is one of the significant characteristics of the coherent state while in each of the stationary states it remains uncertain. Moreover, it is the phase of the order parameter that prohibits spreading the wave packet. The conjugate to the phase variable in the Heisenberg uncertainty relation is the number of quanta corresponding in this case to the coherent state. This does not lead to a contradiction, while the number of energy levels is infinite, and therefore any restrictions in the uncertainty of the number of photons do not occur. On this basis, R. Glauber developed the method of coherent states [5], which, in fact, generalizes the original Schrödinger's result. However, when one tries to extend the notion of the coherent state to the system, other than the harmonic oscillator, four kinds of difficulties arise. First, the spectrum of energy levels, as a rule, is not equidistant, so that construction of an exact coherent state (in the sense of Glauber) is not possible. The proposed procedures of generalization to the systems with a non-equidistant spectrum do not ensure preservation of all the properties of the exact coherent state, providing its proximity to the classical solution [56]. For example, the wave packet spreads with time, and the product of uncertainties of momentum and position is not constant. Second, these procedures are not applicable if one takes into account nonlinearity that arises in the quantum problem when using self-consistent field method for the dimension reduction. Third, Glauber's approach is directly applicable, when a ground state can be identified. It is not so, e.g., in the case of the spin chain, in spite of the fact that the energy spectrum is equidistant in this case. Finally, for a finite number of energy levels the phase cannot be a characteristic of the process because of the above mentioned uncertainty relation. However, its violation does not preclude the existence of the coherence properties, which are studied, for example, in laser physics, based on a two or three-component model [51]. All this compels to think that the usually considered coherence conditions conceal a more general property. We deal here with the manifestation of the coherence effects in the classical and quantum systems, with infinite and the finite spectra, linear and nonlinear. In a brief form, the idea of generalization can be formulated as follows: "For a fixed number of

particles, when the concept of phase has no sense, coherence manifests in certain correlations between the particles. Moreover, these correlations in the case of an indefinite number of the particles lead to the usual notion of the phase (i.e., *the coherent states of Glauber—(LM)*)" [56].

An analogy between the systems of weakly coupled oscillators (linear and nonlinear) and multi-level quantum systems sheds an additional light on this situation. We briefly describe this analogy considering as an example a two-level quantum system and, correspondingly, the classical system of two weakly coupled oscillators.

2 Two-Level Quantum Systems

In quantum mechanics, an arbitrary state $<s|$ of two-component model can be represented as a superposition of two selected basis states $<1|$ and $<2|$ (6) (see, e.g., [61]):

$$< s| = a_1 < 1| + a_2 < 2|\,, \tag{6}$$

where $a_i(\tau)$—the complex amplitude corresponding to the detection of the system in the j-basis state at time τ ($j = 1, 2$).

Then the value of $a_j(\tau + \Delta\tau)$ for small $\Delta\tau$ can be represented as superposition of the basis states at time τ (the causality principle):

$$a_j(\tau + \Delta\tau) = \delta kj + \frac{\mathrm{i}}{\mathrm{h}} c_{kj}(\tau)\Delta\tau, \tag{7}$$

δ_{kj}—the Kronecker delta, and the fundamental quantum equations $(\Delta\tau \to 0)$ with taking into account (7) have the form:

$$\begin{cases} -i\hbar\frac{da_1}{d\tau} = c_{11}a_1 + c_{12}a_2 \\ -i\hbar\frac{da_2}{d\tau} = c_{21}a_1 + c_{22}a_2 \end{cases} \tag{8}$$

In some special cases coefficients c_{ki} in (8) can be considered as independent of the time, and assume that $c_{12} = c_{21}$ is the real number. The basis states, which form a complete system, usually correspond to partial, well distinguishable subsystems. For example, such subsystems in the hydrogen molecule with two electrons having the opposites spins can describe the states close to the atomic ones, and their superposition describes the molecular (valence) bond. In the ammonia molecule they correspond to nitrogen atoms disposition from one or another side of the plane in which the hydrogen atoms arrange. It is understandable that the basis states, generally speaking, do not coincide with those corresponding to the energy levels.

3 The Classical System of Two Weakly Coupled Oscillators

The classical system of two weakly coupled oscillators with identical masses and close frequencies is described (in the dimensionless form) by the following equations

$$\begin{cases} \frac{d^2u_1}{d\tilde{\tau}^2} + u_1 + 2\beta\varepsilon(u_1 - u_2) = 0 \\ \frac{d^2u_2}{d\tilde{\tau}^2} + (1 + 2\varepsilon\gamma)u_2 + 2\beta\varepsilon(u_2 - u_1) = 0 \end{cases}, \tag{9}$$

where $u_j = \frac{U_j}{L_0}$; $\tilde{\tau} = \sqrt{\frac{c_1}{m}}t$; $2\beta\varepsilon = \frac{c_{12}}{c_1}$; $2\varepsilon\gamma = \frac{c_2 - c_1}{c_1}$, t—time, U_j—the displacement of the particle with number j, m—mass of each particle, c_j—the rigidity of the oscillator, c_{12}—the rigidity of coupling, L_0—the distance between the masses in the absence of the deformation, $\varepsilon \ll 1, j = 1, 2$.

Taking into account the smallness of the parameter ε, for asymptotic analysis of equations of motion (9), it is useful to introduce the complex variables

$$\psi_j = (v_j + iu_j);\ \psi_j^* = (v_j - iu_j), \quad v_j = \frac{du_j}{d\tilde{\tau}},\ j = 1, 2 \tag{10}$$

The equations of motion in the variables (10) take the form:

$$\begin{cases} \frac{d\psi_1}{d\tilde{\tau}} - i\psi_1 - i\varepsilon\beta[(\psi_1 - \psi_1^*) - (\psi_2 - \psi_2^*)] = 0 \\ \frac{d\psi_2}{d\tilde{\tau}} - i[(1 + \varepsilon\gamma)\psi_2 - \varepsilon\gamma\psi_2^*)] - i\varepsilon\beta[(\psi_2 - \psi_2^*) - (\psi_1 - \psi_1^*)] = 0 \end{cases} \tag{11}$$

The method of two-scale expansions allows one to introduce explicitly the "slow time" $\tau_1 = \varepsilon\tau_0$ (alongside with the "fast time" $\tilde{\tau} = \tau_0$).

Then, given that

$$\frac{d}{d\tilde{\tau}} = \frac{\partial}{\partial\tau_0} + \varepsilon\frac{\partial}{\partial\tau_1}, \tag{12}$$

and the unknown solution of Eqs. (11) can be represented by the expansions

$$\psi_j(\tau_0, \tau_1) = \psi_{j,0}(\tau_0, \tau_1) + \varepsilon\psi_{j,1}(\tau_0, \tau_1) + \ldots,\ j = 1, 2, \tag{13}$$

with taking into account relation (12), we obtain in the main asymptotic approximation (see Appendix A):

$$\begin{cases} -i\frac{df_{1,0}}{d\tau_1} + \beta(f_{1,0} - f_{2,0}) = 0 \\ -i\frac{df_{2,0}}{d\tau_1} + \beta[(1 - \gamma/\beta)f_{2,0} - f_{1,0}] = 0 \end{cases}, \tag{14}$$

where $f_{j,0}(\tau_1) = \psi_{j,0}e^{-i\tau_0}$, $j = 1, 2$.

4 The Quantum-Classical Analogy

Thus, in this approximation the classical system is described by the same Eqs. (8) as the two-component quantum system with constant real parameters (14), in which

$$a_i = f_{i,0},\ \hbar = 1,\ c_{11} = \beta,\ c_{22} = \beta(1 - \gamma/\beta),\ c_{12} = c_{21} = -\beta,\ \tau_1 = \varepsilon\tilde{\tau} \quad (15)$$

Consequently, while assuming (15), one can give both classical and quantum interpretation of the solutions of these equations.

If we accept for simplification that $\gamma = 0$, then the stationary states of a two-level quantum system corresponding to the normal modes of a classical system of oscillators satisfy the equation

$$\frac{dA}{d\tau_1} = \alpha_1 A;\ \frac{dB}{d\tau_1} = \alpha_2 B, \quad (16)$$

where $A = a_1 + a_2; B = a_1 - a_2, \alpha_1 = c_{11} + c_{12}, \alpha_2 = c_{11} - c_{12}$.

In the quantum mechanics $A = A_0 e^{i\alpha_1\tau_0}$, $B = B_0 e^{i\alpha_2\tau_0}$ are the new basis states with energies α_1 и α_2, respectively. If the system (16) is prepared in one of these stationary states corresponding to the normal modes of the classical system, it can be remained in this state during infinite time interval. If, however, the system starts the evolution from $f_{1.0}(0)$ ($f_{2.0}(0) = 0$), or $f_{2.0}(0)$ ($f_{1.0}(0) = 0$), we can predict the periodic variation of the transition probabilities between the initial basis states corresponding to the process of beating in the classical system of weakly coupled oscillators. An analogy with well-known I. Rabi oscillations which were initially discovered in the atomic nuclei is evident.

5 Analysis of Two-Component Classical and Quantum Models

Using one of the integrals of the complex system: $N = \left|f_{1,0}\right|^2 + \left|f_{2,0}\right|^2$, we introduce new real variables

$$f_{i,0} = \sqrt{N}\,\cos\theta \cdot e^{i\delta_1},\ \ f_{2,0} = \sqrt{N}\,\sin\theta \cdot e^{i\delta_2}. \quad (17)$$

The time evolution equations in the variables (17) take the form

$$\frac{d\theta}{d\tau_1} = \beta\,\sin\Delta$$
$$\sin 2\theta \frac{d\Delta}{d\tau_1} = 2\beta\,\cos 2\theta\,\cos\Delta, \quad (18)$$

where $\Delta = \delta_1 - \delta_2$, and have integral $H_0 = \beta\,\cos\Delta\,\sin 2\theta$.

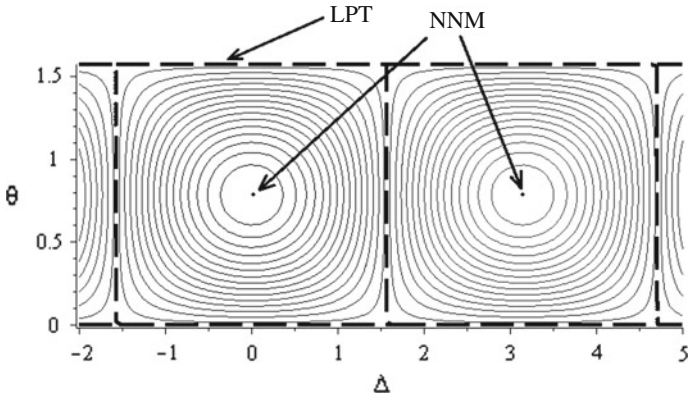

Fig. 1 The phase plane of the variables Δ, θ

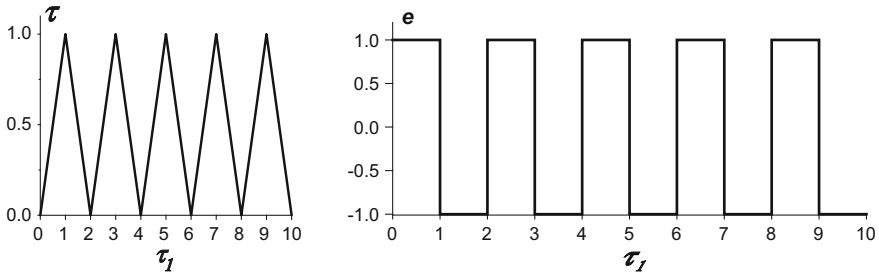

Fig. 2 Time dependence of non-smooth variables

The stationary states of a quantum system (the normal modes of the system of weakly coupled classical oscillators) are the *stationary points* of the phase plane, corresponding to the system (18), which are shown in Fig. 1.

The maximum possible energy exchange between the initial basis states or oscillators (in the classical interpretation) and, therefore, the periodic change of probabilities (in the quantum interpretation) is described by the *limiting phase trajectory* (LPT), which is maximally distant from the stationary points (Fig. 1). The time dependences of the input variables, through which the LPTs can be naturally expressed, are shown in Fig. 2.

To keep the analogy with the classical systems, we assign the term "quantum particle" to each of the original basis states, the linear combinations of which determine the stationary state ("collective" or "wave" excitation). The change in the initial conditions in classical and quantum problems leads to possibility of a transition from the wave (normal mode or stationary state) to a "particle" representation of the process in terms of the LPTs. The feasibility of such a transition is confirmed by the very simple behavior of LPT in time in adequate non-smooth variables: $\theta = \frac{\pi}{2}\tau(\tau_1),\ \Delta = \frac{\pi}{2}e(\tau_1)$ presented in Fig. 2. (see also Appendix B).

This behavior corresponds to the oscillations of a classical particle between rigid walls. Since the function $\theta(\tau_1)$ characterizes actually the ratio of the excitation intensities of the oscillators, its profile gives a fair representation of the energy exchange with some period in slow time (see Appendix B). In the two-level quantum systems, this function describes the periodic dominance of each of the basis states. In the above example with the hydrogen molecule, we are talking about the states in which the electron with a preassigned spin is localized near one or other proton. Measurement at a certain time detects the system in the certain basis state with probability that is expressed in the terms of the saw-tooth function $\theta(\tau_1)$. The described approach is adequately presented in terms of the LPTs with using the non-smooth basis functions. This approach can be naturally extended to nonlinear systems, where the principle of superposition is already not valid.

Note that possible temporal dependence of the parameters of the system in the classical system of weakly coupled oscillators means a change in the elastic and inertial properties. In the quantum case it corresponds, e.g., to the presence of the constant (in time) field. Then the irreversible energy exchange between the classical oscillators, or the quantum tunneling by the well-known Landau-Zener mechanism can be realized [18, 65]. The quantum-classical analogy allows the manifestation of a new type of the energy traps in which an irreversible energy transfer is achieved due to the relatively slow passage through the resonance of the classical system [14, 16, 36].

6 Linear Multi-level System

Our approach to the time-dependent dynamics is naturally extended to the linear systems with many degrees of freedom (oscillatory chains), but we deal here with the "coherence domains" instead the weakly interacting oscillators. The "coherence domains" are formed due to crowding the frequency spectrum near the maximum frequency (Fig. 3), and they include some set of the real particles. With an increase in the number of particles in the oscillatory chain, the number of resonant normal modes, the combination of which forms the coherence domain, also increases.

Figure 4 shows an intense energy exchange between the coherence domains corresponding to the motion over the LPT. In this case each *coherence domain* includes ten real particles. In essence, we are talking about the extension of the concept of the beats to the linear systems with many degrees of freedom. Obviously, the similar results can be obtained for a multi-level quantum system with constant parameters. For example, a number of equidistant (or close to it), i.e., co-resonant levels can coexist with non-equidistant levels. This is the case in the problems of the propagation of the electronic or magnetic excitations in the finite periodic structures in the presence of external fields (respectively, a constant electric field or magnetic field with a constant gradient). In the infinite periodic structures, the electronic and magnetic energy spectra are equidistant [11, 63] but a ground state is absent. Therefore, in this case the Glauber approach is not applicable. However, one can consider that an electron

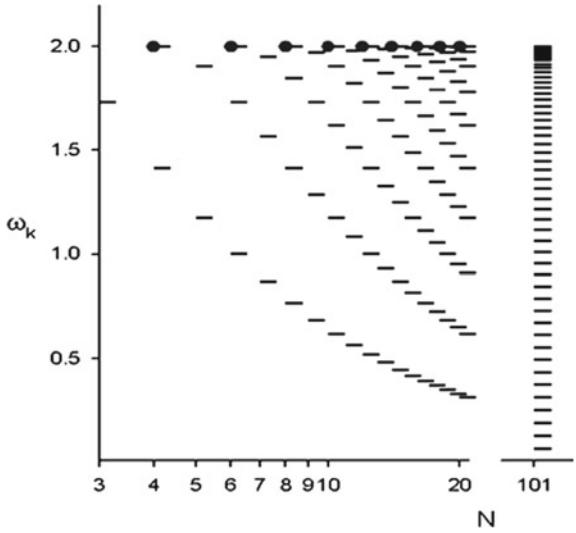

Fig. 3 Crowding of the frequency spectrum with an increase of the number of particles in the linearized system (oscillatory chain with periodic boundary conditions). All modes, except the lowest (not shown, because it has zero frequency) and the mode with the maximum frequency, are double degenerate

moving in a periodic lattice under the influence of a constant electric field is in the coherent state corresponding to the Bloch oscillations (contrary to transitional movement in the absence of a field or a periodic potential). Their frequency depends on the field [49]. In the case of a finite periodic structure, the spectrum is not equidistant. However, then the electronic and magnetic systems can allocate a certain number of co-resonant energy levels [6, 9]. Therefore, the mathematical analogy between the multi-dimensional classical and quantum problems in this case is preserved.

We can say that the seemingly various interpretations of wave-particle duality can come close if we consider that the "wave" approach of Planck, Dirac, and Jordan deals actually with the statistically dependent waves, as well as the "corpuscular" approach S. Bose and A. Einstein deals with statistically dependent particles. However, while the basic variables are selected as dynamically and statistically independent (or almost independent) elementary excitations, they, by necessity, are almost the "wave-like" in the one region of the spectrum, and almost the "particle-like"—in another region. The "wave-particle" duality in this sense is an asymptotic concept with a specific physical and mathematical content, including the notions of "coherence domains" and "limiting phase trajectories."

It is noteworthy that the quantum-classical analogy "works" not only in the abovementioned case of the linear systems with variable parameters [14, 16]. It also holds for nonlinear chains (including the oscillators, weakly interacting with the external field [28, 37, 57, 60]), when the manifestation of the coherence is supplemented by an intermodal interaction.

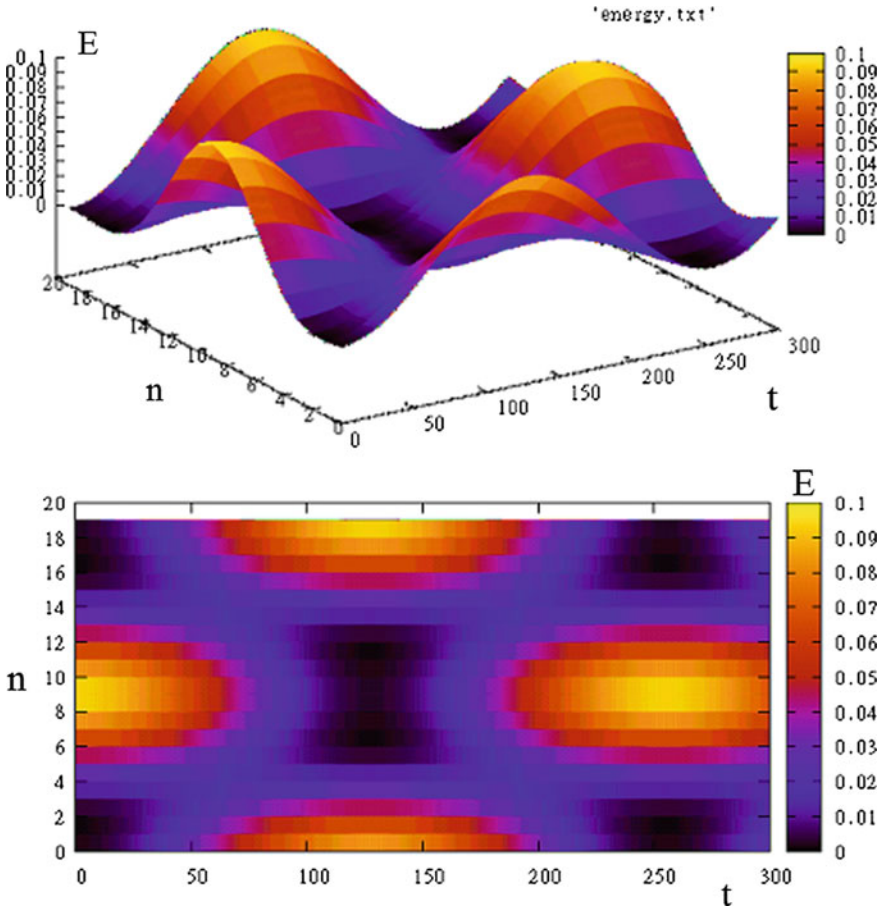

Fig. 4 Energy exchange between the effective particles: upper graph—the energy (vertical) as a function of time and number of particles, the lower graph—a section of the energy surface

7 Nonlinear Systems

In the nonlinear case, as in the linear approximation, an adequate understanding of the intense energy exchange is achieved with the introduction of "coherence domains", whose dynamics is described by the LPTs. In addition, a transition from energy transfer to energy localization can be naturally explained in the terms of LPTs [28, 57]. In essence, this approach reveals also the physical nature of breathers formed in the oscillatory chain with a large number of particles, in particular, in the polymer chains (see, for example, [12, 35]). At the same time, there is a range of the initial conditions, exposure to which determines the applicability of the wave language (NNMs). Let us dwell on the classical nonlinear system—the finite periodic Fermi-Pasta-Ulam (FPU) chain with Hamilton function

$$H = \sum_{j}^{N} \frac{P_j^2}{2m} + V(Q_{j+1} - Q_j)$$
$$V(x) = \frac{1}{2}x^2 + \frac{\alpha}{3}x^3 + \frac{\beta}{4}x^4$$
$$Q_{N+1} = Q_1 \tag{19}$$

The number of particles in (19) is assumed to be even. To simplify the calculations, we assume that $\alpha = 0$. The generalization to the asymmetric system is given in [57, 59]. The strong coupling between the particles induces, as usual, the transition to the normal coordinates with using the canonical transformation (see Appendix C).

The frequencies of the linearized system are defined by the relation $\omega_k = 2\sin(\frac{\pi k}{N}), \quad k = 0, \ldots, N-1$, and the quadratic and quartic components of the Hamiltonian take the form shown in Appendix C.

As in the case of two-dimensional systems, we introduce the complex variables and rewrite the dynamic equations in complex form:

$$\Psi_k = \frac{1}{\sqrt{2}}\left(\frac{d\zeta_k}{dt} + i\omega_k\zeta_k\right), \quad \Psi_k^* = \frac{1}{\sqrt{2}}\left(\frac{d\zeta_k}{dt} - i\omega_k\zeta_k\right) \tag{20}$$

The equations of motion in the variables (20) can be written as follows:

$$i\frac{d\Psi_k}{dt} + \omega_k\Psi_k - \frac{\beta}{8N}\omega_k \sum_{l,m,n=1}^{N-1} C_{k,l,m,n}(\Psi_l - \Psi_l^*)(\Psi_m - \Psi_m^*)(\Psi_n - \Psi_n^*) = 0 \tag{21}$$

The original formulation of the problem does not contain a small parameter, and it would seem that we cannot expect a possible generalization of the above results to the multidimensional case. However, as it was mentioned above, with the increase of the particles number a densification of the frequency spectrum in its upper part is observed. Mathematical reflection of this fact is the appearance of the quantity 1/N in the formula for the natural frequencies, which will be considered as a small parameter appropriate for construction of the asymptotic expansion corresponding to Eq. (21). A quantum analogue of the considered classical model is a non-linear multi-level quantum system.

Presentation of the frequencies $\omega_{\frac{N}{2}\pm1}$ in the form:

$$\omega_{\frac{N}{2}\pm1} = 2\sin\left[\frac{\pi}{N}\left(\frac{N}{2} \pm 1\right)\right] = 2\cos(\frac{\pi}{N}) \approx \omega_{\frac{N}{2}}\left[1 - \frac{1}{2}\left(\frac{\pi}{N}\right)^2\right], \tag{22}$$

where $\omega_{\frac{N}{2}}$—the upper limit frequency in the first Brillouin zone, confirms the spectrum densification at higher frequencies with increasing the number of particles, which is also clearly seen in Fig. 3.

In accordance with the procedure of the multi-scale expansions we supposed that

$$\Psi_k = \varphi_k e^{i\omega_k t} \quad \varphi_k = \sqrt{\varepsilon}(\chi_{k,1} + \varepsilon\chi_{k,2} + \varepsilon^2\chi_{k,3} + \ldots), \quad \tau_0 = t;\ \tau_1 = \varepsilon t;\ \tau_2 = \varepsilon^2 t;\ \varepsilon = 1/N \tag{23}$$

The further calculations starting from relations (23) are presented in Appendix A for the simplest example of weakly coupled linear oscillators.

We write the dynamic equations of the main asymptotic approximation for the highest-frequency mode and two closest in frequency modes of the spectrum (22) (it is clear that such a restriction is possible due to much weaker coupling with other modes)

$$\begin{gathered} i\tfrac{d\chi_{N/2}}{d\tau_2} + \tfrac{3\beta}{4}[|\chi_{N/2}|^2\chi_{N/2} + 2(|\chi_{N/2-1}|^2 + |\chi_{N/2+1}|^2)\chi_{N/2} + \\ (\chi_{N/2-1}^2 + \chi_{N/2+1}^2)\chi_{N/2}^*] = 0 \\ i\tfrac{d\chi_{N/2-1}}{d\tau_2} - \tfrac{\pi^2}{2}\chi_{N/2-1} + \tfrac{3\beta}{8}[(4|\chi_{N/2}|^2 + 3|\chi_{N/2-1}|^2 + \\ 2|\chi_{N/2+1}|^2)\chi_{N/2-1} + (2\chi_{N/2}^2 + \chi_{N/2+1}^2)\chi_{N/2-1}^*] = 0 \\ i\tfrac{d\chi_{N/2+1}}{d\tau_2} - \tfrac{\pi^2}{2}\chi_{N/2+1} + \tfrac{3\beta}{8}[(4|\chi_{N/2}|^2 + 3|\chi_{N/2+1}|^2 + \\ 2|\chi_{N/2-1}|^2)\chi_{N/2+1} + (2\chi_{N/2}^2 + \chi_{N/2-1}^2)\chi_{N/2+1}^*] = 0 \end{gathered} \tag{24}$$

$$X = |\chi_{N/2}|^2 + |\chi_{N/2+1}|^2 + |\chi_{N/2-1}|^2 = const$$

Here we omit the second indices of the functions corresponding to the main asymptotic approximation.

The transition from the waves to the coherence domains is implemented through the change of variables

$$\begin{aligned} \psi_1 &= \frac{\chi_{N/2}}{\sqrt{2}} - \frac{\sqrt{1-2c^2}}{\sqrt{2}}\chi_{N/2-1} - c\chi_{N/2+1} \\ \psi_2 &= \frac{\chi_{N/2}}{\sqrt{2}} + \frac{\sqrt{1-2c^2}}{\sqrt{2}}\chi_{N/2-1} + c\chi_{N/2+1} \\ \varphi &= \sqrt{2}c\chi_{N/2-1} - \sqrt{1-2c^2}\chi_{N/2+1} \end{aligned} \tag{25}$$

In fact, transformation (25) is a natural generalization of the above presented procedure for two weakly coupled oscillators for Eq. (24). The account of the three (not two) modes associates with the degeneracy of the normal modes which are close in frequency to the upper boundary of the spectrum. Parameter "c" reflects the ratio of the degenerate modes contributions in the initial conditions and varies from zero to unity, but it is not present in the equations of motion for the coherence domains.

Preserving the invariant magnitude $X = |\psi_1|^2 + |\psi_2|^2 + |\varphi|^2$, we consider for definiteness the case $\varphi = 0$. Since this invariant quantity is the integral of motion in the slow time, the variables ψ_1 and ψ_2 can be expressed in terms of the angular variables:

$$\psi_1 = \sqrt{X}\,\cos\theta\, e^{i\delta_1};\quad \psi_2 = \sqrt{X}\,\sin\theta\, e^{i\delta_2}. \tag{26}$$

Then the Hamiltonian in the variables (26) takes the form:

$$H(\theta,\Delta) = \frac{X}{64}\big[27\beta X - 16\pi^2 + 2(8\pi^2 - 3\beta X)\cos\Delta\,\sin 2\theta - 3\beta X(8-\cos^2\Delta)\sin^2 2\theta\big], \tag{27}$$

where $\Delta = \delta_2 - \delta_1$.

The equations of motion corresponding to Hamiltonian (27) are written as follows

$$\frac{d\theta}{d\tau_2} + \frac{1}{32}[8\pi^2 - 3\beta X(1-\cos\Delta\,\sin 2\theta)]\sin\Delta = 0$$
$$\sin 2\theta\frac{d\Delta}{d\tau_2} - \frac{1}{32}\cos 2\theta[(8\pi^2 - 3\beta X)\cos\Delta - 3\beta X(8-\cos^2\Delta\,\sin 2\theta] = 0 \tag{28}$$

Let us consider the phase trajectory that characterizes the transition between the states ψ_1 ($\theta = 0$) в ψ_2 ($\theta = \pi/2$). This trajectory, which has two branches, encloses the family of trajectories encircling the stationary points. This is the LPT as well as in the case of two weakly coupled oscillators.

The corresponding temporal process leads to complete energy exchange between two *coherence domains*. These time dependences clearly demonstrate the adequacy of the concept of *coherence domains* and *LPTs.*

The graphs in Figs. 5, 6, 7, 8, 9 demonstrate the evolution of the phase plane with an increase in the nonlinearity parameter, which in this case is denoted as βX. They also illustrate the transition from the intense energy transfer to the energy localization. The first transition mentioned in the captions is associated with the dynamic instability of the boundary normal mode, followed by the birth of two new stable normal modes, and the separatrix separating them. The full energy exchange between the *coherence domains*, which is described by LPT, still remains possible. The second transition occurs at the coincidence of the separatrix and the LPT, which leads to the impossibility of the full energy exchange. As a result, one can observe dominant energy localization on the excited *coherence domain*. The formation of a mobile localized excitation (prototype of a breather in the infinite oscillatory chain) [28, 57–59] also becomes possible.

In the case corresponding to Fig. 5, a periodic FPU chain contains ten particles, from which the two *coherence domains* are formed. The mutual energy exchange is described by LPT. Under initial conditions which are distant from the resonant normal modes, the behavior of the system is adequately described in terms of weakly interacting non-resonating normal modes exhibiting no coherence.

The system shows a complete energy transfer between the *coherence domains* that occurs in spite of the bifurcation of the stationary state corresponding to instability of the boundary normal mode, with the appearance of the new stable stationary points and the separatrix, which encircles them.

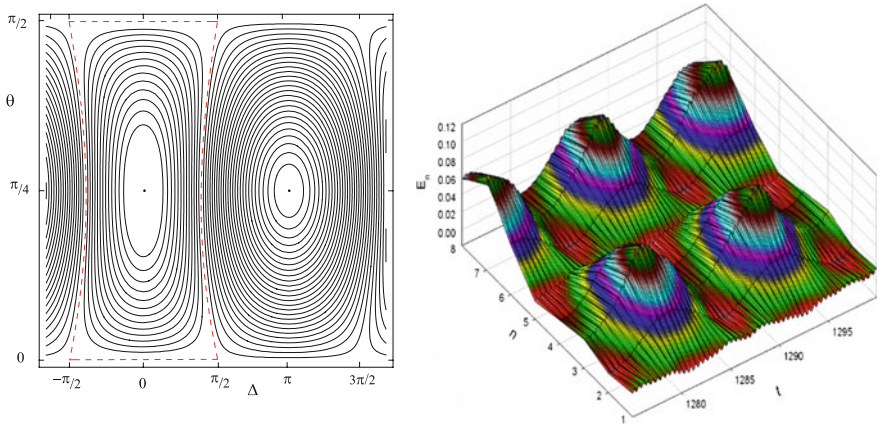

Fig. 5 The energy between the coherence domains before the first dynamical transition

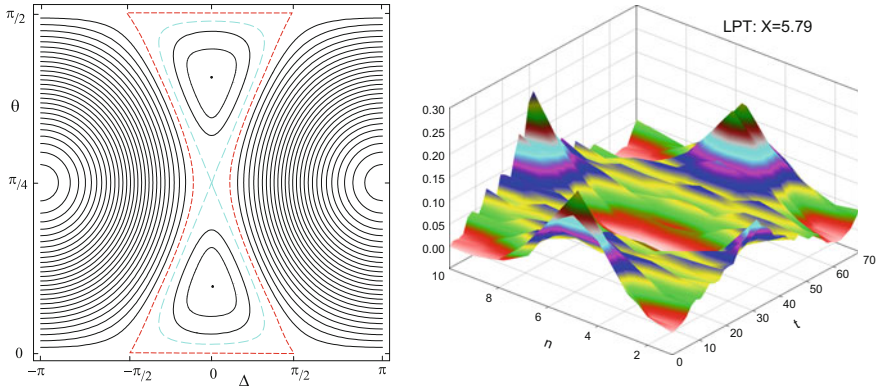

Fig. 6 The energy exchange between the coherence domains after first but before second dynamical transition

The possibility of the energy transfer along the chain is demonstrated in Fig. 9. In fact, alongside with the localized stationary excitation (mobile NNM), similar to the breather with a constant profile in the infinite FPU chain one can observe a localized nonstationary excitation (mobile LPT) with the breather with breathing profile. It turns that the conditions for mobility of both stationary and nonstationary localized excitations are the same, and they correspond to the second dynamical transition. In this connection, we recall some parallels between the classical nonlinear field theory and the quantum field theory. A.B. Migdal's conclusion [40]: "A wonderful idea to take a particle as the quantum states of some field was found to be extremely fruitful; the field is a primary concept" [39] has an important analogy with the classical continuum dynamics. As it is well known, the excitations of a nonlinear material field are not only the periodic waves but also the particle-like waves—solitons, e.g., the

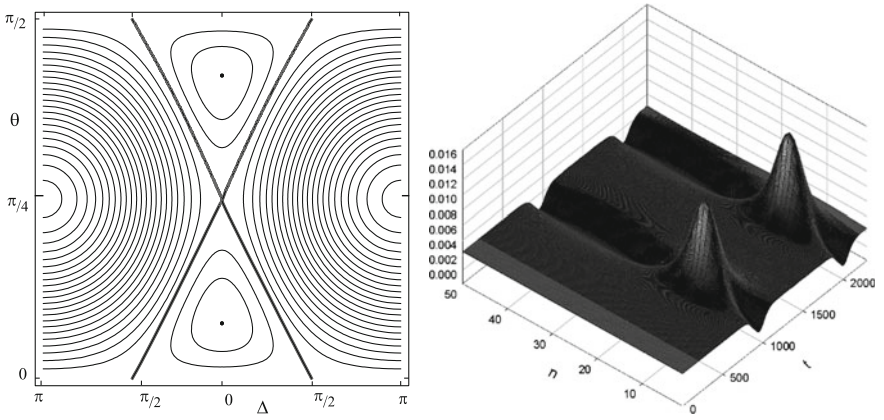

Fig. 7 The second dynamic transition in the periodic FPU chain, consisting of fifty particles. The separatrix becomes the LPT, and a full energy exchange between the coherence domains becomes impossible

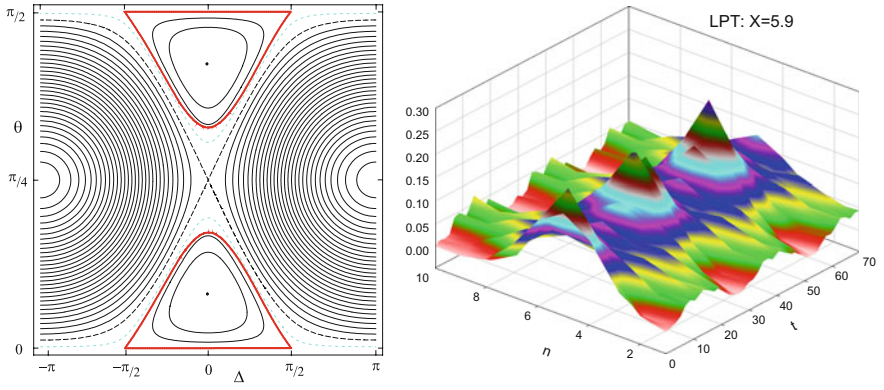

Fig. 8 The energy localization on the excited coherence domain is clearly seen

solitons of the Korteweg-de Vries (KdV) or nonlinear Schrödinger equation (NSE) [2, 43, 55]. However, the consideration of solitons and breathers in terms of particles, not just localized waves (i.e., the use of the classical "wave-particle" duality) is extremely useful in the dynamic and thermodynamic problems [2, 55]. Also, this can be applied to the non-integrable models of nonlinear physics, in particular, the polymer physics [21, 27, 32–35, 41, 53, 54, 64]. The analogy between quantum theory and classical nonlinear field theory can be extended up to the existence of a classical tunneling [42].

The analysis of the finite periodic systems introduces important additional information into these concepts. In this case, as shown above, there are two energy thresholds. They define respectively the instability of the boundary normal mode and merge of LPT with the separatrix which encircles the new stationary points

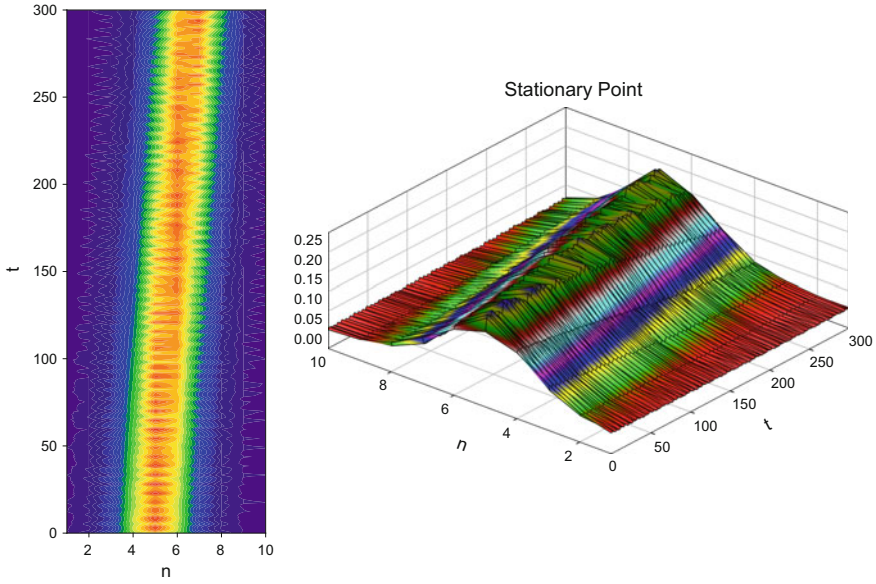

Fig. 9 The mobility of localized excitations (breather analog in the infinite chain) after the second dynamic transition

(NNMs) of new normal modes produced by the bifurcation of the boundary mode. However, the energy thresholds disappear, when the number of the particles as well as the resonances, goes to infinity; and thus it becomes possible an alternative, continuum approach. In this limit, one can use the inverse scattering method [43] in the long-wavelength and short-wavelength approximation (modified KdF and NSE, respectively). But then we cannot identify the stage of the intense energy exchange and the transition to the energy localization, which is specific only for the finite systems. Thus, the physical aspect of the formation of a localized excitation (a weak interaction between the *coherence domains*) remained to be unclarified. Prior to the limiting transition this aspect is crucial, and the concept of the *coherence domains* and *LPT* can describe analytically the intense energy exchange and localization in the finite chains of weakly interacting oscillators (Appendix D).

Note again that the quantum analogue of classical models represents a non-linear multi-level quantum system, in which the emergence of non-linearity is a consequence of the self-consistency procedure (see Appendix E).

The considered LPTs in the conservative systems with constant parameters are not attractors, and in the presence of dissipative factors they occur only at certain stages of non-stationary processes. However, as shown by the analysis of damped Duffing oscillator under biharmonic excitation [60] and weakly coupled self-sustained (Van der Pol—Duffing) oscillators [38], their role in the formation of strongly nonlinear steady-state oscillations in the systems with dissipation can be decisive.

As for the possibility of attractor-like behavior of LPT in the quantum case it is actually implemented in the super-radiant transition between two energy levels, which interact via an electromagnetic field [51].

8 Conclusion

Thus, the "wave—particle" duality in both quantum and classical physics can be viewed as an asymptotic concept, allowing the effective analysis of the energy exchange, localization and transfer in the terms of the *coherence domains* and *LPTs*.

Due to the important role in this concept, the notion of the *coherence domain* should be clarified once more. The discussion of the mechanism of the intensive energy exchange and the transition to the energy localization requires first of all identifying the elementary excitations in the considered system.

In the gaseous media they are almost *free motions of weakly interacting particles* (atoms or molecules), which are involved in the almost free motion. In the oscillatory chain, as in all crystalline solids, the particles interact strongly. In this case the *weakly interacting NNMs of the oscillatory chain as a whole* can be considered as elementary excitations. However, as already noted, with an increase in the number of the particles the resonance relations between the certain frequencies arise. Under strongly asymmetric initial conditions, corresponding to a combination of the resonating normal modes, this leads to the appearance of the *coherence domains*. As a result, the resonating NNMs cannot be considered as the elementary excitations. In a system of two weakly coupled oscillators with strongly asymmetric initial conditions the elementary excitations are the motions of the particles themselves, similarly to the case of the gaseous medium. Their bias can be represented as the sum and the difference of the modal variables; corresponding motion is beating. When the number of the particles increases, in the presence of resonant modes *a motion of the coherence domains,* including a certain number of the real particles, can be considered as the elementary excitation. Its bias (similar to that for two weakly coupled oscillators) is constructed as combination of modal variables. The coupling between the introduced *coherence domains* is weak, although the original equations of motion may not contain a small parameter. Thus, the concept of the beats can be extended to multidimensional systems. In addition, the introduction of the *coherence domains* and LPTs allows an adequate description of the transition from the intense energy exchange to the energy localization with increasing the excitation intensity. Thus, it is possible to trace a connection of discrete models with continuous systems, having localized solutions (breathers). We note that an increase in the number of the resonant modes means that the spatial extent of *coherence domain* is reduced, and it approaches to the profile, typical for the breather in the infinite chain. An increase in the number of such particles occurs when the resonant mode nearest to the boundary of the spectrum is "uninhabited." Of course, outside the intermodal resonance and the coherence manifestation, the wave language is quite adequate. In the terms of

the *coherence domains* and LPTs, a simple analytic description of the intense energy exchange with the use of non-smooth functions can be obtained.

Quantum-classical analogy essentially extends the understanding of the role of coherence, which was initially considered in the classical optics and then was essentially clarified in the quantum theory, first of all in Glauber's method of the coherent states. Contrary to the classical optic fields, for which a partial coherence is typical, this method deals with the complete coherence and can be rarely seen in the textbooks, mainly as an example of non-stationary quantum process. The extension to the case of the non-homogeneous spectrum opens a possibility to apply efficiently the quantum-classical analogy for the study of the non-stationary processes in both classical and quantum systems (linear and nonlinear). As an example, one can mention the Bose-Einstein condensation (BEC), the Landau-Zener tunneling (LZT) [13–15, 52], the superconducting currents in the finite chains of the Josephson junctions [2, 52]. There is a significant difference between the classical and quantum systems in this context. In the former case, the energy exchange as well as the energy localization occurs in a slow time scale as modulations of boundary normal mode. In the latter case, there is no any carrier wave, and the slow time of classical system is the only time scale here. The non-stationary processes and their qualitative change due to an increase of the nonlinearity parameter or to a decrease of the coupling parameter are described in this time scale.

Let us stop once more on the possible interpretation of the wave-particle duality in the quantum statistics. As it is well known, and we have discussed this in connection with Einstein's representation of the energy and momentum fluctuations, the high-frequency and low temperature limit of Planck's distribution correspond to ideal classical gas of distinguishable particles. Certainly, such systems obey the Boltzmann statistics. Meanwhile, Bose's hypothesis of particles identity leads to the Planck distribution. The question is: what is an interpretation of the high-frequency expansion of the Planck distribution, in which the terms following to the Wien law (one, two, etc.) are taken into account? The main term corresponds to the classical ideal gas of the distinguishable particles. Taking into account all terms of the expansion, one deals with the quantum gas of the non-distinguishable particles, but what is a possible interpretation of the intermediate cases? Apparently, the only possible, although unexpected way out is a decrease of the degree of distinguishability with an increase of the number of the terms in the expansion. Such an increase means formally the growth of the statistical dependence of the particles. When the number of the terms in the expansion goes to infinity, one deals with the gas of the absolutely undistinguishable particles with the maximum possible statistical dependence. This fact is coordinated with resolving the well-known Gibss paradox. The paradox relates to the existence of the entropy jump after mixing of the gases consisting of the particles with slightly different characteristics (but this is not true in the limiting case of absolutely identical particles). Resolving of the paradox assumes the existence of partially distinguishable internal states and a possibility of the continuous change of the parameters characterizing the distinguishability [7]. Evidently, the reason of the "tendency to indistinguishability" is a modification of the "particle" properties of the ideal gas at the expense of the wave properties describing by the next terms of the

expansion. From the other side, one can begin from the low-frequency and the high temperature limit, corresponding to the "gas of normal waves". Then, the next terms of the expansion provide a modification of the "wave" properties at the expense of "particle" properties

The low-frequency and high-frequency limits can be used for construction of the two-point Pade-approximate (see, e.g., [1]), which coincides exactly with the Planck distribution (in fact, he has come to his famous result namely by this manner). However, in spite of the fact that the both limits can be obtained with using the classical statistics assuming complete distinguishability of its objects, the corresponding Pade-approximate describes indistinguishable objects, which obey the Bose-Einstein statistics. The wave-particle duality is, in essence, a payment for the use of the classical language of the particles and waves. In the asymptotic interpretation, this means the applicability of the Maxwell–Boltzmann statistics. Surprisingly, this fact is not recognized by certain contemporary physicists. Thus, the author of the instructive book [44] writes about "outrageous Einstein's mistake" in his first paper devoted to quanta: "he has come to the interpretation of the black body radiation as a gas of the light quanta basing on Wien's law instead the Planck law". But the quantum properties of the radiation dominate just in that frequency and temperature ranges, where Wien's law is the adequate approximation of the Planck distribution!

We underline that using the asymptotic interpretation of the wave-particle duality gives the mathematical meaning to the quantum-classical analogy and spreads the area in which it turns out to be an efficient analytical tool up to study of the statistical aspects of classical physics which are significant for thermodynamics [29].

Acknowledgements This work is supported by the Russian Science Foundation under grant 16-13-10302.

Appendix A

In accordance with the procedure of the multi-scale expansions we suppose (see, e.g., [25])

$$\psi_j(\tau_0, \tau_1, \ldots) = \psi_{j,0}(\tau_0, \tau_1,) + \varepsilon\psi_{j,1}(\tau_0, \tau_1, \ldots) + O(\varepsilon^2), \;\; j = 1, 2.$$
$$\tilde{\tau} = \tau_0; \;\; \tau_1 = \varepsilon\tau_0, \ldots$$
$$\frac{d}{d\tilde{\tau}} = \frac{\partial}{\partial\tau_0} + \varepsilon\frac{\partial}{\partial\tau_1} + O(\varepsilon^2)$$

$$
\begin{aligned}
&O(1): \frac{\partial \psi_{j,0}}{\partial \tau_0} - i\psi_{j,0} = 0 \rightarrow \psi_{j,0} = f_{j,0}(\tau_1, \ldots)e^{i\tau_0},\ j = 1, 2\\
&O(\varepsilon): \frac{\partial \psi_{1,1}}{\partial \tau_0} - i\psi_{j,1} + \frac{\partial f_{1,0}}{\partial \tau_1}e^{i\tau_0} - i\beta[(f_{1,0}e^{i\tau_0} - f^*_{1,0}e^{-i\tau_0}) -\\
&\qquad (f_{2,0}e^{i\tau_0} - f^*_{2,0}e^{-i\tau_0})] = 0;\\
&\frac{\partial \psi_{2,1}}{\partial \tau_0} - i(\psi_{2,1} + \gamma\, f_{2,0}e^{i\tau_0} - \gamma\, f^*_{2,0}e^{-i\tau_0}) + \frac{\partial f_{2,0}}{\partial \tau_1}e^{i\tau_0}\\
&-i\beta[(f_{2,0}e^{i\tau_0} - f^*_{2,0}e^{-i\tau_0}) - (f_{1,0}e^{i\tau_0} - f^*_{1,0}e^{-i\tau_0})] = 0;
\end{aligned}
\tag{29}
$$

The condition of the absence of the secular terms leads to the equations of the principal asymptotic approximation:

$$
\begin{cases}
-i\frac{df_{1,0}}{d\tau_1} + \beta(f_{1,0} - f_{2,0}) = 0\\
-i\frac{df_{2,0}}{d\tau_1} + \beta[(1 - \gamma/\beta)f_{2,0} - f_{1,0}] = 0
\end{cases}
\tag{30}
$$

Exclusion of the secular terms is equivalent to averaging over the fast time.

Appendix B

Non-smooth variables were used in connection with the elaboration of the method of non-smooth transformation for analysis of vibro-impact or close to them systems [31, 46, 47, 62]. Far going extension of this method was presented in [46]. It turned out unexpectedly [21, 22] that functions $\tau(\tau_1)$, $e(\tau_1)$ describe adequately the intensive energy exchange in the systems, very different from the vibro-impact ones by both their physical content and original mathematical formulation. They describe the beats by the most simple and obvious manner due to the choice of the appropriate non-smooth variables $\tau(\tau_1)$, $e(\tau_1)$.

The form) of the solution corresponding to LPT leads naturally to introducing the saw-tooth time. After such transformation the solution is described by the smooth functions of the non-smooth time (see Appendix D).

Appendix C

The canonical transformation of the variables for the periodic FPU chain has a view [50]:

$$Q_j = \sum_{k=0}^{N-1} \sigma_{j,k}\zeta_k$$

$$\sigma_{j,k} = \begin{cases} \frac{1}{\sqrt{N}}, & k = 0 \\ \sqrt{\frac{2}{N}}\sin\left(\frac{2\pi kj}{N} + \gamma\right), & k = 1, \ldots \left[\frac{N-1}{2}\right] \\ \frac{(-1)^j}{\sqrt{N}}, & k = \frac{N}{2} \\ \sqrt{\frac{2}{N}}\cos\left(\frac{2\pi kj}{N} - \gamma\right), & k = \frac{N}{2}+1, \ldots, N-1 \end{cases} \tag{31}$$

$$\gamma = \tfrac{\pi}{4}$$

$$\sigma_{j,k} = \tfrac{1}{\sqrt{N}}\left[\sin\left(\tfrac{2\pi kj}{N}\right) + \cos\left(\tfrac{2\pi kj}{N}\right)\right]$$

The quadratic and quartic constituents of the Hamilton function in the normal coordinates of the linearized system are written as follows

$$H_2 = \sum_{k=1}^{N-1} \frac{1}{2}(\eta_k^2 + \omega_k^2\xi_k^2)$$

$$H_4 = \frac{\beta}{8N} \sum_{k,l,m,n=1}^{N-1} \omega_k\omega_l\omega_m\omega_n C_{k,l,m,n}\xi_k\xi_l\xi_m\xi_n$$

$$C_{k,l,m,n} = -\Delta_{k+l+m+n} + \Delta_{k+l-m-n} + \Delta_{k-l+m-n} + \Delta_{k-l-m+n} \tag{32}$$

$$\Delta_r = \begin{cases} (-1)^r, \ if \ r = mN, \ m \in \mathrm{Z} \\ 0 \qquad\quad otherwise. \end{cases}$$

Appendix D

The advantages of the techniques based on the use of the non-smooth variables are evident while dealing with the nonlinear beats (see Appendix B). They can not be presented as linear combination of NNM because the superposition principle is not valid in this case. It was shown earlier [21–24, 26, 30, 50], that an efficient temporal description of LPT in nonlinear chains is attained in the terms of the non-smooth functions of slow time $\tau(\tau_2)$, $e(\tau_2)$. They are plotted in Fig. 2 where $\tau(\tau_1)$ has to be changed to $\tau(\tau_2)$ and $e(\tau_1)$ to $e(\tau_2)$.Then the dependent variables can be presented as [47]

$$\theta = X_1(\tau) + Y_1(\tau)e\left(\frac{\tau_2}{a}\right), \quad \Delta = X_2(\tau) + Y_2(\tau)e\left(\frac{\tau_2}{a}\right) \tag{33}$$

After substitution into the equations of motion of the effective particles one obtains the equations with respect to smooth functions of non-smooth variables $X_i(\tau)$, $Y_i(\tau)$; $i = 1, 2$.

The possibility of similar substitutions is based on the statement that every periodic process, independently on the class of its smoothness, is expressed by the unique manner as an element of the algebra of hyperbolic numbers through the variables τ и e [62]:

$$x(\tau_2) = x(\tau, e) = X(\tau) + e\,Y(\tau), \quad e(\tau_2) = \frac{d\tau}{d\tau_2}. \tag{34}$$

where $X(\tau) = \frac{1}{2}[x(\tau) + x(2 - \tau)]$, $\quad Y(\tau) = \frac{1}{2}[x(\tau) - x(2 - \tau)]$ so, that $x\,(\tau, e) \equiv x(\tau) + e\,Y(\tau\,(t), e\,(t))$.

At that, the pair $\{1, e\}$, where $e^2 = 1$ is a basis, and the algebraic operations as well as differentiation or integration over time preserve the structure of hyperbolic number. This property provides applicability and convenience of the corresponding transformations while solving the differential equations [47].

Interestingly that the hyperbolic numbers which are frequently used for a simplest illustration of the Clifford algebra, were known from the middle of XIX century as abstract mathematical objects without any connection with vibration processes. On the other side, the elliptic complex numbers with the basis $\{1, i\}$ ($i^2 = -1$) and corresponding trigonometric functions turned out, in essence, the main tool for the description of such processes.

The analytical presentation of the solution for the FPU chain in the terms of power series over slow time (the periodicity of the process is taken into account by introducing the independent variable τ) can be written as follows:

$$X_i = \sum_{l=0}^{\infty} X_{j,l}\tau^l, \quad Y_i = \sum_{l=0}^{\infty} Y_{j,l}\tau^l, \tag{35}$$

where $j = 1, 2$, and the plot corresponding to expressions (35) is presented in Fig. 10.

Close results can be obtained for the asymmetric FPU potential [58]. The extension to the case of the chain interacting with an elastic foundation is also possible. Then a minimum frequency in the spectrum of the linearized system differs from zero [28]. The *coherence domains* in this case are formed, contrary to the FPU chain, in the low part of the spectrum (closely to the frequency gap) if one deals with a soft nonlinearity (similarly to the Frenkel-Kontorova model). With such change all the results presented above are valid. They can be applied to the analysis of the nonlinear dynamics of crystalline oligomers in the vicinity of the optic branch of the dispersion curve. This allows one to clarify the most efficient mechanisms of the energy exchange and the transition to energy localization in such systems. Let us

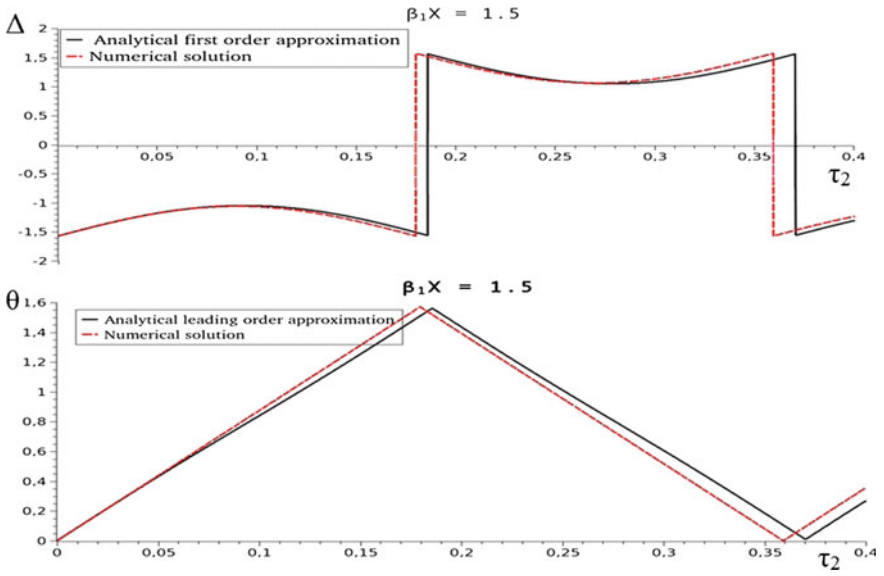

Fig. 10 Time behavior of the symmetric FPU chain corresponding to LPT in coordinates θ, Δ

note that the localization of the vibrations in polyatomic molecules and their role in the relaxation processes are considered in monograph [45] (see also citations there).

Appendix E

We consider the two-level approximation corresponding to the Gross-Pitaevsky equation (GP) [2, 52] as a starting point. The GP equation describes a series of the quantum processes, e.g., the Bose-Einstein condensation (BEC), in the framework of self-consistent field approach that is a source of nonlinearity

$$i\hbar\frac{\partial\Psi(r,t)}{\partial t} = -\frac{\hbar^2}{2m}\nabla^2\Psi(r,t) + \left[V_{trap}(r) + g_0|\Psi(r,t)|^2\right]\Psi(r,t). \tag{36}$$

Then the time evolution of the wave function of GP Eq. (36) can be presented as a superposition of the wave functions corresponding to two natural basic states between which a tunneling is possible:

$$\Psi(r,t) = a_1(t)\Phi_1(r) + a_2(t)\Phi_2(r) \tag{37}$$

The functions $\Phi_{1,2}(r)$ in (37), depending on the space coordinate, are expressed through symmetric $\Phi_+(r)$ и and anti-symmetric $\Phi_-(r)$ stationary GP states as follows [52]:

$$\Phi_1(r) = \frac{\Phi_+ + \Phi_-}{2}$$
$$\Phi_2(r) = \frac{\Phi_+ - \Phi_-}{2} \tag{38}$$

We take into account that $\int \left|\Phi_{1,2}(r)\right|^2 dr = 1$ and $\int \Phi_1(r)\Phi_2(r)dr = 0$. Then, with taking into account (38), we obtain the discrete equations:

$$i\hbar\frac{\partial a_1}{\partial t} = (E_1^0 + U_1|a_1|^2)a_1 - \kappa a_2,$$
$$i\hbar\frac{\partial a_2}{\partial t} = (E_2^0 + U_1|a_2|^2)a_2 - \kappa a_1 \tag{39}$$

This system is similar to that for two weakly interacting classical nonlinear oscillators with cubic nonlinearity, in slow time. Its analysis is performed in [52], and in terms of LPTs in [22, 27]. The detailed development of the LPT concept in application to nonlinear problems is presented in [23, 24, 26, 30].

If one of the parameters of the quantum system (39) depends linearly on the time, the similar procedure leads to the equations which describe a particular case of the nonlinear LZT:

$$i\dot{a}_+ = \varepsilon t a_+ + \Omega a_- + \gamma|a_+|^2 a_+,$$
$$i\dot{a}_- = \Omega a_+ + \gamma|a_-|^2 a_- \tag{40}$$

The limiting magnitudes of the tunneling probabilities (when $t \to \infty$) for system (40) were calculated in [19], and full description of the process is presented in [13]. Here the mathematical analogy is clearly seen with the classical system of weakly coupled nonlinear oscillators the linear stiffness of one of which changes in time. It is possible to note that derivation of both quantum and corresponding classical equations includes the averaging procedure. In quantum case such averaging is a stage of the self-consistence field procedure. In the classical system it is that over the fast time in the method of multiple scale expansions.

References

1. Andrianov, I.V., Barantsev, R.G., Manevich, L.I.: Asymptotic Mathematics and Synergetics. URSS, Moscow (2004)
2. Dauxois, T., Peyrard M.: Physics of Solitons. Cambridge University Press (2006)
3. Fadeev, L.D., Jakubovsky, O.A.: Lekcii po kvantovoj mekhanike dlya studentov matematikov (Quantum mechanics for mathematicians). LGU, Leningrad (1980)
4. Feynman, R.P., Hibbs, A.R.: Quantum Mechanics and Path Integrals. McGraw Hill, New York (1965)
5. Glauber, R.J.: Photon correlations. Phys. Rev. Lett. **10**, 84–86 (1963)
6. Gann, V.V., Kosevich, YuA: Bloch oscillations of spin waves in an inhomogeneous magnetic field. Low Temp. Phys. **36**, 722–735 (2010)

7. Gelfer, J.M., Lyuboshits, V.L., Podgoretsky, M.I.: Gibbs Paradox and the Identity of Particles in Quantum Mechanics (Science). Nauka, Moscow (1975)
8. Heisenberg, W.: Physics and Philosophy. Harper & Row, New York (1958)
9. Kast, M., Pacher, C., Strasser, G., Gornik, E., Werner, W.S.M.: Wannier-Stark states in finite superlattices. Phys. Rev. Lett. **89**, 136803 (2002)
10. Klein, M.J.: Einstein and the wave-particle duality. Nat. Philos. **3**, 3–49 (1964)
11. Kosevich, A.M.: Semiclassical quantization of magnetic solitons. Phys. D **119**, 134–139 (1998)
12. Kovaleva, N.A., Manevitch, L.I.: Complex breather and kink-like excitations in helix oscillatory chain. In: Bernardini, D., Rega, G., Romeo, F. (Eds.) Proceedings of 7th European Nonlinear Dynamics Conference (ENOC 2011), Rome (2011)
13. Kovaleva, A.S., Manevitch, L.I.: Classical analog of quasilinear Landau-Zener tunneling. Phys. Rev. E **85**, 016202 (2012)
14. Kovaleva, A.S., Manevitch, L.I., Kosevich, YuA: Fresnel integrals and irreversible energy transfer in an oscillatory system with time-dependent parameters. Phys. Rev. E **83**, 026602 (2011)
15. Kosevich, YuA, Manevitch, L.I., Savin, A.V.: Wandering breathers and self-trapping in weakly coupled nonlinear chains, Classical counterpart of macroscopic tunneling quantum dynamics. Phys. Rev. E **77**, 046603 (2008)
16. Kosevich, Y.A., Manevitch, L.I., Manevitch, E.L.: Vibrational analogue of nonadiabatic Landau-Zener tunneling and a possibility for the creation of a new type of energy traps. Phys. Usp. **53**, 1281–1286 (2010)
17. Kozhevnikov, A.B.: Dirak i kvantovaya teoriya izlucheniya (Dirac and quantum theory of radiation). In: Ejnshtejnovskij sbornik (Selection of the papers devoted to Einstein), pp. 246–270. Nauka, Moscow (1988)
18. Landau, L.: On the theory of transfer of energy at collisions II. Phys. Z. Sowjetunion **2**, 46–50 (1932)
19. Liu, J., Fu, L., Ou, B.-Y., Chen, S.-G.: Choi, D-Il., Wu, B., Niu, Q.: Theory of nonlinear Landau-Zener tunneling. Phys. Rev. A **66**, 023404 (2002)
20. Malkin, I.A., Man'ko, V.I.: Dinamicheskie simmetrii i kogerentnye sostoyaniya kvantovyh system (Dynamical Symmetries and Coherent States of Quantum Systems). Nauka, Moscow (1979)
21. Manevitch, L.I.: New approach to beating phenomenon in coupled nonlinear oscillators chains. In: Awrejcewicz, J. Sendkowski, D., Mrozowski, J. (eds). Proceedings of 8th Conference on Dynamical Systems - Theory and Applications, Lodz (2005)
22. Manevitch, L.I.: New approach to beating phenomenon in coupled nonlinear oscillatory chains. Arch. Appl. Mech. **77**, 301–312 (2007)
23. Manevitch, L.I.: Vibro-impact models for smooth non-linear systems. In: Ibrahim, R.A., Babitsky, V.I., Okuma, M. (eds.) Lecture Notes in Applied and Computational Mechanics, Vibro-impact Dynamics of Ocean Systems and Related Problems. Lecture Notes in Applied and Computational Mechanics, vol. 44, pp. 191–201. Springer, Berlin (2009)
24. Manevitch, L.I., Gendelman, O.V.: Tractable Models of Solid Mechanics. Formulation, Analysis and Interpretation. Springer, New York (2011)
25. Manevich, A.I., Manevitch, L.I.: Mechanics of Nonlinear Systems with internal resonances. World Scientific, London (2005)
26. Manevitch, L.I., Musienko, A.I.: Limiting phase trajectories and energy exchange between anharmonic oscillator and external force. Nonlinear Dyn. **58**, 633–642 (2009)
27. Manevitch, L.I., Savin, A.V.: Nonlinear modes and energy transfer in polymer chains. Polym. Sci. A **47**, 499–527 (2005)
28. Manevitch, L.I., Smirnov, V.V.: Limiting phase trajectories and the origin of energy localization in nonlinear oscillatory chains. Phys. Rev. E **82**, 036602 (2010)
29. Manevitch, L.I., Smirnov, V.V.: Limiting phase trajectories and thermodynamics of molecular chains. Phys. Dokl. **55**, 324–328 (2010)
30. Manevitch, L.I., Smirnov, V.V.: Resonant energy exchange in nonlinear oscillatory chains and Limiting Phase Trajectories, from small to large system. In: Vakakis, A.F. (ed.) Advanced

Nonlinear Strategies for Vibration Mitigation and System Identification. CISM Courses and Lectures, vol. 518, pp. 207–258. Springer, New York (2010)
31. Manevitch, L.I., Mikhlin, YuV, Pilipchuk, V.N.: Metod normalnyh kolebanij dlya sushchestvenno nelinejnyh sistem (Method of Normal Vibrations for Essentially Nonlinear Systems). Nauka, Moscow (1989)
32. Manevitch, L.I., Savin, A.V., Smirnov, V.V., Volkov, S.N.: Solitons in nondegenerate bistable systems. Phys. Usp. **37**, 859–879 (1994)
33. Manevitch, L.I., Sigalov, G.M., Savin, A.V.: Topological solitons in non-degenerate one-component chains. Phys. Rev. E. **65**(1–22), 036618 (2002)
34. Manevitch, L.I., Savin, A.V., Lamarque, C.-H.: Analytical study and computer simulation of discrete optical in a zigzag chain. Phys. Rev. B. **74**, 014305 (2006)
35. Manevitch, L.I., Savin, A.V., Lamarque, C.-H.: Low-frequency breathers in a polyethylene crystal. Phys. D **237**, 600–612 (2008)
36. Manevitch, L.I., Kosevich, Y.A., Mane, M., Sigalov, G., Bergman, L.A., Vakakis, A.F.: Towards a new type of energy trap, classical analog of quantum Landau-Zener tunneling. Int. J. Non-Linear Mech. **46**, 247–252 (2011)
37. Manevitch, L.I., Kovaleva, A.S., Shepelev, D.S.: Non-smooth approximations of the limiting phase trajectories for the Duffing oscillator near 1,1 resonance. Phys. D **240**, 1–12 (2011)
38. Manevitch, L.I., Kovaleva, M.A., Pilipchuk, V.N.: Non-conventional synchronization of weakly coupled active oscillators. Europhys. Lett. **101**(5), 50002 (2013)
39. Mensky, M.B.: Measurability of quantum fields and the energy-time uncertainty relation. Phys. Usp. **54**, 519–528 (2011)
40. Migdal, A.B.: Kvantovaya fizika i Nils Bor (Quantum Physics and Niels Bohr). Znanie, Moscow (1987)
41. Musienko, A.I., Manevitch, L.I.: Classical mechanical analogs of relativistic effects. Phys. Usp. **47**, 797–820 (2004)
42. Newell, A.C.: Nonlinear Tunnelling. J. of Math. Phys. **19**, 1126–1133 (1978)
43. Novikov, S., Manakov, S.V., Pitaevskij, L.P., Zakharov, V.E.: Theory of Solitons. The Inverse Scattering Methods. Plenum Publishing Corporation, New York; Consultants Bureau, London (1984)
44. Ohanian, H.C.: Einstein's Mistakes, the Human Failings of Genius. W.W. Norton, New York (2008)
45. Ovchinnikov, A.A., Erikhman, N.S., Pronin, K.A.: Vibrational-Relaxational Excitations in Nonlinear Molecular Systems. Kluwer Academic Press, New York (2001)
46. Pilipchuk, V.N.: The calculation of strongly non-linear systems close to vibration impact systems. J. Appl. Math. Mech. **49**, 572–578 (1985)
47. Pilipchuk, V.N.: Nonlinear Dynamics. Between Linear and Impact Limits. Springer, Berlin (2010)
48. Pippard, A.B.: The Physics of Vibration. Cambridge University Press, Cambridge (2007)
49. Pokrovsky, V.L.: Landau and modern physics. Phys. Usp. **179**(11), 1237–1244 (2009). https://doi.org/10.3367/UFNr.0179.200911j
50. Poggi, P., Ruffo, S.: Exact solutions in the FPU oscillator chain. Phys. D **103**, 251–272 (1997)
51. Preparata, G.: An Introduction to a Realistic Quantum Physics. World Scientific, Singapore (2002)
52. Radhavan, S., Smerzi, A., Fantoni, S., Shenoy, R.: Coherent oscillations between two weakly coupled Bose-Einstein condensates, Josephson effects, π oscillations, and macroscopic quantum self-trapping. Phys. Rev. A **59**, 620–633 (1999)
53. Savin, A.V., Manevitch, L.I., Christiansen, P.L., Zolotaryuk, A.V.: Nonlinear Dynamics of zigzag molecular chains. Phys. Usp. **42**, 245–260 (1999)
54. Savin, A.V., Manevitch, L.I.: Solitons in spiral polymeric macromolecules. Phys. Rev. E **61**, 7065–7075 (2000)
55. Scott, E.: Nonlinear Science. Emergence and dynamics of coherent structures. Alwyn Scott, Oxford (2003)
56. Shelepin, L.A.: Kogerentnost (Coherence). Znanie, Moscow (1983)

57. Shepelev D.S., Smirnov V.V., Manevitch L.I.: Limiting Phase Trajectories and Energy Transfer in Asymmetric Fermi-Pasta-Ulam chain. In: Bernardini, D., Rega, G., Romeo, F. (eds). Proceedings of 7th European Nonlinear Dynamics Conference (ENOC 2011), Rome (2011)
58. Smirnov, V.V., Manevitch, L.I.: Limiting phase trajectories and dynamic transitions in nonlinear periodic systems. Acoust. Phys. **57**, 271–276 (2011)
59. Smirnov, V.V., Shepelev, D.S., Manevitch, L.I.: Energy exchange and transition to localization in the asymmetric Fermi-Pasta-Ulam oscillatory chain. Eur. Phys. J. B **86**(1), 10 (2013)
60. Starosvetsky, Y., Manevitch, L.I.: Nonstationary regimes in a Duffing oscillator subject to biharmonic forcing near a primary resonance. Phys. Rev. E **83**, 046211 (2011)
61. Tarasov, L.V.: Osnovy kvantovoj mekhaniki (Foundations of Quantum Mechanics) Librocom (2009)
62. Vakakis, A.F., Manevitch, L.I., Mikhlin, YuV, Pilipchuk, V.N., Zevin, A.A.: Normal Modes and Localization in Nonlinear Systems. Wiley, New York (1996)
63. Wannier, G.H.: Wave functions and effective Hamiltonian for Bloch electrons in an electric field. Phys. Rev. **117**, 432–439 (1960)
64. Yakushevich, L.I., Savin, A.V., Manevitch, L.I.: Nonlinerar dynamics of topological solitons in DMA. Phys. Rev. E **66**, 016614 (2002)
65. Zener, C.: Non-Adiabatic Crossing of Energy Levels. Proc. R. Soc. Lond. A. **137**, 696–702 (1932)

Molecular Simulation of Plastic Deformation of Oligomer Systems

Mikhail A. Mazo, Ivan A. Strelnikov, N. K. Balabaev and Alexander A. Berlin

Abstract Molecular dynamic simulation of low-temperature uniaxial compression and tension of a glass from 1000 molecules of $C_{13}H_{28}$ oligomer is carried out. Stress-strain diagrams, an influence of deformation on density of the glass, and connection between local density and atom rearrangements are discussed. The influence of original level of stress on initial rate of stress relaxation are also investigated. The modeling results of mechanical behavior are in good agreement with experimental data for glassy polymers, which allows one to use MD modeling for further in-depth study of glass behavior mechanisms under mechanical actions.

1 Introduction

Molecular modeling is actively used for studying plastic deformation of amorphous solid materials of various chemical constitution: metallic glasses, covalent materials such as amorphous silicon and SiO_2, and glassy polymers [1–16]. These researches showed that in all these glasses at temperatures lower than ≈0.6 Tg, where Tg—is the temperature of vitrification, a qualitatively similar mechanism of plastic deformation is realized [1, 2, 6, 14, 16]. An overall picture of plasticity is based on the theory of existence of specific structural defects of yield in amorphous solids [1, 2, 6, 7], so called plasticity carriers. Nowadays there are two popular theoretical models where the structure of yield defects in amorphous solids for atomic scale and the character of cooperative transformations in them are proposed. These are the model of shear transformations which first appeared in work [17] and the model of shear transformation zones [18].

M. A. Mazo (✉) · I. A. Strelnikov · A. A. Berlin
N. N. Semenov Institute of Chemical Physics, Russian Academy of Sciences, Moscow 119991, Russia
e-mail: mikhail.mazo1@gmail.com

N. K. Balabaev
Institute of Mathematical Problems of Biology, Keldysh Institute of Applied Mathematics, Russian Academy of Sciences, Pushchino, Moscow Region 142290, Russia

I. V. Andrianov et al. (eds.), *Problems of Nonlinear Mechanics and Physics of Materials*, Advanced Structured Materials 94,
https://doi.org/10.1007/978-3-319-92234-8_17

Progress in conceiving mechanisms of plastic deformation significantly owes to computer simulation of metallic glass. Research of deformation behavior of polymer glass in numerical experiments, in contrast to low molecular systems, faces additional difficulties. A large amount of intramolecular degrees of freedom and a vast variety of local structures makes the analysis of modelling results extremely difficult. For that matter, the research of deformation behavior of oligomeric glasses of interest was carried out only in work [19].

Earlier, we conducted a molecular dynamics simulation of low-temperature deformation of glassy PE [20–23]. Mechanical and thermodynamic characteristics of deformation process were researched, non-affine displacements of carbon atoms and conformational transitions in chains in the direction of deformation were analyzed, the connection of local density with local displacements was studied.

In the present study, we use molecular dynamic (MD) simulation of uniaxial deformation of oligomer glass for analyzing the following questions. How does density of oligomer glass change under uniaxial deformation? Does local density affects structural rearrangements under deformation? What is the difference between annealing before and after the yield peak?

The concept of free volume has already dominated within decades in the examination of structure and dynamics of glassy systems. It is widely accepted that in disordered solids no mobility and deformation displacements are possible if the free volume is sufficient (see, for example, reviews [6, 14, 16]). Earlier, analyzing deformations of PE glass, we have shown that an increase in local volume in the glass actually contributes to nucleation and development of plastic deformations [16]. It is interesting to check whether this conclusion is true for oligomer glass.

Experimental data for the plastic deformation of some polymer films in the modes of stress relaxation and creeping were obtained in, and a phenomenological model was proposed [24, 25]. The model based on the assumption of formation and rise during plastic deformation of some elements of the structure (named plastons). It was interesting to perform MD simulation of the plastic deformation on glasses to check these results and possibly elucidate the nature of structure element responsible for plastic deformation.

2 Molecular Model and Modeling Techniques

Calculations were performed on a system of 1000 molecules of branched $C_{13}H_{28}$ oligomers in the approximation of united atoms (Fig. 1). CH_2 and CH_3 groups distinguished only by their weights, which were 14 and 15 Da, respectively. Valence bonds and valence angles were modelled by harmonic potentials:

$$U(L) = K_L(L - L_0)^2; U(\theta) = K_\theta(\theta - \theta_0)^2,$$

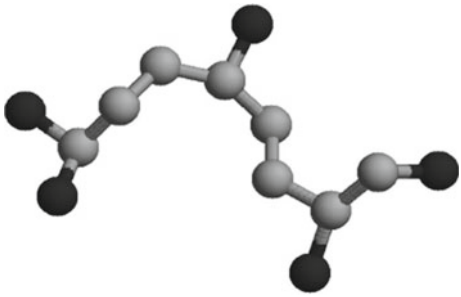

Fig. 1 Structure of $C_{13}H_{31}$ oligomer. Light are CH_2 and CH particles, dark are CH_3

where L is the length of the valence bond, θ is the valence angle, $L_0 = 0.153$ nm, $K_L = 10475$ kJ·mol^{-1} nm^{-2}, $x_0 = 113.0°$ and $K_\theta = 167.6$ kJ·mol^{-1} rad^{-2}. The following potential was used for dihedral angles:

$$U(\varphi) = K_1[1 + \cos(3\varphi)] + K_2[1 + \cos(\varphi)],$$

where ϕ is a rotation angle, $K_1 = 6.7$ kJ·mol^{-1}, and $K_2 = 1.634$ kJ·mol^{-1}. Nonvalent interactions were given by Lennard-Jones potential:

$$U(r_{ij}) = \begin{cases} U_{LJ}(r_{ij}) - U_{LJ}(R_{off});\ r_{ij} < R_{off} \\ 0;\ r_{ij} \geq R_{off} \end{cases}$$

$$U_{LJ}(r_{ij}) = \varepsilon\left[\left(\frac{R_{min}}{r_{ij}}\right)^{12} - 2 \cdot \left(\frac{R_{min}}{r_{ij}}\right)^{6}\right]$$

where r_{ij} is the distance between particles i and j, $\varepsilon = 0.503$ kJ·kg^{-1}, $R_{min} = 0.42654$ nm, and $R_{off} = 1.05$ nm.

Newton equation of motion was numerically integrated with the use of the Verlet velocity algorithm [26] with integration step of 1 fs. The system temperature was maintained with the use of collisional thermostat [27] with parameters $\lambda = 5.5$ ps^{-1} and m0 = 1 which insignificantly (on ~0.01 ps) increased the system viscosity. Pressure was maintained by a Berendsen thermostat [28]. On thousand molecules of branched $C_{13}H_{28}$ oligomers were placed into a computational cubic cell with periodic conditions. To obtain amorphous system for 270 ps, MD modelling was performed at T = 300 K and low density $\rho = 0.28$ g·cm^{-3}.

At the next step, the melt was uniformly cooled at constant pressure of 1 bar with 0.1 K ps^{-1} rate from 300 to 50 K and to 1 K. The systems were allowed to equilibrate so that equilibrium density was reached at these two temperatures. For 50 K and 1 K steady-state densities were to be close to 0.834 and 0.847 g·cm^{-3}, respectively.

3 True Stress—True Strain Curve

In deformation simulation, the key macroscopic characteristics that make it possible to estimate the quality of applied model are the relationship between stress σ and strain ε and the shape of σ–ε curve (presence of the yield peak, strain softening and strengthening, steady plastic flow). Glassy samples at both temperatures, 1 and 50 K, were uniaxially compressed and stretched to $\varepsilon = 32\%$ along one of the coordinate axes at a rate of 10^{-4} ps^{-1}. Along the other two axes of the samples, normal pressure was maintained during loading of the samples.

Figure 2 demonstrates the obtained stress-strain σ–ε diagrams. As it can be seen, the shape of the curves is typical of glassy polymers [14–16]: a linear dependence at low strains ($\varepsilon < 1$–2%) followed by a yield peak ($\varepsilon_y \approx 10\%$) with a yield tooth strain of $\varepsilon_y \sim 9$–13%. At $\varepsilon > 15\%$, steady plastic flow state sets. Table 1 shows calculated Young moduli and stresses σ_y. These values are close to the data of others computer simulations [6, 10, 22]. It is to be expected that at 1 K the samples are harder than at 50 K.

4 Density During Deformation

During uniaxial deformation, density changes appear in a similar manner at both 1 and 50 K (Fig. 3). Compression initially produces a slight rise in sample average density, which attains maximum at $\varepsilon_t \approx 5\%$ and then demonstrates its continuous

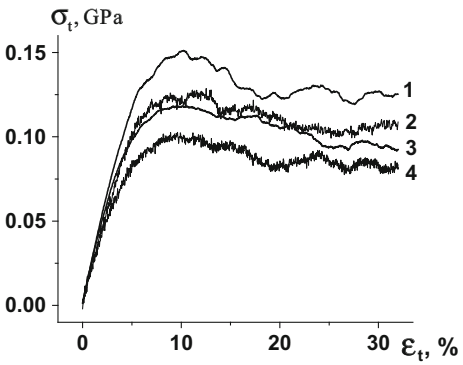

Fig. 2 True stress-true strain curves: uniaxial compression at 1 K (1) and 50 K (2); uniaxial tension at 1 K (3) and 50 K (4)

Table 1 Young moduli and stresses σ_y at the yield points for glassy samples at two temperatures

	Compression		Stretching	
	1 K	50 K	1 K	50 K
E, GPa	2.66 ± 0.07	2.14 ± 0.03	2.49 ± 0.01	2.05 ± 0.03
σ_y, MPa	150	125	120	100

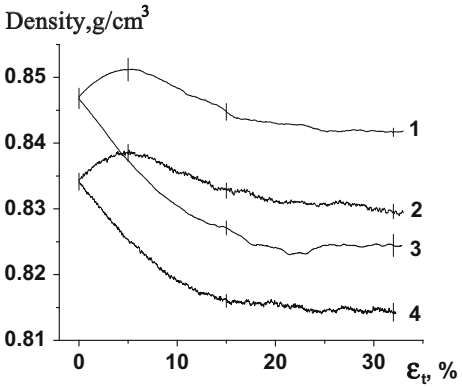

Fig. 3 Density from deformation, statistics by 4 samples. (1) 1 K, compression; (2) 50 K, compression; (3) 1 K, tension; (4) 50 K, tension

reduction. The initial sample density recovers at the range of strain softening at $\varepsilon_t \approx 12\%$. Once a stable flow regime is achieved, density drop decelerates in both cases, and in the simulation of compression to $|\varepsilon_t| > 20$–25% density attains steady-state level. Note that all these density changes in the samples under compression are insignificant and deviation stays in the range of $\pm 1\%$. This behavior of oligomer glass completely agrees with that we received earlier for glass PE [21–24].

Oligomer glass expands during stretching, but just as in the case of compression, density attains the steady-state level, when steady plastic flow state sets in. Here we see the difference from what was observed with PE stretching at the same rate, where a slower relaxation of the system led to appearance of a large and continuously growing with deformation cavity [14, 22]. The total reduction in density of oligomeric glass at stretching was somewhat larger than during compression and was 2.5% for both temperatures.

5 Local Density and Local Rearrangements

As before for amorphous PE [16, 21], we used polygons of Voronoy and Delaunay tessellation for calculating local density around each united atom and proposed by Falk and Langer quantitative estimate of value of local rearrangement $D^2_{\min}$ [29]. For this estimation, Falk and Langer suggested considering root-mean-square value difference between real changes of distances between the particle at issue and its surrounding particles and the changes corresponding to affine displacement ε_{ij} in this region at time Δt:

$$D^2(k, t, \Delta t) = \sum_{n \in R_0} \sum_{i=1}^{3} (r_n^i(t) - r_k^i(t) - \sum_{j=1}^{3} f_{ij}[r_n^j(t - \Delta t) - r_k^j(t - \Delta t)])^2$$

where R_0—the spherical region at issue around particle k, particle n occurs at time t-Δt, $r_n^j(t)$ and $r_k^j(t)$—j components of radius vector of particles k and n correspondingly at time t.

Finding such a value f_{ij}, which minimizes D^2, defines local affine reorganization, which best reflects the affine deformation of the environment, i.e. discrepancy. In this case function f_{ij} has a physical meaning of local tensor of distortion. We modified this expression to some extent, calculating distortion tensor relative to center of mass of particles, occurring in the sphere R_0, which better reflects rearrangements in the sphere:

$$D^2_{c,\min}(k,t,\Delta t) = \min_{f_{ij}} \left\langle \sum_{n\in R_0} \sum_{i=1}^{3} (r_n^i(t) - CM_k^i(t) - \sum_{j=1}^{3} f_{ij}[r_n^j(t-\Delta t) - CM_k^j(t-\Delta t)])^2 \right\rangle$$

For estimate of non-affine displacement of particle k relative to its environment we used the length $\bar{D}_{c,\min}(k,t,\Delta t)$:

$$\bar{D}_{c,\min}(k,t,\Delta t) = \sqrt{D^2_{c,\min}/N},$$

where N –the number of particles in sphere R_0.

At each step of the deformation $\Delta\varepsilon$, we divided all observed non-affine displacements by their size into 5 groups with the same number of elements in each. Figure 4 shows the dependence of volumes averages of Voronoi polytopes V_{av} for each group from deformation ε_t (the segments connect the values of V_{av} for each of these groups at the intervals $[\varepsilon_t, \varepsilon_t + \Delta\varepsilon]$). It can be seen, both in compression and in tension, larger displacements are observed for particles with larger local volume.

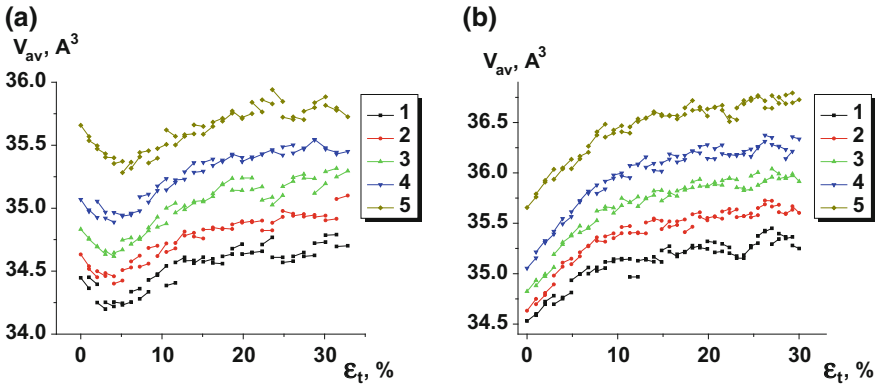

Fig. 4 Dependence of averages of Voronoi polytopes V_{av} for each group of non-affine displacements from deformation ε_t. **a**—compression; **b**—tension. 1—regions with the least non-affine displacements, 5—regions with the largest non-affine displacements

Thus, a larger local volume in glass actually contributes to nucleation and development of plastic deformations. Probably, when analyzing mechanical properties of polymer glasses at such small scales of the order of several nanometers, it is correct to consider their structure as a construction, rather than a homogeneous medium. If so, then relying only on such macroscopic parameters as local volume or a local tensor of tension is possible only with some probability to localize places of the emergence of plastic reorganization at external loading.

6 Relaxation

It was shown previously on polyarylate films that initial rate of stress relaxation $\dot{\sigma}_0$ depends on initial level of stress σ_0. In particular, after the peak the yield $\dot{\sigma}_0$ is significantly greater, than before it [30, 31]. Such behavior of relaxation was explained by forming in the peak area of specific defects, which in these works were named plastons, the number of which with further deformation changed insignificantly. In the work [31] loop formation in dependence $ln\dot{\sigma}_0$ on σ_0 was also observed when with increasing deformation after the yield peakσ_0 decreases a little and stabilization $\dot{\sigma}_0$ occurs. As it turned, the effects are observed in numerical experiment both with tension strain and with compression strain (Figs. 5, 6 and 7).

In the Fig. 5 on diagrams σ-ε we mark the points, at which samples were annealed, and in the Fig. 6—stress relaxation at sample annealing. It's apparent that with equal initial stress σ_x initial velocity of relaxation after yield peak is significantly bigger. We also observed a loop like dependence of $ln\dot{\sigma}_0$ in σ_0 on our model system (Fig. 7).

The results of MD modeling of mechanical behavior of different disordered solid bodies in the complex regimes of deformation completely coincide with the

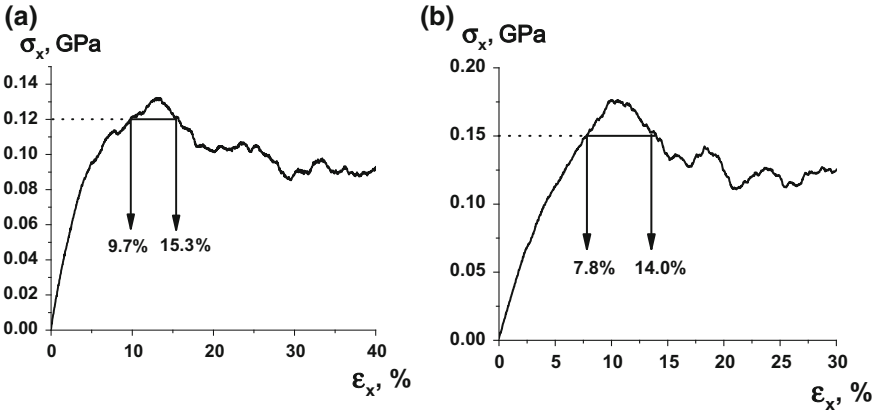

Fig. 5 Deformation dependences with points where samples were annealed (Fig. 6); **a**—tension, **b**—compression. (Reprinted by permission from Springer Nature [19])

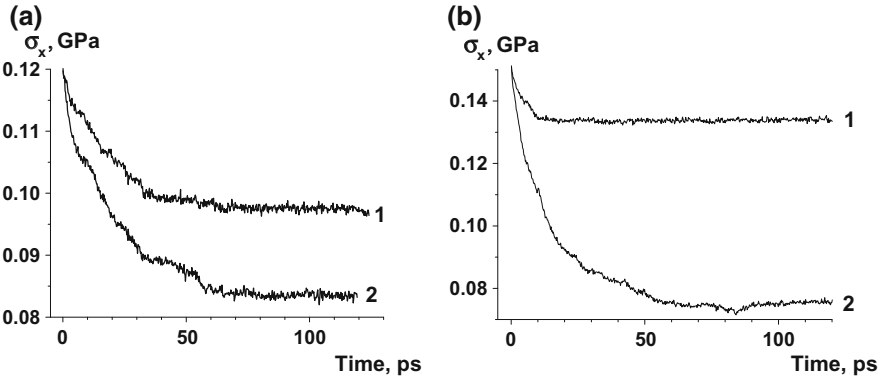

Fig. 6 Stress relaxation curves at T = 1 K at sample annealing: **a** tension at initial deformation of 9.7% (1) and 15.3% (2); **b** compression at initial deformation of 7.8% (1) and 14.0% (2). (Reprinted by permission from Springer Nature [19])

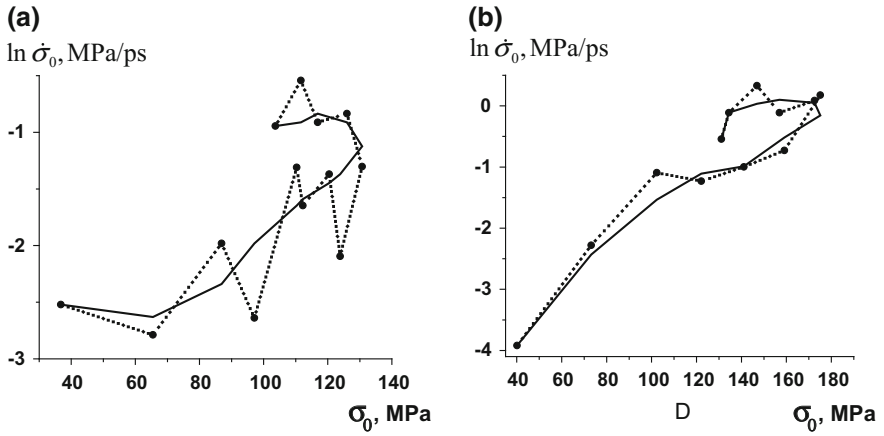

Fig. 7 Dependence of initial rate of stress relaxation $\dot{\sigma}_0$ on initial level of stress σ_0; **a** tension, **b** compression. Points, connected by irregular curves,—estimates obtained at subsequent increasing of deformation. Continuous curves—splines built on these points. (Reprinted by permission from Springer Nature [19])

experimental data for the glassy polymers, which allows one to use MD modeling for the further deep study of glass behavior mechanisms under mechanical actions.

Acknowledgements This work was supported by the Program of Fundamental Research of the Russian Academy of Sciences 2013–2020 (project No 0082-2014-0013, AAAA-A17-117042510268-5). The research was carried out using supercomputers at Joint Supercomputer Center of the Russian Academy of Sciences (JSCC RAS).

References

1. Falk, M.M., Maloney, C.E.: Simulating the mechanical response of amorphous solids using atomistic methods. Eur. Phys. J. B **75**(4), 405–413 (2010)
2. Rodney, D., Tanguy, A., Vandembroucq, D.: Modeling the mechanics of amorphous solids a different length scale and time scale. Model. Simul. Mater. Sci. **19**(8), 083001 (2011)
3. Puosi, F., Rottler, J., Barrat, J.-L.: Time-dependent elastic response to a local shear transformation in amorphous solids. Phys. Rev. E **89**, 042302 (2014)
4. Gendelman, O., Jaiswal, P.K., Procaccia, I., Gupta, B.S., Zylberg, J.: Shear transformation zones: state determined or protocol dependent? Eur. Lett. **109**(1), 16002 (2015)
5. Cubuk, E.D., Ivancic, R.J.S., et al.: Structure-property relationships from universal signatures of plasticity in disordered solids. Science **358**(6366), 1033–1037 (2017)
6. Argon, A.S.: The Physics of Deformation and Fracture of Polymers. Cambridge University Press, New York (2013)
7. Yang, J.S., Jo, W.H., Santos, S., Suter, U.W.: In: Kotelyanskii, M., Theodorou, D.N. (eds.) Simulation Methods for Polymers, p. 389. Marcel Dekker, New York (2004)
8. Clarke, J.H.R.: In: Binder, K. (ed.) Monte Carlo and Molecular Dynamics Simulations in Polymer Science, p. 272. Oxford University Press, New York (1995)
9. Paul, W., Smith, G.D.: Structure and dynamics of amorphous polymers: computer simulations compared to experiment and theory. Rep. Prog. Phys. **67**(7), 1117–1186 (2004)
10. Lyulin, A.V., Vorselaars, B., Mazo, M.A., Balabaev, N.K., Michels, M.A.J.: Strain softening and hardening of amorphous polymers: atomistic simulation of bulk mechanics and local dynamics. Eur. Lett. **71**(4), 618–624 (2005)
11. Rottler J.: Fracture in glassy polymers: a molecular modeling perspective. J. Phys. Condens. Matter. **21**(46) 463101 (2009)
12. Barrat, J.-L., Baschnagel, J., Lyulin, A.: Molecular dynamics simulations of glassy polymers. Soft Matter **6**(15), 3430–3446 (2010)
13. Lyulin S.V., Larin S.V., Nazarychev V.M., Fal'kovich S.G., Kenny J.M.: Multiscale computer simulation of polymer nanocomposites based on thermoplastics. Polym. Sci. C **58**(1), 2–15 (2016)
14. Oleinik E.F., Rudnev S.N., Salamatina O.B., Mazo M.A., Strelnikov I.A., Koteljansky M.I.: In: Hubbard, D. (ed.) Plastic Deformation: Processes, Properties and Applications, p. 45. Nova Science Publishers, New York (2016)
15. Haward, R.N., Young, R.J. (ed.): The Physics of Glassy Polymers. Chapman and Hall, London (1997)
16. Oleinik, E.F., Mazo, M.A., Strelnikov, I.A., Rudnev, S.N., Salamatina, O.B.: Plasticity mechanism for glassy polymers: computer simulations picture. Polym. Sci. Ser. A **60**(1), 3–57 (2018)
17. Argon, A.S.: Plastic deformation in metallic glasses. Acta Metall. **27**(1), 47–58 (1979)
18. Langer, J.S.: Anomalous diffusion and stretched exponentials in heterogeneous glass-forming liquids: low-temperature behavior. Phys. Rev. E **77**(2), 061505 (2008)
19. Berlin, Al.Al., Mazo, M.A., Strel'nikov, I.A., Balabaev, N.K.: Modeling of plastic deformation of glasses in creeping and stress relaxation regimes. Polym. Sci. D **8**(2), 85–91 (2015)
20. Balabaev, N.K., Mazo, M.A., Lyulin, A.V., Oleinik, E.F.: Plastic deformation of glassy polymethylene: Computer_AidedMolecular_Dynamic Simulation. Polym. Sci. A **52**(6), 633–644 (2010)
21. StrelnikovI, A., Balabaev, N.K., Mazo, M.A., Oleinik, E.F.: Analysis of local rearrangements in chains during simulation of the plastic deformation of glassy polymethylene. Polym. Sci. A **56**(2), 219–227 (2014)
22. Strelnikov, I.A., Mazo, M.A., Balabaev, N.K., Oleinik, E.F.: Computer simulation of rearrangements in chains of glassy polymethylene subjected at low temperature inelastic deformation. Polym. Sci. A **56**(4), 511–521 (2014)
23. Strelnikov, I.A., Mazo, M.A., Balabaev, N.K., Oleinik, E.F., Berlin, A.A.: Energy storage in plastic deformation of glassy polymethylene. Dokl. Phys. Chem. **457**(1), 108–111 (2014)

24. Berlin, Al.Al., Manevich, L.I., et al.: On the plastic flow and the destruction of glassy bodies. Dokl. Akad. Nauk SSSR **268**(6), 1426–1430 (1983)
25. Berlin, Al.Al., Grineva, N.S., Aleksanyan, G.G., Karpenko, Yu.P., Manevich, L.I.: Features of plastic deformation of amorphous glassy polymers in stress relaxation and creep regimes. Polym. Sci. A **28**(12), 2781–2786 (1986)
26. Allen, M.P., Tildesley, D.J.: Computer Simulation of Liquids. Clarendon Press, Oxford (1987)
27. Lemak, A.S., Balabaev, N.K.J.: Molecular dynamics simulation of polymer chain in solution by collisional dynamics method. J. Comput. Chem. **17**(15), 1685–1695 (1996)
28. Berendsen, H.J.C., Postma, J.P.M., et al.: Molecular dynamics with coupling to an exteral bath. J. Chem. Phys. **81**(8), 3684–3690 (1984)
29. Falk, M.L., Langer, J.S.: Dynamics of viscoplastic deformation in amorphous solids. Phys. Rev. E **57**(6), 7192–7205 (1998)
30. Berlin, Al.Al., Manevich, L.I., et al.: On the plastic flow and the destruction of glassy bodies. Dokl. Akad. Nauk SSSR **268**(6), 1426–1430 (1983)
31. Berlin, Al.Al., Grineva, N.S., Aleksanyan, G.G., Karpenko, Yu.P., Manevich L.I.: Features of plastic deformation of amorphous glassy polymers in stress relaxation and creep regimes. Polym. Sci. A **28**(12), 2781–2786 (1986)

Plastic Deformation in Disordered Solids: The State of the Art and Unresolved Problems

Eduard F. Oleinik, Mikhail A. Mazo, Michael I. Kotelyanskii, Sergey N. Rudnev and Olga B. Salamatina

Abstract Crystalline materials are deformed plastically through crystallographic mechanisms based on the lattice's periodicity. However, plasticity of disordered solids can't be described in these terms due to an absence of regular lattices. To find the best way of the description of plastic response for disordered solids (DSs) became a serious challenge for material science and solid-state physics. This paper discusses current views on mechanism of plastic deformation in DSs and touches some problems in the field. It is broadly accepted now that one, common mechanism of plasticity operates in all DSs, independent on their chemical nature and interaction potentials. Such mechanism is dictated by the structural disorder of glasses. Many details of the mechanism are not well understood yet. Important features of the mechanism are discussed in this paper, and several problems, which do not permit the field to develop further successfully are considered.

1 Introduction

Plasticity of disordered solids (DSs) became the hot point of modern solid-state physics during the last two decades [1–7]. It is not surprising due to practical and academic reasons: many disordered solids like glassy polymers (PGs), metallic glasses (MGs), covalent amorphous solids and many others became important engineering materials. From academic point of view physical processes of molecular relaxations, mechanism of plastic deformation, static and dynamic heterogeneities, change in potential energy landscape during an ageing and deformation and others attract interest of researches [1, 4, 8]. Prof. L.I. Manevich was always interested by scientific problems of DSs. In the 90-ties, together with his student Gendelman they found

E. F. Oleinik (✉) · M. A. Mazo · S. N. Rudnev · O. B. Salamatina
Department Polymer and Composite Materials, Semenov Institute of Chemical Physics RAS, Moscow 119991, Russia
e-mail: efoleinik@gmail.com

M. I. Kotelyanskii
Rudolph Technologies Inc., Mount Olive, NJ 07828, USA

I. V. Andrianov et al. (eds.), *Problems of Nonlinear Mechanics and Physics of Materials*, Advanced Structured Materials 94,
https://doi.org/10.1007/978-3-319-92234-8_18

and described some specific defects characteristic for DSs [9]. Gendelman develops this study further and found recently, that the deformation response of glasses is the test protocol sensitive: different loading protocols give different spatial distribution of plastic events in the deformed glassy samples [10]. This finding is very important for understanding of plastic deformation mechanism in DSs. It possibly shows that specific sites in glass, which may operate as the structural precursors facilitating nucleation of new plastic events, do not exist in non-deformed DSs, and search for them becomes pointless.

Study of DSs demonstrates serious progress during the last 20–25 years. Many important features of their plasticity were discovered and analyzed by different techniques, computer modeling, first of all [11–13]. New approaches in creation of the analytical theories had appeared also [5–7]. Important common features of deformation behavior of glassy solids were discovered [2, 3, 5–7, 14]. However, many problems are still left unresolved and some serious challenges still exist in the field of physics and mechanics of solid materials. In this paper we will outline briefly several key features of the plastic deformation of DSs and will point out some problems interfering with the field development.

2 Key Features of Inelastic Deformation of DSs

We consider the following common characteristics of deformation process in disordered solids to be the key features of their response to external load. These features are:

- It is broadly accepted now [1, 2] that plastic deformation in DSs is nucleated and develops through a single mechanism, common for any DS in spite of different chemical nature and interparticle interaction potentials, binding atoms and molecules in different glassy solids (metallic and inorganic covalent, organic polymeric and non-polymeric, frozen colloidal glasses and pastes) [1–3, 8]. An existence of one mechanism of plasticity in DSs does not mean that the kinetics and other quantitative characteristics of deformation processes in them are the same. Activation parameters of a nucleation of local plastic events, free energy of the plasticity carriers, scale of plastic rearrangements, scale and type of disorder in rearranging atomic/molecular clusters, different strength of constrains and rates of their relaxations create quantitative differences in the process kinetics.
- The plasticity carriers are nucleated in glass by an action of applied load. Temperature facilitates the nucleation. However, the temperature accelerates relaxation of DS at loading. The nucleated primary plasticity carriers experience complex atomic/molecular level local rearrangements under load and form final carriers of plasticity. Final, the macroscopic plasticity carriers have the structure of shear transformations (STs) [1–3, 14–16]. Such STs have analogs in the plasticity of crystalline solids. The analogs are the sessile dislocations [1, 15], or twins and martensitic transformations [1, 17, 18]. Plasticity carriers in DSs have much in

common with their crystalline analogs but are less constrained. The nucleated carriers always carry increments of plastic strain γ^T in their structure. They are highly localized [1–3, 10, 14]. The number of plasticity carriers grows up with an increase of an applied stress and strain through new local nucleation events. An increase of the carrier's concentration increases the total macroscopic plastic strain of a sample also [1]. Nucleation of STs always raises total internal potential energy of DSs under deformation because an external mechanical work is expended for their nucleation [5, 19–21]. After straining of glass DSs become excited.

- The nucleation of carriers is the kinetic step controlling whole plasticity process in DSs.
- DSs internal energy growth with macroscopic strain (ε) usually proceeds in a form of the S-shaped curve eventually approaching a constant value ΔU_{max} [5, 19–21]. The ΔU_{max} level is different for each glass (for PGs and MGs at least). The kinetics of the ΔU_{max} increase with strain ε exactly reflects the accumulation of the plastic carriers in GSs. ΔU_{max} in each compound is directly related to the concentration of plastic carriers necessary for developing a macroscopic steady plastic flow in a given sample. The level of ΔU_{max} accumulated during loading of PGs is about 5–25 KJ·g^{-1} for glassy polymers at T_{room} [1, 19–22].
- Mechanical work W of deformation in a solid is always transformed in two ways: partly into the deformation heat Q (dissipation processes), and partly into ΔU (the change of structure of glass) [19, 21, 22]. About 95% or more of the expended W at loading of crystalline metals at early stages of deformation is transformed into the deformation heat [23, 24]. Such strong dissipation occurs during the process of dislocation glide. We think, that friction of dislocations at their glide over a crystalline lattice produces total deformation heat Q_{def}. Completely different situation occurs in GSs, in glassy polymers for example [4, 19, 21–25]. About 95% of the work W expended at T_{room} on compressive straining of GPs is transformed into energy excess of a sample. Dissipation practically absent at early stages of GPs' deformation [19, 21]. Dissipation in GPs becomes noticeable at nominal strains $\varepsilon > 30\%$ at T_{room}. Undoubtedly, the work W is expended in GPs mainly for nucleation of the excited carriers of plastic strain. Computer modeling had shown that in GPs the carriers appear mainly due to the perturbations of the van-der-Waals inter-chain interactions [25].
- The mechanics of the nucleated STs is well described in terms of the Eshelby inclusion model [26]. Long-range elastic fields appear around STs. These elastic fields work as a main source of the energy excess ΔU measured experimentally for plastically deformed GPs [19, 21].
- Nucleation process of STs in GSs rises an important question: are any structural precursors, facilitating the nucleation of STs necessary to be present in an initial glass structure for nucleation of plastic events in it? Some deformation models do suggest the necessity of precursors, but others don't.

DSs are always the excited state of matter (both, deformed and nondeformed). Thermodynamic characteristics of DSs strongly correlate with their structural disorder [14]. Structure of glasses is highly constrained due to disorder. The constrains

manifest themselves through the enthalpy excess, which always exists in glasses. Plastic deformation increases an excitation of DSs. For example, in organic glassy polymers the enthalpy ΔH excess or elastic energy of deformation accumulated in the excessive pressure field were calculated from local tensors of hydrostatic pressure $\Delta H_{\langle p\rangle}$ and deviatoric stresses $\Delta H_{<\tau>}$ [1].

Estimations gave [1]:

$$\Delta H_{\langle p\rangle} = 1/2 \sum_i c_i \langle p_i\rangle 2/K \text{ and } \Delta H_{\langle \tau\rangle} = 1/2 \sum_i c_i \langle \tau_i\rangle 2/\mu, \qquad (1)$$

where K is the bulk and μ is shear modules, and c_i—fractions of chemically different environments. The calculated values are $\Delta H_{\langle p\rangle} = 0.198 \times 10^{10}$ J·m^{-3} and $\Delta H_{\langle \tau\rangle} = 1.221 \times 10^{10}$ J·m^{-3}. Total enthalpy is $\Delta H = 1.42 \times 10^{10}$ J·m^{-3}. These data indicate that about 86% of the whole enthalpy excess is contained in the shear strain field and only 14% is contained in the pressure strain field. Because of disorder in the system, the excess of enthalpy for the amorphous PP, for example, is higher by a factor of ~70 than the density of cohesion energy. Such excitation gave an important cause for high sensitivity of DS's properties and deformation on their thermal prehistory [1].

PGs always show additional amorphisation (anti-ageing process) at plastic deformation [22, 27] at constant temperature. It, we believe, should be general for all glasses. Amorphisation (additional disordering) is the result of creation of new free volume at plastic deformation of PG's. It was proved by PALS measurements [28] and by computer modeling [25, 29].

For the macroscopic plasticity in DSs to occur, the percolation of plastic carriers through whole sample is necessary. Study of plasticity of the amorphous Si [1, 3] had shown, that the quantity, controlling start of the macroscopic plastic flow is not the total free volume in the system, but the concentration of liquid-like structural cells.

3 The Mechanism of Plasticity in DSs

We accept, together with many researchers in the world, that one common mechanism of plasticity operates in all DSs with different chemistry and inter-particle interaction potentials [1–3, 30, 31]. The mechanism was carefully analyzed and checked for several objects: a-Si (amorphous Si) [1, 3] MGs [14, 30, 31] and PGs [1–3]. However, several approaches exist within this common mechanism and different approaches give different views on stages of DS's plasticity and sometimes guide a reader to important differences in conclusions. Below we will shortly describe some of the approaches.

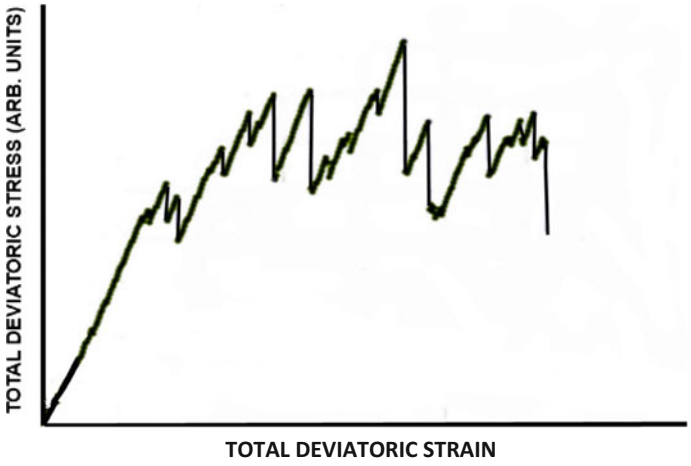

Fig. 1 A typical computer-simulated stress-strain curve for an amorphous Si at 0 K [1.3]. Stress jumps (jumps down at sample loading) are the processes of irreversible plastic relaxations which occur locally in glassy sample under loading. The linear elastic stress rises between mentioned relaxation jumps mirror a local stress increase. Local increments of plastic strain are nucleated at each linear stress rise. At the end of these linear rises local mechanical instabilities are nucleated in a glassy sample

3.1 The Shear Transformations (STs) Nucleation Model [1, 3, 20]

Figure 1 shows a stress-strain curve of shear deformation of amorphous Si, demonstrating main important features of deformation response of all DSs. The curve consists of number of sharp drops and rises of stress and pressure. Stress and pressure drops occur also at sample unloading. Pressure drops appear in the system at the same strains as shown stress drops. Each drop mirrors one of many unit plastic events, which are nucleated under the action of an external load. Similar curves with stress drops were registered for many different polymeric and non-polymeric GSs [1–3].

Macroscopic plasticity in GSs proceeds as series of localized random rearrangements in atomic clusters of volume Ωi, each having the overall nature of a ST [1, 3]. The atomic sites that suffer distortions are identified as the plastically rearranging clusters, accompanied by a local dilatation or compaction. It was found, that appeared transformation is triggered at the threshold stress τ_{tr} in a small sub-cluster, with number of atoms 7 ± 5.2 for a-Si. Local mechanical instability in volume Ω_f becomes nucleated in the representative volume V of glass. A local stress increment is accumulated at each stress rise step, but not at a relaxation step. The volume element Ω_f has value about $8 \cdot 10^{-27}$ m^3 for deformation of a-Si and $8 \cdot 10^{-30}$ m^3 for MGs [1]. The volume element Ω_i increases in size with increasing kinematical constraints imposed on relaxations by the nature of the atomic bonding [3].

The sizes of stress drops point out that volume elements comprising individual events are substantial in size relative to the size of the simulation cell. Thus, the appearance of smooth plastic flow would be achieved only when the deforming model volume becomes much larger than the volume of individual relaxation events and contains a substantial number of uncorrelated events. An appearance of the relaxation stress drops on a stress-strain curve is clear reflection of the fact that plastic flow is an intrinsically non-affine process, unlike elasticity [1, 3].

Visualization of the atomic clusters [1, 3], within which the ST occurs develops deeper understanding of the elementary plastic relaxation processes. The atomic site that is identified as having undergone only an elastic change is considered to be a part of the elastically flexing background matrix material. The atomic sites that suffer distortions falling well outside this conservative range are identified as being part of the plastically rearranging cluster. The contiguity of atomic sites that have suffered large local changes identifies the transforming cluster undergoing a plastic relaxation event. Plastic events of different sizes behave differently: small event consisted only of a single relaxation step, the larger event is made up of a series of consecutive relaxation steps. Some of small (triggering sub-clusters) do not participate in avalanche, but bigger sub-clusters are involved. The most important feature of the nucleated sub-clusters is that the transforming atomic clusters are indeed the principal source of the plastic strain production in GSs [1–3].

Following the stress threshold (stress level before a stress drop) the next important process becomes triggered. An autocatalytic avalanche of successive relaxations starts. The relaxations continue up to the moment, when the volume Ω_i becomes completely unloaded. The avalanche normally nucleates structures with significantly larger number of atoms in comparison with the initial sub-clusters. Some of after-avalanche structures in GSs involve only few additional atoms to initial sub-clusters (small stress drops on σ-ε curves). However, some of them (after large stress drops in the curve) include about 400 atoms in average [1, 3]. One may observe such after-avalanche structures play role of the strain carriers of the macroscopic plastic flow in GSs.

And the final event appearing in this sequence of deformation steps in the ST model of plasticity is related to the evolution of free volume of whole system. Not only stress relaxes, but the internal potential energy and pressure are changed simultaneously in the new cluster [1]. Atomic diffusion starts also, and the diffusion changes ratio between liquid-like (LL) and the solid-like (SL) free volume Cohen-Grest [32] cells. It was found that in a-Si fluidity is mediated not by sites with free volume excess but by the atomic level environment with LL character [1]. LL cells later become facilitators of the global plastic flow. The change of LL cells into the SL cells and back occurs due to atomic diffusion. The fraction φ of the LL cells to the final level of the stationary flow state ($\varphi \approx 0.5$–0.55 [1, 3]) atom environments have undergone transitions from SL to LL or vice versa during plastic flow of a-Si. During plastic relaxation, atomic environments inside the transformation inclusion can change their character from the SL (coordination number in a-Si close to 4) to the LL (coordination number close to 5) and vice versa [3].

Evidently, using a simple separation of complex plastic rearrangements in ST mechanism of plasticity of GSs is quite artificial. In reality, all processes go continuously, and an appearance of the first structure (triggering sub-cluster) already suggests the following processes (the avalanche and accumulation of the LL cells). However, we used such separation for better understanding of the GS's plasticity details.

3.2 Shear Transformation Zone (STZ) Model [2, 5, 7]

Falk and Langer [2, 5, 7] formulated the model, where the structure and behavior of fundamental unit plastic flow events looks differently compared to ST model. After publication of the first paper the term shear transformation zone (STZ) had appeared in scientific literature. In this model the nucleation of a local structure accommodating plastic flow in GSs remain the main, rate controlling event of whole deformation mechanism. Atomic level rearrangements, leading to unit plastic strain production occur in this model as rearrangement of small group of atoms (4–10 atoms in metallic glass) surrounded by more densely packed matrix [2]. When shear stress is applied to the sample the atoms undergone orientation coordinated rearrangement and an increment of shear strain γ^{T} appears in 3D local zone where rearranging atoms are located. Local orientation of group of atoms is the main event differing the STZ model from the ST model. Local strain increment appears in glass due to the orientation. Integration over all such local strain increments gives total macroscopic strain of a sample. Atoms in the zone undergone some displacements in all 3D directions, but the main displacements occur in the direction of new orientation axes. The surrounding matrix remains in the pure Hookean elastic state [2, 30, 31].

Computer simulations have shown that STs are associated with regions of enhanced structural disorder and are sensitive to pressure [14]. There are fundamental differences between the STZ-based interpretations of plastic response of GSs [3, 5, 7] and the view of the basic ST model. In [2] it was visualized that shape of nucleated STZ should be elongated zones of atoms that can result in a two-level relaxation process by flipping principal axes under stress (orientation displacement) [3]. In this view STZs appear to be pre-existing in the structure and are considered something like fertile material elements in basic ST model. Under stress, these zones appear to be polarized by flipping from initially unrelaxed to relaxed form. This is radically different from understanding of STs, which do not pre-exist in the structure but are a consequence of complex structural relaxations in clusters of atoms, giving rise eventually to net transformation shear strains γ^{T} of only a few percent. Because in the relaxation process load is shed from the unrelaxed cluster to its immediate surroundings, local back stresses are established causing Bauschinger effects [3]. In paper [30] existence of STZs was confirmed experimentally in a colloidal glassy system. It was shown also that the STZs are irreversible and thermally activated, and that their transformation can induce the formation of new STZs. Furthermore, they quantify the stress needed to cause a STZ to transform. Such theories are needed to

pave the way for new materials that take advantage of the disorder inherent in glasses, which may in the years ahead provide as rich a source of new materials advances as crystals have to date [2].

3.3 *Deformation of 2D Lennard–Jones (LD) Glass [33, 34]*

Computer modeling of inelastic deformation of 2D LD glass [33, 34] demonstrated a little different (in comparison with the basic ST model) picture of deformation at its second stage. At Fig. 2 atomic level deformation rearrangements are shown. 2D glass containing 539 spherical particles of two different diameters was simulated. Particles interacted in accordance with the Lennard–Jones (LJ) potential. Shear was applied to the system through the displacements of rigid walls on its boundary. Figure 2 depicts the nucleation and accumulation of local deformation events in the glass during boundary displacements. Figure 2a illustrates the arrangement of particles in the non-deformed glassy sample. The macroscopic shear strain γ was measured from the displacement of boundaries.

Whole deformation process occurs as a sequence of localizes small-medium scale atomic rearrangements (inelastic events ST-I—ST-III in Fig. 2), where inelastic strain is accumulated. An increase of the external shear stress τ changes the behavior of the system: at $f \approx 16–17 \times 10^{-23}$ N the inelastic deformation starts (Fig. 2b).

Local shear strains were determined after Delaunay tessellation applied to whole samples. The measures of local strains are the dashed areas of Delaunay triangles, which are shown in Fig. 2a, c–e (in Fig. 2c–e atoms do not shown; only dots representing centers of atoms are shown). In Figs. 2c–2e nucleation of events producing new plastic strain during sample loading are represented (events ST-I, ST-II and ST-III).

The first plastic event in the system was registered at $f > 2 \cdot 10^{-22}$ N and $\gamma > 0.04$. The growth of f leads to the emergence of local events, carrying newly produced inelastic strains. Figure 2c shows the first unit local deformation event (ST-I). Deformation of all regions beyond the shear ST-1 zone is elastic, and the coordinates of atoms immediately regain their initial positions upon sample unloading. However, newly formed region ST-I behaves differently. The residual strain stays in the region ST-I after sample unloading. Macroscopic strain of the whole sample is $\gamma = 0.025$, even though the strain in ST-1 region is much higher (Fig. 2c).

All macroscopic residual strain is concentrated only in the region of ST-1 structure. Dimensions of the ST-I are small and involve only 2–3 neighboring coordination spheres around the central atom of the event. All inelastic excessive deformation energy ΔU total consists of localized plastic events. So, the stored deformation energy is a local quantity also. The remainder areas of the sample contain only the elastic component of excessive strain, stress and energy that immediately vanish upon unloading (the stored energy is transformed into heat).

Further macroscopic straining entails the development of the second localized sheared region ST-II (Fig. 2d). Characteristics of the ST-II region are similar to those

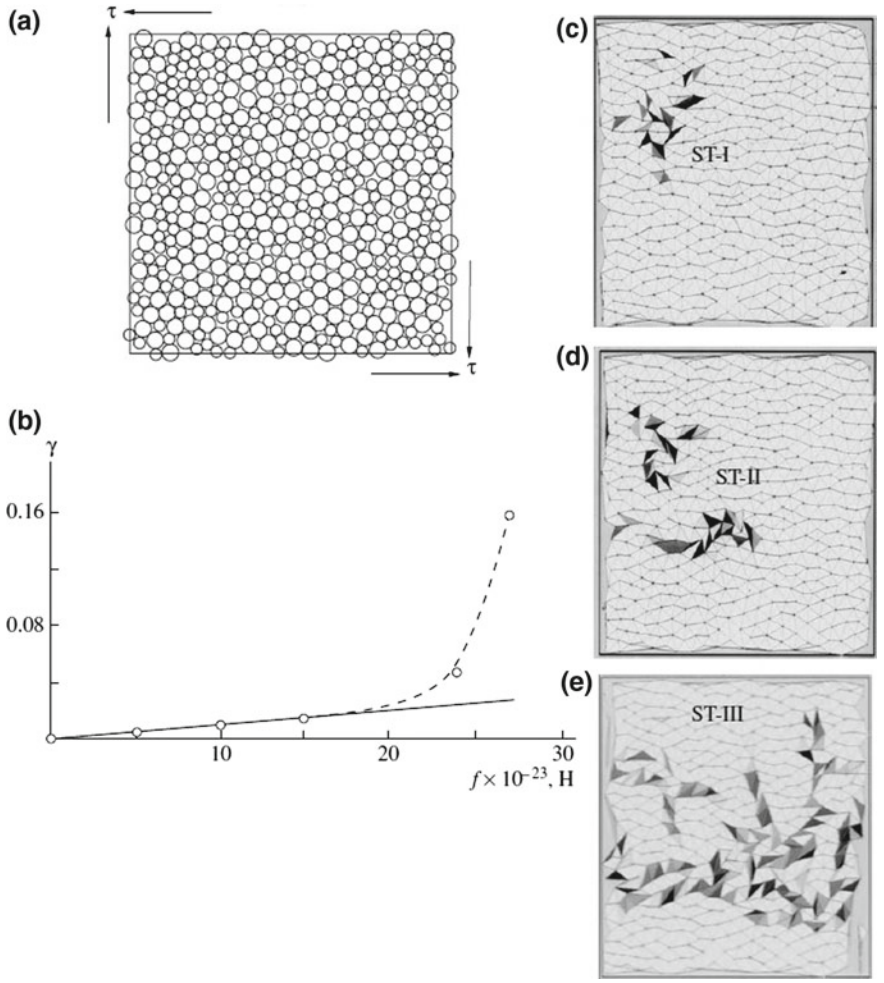

Fig. 2 **a** Initial bi-component glassy system for computer simulation of deformation [34]; **b** force f—shear strain diagram; **c**–**e** structural rearrangements in a computer glass in the course of shear straining; nucleation of unit plastic events: **c** event ST-I, **d** event ST-II, and **e** event ST-III. Centers of atoms—points and the Delaunay tessellation—triangles. Local strain is estimated through the area of Delaunay triangles. Local shear strain $\gamma = 1.0$ (black triangles), 0.5 (dark grey triangles), 0.3 (light grey triangles), and <0.02 (white triangles). τ—is the shear stress. (Reprinted by permission from Springer Nature [34])

of ST-I. It is important that the ST-II region arises not by the growth of the ST-I region, but at a certain distance from it. This result shows that each next plastic event occurs by new nucleation process. It is seen from Fig. 2d that the ST-I region experiences only very slight structural rearrangements upon nucleation of the ST-II event. The net strain of the sample after appearance of the ST-II event becomes

$\gamma = 0.05$. The above results clearly show that the plastic deformation in the material is accumulated via formation of independent localized STs; in other words, this process is heterogeneous. An analysis of the above evidence demonstrated that, in ST-I and ST-II, no dilation takes place. Each ST carries inelastic strain and excessive potential energy appearing from the elastic field around local events ST-I and ST-II.

The nucleation of ST-III event changes all previous strain distribution picture. Practically all sample cross section is covered by Delaunay triangles with local strains markedly higher than the average over the sample. Many new strained triangles had appeared. It is difficult now to separate all individual STs. Possibly more than only one plastic event is nucleated in the sample at this stage of the process. Or there is the other possibility: all previously nucleated local plastic events become united (coalescence stage of plasticity). At this deformation stage the percolation of plastic carriers appear in glassy solid.

Contours of ST-I and ST-II events had changed at this stage of the process remarkably. Whole deformed region (ST-I + ST-II + ST-III) looks like an embryo of a shear band. It looks that steady macroscopic plastic flow starts after formation of event ST-III due to the percolation of carriers over entire sample. The main deviation of the described deformation process from the basic ST model (Sect. 3.1) is that we do not see any avalanche process. We do not see any growth of events ST-I and ST-II. And we did not find any dilation or contraction in the events ST-I and ST-II. The reason for such behavior in our 2D glass model is not clear yet.

Analysis of results shown in Fig. 3a–d leads to several important conclusions:

- Plastic deformation proceeds in the studied LD glass along the line, which coincide with basic ST model, described in the Sect. 1. Plasticity on a sample scale is accumulated by increase in number of individual localized deformation events. It appears that each event is the final result of nucleation of rearranging clusters, i.e. local structures which carry plastic strain increment.
- All plastic events appear consequently and cover all sample cross section before a macroscopic steady plastic flow starts.
- The third event creates some global superstructure, which may be an embryo of shear band or the structure, which where percolation occurs and the homogeneous macroscopic plastic flow begins in a sample.
- Potential energy and shear stresses are distributed heterogeneously and localized strongly inside of events ST-I through ST-III. Plastic deformation is substantially heterogeneous both, with respect to the space of the sample and within each individual event (from ST-I through ST-III). Delaunay triangles inside the event ST-I, for example, carry strains $\gamma \approx 0{,}3$ up to 1,0. However, we do not see some important details existing in the ST model. We do not see the avalanche stage and change of ST's volume. The results say that the inelastic deformation process in 2D glass does not coincide in some details with ST and with STZ models, and this fact should find explanations in the future.

4 Rearrangements in DSs by Structural Quantity "Softness"

Recently, different approach to the description of rearrangements in DSs was proposed [31, 35]. Below we will introduce the approach on the bases of these papers. The approach is based on introduction of a microscopic structural quantity named "softness". Softness is a weighted integral over the local pair correlation function $g_i(r)$. It was shown, that the probability that particles in DSs will rearrange is a function of their softness. The most important structural features contributing to softness are the density of neighbors at the first peaks of the radial distribution functions g_{AA} (r) and g_{AB} (r); these two features alone give 77% prediction accuracy for rearrangements. Particles with more neighbors at the first peaks of $g_i(r)$ have a lower softness and are thus more stable. These results are reminiscent of the cage picture, in which an increase of population in the first-neighbor shell suppresses rearrangements, or the free-volume picture, in which particles whose surroundings are closely packed are more stable than those with more loosely packed neighborhoods. Overall, soft particles typically have a structure that is looks like a higher-temperature liquid, where there are more rearrangements, whereas hard particles have a structure that is closer to a lower-temperature liquid.

Experiments and simulations enabled authors to measure the spatial correlations and strain response of softness, as well as two measures of plasticity: the size of rearrangements and the yield strain. All four quantities maintained remarkable commonality in their values for many DSs ranging from atoms to grains, spanning seven orders of magnitude in diameter and 13 orders of magnitude in elastic modulus. These commonalities link the spatial correlations for strain and strain response of softness to rearrangement size and yield strain, respectively [35].

The probability that particles rearrange is a function of their softness. This probability $P_R(S)$ is calculated as the fraction of particles of a softness S, that are rearranging at a given time. At each temperature probability $P_R(S)$ is a strong function of softness, increasing by several orders of magnitude, especially at the lower temperatures, in the range $S > -3$ to $S = +3$.

First, characterization of the size of rearrangements, which are the precursors to global plasticity was performed in this work [35]. Rearrangements (or the initial rearrangements in an avalanche) have been recognized as being localized in several DSs systems, such as LD glasses, bubble rafts, foams, and colloidal glasses. To do this, the quantity D^2_{min} between times t and $t + \Delta t$, introduced in [7] and modified in [25] was used. This quantity captures the mean square deviation of a particle's position from the best-fit affine deformation of its neighborhood, and therefore measures the non-affine motion of particle k at time t [4, 25]:

$$D^2_{min} = 1/M_k \sum [\mathbf{r}_{ik}(t + \Delta t) - \mathbf{J}_k(t)\mathbf{r}_{ik}(t)]^2 \quad (2)$$

where $\mathbf{r}_{ik}(t)$ is the displacement vector between particles i and k at time t, $\mathbf{J}_k(t)$ is the "best fit" local deformation gradient tensor about particle k that minimize D^2_{min} (k; t). Summation runs over the M_k particles within a radius R_c^D of particle k.

To focus on the initial rearrangements, we calculate D^2_{min} at the value of Δt corresponding to the minimum of the correlation length ξ_r. All experiments show that the correlations are reasonably well described by an exponential decay with a correlation length ξ_r. Therefore, the size of rearrangements was characterized by $\xi_{r.}$ To measure the spatial extent of rearrangements, the normalized correlation function was considered:

$$\langle \delta D^2_{min}(0) \delta D^2_{min}(r) \rangle \equiv \langle D^2_{min}(0)\, D^2_{min}(r) \rangle - \langle D^2_{min}(r) \rangle^2 / \langle [D_{min}]^2 \rangle - \langle D^2_{min} \rangle^2 \qquad (3)$$

Analysis of number of disordered solids draws a striking contrast with crystalline solids. Overall 12 different systems were studied. For six of these systems, which span almost the entire range of Young's modulus, particle size, and particle interactions were obtained The particle positions versus time data needed for the analysis of rearrangement size. Results for ξ_r versus particle diameter fall very close to the line of best fit, $\xi_r/d = 1.1 \pm 0.2$, where d is the effective particle diameter. The result shows that all studied DSs have only one size of rearrangements, close to a particle diameter. In other words, common rearrangement size is typical feature of DSs. There are no rearrangements of different sizes in DSs. This results is difficult to explain in the framework of plasticity models described above.

4.1 Relationship of Softness to Rearrangements

It was found that local structure of DSs alone can be used to develop a predictive description of dynamics in glassy liquid sand and aged glasses, because the "softness" depends only on the local structural environment of the particle. Thus, softness can be determined from any static picture (or snapshot) of the structure along deformation, time, or temperature trajectories. It has been shown that for LD and oligomer glasses the energy barrier that must be surmounted for the particle to rearrange *decreases linearly with increasing softness*. Thus, rearrangements are exponentially more likely to involve particles with high softness. Note that not all high-softness particles participate in rearrangements, like particles surrounding dislocations in crystals. Soft particles are simply more likely to rearrange than others. Therefore, one would expect the size of a rearrangement to be limited by the spatial extent of high-softness regions of glass.

In analogy to the previous discussion of D^2_{min}, the size of structural heterogeneities was quantified by considering the normalized spatial correlation function:

$$\langle \delta S(0) \delta S(r) \rangle \equiv \langle \delta S(0) \delta S(r) \rangle - \langle S \rangle^2 / \langle S^2 \rangle - \langle S \rangle^2 \qquad (4)$$

As with D^2_{min}, it was found that $\delta S(0)\ \delta S(r)$ decays approximately exponentially with the correlation length ξ_s. Thus, ξ_s is a good measure of the size of high-softness regions that are more likely to rearrange. Authors find that the emergent correlations of S are nearly universal. The spatial correlation length for softness (the size of soft regions), ξ_s, falls on a common line $\xi_s/d = 1.1 \pm 0.2$ for all systems studied. (In the case of oligomers d = the monomer size, which also seriously contradicts with results of ST and STZ models.) Results show the ratio $\xi_r/\xi_s = 0.97 \pm 0.07$, with a scatter significantly smaller than for ξ_r/d or ξ_s/d. The analysis provides compelling evidence that the size of rearrangements, ξ_r, is encoded in the size of correlated soft regions in the system, ξ_s, independent of the nature and even the sign of interactions, the dimensionality of the system, and how the rearrangements were induced.

All provided data show, that the essential differences between plasticity in crystals and plasticity in DSs can be summarized as follows. In crystals, there is universality in the definition of the microscopic structural features which are correlated with rearrangements. But DSs behave differently. In DSs there is emergent universality in the properties like yield strain and rearrangement size, but there is not in crystals. The origin of this universality is not yet understood. Results of the work [31, 35], however, point to the possibility of a unifying framework and simplification of understanding of plasticity in DSs.

5 Some Unresolved Problems in Plasticity of DSs

General picture of plasticity of DSs appears as reasonably understandable [1–3]. The main event defining the development of plasticity in DSs is the nucleation of the primary carriers, STs or STZs, in a body. This process controls the kinetics of all further rearrangements. Then further reorganizations of primary carriers occur. Main of them is an avalanche which create the final size of the macroscopic plasticity carriers and their size distribution. Plasticity carriers can't glide in dislocation-like manner in a glass. Therefore, repeating nucleation of them guides the whole plastic processes in GSs. The concentration of the plasticity carriers necessary for the steady flow is different in DSs of different chemistry. Characteristic of GSs responsible for steady concentration of plasticity carriers in them is not clear yet also. The internal potential energy ΔU of a deformed DS is defined by concentration of the carriers. The steady plastic flow starts when percolation of the macroscopic carriers over whole sample occurs.

However, deep penetration in the plasticity mechanism demonstrates that many important details of plastic rearrangements look controversial and not yet clear enough. In the following we will describe some of such features. Many features of nucleation of the primary carriers of plasticity in the model of softness in not clear. Definitely, the carriers in this model should have the ST structure. However, relation of their structure and size to the softness of glass is not understood now yet. Below we'll consider several unresolved problems in plastic deformation of DSs

5.1 Is It Necessary for DSs to Have the Structural Precursors for Development of Plastic Deformation?

Today there are two conflicting points of view. One group of researches considers plasticity of DSs as an inherent local mechanical instability. This instability can be understood by focusing on the Hessian matrix of the material with an eigen value that goes to zero following a saddle-node bifurcation [1, 2, 10]. In the instability way of thinking this is explained by the localization of the eigenvalue function associated with the going them to zero eigenvalue [1, 10].

The other way of a system to react on an external load is the nucleation of STs in some special (fertile [1, 3]) sites of a glass. In papers [2, 3, 14, 31, 35] it was suggested, that local structural precursors should exist in a virgin glass, and the plasticity starts in such specific, some pre-existing structures occur in a virgin (non-deformed) glass. In works [2, 35, 36] the size and internal complexity of the transformations must be related to local cluster of misfit and the *pre-existing excess enthalpy* [3]. STZs appear when, and these structures become polarized by external stress flipping from initially unrelaxed to relaxed structural forms [2]. In the ST model plastic strain increment γ^{T} is accumulated inside of each ST. But in STZ model the increment appears due to an orientation of an STZs. This is radical difference between the ST and STZ models. It suggests that for nucleation of STZ in glass some structural precursor should exist in glass before its loading [1, 3]. Do precursors exist in non-deformed glasses or not we can't say now.

5.2 Sizes of the Unit Plastic Events

The volume of an individual plastic event Ω_i is the other important parameter of the plastic process in GSs. Relaxations, leading to the formation of shear rearrangements occur in this volume. In metallic glasses, where atomic interactions are nearly isotropic, the relaxation volume is the smallest and is estimated as $8{\cdot}10^{-30}$ m^3 [1, 3]. By contrast, in the flexible chain glassy polymers, where the principal kinematical forms of a plastic strain accommodation are rotations around single bonds of the backbone, the volume Ω_i is the largest for all studied DSs and has been estimated to be $5{\cdot}10^{-25}$ m^3 [1, 3]. For a-Si, as a representative of a simple space network glass, with more isotropic kinematical restrictions, estimates for Ω_i are $8{\cdot}10^{-27}$ m^3, i.e., intermediate between the values for metallic and polymeric glasses. The average transformation shear strain γ^T was guessed to be 2 to 3% in metallic glasses [3], measured to be in the range of 1.7% in flexible chain glassy polymers by computer simulation, and was determined to be 3.6% for a-Si [3].

The higher the kinematic constraints acting on the relaxation process in volume Ω_{i}, the larger is Ω_{i} [1]. The type of atoms bonding in the glass undoubtedly affects the strength of constraints. For example, polymer glasses composed of flexible chains, this parameter is the highest among the materials at hand, $\Omega_i \approx 5{\cdot}10^{-25}$ m^3, which

is expectable. Calculating in number of monomer units the sizes of rearranging segments are: 1267 (PS), 4500 (PC), 6500 (PET) and 8600 (Kapton) monomers [1]. According to other authors, for PMMA the segment size is 3000 monomers [37, 38]. Evidently, such large values of Ω_i for organic polymers may occur due to participation of segmental motions in rearrangements and relaxation processes. The other reason is strong anisotropy of polymer chains (and ordered structures) along and across of chain axes [1, 3]. In [1, 20] is assumed that the size of the plastic segment is much larger than the size of a computation cell. Such sizes of plastic rearrangements seem to be too large. The simulation of glassy PE [25, 29, 39, 40] that the average length of the segment participating in a single plastic event at $T_{def} = 50$ K is as low as 14 methylene groups for the full-atom model and 24 for the united-atom model. Data of papers [31, 35] demonstrate very different picture. In work [31] the sizes of rearranging units occur to be about the diameter of monomer unit for oligomers. The contradiction of the estimations is evident. A precise evaluation, however, requires STZs direct observation, which is not feasible since STZs are local transition events rather than being actual defects like dislocation.

Another question appears in the connection with structural description of DSs, introduced in papers [41–43]. Authors found three types of atomic level defects in DSs: n-, p- and τ—defects in computer simulations of structure of MGs. The defects describe internal stresses in MG structure (or in dislocation cores of crystals), long range elastic stress fields around the defects and symmetry of the defects. The picture represents well many structural features and enthalpy excess in DSs [4]. However, attempts to check abilities of the defects to initiate local plastic deformation in glasses were not successful. And it is not clear why. At least two suggestions might be considered: the first one—any structural precursors (atomic level defects in this case and stress fields surrounding the defects) are not necessary for nucleation of plastic rearrangements in DSs; the second assumption—n-, p- and τ—defects have too small sizes (free volume) to nucleate plastic rearrangements in glasses. The question is not resolved yet, but it looks that the resolution may appear soon. We believe that if we will be able to find critical size (critical free volume) and type of a defect able to nucleate a unit plastic event under action of external stress, it may strongly move us to understanding of key features of plasticity in DSs.

5.3 Free and Activation Volumes in GSs

Method PALS gave possibility to measure the sizes and shape of the free volume holes in glasses [28]. It is known now that the average size of the free volume holes is about an order of magnitude smaller than that of the shear activation volume V* (couple of hundred cubic angstroms compared to a couple of cubic nanometer, respectively) [28, 44–46]. From this comparison important conclusion might be deduced: the free volume holes serve only as active sites for shear transformations rather than accommodating them. Therefore, larger free volume cavities can support more localized shear events with smaller sizes. In smaller holes the localization effect

is less dominant, and broad regions of DSs undergo shear deformation. This hypothesis [45], however, requires further investigation via direct visualization of STZs. By examining the strain rate and temperature sensitivity of the flow, it was found that the geometrical properties of the STZs are only slightly dependent on the thermal history of the sample. In PC, STZs are shown to occur in almost flat ellipsoidal regions with the volume about 480 nm^3 which encompasses 5700 monomers, and with the transformation shear strain of about 0.02. The nucleation Helmholtz free energy for a single STZ is identified to be almost strain rate insensitive and is calculated to be about 1.35 eV for the close strain rates [44]. Authors made these conclusions from nano-indentation data [44, 45]. They came to the following inferences:

- The nucleation energy of a single STZ in PGs is about unity in eV units which is not significantly smaller than that of the MGs. While the nucleation energy of an STZ is directly related to the shear modulus of the material, one expects this energy to be orders of magnitude bigger for MGs according to their considerably higher shear modulus. However, the nucleation energy also depends on the size of the STZ. The huge size of the STZs in PGs compared to MGs compensates for their shear modulus discrepancy, and levels of activation energy in two materials.
- The transformation shear strain γ^T is not a universal value in PGs. The transformation shear strain is assumed to be about 0.015 in all types of glassy polymers [1, 3, 20], however, current analyses show that the value of this parameter is material dependent and is about 0.02 in PC and 0.03 in PMMA. The shape of the STZs in all types of glassy solids are assumed to be spherical [1, 3, 37, 38, 47]; however, current studies suggest that the shear transformation zones are formed in the regions with the shape close to the flat ellipsoids in PMMA and PC. All these data are close to results received in [1, 3], however, show some deviations. All presented results tell as, that our vision of the size and shape of Ω_i in GSs is not very definite yet.

5.4 *Enhancement of Molecular Motions in DSs During Deformation*

One of the most unexpected effects in deformation of DSs is a drastic acceleration of the segmental dynamics of polymer chains under the action of external stress. The effect was first discovered experimentally for a deuterated Nylon-6, where enhanced mobility of the amorphous phase was found by NMR measurements [48, 49]. Next evidences were discovered by the computer simulations of LD glasses. Much more information was received in simulations of glassy PE subjected to the active uniaxial compression [50, 51]. These simulations had shown:

- The rate of transitions between the states of PE chain with different conformations grows by two to three orders of magnitude. The new flip-type molecular motions along PE chains appear [52].

- The acceleration of chain dynamics has almost no effect on the conformational composition of PE glass.
- Once loading is stopped, the rates of conformational transitions decrease, and the flip-type motions becomes hindered again.
- In the glassy state of PE conformational transitions are spatially heterogeneously distributed in the system. Dynamic heterogeneity appearing in the deformation process is not related to the heterogeneity of local density of the glass. The acceleration of molecular dynamics during the deformation of glassy polymers was also supported in experiments with rotational dynamics of the fluorescent probe in the glassy PMMA [53]. Creep experiments ($\sigma = 0.54\ \sigma_y$) had shown that the segmental motions in glassy PMMA at a constant loading rate accelerates from the very onset of loading. The rate of segmental dynamics in PMMA increases by several orders of magnitude by the end of the deformation process. The increase in segmental mobility was also observed in the simulation of shear deformation in the atactic glassy PS film [47]. All the results confirmed data received on PE simulations [51].

The data on the acceleration of molecular dynamics under loading of glassy polymers are often interpreted in terms of free volume grows during deformation. However, as was shown in [54], there are two types of behavior in changes of dynamics. In tensile deformation, the acceleration correlates with the growth of volume, but during uniaxial compression, macroscopic changes in volume are insignificant (less than 0.5%) at all stresses, although mobility is nevertheless enhanced. It was also shown that molecular mobility in chains is enhanced to the same extent for both tensile and compression deformation protocols. Hence, it follows that a change in the shape of potential energy surface rather than increase in volume during deformation is responsible for the observed acceleration of dynamics.

Two dynamic characteristics of glassy polymers are very sensitive to deformation. First is the rate of segmental mobility of chains, and the dynamic heterogeneity of polymer glasses. The acceleration of the dynamics of chains is currently explained in terms of two factors. One of them is the rejuvenation phenomenon moving the system upward along potential energy surface, and the second factor is related to the action of an applied stress, which "inclines" potential energy surface and thus reduces the activation barrier of mobility and does not change the position of energy minima [55]. Simulations in many cases are consistent with this viewpoint [56, 57]. Both of these acceleration mechanisms operate also in the theory advanced in [58].

All mentioned problems of plastic deformation of GSs undoubtedly will be resolved in near future. And one may expect that new knowledge will provide deeper understanding of the deformation behavior of DSs.

Acknowledgements This work was supported by the Program of Fundamental Research of the Russian Academy of Sciences 2013-2020 (project No 0082-2014-0013, AAAA-A17-117042510268-5). The research was carried out using supercomputers at Joint Supercomputer Center of the Russian Academy of Sciences (JSCC RAS).

References

1. Argon, A.S.: The Physics of Deformation and Fracture of Polymers. Cambridge University Press, New York (2013)
2. Falk, M.L.: The flow of glass. Science **318**, 1880–1881 (2007)
3. Argon, A.S., Demkowicz, M.J.: What can plasticity of amorphous silicon tell us about plasticity of metallic glasses? Metall. Mater. Trans. A **39**, 1762–1778 (2008)
4. Oleinik, E.F., Mazo, M.A., Strelnikov, M.I., Rudnev, S.N., Salamatina, O.B.: Plasticity mechanism for glassy polymers: computer simulation picture. Polymer Sci. Ser. A+ **60**, 1–49 (2018)
5. Falk, M.L., Langer, J.S.: Dynamics of viscoplastic deformation in amorphous solids. Phys. Rev. E **57**, 7192–7205 (1998)
6. Falk, M.L., Maloney, C.E.: Simulating the mechanical response of amorphous solids using atomistic methods. Eur. Phys. J. B **75**, 405–413 (2010)
7. Falk, M.L., Langer, J.S.: Deformation and failure of amorphous, solid like materials. Annu. Rev. Condens. Matter. Phys. **2**, 353–373 (2011)
8. Rodney, D., Tanguy, A., Vandembroucq, D.: Modeling the mechanics of amorphous solids at different length scale and time scale. Model. Simul. Mater. Sci. **19**, 083001 (2011)
9. Gendelman, O.V., Manevitch, L.I.: A model of plastic deformation and localized vibration modes in 3D glass. J. Phys.-Condens. Matter **7**, 6993–7004 (1995)
10. Gendelman, O., Jaiswal, P.K., Procaccia, I., Gupta, B.S., Zylberg, J.: Shear transformation zones: state determined or protocol dependent? EPL-Europhys. Lett. **109**, 16002 (2015)
11. Bulatov, V.V., Argon, A.S.A stochastic model for continuum elasto-plastic behavior. I. Numerical approach and strain localization. Model. Simul. Mater. Sci. **2**, 167–184 (1994)
12. Bulatov, V.V., Argon, A.S.: A stochastic model for continuum elasto-plastic behavior. II. A study of the glass transition and structural relaxation. Model. Simul. Mater. Sci. **2**, 185–202 (1994)
13. Bulatov, V.V., Argon, A.S.: A stochastic model for continuum elasto-plastic behavior. III. Plasticity in ordered versus disordered solids. Model. Simul. Mater. Sci. **2**, 203–222 (1994)
14. Schuh, C.A., Lund, A.C.: Atomistic basis for the plastic yield criterion of metallic glass. Nat. Mater. **2**, 449–452 (2003)
15. Argon, A.S.: Plastic deformation in metallic glasses. Acta Metall. Mater. **27**, 47–58 (1979)
16. Spaepen, F.: A microscopic mechanism for steady state inhomogeneous flow in metallic glasses. Acta Metall. Mater. **25**, 407–415 (1977)
17. Boiko, V.S., Garber, R.I., Kosevich, A.M.: Reversible Plasticity of Crystals. Nauka, Moscow (1991) (in Russian)
18. Likhachev, V.A., Kuz'min, S.L., Kamentceva, Z.P.: Shape Memory Effect. LGU Publication, Leningrad (1987) (in Russian)
19. Oleinik, E.F.: Distortional plasticity in organic glassy polymers. In: Baer, E., Moet, S. (eds.) High Performance Polymers, pp. 79–102. Hanser Verlag, Munchen (1990)
20. Mott, P.H., Argon, A.S., Suter, U.W.: Atomistic modeling of plastic deformation of glassy polymers. Philos. Mag. A **67**, 931–978 (1993)
21. Oleinik, E.F., Salamatina, O.B., Rudnev, S.N., Shenogin, S.V.: A new approach to treating plastic strain in glassy polymers. Vysokomol. Soedin. A **35**, 1819–1849 (1993). (in Russian)
22. Hasan, O.A., Boyce, M.C.: Energy storage during inelastic deformation of glassy polymers. Polymer **34**, 5085–5092 (1993)
23. Bol'shanina, M.A., Panin, V.E.: Latent energy of deformation. Book of Paper of Tomsk State University, pp. 193–225 (1957) (in Russian)
24. Bever, M.B., Holt, D.L., Titchener, A.L.: The stored energy of cold work. Prog. Mater Sci. **17**, 5–177 (1972)
25. Strelnikov, I.A., Mazo, M.A., Balabaev, N.K., Oleinik, E.F.: Computer simulation of rearrangements in chains of glassy polymethylene subjected at low temperature inelastic deformation. Polymer Sci. Ser. A+ **56**, 511–521 (2014)
26. Eshelby, J.D.: The determination of the elastic field of an ellipsoidal inclusion, and related problems. Proc. R. Soc. A Math. Phys. **241**, 376–396 (1957)

27. Oleinik, E.F., Shenogin, S.V., Paramzina, T.V., Rudnev, S.N., Shantarovich, V.P., Azamatova, Z.K., Pakula, T., Fisher, E.W.: Molecular mobility in plastically deformed glassy polymers. Polymer Sci. Ser. A+ **40**, 1187–1202 (1998)
28. Consolati, G., Quasso, F.: Morphology of free-volume holes in amorphous polymers by means of positron annihilation lifetime spectroscopy. In: Utracki, L.A., Jameson, A.M. (eds.) Polymer Physics. From Suspensions to Nanocomposites and Beyond, pp. 391–419. Wiley, Hoboken (2010)
29. Pacheco, A.A., Batra, R.C.: Analysis of structural changes during plastic deformations of amorphous polyethylene. Polymer **54**, 819–840 (2013)
30. Schall, P., Weitz, D.A., Spaepen, F.: Structural rearrangements that govern flow in colloidal glasses. Science **318**, 1895–1899 (2007)
31. Schoenholz, S.S., Cubuk, E.D., Sussman, D.M., Kaxiras, E., Liu, A.J.: A structural approach to relaxation in glassy liquids. Nat. Phys. **12**, 469–471 (2016)
32. Cohen, M.H., Grest, G.S.: Liquid–glass transition, a free volume approach. Phys. Rev. B **20**, 1077–1098 (1979)
33. Kotelyanskii, M.J., Mazo, M.A., Oleynik, E.F., Grivtsov, A.G.: Molecular dynamics of vitrification and plastic deformation of a two-dimensional Lennard-Jones mixture. Phys. Status Solidi B **166**, 25–42 (1991)
34. Oleinik, E.F., Rudnev, S.N., Salamatina, O.B.: Evolution in concepts concerning the mechanism of plasticity in solid polymers after the 1950s. Polymer Sci. Ser. A+ **49**, 1302–1327 (2007)
35. Cubuk, E.D., et al.: Structure-property relationships from universal signatures of plasticity in disordered solids. Science **358**, 1033–1037 (2017)
36. Demkowicz, M.J., Argon, A.S.: Liquidlike atomic environments act as plasticity carriers in amorphous silicon. Phys. Rev. B. **72**, 245205 (2005)
37. Malekmotiei, L., Samadi-Dooki, A., Voyiadjis, G.Z.: Nanoindentation study of yielding and plasticity of poly(methyl methacrylate). Macromolecules **48**, 5348–5357 (2015)
38. Malekmotiei, L., Voyiadjis, G.Z., Samadi-Dooki, A., Lu, F., Zhou, J.: Effect of annealing temperature on interrelation between the microstructural evolution and plastic deformation in polymers. J. Polymer Sci. Polymer Phys. **55**, 1286–1297 (2017)
39. Balabaev, N.K., Mazo, M.A., Lyulin, A.V., Oleinik, E.F.: Plastic deformation of glassy polymethylene: computer aided molecular dynamic simulation. Polymer Sci. Ser. A+ **52**, 633–644 (2010)
40. Strelnikov, I.A., Mazo, M.A., Balabaev, N.K., Oleinik, E.F., Berlin, A.A.: Energy storage in plastic deformation of glassy polymethylene. Dokl. Phys. Chem. **457**, 108–111 (2014)
41. Srolovitz, D., Egami, T., Vitek, V.: Radial distribution function and structural relaxation in amorphous solids. Phys. Rev. B **24**, 6936–6944 (1981)
42. Srolovitz, D., Maeda, K., Vitek, V., Egami, T.: Structural defects in amorphous solids statistical of a computer model. Philos. Mag. A **44**, 847–866 (1981)
43. Maeda, K., Takeuchi, S.: Computer simulation of deformation in two-dimensional amorphous structures. Phys. Status Solidi A **49**, 685–696 (1978)
44. Samadi-Dooki, A., Malekmotiei, L., Voyiadjis, G.Z.: Characterizing shear transformation zones in polycarbonate using nanoindentation. Polymer **82**, 238–245 (2016)
45. Voyiadjis, G.Z., Samadi-Dooki, A.: Constitutive modeling of large inelastic deformation of amorphous polymers: free volume and shear transformation zone dynamics. J. Appl. Phys. **119**, 225104 (2016)
46. Zimmerman, J.A., Kelchner, C.L., Klein, P.A., Hamilton, J.C., Foiles, S.M.: Surface step effects on nanoindentation. Phys. Rev. Lett. **87**, 165507 (2001)
47. Chung, Y.G., Lacks, D.J.: Atomic mobility in strained glassy polymers: the role of fold catastrophes on the potential energy surface. J. Polymer Sci. Polymer Phys. **50**, 1733–1739 (2012)
48. Loo, L.S., Cohen, R.E., Gleason, K.K.: Deuterium nuclear magnetic resonance of deuterium oxide in nylon 6 under active uniaxial deformation. Polymer **41**, 7699–7704 (2000)
49. Loo, L.S., Cohen, R.E., Gleason, K.K.: Chain mobility in the amorphous region of nylon 6 observed under active uniaxial deformation. Science **288**, 116–119 (2000)

50. Brown, D., Clarke, J.H.R.: Molecular dynamics simulation of an amorphous polymer under tension. 1. Phenomenology. Macromolecules **24**, 2075–2082 (1991)
51. Capaldi, F.M., Boyce, M.C., Rutledge, G.C.: Molecular response of a glassy polymer to active deformation. Polymer **45**, 1391–1399 (2004)
52. Smessaert, A., Rottler, J.: Recovery of polymer glasses from mechanical perturbation. Macromolecules **45**, 2928–2935 (2012)
53. Riggleman, R.A., Lee, H.-N., de Ediger, M.D., Pablo, J.J.: Heterogeneous dynamics during deformation of a polymer glass. Soft Matter **6**, 287–291 (2010)
54. Riggleman, R.A., Lee, H.-N., Ediger, M.D., de Pablo, J.J.: Free volume and finite-size effects in a polymer glass under stress. Phys. Rev. Lett. **99**, 215501 (2007)
55. Hebert, K., Ediger, M.D.: Reversing strain deformation probes mechanisms for enhanced segmental mobility of polymer glasses. Macromolecules **50**, 1016–1026 (2017)
56. Riggleman, R.A., Schweizer, K.S., de Pablo, J.J.: Nonlinear creep in a polymer glass. Macromolecules **41**, 4969–4977 (2008)
57. Riggleman, R.A., Toepperwein, G.N., Papakonstantopoulos, G.J., de Pablo, J.J.: Dynamics of a glassy polymer nanocomposite during active deformation. Macromolecules **42**, 3632–3640 (2009)
58. Chen, K., Schweizer, K.S.: Theory of yielding, strain softening and plastic flow in polymer glasses under constant strain deformation. Macromolecules **44**, 3988–4000 (2011)

Shockwaves and Kinks in Exothermic Nonlinear Chains

Itzik B. Shiroky and Oleg V. Gendelman

Abstract We address the problem of a transition front propagation in chains with a bi-stable nondegenerate on-site potential and a nonlinear gradient coupling. For a generic nonlinear coupling, one encounters a special regime of transitions, characterized by extremely narrow fronts, far supersonic velocities of the front propagation, and long waves in the oscillatory tail. This regime is qualitatively associated with a shock wave. In this case, the front propagation can be described with the help of a simple reduced-order model; the latter delivers a kinetic law, which is almost not sensitive to the fine details of the on-site potential. Besides, it is possible to predict all main characteristics of the transition front, including its velocity, as well as the frequency and the amplitude of the oscillatory tail. Numerical results are in a good agreement with the analytical predictions. The suggested approach allows one to consider the effects an on-site damping. When the damping is moderate, it is possible to consider the shock propagation in the damped chain as a perturbation of the undamped dynamics. This approach also yields reasonable predictions. When the damping is high, the transition front enters a completely different asymptotic regime of a subsonic kink. The gradient nonlinearity generically turns negligible, and the propagating front converges to the regime described by simple exact solution for continuous model with a linear coupling.

1 Introduction

Transition fronts, also known as phase boundaries, are common in systems in which the potential energy has more than one state of a stable equilibrium. A broad variety of processes in real systems and materials can be described by such switching of states. Among many possible applications, one encounters dislocations in metals [1–3], dry friction [4], dynamics of carbon nano tubes foams [5], pulse propagation in cardio physiology [6], lattice distortions around twin boundaries [7], domain walls

I. B. Shiroky · O. V. Gendelman (✉)
Faculty of Mechanical Engineering, Technion, 32000 Haifa, Israel
e-mail: ovgend@technion.ac.il

I. V. Andrianov et al. (eds.), *Problems of Nonlinear Mechanics and Physics of Materials*, Advanced Structured Materials 94,
https://doi.org/10.1007/978-3-319-92234-8_19

in ferroelectrics [8], crack propagation [9, 10], motion of fronts in semiconductor superlattices [11], surface reconstruction phenomena [12], calcium release in cells [13] and statistical mechanics [14]. Truskinovsky and Vainchtein in [15] addressed martensitic phase transitions by presenting a discrete model with long- range interactions. The model allows the derivation of a macroscopic dissipation law specified as a relation between force and velocity. The dissipation is due to radiation of lattice waves that carry energy from the front. Dynamics of crowdions in anisotropic crystals was studied in [16, 17]. In [18] the damped and externally driven FK chain is studied and the threshold forcing amplitude is found. This model may be beneficial in describing a chain of ions trapped on a metallic surface with an external AC electric field as the drive, as well as in the study of Josephson junctions. Other applications can be found in the comprehensive review of Braun and Kivshar [2].

It is beneficial in many cases to invoke discrete models for description of these phenomena. In such models, the transition front (or other structural defect) is to overcome the potential barrier caused by the discrete lattice. For this sake, it requires either external forcing or energy supply in the lattice due to the front propagation. This micro-scale effect disappears in continuous models, where the solutions, which represent defects, can move freely without drag. On the other hand, discrete models allow derivation of a relation between the external force or energy gain and the front velocity, commonly known as the "kinetic relation". At the micro level, when no dissipation is assumed, the effect which describes the removal of the released energy is known in literature as "radiative damping" [19]. The lattice waves that accompany the transition front, have to remove at least the major portion of the gained energy, while the rest of the energy may be spent for creating new surfaces as it happens in the case of crack initiation [20, 21].

The broad family of the discrete models that describe such transitional phenomena can be categorized to sub-classes. The multi-stability can appear in the on-site potential [1, 19, 22–25], or in the interparticle coupling to describe, for instance, martensitic phase transition [15, 26]. These models are often considered as Hamiltonian [1, 27, 28]. However, in certain cases the dissipation is included explicitly [22, 29–31]. Nevertheless, the main reason for the ongoing growth in studies of these systems is the numerous possible configurations of the multi-stable potentials. The pioneering work of Frenkel and Kontorova [28] considered a sinusoidal on-site potential, thus introducing the discrete version of the sine-Gordon equation. Zolotaryuk considers a different periodic degenerate on-site potential and shows that kinks can propagate even when the barriers are nearly flat and the wells are narrow [32]. Smooth layouts of the on-site potentials (also referred to as fully nonlinear) are studied numerically in [33, 34], and show that these might result in slower velocity of the defect propagation. In [22] a linear chain with the smooth on-site potential is studied by means of an approximate model.

A common configuration that has been adopted in many works, is that of a bi-stable on-site potential [19, 27, 35]. The most interesting case is the non-degenerate on-site potential with a certain energetic difference between the minima; this difference dictates the direction of the front propagation. The simplest model of linearly coupled chain an a bi-parabolic on-site potential with equal curvature wells was considered

in the work of Atkinson and Cabrera [1], and further explored in the early works of Ishioka [30] and Celli [36] and later works [19, 22, 27, 37]. The advantage of this potential is that an analytical solution can be obtained through a direct Fourier transform. The solution can be generalized to include also an on-site linear dissipation [38]. The case with different well curvatures requires application of the Wiener–Hopf method as was implemented in [39]. Paper [26] studies a modification of the bi-parabolic potential by an inclusion of a non-convex region (a spinodal region) that smoothens the cusp of the pure bi-parabolic potential.

Dynamics of the transition fronts in chains with a bi-stable on-site potential and a nonlinear gradient coupling is much less explored. In weakly nonlinear lattices, directional waveguiding has been achieved by using cubic Kerr nonlinearities in nonhomogeneous systems [40]. In strongly nonlinear chains of elastically coupled rotational pendula, a steady front propagation was observed in [41]. Recent studies [29, 42] have addressed the case of a generic coupling with on-site dissipation and suggested a law that connects the transported energy with the velocity and dissipation ratio. The results were verified experimentally. Paper [43] explores a topological soliton in a degenerate φ^4 model with a cubic gradient nonlinearity. It is demonstrated that the soliton has a finite number of velocity values in which the propagation isn't accompanied by emission of phonons, and in such case a continuous approximation holds. Further numerical exploration of a similar model is presented in [44] by applying a pseudo-spectral technique. It is found that a single fixed point exists for the explored solitons and it depends on the non-linearity parameter and the barrier of the degenerate potential. The lattice with cubic nonlinearity and φ^4 substrate potential is addressed in [45]. The paper includes analytical results for wide kinks by application of a continuum limit, while it is pointed out that narrow kinks exhibit essentially different dynamics and require a different approach. Milchev [46] studies a system with nonconvex inter-particle interaction. An analytical solution is obtained in the continuum limit and it is shown that distortive waves and breakdown of conventional kinks might be related to the inflection point of the nonconvex potential. A numerical study of a one-dimensional chain with a nonlinear coupling and a non-degenerate on-site potential was presented in [47]. It was shown that even at relatively weak gradient nonlinearities, the velocity of the kink propagation increases dramatically. It was also revealed numerically that for high values of nonlinear coupling β, the front velocity is proportional to $\sqrt{\beta}$.

In several works, dynamics of Frenkel–Kontorova-based systems is analyzed by means of equivalent reduced models [22, 31, 48, 49]. In [22] an approach named "active point theory" is applied to construct approximate solutions for the case of a damped chain with an on-site potential with cubic nonlinearity. A similar method is used in [48]. In [31] the "local mode approximation" is employed to reduce the damped Frenkel–Kontorova problem to an equivalent model of pendula. Generally, these works demonstrate a good agreement of the simplistic models with the numerical integration of the full multi-particle nonlinear equations.

The aforementioned studies, as well as the results obtained for some other models, demonstrate that the transition fronts can be crudely classified as belonging to one of two categories: kinks and shocks, or shockwaves [50]. The kinks normally

have a subsonic or slightly supersonic velocity, and strongly depend on fine details of the model potentials. Contrary to that, the shockwaves can have far supersonic velocities, and their dynamics is governed by conservation laws, similar to classical Rankine–Hugoniot conditions for shockwaves in gases. In the latter case, the fine details of the model potentials are less significant.

In the current report that is based on publications [51, 52], we explore chains with a nonlinear coupling and a non-degenerate bi-stable potential. As the coupling nonlinearity increases, the regime of front propagation gains clear features of a shockwave. The characteristics of the transition front change dramatically compared to the case of linear coupling: the front becomes very narrow with an extreme energy concentration, the front velocity become far supersonic, and the wavenumbers in the oscillatory tail are very low. These properties allow a construction of a simple reduced model applicable to arbitrary nonlinear couplings that depends only on general characteristics of the on-site potential rather than on its fine details. The analytical approach proposed is tested for important cases of asymmetric (Fermi-Pasta-Ulam, FPU) and saturating (Lennard-Jones, LJ) coupling potentials. The discussion is further expanded to include an on-site linear damping is studied for two opposite limiting cases. It is shown that the small damping can be considered as a perturbation of the conservative case, where the propagation is still governed by the shockwave dynamics. In the opposite limit of high damping, the front propagation can be described by means of a simple continuous linear model that describes the propagation of the subsonic kink.

2 Conservative Bi-Stable Chains

2.1 The Model

We consider a chain with a bi-stable nondegenerate on-site potential [27, 51] with a generic nonlinear gradient coupling. Hamiltonian of this chain is written as follows:

$$H = \sum_{n=1}^{\infty} \left[\frac{p_n^2}{2} + U_1(\varphi_{n+1} - \varphi_n) + U_2(\varphi_n) \right]. \tag{1}$$

Here φ_n is the displacement of the nth particle from the initial equilibrium state (meta-stable), $U_1(\varphi_{n+1} - \varphi_n)$ is the gradient potential of the interparticle interaction, $U_2(\varphi_n)$ is a non-degenerate bi-stable on-site potential; $p_n = \dot{\varphi}_n$, masses of all particles are set to unity. $U_2(\varphi_n)$ is defined by three main characteristics: the energetic effect Q, the height of the potential barrier B, and the coordinate difference between the stable and meta-stable states φ^*. Minimum of the meta-stable state is set to $\varphi = 0$ without affecting the generality. Obviously, infinite number of possible bi-stable potentials have such characteristics. In the examples that are presented in this paper we restrict ourselves to three typical shapes:

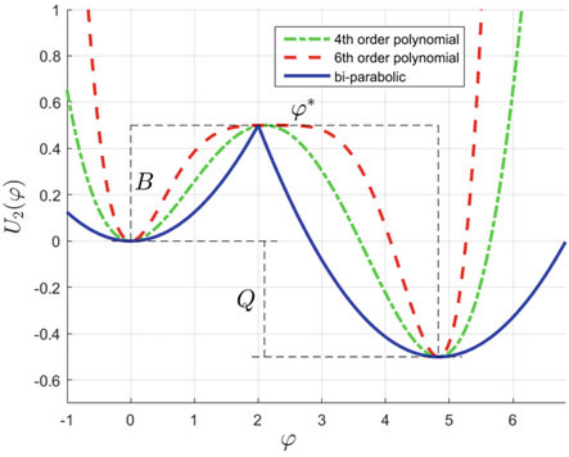

Fig. 1 On-site nondegenerate potential $U_2(\varphi)$. Three possible approximations with the same basic shape parameters are presented: solid-blue—bi-parabolic potential, line-dotted green—4th order polynomial, dashed red—6th order polynomial

(1) Bi-parabolic potential with same curvatures of the two wells ω_0:

$$U_2(\varphi_n) = \begin{cases} \frac{\omega_0^2}{2}\varphi_n^2 & \varphi_n \le b = \frac{\sqrt{2B}}{\omega_0} \\ \frac{\omega_0^2}{2}(\varphi_n - \varphi^*)^2 - Q & \varphi_n > b \end{cases} \tag{2}$$

Here, $\varphi^* = \frac{\sqrt{2(Q+B)}}{\omega_0} + \frac{\sqrt{2B}}{\omega_0}$

(2) 4th order polynomial potential

$$U_2(\varphi_n) = a_2\varphi_n^2 + a_3\varphi_n^3 + a_4\varphi_n^4 \tag{3}$$

(3) 6th order polynomial:

$$U_2(\varphi_n) = b_2\varphi_n^2 + b_3\varphi_n^3 + b_4\varphi_n^4 + b_5\varphi_n^5 + b_6\varphi_n^6 \tag{4}$$

For the 4th order polynomial, the constraints on B, Q, φ^* uniquely define all coefficients. For the 6th order polynomial there is more freedom with 5 coefficients to choose. To obtain the essential deviation from the bi-parabolic potential, the coefficients are chosen to annihilate the second derivative at the maximum (additional condition stems from the fact that the third derivative in this point also must be zero).

The three examples are shown in Fig. 1. The necessary condition for nondegeneracy of the potentials is $Q > 0$. In other terms, the energetic effect Q is the driving force which determines the favorable direction of the reaction. While the three potentials possess the same basic characteristics, the details are different. A notable difference is the shape of the concave area which is sharp for the bi-parabolic potential, smooth for the 4th order polynomial, and nearly flat for the 6th order polynomial.

2.2 The Dynamics of Propagation in the Case of a Subsonic Kink

The main interest of the current paper is the formation and the dynamics a supersonic shockwave in lattices described by Hamiltonian (1). Here, we briefly provide a short description of the subsonic kinks that are also valid solutions of this system for the sake of completeness and to clarify the essential differences when compared to shockwaves. For instance, a kink is formed when the gradient potential is harmonic, $U_1(r) = r^2/2$, as was previously studied in several works [1, 19, 27, 39]. If one considers the classical bi-parabolic potential (2), the dispersion relation in each well can be presented as follows:

$$\omega^2 = 4\sin^2\left(\frac{k}{2}\right) + \omega_0^2 \tag{5}$$

Here ω is a frequency of linear waves in the system. Typical dynamic response in this case is shown in Fig. 2 for a certain time instance. The only nonzero initial condition is the velocity of particle #1 $-\ \dot{\varphi}_1(0) = 10$. From here on, this condition is denoted in figures as "impulse 10". One can observe that the transition zone includes about 5 particles simultaneously.

For the stationary propagation of the transition it is necessary that the front velocity is equal to the phase velocity of the accompanying oscillatory tail, $V = V_{ph}$. We are primarily interested in the cases of rapid and stable front propagation, and therefore assume that the velocity is large enough, so that it corresponds to a single value of real wavevector $k = k^*$. Then, one obtains:

$$V = V_{ph} = \omega^*/k^* \tag{6}$$

Let us denote:

$$L(k) = \omega_0^2 + 4\sin^2\left(\frac{k}{2}\right) - k^2 V_{ph}^2 \tag{7}$$

It is shown in [19] that the phase velocity can be expressed analytically as a function of the energetic effect Q through the following "kinetic relation":

$$\frac{\sqrt{1+Q/B}-1}{\sqrt{1+Q/B}+1} = \omega_0^2 \sum_{k\in N\pm} \frac{1}{|kL'(k)|} \tag{8}$$

Here, $N\pm$ are the real roots of the dispersion relation (5) of the chain. The phase velocity is implicitly determined for any set of the system parameters, as Eq. (8) can be satisfied only by a unique set of roots $N\pm$ that are found from the dispersion relation for a single value of frequency $\omega = \omega^*$.

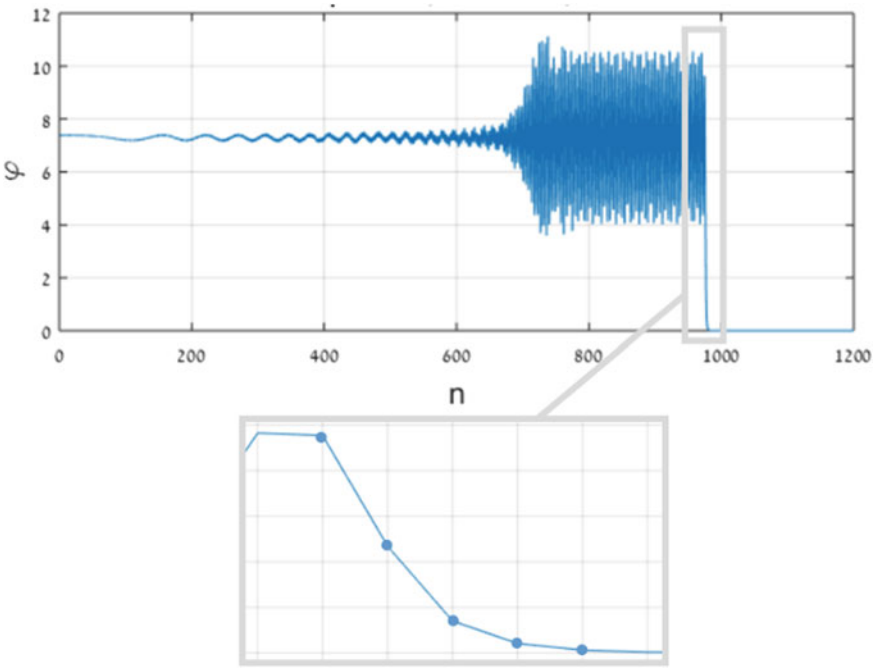

Fig. 2 Particle displacements in the chain with linear coupling. at $t = 1000$. Detailed structure of the front zone is presented in the inset. Parameters: $Q/B = 6$, $\omega_0 = 0.5$, initial conditions: impulse 10. The inset depicts the front zone in details

To examine the sensitivity of solution (6)–(8) to variations in the shape of the on-site potential, we numerically integrate the evolution equations obtained from Hamiltonian (1), with $U_1(r) = r^2/2$ for on-site potentials (3), (4). The front velocity as a function of φ^* is presented in Fig. 3 for all three potential shapes. It easy to notice that the results differ, as one would expect, but the difference in velocities is within 10–15% margin. Qualitative shapes of the curves are similar.

For the 6th order polynomial potential (4) one observes an interesting peculiarity—time delay in the front initiation. Initially, the excitation remains almost perfectly localized at the first particle in a regime of oscillations over both wells. In the conducted numerical simulations, after periods of time that get longer with increasing φ^*, the localized solution disintegrates into the propagating front. This finding is demonstrated in a $\varphi = \varphi(n, t)$ plot in Fig. 4. The excitation remains almost perfectly localized at the first particle for about 790 time units. Small amount of energy is irradiated into the rest of the chain, until the energy of the first particle reaches a critical point, where the propagating front regime is established. This localization and delay of the front initiation occur due to nonlinearity of the on-site potential.

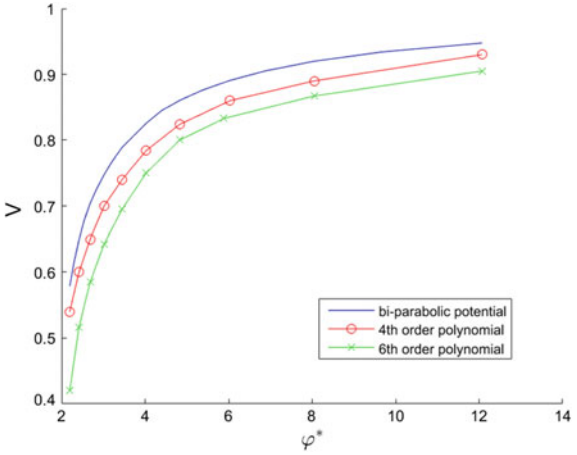

Fig. 3 Front velocity as a function of φ^*; Solid blue—bi-parabolic potential, 'o' red—4th order polynomial potential, 'x' green—6th order polynomial potential; parameters: $Q/B = 1$

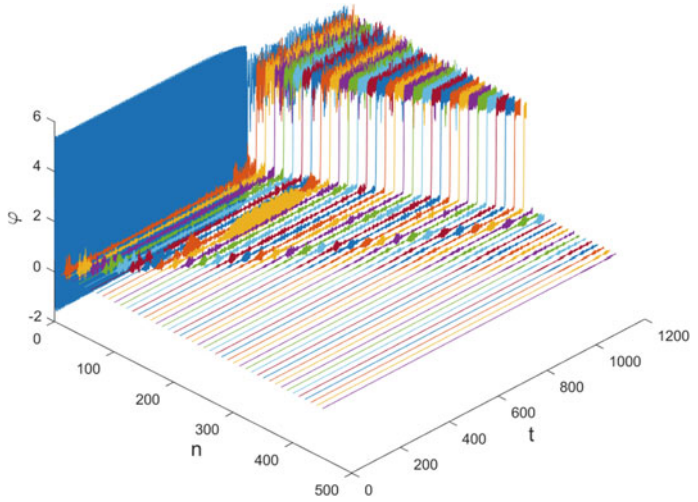

Fig. 4 Delay of the front propagation for the 6th order polynomial potential (4), $\varphi = \varphi(n, t)$; parameters: $Q/B = 1$, $\varphi^* = 4.02$, initial conditions: impulse 8

Similar localization gives rise to well-known discrete breather solutions. Thus, the excitation of the propagating front can be interpreted as a loss of stability of the discrete breather in the chain. Similar effect should be observed also for on-site potential (3), but presumably for larger initial excitations.

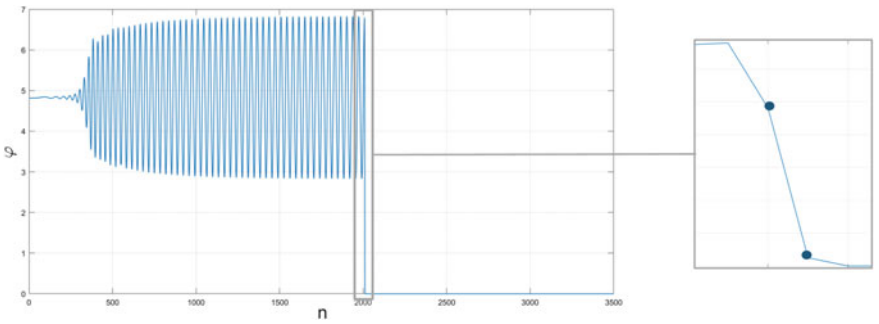

Fig. 5 Dynamic response of the chain with LJ coupling, $\sigma = 20$, $\varepsilon = 2^{1/3}\sigma^2/18$, for $t = 700$. On-site potential: bi-parabolic with parameters: $Q = B = 0.5$, $\omega_0 = 0.5$, Initial conditions: impulse 10. The inset depicts the front zone in details

2.3 *The Supersonic Shockwave Dominated by Gradient Nonlinearities*

In contrast to the previous subsection, if the gradient potential is nonlinear, the front propagation can enter the shockwave regime completely dominated by the coupling nonlinearity, rather than by the specific details of $U_2(\varphi_n)$. To illustrate the phenomenon, we present the simulation results for the well-known LJ coupling potential: $U_1(r) = \varepsilon\left[\sigma^{12}\left(r + 2^{1/6}\sigma\right)^{-12} - \sigma^6\left(r + 2^{1/6}\sigma\right)^{-6}\right]$. A typical response of the chain is presented in $n - \varphi$ plane for a fixed time instance (Fig. 5). The only nonzero initial condition is the velocity of particle #1 $-\ \dot{\varphi}(0) = 10$.

The specific example of the LJ coupling potential is considered in details in Sect. 2.5. Here we suggest a generic simplified model for the description of shockwaves qualitatively similar to the one presented above without restricting ourselves to any particular shape. We base the formulation of the model on the following observations. First, we observe that the velocity is far supersonic. For instance, for the response in Fig. 5, the front propagates with velocity equal to 3.02 (for parameters used in this simulation, the sound velocity is unit). In contrast, for the same on-site potential, but with a linear coupling, the front would propagate with a velocity of 0.86. Then, we admit that the transition area is extremely narrow and includes only 1–2 particles, as in the typical example in Fig. 5. In addition, one observes that the oscillatory tail has a very large wavelength compared to the narrow front area. In the discussed example, each period of oscillations within the tail consists of about 36 particles. The combination of the last two observation yields that the energy concentration in the front is very large compared to other parts of the system, and it happens by virtue of the nonlinear coupling potential. To see that, we evaluate the average density of the strain energy as follows:

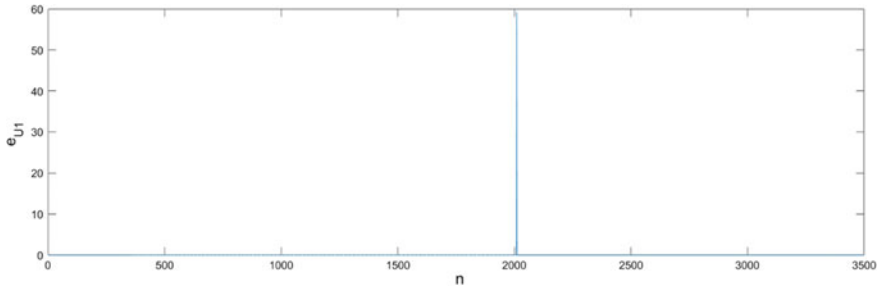

Fig. 6 Nearest-neighbor interaction energy of the chain with LJ coupling term $\sigma = 20$, $\varepsilon = 2^{1/3}\sigma^2/18$ at $t = 700$; On-site potential: bi-parabolic with: $Q = B = 0.5, \omega_0 = 0.5$, initial conditions: impulse 10

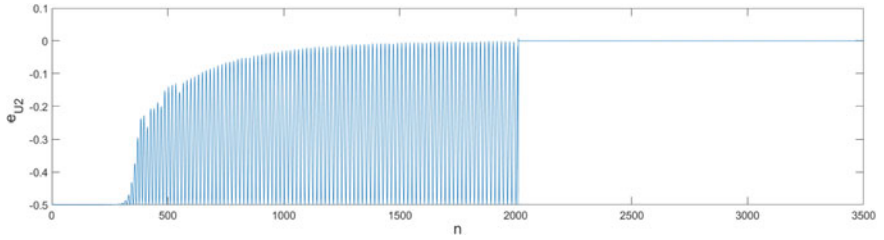

Fig. 7 On-site interaction energy of the chain with LJ coupling term $\sigma = 20$, $\varepsilon = 2^{1/3}\sigma^2/18$ at $t = 700$; On-site potential: bi-parabolic with: $Q = B = 0.5, \omega_0 = 0.5$, initial conditions: impulse 10

$$\bar{e}_{U_1}(n) = \frac{1}{\tau}\int_{t_1}^{t_1+\tau} U_1(\varphi_n(t) - \varphi_{n-1}(t))dt \tag{9}$$

Here $\tau = 1/V$ is the characteristic time of transition, such that for particles within the transition region $\varphi_n(t) = \varphi_{n+1}(t+\tau)$. Typical numerical results for the chain with LJ coupling are presented in Fig. 6. One admits that the concentration of energy is extremely high in the narrow transition area when compared to the rest of the chain.

To construct the simplified model, we first assume the dominance of the nonlinear term (Fig. 6) in the transition area, compared to contribution of the on-site potential (the latter is illustrated in Fig. 7). The maximal energy of the on-site potential is 0.5, which is less than 1% of the energy concentrated in the front zone due to the coupling potential. Therefore, when describing the front zone, we can omit $U_2(\varphi_n)$ in Eq. (1). However, the on-site potential affects the boundary conditions of the solution and the oscillatory tail, as it will be demonstrated below. Hence, we obtain the following approximate Hamiltonian for the transitional area:

$$H_{transition} \approx \sum_j \left[\frac{\dot{\varphi}_j^2}{2} + U_1\big(\varphi_{j+1} - \varphi_j\big)\right] \tag{10}$$

Here j are the indices of particles that belong to the transitional area.

Then, as was mentioned earlier, the transition area is extremely narrow (cf. Fig. 5). Therefore, only these few particles contribute in the summation in Eq. (10). We simplify the problem further and admit that, at large enough velocities, the approximation can take into account only the rapid transition of a single particle from the meta-stable state to the vicinity of the stable state.

To complete the construction of the approximate model, we further observe that the gradient in the transitional region is extremely large compared to both the pre-front zone and the oscillatory tail. So, it is possible to assume that at one edge the transitional region is attached to an almost a fixed particle that still has not left the metastable position $\varphi = 0$.

At the other edge, the transition region is attached to the oscillatory tail. In order to analyze the essence of the interaction of the particle in transition with the tail, we first evaluate the dispersion relation in this area for the test case where the coupling potential is in the form $U_1(r) = \frac{1}{2}r^2 + \frac{\beta}{4}r^4$, and the on-site potential is bi-parabolic (2). Let us introduce a complex variable [53]:

$$\Psi_n = \dot{\varphi}_n + i\omega\varphi_n \tag{11}$$

The derivatives in terms of Ψ are written as follows:

$$\varphi_n = -i\frac{\Psi_n - \Psi_n^*}{2\omega}, \dot{\varphi}_n = \frac{\Psi_n + \Psi_n^*}{2}, \quad \ddot{\varphi}_n = \dot{\Psi}_n - \frac{i\omega}{2}\left(\Psi_n + \Psi_n^*\right) \tag{12}$$

Substitution into the equations of motion for the stable branch and substitution of the modulated harmonic function: $\Psi_n = \phi_n e^{i\omega t}$, $\dot{\Psi}_n = \dot{\phi}_n e^{i\omega t} + i\omega\phi e^{i\omega t}$ yield:

$$\begin{aligned}
&\dot{\phi}_n e^{i\omega t} + \frac{i\omega}{2}\phi_n e^{i\omega t} - \frac{i\omega}{2}\phi_n^* e^{-i\omega t} - \frac{i\omega_0^2}{2\omega}\left(\phi_n e^{i\omega t} - \phi_n^* e^{-i\omega t}\right) \\
&- \frac{i}{2\omega}\left[(2\phi_n - \phi_{n-1} - \phi_{n+1})e^{i\omega t} - \left(2\phi_n^* - \phi_{n-1}^* - \phi_{n+1}^*\right)e^{-i\omega t}\right] \\
&+ \frac{i}{8\omega^3}\beta\Big[\left((\phi_n - \phi_{n+1})e^{i\omega t} - \left(\phi_n^* - \phi_{n+1}^*\right)e^{-i\omega t}\right)^3 \\
&\qquad + \left((\phi_n - \phi_{n-1})e^{i\omega t} - \left(\phi_n^* - \phi_{n-1}^*\right)e^{-i\omega t}\right)^3\Big] = 0
\end{aligned} \tag{13}$$

Division by $e^{i\omega t}$ and subsequent averaging leads to the following slow-flow equations for the wave amplitudes:

$$\begin{aligned}
&\frac{2\omega}{i}\dot{\phi}_n + \omega^2\phi_n - \omega_0^2\phi_n - (2\phi_n - \phi_{n-1} - \phi_{n+1}) \\
&\quad - \frac{3}{4\omega^2}\beta\begin{bmatrix}(\phi_n - \phi_{n+1})^2\left(\phi_n^* - \phi_{n+1}^*\right) + \\ +(\phi_n - \phi_{n-1})^2\left(\phi_n^* - \phi_{n-1}^*\right)\end{bmatrix} = 0
\end{aligned} \tag{14}$$

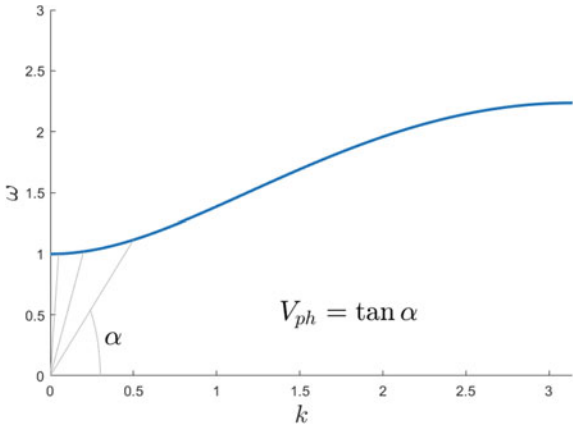

Fig. 8 A typical dispersion relation plot

By substituting $\phi_n = Ae^{ikn}$ one obtains the desired approximate nonlinear dispersion relation:

$$\omega^2 - \omega_0^2 - 4\sin^2\frac{k}{2} + \frac{3\beta A^2}{\omega^2}\left[\sin^2 k - 4\sin^2\frac{k}{2}\right] = 0 \tag{15}$$

The immediate conclusion from (15) is that in the presence of nonlinear coupling the nonlinear dispersion relation is a perturbation of the linear dispersion relation presented in Fig. 8 and it can be used for the following conjecture. Clearly, in a steady state propagation, the phase velocity ($V_{ph} = \omega/k$) must be equal to the front velocity (V) and when the latter is very high, the wavenumber k in the tail must be very small, since it is the only possibility to obtain far supersonic phase velocity for a given linear dispersion relation (Fig. 8). Thus, one can assume the particle at the front approaches a nearly fixed point with coordinate Δ, defined as the first maximum of the oscillatory tail behind the transition (see Fig. 9).

To find the value of Δ one should notice that close to the left bandgap of the linear dispersion relation (Fig. 8), the group velocity is small. So, the energy transport through the oscillatory tail can be neglected and the energy released due to the front propagation is almost not transferred towards or from the front. Moreover, the inter-particle energy can be neglected due to the low-strain in the tail. Due to these peculiarities of the propagation, each particle in the tail oscillates approximately with the energy released by the front at the single site. Hence, the energy balance for an arbitrary particle n in the oscillatory tail can be simply expressed as:

$$\frac{\dot{\varphi}_n^2}{2} + U_2(\varphi_n) = 0 \tag{16}$$

The peak of the oscillation, $\varphi_n = \Delta$, occurs when $\dot{\varphi}_n = 0$. Therefore, one has to extract Δ from the following relation and to choose the relevant root:

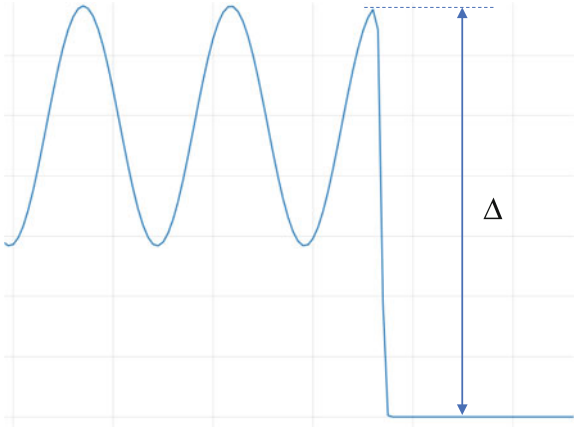

Fig. 9 Definition of Δ

$$U_2(\Delta) = 0 \tag{17}$$

Specifically, for specific potentials used as examples in Fig. 1 we can obtain the following exact expressions for Δ:

Bi-parabolic potential (2):

$$\Delta = \varphi^* + \frac{\sqrt{2Q}}{\omega_0} \tag{18}$$

4th order polynomial potential (3):

$$\Delta = \frac{1}{2a_4}\left(-a_3 + \sqrt{a_3^2 - 4a_4a_2}\right) \tag{19}$$

For the 6th order polynomial (4) potential the expression is somewhat more awkward, but easily computable.

To confirm these findings, we present in Fig. 10 the dependence of numerically determined amplitude Δ versus β and compare it to analytic estimations (18), (19). The amplitude converges to the asymptotic value for both considered cases. For the case of the bi-parabolic potential the convergence is faster due to higher front velocities for the same β. At value of $\beta = 0.1$ the convergence is within 1% of the limit value for the bi-parabolic potential.

The resulting approximate single-DOF Hamiltonian for the particle inside the transition front is written as follows:

$$H = \frac{\dot{\varphi}^2}{2} + U_1(0 - \varphi) + U_1(\varphi - \Delta) \tag{20}$$

From Hamiltonian (20), one obtains:

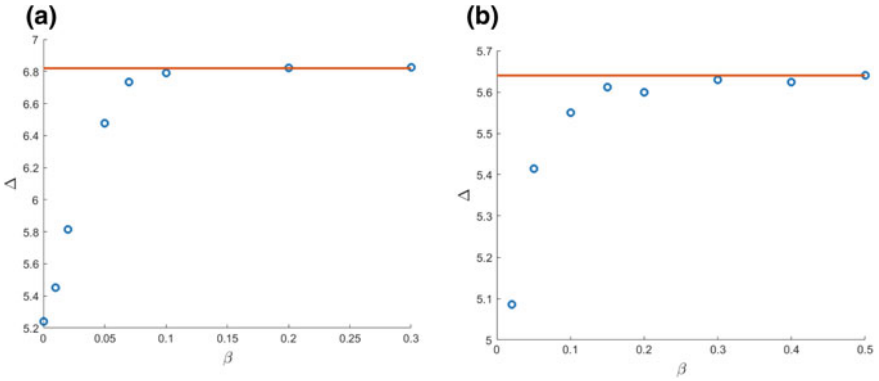

Fig. 10 Amplitude of the transition front Δ as a function of β; Solid line—analytical value of Δ, 'o'—numerical values of Δ; **a** bi-parabolic potential, **b** 4th order polynomial potential; parameters: $Q/B = 1, \omega_0 = 0.5$

$$dt = \frac{d\varphi}{\sqrt{2}\sqrt{U_1(0) + U_1(-\Delta) - U_1(-\varphi) - U_1(\varphi - \Delta)}} \tag{21}$$

By using $V = 1/\int_{t=0}^{t(\varphi=\Delta)} dt$, the corresponding velocity is found from the following expression:

$$V \approx \frac{1}{\int_0^{\Delta} \frac{d\varphi}{\sqrt{2}\sqrt{U_1(0)+U_1(-\Delta)-U_1(-\varphi)-U_1(\varphi-\Delta)}}} \tag{22}$$

Expression (22) is the general formulation of the approximate model for the case of the nonlinear gradient potential U_1. In Sects. 2.4 and 2.5 we verify the result for two specific examples and test it for robustness to variations in the shape of the on-site potential.

One should notice, that although the treatment is general, the specific parameters for which the nonlinear regime is fully developed (a shock wave is formed), depend on the parameters of the potentials. As a rule of thumb, this treatment holds for responses with front velocity $V > 2$. For lower velocities, the coupling nonlinearity expresses itself to a smaller extent, the front exhibits a crossover to the kink pattern, and approximate model (16)–(22) loses its validity. A further explanation on the validity of the shockwave analysis are provided in Sect. 2.6.

2.4 Polynomial Coupling Potential in the Form of Fermi-Pasta-Ulam (FPU)

The first specific gradient potential to illustrate the approach developed above is a generalization of the linear-cubic coupling studied in [51]. This celebrated potential (α-β—FPU) can be seen as a Taylor expansion of more general potentials, and is presented in the following form:

$$U_1(r) = \frac{1}{2}r^2 + \frac{\alpha}{3}r^3 + \frac{\beta}{4}r^4 \tag{23}$$

α and β are the stiffnesses of the quadratic and cubic nearest-neighbor springs respectively. Without loss of generality the linear stiffness is set to unity. In the regime dominated by the nonlinearities of the inter-particle interaction, the energy that is contained within the linear portion of coupling is negligible compared to the nonlinear terms. We neglect the linear coupling term, and by substitution of (23) into (20) obtain the following Hamiltonian that describes the single particle dynamics in the region of the front:

$$H = \frac{\dot{\varphi}^2}{2} + \frac{\beta}{4}\left[\varphi^4 + (\varphi - \Delta)^4\right] + \frac{\alpha}{3}\left[-\varphi^3 + (\varphi - \Delta)^3\right] \tag{24}$$

By substituting $z = \varphi/\Delta$, integrating over the entire motion range $0 < z < 1$, the following solution is obtained for the SDOF model:

$$V = \frac{\Delta\sqrt{\beta}}{\sqrt{2}} \frac{1}{\int\limits_0^1 \frac{dz}{\sqrt{\left[1-z^4-(1-z)^4\right] - \frac{4}{3}\frac{\alpha}{\beta\Delta}\left[1-z^3-(1-z)^3\right]}}} \tag{25}$$

Expression (25) involves a somewhat awkward elliptic integral. However, a simple approximated expression can be obtained by defining a small parameter $\mu \equiv \frac{4}{3}\frac{\alpha}{\beta\Delta} \ll 1$:

$$V = \frac{\Delta\sqrt{\beta}}{\sqrt{2}} \frac{1}{\int\limits_0^1 \frac{dz}{\sqrt{1-z^4-(1-z)^4}} - \frac{\mu}{2}\int\limits_0^1 \frac{\left[-1+z^3+(1-z)^3\right]dz}{\left[1-z^4-(1-z)^4\right]^{\frac{3}{2}}} + O\left(\mu^2\right)} \tag{26}$$

Neglecting $O\left(\mu^2\right)$ terms and integrating, one obtains:

$$V \approx \frac{\Delta\sqrt{\beta}}{\sqrt{2}} \frac{1}{\left(K\left(\frac{\sqrt{2}}{4}\right) + \mu\frac{3}{7}E\left(\frac{\sqrt{2}}{4}\right)\right)} \quad \approx f_1(\beta, \Delta) + f_2(\alpha, \beta)$$

$$f_1(\beta, \Delta) = \frac{1}{\sqrt{2}K\left(\frac{\sqrt{2}}{4}\right)}\Delta\sqrt{\beta}, \quad f_2(\alpha, \beta) = -\frac{4E\left(\frac{\sqrt{2}}{4}\right)}{7\sqrt{2}K\left(\frac{\sqrt{2}}{4}\right)^2}\frac{\alpha}{\sqrt{\beta}} \tag{27}$$

Here K and E are complete elliptic integrals of the first and the second kind respectively. This analysis leads to a conclusion that the $\alpha - \beta$ problem can be treated as two separate problems: the basic velocity due to the $\beta - FPU$ nonlinearity (f_1), and the modification of the basic velocity due to inclusion of a non-zero $\alpha - FPU$ term (f_2).

It was found from numerical simulations that in order to obtain a very good quantitative agreement, it is enough to multiply f_1 and f_2 by constant coefficients $\gamma_1 \approx 1.33$ and $\gamma_2 \approx 1.6$. Necessity of these corrections stems from the simplification and assumptions taken. These factors were extracted from numerous numerical simulations for varying α, β, Δ and although their chosen values should be treated as an assumption, they remained nearly constant for the range of the front velocities $V > 2$. Therefore, it is reasonable to assume that, with good accuracy, these factors are nearly constant.

2.4.1 The Contribution of $\beta - FPU$

The basic problem is the pure β problem (f_1) which determines the nominal velocity through values of β and Δ. The β contribution can be effectively described by the following scaling law:

$$V(\alpha = 0) = f_1(\beta, \Delta) \quad \sim \quad \Delta\sqrt{\beta} \tag{28}$$

Kinetic relation (28) implies that the following relations should be satisfied with a sufficient accuracy:

$$\begin{aligned} &(a) \quad \ln V = 1 \cdot \ln(\Delta) + \ln\left(\gamma_1\left[\sqrt{2}\mathrm{K}\left(\tfrac{\sqrt{2}}{4}\right)\right]^{-1}\sqrt{\beta}\right) \\ &(b) \quad \ln V = \tfrac{1}{2} \cdot \ln(\beta) + \ln\left(\gamma_1\left[\sqrt{2}\mathrm{K}\left(\tfrac{\sqrt{2}}{4}\right)\right]^{-1}\Delta\right) \end{aligned} \tag{29}$$

Direct comparison between the numerical and the analytical results for the front velocity are presented in Figs. 11 and 12 as functions of β and Δ respectively. In Fig. 11 we see that for $\beta < 0.1$ the system is not yet in the regime dominated by the nonlinear term, while for β above this threshold, the system can be described by the proposed simple scaling law.

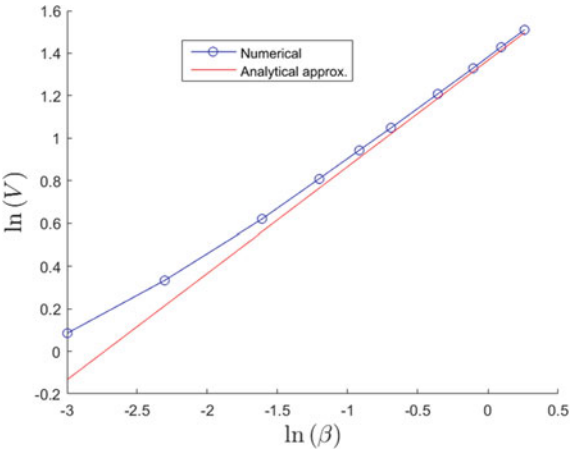

Fig. 11 Validation of scaling law (28) for the front velocity versus the nonlinear stiffness coefficient; Line-dotted blue—Numerical, Solid red —Analytical; parameters: $Q/B = 1, \omega_0 = 0.5$

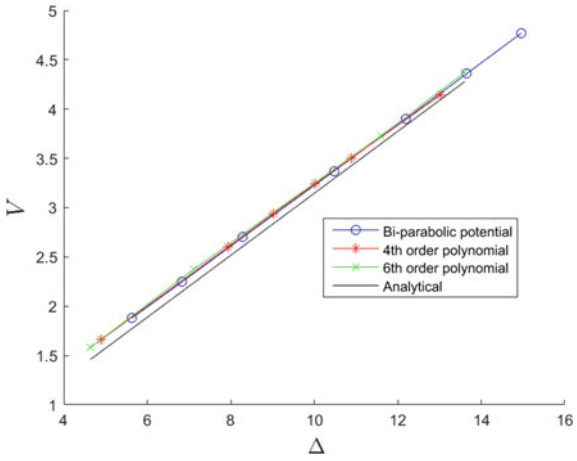

Fig. 12 Front velocity as a function of potential parameter Δ; 'o' blue—parabolic potential (2), '*' red—4th order polynomial (3), 'x' green—6th order polynomial (4); solid black – Analytical; Parameters: $\beta = 0.3, \quad B = 0.5, \quad \omega_0 = 0.5$

One of the main assumptions that led to derivation of the simplified model was the possibility to neglect the particularities of the on-site potential. The characteristics of the potential affected only the single parameter—fixed value of the "amplitude of transition" Δ. Each on-site potential yields a different value of Δ; however, the scaling law (28) that relates between the front velocity and Δ is valid for broad range of the on-site potentials with similar general characteristics (B, Q, φ^*). To check this claim, we examine three different potentials mentioned above: bi-parabolic, 4 and 6th order polynomials with similar characteristics (Eqs. (2)–(4), Fig. 1). The comparison between these simulations and the analytical model is presented in Fig. 12 (V vs. Δ). The results for all three potentials collapse on the same straight line. This

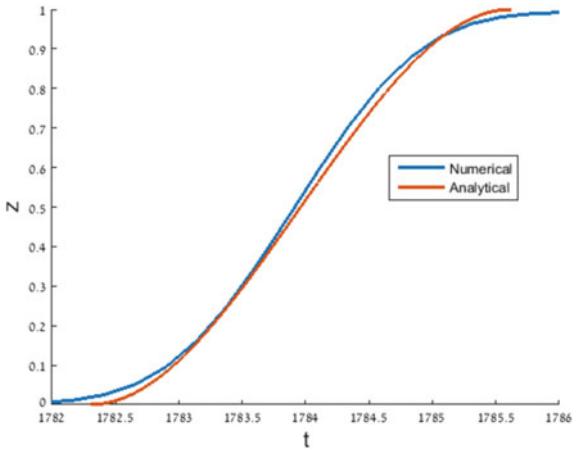

Fig. 13 Comparison between analytical prediction and numerical result for the rescaled front shape in the case of $\beta - FPU$ coupling

result supports the conjecture that the front velocity depends only on the parameter Δ, rather than on the exact potential shape. This weak dependence leads to an important conclusion, that the model (28) is universal for modified shapes of the on-site potential, when the nonlinear term is dominant and above the threshold value. Also, the approximate model provides a good estimation of the numerical results with accuracy that asymptotically improves at higher velocities.

The approximate model allows one can also obtain an approximate equation for the time history of the particle inside the propagating front $z = z(\tilde{t})$. For the particular case of $\beta - FPU$ nonlinearity without an $\alpha - FPU$ term it immediately follows from (21):

$$\tilde{t} = \frac{\sqrt{2}}{\gamma} \int_0^z \frac{dz}{\sqrt{1 - z^4 - (z-1)^4}}, \qquad 0 < z < 1 \tag{30}$$

Here the values of the actual time and φ can be obtained from: $t = \left(\Delta\sqrt{\beta}\right)^{-1}\tilde{t}, \quad \varphi = \Delta z$.

Equation (30) describes the movement of the considered single particle inside the front. The absence of system parameters in the rescaled representation implies that the basic structure of the front in the case of a shockwave does not depend on the system parameters and any specific solution can be obtained by the appropriate rescaling of this basic shape. Comparison of this rescaled shape of the transition region to the one obtained numerically in the complete system is presented in Fig. 13. The agreement is reasonable, albeit not perfect.

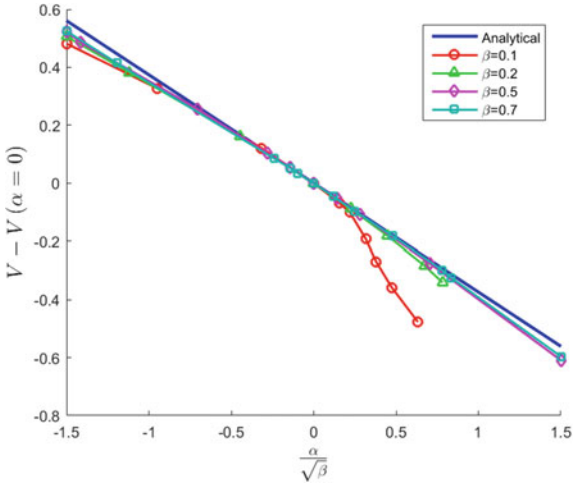

Fig. 14 Modification of the front velocity due to α; solid blue—analytical estimation, circles red—$\beta = 0.1$, triangles green—$\beta = 0.2$, diamonds purple—$\beta = 0.5$, squares turquoise—$\beta = 0.7$; On-site potential: bi-parabolic with parameters: $Q = 0.5,\ B = 0.5,\ \omega_0 = 0.5$

2.4.2 The Contribution of $\alpha - FPU$

The second problem is the contribution of α to the nominal velocity—f_2. The contribution can be described as a modification of the velocity established and dominated by β term alone according to the following law:

$$V - V(\alpha = 0) = f_2(\alpha, \beta) \quad \sim \quad -\frac{\alpha}{\sqrt{\beta}} \tag{31}$$

In Fig. 14 the modification of the front velocity is presented for different β and is compared to the analytical predictions. It is seen that for $\beta \geq 0.2$ the approximation reasonably conforms to the numeric results. At $\beta = 0.1$ the approximation fails to describe the front velocity accurately for positive α. This combination of parameters corresponds to low front velocities, that lie beyond the scope of validity of the simplified model, and thus cannot be classified as the shockwaves.

Remarkably, in expression (27), the contribution of α to the front velocity doesn't involve any characteristics of the on-site potential. Hence, unlike the β contribution that depends on knowing the potential shape (through expression (17)), the α contribution can be determined for all potentials. To examine the legitimacy of this statement, we present the results for three bi-stable on-site potentials defined above (Fig. 1) in Fig. 15. All results collapse on the same line with a considerable accuracy.

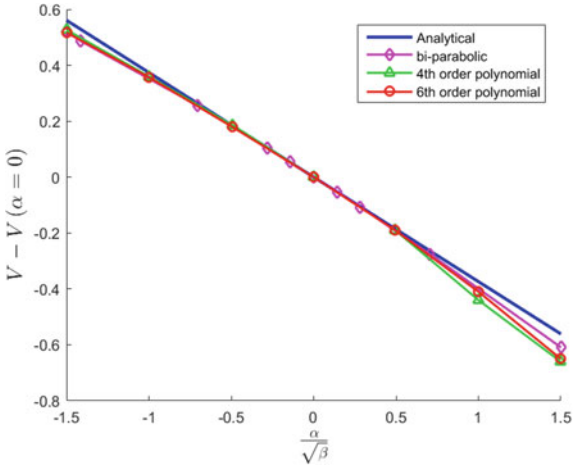

Fig. 15 Robustness of the α contribution to front velocity to different on-site potentials; solid blue—analytical estimation, diamonds purple—bi-parabolic potential; triangles green—4th order polynomial potential; circles red—6th order polynomial potential, common parameters: $Q = 0.5$, $B = 0.5$, $\varphi^* = 4.82$

2.5 LJ Coupling Potential

In more realistic models, one should consider also non-polynomial coupling potentials, and, in particular, the potentials that allow dissociation. Here we come back to the LJ coupling in the following common form:

$$U_1(r) = U_{LJ}(r) = \varepsilon\left[\left(\frac{\sigma}{r + r^*}\right)^{12} - \left(\frac{\sigma}{r + r^*}\right)^{6}\right] \tag{32}$$

To set the force to zero at $r = 0$, the following condition should be satisfied:

$$\frac{dU_{LJ}}{dr}(r = 0) = 0 \rightarrow r^* = 2^{1/6}\sigma \tag{33}$$

A typical response of a chain with the LJ coupling was presented in Fig. 5. As it was mentioned above, this regime can be classified as a shockwave. To describe the regime analytically, we employ the SDOF approximation (17), (22) and consider the following SDOF Hamiltonian:

$$H = \frac{\dot{\varphi}^2}{2} + U_{LJ}(-\varphi) + U_{LJ}(\varphi - \Delta) \tag{34}$$

One obtains the following expression for the front velocity:

$$V \approx \frac{1}{\int_0^{\Delta} \frac{d\varphi}{\sqrt{2}\sqrt{U_{LJ}(0)+U_{LJ}(-\Delta)-U_{LJ}(-\varphi)-U_{LJ}(\varphi-\Delta)}}} \tag{35}$$

The argument of the square root in (35) can be expanded to a Taylor series in the following way:

$$\begin{aligned} &U_{LJ}(0) + U_{LJ}(-\Delta) - U_{LJ}(-\varphi) - U_{LJ}(\varphi - \Delta) \\ &\approx \varepsilon \left[\frac{6\sigma^6}{\left(\Delta - 2^{1/6}\sigma\right)^7} - \frac{12\sigma^{12}}{\left(\Delta - 2^{1/6}\sigma\right)^{13}} \right] \varphi \end{aligned} \tag{36}$$

The substitution of (36) into (35) yields:

$$V \approx \frac{1}{2^{17/12}\sqrt{3}\sqrt{\Delta}} \sqrt{\frac{\sigma^{14}}{\left(\sigma - 2^{-1/6}\Delta\right)^{13}} - \frac{\sigma^8}{\left(\sigma - 2^{-1/6}\Delta\right)^7}} \tag{37}$$

From (37) one deduces that the velocity tends to infinity for $\sigma \to 2^{-1/6}\Delta$. Also, we see that no simple scaling law exists between the velocity and the governing parameters σ, Δ.

To study the behavior for relatively low velocities, we adopt the previously addressed FPU model as an approximation for the LJ potential, by means of a Taylor expansion of the full potential. Taylor expansion of (32) yields:

$$U = U(0) + \frac{1}{2}\frac{18\varepsilon}{2^{1/3}\sigma^2}r^2 - \frac{1}{3}\frac{189\varepsilon}{2^{1/2}\sigma^3}r^3 + \frac{1}{4}\frac{1113\varepsilon}{2^{2/3}\sigma^4}r^4 + O\left(r^5\right) \tag{38}$$

Without affecting the generality, we set the coefficient of linear coupling to 1, achieve a constraint on ε and express α, β as follows:

$$\frac{18\varepsilon}{2^{1/3}\sigma^2} = 1 \Bigg| \to \varepsilon = \frac{2^{1/3}\sigma^2}{18} \quad \to \quad \alpha = -\frac{21}{2^{7/6}\sigma} \qquad \beta = \frac{371}{6 \cdot 2^{1/3}\sigma^2} \tag{39}$$

This leads to the approximated FPU potential that is a function of a single parameter σ:

$$U_{\alpha-\beta} = U(0) + \frac{1}{2}r^2 + \frac{1}{3}\frac{-21}{2^{7/6}\sigma}r^3 + \frac{1}{4}\frac{371}{6 \cdot 2^{1/3}\sigma^2}r^4 \tag{40}$$

The FPU approximation is expected to work for small values of r. This correlates with high σ. In turn, high σ yields small values of α, β. This leads to a conclusion that at high σ the value of velocity of the system with LJ coupling potential asymptotically converges to the velocity with the linear coupling with potential $1/2r^2$. This value can be expressed in closed analytic form, if the on-site potential is piecewise parabolic [19, 22], and rescaled to the parametrization of the current analysis (8). In Fig. 16 the results of the velocity for the chain with LJ potential are presented. One observes

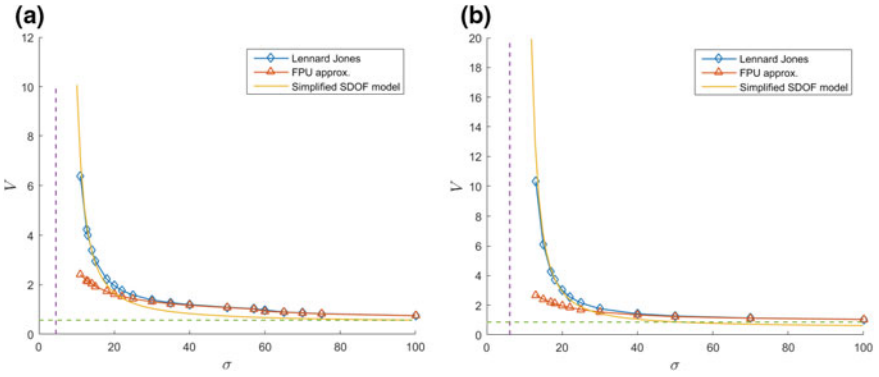

Fig. 16 Front velocity of the chain with LJ coupling; blue-diamonds—numerical result of the full LJ potential with $\sigma = 20$, red-triangles—numerical result of the approximated $\alpha - \beta$ potential, solid yellow—SDOF model solution, horizontal dashed green—asymptotic value of the linearly coupled chain, vertical dashed purple – asymptotic σ for which $V \to \infty$. On-site potential is bi-parabolic with $B = 0.5,\ \omega_0 = 0.5$; **a** $Q = 0.1$, **b** $Q = 0.5$

that the full solution converges to that with the FPU coupling at low velocities and to the SDOF model at high velocities (in the fully established shockwave regime).

The main assumption that is taken during the analysis is that the only parameter of the on-site potential that has a direct effect on the front velocity is Δ (Fig. 9). In the current case, the relationship can't be scaled by a simple law as can be seen even from approximation (37). Hence, we check the self-consistency of the assumption by numerically extracting the relationship between V and Δ for different on-site potentials (Fig. 17), and discover that all results collapse on the same curve.

2.6 *Validity of the Shock Wave Dynamics*

The dynamic behavior that is described by simplified model (16)–(22) can be associated with the shockwave for two reasons: it is far supersonic, and it is described by basic laws of conservation, without requiring additional conditions that are related to fine structure of the on-site potential [50]. This comes in contrast to the dynamics of the kink that is observed for linear coupling and described by kinetic relation (8). Although, as it was demonstrated in the examples, the analytical description of the shockwaves corresponds well to numerical simulations, the formal limit of its validity is bounded to relatively high front velocities. Specifically, in the example with LJ potential (Fig. 16) the assumption of shockwave is self-consistent for $V > 2.5$. In a different example of FPU (Fig. 14), a discrepancy is between the results is seen for $\alpha/\sqrt{\beta} < 0,\ \ \beta = 0.1$; in this parametric region, the shock wave assumptions are no more consistent. Together with results of [51], one can conclude that there

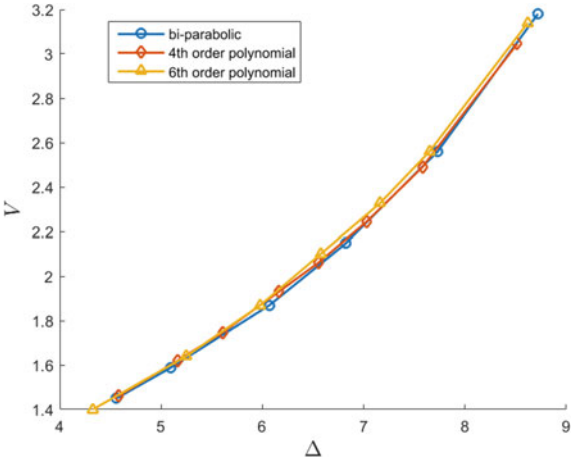

Fig. 17 Front velocity of a chain with LJ interaction for different on-site potentials; blue circles—bi-parabolic potential, red diamonds—4th order polynomial potential, yellow triangles—6th order polynomial potential; common parameters: $\sigma = 25$, $B = 0.5$

is no distinct transition from a kink to a shockwave; instead, a smooth crossover is observed.

A special attention has to be paid to the limiting case of $Q = 0$. This case was addressed previously in [43, 44]. According to notations used in the paper, this situation corresponds to a particular case $\Delta = \varphi^*$. Due to a lack of energy input from the on-site potential, the steady propagation of the transition front is possible only if the total energy of the tail reaches a constant value. To examine whether this scenario is possible, we numerically excite the shock with different initial conditions. First, we show in Fig. 18 the total energy within the propagating front as a function of time. Expectedly, there is a minimal amount of energy required to initiate the shock; in the current example it is $E_{\min} = 21.77$ and it corresponds to a minimal initial velocity applied to the first particle of $\dot{\varphi}_0(0) = \sqrt{2E_{\min}} = 6.6$. For two initial conditions above this threshold: "impulse 7" and "impulse 10", the energy of the front converges after a sufficiently long time to $E_{\min}$. Since the system is energy conserving, the rest of the initial energy is located within the tail and must remain constant. According to Fig. 19 this requirement is satisfied, as the amplitude of oscillations within the tail gradually vanishes as the time increases.

Figure 20 presents the dependence of the shock velocity versus parameter Δ defined above (Eq. (17) and Fig. 9) for the case of bi-parabolic on-site potential with varying Q and linear—cubic nearest—neighbor coupling. One observes that the front velocity in the limit $Q \to 0$ is close to the linear trend obtained for $Q > 0$ [51], but demonstrates slight deviation in the vicinity of $Q = 0$. This deviation points on certain inaccuracy of the approximate analytic model in this limit. Possible reason for this inaccuracy lies in the fact that the model predicts strictly zero amplitude of the oscillatory tail. In such case, the motion of particles in the vicinity of the front

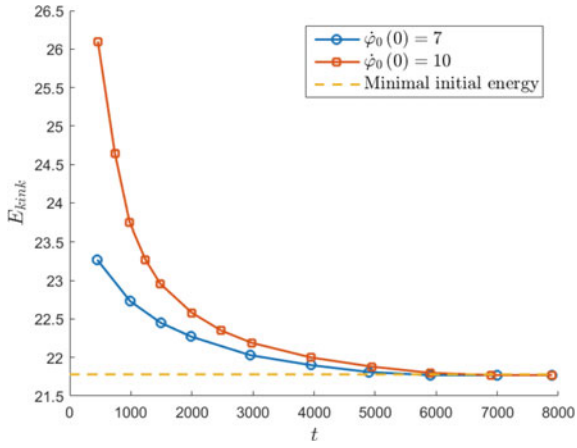

Fig. 18 Convergence of the front energy to the terminal value for $Q = 0$; circles—initial conditions: impulse 7, squares—initial conditions: impulse 10, horizontal dashed yellow—minimal energy required for the front initiation. The gradient nonlinearity is cubic with $\beta = 0.5$; the on-site potential is bi-parabolic with $Q = 0$, $B = 0.5$, $\omega_0 = 0.5$

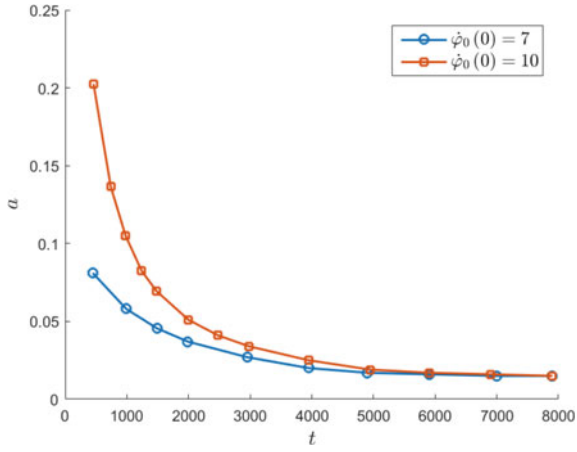

Fig. 19 Decay of amplitude of the tail oscillations for $Q = 0$; circles—initial conditions: impulse 7, squares—initial conditions: impulse 10; The gradient nonlinearity is cubic with $\beta = 0.5$; the on-site potential is bi–parabolic with $B = 0.5$, $\omega_0 = 0.5$

becomes quite significant, and dynamics of the front must be considered with higher accuracy than simple single-particle approximation (20). From the other side, the simulation cannot exclude the possibility of low-amplitude energy irradiation from the front after approaching the "steady-state" velocity.

3 Transition Fronts in the Chain with On-Site Linear Damping

So far, we addressed conservative systems. Here we present an approach that allows an account of the on-site linear damping in the frame of the previously developed approach.

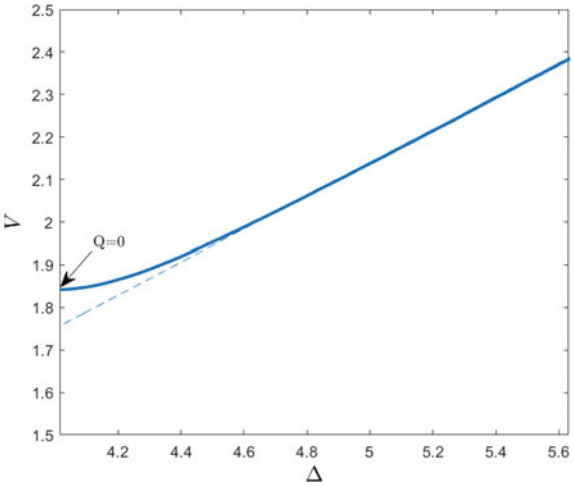

Fig. 20 Front velocity versus Δ for $Q \to 0$; Solid—numerical results, dashed—analytical prediction [51]. The gradient nonlinearity is cubic with $\beta = 0.5$; the on-site potential is bi–parabolic with $B = 0.5,\ \omega_0 = 0.5$

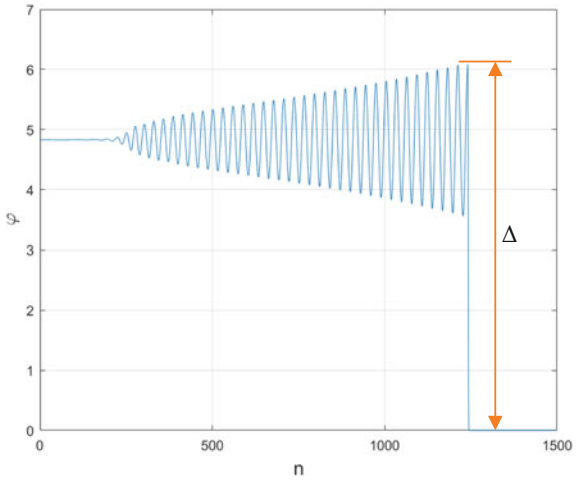

Fig. 21 A dynamic response in the presence of on-site damping; Gradient potential: cubic with $\beta = 0.5$; On-site potential: bi-parabolic with $Q = 0.5$, $B = 0.5,\ \omega_0 = 0.5$; damping coefficient: $\xi = 0.005$, initial conditions: Impulse 10

3.1 The Case of Low Damping

We first consider the case of a small linear damping. In this case, the shockwave pattern persists, and the impact of the damping can be described as a perturbation of the solution for a Hamiltonian system (22), (17). In the frame of the single—particle model, the only effect of the on-site damping on the front velocity comes by modification of Δ for the first particle within the stable well (Fig. 21). The energy dissipation along the oscillatory tail has no effect on the front velocity.

We assume that for low value of onsite damping coefficient ξ, the dynamics of the particle within the transitional region can be approximately described by the same single DOF Hamiltonian (20). During the motion of the single particle, energy is dissipated from the system, and its total amount, in the first-order approximation, can be expressed as follows:

$$W_\xi = \xi \int_0^\Delta \dot{\varphi} d\varphi = \sqrt{2}\xi \int_0^\Delta \sqrt{U_1(0) + U_1(-\Delta) - U_1(-\varphi) - U_1(\varphi - \Delta)} d\varphi \quad (41)$$

The value Δ is found through a modification of Eq. (17). In the current case, the energy dissipated during the motion through the front has to be included in the energetic balance. So, the modified balance of energy for the particle that has entered the stable well can be expressed as follows:

$$U_2(\Delta) + W_\xi = 0 \quad (42)$$

After Δ is extracted from Eq. (42), the front velocity can be determined from (22). This treatment is general for any combination of U_1, U_2. Here, we bring a specific example with the following selection of potentials: $U_1 = \frac{r^2}{2} + \frac{\beta r^4}{4}$, U_2 a piecewise parabolic potential (2). However, when the nonlinearity is dominant, and the damping is small enough, we can neglect the contribution of the quadratic term. The work done by the damping in this case is calculated as:

$$W_\xi = \frac{\xi \Delta^3 \sqrt{\beta}}{\sqrt{2}} \int_0^1 \sqrt{1 - z^4 - (z-1)^4} dz = \frac{I_1 \xi \Delta^3 \sqrt{\beta}}{\sqrt{2}}, \quad I_1 = \left(\frac{7}{3} K\left(\frac{\sqrt{2}}{4}\right) - 2E\left(\frac{\sqrt{2}}{4}\right) \right) \quad (43)$$

Substitution of Eq. (43) and of the expression for the stable branch of the bi-parabolic on-site potential (2) into (42) yields:

$$\frac{\omega_0^2}{2}\left(\Delta - \varphi^*\right)^2 - Q + \frac{I_1}{\sqrt{2} c_d} \xi \Delta^3 \beta = 0 \quad (44)$$

The value of Δ can be extracted for any set of parameters. Here, contrary to the conservative case, its value depends not only on the parameters of potential U_2, but also on β and ξ. In (44) a correction factor c_d is introduced, which is a result of approximations and assumptions that were taken in the estimation of W_ξ. Yet, for the selected potentials, its value was found numerically to be nearly constant $c_d \approx 1.5$, from verifications of the expression for different ξ and β. Once the value of Δ is extracted, the velocity is found from the same expression as in the conservative case (22). The results for the benchmark case of a bi-parabolic on-site potential and a cubic gradient potential are presented in Fig. 22. The numerical results are in a good agreement with the analytical model for front velocities which higher than 2, which complies with all other findings in this work.

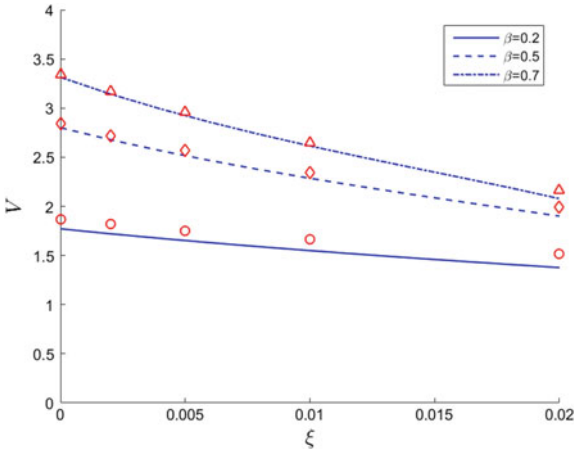

Fig. 22 Front velocity in the presence of on-site damping; Solid line: analytical result for $\beta = 0.2$, dashed line: analytical result for $\beta = 0.5$, line-dotted line: analytical result for $\beta = 0.7$; Gradient potential: cubic; On-site potential: bi-parabolic with $Q = 0.5$, $B = 0.5$, $\omega_0 = 0.5$

For $\xi \to 0$ the following approximation for Δ is obtained:

$$\Delta = \Delta_0 - \frac{\left(\omega_0\varphi^* + \sqrt{2Q}\right)^3 I_1}{2c_d\sqrt{Q}\omega_0^4}\xi\sqrt{\beta}, \qquad \Delta_0 = \varphi^* + \frac{\sqrt{2Q}}{\omega_0} \tag{45}$$

Thus, the approximate expression for the change in velocity due to incorporation of on-site damping is:

$$V - V(\xi = 0) \approx -\frac{\gamma_1\left(\omega_0\varphi^* + \sqrt{2Q}\right)^3 I_1 I_2}{2c_d\sqrt{Q}\omega_0^4}\xi\beta, \qquad I_2 = \left(\sqrt{2}K\left(\frac{\sqrt{2}}{4}\right)\right)^{-1} \tag{46}$$

It turns out that the modification of the front velocity due to inclusion of the on-site damping is proportional to β and ξ when the damping is small. To further justify the claim that the inclusion of damping is a perturbation of the Hamiltonian system, we examine the kinetic energy of the system. In Fig. 23 the dependencies of total kinetic energy and the kinetic energy in the front region are shown. It is seen that the kinetic energy of the front slightly decreases as the damping increased and complies to the perturbative analytical result. On the other hand, the total kinetic energy is asymptotically infinite as the damping tends to zero, and can't be related to the perturbative nature of the damping effect on the dynamics. This is yet another evidence that the response in the strongly nonlinear shockwave regime is mostly affected by the internal energy conversion within the front region, rather than on the dynamics of the entire chain.

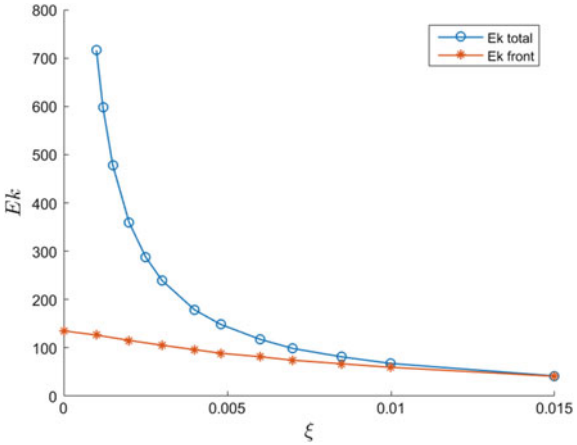

Fig. 23 Kinetic energy as a function of damping coefficient, 'o'- total kinetic energy, '*'—kinetic energy of the front; Gradient potential: cubic with $\beta = 0.5$; On-site potential: bi-parabolic with $Q = 0.5$, $B = 0.5$, $\omega_0 = 0.5$. Initial conditions: Impulse 10

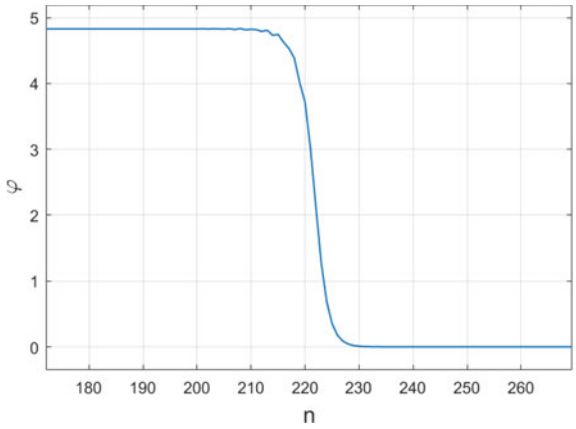

Fig. 24 A typical response in the presence of high damping; gradient potential: cubic with $\beta = 0.5$; on-site potential: bi-parabolic with $Q = 0.5$, $B = 0.5$, $\omega_0 = 0.5$. Damping coefficient - $\xi = 0.3$; Initial conditions: Impulse 10

3.2 The Case of Large Damping

Here we address the opposite case of a large damping. In this limiting case, the propagating front conforms to the pattern of the subsonic kink. A typical response is shown in Fig. 24. We see that when damping is high enough, it completely suppresses the oscillations in the tail. Moreover, the front area becomes very wide (in this example—20 particles).

The kink is smooth enough to consider the continuum limit. Besides, all gradients are small enough to suppress the effect of nonlinear terms in the coupling forces. Thus, for the sake of analytical treatment, we consider a linear chain with a linear on-

site damping (with damping coefficient ξ), subject to the non-degenerate substrate potential (U_2). Equations of motion are written in the following general form:

$$\ddot{\varphi}_n + \xi\dot{\varphi}_n + (2\varphi_n - \varphi_{n-1} - \varphi_{n+1}) = -\frac{\partial U_2(\varphi_n)}{\partial \varphi_n} \tag{47}$$

Continuum limit of System (47) is written for the continuous field of displacement $\varphi(x, t)$ as follows:

$$\ddot{\varphi} + \xi\dot{\varphi} - \varphi'' = -\frac{\partial U_2(\varphi)}{\partial \varphi} \tag{48}$$

According to previous treatment (Fig. 1 and Eq. (2)), the potential function obeys the relationships:

$$U_2(\varphi) = \begin{cases} \frac{\omega_0^2\varphi^2}{2} + O\left(\varphi^3\right), \varphi \to 0 \\ \frac{\omega_0^2(\varphi-\varphi^*)^2}{2} - Q + O\left[(\varphi-\varphi^*)^3\right], \varphi \to \varphi^* \end{cases} \tag{49}$$

We would like to describe the propagating kink that transmits the system from upper to lower well and suppose the existence of travelling-wave solution in a form:

$$\varphi(x, t) = \varphi(x - Vt), \varphi(x \to -\infty) = \varphi^*, \varphi(x \to \infty) = 0 \tag{50}$$

Travelling-wave ansatz (50) converts Eq. (48) to an ODE:

$$(V^2 - 1)\varphi_{\zeta\zeta} - V\xi\varphi_\zeta = -\frac{\partial U_2(\varphi)}{\partial \varphi}, \ \zeta = x - Vt \tag{51}$$

For general potential shape $U_2(\varphi)$ and for nonzero damping coefficient solution of Eq. (51) is not known. To obtain a closed-form solution for the transition kink we first adopt a piecewise parabolic approximation for the on-site potential (Eq. 2):

$$U_2(\varphi) = \begin{cases} \frac{\omega_0^2\varphi^2}{2}, & \varphi < b \\ \frac{\omega_0^2(\varphi-\varphi^*)^2}{2} - Q, & \varphi > b \end{cases} \tag{52}$$

It is obvious that $B = \omega_0^2 b^2 \big/ 2$. Then, to obtain a continuous potential function, one should satisfy the following relationships:

$$\frac{\omega_0^2 b^2}{2} = \frac{\omega_0^2(b-\varphi^*)^2}{2} - Q \quad \Rightarrow \quad \varphi^* - b = \frac{\sqrt{2(B+Q)}}{\omega_0} \tag{53}$$

So, we see that for selected potential function the parameters are not independent. To derive the expression for the kink, we adopt that the transition between two wells

of potential function (52) occurs at the point $\zeta = 0\,(x = Vt)$. Then, for the region $\zeta > 0$ Eq. (51) with potential (52) is reduced to the form:

$$\left(V^2 - 1\right)\varphi_{\zeta\zeta} - V\xi\varphi_\zeta = -\omega_0^2\varphi \tag{54}$$

As it will be demonstrated below, the regime of transitions between the two wells exists only for $V < 1$. The solution (54) of that decays to zero at infinity, is written as:

$$\varphi_+(\zeta) = C_+\exp(\lambda_+\zeta),\ \zeta > 0,\ \lambda_+ = -\frac{\sqrt{\xi^2V^2 + 4\omega_0^2\left(1 - V^2\right)} + \xi V}{2\left(1 - V^2\right)} \tag{55}$$

For the region $\xi < 0$ Eq. (51) with potential (52) is reduced to the form:

$$\left(V^2 - 1\right)\varphi_{\zeta\zeta} - V\xi\varphi_\zeta = -\omega_0^2\left(\varphi - \varphi^*\right) \tag{56}$$

Solution (56) of that satisfies the boundary condition at $\zeta \to -\infty$ is written as:

$$\varphi_-(\zeta) = \varphi^* - C_-\exp(\lambda_-\zeta),\ \zeta < 0,\ \lambda_- = \frac{\sqrt{\xi^2V^2 + 4\omega_0^2\left(1 - V^2\right)} - \xi V}{2\left(1 - V^2\right)} \tag{57}$$

Expressions (55) and (57) should satisfy the following matching conditions at $\zeta = 0$:

$$\varphi_+(0) = \varphi_-(0) = b,\ d\varphi_+(\zeta)/d\zeta|_{\zeta=0} = d\varphi_-(\zeta)/d\zeta|_{\zeta=0} \tag{58}$$

Matching conditions (58) yield the following expressions:

$$C_+ = b,\quad C_- = \varphi^* - b,\quad C_+\lambda_+ = -C_-\lambda_- \tag{59}$$

Substitution of (53), (55) and (57) into (59) yields:

$$\frac{\sqrt{\xi^2V^2 + 4\omega_0^2\left(1 - V^2\right)} - \xi V}{\sqrt{\xi^2V^2 + 4\omega_0^2\left(1 - V^2\right)} + \xi V} = \sqrt{\frac{B}{B + Q}} \tag{60}$$

It is easy to see that for $\xi = 0$ Eq. (60) is automatically satisfied for any velocity V, but only for the degenerate case $Q = 0$. In the non-degenerate case and for nonzero damping equation (60) determines unique velocity of the kink. The front velocity can be expressed explicitly as follows:

$$V = \frac{\omega_0(1 - a)}{\sqrt{a\xi^2 + \omega_0^2(1 - a)^2}} \le 1 \quad a = \sqrt{\frac{B}{B + Q}} \tag{61}$$

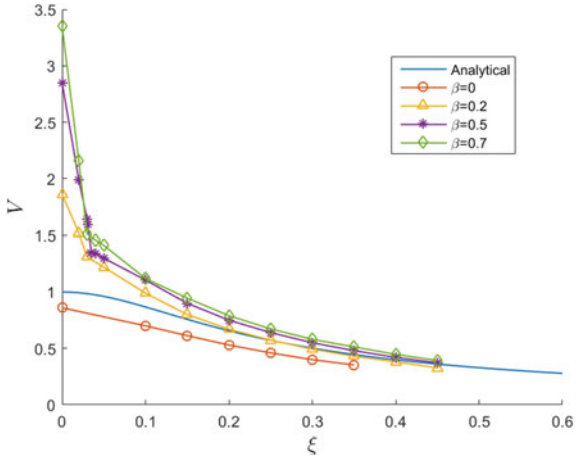

Fig. 25 Front velocity as a function of damping coefficient, solid blue – analytical, 'o'—$\beta = 0$, 'triangles'—$\beta = 0.2$, '*'—$\beta = 0.5$, 'diamonds' – $\beta = 0.7$; Gradient potential: cubic; On-site potential: bi-parabolic with $Q = 0.5$, $B = 0.5$, $\omega_0 = 0.5$. Initial conditions: Impulse 10

As one could expect in the case of the subsonic kink, the velocity of propagation depends on the internal structure of the on-site potential (B, Q, ω_0) as was the case in (8). The results of front velocity as a function of damping per (61) compared to results obtained from numerical simulations are plotted in Fig. 25. Each curve corresponds to a different value of nonlinear coefficient β. At very high damping we observe that the curves tend to the analytical estimation. At the lower damping (under $\xi < 0.1$) the continuum model fails to describe the dynamics, as the effect of cubic nonlinearity becomes dominant and the front becomes accompanied by considerable oscillations within the tail region responsible for the radiative damping.

Concluding Remarks

Inclusion of a nonlinear gradient coupling in lattices with a bi-stable on-site potential leads to a dynamic behavior characteristic to shockwaves: supersonic velocity, narrow front, low wavenumber of the oscillatory tail and an extreme energy concentration in the front zone. This regime is not unique to a particular gradient nonlinearity; rather it turns out to be a generic scenario for couplings above a certain threshold. In such cases, properties of the front can be described in the framework of a reduced analytical model with a single degree of freedom and appropriate boundary conditions. Unlike the well-known kinks of the Atkinson-Cabrera model, the propagation of the discussed shockwaves doesn't depend on fine-details of the on-site potential. Instead, the only parameter of the on-site potential that substantially affects the shock is the coordinate Δ (Eq. (17)), easily computable to arbitrary on-site potentials. The energetic effect of the transition Q is required only for evaluation of the oscillatory tail amplitude. As specific examples we considered the FPU and LJ models and the analytical predictions were in a good agreement with the numerical data.

Furthermore, it was demonstrated that the weak on-site linear damping can be treated as a perturbation of the reduced model as far as the features of the shockwave regime are preserved. On the other hand, the case of large damping corresponds to

the opposite asymptotic limit of a subsonic kink propagation and can be treated with a continuous approximate model that naturally yields a Q dependent kinetic relation.

The treatment presented above leaves many questions for further investigation. First, the derived simplified model works fine only if the front propagation velocity is relatively high. This regime requires considerable nonlinear component of the coupling force. The crossover from kink to shockwave front propagation patterns requires a more refined analytic technique. Other interesting problem is possible extension of the simplified local model for higher dimensions.

Acknowledgements The authors are very grateful to Israel Science Foundation (grant 1696/17) for financial support.

References

1. Atkinson, W., Cabrera, N.: Motion of a Frenkel-Kontorova dislocation in a one-dimensional crystal. Phys. Rev. A **138**(3), A763–A766 (1965)
2. Braun, O.M., Kivshar, Y.S.: Nonlinear dynamics of the Frenkel-Kontorova model. Phys. Rep. **306**, 1–108 (1998)
3. Nabarro, F.: Theory of Crystal Dislocations. Oxford University, Oxford (1967)
4. Weiss, M., Elmer, F.J.: Dry friction in the Frenkel-Kontorova-Tomlinson model: dynamical properties. Zeitschrift für Physik B Condensed Matter **104**(1), 55–69 (1997)
5. Fraternali, F., Blesgen, T., Amendola, A., Daraio, C.: Multiscale mass-spring models of carbon nanotube foams. J. Mech. Phys. Solids **59**(1), 89–102 (2011)
6. Keizer, J., Smith, G.D.: Spark-to-wave transition: saltatory transmission of calcium waves in cardiac myocytes. Biophys. Chem. **72**, 87–100 (1998)
7. Suezawa, M., Sumino, K.: Lattice distortion and the effective shear modulus along a coherent twin boundary. Phys. Status Solidi (A) Appl. Res. **36**, 263–268 (1976)
8. Bruce, D.A.: Scattering properties of ferroelectric domain walls. J. Phys. C **14**, 5195–5214 (1981)
9. Marder, M., Gross, S.: Origin of crack tip instabilities. J. Mech. Phys. Solids **43**(1), 1–48 (1995)
10. Slepyan, L.I.: Dynamics of a crack in a lattice. Sov. Phys.-Dokl. **26**(5), 538–540 (1981)
11. Carpio, A., Bonilla, L.L., Dell'Acqua, G.: Motion of wave fronts in semiconductor superlattices. Phys. Rev. E **64**(3), 036204 (2001)
12. Harten, U., Lahee, A.M., Peter Toennies, J., Wöll, C.: Observation of a soliton reconstruction of Au(111) by high-resolution helium-atom Diffraction. Phys. Rev. Lett. 54(24), 2619 (1985)
13. Keener, J.P., Sneyd, J.: Mathematical Physiology. Springer, New York (1998)
14. Nelson, D.R.: Defects and Geometry in Condensed Matter, Cambridge. Cambridge University Press, UK (2002)
15. Truskinovsky, L., Vainchtein, A.: Kinetics of martensitic transitions: lattice model. SIAM J. Appl. Math. **66**(2), 533–553 (2005)
16. Landau, A.I., Kovalev, A.S., Kondratyuk, A.D.: Model of interacting atomic chains and its application to the description of the crowdion in an anisotropic crystal. Phys. Status Solidi (b), **179**(2), 373–381 (1993)
17. Kovalev, A.S., Kondratyuk, A.D., Kosevich, A.M., Landau, A.I.: Theoretical description of the crowdion in an anisotropic crystal based on the frenkel-kontorova model including and elastic three-dimensional medium. Phys. Status Solidi (b) **177**, 117–127 (1993)
18. Bonilla, L.L., Malomed, B.: Motion of kinks in the ac-driven damped Frenkel-Kontorova chain. Phys. Rev. B **43**(13), 11539–11541 (1991)
19. Kresse, O., Truskinovsky, L.: Mobility of lattice defects: discrete and continuum approaches. J. Mech. Phys. Solids **51**, 1305–1332 (2003)

20. Balk, A.M., Cherkaev, A.V., Slepyan, L.I.: Dynamics of chains with non-monotone stress–strain relations. I. Model and numerical experiments. J. Mech. Phys. Solids **49**(1), 131–148 (2001)
21. Balk, A.M., Cherkaev, A.V., Slepyan, L.I.: Dynamics of chains with non-monotone stress–strain relations. II. Nonlinear waves and waves of phase transition. J. Mech. Phys. Solids **49**(1), 149–171 (2001)
22. Carpio, A., Bonilla, L.L.: Oscillatory wave fronts in chains of coupled nonlinear oscillators. Phys. Rev. E **67**(5), 56621–1-11 (2003)
23. Manevitch, L.I., Sigalov, G.M.: Solitonic mechanism of structural transformations in a nondegenerate chain of particles with anharmonic and commpeting interactions. Phys. Lett. A **210**, 423–428 (1996)
24. Manevitch, L.I., Savin, A., Smirnov, V., Volkov, S.: Solitons in nondegenerate bistable systems. Phys. Usp. **37**, 859 (1994)
25. Manevitch, L.I., Smirnov, V.V.: Propagation of exothermic reactions in condensed matter. Phys. Lett. A **165**, 427–431 (1992)
26. Vainchtein, A.: The role of spinodal region in the kinetics of lattice phase transitions. J. Mech. Phys. Solids **58**, 227–240 (2010)
27. Smirnov, V.V., Gendelman, O.V., Manevitch, L.I.: Front propagation in a bistable system: how the energy is released. Phys. Rev. E **89**, 050901 (2014)
28. Frenkel, Y.I., Kontorova, T.: On the theory of plastic deformation and twinning. Phys. Z. Sowietunion **13**, 1–10 (1938)
29. Nadkarni, N., Daraio, C., Abeyarante, R., Kochmann, M.: Universal energy transport law for dissipative and diffusive phase transitions. Phys. Rev. B **93**, 104109 (2016)
30. Ishioka, S.: Steady motion of a dislocation in a lattice. J. Phys. Soc. Jpn. **34**, 462–469 (1973)
31. Perchak, D., Weiner, J.H.: Local mode approximations in the Frenkel-Kontorova or sine-Gordon chain. Phys. Rev. B **22**(6), 2683–2694 (1980)
32. Zolotaryuk, Y.: Moving topological solitons in the discrete Klein-Gordon equation. Nonlinear Waves: Classical and Quantum Aspects, pp. 521–528
33. Peyrard, M., Kruskal, M.D.: Kink dynamics in the highly discrete sine-Gordon system. Phys. D **14**, 88–102 (1984)
34. Vainchtein, A.: Effect of nonlinearity on the steady motion of a twinning dislocation. Phys. D **239**, 1170–1179 (2010)
35. Slepyan, L.I.: Dynamic factor in impact, phase transition and fracture. J. Mech. Phys. Solids **48**, 927–960 (2000)
36. Celli, V., Flytzanis, N.: Motion of a screw dislocation in a crysta. J. Appl. Phys. **41**(11), 4443–4447 (1970)
37. Rosakis, P., Vainchtein, A.: New solutions for slow moving kinks in a forced Frenkel–Kontorova chain. J. Nonlinear Sci. **23**(6), 1089–1110 (2012)
38. Kresse, O., Truskinovsky, L.: Prototypical lattice model of a moving defect: the role of environmental viscosity. Izv. Phys. Solid Earth **43**, 63–66 (2007)
39. Kresse, O., Truskinovsky, L.: Lattice friction for crystalline defects: from dislocations to cracks. J. Mech. Phys. Solids **52**, 2521–2543 (2004)
40. Scalora, M., Dowling, J., Bowden, C., Bloemer, M.: The photonic band edge optical diode. J. Appl. Phys. **96**(4), 2023 1994
41. Scott, A.: A nonlinear Klein-Gordon equation. Am. J. Phys. **37**, 52 (1969)
42. Nadkarni, N., Arrieta, A.F., Chong, C., Kochmann, D., Daraio, C.: Unidirectional transition waves in bistable lattices. Phys. Rev. Lett. **118**, 244501 (2016)
43. Savin, A.V.: Supersonic regimes of motion in a topological soliton. JETP **81**, 608 (1995)
44. Zolotaryuk, Y., Eilbeck, J., Savin, A.: Bound states of lattice solitons and their bifurcations. Phys. D **81**, 108 (1997)
45. Pnevmatikos, S., Flytzanis, N., Bishop, A.R.: Soliton dynamics of an extended phi4 model with dissipation and an external field. J. Phys. C **20**, 2828–2851 (1987)
46. Milchev, A.: Solitary waves in a Frenkel-Kontorova model with non-convex interactions. Phys. D **41**, 262–274 (1990)

47. Halioua, G.: Waves of collapse in nondegenerate chain arrays. MSc thesis, under supervision of Prof. O.V. Gendelman, Technion - Israel Institute of Technology, Haifa (2014)
48. Carpio, A., Bonilla, L.L.: Wave front depinning transition in discrete one-dimensional reaction-diffusion systems. Phys. Rev. Lett. **86**(26), 6034–6037 (2001)
49. Defontaines, Y.D., Pomeau, Y.: Chain of coupled bistable oscillators: a model. Phys. D **46**, 201–216 (1990)
50. Truskinovsky, L.: Kinks versus shocks. Shock Induced Transitions and Phase Structures in General Media, pp. 185–229. Springer, New York (1993)
51. Shiroky, I.B., Gendelman, O.V.: Propagation of transition front in bi-stable nondegenerate chains: model dependence and universality. J. Mech. Phys. Solids **104**, 144–156 (2017)
52. Shiroky, I.B., Gendelman, O.V.: Propagation of transition fronts in nonlinear chains with non-degenerate on-site potentials. Chaos **28**, 023104 (2018)
53. Gendelman, O.V., Manevitch, L.I., Vakakis, A.F., M'Closkey, R.: Energy pumping in nonlinear mechanical oscillators: Part I—dynamics of the underlying hamiltonian systems. J. Appl. Mech. **68**(1), 34–41 (2000)

Part IV
Theory of Beams, Plates and Shells

Local Buckling of Cylindrical Shells. Pogorelov's Geometrical Method

A. Yu. Evkin

Abstract The important role of local dimple-like equilibrium states in the buckling mechanism of compressed cylindrical shell has been revealed in many experiments. In the present paper a mathematical model describing features of local buckling of the shells is suggested. It is based on Pogorelov's geometrical method. Derived simple analytical solution allowed estimating buckling loads and corresponding conditions. Especially the influence of local external perturbations was studied. Simple formula is suggested for design buckling load of elastic thin axially compressed cylindrical shells, which is based on energy criterion as a measure of perturbations.

1 Introduction and a Brief Historical Excurse

Massive experiments were performed in the research Laboratory of Strength and Reliability of Structures of Dnepropetrovsk State University in 1970 s, especially when the Lab moved to a new building equipped with modern testing machines and appliances. Most of tested specimens were cylindrical shells subject to axially compressive load. The previous experimental data obtained by different researchers had extremely wide dispersion and were hardly to predict theoretically. This "classical buckling problem" attracted attention of many researchers because they tried to explain the significant discrepancy between theoretical and experimental results. It was already clear that the significant difference between theoretical and experimental results was mainly caused by structure imperfections and first of all by initial deflections. However, the mechanism of the shell buckling was not explained and therefore the problem of estimating design buckling load of real structures remained not resolved.

A significant achievement was made when local dimple-like post-buckling equilibrium states were discovered by Vladimirov et al. [1] and Ricardo [2]. This special post-buckling pattern of the shell middle surface was observed at the load range

A. Yu. Evkin (✉)
Software for Structures, Toronto, Canada
e-mail: alexyevkin@hotmail.com

I. V. Andrianov et al. (eds.), *Problems of Nonlinear Mechanics and Physics of Materials*, Advanced Structured Materials 94,
https://doi.org/10.1007/978-3-319-92234-8_20

of about 35–50% of classical buckling load when an additional lateral force was applied as an external perturbation. The local equilibrium state with one buckle also can occur if the cylindrical shell has a local dimple-like geometrical imperfection. However, further increase of compressive load to approximately 50% of classical buckling load led to global buckling of the shell with loss of its load-carrying capacity. This axial compressive load was called "*upper local buckling load*". On the other hand, minimum compressive load was discovered when the local equilibrium shape existed. This load was called "*lower local buckling load*". Both local buckling loads were studied in the Lab, especially their dependence on shell geometrical parameters. The domain when local stable equilibrium state existed was relatively small (approximately from 35% to 50% of classical buckling load). It was the reason why this equilibrium state was not observed before without applying special additional local perturbations.

Next very important step in the research in this direction was made by Tennyson [3] and Eßlinger [4]. Using high-speed camera, they observed the buckling process of the shells and discovered that the process began with appearance of local dents (one or several) and then in the buckling process intensive bending deformation of the shell surface spread across the most part of the shell. This experimental result has shown the importance of local equilibrium states of the shell in the mechanism of shell buckling and gave another impulse to experimental study of local buckles in the Lab. The result was published in Mossakovskii et al. [5], Manevich et al. [6] and in other interesting research papers which we are not citing here because they are published in Russian and are not easily accessible for readers.

Then the most important question arose: how to use this knowledge for design buckling load estimation of real structures? It was obvious that perturbations (internal and external) should be taken into account. Initial geometrical imperfections of large scale real structures were not easy to measure. In addition, they significantly depend on manufacturing technology therefore can vary from one type of structure to another. Some of them (for example initial bending stresses) are hard to control. The current NASA (1968) design recommendation [7] suggests a lower bound estimation of design buckling load which is based on experimental data collected at that time. But the estimation is overly conservative, especially nowadays when the quality of structures increased significantly since the guidelines have been published.

Friedrichs [8] and Tsien [9] suggested energy criterion buckling load at some value where total potential energy in initial trivial state is equal to total potential energy at a stable post-buckling one. Certainly, the energy measure is the most universal one in physics, however the suggested criterion seems to never have been considered seriously [10] because initial equilibrium state A is separated from post-buckling stable state D by energy barrier Π_{AB} which in Fig. 1b corresponds to intermediate not stable equilibrium state B. Probably Jones [11] was the first who suggested to use energy barrier as a measure of shell stability. Unfortunately, he made a methodological mistake in the energy barrier calculation (see [12]) and, in addition, applied a too rough estimation method.

Professor L.I. Manevich suggested estimating energy barrier corresponding to local buckling of axially compressed cylindrical shells. The energy was measured

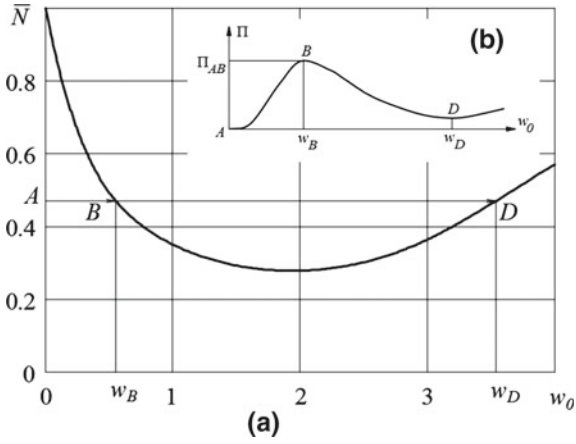

Fig. 1 **a** Post-buckling load deflection diagram and **b** energy deflection diagram corresponding to snap through equilibrium states A–B–D

directly in the experiments Mossakovskii et al. [5] and Manevich et al. [6] by dropping a steel ball on the surface of compressed cylindrical shell. The behaviour of shells in these experiments was similar to behaviour of cylinders tested with static local perturbations. At certain level of main compressive load and perturbation energy local post-buckling patterns of the shell were observed. In addition, the energy barrier was estimated whose order was about 1% of the shell deformation energy in its initial unbuckled equilibrium state at compressive load level close to lower local buckling load. Local post-buckling equilibrium states with 1, 2, 3, … coupled dimples were discovered in the experiments. Corresponding lower buckling load values decreased slightly with number of buckles. However, the energy barrier increased approximately proportionally to this number. It was intuitively reasonable to assume that post-buckling equilibrium shape with one local dimple corresponds to minimal buckling energy barrier.

One can conclude that the snap through to equilibrium state of the shell with one buckle is very likely at lower local buckling load because of presence of external and internal perturbations in engineering applications. Furthermore, the perturbations usually (or, again, more likely) have local character. Therefore lower local buckling load can be a good candidate for a criterion for estimation of design buckling load. Another candidate is the upper local buckling load which leads to loss of load-carrying capacity of the structure. From this point of view, studying local equilibrium states of the shell with one or several buckles and their dependence on different geometrical parameters of the structure and boundary conditions was very important.

Such experimental research was done in the Lab. I was a student at that time and observed all experiments. Professor L.I. Manevich was my Masters Degree thesis supervisor. He suggested I create a mathematical model of local buckling behavior of cylindrical shells and apply energy barrier concept to design buckling load estimation of the compressed shells. Furthermore, he proposed to apply Pogorelov's geometrical method which was (as I understood later) the most adequate approach at that time. This suggestion was the best luck in my research carrier.

It is remarkable that concepts described above are being intensively developed now. The energy barrier conception was developed by Horak et al. [13], Hutchinson and Thompson [14], Hutchinson [10], Evkin and Lykhachova [12]. Horak et al. have shown that minimum energy barrier of cylindrical shell buckling corresponds to local buckle. This was intuitively understandable before, but they proved this assumption by numerical analysis. In Evkin and Lykhachova [12] the energy criterion in combination with asymptotic method allowed obtaining formula for design buckling external pressure of spherical shell. The formula improved an overly conservative corresponding NASA design recommendation. In Haynie et al. [15] and Wagner et al. [16, 17] concepts of additional local perturbations of different types were used for design buckling load estimation of cylindrical shells subject to axial compression. Nowadays, software packages like ANSYS and ABAQUS, which are based on finite element method, allow behaviour simulation of compressed cylindrical shells with local perturbations [15, 18]. For more references concerning the subject, see papers cited in this paragraph.

2 Pogorelov's Geometrical Method

From mathematical point of view, the problem has two main specifics. First, the post-buckling shape is localized in both directions and it cannot be described by classical buckling modes (trigonometrical functions), which are usually used in common analytical methods. Second, the deflections corresponding to lower (or upper) local buckling load are not small compared to shell thickness. Deflection amplitude is around 3–5 times the shell thickness at lower local buckling load, therefore linear buckling solution is almost useless, even as a rough approximation. In Fig. 2 the picture of cylindrical shell compressed by load which is close to lower local buckling one is shown. Three different zones of deformed shell surface can be observed. First zone F_e is a surface which is very close to initial cylindrical one. The second part F_i is characterized by intensive bending and can be approximated by cylindrical surface with horizontal generatrixes. Two parts F_e and F_i are separated by narrow zone (along the curve γ) with intensive bending and membrane deformations. The curve γ is moving and the area of part F_i is increasing while deflection amplitude of the post-buckling dimple is increasing.

The described situation (fast changing deformation zone γ whose location is not fixed, plus significant non-linearity) caused the major problem for numerical methods. First reliable numerical solution for spherical shell with large deflections was obtained by Gabril'iants and Feodos'ev [19] for the case of axially symmetric deformation. Efficient finite element methods for significantly two-dimensional non-linear problems had developed only at the end of the last century. They were implemented and are available now in such commercial software as ANSYS and ABAQUS. In addition to experimental data we will use results of ANSYS simulation for validation of our analytical method which is based on Pogorelov's geometrical approach.

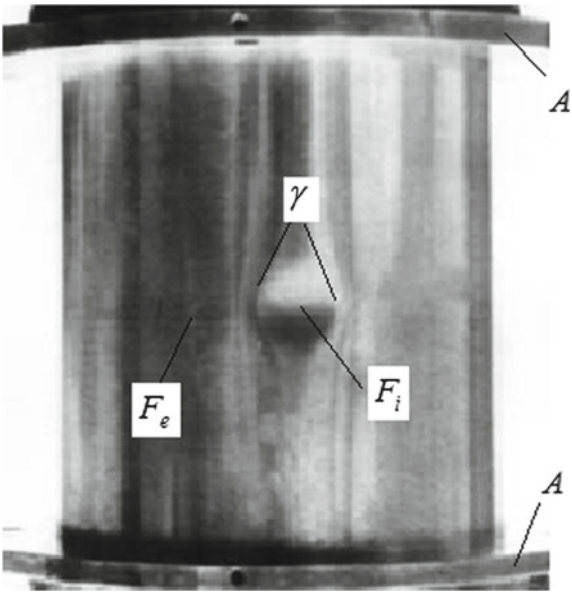

Fig. 2 Picture of compressed cylindrical shell with local dimple-like buckle

Pogorelov [20] developed geometrical method for describing behaviour of thin shell with large deflections. It is based on assumption that middle shell surface of the shell in post-buckling stage is close to some isometric mapping of the initial surface. This type of deformation is pure bending which requires much less energy than membrane type deformation, especially if deflections are large. However, load carrying structures are designed in such manner that the pure bending is not allowed because of boundary conditions (for cylindrical shells) or because of initial shell shape (spherical shells). Pogorelov suggested to consider isometric mapping in the set of not smooth surfaces. For spherical shell it is an inversion (mirror reflection) of a spherical segment. There is a sharp crease which is a junction of two parts of the shell (initial and inverted). In such mapping the surface is inextensional and Gaussian curvature remains constant. For cylindrical shell this mapping is more complicated than for spherical shell and will be considered in the next section. The main deformation energy is concentered in the narrow zone of inner boundary layer smoothing the unsmooth connection between two parts of the shell surface. Pogorelov obtained the following formula for this deformation energy

$$U_\gamma = cEh^{5/2} \int\limits_\gamma \frac{\alpha^{5/2}}{\sqrt{r}} ds_\gamma + \frac{Eh^3}{12\left(1-\nu^2\right)} \int\limits_\gamma \alpha(k_e + k_i)\, ds_\gamma, \tag{2.1}$$

where h is shell thickness, E is elasticity modulus, ν is Poisson's ratio. The integral should be evaluated along the curve γ separating two parts of the shell middle surface obtained after isometric mapping. Here r is curvature radius of the curve γ, k_e and

k_i are normal curvatures of the surface in direction perpendicular to the curve; 2α is the angle between planes tangent to the surfaces along the curve γ.

In Evkin [21] it is shown that Pogorelov's approach and its formula can be obtained by asymptotic analysis of convex shallow shell theory equations introducing a new small parameter proportional to ratio of shell thickness to the deflection amplitude. The second term in (2.1) belongs to terms of higher order of asymptotic solution and exactly equals zero for spherical shell, therefore we will neglect this term in the future consideration. There is a small difference in coefficient c calculations using asymptotic formula and Pogorelov's one. There is only an additional multiplier in asymptotic formula, which is equal to $\sqrt[4]{(1-\nu^2)}$. Here we used the result obtained by asymptotic method: $c = 1.12/\left[12(1-\nu^2)\right]^{3/4}$.

It is remarkable that the solutions of the asymptotic and Pogorelov's methods are more accurate for large (compared to shell thickness) deflections, therefore these methods complement Koiter's one, which is in contrast more accurate for small deflections. Unfortunately, the asymptotic method has not been proved yet for cylindrical shells, however it is clear that the geometrical method can be quite an adequate analytical one for studying the behaviour of buckled shells.

3 The Mathematical Model

The construction of the model describing behaviour of compressed cylindrical shells with local buckles was based on experimental data and observations of such post-buckling equilibrium states, as well as on author's experience in applying geometrical and asymptotic methods. The model was then verified by comparison with experimental results and numerical simulations.

According to the geometrical method, we have to construct a surface which is an isometric mapping of the initial cylinder. The Gaussian curvature of this surface should be equal to zero. In Mossakovskii et al. [22] this surface had two parts: one part was the initial cylinder and the second part was a cylindrical surface with horizontal generatrixes. They were separated by a curve, which was located on the initial cylindrical surface. Created corresponding model provided a lower bound estimation of shell buckling load parameters. However, it was inconsistent with Pogorelov's concept: the post-buckling surface had length of cross section perimeter less than that of the initial circle. In Evkin and Krasovsky [23] this inconsistency was omitted and the geometrical method was applied more accurately in case of local buckling of cylindrical shells under uniform external pressure. In the present paper we will develop the same approach for the case of axially compressed cylindrical shell.

The fragment of an isometric mapping suggested by Pogorelov for cylindrical shell is represented in Fig. 3. Curve γ (geometrical rib) separates cylindrical part with horizontal generatrixes F_i from ruled surface F_e. There is a plane triangle connecting ruled surface with initial circular cylinder. Circle γ_0 could be a boundary

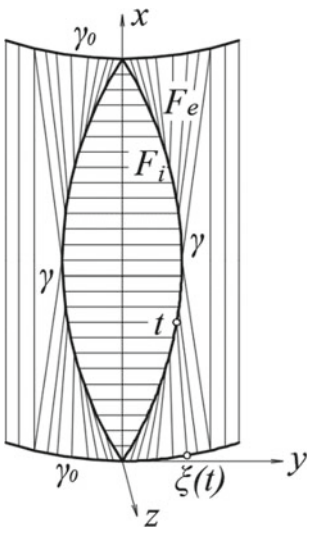

Fig. 3 Fragment of isometric mapping of cylindrical shell surface with local buckle

of a shell if it is under uniform compression (like in Evkin and Krasovsky [23]) or (in our case) it is another geometrical rib. Deformation in the zone around γ_0 can be neglected because radius of corresponding curvature is much larger compared to that of curve γ.

The equations of the curve γ is represented as the following

$$x = t, \quad y = \beta(t), \quad z = \lambda(t) \tag{3.1}$$

under assumption that $(\lambda')^2 << 1$.

There is an important condition coupling above functions derived by Pogorelov [20]:

$$\lambda'' = \frac{3\beta''}{4R}\left(\beta - \beta' t\right), \quad \xi(t) = \frac{3}{2}\left(\beta - \beta' t\right), \tag{3.2}$$

where R is the shell radius.

These equations were derived from the condition that the surface represented in Fig. 3 must map a plane without discontinuities along the curve γ. In this case the angles between contagious plane at any point of γ and corresponding tangent planes from left and right sides should be equal. For the axisymmetric inversion of a shell of revolution this condition is satisfied automatically.

We obtained the following formulae for geometric parameters of the isometric mapping:

$$\alpha = 0.5\,\xi\, d/R, \quad 1/r = \left|\beta''\right|/d^3, \quad ds_\gamma = d\,dt, \tag{3.3}$$

where $d = \sqrt{1 + (\beta')^2}$.

We introduce dimensions of the buckle (surface F_i): in the axial direction it is $2l_x$ and in the circumferential direction it is $2l_y$. We assume that buckles are located in the middle of the cylinder length. Because of symmetry with respect to two (vertical and horizontal) planes, we can consider only quarter of the surface plotted in Fig. 3, therefore integration can be performed from 0 to l_x. Finally, we have equation for the first term of (2.1) in the form

$$U_\gamma = 4cEh^{5/2} \int_0^{l_x} \sqrt{|\beta''|}\, d^2 (0.5\xi/R)^{5/2} dt. \tag{3.4}$$

This is deformation energy concentrated at narrow zone along the curve γ. Estimating bending deformation energy at the rest of the shell, we will neglect the curvature changes of F_e, as well as curvature change of F_i in circumferential direction, because by large deflections they are much smaller compared to curvature change of F_i in axial direction. The last one is approximately equal to λ''. Therefore the bending deformation energy at F_i is

$$U_i = 2D \int_0^{l_x} \beta(\lambda'')^2 dt, \tag{3.5}$$

where $D = Eh^3/\left[12\left(1 - \nu^2\right)\right]$ is bending stiffness of the shell.

Deflection amplitude w_0 at $t = l_x$ is

$$w_0 = \frac{3l_y^2}{8R}. \tag{3.6}$$

Therefore corresponding virtual work of lateral concentrated force Q applied at this point of the shell surface is

$$A_Q = Qw_0 = Q\frac{3l_y^2}{8R}. \tag{3.7}$$

We approximated curve γ by parabola with two parameters, l_y (which defines deflection amplitude according (3.6)) and l_x:

$$\beta\left(\bar{t}\right) = l_y\left(2\bar{t} - \bar{t}^2\right), \tag{3.8}$$

where $\bar{t} = t/l_x$. Then according to (3.2)

$$\lambda'' = 0.5\, l_y^2\left(\bar{t} - 0.25\bar{t}^4\right), \quad \xi = 1.5\bar{t}^2. \tag{3.9}$$

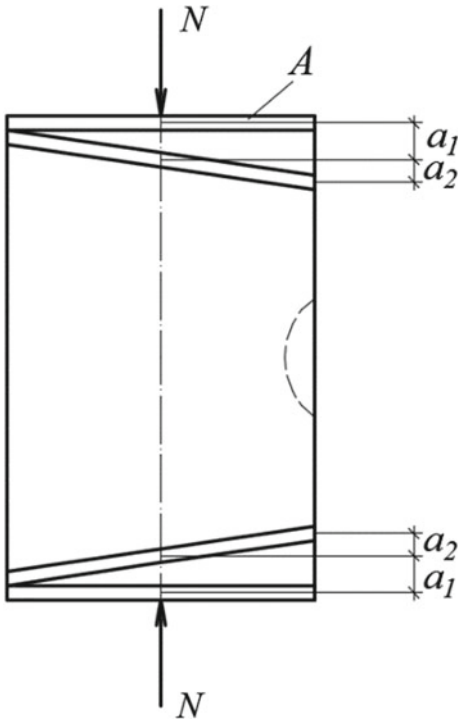

Fig. 4 Loading and boundary conditions of a cylindrical shell

In Fig. 4 boundary and loading conditions are shown which were realized in most experiments. The compressive load N was applied to the shell through rigid elements A which had 2 degrees of freedom described by parameters a_1 and a_2. The displacement function of element A and therefore displacement of the shell edge is

$$u = u_0 + a_1 + a_2 \cos(y/R), \tag{3.10}$$

where u_0 is displacement caused by shell loading in initial pre-buckling stage. Virtual work of main compressive load at buckling stage can be easily calculated as $A_N = 2a_1 N$. The following two equilibrium equations of rigid element are used for calculation of parameters a_1 and a_2:

$$\int_0^{2\pi R} \sigma(y)\, h\, dy = N, \tag{3.11}$$

$$\int_0^{2\pi R} \sigma(y)\, h\, R\, \cos(y/R) dy = 0. \tag{3.12}$$

Normal stresses σ are uniformly distributed along edge circle of the shell at initial equilibrium stage, however after shell dimple-like buckling the distribution became significantly non-homogenous and, therefore, the membrane deformation energy is changed. Calculating this energy we will neglect shear stresses. In addition to the geometrical method assumption (deflections are large compared to shell thickness), this is another one which allowed us to significantly simplify analytical solution. According to this assumption, we consider each longitudinal strip of the shell as a compressed and bended column. Because deflections are very small compared to shell length L, we can separate boundary displacement into two types: boundary displacement caused by bending (only surface F_i is taken into account)

$$u_b = 0.5 \int_0^{t(y)} (\lambda')^2 dt \tag{3.13}$$

and displacement $u_c(y)$ caused by column compressive deformation $\varepsilon(y)$, which, according to our assumption, is constant along the column. Therefore we have

$$\varepsilon(y) = 2u_c(y)/L, \quad \sigma(y) = E\varepsilon(y). \tag{3.14}$$

Equations (3.10)–(3.13) allowed to derive formulae for parameters a_1 and a_2

$$a_2 = 2a_1, \quad a_1 = B_1/\pi, \quad B_1 = \frac{1}{R} \int_0^{\pi R} \int_0^{t(y)} (\lambda')^2 dt\, dy. \tag{3.15}$$

Membrane deformation energy in post-buckling stage can be calculated using the obtained formula

$$U_c = U_0 + \frac{2Eh}{L} \left(B_3 - \frac{3RB_1^2}{2\pi} \right), \tag{3.16}$$

where $B_3 = \frac{1}{2R} \int_0^{\pi R} \left(\int_0^{t(y)} (\lambda')^2 \right)^2 dy$ and $U_0 = \frac{N^2 L}{4\pi RhE}$ is shell deformation energy in its initial bendingless state.

Actually, loading conditions represented in Fig. 4 allow to consider 4 different types of them [24]. The first one is described above. It has two parameters (free parallel displacement and rotation of the rigid element), which can be defined by equilibrium Eqs. (3.11) and (3.12). The second type is characterized by rotation only, but parallel displacement is restricted in this case. We put $a_1 = 0$ instead of using Eq. (3.11) in this case. In the third type rotation is restricted: equation $a_2 = 0$ is used instead of (3.12). Finally, $a_1 = 0$ and $a_2 = 0$ in the fourth type, which is rigid loading. We assigned index values $k = 3,\ 2,\ 1,\ 0$ corresponding to each of these four described loading types respectively.

In addition, we included equilibrium states with n dimple-like buckles in the consideration. For loading types 1 and 2 (with rotation) the buckles should be located (according to our model) close to each other in the not large part of the shell cross section perimeter (less than shell radius).

For the case of parabola approximation (3.8) of a geometrical rib γ, we obtained the formula for change of full potential energy U of the system, which includes virtual works of both compressive load N and lateral force Q:

$$\overline{U} = \frac{3nb\,\overline{\Pi}\left(\overline{N},\ \overline{Q}\right)}{\pi\, Z\overline{N}^2}, \tag{3.17}$$

$$\overline{\Pi} = 0.19\eta^3\overline{w}_0 + 0.35\overline{w}_0^{3/2}\left(1 + 0.143\eta^2\right) + 0.29\frac{\overline{w}_0^{3.5}\eta^2}{\sqrt{Z}}\left(1 - 0.46knb\sqrt{\frac{\overline{w}_0}{Z}}\right) - 0.7\overline{N}\overline{w}_0^2\eta - \overline{Q}\overline{w}_0. \tag{3.18}$$

Here the following normalization is introduced

$$\overline{U} = \frac{U}{U_0},\quad \overline{w}_0 = \frac{w_0}{h}\sqrt{1-\nu^2},\quad \eta = \frac{l_y}{l_x},\quad Z = \frac{L^2}{Rh}\sqrt{1-\nu^2},\quad \overline{Q} = \frac{\left(1-\nu^2\right)RQ}{Eh^3},\quad \overline{N} = \frac{N}{N_{cl}}, \tag{3.19}$$

where $N_{cl} = 2\pi Eh^2/\sqrt{3\left(1-\nu^2\right)}$ is classical buckling load, $b = L/R$.

Taking derivatives with respect to two variables η and $\overline{w}_0$, we obtain the final equations corresponding to equilibrium state of buckled shell loaded both by lateral and axially compressive force

$$0.57\eta^2 + 0.0985\eta\sqrt{\overline{w}_0} + 0.582\eta\frac{\overline{w}_0^{2.5}}{\sqrt{Z}}\left(1 - 0.46knb\sqrt{\frac{\overline{w}_0}{Z}}\right) - 0.7\overline{w}_0\overline{N} = 0, \tag{3.20}$$

$$\overline{Q} = 0.19\eta^3 + 0.522\sqrt{\overline{w}_0}\left(1 + 0.143\eta^2\right) + 1.02\eta^2\frac{\overline{w}_0^{2.5}}{\sqrt{Z}}\left(1 - 0.46knb\sqrt{\frac{\overline{w}_0}{Z}}\right) - 1.4\overline{w}_0\eta\overline{N}. \tag{3.21}$$

The first equation is quadratic one with respect to η. Solving it for given compressive load parameter $\overline{N}$ and normalized deflection amplitude $\overline{w}_0$ and then substituting the solution in (3.21), we obtained the dependence $\overline{Q}(\overline{w}_0)$. A typical one is shown in Fig. 5.

4 Validation and Analysis of the Model

There are two main assumptions used in our model. The first one is the assumption about large deflections of considered equilibrium states of the shells. According to our experience of applying asymptotic and geometrical methods, the obtained solution can be not bad lower bound estimation of main compressive load, deflections and full potential energy even for moderate values of deflection amplitude. Accord-

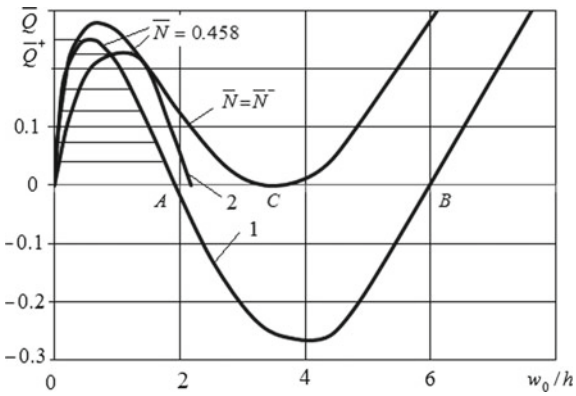

Fig. 5 Lateral load deflection diagrams of compressed cylinder ($L/R = 2.0,\ R/h = 210$)

ing to the second assumption, we neglect shear stresses and therefore can assume that normal axial stresses and deformations are constant in the longitudinal direction. The model based on the assumptions was validated by finite element simulation and experimental results. In all experiments considered below the specimens were manufactured from steel sheets (Poisson's ratio $\nu = 0.3$). The loading type 1 was realized. But there was a difference in the attaching shell edges to the rigid elements. In most experiments (Vladimirov et al. [1], Manevich et al. [6], Mossakovskii et al. [5]) and in all numerical simulations the shells were considered as clamped to the rigid plate. However in experiments completed by Krasovsky [25] and then cited in Evkin et al. [24] the boundary condition in circumferential direction was significantly weaker. This boundary condition matches our model more, because in this case shear stresses are equal to zero not only in two symmetry planes and in the not buckled main part of the shell, but also at the edges of the shells. In Krasovsky's experiments displacement parameters of the rigid plate were measured and the obtained result confirmed the formula (3.15) derived from our model under the considered assumption. The following relationship $a_2 = (2.006 \pm 0.082)\, a_1$ was obtained in the test. We have to note that neglecting shear stresses we obtain lower bound estimation as a result of our model analysis.

The analytical method allows us to make a conclusion about system dependence on its important parameters. According to normalization (3.19) and Eqs. (3.20), (3.21), it depends only on Batdorf parameter $Z = L^2\sqrt{1-\nu^2}/(Rh)$ if loading condition is of type 4 (absolutely rigid loading, $k = 0$). For other types of loading conditions it slightly depends on these types (on index k and radius to thickness ratio) if we have just one local buckle ($n = 1$). For deflection amplitude $w_0/h \leq 1$ the normalized system parameters do not depend on any geometrical and rigid structure parameters at all. Certainly, this conclusion is valid in the scope of our model.

The structure behaviour in the dimple-like post-buckling stage depends on the shell length, which is included in deformation energy (3.16). Even though the deformation seems to be localized, the axial stresses are spread along the shell length and

their distribution change in circumferential direction causes the dependence on shell length in the case of local buckling.

4.1 Axially Compressed Cylindrical Shells Under Local External Perturbations

In Fig. 5 the theoretical (curve 1) and experimental (curve 2) [24, 25], dependences of lateral force parameter $\overline{Q}$ on normalized deflection amplitude are plotted for the fixed value of main load parameter $\overline{N} = 0.458$. Maximum $\overline{Q}^{+}$ corresponds to buckling state of the shell under considered load combination. Even though the maximum is reached at not large deflection amplitude, the theoretical solution does not exceed experimental result of shell testing (with geometrical parameters $L/R = 2.0,\ R/h = 210$) by much.

Some more useful information can be derived from the graphs. Points A and B when $\overline{Q} = 0$ correspond to post-buckling equilibrium states of the compressed shells without external perturbations. Point A with deflection amplitude w_0 corresponds to intermediate unstable equilibrium state, whose energy level (barrier) can be calculated as dashed area under the curve. At some value of compressive load parameter $\overline{N} = \overline{N}^{-}$ there is only one point C when $\overline{Q} = 0$ and the load deflection curve is tangent to the horizontal axis. For $\overline{N} < \overline{N}^{-}$ the equilibrium state with one dimple does not exist. Value $\overline{N}^{-}$ is lower local buckling load parameter. Point B corresponds to post-buckling equilibrium state, which becomes unstable if compressive load exceeds upper local buckling load $\overline{N}^{+}$.

Buckling load combinations of compressive and lateral load are shown in Fig. 6. Result of our calculations is represented by curve 1 ($L/R = 2.0,\ R/h = 210$) and compared with numerical simulation obtained by Marchenko [26] (curve 2). There is a good agreement in the interval $0.3 \le \overline{N} \le 0.6$. For greater compressive load, the maximum of perturbation load is reached in the range, where deflection amplitude is small compared to shell thickness and geometrical method yields wrong result.

Experimental data obtained in Krasovsky [25] and published in Evkin et al. [25] are shown by triangle symbols ($L/R = 2.0,\ R/h = 210$). Two types of loading sequence were applied in the experiment. Empty triangle symbols correspond to the case when local lateral load was applied first. Filled triangle symbols correspond to the case when compressive load was applied first and then the local lateral force was applied. No significant difference in the sequence of load applying was observed in the tests. Theoretical results obtained by numerical method by Wagner et al. (2017) ($L/R = 3.0,\ R/h = 330$) are shown by diamonds. Empty symbols correspond to local and filled diamonds to global buckling of the structure.

Equations (3.20) and (3.21) can be simplified assuming that the load combination is reached at moderate deflection amplitude $w_0/h \sim 1$. Neglecting small terms we obtain

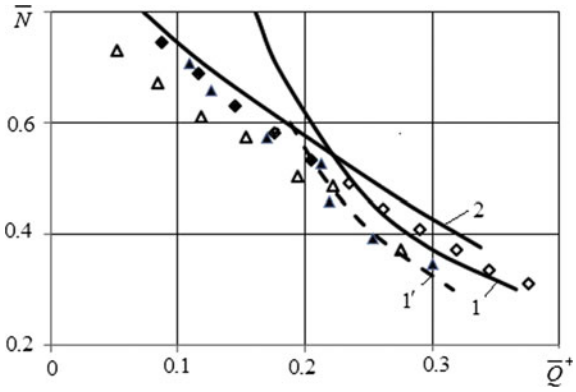

Fig. 6 Experimental and theoretical buckling load combinations

$$0.57\eta^2 - 0.7\overline{w}_0\overline{N} = 0, \tag{4.1}$$

$$\overline{Q} = 0.19\eta^3 + 0.522\sqrt{\overline{w}_0} - 1.4\overline{w}_0\overline{N}. \tag{4.2}$$

Finally we have very simple formula for buckling load combination

$$\overline{Q} = 0.128/\overline{N}^{0.75}, \quad 0.3 \le \overline{N} \le 0.6. \tag{4.3}$$

The formula is represented by curve $1'$ in Fig. 6. One can see that it is in good agreement with experimental data in the range $0.3 \le \overline{N} \le 0.6$ and yields slightly more conservative result with respect to numerical solution. The formula can be efficiently used for preliminary estimation of structure stability in the mentioned above compressive load range, which is the most important from practical point of view.

Let us compare buckling lateral perturbation load with main axial compressive one considering the ratio

$$\frac{Q}{N} = \frac{0.128h}{2\pi\, R\overline{N}^{1.75}}\sqrt{\frac{3}{\left(1-\nu^2\right)}}. \tag{4.4}$$

Perturbation load is extremely small compared to the main load. For example, if $\nu = 0.3$, $\overline{N} = 0.5$ we have $Q/N = 0.12h/R$. For $R/h = 480$ we obtain $Q = 0.00025N$. If we take realistic load value of a large scale missile $N=1000kN$, we have corresponding buckling lateral force $Q=0.25kN$. This load can be applied just by kicking the structure by boots. In addition, if compressive load is greater than upper local buckling load, the structures can completely lose its capacity with severe consequences. Therefore knockdown factor should be significantly less than 0.5 for this shell.

We considered inward lateral force as a local perturbation. There could be another so called *kinematic perturbation* type when the deflection is given. In the experiments by Krasovky [25], Evkin et al. [24] these perturbations were realized by

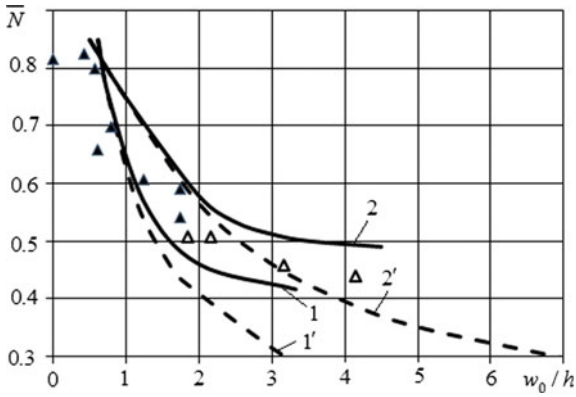

Fig. 7 Compressive load parameter versus normalized deflection amplitude ($L/R = 2.0,\ R/h = 150$)

loading screw with one side constraint on the shell surface. The buckling occurred at deflection amplitude w_0 when reaction from the shell was equal to zero ($\overline{Q} = 0$), therefore it corresponded to intermediate equilibrium state of the structure without perturbations. Corresponding compressive load deflection diagrams are shown in Fig. 7 in normalized form. Curves 1 and 1′ represent result of calculations based on our model. Curves 2 and 2′ were obtained by Marchenko [26] by numerical method. Dashed lines 1′ and 2′ correspond to classical loading type when compressive normal stresses are uniformly distributed in the circumferential direction at the shell edge even in post-buckling stage. To model this case we neglected membrane energy U_c in our calculations. There is no minimum in the diagrams corresponding to lower local buckling loads in this type of loading. Therefore minimum can occur only if there is a reinforcement at the shell edge causing some not homogeneous stress distribution in circumferential direction in post-buckling shell equilibrium state with localized bending deformation of the shell.

Experimental results obtained by Krasovsky [25] are shown by triangle symbols. Shells of good quality were tested: buckling load of specimens without external perturbations exceeded 80% of classical buckling load. Two ways of loading were examined in the test with different sequence of loading by main compressive load and external kinematic perturbation. No difference in buckling combination was observed in the experiment. Empty triangles correspond to the case when only one dimple was realized after buckling. Filled triangles represent global shell buckling when almost all shell surface was bended in the final post-buckling stage. The boundary between these types of buckling is separated by upper local buckling load. The dimple-like equilibrium state of the shell became unstable at compressive load greater than upper local buckling load and any local perturbations lead to global shell buckling with loss of load-carrying capacity. From practical point of view, it is very important to study both lower and upper local buckling loads and conditions when the snap through to local buckling form can be realized. Unfortunately, our model does not allow obtaining solution for upper local buckling load, because this is a much more complicated problem, but it yields good results for lower local buckling load.

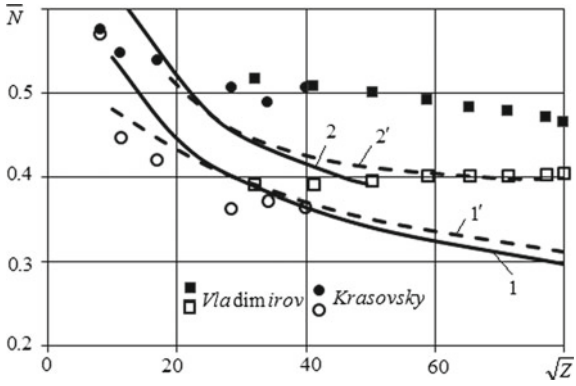

Fig. 8 Local buckling loads depending on Batdorf parameter

The result of our calculations matches experimental data in Fig. 7 except zone with high compressive load ($\overline{N} \leq 0.75$) with corresponding small deflection amplitude. But it is slightly lower compared to the numerical solution, because in our model, as well as in the experiment, weaker boundary conditions in circumferential direction were considered.

4.2 Lower and Upper Local Buckling Loads

As we mentioned above, Batdorf parameter Z is the main one of the system. Curves 1 and $1'$ in Fig. 8 represent result of our calculations of lower local buckling load. Curve 1 was obtained with fixed ratio $R/h = 210$ and therefore ratio L/R was changed, curve $1'$ was obtained with fixed ratio $L/R = 2$. The same approach was used by Marchenko [26] in numerical analysis. The result is shown by curves 2 and $2''$ respectively. Experimental data are shown by circles [25] and rectangles [1]). Empty symbols correspond to lower local buckling load, filled – to upper local buckling load. In Vladimirov's experiment [1] only ratio R/h was changed and clamped shells were tested. In Krasovsky's experiment [25] shorter specimens with different ratio L/R were tested but with weaker boundary conditions. Our result matches experimental data well in the most practically important range $100 \leq Z \leq 1600$. For greater values of Batdorf parameter it yields lower bound estimation if the shell is clamped.

Lower local buckling load depends on the number of buckles n. This dependence is illustrated in the Table 1 by parameter $\overline{N}_e^-$ for shells ($L/R = 1.76,\ R/h = 280$), which were tested in Mossakovskii et al. [5]. Result of our calculations is noted by $\overline{N}^-$. It is limited by buckle number $n = 1,\ 2$ because of restriction $(y/R)^2 << 1$ for loading type condition 1, 2 with free rotation of rigid elements.

In the experiment Evkin et al. [27] ($L/R = 1.4,\ R/h = 370$) lateral forces were applied periodically in the circumferential direction, therefore loading type condition 3 can be considered in this case. We put $k = 1$ in our calculations and

Table 1 Upper and lower local buckling loads depending on number n of buckles (loading type condition 1, $L/R = 1.76,\ R/h = 280$)

n	1	2	3	4	5	6
$\overline{N}_e^-$	0.413	0.360	0.328	0.309	0.303	0.296
$\overline{N}^-$	0.404	0.38	----	----	----	----
$\overline{U}(\%)$	0.6	1.6	----	----	----	----

Table 2 Upper and lower local buckling loads depending on number n of buckles (loading type condition 3, $L/R = 1.4,\ R/h = 370$)

n	2	3	4	6	8	12	16
$\overline{N}_e^+$	0.533	0.505	0.469	0.429	0.403	0.397	0.472
$\overline{N}_e^-$	0.445	0.438	0.418	0.403	0.387	0.363	0.444
$\overline{N}^-$	0.423	0.416	0.411	0.397	0.380	--.	--.
$\overline{U}(\%)$	0.95	1.5	2.1	3.7	6.2	--.	--.

Table 3 Upper and lower local buckling loads for different types of load conditions ($L/R = 2.0,\ R/h = 150$)

k	3	2	1	0
$\overline{N}_c^+$	0.555	0.560	0.616	0.623
$\overline{N}_c^-$	0.487	0.498	0.510	0.520
$\overline{N}^-$	0.420	0.428	0.438	0.447
$\overline{U}(\%)$	0.8	0.76	0.68	0.62

obtained result noted in Table 2 as $\overline{N}^-$. Experimental data corresponding to lower $\overline{N}_e^-$ and upper $\overline{N}_e^+$ local buckling loads are shown in the Table 2 as well. There is good agreement between theoretical and experimental data. Both upper and lower local buckling loads reached minimum because buckles were stiffened by each other when their number increased enough. We did not study this effect in our model.

In the Table 3 our calculation result for lower local buckling load parameter $\overline{N}^-$ is compared with the result of numerical analysis by Marchenko [26]. Numerically obtained upper local buckling load parameter is noted as $\overline{N}_c^+$ here. Both methods yield slight dependence of buckling loads on loading type conditions.

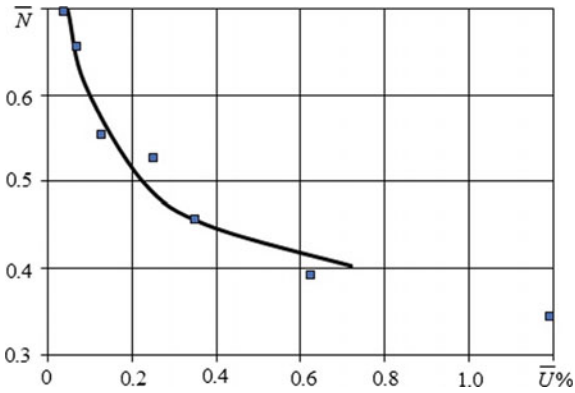

Fig. 9 Theoretical and experimental estimation of energy barrier depending on load parameter ($L/R = 2.0,\ R/h = 210$)

4.3 Energy Barrier and Design Buckling Load

One can see from Table 3 that relative energy barrier $\overline{U}$ does not depend much on loading type conditions remaining very small compared to deformation energy of the structure in initial equilibrium state. But the barrier increases fast with the number of buckles (Tables 1 and 2). In the Tables the energy barrier is calculated at the compressive load, which is equal to lower local buckling one. Diagram of the energy barrier depending on the compressive load level is shown in Fig. 9. Here our result is compared with experimental data obtained by Krasovsky ($L/R = 2.0,\ R/h = 210$). Author used static loading by lateral force, obtained a diagram similar to that in Fig. 5 and then calculated corresponding area. There is excellent agreement between theory and experiment.

The following formula is suggested by NASA (1968) [7] for knockdown factor for axially compressed cylindrical shells

$$\rho = 1 - 0.902\left(1 - e^{-\left(\frac{1}{16}\sqrt{\frac{R}{h}}\right)}\right). \tag{4.5}$$

The approach has two disadvantages: it yields overly conservative estimation of design buckling load for thin shells and it does not depend on the shell length. The classical buckling load value does not depend on shell length, but from local perturbation concept this dependence is very important. The formula is represented in Fig. 10 for the case when ratio $L/R = 2.0$. Formula for knockdown factor suggested by Wagner and Hühne [17] included dependence from shell length. It has the following form

$$\rho = \Omega_{TH}(R/h)^{-\eta_{TH}}, \tag{4.6}$$

$$\Omega_{TH} = -0.0196(L/R)^2 - 0.0635(L/R) + 1.3212, \tag{4.7}$$

$$\eta_{TH} = -0.0113(L/R)^2 + 0.061(L/R) + 0.08. \tag{4.8}$$

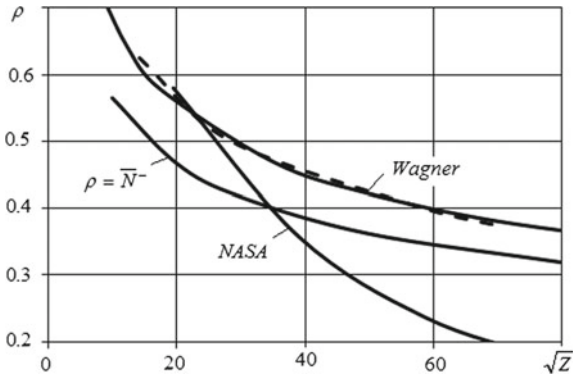

Fig. 10 Knockdown factor depending on Batdorf parameter

Table 4 Relative energy barrier at lower local buckling load versus Batdorf parameter

Z	100	400	900	2500	6400
$\overline{U}(\%)$	1.26	0.73	0.53	0.35	0.24

The formulae were derived taking into account geometric and loading imperfections as perturbations at the same time.

We calculated knockdown factor ρ following these formulae in two ways: fixing ratio $L/R = 2.0$ first and changing another geometrical parameter R/h (solid lane in Fig. 10), and then fixing $R/h = 210$ and changing relative length of the shell L/R(dashed line in Fig. 10). There is no difference in the results if they are represented as load dependence from Batdorf parameter. Therefore two geometrical parameters R/h and L/R can be reduced to just one Batdorf parameter Z. We derived the same conclusion above from analysis of our model.

We suggest lower local buckling load as a design buckling one. The corresponding curve 1 in Fig. 10 is the result of calculations based on our model. The loading type 4 is considered, which corresponds to loading type in the research of Wagner and Hühne [17]. In this case $k = 0$ and the system (according to our model) exactly depends only on Batdorf parameter. The curve $\rho = \overline{N}^{-}\left(\sqrt{Z}\right)$ repeats result obtained by Wagner and Hühne, but yields about 15% smaller knockdown factor. The difference can be considered as additional safety factor or result of boundary condition imperfections, because in our model we considered weaker connection of the shell edges to the loading plates. The energy barrier analysis shows that extremely small perturbations are enough for shell buckling at lower local buckling load. The energy barrier is decreasing with the increase of Batdorf parameter and can be about 1% of deformation energy of the structure in initial pre-buckling equilibrium state or even significantly less. The energy barrier calculated at lower local buckling load is shown in the Table 4.

We also compared our solutions with result obtained by Horak et al. [13]. As we mentioned above, authors proved that minimum energy barrier corresponds to potential of dimple-like equilibrium state of the shell. In addition, one can conclude

Table 5 Comparison of lower local buckling load with Horak's result noted as $\overline{N}_H^-$

a	50	100	200
$\overline{N}_H^-$	0.345	0.297	0.256
$\overline{N}^-$	0.355	0.293	0.243

from Fig. 4.3 (left) of the cited paper that the obtained solution depends only on domain $(-a,\ a)$ of longitudinal variable x. Shell parameter a is proportional to square root of Batdorf parameter $a = \sqrt[4]{192}\sqrt{Z}/\pi$, therefore Batdorf parameter is the main structure characteristic if buckling of the structure is localized in circumferential direction. It is also interesting that Horak et al. [13] obtained formula (5.1) for relative full potential energy, which can be represented in the form

$$\overline{U} = \frac{b\, V\left(\overline{N}\right)}{8\pi\sqrt{3}Z\overline{N}^2}. \tag{4.9}$$

It is similar to our Eq. (3.17).

In the Table 5 we compare result of our calculation ($k = 0$) of lower local buckling load with corresponding data from Horak et al. [13] by reading results represented in Fig. 4.3 (left) of the paper. There is good agreement between data in Table 5. However, energy barrier values obtained in the cited paper are approximately two times greater than that obtained in our calculations and experiments.

The energy criterion for design buckling load estimation has obvious advantages. The energy is the most general measure in mechanics and therefore can accumulate impacts of any perturbations including external ones and geometrical imperfections. We believe that there is a correlation between geometrical and external perturbations (see Evkin and Lykhachova [12]). In addition, the energy barrier concept allows estimating sensitivity of the structure to the perturbations, but it does not require information about initial structure imperfections, which are hard to control in practice.

We observed that if we take any pair $\sqrt{Z_1}$ and $\sqrt{Z_2}$ such that $\sqrt{Z_1}/\sqrt{Z_2} = 2$ the ratio $\overline{N}^-\left(\sqrt{Z_2}\right)/\overline{N}^-\left(\sqrt{Z_1}\right) = 1.21$ will be almost constant, therefore the obtained dependence $\rho = \overline{N}^-\left(\sqrt{Z}\right)$ (plotted in Fig. 10) can be approximated with good accuracy as the following simple formula

$$\rho = 1.07Z^{-0.138}, \quad 50 \le Z \le 7000. \tag{4.10}$$

It is not shown in the Fig. 10 because corresponding curve almost coincides with the plotted curve $\rho = \overline{N}^-\left(\sqrt{Z}\right)$. We suggest (4.10) as a formula for knockdown factor of design buckling load $N_{des} = \rho N_{cl}$. Dependence obtained by Wagner and Hühne [17] yields result which is about 15% greater. With good accuracy it can be approximated as

$$\rho = 1.23Z^{-0.138}. \tag{4.11}$$

Another candidate for design buckling load, which discussed in literature, is upper local buckling load. It can exceed the lower local buckling load by about 20%, but the difference is decreasing for thinner shells (see experimental results in Fig. 8). Energy barrier at upper local buckling load is extremely small fraction of the shell deformation energy at initial equilibrium state. Certainly, nowadays it is possible to manufacture and test small specimens in the lab and obtain high values of buckling load, but in reality external perturbations and initial geometrical imperfections always exist and will make buckling of large scale structures almost inevitable at upper local buckling load, therefore this load cannot be considered as a lower bound estimation for design buckling load. Comparison with experimental data shows that selecting upper local buckling load as design buckling load can overestimate empirical data substantially (see for example Wagner et al. [16]). In addition, buckling at upper local buckling load will cause global shell buckling with loss of load-carrying capacity. This can lead to catastrophic consequences and therefore it should be compensated by additional safety factor. Our approach suggests somewhat conservative lower bound estimation of design buckling load.

5 Conclusion

Suggested simple analytical model based on Pogorelov's geometrical method is developed and validated by experimental results and numerical simulations. The model revealed and explained important buckling features of compressed thin cylindrical shells. In particular, introduced parameter normalization shows that the Batdorf parameter is the most important one describing behavior of the system.

Obtained simple formulae can be useful in engineering practice for stability estimation of compressed elastic cylindrical shells subject to possible external local perturbations. The perturbation approach and energy barrier concept allowed to conclude that the so called lower local buckling load can be suggested as a lower bound estimation of the design buckling load of the structure.

We also provided some experimental data, which were published only in Russian or they are difficult to find because most experiments were performed in 1970s. Recently this topic became very popular in the shell buckling theory. Latest research concerning the subject can be found in the reference lists of papers [10, 14, 16, 17].

References

1. Vladimirov, S.A., Konokh, V.I., Mossakovskii, V.I., Smelyi, G.N.: Experimental investigation of local loss of stability of a cylindrical shell during axial compression. Mech. Solids **4**(4), 161–165 (1969)
2. Ricardo, O.G.S.: An experimental investigation of the radial displacements of a thin-walled cylinder. NASA-CR-934 rep. California Institute of Technology, Pasadena, CA (1967)
3. Tennyson, R.C.: Buckling modes of circular cylindrical shells under axial compression. AIAA J. **7**(8), 1481–1487 (1969)
4. Eßlinger, M.: Hochgeschwindigkeitsaufnahmen vom Beulvorgang dünnwandiger axialbelasteter Zylinder. Stahlbau **39**(3), 73–76 (1970)
5. Mossakovskii, V.I., Manevich, L.I., Prokopalo, E.F.: Investigation of post-critical behaviour of cylindrical shells (in Russian). Proc. USSR Acad. Sci. **206**(2), 297–298 (1972)
6. Manevich, L.I., Mossakovskii, V.I., Prokopalo, E.F.: Experimental study of the transcritical behaviour of shells. Mech. Solids **10**(1), 145–150 (1975)
7. NASA: Buckling of thin-walled circular cylinders, NASA SP-8007 (1968)
8. Friedrichs, K.O.: On the minimum buckling load for spherical shells. In: Theodore von Karman Anniversary volume. California Institute of Technology, Pasadena, CA, pp. 258–282 (1941)
9. Tsien, H.S.: A theory for the buckling of thin shells. J. Aeronaut. Sci. **9**(10), 373–384 (1942)
10. Hutchinson J.W.: Buckling of spherical shells revisited. Proc. R. Soc. A **472**:2160577, 25 pp (2016)
11. Jones, R.M.: Toward a new snap-through buckling criterion for axially compressed circular cylindrical shells. AIAA J. **4**(9), 1526–1530 (1966)
12. Evkin, AYu., Lykhachova, O.V.: Energy barrier as a criterion for stability estimation of spherical shell under uniform external pressure. Int. J. Solids Struct. **118**(July), 14–23 (2017)
13. Horak, J., Lord, G.J., Peletier, M.A.: Cylinder buckling: the mountain pass as an organizing centre. SIAM J. Appl. Math. **66**(5), 1793–1824 (2006)
14. Hutchinson, J.W., Thompson, J.M.T.: Nonlinear buckling of spherical shells: barriers and symmetry-breaking dimples. Philos. Trans. R. Soc. A, 25 pp (2016)
15. Haynie, W.T., Hilburger, M.W., Bogge, M., Maspoli, M., Kriegesmann, B.: Validation of lower-bound estimates for compression-loaded cylindrical shells. In: Collection of Technical Papers - AIAA/ASME/ASCE/AHS/ASC Structures, Structural Dynamics and Materials Conference, April 2012. https://doi.org/10.2514/6.2012-1689
16. Wagner, H.N.R., Hühne, C., Niemann, S., Khakimiva, R.: Robust design criterion for axially loaded cylindrical shells—Simulation and validation. Thin-Walled Struct. **115**, 154–162 (2017)
17. Wagner, H.N.R., Hühne, C.: Robust knockdown factors for design of cylindrical shells under axil compression: potentials, practical application and reliability analysis. Int. J. Mech. Sci. **135**, 410–430 (2018)
18. Krasovsky, V., Marchenko, V., Schmidt, R.: Deformation and buckling of axially compressed cylindrical shells with local loads in numerical simulation and experiments. Thin-Walled Struct. **49**, 576–580 (2011)
19. Gabril'iants, A.G., Feodos'ev, V.I.: Axially-symmetric forms of equilibrium of an elastic spherical shell under uniform distributed pressure. J. Appl. Math. Mech. (PMM) **25**(6), 1629–1642 (1961)
20. Pogorelov, A.V.: Bending of Surfaces and Stability of Shells. Translation of Mathematical Monographs, vol. 72. American Mathematical Society (1988)
21. Evkin, AYu.: A new approach to the asymptotic integration of the equations of shallow convex shell theory in the postcritical stage. J. Appl. Math. Mech. **53**(1), 92–96 (1989)
22. Mossakovskii, V.I., Manevich, L.I., Evkin, AYu.: A study of the post-critical equilibrium configurations of a cylindrical shell under compression. Soviet Appl. Mech. **11**(11), 1155–1159 (1975)
23. Evkin, AYu., Krasovsky, V.L.: Post-critical deformation and estimation of the stability of real cylindrical shells under external pressure. Soviet Appl. Mech. **27**(3), 290–296 (1991)

24. Evkin, AYu., Krasovsky, V.L., Manevich, L.I.: Stability of longitudinally compressed shells under quasi-static local disturbances. Mech. Solids **13**(6), 83–88 (1978)
25. Krasovsky, V.L.: Experimental investigation of behaviour and load-carrying capacity of axially compressed circular cylindrical shells with structural imperfections and external perturbations [in Russian]. Ph.D. thesis, Dnepropetrovsk (1973)
26. Marchenko, V.A.: Non-linear strain and buckling of the axially compressed cylindrical shells subject to subject to local quasistatic transversal perturbations [in Russian]. Ph.D. thesis, Dnepropetrovsk (2013)
27. Evkin, A.Yu., Prokopalo, E.F., Shukurov A.H.: On post-buckling equilibrium forms of axially compressed cylindrical shell [in Russian]. In: Conference Proceedings: Nonlinear Theory of Shells and Plates, Kazan, pp. 63–65 (1980)

Stretching of Reinforced Orthotropic Plate

S. Koblik

Abstract The stress-strain state of an orthotropic plate reinforced by a doubly periodic system of inextensible one-dimensional inclusions and subjected to loading simulating uniaxial tension in the direction of the inclusions is studied. Using the asymptotic method, developed for the case of the strong anisotropy, using the theory of Weierstrass elliptic functions, the theory of boundary value problems of analytic functions, and the Keldysh-Sedov formula an approximate closed solution of the problem is obtained. A comparison with the exact solution, which is known for the case of one inclusion in the plane, shows that the error of the asymptotic solution does not exceed 9% at case of an isotropic plate. This case is the worst one from the point of view of the method. The approximate solution obtained is used to calculate the effective modulus of elasticity in the direction of the inclusions. The dependence of this modulus on the size of the periodicity cell and the mutual arrangement of the inclusions is demonstrated.

1 Introduction

The problem of extension of an elastic plate with a thin inextensible or elastic inclusion was studied in the number of papers [1–5]. The purpose of these articles was analysis of the stress-strain state near the inclusion. The related problems of stress-strain state of plates with doubly-periodic structure was studied in [6–8]. Effective elastic characteristics of such solids have also been identified. However, the case of reinforcement of an elastic plane by a doubly-periodic system of one-dimensional elastic or inextensible inclusions was not considered. In present paper the effective stiffness of reinforced plane is estimated, based on the approximate asymptotic solution of the problem of stretching elastic plane reinforced by the doubly-periodic lattice of inextensible one-dimensional inclusions.

S. Koblik (✉)
8110 Birchfield Dr, Indianapolis, IN, USA
e-mail: Stevekoblik8110@comcast.net

I. V. Andrianov et al. (eds.), *Problems of Nonlinear Mechanics and Physics of Materials*, Advanced Structured Materials 94,
https://doi.org/10.1007/978-3-319-92234-8_21

A similar problem of determining the effective shear modules of elasticity in case of antiplane loading orthotropic solid, weakened by doubly periodic crack system, discussed in [9], where effective moduli are found using the exact solution of antiplane problem for rectangular cells, that obtained using the conformal mapping the half of the cell onto the upper half-plane.

Unlike work [9], in which the exact solution of harmonic problem is found, the exact solution of the biharmonic problem of stretching of reinforced plate is unknown. To get an approximate solution of the problem, the asymptotic method, proposed in [10] and described in detail in [11, 12], is used. According to this method the solution is represented as an asymptotic expansion on parameter $\varepsilon = G^2 \big/ B_1 B_2$. Since this approach is little known, its application will be illustrated on the example of the stretching of orthotropic plane with one inextensible one-dimensional inclusion.

Let us consider the plane stress-strain state of an orthotropic plate for which the principal lines of orthotropy are coincide with the coordinate axes. The solution of boundary value problems for such a plate can be reduced to solution of the equations of equilibrium of the planar orthotropic media in displacements

$$\begin{aligned} B_1 \frac{\partial^2 u}{\partial x^2} + G \frac{\partial^2 u}{\partial y^2} + Ge \frac{\partial^2 v}{\partial x \partial y} &= 0, \\ G \frac{\partial^2 v}{\partial x^2} + B_2 \frac{\partial^2 v}{\partial y^2} + Ge \frac{\partial^2 u}{\partial x \partial y} &= 0, \end{aligned} \tag{1}$$

under given boundary conditions.

Here

$$B_j = \frac{E_j}{1 - \nu_{12}\nu_{21}}, \quad j = 1, 2; \quad G = G_{12}; \quad e = 1 + \nu_{21} \frac{B_1}{G} = 1 + \nu_{12} \frac{B_2}{G}, \tag{2}$$

E_1, E_2 and G are elastic moduli in the directions x, y and shear modulus; ν_{12} and ν_{21} are Poisson's ratios, where $\nu_{12} E_2 = \nu_{21} E_1$. The tensile and shear stresses in the plane are determined by the expressions

$$\begin{aligned} \sigma_x &= B_1 \frac{\partial u}{\partial x} + G(e-1) \frac{\partial v}{\partial y}, \\ \sigma_y &= B_2 \frac{\partial v}{\partial y} + G(e-1) \frac{\partial u}{\partial x}, \\ \tau_{xy} &= G \left(\frac{\partial u}{\partial y} + \frac{\partial v}{\partial x} \right). \end{aligned} \tag{3}$$

In order to pose the corresponding boundary value problem for Eq. (1), the boundary conditions have to be added and, in the case of the mixed boundary problem for the orthotropic strip ($0 \le y \le H$, $|x| < \infty$), they have to be formulated as follows: the boundary of the strip $\left(L = L' + L''\right)$ is separated into the parts with different boundary conditions, e.g.

$$\sigma_x = F(x), \quad \tau_{xy} = P(x), \quad \left(x \in L'\right),$$
$$u = u^*(x), \quad v = v^*(x), \quad \left(x \in L''\right). \tag{4}$$

Let us suppose case of strong anisotropy $B_1 \sim B_2 \gg G$. Then the quantity $\varepsilon = G^2 \big/ B_1 B_2$ may considered as a small parameter. This condition explicitly defines the essential anisotropy of the medium in the considered problem—for isotropic medium the Young's modulus and the shear modulus should be of the same order.

Let us introduce the affine transformation

$$x = \varepsilon^{-1/4} q^{-1/4} x_1, \quad y = y_1, \quad u = U^{(1)}, \quad v = \varepsilon^{3/4} q^{-1/4} V^{(1)}, \tag{5}$$
$$x = \varepsilon^{1/4} q^{-1/4} x_2, \quad y = y_2, \quad u = \varepsilon q^{1/4} U^{(2)}, \quad v = \varepsilon^{1/4} V^{(2)}, \tag{6}$$

where $q = B_1 \big/ B_2 \sim 1$.

Substitution of the transformations (5) and then (6) into Eq. (1) leads to systems (7) and (8) respectively

$$\begin{aligned} &U^1_{,xx} + U^1_{,yy} + \varepsilon e V^1_{,xy} = 0, \\ &V^{(1)}_{,yy} + e U^{(1)}_{,xy} + \varepsilon V^{(1)}_{,xx} = 0. \end{aligned} \tag{7}$$
$$\begin{aligned} &U^{(2)}_{,xx} + e V^{(2)}_{,xy} + \varepsilon U^{(2)}_{,yy} = 0, \\ &V^{(1)}_{,xx} + V^{(2)}_{,yy} + \varepsilon e U^{(2)}_{,xy} = 0. \end{aligned} \tag{8}$$

Here and below the following notations are accepted for brevity:

$$\frac{\partial \varphi^{(i)}}{\partial x_i} = \varphi^{(i)}_{,x}, \quad \frac{\partial \varphi^{(i)}}{\partial y_i} = \varphi^{(i)}_{,y}.$$

The solution of the system (7) varies along x-axis more slow than the similar solution of system (8).

(In the former case $\frac{\partial}{\partial x} = \varepsilon^{1/4} q^{1/4} \frac{\partial}{\partial x_1}$, in the latter $\frac{\partial}{\partial x} = \varepsilon^{-1/4} q^{1/4} \frac{\partial}{\partial x_2}$.)

The components of the displacement vector are presented by superposition of the solutions of both types

$$u = u_1 + u_2\,, \; v = v_1 + v_2. \tag{9}$$

We will look for the functions $U^{(n)}$, $V^{(n)}$ $(n = 1, 2)$ as series in small parameter $\varepsilon^{1/4}$:

$$U^{(n)} = \sum_{m=0}^{\infty} \sum_{j=0}^{3} \varepsilon^{m+j/4} U^{n,4m+j},$$
$$V^{(n)} = \sum_{m=0}^{\infty} \sum_{j=0}^{3} \varepsilon^{m+j/4} V^{n,4m+j}. \tag{10}$$

It is convenient to introduce additional transformations of the coordinates

$$\xi_1 = x_1 \sum_{m=0}^{\infty} \alpha_m \varepsilon^m, \ \eta_1 = y_1, \tag{11}$$

$$\xi_2 = x_2 \sum_{m=0}^{\infty} \beta_m \varepsilon^m, \ \eta_2 = y_2. \tag{12}$$

Here the coefficients α_0, β_0 are equal to unity, because the equations of the zeroes approximation have to coincide with the limiting systems which can be obtained from Eqs. (7) and (8) if $\varepsilon \to 0$. The coefficients α_m, β_m ($m=1, 2,\ldots$) are calculated from the recursion formulas [11, p.77], [12, p.274] and are used for simplification of the equations for higher approximations. By substitution of series (10) and (11) into the system (7) and by splitting the obtained expressions by parameter $\varepsilon^{1/4}$ we obtain for the stress state of the first type:

$$U^{1,4m+j}_{,\xi\xi} c_0 + U^{1,4m+j}_{,\eta\eta} = -\sum_{\nu=0}^{m-1} \left(U^{1,4\nu+j}_{,\xi\xi} c_{m-\nu} + e V^{1,4\nu+j}_{,\xi\eta} \alpha_{m-\nu-1} \right), \tag{13}$$

$$V^{1,4m+j}_{,\eta\eta} = -eU^{1,4m+j}_{,\xi\eta} \alpha_0 - \sum_{\nu=0}^{m-1} \left(eU^{1,4\nu+j}_{,\xi\eta} \alpha_{m-\nu} + V^{1,4\nu+j}_{,\xi\xi} c_{m-\nu-1} \right), \tag{14}$$

where $c_p = \sum_{s=0}^{p} \alpha_s \alpha_{p-s}$.

Similarly, after substitution of the series (10) and (12) (for $n = 2$) into system (8) one can find for the stress state of the second type:

$$U^{2,4m+j}_{,\xi\xi} = -eV^{2,4m+j}_{,\xi\eta} \beta_0 - U^{2,4(m-1)+j}_{,\eta\eta} - \sum_{\nu=0}^{m-1} \left(U^{2,4\nu+j}_{,\xi\xi} d_{m-\nu} + eV^{2,4\nu+j}_{,\xi\eta} \beta_{m-\nu} \right), \tag{15}$$

$$V^{2,4m+j}_{,\xi\xi} d_0 + V^{2,4m+j}_{,\eta\eta} = -\sum_{\nu=0}^{m-1} \left(V^{2,4\nu+j}_{,\xi\xi} d_{m-\nu} + eU^{2,4\nu+j}_{,\xi\eta} \beta_{m-\nu} \right), \tag{16}$$

where $d_p = \sum_{s=0}^{p} \beta_s \beta_{p-s}$.

As it is shown in [11, 12], the coefficients α_m, β_m (m = 1, 2, …) can be determined in a way that Eqs. (13)–(16) will be written as follows

$$U^{1,4m+j}_{,\xi\xi} + U^{1,4m+j}_{,\eta\eta} = 0, \tag{17}$$

$$V^{1,4m+j}_{,\eta\eta} = -eU^{1,4m+j}_{,\xi\eta} - \sum_{\nu=0}^{m-1} \left(eU^{1,4\nu+j}_{,\xi\eta} \alpha_{m-\nu} + V^{1,4\nu+j}_{,\xi\xi} c_{m-\nu-1} \right), \tag{18}$$

$$U^{2,4m+j}_{,\xi\xi} = -eV^{2,4m+j}_{,\xi\eta} - U^{2,4(m-1)+j}_{,\eta\eta} - \sum_{\nu=0}^{m-1}\left(U^{2,4\nu+j}_{,\xi\xi}d_{m-\nu} + eV^{2,4\nu+j}_{,\xi\eta}\beta_{m-\nu}\right), \quad (19)$$

$$V^{2,4m+j}_{,\xi\xi} + V^{2,4m+j}_{,\eta\eta} = 0. \quad (20)$$

If in Eqs. (18) and (19) the upper limit of a sum is less than its lower limit, then the sum equals to zero. Similarly, if the second upper index of a function $U^{n,k}$ or $V^{n,k}$ is negative, then this function equals to zero.

By substituting the sums (9) and corresponding transformations (10)–(12) into expressions for the displacements u, v and stresses (3) we obtain

$$u = U^{(1)} + \varepsilon q^{1/4}U^{(2)} = \sum_{m=0}^{\infty}\sum_{l=0}^{3}\varepsilon^{m+j/4}\left(U^{1,4m+j} + \varepsilon q^{1/4}U^{2,4m+j}\right),$$

$$v = \varepsilon^{3/4}q^{-1/4}V^{(1)} + \varepsilon^{1/4}V^{(2)} = \sum_{m=0}^{\infty}\sum_{l=0}^{3}\varepsilon^{m+\frac{j+1}{4}}\left(V^{2,4m+j} + \varepsilon^{1/2}q^{-1/4}V^{1,4m+j}\right). \quad (21)$$

In similar way the stresses are represented as expansions

$$\begin{aligned}\sigma_x &= B_1\left(u_{,x} + \nu_{21}v_{,y}\right)\\ &= B_1\varepsilon^{1/4}q^{1/4}\sum_{m=0}^{\infty}\sum_{j=0}^{3}\varepsilon^{m+j/4}\left[\sum_{\nu=0}^{m}U^{1,4\nu+j}_{,\xi}\alpha_{m-\nu}\right.\\ &\quad\left.+\varepsilon^{1/2}q^{1/4}\left(\sum_{\nu=0}^{m}U^{2,4\nu+j}_{,\xi}\beta_{m-\nu} + (e-1)V^{2,4m+j}_{,\eta}\right) + \varepsilon(e-1)V^{1,4m+j}_{,\eta}\right] \quad (22)\end{aligned}$$

$$\begin{aligned}\sigma_y &= B_2\left(v_{,y} + \nu_{12}u_{,x}\right)\\ &= B_2\varepsilon^{1/4}\sum_{m=0}^{\infty}\sum_{j=0}^{3}\varepsilon^{m+j/4}\left[V^{2,4m+j}_{,\eta}\right.\\ &\quad\left.+\varepsilon^{1/2}q^{-1/4}\left(V^{1,4m+j}_{,\eta} + (e-1)\sum_{\nu=0}^{m}U^{1,4\nu+j}_{,\xi}\alpha_{m-\nu}\right) + \varepsilon(e-1)\sum_{\nu=0}^{m}U^{2,4\nu+j}_{,\xi}\beta_{m-\nu}\right], \quad (23)\end{aligned}$$

$$\begin{aligned}T_{xy} &= G\left(u_{,y} + v_{,x}\right)\\ &= G\sum_{m=0}^{\infty}\sum_{j=0}^{3}\varepsilon^{m+j/4}\left[U^{1,4m+j}_{,\eta}\right.\\ &\quad\left.+q^{1/4}\sum_{\nu=0}^{m}V^{2,4\nu+j}_{,\xi}\beta_{m-\nu} + \varepsilon\left(q^{1/4}U^{2,4m+j}_{,\eta} + \sum_{\nu=0}^{m}V^{1,4\nu+j}_{,\xi}\alpha_{m-\nu}\right)\right]. \quad (24)\end{aligned}$$

The substitution of series (21)–(24) into boundary conditions and the following splitting by parameter $\varepsilon^{1/4}$ allows one to find the boundary conditions corresponding to the boundary value problems for the functions $U^{1,4m+j}$, $V^{2,4m+j}$. The functions $V^{1,4m+j}$ and $U^{2,4m+j}$ are calculated by simple integration of the expressions (14) and

(15). One can see from (17)–(24) that the stress-strain states of both types are coupled only via the boundary conditions.

The displacement u has the dominant effect on the stress-strain state of the first type as well as on a corresponding stress σ_x and component of the shear stress τ_{xy} depending on u.

As for the dominant components of the second stress-strain state, they are displacement v, stress σ_y and component of the shear stress τ_{xy} depending on v.

So, for $m = 0$ and $j = 0$ one obtains

$$U^{1,4m+j}_{,\xi\xi} + U^{1,4m+j}_{,\eta\eta} = 0,$$

$$V^{1,4m+j}_{,\eta\eta} = -eU^{1,4m+j}_{,\xi\eta}, \tag{25}$$

$$u^{1.0} = U^{1.0}, \tag{26}$$

$$\sigma^{1,0}_x = B_1\varepsilon^{1/4}q^{1/4}U^{1,0}_{,\xi} \tag{27}$$

for the state of the first type and

$$U^{2,4m+j}_{,\xi\xi} = -eV^{2,4m+j}_{,\xi\eta},$$

$$V^{2,4m+j}_{,\xi\xi} + V^{2,4m+j}_{,\eta\eta} = 0, \tag{28}$$

$$v^{2,0} = \varepsilon^{1/4}V^{2,0}, \tag{29}$$

$$\sigma^{2,0}_y = B_2\varepsilon^{1/4}V^{2,0}_{,\eta} \tag{30}$$

for the state of the second type.

The shear stress depends on both states

$$\tau^0_{xy} = \tau^{1,0}_{xy} + \tau^{2,0}_{xy} = G\left(U^{1,0}_{,\eta} + q^{1/4}V^{2,0}_{,\xi}\right). \tag{31}$$

Let us demonstrate the method efficiency on the model problem about stretching elastic plane with inextensible one-dimensional inclusion that is oriented along the x-axis. The plane is loaded by applied at infinity stress σ^∞_x. This problem has the exact solution that allows estimate the accuracy of the method.

Let us place the origin of the frame of reference in the middle of inclusion. Then inclusion is located in segment ($|x| \le a,\ y = 0$), and, by the virtue of symmetry, displacement u and stresses $\sigma_x,\ \sigma_y$ are even functions of y, while v and shear stress τ_{xy} are odd functions of$y$. It follows that the offset v vanish in the x-axis and hence

$$\partial v \big/ \partial x = 0 \quad (-\infty < x < \infty,\ \ y = 0), \tag{32}$$

while the shear stresses on the sides of the inclusion, as antisymmetric, satisfy equality

$$\tau^+_{xy} = -\tau^-_{xy}, \tag{33}$$

where $\tau_{xy}^{+} = \lim\limits_{y\to+0} \tau_{xy}, \quad \tau_{xy}^{-} = \lim\limits_{y\to-0} \tau_{xy} \quad (|x| < a)$.

From Eqs. (31)–(33) it follows that on the sides of inclusion

$$U_{,\eta}^{1,0}(\xi_1, +0) = -U_{,\eta}^{1,0}(\xi_1, -0). \tag{34}$$

Because the inclusion is inextensible, the strain

$$U_{,\xi}^{1,0} = 0 \text{ for}(|\xi_1| \le a_1, \ \eta_1 = 0). \tag{35}$$

Thus for the zeroes approximation the following equations and boundary conditions are obtained:

$$U_{,\xi\xi}^{1,0} + U_{,\eta\eta}^{1,0} = 0, \tag{36}$$

$$\begin{aligned} &U_{,\xi}^{1,0}(\xi_1, 0) = 0 && |\xi_1| \le a_1, \\ &U_{,\eta}^{1,0}(\xi_1, +0) = -U_{,\eta}^{1,0}(\xi_1, -0) && |\xi_1| \le a_1, \\ &\lim_{|\xi_1|\to\infty} \sigma_x^{1,0} = \lim_{|\xi_1|\to\infty} B_1 \varepsilon^{1/4} q^{1/4} U_{,\xi}^{1,0} = \sigma_x^{\infty} \end{aligned} \tag{37}$$

for the state of the first type and

$$V_{,\xi\xi}^{2,0} + V_{,\eta\eta}^{2,0} = 0, \tag{38}$$

$$\begin{aligned} &V_{,\xi}^{2,0} = 0 && (|\xi_2| \le \infty, \ \eta_2 = 0), \\ &V_{,\eta}^{2,0}(\xi_2, +0) = V_{,\eta}^{2,0}(\xi_2, -0) && (|\xi_2| \le \infty), \\ &\lim_{|\eta_2|\to\infty} \sigma_y^{1,0} = \lim_{|\eta_2|\to\infty} B_2 \varepsilon^{1/4} V_{,\eta}^{2,0} = 0 \end{aligned} \tag{39}$$

for the state of the second type.

To solve the boundary value problems (36), (37) and (38), (39), let us introduce the holomorphic functions of complex variables

$$\Phi^{1,0}(\zeta_1) = U_{,\xi}^{1,0} - iU_{,\eta}^{1,0}, \ \text{where } \zeta_1 = \xi_1 + i\eta_1, \tag{40}$$

$$\Phi^{2,0}(\zeta_1) = U_{,\xi}^{2,0} - iU_{,\eta}^{2,0}, \ \text{where } \zeta_2 = \xi_2 + i\eta_2. \tag{41}$$

Then, due to the boundary condition (37) and (39), the problem is reduced to two Riemann-Hilbert problems:

$$\begin{aligned} &\Phi^{1,0+}(\xi_1) = -\Phi^{1,0-}(\xi_1), && (-a_1 \le \xi_1 \le a_1), \\ &\lim_{\zeta_1\to\infty} \Phi^{1,0}(\zeta_1) = \tfrac{\sigma_x^{\infty}}{B_1} \varepsilon^{-1/4} q^{-1/4}. \end{aligned} \tag{42}$$

$$\Phi^{2,0+}(\xi_2) = \Phi^{2,0-}(\xi_2),\ (-\infty \le \xi_2 \le \infty),$$
$$\lim_{\zeta_2 \to \infty} \Phi^{2,0}(\zeta_2) = 0. \tag{43}$$

The problems have solutions

$$\Phi^{1,0}(\zeta_1) = \frac{\sigma_x^\infty}{B_1} \varepsilon^{-1/4} q^{-1/4} \frac{\zeta_1}{\sqrt{\zeta_1^2 - a_1^2}}, \tag{44}$$

$$\Phi^{2,0}(\zeta_2) = 0. \tag{45}$$

The shear stresses on the top side of inclusion are

$$\tau_{xy}^+ = G U_{,\eta}^{1,0+} = -G \mathrm{Im}(\Phi^+(\xi_1)) = G \frac{\sigma_x^\infty}{B_1} \varepsilon^{-1/4} q^{-1/4} \frac{\xi_1}{\sqrt{\xi_1^2 - a_1^2}} = \sigma_x^\infty \varepsilon^{1/4} q^{1/4} \frac{x}{\sqrt{x^2 - a^2}}. \tag{46}$$

For isotropic plane $q = 1$,
$\varepsilon^{1/4} = \sqrt{(1-\nu)/2}$ for plane strain,
and $\varepsilon^{1/4} = 1/\sqrt{2(1+\nu)}$ for generalized plane stress.
The exact solution of the problem for isotropic plane is [13]:

$$\tau_{xy}^+ = \frac{\sigma_x^\infty}{8} \frac{(1+\kappa)^2}{\kappa} \frac{x}{\sqrt{x^2 - a^2}}, \tag{47}$$

where $\kappa = 3 - 4\nu$ for plane strain and $\kappa = \frac{3-\nu}{1+\nu}$ for generalized plane stress.

Expressions (46) and (47) differs only in coefficients; a comparison between the exact solution (47) and the approximate one (46) in the worst, from the point of view of the described asymptotic method, case of isotropic plane shows that the difference is less than 9% for both plane strain and generalized plane stress.

2 Statement of the Problem and Solution

Orthotropic plane with principal axes, which coincide with the axes of frame of reference, is reinforced by doubly periodic lattice of one-dimensional inextensible inclusions, oriented along the x-axis. The plane is stretched in x-axis direction. The challenge is to define the stress-strain state and evaluate effective stiffness of the reinforced plane in the x-axis direction (Fig. 1).

Here $2l$ is the length of cell of a doubly-periodic lattice, $2h$ is the height of the cell.

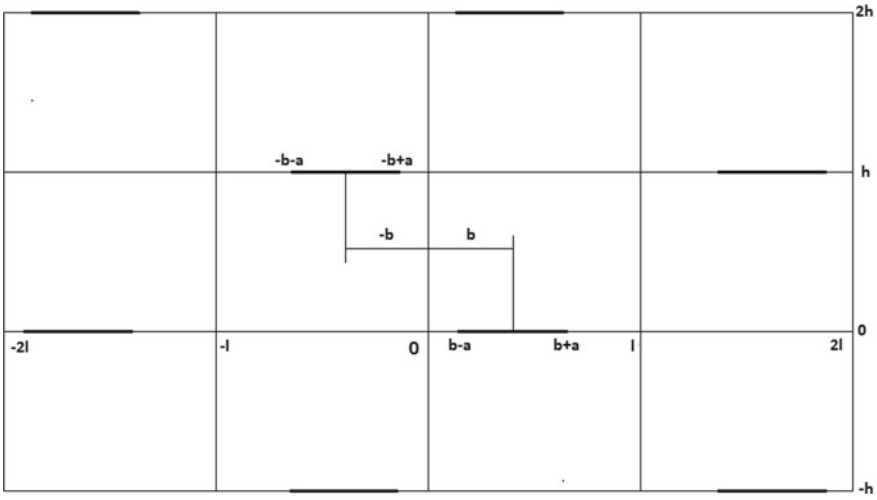

Fig. 1 Doubly-periodic lattice of inclusions

All inclusions have length $2a \quad (0 < a < l)$ and located on segments:

$$\begin{aligned} &b - a + 2kl \le x \le b + a + 2kl, \qquad y = 2mh, \qquad k = 0, \pm 1, \pm 2, \ldots, \\ &-b - a + 2kl \le x \le -b + a + 2kl, \; y = (2m+1)h, \; m = 0, \pm 1, \pm 2, \ldots \end{aligned} \tag{48}$$

To determine the effective tensile modulus, let us consider such load of the plane, which simulates the uniaxial tension and the doubly periodicity is not violated, although the shape of the cell may changes. We assume that the straight lines where inclusions are located remain straight and parallel to the x-axis and displacements u and v are symmetric and antisymmetric respectively about the straight lines $y = mh$, $m = 0, \pm 1, \pm 2, \ldots$ Thus derivative $\partial u \big/ \partial y$ and the shear stresses τ_{xy} will be antisymmetric about the same straight lines, while derivative $\partial v \big/ \partial y$ and the tensile stresses σ_x, σ_y are symmetric about those lines. It follows that in the sides of the inclusions

$$\frac{\partial u}{\partial y}^{+} = -\frac{\partial u}{\partial y}^{-} \text{ and } \frac{\partial v}{\partial y}^{+} = \frac{\partial v}{\partial y}^{-}.$$

Since the inclusions are inextensible, the tensile strain vanishes $\left(\partial u \big/ \partial x = 0\right)$ at the points adjacent to the inclusions. It is obvious, that outside of inclusions the displacements and its derivatives are continuous, and because the displacement v is antisymmetric about lines, which hosts inclusions, v vanishes there as well as the shear stresses τ_{xy} vanish in the continuation of inclusions (see Fig. 2).

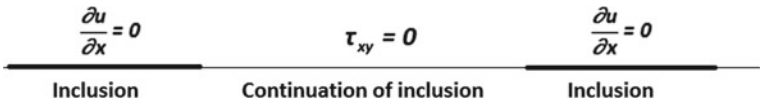

Fig. 2 The boundary conditions

Thus in any line $y = mh$, $m = 0, \pm 1, \pm 2, \ldots$ we have $v(x, y) = 0$ and $\frac{\partial v(x, y)}{\partial x} = 0$. Therefore, from $\tau_{xy}(x, y) = 0$ it follows that $\partial u/\partial y = 0$ in the continuation of inclusions.

Because the doubly-periodicity is not violated we can consider the only cell.

In this case we define the average linear strain as

$$\varepsilon_{av} = \frac{1}{\Omega} \int\limits_{\Omega} \int \varepsilon_x d\Omega = \frac{1}{2h} \int\limits_{-h}^{h} \left(\frac{1}{2l} \int\limits_{-l}^{l} \varepsilon_x dx \right) dy, \tag{49}$$

and define the average tensile stress as

$$\sigma_{av} = \frac{P_x}{2h} = \frac{1}{2h} \left[\int\limits_{-h}^{h} \sigma_x|_{x=\tilde{x}} dy + T_x(\tilde{x}) \right] \tag{50}$$

where

P_x is the total extending force applied to the cell in direction of x-axis,

$T_x(\tilde{x})$ is the stretching load in the inclusion at the point $\tilde{x}$, which is selected in a such way, that straight line $x = \tilde{x}$ crosses only the inclusion located in x-axis in the cell, or it does not intersect any inclusion at all, hence

$$T_x(\tilde{x}) = -(H(\tilde{x} - (b - a)) - H(\tilde{x} - (b + a))) \int\limits_{b-a}^{\tilde{x}} \left(\tau_{xy}^{+} - \tau_{xy}^{-} \right) dx, \tag{51}$$

$H(x)$ is the Heaviside step function,

$-\tau_{xy}^{+}$ and $-\tau_{xy}^{-}$ are shear stresses applied to the upper and lower side of inclusion.

Hence, the effective stiffness in x-axis direction is

$$B_{eff} = \frac{\sigma_{av}}{\varepsilon_{av}} = \left[\int\limits_{-h}^{h} \sigma_x|_{x=\tilde{x}} dy + T_x(\tilde{x}) \right] / \frac{1}{2l} \int\limits_{-h}^{h} \left(\int\limits_{-l}^{l} \varepsilon_x dx \right) dy. \tag{52}$$

It is obvious, that σ_x and ε_x are symmetric functions about x-axis, while τ_{xy} is an antisymmetric function about the same axis. Hence, formulas (49)–(52) could be rewritten

$$\varepsilon_{av} = \frac{1}{h}\int_0^h \left(\frac{1}{2l}\int_{-l}^{l} \varepsilon_x dx\right) dy, \tag{53}$$

$$\sigma_{av} = \frac{1}{h}\left[\int_0^h \sigma_x|_{x=\tilde{x}} dy + \frac{1}{2}T_x(\tilde{x})\right], \tag{54}$$

$$T_x(\tilde{x}) = -2(H(\tilde{x}-(b-a)) - H(\tilde{x}-(b+a)))\int_{b-a}^{\tilde{x}} \tau_{xy}^{+} dx, \tag{55}$$

$$B_{eff} = \frac{\sigma_{av}}{\varepsilon_{av}} = \left[\int_0^h \sigma_x|_{x=\tilde{x}} dy + T_x(\tilde{x})\right] / \frac{1}{2l}\int_0^h \left(\int_{-l}^{l} \varepsilon_x dx\right) dy. \tag{56}$$

To find the effective stiffness we need to solve equations of the plane theory of orthotropic elasticity (1)

with following boundary conditions:

$$\frac{\partial u}{\partial x} = 0 \text{ in each inclusion}, \quad \tau_{xy} = 0 \text{ in continuations of inclusions}. \tag{57}$$

We need also take into account the condition of equilibrium of cell

$$2\int_0^h \sigma_x|_{x=\tilde{x}} dy + T_x(\tilde{x}) = P_x, \tag{58}$$

and the condition of equilibrium of inclusion

$$\int_{b-a}^{b+a} \tau_{xy}^{+}\big|_{y=0} dx = 0. \tag{59}$$

To get an approximate solution of the problem, the aforementioned asymptotic method is used.

The first term of the main part of asymptotic expansion is found from equation

$$U^{1,0}_{,\xi\xi} + U^{1,0}_{,\eta\eta} = 0 \tag{60}$$

with boundary conditions:

$$U^{1,0}_{,\xi} = 0 \text{ in each inclusion}; \quad U^{1,0}_{,\eta} = 0 \text{ in continuations of the inclusions}. \tag{61}$$

Condition of equilibrium of cell is

$$2\int_0^h \sigma_x|_{x=\tilde{x}}dy + T_x(\tilde{x})$$
$$= 2B_1\varepsilon^{1/4}q^{1/4}\left[\int_0^{h_1} U^{1,0}_{,\xi}d\eta_1 - \Big(H\Big(\tilde{\xi}_1-(b_1-a_1)\Big) - H\Big(\tilde{\xi}_1-(b_1+a_1)\Big)\Big)\int_{b_1-a_1}^{\tilde{x}_1} U^{1,0}_{,\eta}d\xi_1\right] = P_x. \tag{62}$$

Condition of equilibrium of inclusion is

$$\int_{b_1-a_1}^{b_1+a_1} U^{1,0}_{\eta}d\xi_1 = 0. \tag{63}$$

The load in the inclusion is defined by formula

$$T_x = -2\Big(H\Big(\tilde{\xi}_1-(b_1-a_1)\Big) - H\Big(\tilde{\xi}_1-(b_1+a_1)\Big)\Big)B_1\varepsilon^{1/4}q^{1/4}\int_{b_1-a_1}^{\tilde{\xi}_1} U^{1,0}_{,\eta}d\xi_1. \tag{64}$$

Let us introduce the analytic function $\Phi^{1,0}(\zeta_1) = U^{1,0}_{,\xi} - iU^{1,0}_{,\eta}$ of complex variable $\zeta_1 = \xi_1 + i\eta_1$. Then we have to find a doubly-periodic function $\Phi^{1,0}(\zeta_1)$ that satisfies to conditions: $\mathrm{Re}\big(\Phi^{1,0}(\zeta_1)\big) = 0$ in each inclusion and $\mathrm{Im}\big(\Phi^{1,0}(\zeta_1)\big) = 0$ in continuations of inclusions.

This problem is solved by Keldysh-Sedov formula [14]

$$\Phi^{1,0}(\zeta_1) = A\frac{\sigma(\zeta_1-c_1)\sigma_3(\zeta_1+c_1)}{\sqrt{\sigma(\zeta_1-(b_1-a_1))\sigma(\zeta_1-(b_1+a_1))\sigma_3(\zeta_1+(b_1-a_1))\sigma_3(\zeta_1+(b_1+a_1))}}, \tag{65}$$

where $\sigma(\zeta_1)$ and $\sigma_3(\zeta_1)$ are the Weierstrass sigma functions.

Since functions $\sigma(z_1)$ and $\sigma_3(z_1)$ are antisymmetric ones about the origin, it is obvious that $\sigma(\zeta_1 - c_1)$ and $\sigma_3(\zeta_1 + c_1)$ change sign and vanish at points $\zeta_1 = c_1$ and $\zeta_1 = -c_1 + ih_1$ accordingly.

In contrast to the approach taken in article [9], which uses the conformal mapping, the usage of Keldysh-Sedov formula allows to solve the problem (60)–(63), without the knowledge of boundary conditions at the vertical boundaries ($|\xi_1| = \pm l_1,\ \ |\eta_1| \le h_1$) of cell of periodicity, which gives the opportunity to explore the unsymmetrical, regarding those boundaries, stress-strain state.

Formula (65) contains two unknown parameters: A and c_1. The latter can be defined by using condition of equilibrium of inclusion $\int_{b_1-a_1}^{b_1+a_1} \mathrm{Im}\big(\Phi^{1,0}(\xi_1+i0)\big)d\xi_1 = 0$, while to find A we must use the equilibrium of the cell

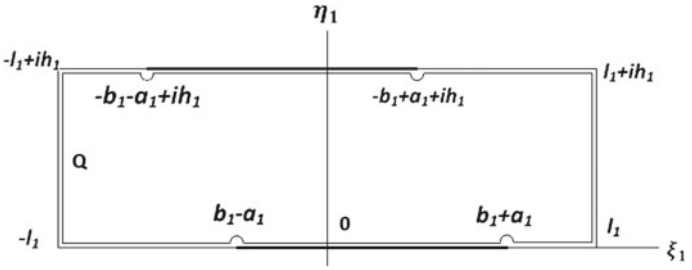

Fig. 3 Integration line of the curvilinear integral

$$2B_1\varepsilon^{1/4}q^{1/4}\left[\int_0^{h_1}\mathrm{Re}\left(\Phi^{1,0}\left(\tilde{\xi}_1+i\eta_1\right)\right)d\eta_1+\left(H\left(\tilde{\xi}_1-(b_1-a_1)\right)-H\left(\tilde{\xi}_1-(b_1+a_1)\right)\right)\int_{b_1-a_1}^{\tilde{x}_1}\mathrm{Im}\left(\Phi^{1,0}(\xi_1+i0)\right)d\xi_1\right]=P_x.$$

Because $\sigma(\zeta_1)$ and $\sigma_3(\zeta_1)$ are the entire functions, $\Phi^{1,0}(\zeta_1)$ is an analytic function everywhere in the cell of periodicity, except points $b_1-a_1,\ \ b_1+a_1,\ \ -b_1-a_1+ih_1,\ \ -b_1+a_1+ih_1$. In accordance to Cauchy's theorem the curvilinear integral alone a path Q (located in the upper half of the cell) vanishes (Fig. 3).

$$\int_Q\Phi^{1,0}(\zeta_1)d\zeta_1=\int_{-l_1}^{l_1}\Phi^{1,0}(\zeta_1)d\zeta_1+\int_{l_1}^{l_1+ih_1}\Phi^{1,0}(\zeta_1)d\zeta_1+\int_{l_1+ih_1}^{-l_1+ih_1}\Phi^{1,0}(\zeta_1)d\zeta_1+\int_{-l_1+ih_1}^{-l_1}\Phi^{1,0}(\zeta_1)d\zeta_1=0. \quad (66)$$

By the virtue of periodicity $\Phi^{1,0}(-l_1+i\eta_1)=\Phi^{1,0}(l_1+i\eta_1)$, thus

$$\begin{aligned}\int_{l_1}^{l_1+ih_1}\Phi^{1,0}(\zeta_1)d\zeta_1&=\int_0^{ih_1}\Phi^{1,0}(l_1+i\eta_1)id\eta_1\\&=\int_0^{ih_1}\Phi^{1,0}(-l_1+i\eta_1)id\eta_1\\&=-\int_{ih}^{0}\Phi^{1,0}(-l_1+i\eta_1)id\eta_1\\&=-\int_{-l_1+ih_1}^{-l_1}\Phi^{1,0}(\zeta_1)d\zeta_1.\end{aligned}$$

Hence the Eq. (66) takes the form

$$\int_{-l_1}^{l_1} \Phi^{1,0}(\zeta_1)d\zeta_1 + \int_{l_1+ih_1}^{-l_1+ih_1} \Phi^{1,0}(\zeta_1)d\zeta_1 = 0 \quad \text{or} \quad \int_{-l_1}^{l_1} \Phi^{1,0}(\zeta_1)d\zeta_1 = \int_{-l_1+ih_1}^{l_1+ih_1} \Phi^{1,0}(\zeta_1)d\zeta_1$$

In the same way one obtains

$$\int_{-l_1}^{l_1} \Phi^{1,0}(\zeta_1)d\zeta_1 = \int_{-l_1+\tilde{y}}^{l_1+\tilde{y}} \Phi^{1,0}(\zeta_1)d\zeta_1 \ for\, any \quad 0<\eta_1 <h_1. \tag{67}$$

By taking into account that $\Phi^{1,0}(\zeta_1) = U^{1,0}_{,\xi} - iU^{1,0}_{,\eta}$ and separating the real and imaginary parts in (67) one obtains

$$\int_{-l_1+\tilde{\eta}_1}^{l_1+\tilde{\eta}_1} \mathrm{Re}\Big(\Phi^{1,0}(\zeta_1)\Big)d\zeta_1 = \int_{-l_1}^{l_1} \mathrm{Re}\Big(\Phi^{1,0}(\xi_1 + i\tilde{\eta}_1)\Big)d\zeta_1 = \int_{-l_1}^{l_1} U^{1,0}_{,\xi} d\xi_1 = U^{1,0}\Big|_{-l_1}^{l_1} = const.$$

That means the elongation of any segment, which length equals to the length of cell and that is parallel to x-axis, is the same. Thus formula (53) is simplified

$$\varepsilon_{av} = \frac{1}{2l}\int_{-l}^{l} \varepsilon_x dx = \frac{1}{2l}\int_{-l_1}^{l_1} \mathrm{Re}\big(\Phi^{1,0}(\zeta_1)\big)d\xi_1. \tag{68}$$

And eventually one obtains

$$B_{eff} = B_1 \varepsilon^{1/4} q^{1/4} \frac{2l}{h} \frac{\int_0^{h_1} \mathrm{Re}\Big(\Phi^{1,0}(\zeta_1)\Big)d\eta_1 + \Big(H\big(\tilde{\xi}_1 - (b_1 - a_1)\big) - H\big(\tilde{\xi}_1 - (b_1 + a_1)\big)\Big)\int_{b_1-a_1}^{\tilde{\xi}_1} \mathrm{Im}\Big(\Phi^{1,0}(\zeta_1)\Big)d\xi_1}{\int_{-l_1}^{l_1} \mathrm{Re}\big(\Phi^{1,0}(\zeta_1)\big)d\xi_1}. \tag{69}$$

The dependency of point c_1 on offset of the middle of inclusions b_1 is shown below.

From the Fig. 4 one can see, that point c, where the shear stress on the inclusion changes sign, matches the middle point of inclusion b when $b = 0$ or $b = l/2$. For other values of b, point c and b vary, and this difference is growing, when height of the cell of double-periodicity is decreasing.

The layouts of inclusions for $b = 0$ and $b = l/2$ are symmetrical ones and shown below (Fig. 5).

The shear stress at adjacent to the top side of inclusion points of the plain is given by formula

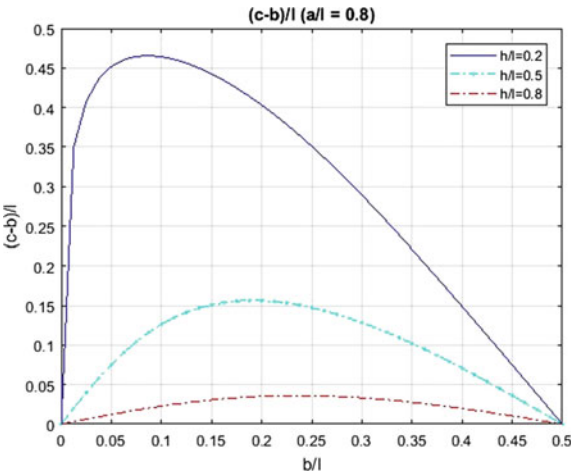

Fig. 4 Dependence of point c_1 on offset of the middle of inclusions b_1

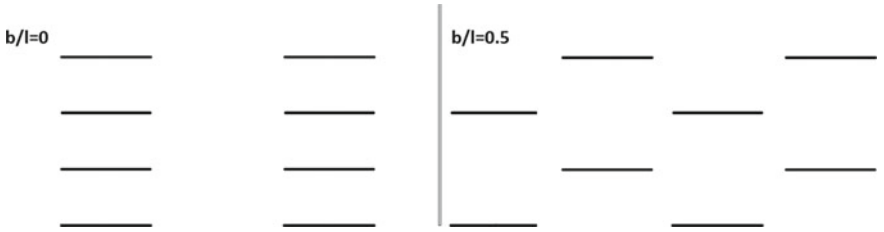

Fig. 5 Inclusions layout for two symmetrical cases

$$\tau_{xy}^{1.0+} = -G\mathrm{Im}\left(\frac{A\sigma(\xi_1 - c_1)\sigma_3(\xi_1 + c_1)}{\sqrt{\sigma(\xi_1 - (b_1 - a_1))\sigma(\xi_1 - (b_1 + a_1))\sigma_3(\xi_1 + (b_1 - a_1))\sigma_3(\xi_1 + (b_1 + a_1))}}\right), \tag{70}$$

where $b_1 - a_1 \le \xi_1 \le b_1 + a_1$.

Distribution of shear stresses and loads on the left half of the inclusion for these two cases with different values of a/l and h/l are shown below.

The distribution of dimensionless shear stress $\tau_{xy}^{+}/\sigma_{av}$ along the left-hand side of inclusion is shown on Fig. 6, while the distribution of dimensionless loads T_x/P_x is shown on Fig. 7. The left-hand graphs are built for short inclusions $(a/l = 0.2)$, which are small compared to the length of the cell. The middle graphs are depicted for $a/l = 0.5$, and right-hand graphs are built for $a/l = 0.8$. In case of short inclusions, one can see that for relatively high cell $(h/l = 0.5)$ shear stresses and loads do not depend on the position of inclusions in the cell. Graphs for $b/l = 0$ and $b/l = 0.5$ are virtually identical: the interaction of elements of doubly-periodic lattice is negligible. However, for $h/l = 0.1$ this dependence is obvious: load in the middle of inclusion for $b/l = 0.5$ is about 30% more than the corresponding loads for $b/l = 0$. That

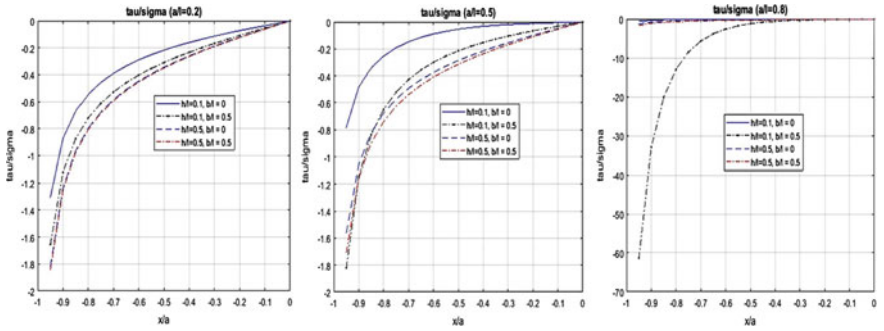

Fig. 6 Distribution of shear stresses on the left half of the inclusion

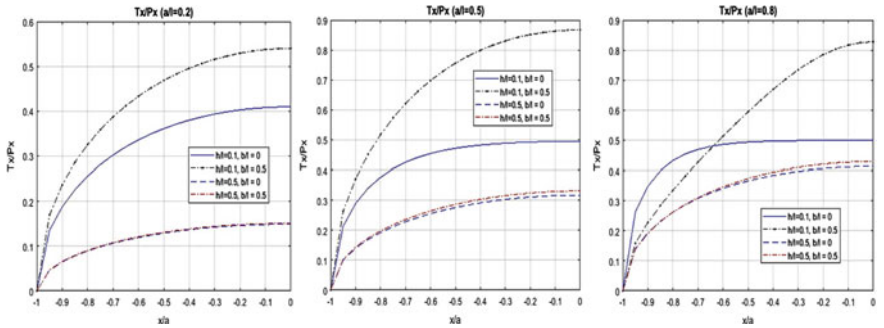

Fig. 7 Distribution of loads on the left half of the inclusion

is due to fact that the distance between the inclusions in a column in the first case is twice as large as in the second one.

If the length of the inclusion is the half of cell's length, the difference between curves $b/l = 0$ and $b/l = 0.5$ is large enough for all values of the parameter h/l. If $b/l = 0$, T_x/P_x reaches half of the load applied to the cell in a considerable part of inclusion. While for $b/l = 0.5$, load in inclusion T_x/P_x reaches almost to 0.9 of such load, although only in central part of inclusion.

When $a/l = 0.8$ (right-hand graphs) shear stresses are very small almost everywhere at the central part of inclusion. An exception is the case $h/l = 0.1, b/l = 0.5$, where shear stresses are large. The difference is due to the fact that for low cell and long inclusions the strong interaction appears between inclusions of neighboring "columns", and, as a consequence, there are additional shear stresses. The load in this case grows until almost the middle of inclusion. The greatest value of the loads is lesser, then for $a/l = 0.5$ because the distance (along the y - axis) between the inclusions of neighboring columns is half the distance between the elements in the same column. For other cases loads are basically no different from the middle graph.

Thus, in the case of $b/l = 0.5$ the reinforcing elements are loaded more than in case $b/l = 0$. This suggests that effective stiffness for $b/l = 0.5$ is more than for

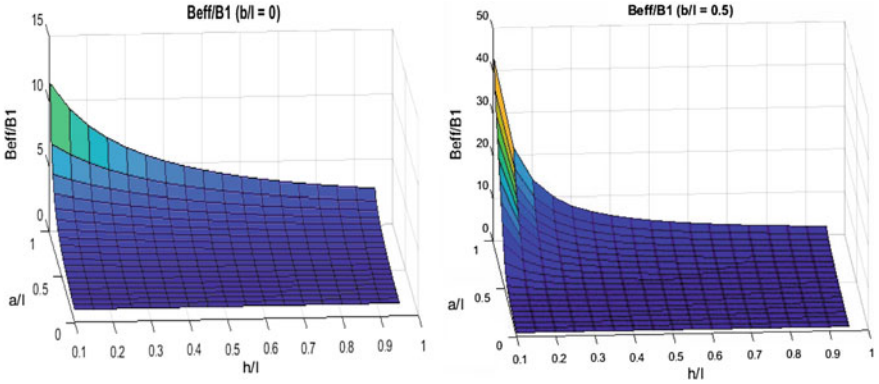

Fig. 8 Dependence of B_{eff}/B_1 on h/l and a/l

$b/l = 0$. This expectation is confirmed by the results of the calculation by formula (69). The effective stiffness for these two cases was computed for isotropic material with Poisson's ratio equals 0.3.

One can see from Fig. 8 that for $b/l = 0.5$ the stiffness is about 4 times greater than for $b/l = 0$.

The reason is that for $b/l = 0$ there are vertical "columns" in the plane which do not contain any inclusion, and where almost all deformation occurs. On the contrary for $b/l = 0.5$ such "columns" do not exist (for $a/l > 0.5$) and instead of stretching deformation the shear strain occurs between the closely spaced inclusions.

3 Conclusion

The problem of extension of an elastic orthotropic plane enforced by a doubly periodic lattice of one-dimensional inextensible inclusions is investigated. An approximate solution to the problem is obtained by employing the asymptotic method, specially tailored for orthotropic plane, Weierstrass elliptic functions and Keldysh-Sedov formula to solve boundary value problem for analytic functions.

The closed form formulae for the shear stresses and the effective tensile modulus of the reinforced plane are presented. It is shown that the error of an approximate solution does not exceed 9% in the worst, from the point of view of method, case of isotropy. The use a Keldysh-Sedov formula provided the solution of the problem without assumptions about the behavior of solutions at the vertical boundaries of cell. In addition, let us mention, that the solution is suitable not only for the rectangular cell of periodicity, but for the cell having the form of a parallelogram as well.

References

1. Argatov, I.I.: Extension of an elastic space with a rigid bar. J. Appl. Mech. Tech. Phys. **49**(1), 98–104 (2008)
2. Nikishkov, G.P., Cherepanov, G.P.: Extension of an elastic space with an isolated stiff rod. J. Appl. Math. Mech. **48**(3), 332–335 (1984)
3. Grilitskii, D.V., Sulim, G.T.: Periodic problem for an elastic plane with thin-walled inclusions. J. Appl. Math. Mech. **39**(3), 520–529 (1975)
4. Grilitskii, D.V., Evtushenko, A.A., Sulim, G.T.: Stress distribution in a strip with a thin elastic inclusion. J. Appl. Math. Mech. **43**(3), 542–549 (1979)
5. Koblik, S.G.: Stretching of elastic orthotropic plane reinforces by the lattice of inextensible inclusions. Mech. Solids 22(4) (1987)
6. Grigolyuk, E.I., Filshtinsky, L.A.: Perforated Plates and Shells. Nauka (1970) (in Russian)
7. Grigolyuk, E.I., Filshtinsky, L.A.: Regular Piecewise Homogeneous Structures with Defects. PhysMatGiz (1994). (in Russian)
8. Bardzokas, D.I., Filshtinsky, M.L., Filshtinsky, L.A.: Mathematical Methods in Electro-Magneto-elasticity. Springer, Berlin (2007)
9. Xiao, J., Jiang, C.P.: Exact solution for orthotropic materials weakened by doubly periodic cracks of unequal size under antiplane shear. Acta Mech. Solida Sin. **22**(1), 53–63 (2009)
10. Manevitch, L.I., Pavlenko, A.V., Shamrovskii, A.D.: Application of the group theory methods to the dynamical problems for orthotropic plates. In: Trudy 7 Vsesoyuznoi Conference po Plastinam i Obolochkam (Proceedings of the 7th All-Union Conference on Plates and Shells). Dnepropetrovsk (1969). Nauka, pp. 408–412 (1970) (in Russian)
11. Manevitch, L.I., Pavlenko, A.V., Koblik, S.G.: Asymptotic Methods in Theory of Elasticity of Orthotropic Solid. Vyshcha Shkola (1982) (in Russian)
12. Manevitch, L.I., Gendelman, O.V.: Tractable Models of Solid Mechanics. Springer, Berlin (2011)
13. Muskhelishvili, N.I.: Some Basic Problems of the Mathematical Theory of Elasticity. Springer, Berlin (1977)
14. Sedov, L.I.: Two-Dimensional Problems in Hydrodynamics and Aerodynamics. Interscience (1965)

Features of Deformation of Smooth and Stringer Cylindrical Shells at Axial Compression and Statistical Properties of Their Critical Loads

Vasiliy L. Krasovsky

Abstract Three sets of thin cylindrical shells have been tested: smooth cylinders and shells stiffened by outside and inside stringers. All specimens were of relatively high quality and manufactured with using identical technologies. Statistical properties of the obtained experimental critical loads have been analyzed. Buckling loads of smooth cylinders had significantly higher dispersion compared to reinforced shells. The important role of nonlinear pre-buckling deformation and local shell skin buckling between stringers was observed in the experiment.

1 Introduction and Statement of the Problem

It is known that experimental data on load-carrying capacity of axially compressed smooth isotropic circular thin-walled cylinders are characterized by significant dispersion and uncertainty. It is due to extremely high sensitivity of buckling parameters of such shells to intensity of various, as a rule, revolting technological factors and, first of all, to small initial geometrical imperfections of the shell middle surface. Usually, the initial imperfections are randomly and non-uniformly distributed across the shell surface and hardly controllable. It is obvious that there is a necessity of studying statistical properties of shell buckling loads at the analysis of experimental data and estimation of design buckling loads.

Researches in this direction for smooth cylinders were carried out since setting the problem (see, e.g., review by Grigolyuk and Kabanov [2]) and were being conducted with various intensity (in the process of accumulation of experimental data) until present time. Essential results have been obtained in the sixtieth-seventieth years of the last century when there were conditions and opportunities of carrying out massive experiments [8, 11]. Several hundred specimens of smooth thin cylindrical shells with different nominal sizes were tested by Manevitch and Prokopalo [8]. Statistical analysis of the obtained results has been performed, with emphasis on the

V. L. Krasovsky (✉)
Pridneprovskaja State Academy of Civil Engineering and Architecture, Dnipro, Ukraine
e-mail: stmehanika@gmail.com

I. V. Andrianov et al. (eds.), *Problems of Nonlinear Mechanics and Physics of Materials*, Advanced Structured Materials 94,
https://doi.org/10.1007/978-3-319-92234-8_22

effect of radius to shell thickness ratio. We believe that the obtained results are still valuable for practical engineering design of the structures.

At the same time, for the stiffened shells, despite their wider practical applications, statistical properties of buckling loads are studied much less [1]. It was caused not only by higher complexity and cost of the experimental research, but also due to essential increase of number of geometrical and stiffness structure parameters which can affect disorder in experimental data analysis. Nevertheless, it is considered conventionally, that the dispersion of buckling loads of the stiffened shells is less, than that of smooth ones. In addition, there are various design features of stiffened cylinders that, basically, are not casual and give the possibility to be controlled. Unfortunately, till now there are not enough experimental buckling load data of homogeneous samples with the same nominal parameters of stiffened shells even for certain limited classes. Lack of experimental data leads to necessity to unite results of diverse tests in one general set [7] in the analysis. Thus some design features, in particular, omitted in the analysis, can cause wrongfully wide scatter of buckling load values of the stiffened cylinders [7].

Let us note one more important feature of the stiffened shells, connected with the statistical analysis of buckling loads. Presence of reinforcements essentially complicates the behavior of shells at loading and buckling process. Thus, smooth cylinder buckling load is associated usually with its load-carrying ability which in diverse tests is determined simply enough. However, in case of the stiffened shells there are several critical points and, in particular, the general buckling load can differ from limit one [9]. It leads to ambiguity in choosing of buckling criteria in various experiments. Besides, in connection with various practical operational requirements, statistical properties of not only load-carrying ability of a shell are of interest, but also properties of loads corresponding to other critical conditions, for example, to local buckling of a shell skin between stringers. It specifies necessity of our research of the shell behavior at all stages of its deformation down to destruction, at carrying out of the statistical analysis of critical loads.

In the present chapter results of experimental study of behavior and buckling features are brought and discussed, as well as statistical analysis of buckling loads of axially-stiffened and unstiffened circular cylindrical shells subject to axial compression is provided. Researches were carried out on small-size specimens. The specifics of the experiments are in the following: (1) all shells (stiffened and unstiffened) had the identical nominal sizes (radius, length and thickness); (2) they were made of the same material using uniform technology; and (3) they were tested in laboratory conditions (there were no external influences) using uniform technique and requirements to supervision and measurements. It allowed leading the comparative analysis of statistical characteristics of critical loads of the smooth and stiffened cylinders which dispersion has been caused, as a matter of fact, only by casual technological factors, basically, by initial geometrical imperfections.

2 Specimens and Technique of the Experiment

The specimens were grouped in three sets: Set 1—smooth cylinders (10 samples), Sets 2 and 3—shells with inside and outside reinforcement by stringers, accordingly (five identical samples in each set). Samples had the following dimensions: internal diameter—$2R = 171.6$ mm, thickness—$h = 0.19$ mm, length—$L = 172$ mm ($R/h = 450$, $L/R = 2$). Each stiffened shell was equipped with 24 identical equidistant thin-walled stringers of angular profile with dimensions: $4.0 \times 4.3 \times 0.34$ mm.

Shells were made from sheet of cold-rolled stainless steel X18H9H (the elasticity modulus—$E = 191$ GPa, conditional yield stress—$\sigma_{02} = 800$ MPa, Poisson's ratio—$\nu = 0.3$) by spot welding with one longitudinal lapped seam (with two welding rows). The width of the lapped seam was 2% of the shell perimeter. The high value of conditional yield stress of the material eliminated the plasticity effects not only at pre-buckling stages, but also at the stage of initial post-buckling deformation. Stringers were made from preliminary cut strips of the same steel sheet (thickness—0.34 mm) by rolling on multilane rolling appliance and welded to a shell by one row spots (welding on the narrow side of the stringer).

Before installation to the testing machine, the shells were equipped with special face test adaptations consisting of flat rigid discs, carrying out the transfer of the load from compression machine to the end faces of the sample, and directing disks which aligned a specimen in adaptations and retained circular form at the shell edges. Directing disks for testing of unstiffened shells had conic surface with the maximal diameter corresponding to internal diameter of the shell. Disks with special cuttings for internal stringers (in the form of a cogwheel) [9] were used while testing stiffened shells. Diameter of these disks was a little bit less than that of the disk for smooth cylinders. The disks had identical thickness equal to 8 mm.

Preliminary, to maintain identical boundary conditions (close to free support) at different types of reinforcements, edges of walls of the stringers of all shells were cut under corner of 12°–15° to plane of the end face [9]. For elimination of the load eccentricity with respect to a "neutral" surface (various at internal and external reinforcements), compensating basic overlays were welded to the shell skin at the stringer side. First, intermediate overlays were installed on the shell skin between stringers (see Fig. 1.) They had the following dimensions: length 17 mm, width 8 mm, and thickness 0.34 mm. Edges of these overlays coincided with the shell edges. Then through intermediate overlays and shelves of the stringers basic overlays (length 20 mm, width 10 mm, and thickness 0.49 mm) were welded. They acted on 1.0–1.5 mm above the plane of shell face section.

Uniformity of the load distribution on perimeter was reached by careful grinding in of shell edges (all over again smooth, and then equipped by overlays) using abrasive plates. After grinding in, the overlays edges were sharpened up to a level of 0.35 mm on thickness (Fig. 1). In this case load transfer to the shells through the overlays provided practically identical loading conditions of the samples with internal and external stringers. Centering steel balls between test adaptations and compression

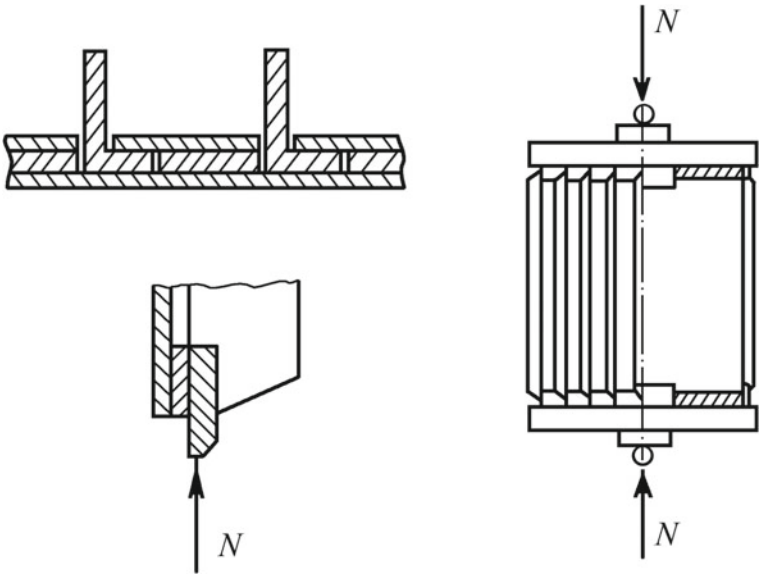

Fig. 1 The scheme of loading transfer on the stringer shell

machine plates were used for elimination of loading eccentricity with respect to the shell axis (Fig. 1).

The compressing force was created by the universal testing machine of mechanical type with rigidity of 66.2 kN/mm. The machine allowed to carry out kinematic loading (displacement was set) with various constant speeds. All samples have been tested at speed of 0.05 mm/min. During loading, the diagram "load (N)—displacement of press plates (ΔL)" was registered for all shells. Radial displacements of three shells of each set (at all stages of deformation, down to destruction) were measured in zones of maximal initial deflections.

The accepted manufacturing technique of smooth shells and technique of their preparation for testing provided:

(1) deviation of internal diameter within shell thickness h;
(2) deviation of the shell thickness from nominal not more than 0.02 h;
(3) deviation of a surface of end faces from a plane no more than 10 microns (the maximal amplitudes corresponded to the 2–4 t harmonics of decomposition of deviation function in a trigonometric series);
(4) non-perpendicularity of end face planes with respect to shell axis not more than 1°;
(5) non-parallelism of these planes did not exceed 2°.

Deviations of middle surface of the smooth shells from a perfect cylinder (were determined after assembly of the shells with face adaptations) were as follows:

(1) conicity (no more 0.5°);

(2) local (in the area of a welded seam) and the general (ovalization) deviations of the cylinder from a circular one (no more 2.0 h);
(3) casual local dents and bulges (curvature in longitudinal direction and cross-section curvature change).

The maximal amplitude of last kind of imperfection was marked in a zone of welding lapped seam and was up to 2.0 h. As a rule, first harmonic prevailed in decomposition of the deviation function in trigonometric series. The imperfection amplitude on another part of surface of the shells did not exceed 0.5 h.

Equipment of shells by stringers and overlays led to change of a picture of initial deflections. In circumferential direction, the initial deflection harmonic corresponding to number of stringers was observed at all samples. In a stringer zone the deflection has been directed inside of the shell, in the middle part of the panel - outside. The amplitude of this harmonic is insignificant—up to (0.15–0.2) h, however large deflection amplitude values were observed on the shells with internal stringers. Casual deviations from the circular shape were characterized by small change in circumferential direction with rather essential amplitudes—(2, 3) h. In the longitudinal direction, practically on all shells, deflections (directed to the center of curvature and almost asymmetrical) were marked at the edge of the structure. They connected, apparently, with presence of regional overlays. These longitudinal curvature changes have caused deflections in the majority of shell cross sections. These deflections can be precisely expressed by harmonics with three half waves on the shell length. Corresponding maximal deflection amplitude of some samples reached thickness of a shell. Other initial deflection components, specific for all or majority of the shells were not revealed. On the most part of a shell surface casual, local dents and gouges with the maximal depth which is not exceeded (0.7–0.9) h in the middle part of panels and with depth about (0.5–0.7) h near stringers were marked. In zones of welding lapped seam, similar to smooth shells, the initial deflection amplitude increased up to 2 h (corresponding, as a rule, to the first and third harmonics). Typical diagrams of initial deflections of stiffened shells are shown in Fig. 2. Initial deflections (w_0) toward the center of shell curvature are accepted as negative.

Samples which quality did not satisfy the conditions above were rejected. In total, it has been rejected three smooth samples and one shell with an external reinforcement. Presence of a large dent (with one half wave in the longitudinal direction) in a zone of welding lapped seam was a main cause of the rejection in all cases.

3 Test Results

3.1 Smooth Shells

During the pre-buckling deformation of smooth shells, the development of initial imperfections, which played a main role at definition of critical conditions, was observed. Load-carrying capacity of these shells was determined by loads corre-

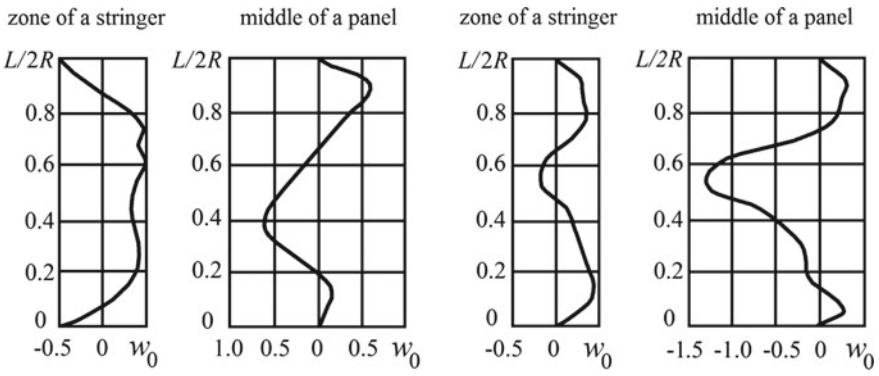

Fig. 2 Imperfections in longitudinal direction in stiffened shells ($\overline{w}_0 = w_0/h$)

Table 1 Smooth shell test results (Set 1)

No.	N^{cr} (kN)	σ^{cr} (MPa)	$\overline{\sigma}^{cr}$
1	15.4	148	0.578
2	13.8	133	0.52
3	17.4	167	0.652
4	18.1	174	0.68
5	12.0/13.3	115/128	0.449/0.500
6	14.4	138	0.539
7	16	154	0.602
8	13.0/13.2	125/127	0.488/0,496
9	15.6	150	0.586
10	14.9	143	0.559

sponding to general loss of stability, which occurred, basically, in two ways [3, 4]. The first way was realized in the form of continuous process of the general wave formation during fraction of a second, accompanied by a sharp clap and significant reduction of carrying ability of a shell. Thus the surface of the cylinder became covered by characteristic diamond-like dents located in two-three rows, covering (60–80)% of its perimeter (see a photo in Fig. 5a). The amount of dents (at the rate of their formations on all perimeter) was 8–10. The described process of the general buckling has been recorded at tests of 8 samples. Buckling of two shells occurred stage by stage as transition through stable post-buckling configuration with just one local dent. On both shells post-buckling dent was formed by a soft clap as a result of development of initial deflection in the field of a welding lapped seam. The further loading of these shells led to the general buckling which occurred at so called maximal local critical load [10]. Values of critical loads (N^{cr}) of the shells of a series 1 are resulted in Table 1.

In the same row of the table corresponding values of absolute (σ^{cr}) and relative ($\overline{\sigma}^{cr}$) critical stresses are presented. Here $\overline{\sigma}^{cr} = \sigma^{cr}/\sigma^{cl}$, σ^{cl} is classical value of critical stress of thin isotropic elastic cylinder at axial compression

$$\sigma^{cl} = \frac{Eh}{R\sqrt{3(1-\nu^2)}}, \text{ at } \nu = 0.3, \ \sigma^{cl} = 0.605\frac{Eh}{R}$$

For shells with number 5 and 8 critical parameters resulted in the numerator correspond to local and in the denominator to the general buckling. Note that tested smooth shells are the structures of average quality according to the classification of shell quality [5].

3.2 Stringer-Stiffened Shells

The behavior of the stiffened shells was determined, basically, by character of an arrangement of stringers, their stiffness parameters and intensity of initial imperfections. Typical deformation diagrams "$N - \Delta L$" of these shells are presented in Fig. 3.

On the diagrams some characteristic points, and also number of the formed dents of the general loss of stability (n_r) are specified. A concentrated force at the center of the top end plate was applied by testing machine by means of loading screw and a ball bearing in a hemispherical cup seated on top plate. Diagrams were plotted by points with step of moving plates, equaled to 0.025 mm. Load change within each step was accepted as linear on the diagram. We have to mention, that ΔL represents relative displacement of press plates of the test machine, instead of displacement of end plates which value will be a little bit less, because of presence of elastic elements (aligning spherical balls and loading adaptations) in the loading chain.

Dependence "$N - \Delta L$" was strictly linear at the initial stage of loading. On samples with an identical arrangement of shell edges, intensity of relative shortening of shells $\Delta L/L$ was practically identical, and at an external reinforcement it was greater about (13–15)%, than that at internal one. During this part of loading, the first dents of local buckling between stringers are formed (as a rule, by a soft clap). Corresponding load values (N^{m1}), depend on character and intensity of initial deflections and essentially differed for various shells. We have to note that formation of the first local dents did not influence the slope of a straight line of the diagram "$N - \Delta L$".

At the certain level of load, the process of intensive local wave formation began which was reflected in the diagram of deformation in the form of a break (see diagrams in Fig. 3). These loads were accepted as loads of skin buckling between stringers (N^m). Values N^{m1} and N^m, corresponding average critical stress (σ^{m1} and σ^m) as well as ratios $\overline{\sigma}^{m1} = \sigma^{m1}/\sigma^{cl}$ and $\overline{\sigma}^m = \sigma^m/\sigma^{cl}$ for shells with internal and external reinforcement, are resulted in Tables 2 and 3.

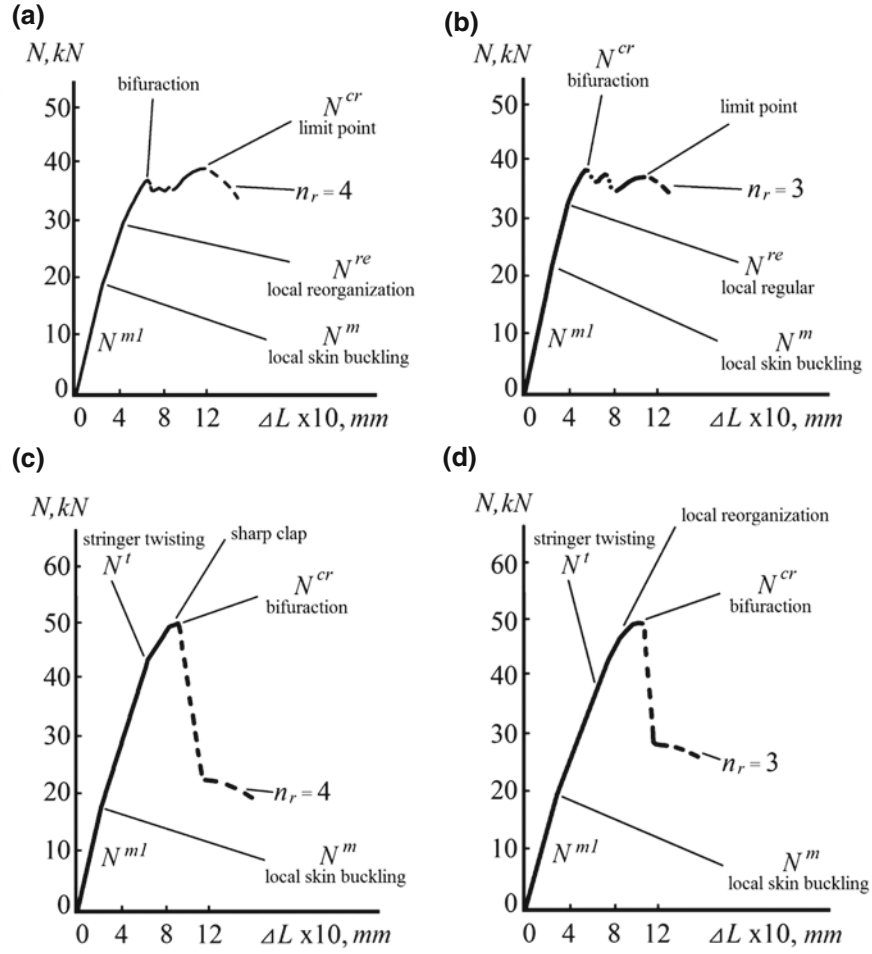

Fig. 3 Deformation diagrams of stiffened shells (**a**, **b** - internal; **c**, **d** - external stringers)

Formation of dents (skin buckling) occurred by claps at load value N^m. It was marked insignificant (0.1–0.3 kN) decrease in load (in case of continuous record of the diagram "$N - \Delta L$" this part of it would represent "serrati form" dependence). During the further loading the dependences "$N - \Delta L$" remained practically linear and characteristics of longitudinal deformation $E\Delta L/\sigma L$ of shells with internal and external reinforcement were equalized. As a result of the process of "rough" wave formation of the shell skin, the local post-buckling configuration with an arrangement of dents in the "chess" order was formed. The number of dents along the length of the panel (3, 4) of shells with external stringers, as a rule, was more, than that of samples with an internal reinforcement (2, 3).

Table 2 Shells with internal reinforcement test results

No.	1	2	3	4	5
N^{m1} (kN)	11.4	07.8	09.5	17.8	12.0
σ^{m1} (MPa)	66.4	45.4	55.3	104	67.8
$\overline{\sigma}^{m1}$	0.259	0.177	0.216	0.406	0.265
N^{m} (kN)	20.8	22.5	21.5	23.2	22.5
σ^{m} (MPa)	121	131	125	135	131
$\overline{\sigma}^{m}$	0.473	0.512	0.488	0.528	0.512
N^{re} (kN)	29.5	32.5	31.5	32.5	31.5
σ^{re} (MPa)	172	189	183	189	183
$\overline{\sigma}^{re}$	0.673	0.738	0.715	0.738	0.715
N^{cr} (kN)	37.8	36.7	37.4	39.0	37.1
σ^{cr} (MPa)	220	214	218	227	216
$\overline{\sigma}^{cr}$	0.859	0.836	0.852	0.887	0.844

Table 3 Shells with external reinforcement test results

No	1	2	3	4	5
N^{m1} (kN)	8.4	12.2	11.9	14.0	07.5
σ^{m1} (MPa)	48.9	71.0	69.3	81.5	43.7
$\overline{\sigma}^{m1}$	0.191	0.278	0.270	0.320	0.172
N^{m} (kN)	17.0	19.2	17.0	18.1	18.7
σ^{m} (MPa)	99	112	99	105	109
$\overline{\sigma}^{m}$	0.387	0.438	0.387	0.410	0.425
N^{t} (kN)	42.5	38.5	37.5	38.5	41.5
σ^{t} (MPa)	248	224	218	224	242
$\overline{\sigma}^{t}$	0.969	0.875	0.852	0.875	0.945
N^{cr} (kN)	50.0	48.6	50.6	51.8	47.4
σ^{cr} (MPa)	291	283	295	302	276
$\overline{\sigma}^{cr}$	1.137	1.105	1.152	1.180	1.078

The shape of the panel at local skin buckling with external stringers (on distance of 3 mm from a stringer) is resulted in Fig. 4 (left). From the figure it is visible that amplitude of internal deflections considerably (6–7 times) exceeds amplitude of external deflections. Character of local post-buckling waves practically was not connected with the initial deflections. Local dents intensively developed at increasing load. In Fig. 4 (right) load-deflection dependence at the center of a local dent located at 3 mm from a stringer is resulted.

At certain load in shells with internal reinforcement a reorganization of the local form was marked (for three shells). It occurred dynamically at certain value N^{re} by one clap with increase in number of dents at panels from two to three.

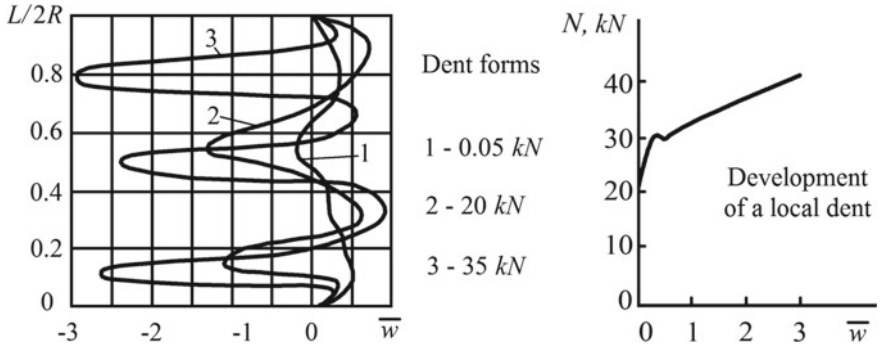

Fig. 4 The form and development of local configurations

This reorganization led to a new break in the diagram "$N - \Delta L$" (Fig. 3a). On two shells approximately at the same load, regular local post-buckling configurations were finally issued, which also was reflected by a break on "$N - \Delta L$" diagram (Fig. 3b). Reorganization of a local post-buckling configuration of shells with external reinforcement has been noted only for one specimen (the pattern with 3 dents was replaced by a pattern with 4 dents). It was happened at the load value close to the limit one (Fig. 3d). At the same time for shells with external reinforcement, development of the local shape led to clear twisting of stringers. The beginning of development of this process coincided with formation of regular local post-buckling configurations and also was reflected at the diagram "$N - \Delta L$" by a break (Fig. 3c, d).

After formation of regular local post-buckling configurations and beginning of the process of stringer twisting, the load-displacement dependence became nonlinear. Character of this dependence essentially depends on arrangement of the reinforcement. On shells with external stringers at the load about (98–99)% of general buckling critical load (N^{cr}), dents started increasing sharply. That was visually observed as a turn (skew) of their horizontal diagonals (Fig. 3c). The general loss of stability of shells with an external reinforcement was accompanied by sharp clap and "folding" of walls of stringers [9]. Thus there were formed 3–4 large global dents (with one half wave on shell length), each of which in the circumferential direction involved four stringers (see Fig. 5d). The load during this clap sharply decreased. The further loading of the shells led to development of global dents and smooth decrease of the load caused by plastic deformations. Let us note that the shell capacity level in post-buckling stages (N^z), depended on number of formed dents, and their concrete number were rather stable (at $n_r = 3$ and 4 accordingly $N^z = 27.5$ and 20.5 kN) (Fig. 3c, d).

The clap has been poorly expressed at loss of stability of the shells with internal stringers. The beginning of the general wave formation (bifurcation) of two shells did not coincide with a maximum load (Fig. 3a). Two and four waves covering 3–4 stringers were softly formed. The load decreased by (4–6) %. Dents developed at further loading, and their amplitude was defined, basically, by level of applied load

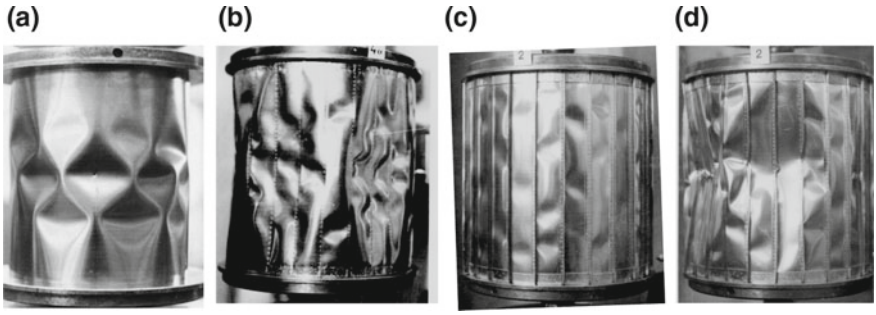

Fig. 5 Buckling forms of smooth (**a**) and stiffened shells (**b**—internal; **c**, **d**—external stringers)

and did not depend on the limit one (N^{cr}). Loss of load-carrying capacity of these shells occurred smoothly during development and formation of new dents and the beginning of plastic deformation. Values of maximum load were close to bifurcation one (difference did not exceed 2%). Maximum loads for three shells coincided with their bifurcation loads (Fig. 3b). Initial post-buckling deformation of these samples did not differ from that described earlier. The form of the general loss of stability is resulted in Fig. 5b.

Values of the general buckling load for the stiffened shells (for two samples with internal stringers) are presented in Tables 2 and 3 (maximum load values (N^{cr}, Fig. 3a), average stresses (σ^{cr}), and also relative stresses $\overline{\sigma}^{cr}$). In Table 2 the buckling parameters corresponding to reorganization or formation of regular local post-buckling configurations (N^{re}, σ^{re}, $\overline{\sigma}^{re}$) are given. In addition, in Table 3 values corresponding to twisting of stringers (N^{t}, σ^{t}, $\overline{\sigma}^{t}$) are represented.

4 Discussion of the Results

One can see from Tables 1, 2, 3, that buckling of all the shells occurred in elastic stage of deformation, because membrane stresses, corresponding to maximum loads, for smooth samples did not exceed 23% and for stiffened shells—38% of the value of the elastic limit of the shell material.

For all considered above shells the statistical characteristics of relative critical parameters are resulted in the Table 4: average values ($\sigma*$), root-mean-square deviations (S) and variation factors ($V=3S/\sigma* \times 100\%$), defining confidence interval of parameters with probability confidence level 0.997. For smooth shells (Set 1) data concerning buckling (general or local) had been incorporated by the parameter $\bar{\sigma}^{cr}$, parameter $\bar{\sigma}^{lim}$ corresponds to data concerning load-carrying capacity of the shells.

Let us lead the analysis of the obtained data without considering comparison of experimental and theoretical results. First of all, we shall note that stringer equipment

Table 4 Statistical properties of critical loads

Sets	Parameters	$\sigma*$	S	V (%)
Set 1	$\overline{\sigma}^{cr}$	0.556	0.0702	37.2
	$\overline{\sigma}^{lim}$	**0.572**	**0.0604**	**31.7**
Set 2	$\overline{\sigma}^{m1}$	0.265	0.0867	98.1
	$\overline{\sigma}^{m}$	0.503	0.0217	13.0
	$\overline{\sigma}^{re}$	0.716	0.0269	11.2
	$\overline{\sigma}^{cr}$	**0.856**	**0.0202**	**7.08**
Set 3	$\overline{\sigma}^{m1}$	0.426	0.0624	76.1
	$\overline{\sigma}^{m}$	0.401	0.0227	16.7
	$\overline{\sigma}^{t}$	0.903	0.0396	13.2
	$\overline{\sigma}^{cr}$	**1.130**	**0.0399**	**10.6**

of the shells and regional overlays has led to significant growth (compared to smooth shells) of the stresses corresponding to maximum loads, and also to the essential statistical stabilization of buckling load values. Indeed, average values σ^{cr} at internal reinforcement have increased by 1.5 times, at external—by 2.3 times. Carrying load-capacity of shells has increased accordingly by 2.47 and 3.26 times. Exclusively small variation of maximum loads of shells with an internal reinforcement ($V = 7.08\%$) is observed. The variation of carrying load-capacity at the external reinforcement has appeared a little bit greater ($V = 10.6\%$), however, in comparison with smooth shells ($V = 31.7\%$), it is possible to consider it much less significant. High enough stability is a characteristic also for the parameters corresponding to critical points which were reflected in diagrams "$N - \Delta L$" in form of breaks or changes in its character ($\overline{\sigma}^{m}, \overline{\sigma}^{re}, \overline{\sigma}^{t}$). At the same time extremely wide scatter of values was noted for stress $\overline{\sigma}^{m1}$ (for shells with internal reinforcement $V = 98.1\%$, with external $V = 76.1\%$).

Let us notice that this fact is rather indicative. The integrated characteristic of initial imperfection intensity which can be indirectly estimated by parameter $E\Delta L/\sigma L$, was approximately identical for all samples of each shell set (at much higher level of geometrical imperfection intensity of stiffened shells). At the same time at any distribution of initial geometrical imperfection on a surface of a shell its local characteristics on various shells of one set can significantly differ. It is obvious, that local imperfection fluctuations are capable to change essentially the local critical parameters (for example, critical stress σ^{m1}). However, much less significant influence on integrated critical characteristics was observed. First of all, it is related to stresses of general buckling, and also to stresses corresponding to critical points which change character of dependence "$N - \Delta L$". In this connection the wide scatter of values $\overline{\sigma}^{lim}$ is an evidence that the process of the general smooth shell buckling has the local nature [3].

Let us consider the influence of some design shell features on its critical parameters. First, the effect of stringer eccentricity sign was statistically confirmed for the tested samples. The influence of arrangement of stringers on behavior of shells and

value σ^{cr} is well studied, and data obtained in this work concerning σ^{cr} do not contradict with obtained before results. Rather significant difference between σ^{m} for shells with external and internal stringers can be explained by character of pre-buckling behavior of these shells [6] and also by technology of their manufacturing.

Increase in capability of stiffened shells is caused not only by longitudinal reinforcement, but also by the boundary constraint on longitudinal displacement and on turn angle at shell edges (due to the end plates). Test results for three pairs of shells (with an internal and external reinforcement) which differed from samples of Sets 2 and 3, as a matter of fact, only by absence of additional boundary restrictions are resulted by Manevich et al. [9]. Behavior character and destruction of these shells practically did not differ from considered above, except for one feature connected with general buckling of samples with an internal reinforcement: maximum loads at these shells exceeded (8% in average) load values of the general buckling. Variation factors of capability and bifurcation loads at an external and internal reinforcement were approximately identical and made of (20–25)%. Average values σ^{cr} were less, than that of shells with our boundary conditions, by about 17% in case of internal reinforcement and 14% in case of external one.

Basing on the provided comparison, it is possible to assume, that the additional controllable design features influencing the pre-bucking deformation and the value of general buckling load promote, as a rule, statistical stabilization of shell capability. This can be explained by the following. The influence of controllable shell inhomogeneity caused by reinforcement, usually dominate over uncontrolled technological imperfections. It leads to decrease of the role of uncontrolled factors in the mechanism of buckling and as a consequence, reduces dispersion of critical loads of stringer shells.

References

1. Amiro I.Ya., Zarutskii V.A.: Statics, dynamics, and stability of stiffened shells. Itogi nauki i tekhniki. VINITI, 21, 132–191 (1990) (in Russian)
2. Grigolyuk, E.I., Kabanov, V.V.: Stability of Shells. Nauka, Moscow (1978) (in Russian)
3. Krasovsky, V.L.: Features of buckling process of real cylindrical shells under axial compression. Tezisy dokladov V Vsesoyuznoy konferencii po problemam ustoychivosti v stroitel'noy mekhanike, Moscow, pp. 142–143 (1977) (in Russian)
4. Krasovsky, V.L.: Behavior and stability of compressed thin cylindrical shells with local imperfections. Trudy XV Vsesoyuznoy konferencii po teorii obolochek i plastin, Kazan',pp. 303–308 (1990) (in Russian)
5. Krasovsky V.L.: Experimental investigation of buckling of compressed cylindrical shells (quality of shells and mechanisms of buckling). In: Static, Dynamics and Stability of Structures, Poland, Lodz, vol. 2, pp. 447–476 (2012)
6. Krasovsky V.L., Kostirko V.V.: Prebuckling deforming of shells stiffened with stringers at axial compression. In: Proceedings of 15th Canadian Congress on Applied Mechanics, Canada, Victoria, British Columbia, vol. 1, pp. 288–289 (1995)
7. Lipovskiy, D.E., Altukher, G.M., Koc, V.M., Nazarov, V.A., Todchuk, V.A., Shun, V.M.: Statistical estimation of influence of random perturbations on stability of reinforced shell based on

experimental research. In: Raschet prostranstvennyh konstrukciy, Moscow, vol.17, pp. 32–44 (1977) (in Russian)
8. Manevitch, L.I., Prokopalo, E. F.: Statistical properties of load-carrying capacity of smooth cylindrical shells. Problemy nadezhnosti v stroitel'noy mekhanike. In: Materialy II Vsesoyuznoy konferecii po problemam nadezhnosti v stroitel'noy mekhanike, Vil'nyus, pp. 182–187 (1968) (in Russian)
9. Manevich, A.I, Demeshko, M.A., Krasovsky, V.L., Kucherenko, V.M.: Experimental investigation of buckling of longitudinally stiffened cylindrical shells under axial compression. In: Raschet prostranstvennyh konstrukciy, Moscow, vol. 14, pp. 87–102 (1971) (in Russian)
10. Vladimirov, S., Konoch, V., Mossakovskii, V.: Experimental investigation of local stability of a cylindrical shell under axial compression. Mech. Solids **4**(4), 158–161 (1969)
11. Weingarten, V.I., Morgan, E.J., Seide, P.: Elastic stability of thin-walled cylindrical and conical shells under axial compression. AIAA J. **3**(3), 500–505 (1965)

Discontinuities in Viscoelastic Timoshenko Beam Under Moving Concentrated Loads

Arkadiy I. Manevich

Abstract Direct determination of jumps in internal forces and bending moments in elastic and viscoelastic Timoshenko beams under action of moving concentrated forces and moments is presented. Some "paradoxical" changes in the internal forces jumps in elastic beams at transitions through critical velocities are revealed, and an explanation to them is given. There is shown that the account of viscous internal friction is of principal importance for the dynamical Timoshenko beam model.

1 Introduction

At analysis of stress-strain state in beams under moving loads the question arises: how the velocity of a load affects discontinuities in internal forces and bending moments at points of the load application? The answer to this question depends on the beam model employed. If the classical Euler–Bernoulli (E-B) model is used for an elastic beam, there are no reasons for differences between static and dynamic jumps in the internal forces. However, at employing more exact and complicated models for beam and material, e.g., Timoshenko beam (TB) made of the elastic or viscoelastic material, the picture becomes more complicated and needs careful highlighting. As has been shown by Achenbach and Sun [1], if a concentrated force moves along an elastic Timoshenko beam on elastic or viscoelastic foundation, velocity of the force affects the discontinuity magnitude in the first derivative of the total displacement and therefore changes discontinuity in the shear force. Any physical explanation of this fact has not been proposed. To our knowledge, the question was not discussed in literature later.

The correct description of jumps in the internal force factors at the point of application of the moving concentrated load is of principal interest at solving dynamics problems with the use of conjunction conditions for two parts of beam –ahead of and behind the load. In particular, this approach was used for description of the steady-

A. I. Manevich (✉)
Dniepr National University, Gagarin Av. 72, Dniepr 49010, Ukraine
e-mail: armanevich2@gmail.com

I. V. Andrianov et al. (eds.), *Problems of Nonlinear Mechanics and Physics of Materials*, Advanced Structured Materials 94,
https://doi.org/10.1007/978-3-319-92234-8_23

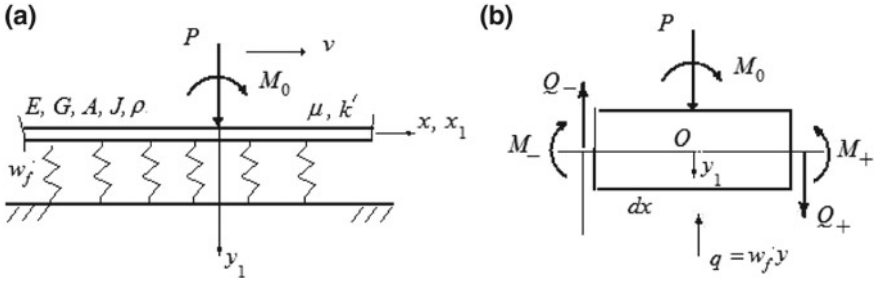

Fig. 1 **a** An infinite Timoshenko beam on elastic foundation; **b** The beam element containing the traveling force P and moment M_0

state running waves in infinite beams on elastic foundation, either within framework of the E-B theory (Kenney [6], see also Panovko and Gubanova [9], Fryba [2], Grigoluk and Selezov [3]), or using the TB model (Gulyaev et al. [4] and others).

In this work we give the direct derivation of expressions for jumps in internal forces and bending moments in elastic and viscoelastic Timoshenko beams under moving concentrated forces and bending moments (without solving concrete dynamic problems). It is shown that in elastic TBs some "paradoxical" changes in the internal forces jumps appear at transitions through critical velocities, but these jumps become independent on force velocity in viscoelastic beams. So accounting internal viscous friction is of principal importance for the dynamical TB model.

2 Governing Equations

We consider, for definiteness and simplicity, stationary running waves in an infinite viscoelastic Timoshenko beam under a concentrated force P and a moment M_0 moving with velocity v (Fig. 1a). The beam lies on the elastic foundation with stiffness factor w_f. The material of the beam is assumed to obey the Voigt law.

Deformations of the Timoshenko beam are described by two independent functions – the total transverse deflection $y(x, t)$ and the angle of cross section rotation ψ. The total slope of the bent axis is $\partial y/\partial x = \psi + \gamma$, where γ is the shear angle (here both angles ψ and γ are counted off in one direction). Constitutive relations are assumed according to the Voigt law for normal stresses σ_x as well as for shear stresses τ in the form

$$\sigma_x = E\varepsilon_x + k_1\frac{\partial \varepsilon_x}{\partial t} = E\left(1 + \mu_1\frac{\partial}{\partial t}\right)\varepsilon_x \;\; \tau = G\gamma + k_2\frac{\partial \gamma}{\partial t} = G\left(1 + \mu_2\frac{\partial}{\partial t}\right)\gamma, \quad (1)$$

($k_{1,2}$ and $\mu_1 = k_1/E$, $\mu_2 = k_2/G$ are the viscosity parameters, E and G are the elasticity modulus in tension and shear, respectively). The bending moment and the

transverse shear force in the cross section are specified by expressions (see, e.g., A. Manevich and Kolakowsky [7])

$$M = -EJ\left(1+\mu_1\frac{\partial}{\partial t}\right)\frac{\partial\psi}{\partial x},\ Q = k'A\,\tau = k'AG\left(1+\mu_2\frac{\partial}{\partial t}\right)\left(\frac{\partial y}{\partial x}-\psi\right) \quad (2)$$

(k' is the shear coefficient, which depends upon the cross section shape, A and J are the cross section area and moment of inertia).

Let us consider the beam element dx containing the force P and moment M_0 (Fig. 1b). In the coordinate system $x_1 = x - v\,t$, $y_1 = y$, moving with the load at velocity v, the force and the moment are applied at the origin O. Note that for stationary waves $y(x_1) = y(x - v\,t)$ derivatives in time t are expressed through derivatives in x:

$$\frac{\partial y}{\partial t} = -v\frac{\partial y}{\partial x_1},\ \frac{\partial^2 y}{\partial t^2} = v^2\frac{\partial^2 y}{\partial x_1^2} \quad (3)$$

(similar relations hold also for angle ψ).

Equations of the forces balance for this element with account of inertia forces, their moment and the distributive reactive force from the foundation $q_f = -w_f y$ are as follows

$$Q_+ - Q_- - \rho A\frac{\partial^2 y}{\partial t^2}dx - w_f y dx + P = 0, \quad (4)$$

$$-\rho J\frac{\partial^2\psi}{\partial\,t^2}\,d\,x + (Q_+ + Q_-)\,d\,x - (M_+ - M_-) + M_0 = 0 \quad (5)$$

(lower indexes "−" and "+" relate to quantities at the left and right edges of the element). Accordingly to (3) one has

$$\frac{\partial^2 y}{\partial t^2}dx = v^2\frac{\partial^2 y}{\partial x_1^2}dx = v^2\left[\left(\frac{\partial y}{\partial x_1}\right)_+ - \left(\frac{\partial y}{\partial x_1}\right)_-\right] = v^2\left(\frac{\partial y}{\partial x_1}\right)_-^+, \quad (6)$$

$$\frac{\partial^2\psi}{\partial\,t^2}\,d\,x = v^2\frac{\partial^2\psi}{\partial\,x_1^2}d\,x = v^2\left(\frac{\partial\,\psi}{\partial\,x_1}\right)_-^+$$

(here notation $(\ldots)_-^+ = (\ldots)_+ - (\ldots)_-$ is introduced). Expressions (2) are similarly reduced to

$$M = -EJ\left(1-\mu_1 v\frac{d}{dx_1}\right)\frac{d\psi}{dx_1},\ Q = k'AG\left(1-\mu_2 v\frac{d}{dx_1}\right)\left(\frac{dy}{dx_1}-\psi\right) \quad (7)$$

After substitution of (6) and (7) into (4) and (5) we obtain

$$k'AG\left(1-\mu_2 v\frac{d}{dx_1}\right)\left(\frac{dy}{dx_1}-\psi\right)_-^+ - \rho A v^2\left(\frac{dy}{dx_1}\right)_-^+ - w_f y dx + P = 0, \tag{8}$$

$$-\rho J v^2\left(\frac{d\psi}{dx_1}\right)_-^+ + k'AG\left(1-\mu_2 v\frac{d}{dx_1}\right)\left[\left(\frac{dy}{dx_1}-\psi\right)_+ + \left(\frac{dy}{dx_1}-\psi\right)_-\right]dx + EJ\left(1-\mu_1 v\frac{d}{dx_1}\right)\left(\frac{d\psi}{dx_1}\right)_-^+ + M_0 = 0 \tag{9}$$

The deflection y and angle ψ cannot have discontinuities: $y_+ = y_-$, $\psi_+ = \psi_-$. All terms with factor dx should be disregarded for the infinitesimal element, therefore Eqs. (8) and (9) result in conditions

$$\left(1-\frac{\rho v^2}{k'G}-\mu_2 v\frac{d}{dx_1}\right)\left(\frac{dy}{dx_1}\right)_-^+ + \frac{P}{k'AG} = 0, \tag{10}$$

$$\left(1-\frac{\rho\, v^2}{E}-\mu_1 v\frac{d}{d\, x_1}\right)\left(\frac{d\,\psi}{d\,x_1}\right)_-^+ + \frac{M_0}{EJ} = 0 \tag{11}$$

Relationships (10) and (11) determine jumps in derivatives and corresponding jumps in internal force factors M and Q (2) at transition through the point of applying the concentrated load. Let us rewrite these expressions in dimensionless variables and parameters [7, 8]

$$z = \frac{x_1}{r_0}, Y = \frac{y}{r_0}, \tau = \frac{c}{r_0}t, \chi = \frac{E}{k'G}, \mu^* = \frac{c}{r_0}\mu, v^* = \frac{v}{c}, P^* = \frac{P}{EA}, Q^* = \frac{Q}{EA}, M^* = \frac{Mr_0}{EJ} \tag{12}$$

($r_0 = \sqrt{J/A}$ is the cross section radius of inertia, $c = \sqrt{E/\rho}$ is the sound velocity in the beam material, χ is the shear deformability parameter, μ^* is the dimensionless viscous parameter; for classical Euler–Bernoulli and Rayleigh models $\chi = 0$). In these variables and parameters physical relationships (7) take the form

$$M^* = -\left(1-\mu_1^* v^*\frac{d}{d\,z}\right)\frac{d\,\psi}{d\,z},\ \ Q^* = \frac{1}{\chi}\left(1-\mu_2^* v^*\frac{d}{d\,z}\right)\left(\frac{d\,Y}{d\,z}-\psi\right), \tag{13}$$

Expressions for the jumps (10), (11) transform into

$$\left(1-\chi v^{*2}\right)\left(\frac{d\,Y}{d\,z}\right)_-^+ - \mu_2^* v^*\left(\frac{d^2 Y}{d\,z^2}\right)_-^+ + P^*\chi = 0 \tag{14}$$

$$\left(1-v^{*2}\right)\left(\frac{d\,\psi}{d\,z}\right)_-^+ - \mu_1^* v^*\left(\frac{d^2\psi}{d\,z^2}\right)_-^+ + M_0^* = 0. \tag{15}$$

3 Elastic Timoshenko Beam

Consider the case of elastic beam $\mu_1 = \mu_2 = 0$ first. Then expressions (14), (15) yield to following jumps in the first derivatives:

$$\left(\frac{d\,Y}{d\,z}\right)_{-}^{+} = -\frac{P^*\chi}{1-\chi v^{*2}},\ \left(\frac{d\,\psi}{d\,z}\right)_{-}^{+} = -\frac{M_0^*}{1-v^{*2}} \tag{16}$$

Corresponding jumps in dimensionless internal force factors Q^* and M^* accordingly to (13) are as follows:

$$Q_+^* - Q_-^* = -\frac{P^*}{1-\chi v^{*2}},\ M_+^* - M_-^* = \frac{M_0^*}{1-v^{*2}} \tag{17}$$

The first formula (17) coincides with the expression obtained by Achenbach and Sun [1] for the case of a concentrated force (formula (85), in other notations); the case of a concentrated moment was not considered there. In our opinion, the way the formula has been derived in that article, is not enough transparent and is essentially based on the traveling wave solution obtained there.

The most interesting question is: what physical reason leads to dependence of the jumps on the velocity of concentrated loads in elastic beams. As has been shown above, this dependence is due to the way the inertia forces are distributed in the neighborhood of the cross section where the concentrated force and/or moment are applied. An inevitable jump in the shear force yields in the TB model to a jump in the first derivative of the displacement (expression (2) for Q). As can be seen from expressions (6), the moving jump in the first derivative inevitably results in a *concentrated* inertia force in this cross-section. Similarly, the moving concentrated moment, causing the jump in the derivative of the angle of cross section rotation (2), generates the *concentrated* moment of inertia forces.

From this explanation it is clear now, why an elastic foundation does not influence the considered peculiarity – a reactive force from the foundation depends on the total displacement and, as a continuous function, is not able to produce any concentrated effect (as well as distributed forces of viscous friction in a viscoelastic foundation).

Evidently, in the E-B model with jumps only in the second and third derivatives of the displacement (caused by the force P and the moment of forces M_0) the concentrated inertia forces and their moment do not appear. That is why the motion of concentrated loads in E-B model does not affect jumps in the internal forces.

Even without complete solution of a dynamical problem, expressions (17) enable us to make conclusions on the "critical velocities" at moving load for the elastic TB. The jumps in the shear force and bending moment become indefinitely large when the velocities are equal to the following values, respectively:

$$v_1^* = \frac{1}{\sqrt{\chi}},\ v_2^* = 1 \tag{18}$$

(in the original dimensional variables these velocities v_1^* and v_2^* correspond, accordingly to (13), to values $v_1 = c/\sqrt{\chi} = \sqrt{k'G/\rho}$, $v_2 = c = \sqrt{E/\rho}$, which are the velocity of shear waves and the longitudinal waves, respectively (the latter equals to the speed of perturbation propagation in the bending moment).

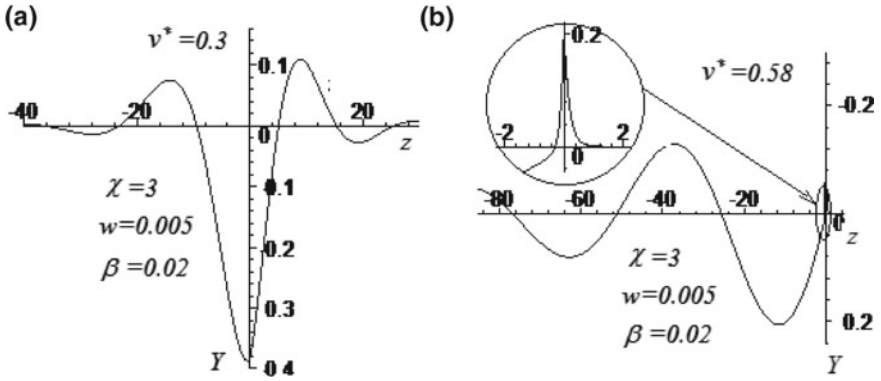

Fig. 2 Stationary running waves in TB on the viscoelastic foundation ($\chi = 3$, $w = 0.005$; $\beta = 0.02$) for two velocities: **a** $v^* = 0.3$ (pre-critical velocity interval); **b** $v^* = 0.58$ (the first supercritical interval)

Hence, at these two velocities of motion for the force and moment, steady-state running waves do not exist (in elastic TB). However, such waves exist at bigger velocities – in supercritical intervals $v_1 < v < v_2$ and $v > v_2$ (i.e. $v^* > 1$).

At these velocities of a concentrated load "paradoxical" transitions take place in elastic TB. When the speed falls in interval $v_1 < v < v_2$, the jumps in the total slope of the bent axis and in the shear force change their signs. At transition to supercritical interval $v > v_2$, the jumps in the derivative for both the cross section angle of rotation and bending moment experience the same inversion.

The profiles of the stationary running waves in an elastic TB ($\chi = 3, v_1^* = 0.57735$) on a viscoelastic foundation with dimensionless stiffness parameter $w = w_f r_0^2/EA = 0.005$ are shown in Fig. 2 for two values of dimensionless velocity: $v^* = 0.3$ (pre-critical interval, plot *a*) and $v^* = 0.58$ (the first supercritical interval, plot *b*).

Details of the solution are given in A. Manevich [8] (note that viscosity parameter of the foundation β does not affect the jumps). In the moving coordinate system the force is applied at the origin ($z = x/r_0 = 0$) and is directed vertically downwards. We see that in case $v^* = 0.58$ *the beam deflection at point of the force application is directed oppositely to the force direction*. This inversion is due to the fact that the jump in the inertia force caused by the running fissure of the bent axis in Timoshenko model become prevailing – it exceeds the magnitude of force P.

4 Viscoelastic Timoshenko Beam

Let us now return to the general case of viscoelastic TB. It follows from (14), (15) that a concentrated force or a moment lead to a jump in the corresponding second

derivatives, but the first derivatives are smooth (otherwise the second derivatives would be infinite). The jumps in the second derivatives are

$$\left(\frac{d^2Y}{d\,z^2}\right)_-^+ = \frac{P^*\chi}{\mu_2^* v^*},\ \left(\frac{d^2\psi}{d\,z^2}\right)_-^+ = \frac{M_0^*}{\mu_1^* v^*} \tag{19}$$

But then it follows from (13) with account of continuity of the first derivatives ($(dY/d\,z)_-^+ = 0$ and $(d\,\psi/d\,z)_-^+ = 0$) that corresponding jumps in dimensionless internal force factors Q^* and M^* are

$$Q_+^* - Q_-^* = -P^*,\ M_+^* - M_-^* = M_0^* \tag{20}$$

So these jumps become independent on the velocity. The account of the internal viscous friction eliminates the moving fissure of the bent axis in Timoshenko model, and associated with it concentrated inertia forces disappear. So the jumps in the internal force factors remain the same as in statics.

We come to conclusion that the Timoshenko model for elastic beams in dynamical problems can result in some effects that disappear at employing more physical viscoelastic Timoshenko beam model.

5 Conclusions

Jumps in internal forces in elastic and viscoelastic Timoshenko beams under action of moving concentrated forces and moments can be determined directly from equations of the force balance for the beam element containing the force and the moment and moving with the load velocity. For the elastic TB at supercritical velocities of loads the force jumps can change their signs, as well as corresponding deformations. We give an explanation to the revealed differences between static and dynamic jumps in forces and moments caused by the moving fissure of the bent axis in the elastic TB model yielding to concentrated inertia forces and moments. These effects disappear in the viscoelastic TB model, so account of internal viscous friction is of principal importance for the dynamical TB model.

References

1. Achenbach, J.D., Sun, C.T.: Moving load on a flexibly supported Timoshenko beam. Int. J. Solids Struct. **1**(4), 353–370 (1965)
2. Fryba L.: Vibration of Solids and Structures under Moving Loads. 1st edn. Noordhoff International, The Netherlands (1972); 3rd edn. Thomas Telford Ltd (1999)
3. Grigoluk, E.I., Selezov I.T.: Nonclassical theories of oscillations of rods, plates and shells. In: Itogi nauki i tekhniki, Series: Mekhanika tviordykh deformiruemykh tel, vol. **5.** VINITI, Moscow (1973) (in Russian)

4. Gulyaev, V.I., Melnik, V.M., Yakovenko Ye.V.: Dynamics of beam on elastic foundation under action of moving force and moment (Timoshenko model). Int. Appl. Mech., Kiev, **36**(12), 121–127 (2000) (in Russian)
5. Gulyaev, V.I., Nabil M.: Resonance interaction of beam and elastic foundation at motion of a periodic system of concentrated loads. Int. Appl. Mech. **41**(5), 116–123 (2005) (in Russian)
6. Kenney, J.T., jr.: Steady-state vibrations of beam on elastic foundation for moving load. J. Appl. Mech. Trans. ASME **76**, 359–364 (1954)
7. Manevich, A., Kolakowsky, Z.: Free and forced oscillations of Timoshenko beam made of viscoelastic material. J. Theor. Appl. Mech. Warsaw **49** (1), 3–16 (2011)
8. Manevich, A.I.: Supercritical stationary regimes in Timoshenko beam on viscoelastic foundation under moving load. In: Mania, R. (ed.) Statics, Dynamics and Stability of Structures, Research Advances in Applied Mechanics. A Series of Monographs, vol. **6**,. Lodz University of Technology, Lodz, pp. 147–168 (2016)
9. Panovko, Ya.G., Gubanova, I.I.: Stability and Oscillations of Elastic systems. Modern Conceptions, Paradoxes and Errors, 2nd edn. Nauka, Moscow (1967) (in Russian)

Part V
Theory of Elasticity and Thermo-elasticity

Analytical Study of a Nonlinear Beam Including a Piezoelectric Patch

V. Guillot, A. Ture Savadkoohi and C.-H. Lamarque

Abstract The chapter presents modal responses and nonlinear interactions of a multi-physics nonlinear beam. It is composed of a piezoelectric material which is patched on a two-dimensional nonlinear Euler–Bernoulli beam. The spatio-temporal variables of governing equations of the composite beam are separated. Traced frequencies and mode shapes of the overall beam show modifications of its modal response due to the piezoelectric patch and its position on the beam. Studying the system in time domain via a multiple scale technique, leads to detection of its responses as function of frequency of excitation which present strongly nonlinear response due to nonlinearity of the beam and also presence of the piezoelectric patch.

1 Introduction

Piezoelectric systems are used widely for control [1, 2] and vibratory energy harvesting [3, 4]. To this end, they are patched to main structural systems such as beams for controlling or harvesting their vibratory energies. Proper modelling and treatments of these composite structures are essential steps for the design of piezoelectric materials. Modelling and detection of nonlinear responses of Euler–Bernoulli beam elements are quite mature. As some few representations of extensive works in this domain we can mention followings: Ref. [5] developed nonlinear equations of a beam which relate different internal actions such as torsion and bendings to deformed variables. As an example they derived governing equations of a rotating cantilever beam that undergoes coupled axial deflection and flap (out-of-plane) bending. Ref-

V. Guillot (✉) · A. Ture Savadkoohi · C.-H. Lamarque
Univ Lyon, ENTPE, LTDS UMR CNRS 5513, 69518 Vaulx-en-Velin,
rue Maurice Audin, France
e-mail: vinciane.guillot@entpe.fr

A. Ture Savadkoohi
e-mail: alireza.turesavadkoohi@entpe.fr

C.-H. Lamarque
e-mail: claude.lamarque@entpe.fr

I. V. Andrianov et al. (eds.), *Problems of Nonlinear Mechanics and Physics of Materials*, Advanced Structured Materials 94,
https://doi.org/10.1007/978-3-319-92234-8_24

erences [6, 7] developed nonlinear governing differential equations of an extensible Euler–Bernoulli beam experiencing flexure along two principal directions and torsion. They studied responses of such beams with some different boundary conditions, eg. clamped-pined, clamped-clamped, under distributed periodic excitation being in resonance with one of the modes. References [8–10] developed nonlinear differential equations of Euler–Bernoulli inextensible beams. They studied some special cases such as flap-wise and chord-wise excitations for systems with internal resonances. There are some research works for modelling and treating composite beams, i.e. a homogeneous beam and piezoelectric patches which we summarize some of recent works here: Refs. [11–13] studied the energy harvesting problem of a two-dimensional model of a parametrically excited two-layered cantilever beam, i.e. a layer of a homogeneous beam and a piezoelectric one, with a tip mass. Reference [14] studied a parametrically excited two-dimensional cantilevered beam with two patches of a piezoelectric material with given length and given position at either sides of the beam.

In this chapter, we are interested to analyse spatio-temporal responses of a two-dimensional cantilever beam with a patch of piezoelectric material on the beam. The chapter is structured as it follows: developments of governing equations of a two-dimensional nonlinear composite beam are presented in Sect. 2. In Sect. 3, spatio-temporal variables of system are separated and space and time variables are treated via an adapted method. In Sect. 4, an example of modal responses of a composite beam is illustrated. Finally, the chapter is concluded in Sect. 5.

2 Beam and Piezoelectric Material Model

2.1 Beam Model

Let us consider the deformation of a beam from an inertial coordinate system $(\vec{\mathbf{e}}_x, \vec{\mathbf{e}}_y, \vec{\mathbf{e}}_z)$ to a rotational coordinate system $(\vec{\mathbf{e}}_\eta, \vec{\mathbf{e}}_\zeta, \vec{\mathbf{e}}_\xi)$, see Fig. 1. We

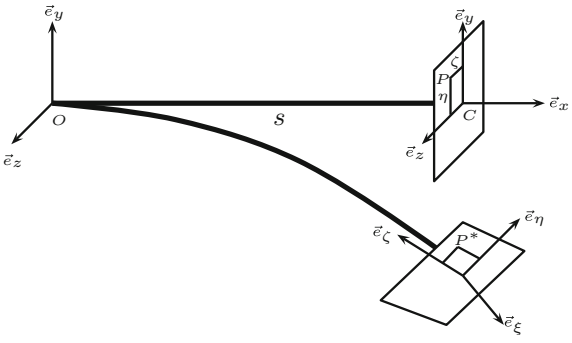

Fig. 1 Deformation of the beam from the inertial coordinate system $(\vec{\mathbf{e}}_x, \vec{\mathbf{e}}_y, \vec{\mathbf{e}}_z)$ to the rotational coordinate system $(\vec{\mathbf{e}}_\eta, \vec{\mathbf{e}}_\zeta, \vec{\mathbf{e}}_\xi)$ [15]

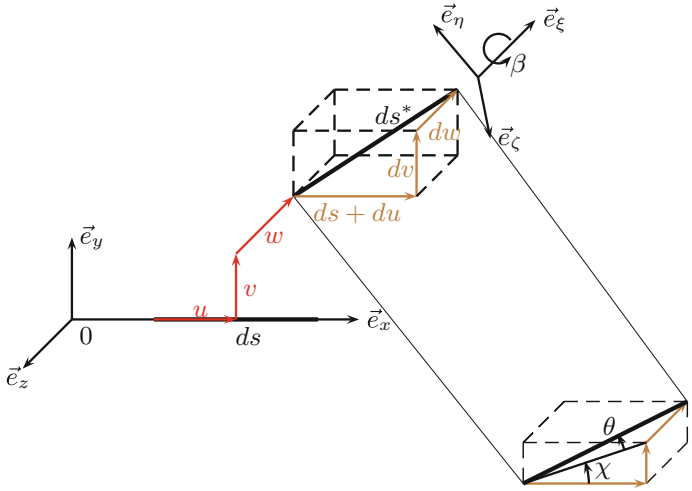

Fig. 2 Deformation u v and w of the neutral axis of the beam in inertial coordinates

use the Euler–Bernoulli beam theory for modeling the system. We assume that the Poisson coefficient can be neglected and we set E_b and G to be the Young and shear moduli of the beam, respectively. We also assume that the section of the beam is not deformed, this way we are only interested in the deformation of the neutral axis, as despicted in Fig. 2. We suppose a displacement (u, v, w) in the inertial coordinate, i.e. $(\vec{\mathbf{e}}_x, \vec{\mathbf{e}}_y, \vec{\mathbf{e}}_z)$. The beam is assumed to be inextensible, thus we use a Lagrange multiplier λ in the equations. The translational kinetic energy reads as:

$$T = \frac{1}{2} m_b \int_0^L (\dot{u}^2 + \dot{v}^2 + \dot{w}^2) ds \tag{1}$$

m_b is the linear density of the mass, $'\dot{}'$ stands for the time derivative of a variable and L is the length of the beam. We neglect the rotational kinetic energy, assuming that the principal moments of inertia can be omitted. The potential energy V is written as:

$$V = \int_\vartheta (\boldsymbol{\sigma} : \boldsymbol{\epsilon}) \, \mathrm{d}\vartheta \tag{2}$$

σ and ϵ are the tensors of stress and strain, respectively. V can be rewritten as:

$$V = \frac{1}{2} \int_0^L (D_\xi \rho_\xi^2 + D_\eta \rho_\eta^2 + D_\zeta \rho_\zeta^2) ds \tag{3}$$

where,

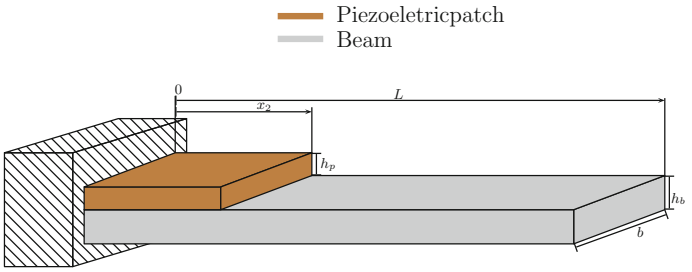

Fig. 3 Schema of the beam with the piezoelectric material

$$D_\xi = G \int_A (\eta^2 + \zeta^2)\, dA \tag{4}$$

$$D_\eta = E_b \int_A \zeta^2\, dA \tag{5}$$

$$D_\zeta = E_b \int_A \eta^2\, dA \tag{6}$$

when $\rho_\xi, \rho_\eta, \rho_\zeta$ are the curvatures in the rotational coordinate system ($\vec{\mathbf{e}}_\eta, \vec{\mathbf{e}}_\zeta, \vec{\mathbf{e}}_\xi$), [15].

2.2 Modelling of the Piezoelectric Material

The goal is to model the multi-physics beam which is illustrated in Fig. 3. The first step with a piezoelectric material is to define its free density energy H that depends on the strain tensor ϵ written in a vectorial maner and the electric field E. We suppose that the piezoelectric material is polarized in the direction $\vec{\mathbf{e}}_y$, i.e. $E_x \simeq 0 \simeq E_z$, see Fig. 3. Since the piezoelectric patch is going to be on the beam, we can assume that it has the same displacement as the beam. In this case, they share the same strain tensor. Thus, the free density energy H reads:

$$\begin{aligned} H(\rho_\eta, \rho_\xi, \rho_\zeta, E_y) = A_{n1} E_y \rho_\eta + A_{e1} E_y \rho_\xi + A_{c1} E_y \rho_\zeta + T_{no} \rho_\eta^2 + T_{co} \rho_\zeta^2 \\ + T_{eo} \rho_\xi^2 + \tfrac{1}{2} \xi_{33} E_y^2 + G(E_y, \rho_\eta, \rho_\zeta, \rho_\xi) \end{aligned} \tag{7}$$

with $G(E_y, \rho_\eta, \rho_\zeta, \rho_\xi)$ a function of higher order terms in $E_y, \rho_\eta, \rho_\zeta, \rho_\xi$ and A_{n1}, A_{e1}, A_{c1}, T_{no}, T_{co}, T_{eo} and ξ_{33} are constants of the piezoelectric material [12]. From this constitutive law, we can define the potential energy of the piezoelectric material V_{piezo}:

$$V_{piezo} = \int_\vartheta H(\rho_\eta, \rho_\xi, \rho_\zeta, E_y) d\vartheta \tag{8}$$

The kinetic translational energy T_{piezo} yields to:

$$T_{piezo} = \frac{1}{2} m_p \int_{x_1}^{x_2} (\dot{u}^2 + \dot{v}^2 + \dot{w}^2) ds \tag{9}$$

with m_p being the linear density of the piezoelectric material, and x_1, x_2 are the coordinates representing the position of the piezolectric materials in the x direction. u, v, w are displacements of the pieozelectric material in the inertial coordinates $(\vec{\mathbf{e}}_x, \vec{\mathbf{e}}_y, \vec{\mathbf{e}}_z)$. There is also an electrical equation, deduced from the electrical circuit linked to the piezoelectric material and also from its constitutive law. In fact, J the electrical intensity in the circuit [16] reads:

$$J = -\int \int_{y=h} \frac{\partial}{\partial t} \left(\frac{\partial H(\rho_\eta, \rho_\xi, \rho_\zeta, E_y)}{\partial E_y} \right) dA \tag{10}$$

The integration on the section of the piezoelectric material is carried out in $y = h$, where h is the distance between the neutral axis and the electrode on the piezoelectric material.

2.3 Governing Equations of the Multi-physics Beam

Let us consider a two-dimensional non-linear beam model, with a piezoelectric material on it. The piezoelectric material is patched at the beginning of the beam until $s = x_2$, as depicted in Fig. 3. As the kinetic and potential energies of each part of the multi-physics beam have been clarified already, we can define the Lagrangian l of the system as:

$$l = T(s) - V(s) + T_{piezo}(s) - V_{piezo}(s) - \mathcal{H}(s - x_2)\big(T_{piezo}(s) - V_{piezo}(s)\big) \tag{11}$$

where $\mathcal{H}(s - x_2)$ stands for the Heaviside function. The Hamilton's principle imposes:

$$\int_{t_1}^{t_2} (\delta l + \delta W_{nc}) \mathrm{d}t = 0 \tag{12}$$

where W_{nc} is the non conservative work.

We reduce the dimension of the system to two-dimensional by setting $w = 0$. We obtain three equations, two electro-mechanical ones corresponding to the three generalised coordinate of the problem [15] and an electrical equation. Supposing the piezoelectric material has a electrical circuit with a resistor R:

$$m(s)\ddot{u} = [\lambda(1 + u')]' + N_1(E_y, u, v, \gamma) \tag{13}$$

$$m(s)\ddot{v} = [EI_v(s)v'']'' + N_2(E_y, u, v, \gamma) \tag{14}$$

$$\xi_{33}\dot{E}_y + \frac{E_y}{R} + N_3(E_y, u, v, \gamma) = 0 \tag{15}$$

where " $'$ " stands for the space derivative of a variable and the N_j, $j = 1, 2, 3$ are nonlinear functions of E_y, u, v, γ with higher order terms in those variables, with γ being the real twist angle [15]. We define:

$$m(s) = \begin{cases} m_b + m_p, & \text{if } s \leq x_2 \\ m_b, & \text{if } s > x_2 \end{cases} \tag{16}$$

$$EI_v(s) = \begin{cases} EI_1 = D_\eta + T_{no}, & \text{if } s \leq x_2 \\ EI_2 = D_\eta, & \text{if } s > x_2 \end{cases} \tag{17}$$

We take the equation obtain from inextensibility condition, i.e.:

$$(1 + u')^2 = 1 - v'^2 \tag{18}$$

and the Eq. (13) to deduce λ [15] and we replace them in the Eq. (14).

3 Treatments of System Equations

We suppose the following separation of variables for the displacement $v(s, t)$ as:

$$v(s, t) = \phi(s)g(t) \tag{19}$$

we inject it in Eq. (14). In this case we can obtain two sets of equations, as functions of time and space.

3.1 The Problem in Space

Thus, we can define a problem in space only by keeping the linear part in $g(t)$ of the equation:

$$\frac{\ddot{g}(t)}{g(t)} = -\frac{1}{\phi(s)m(s)}\frac{\partial^2}{\partial s^2}\left(\phi(s)''EI_v(s)\right) = \omega_v^2 \tag{20}$$

where ω_v is a constant.

In order to treat the spatial equations of system (20) that are with variable coefficients, we define:

$$\phi(s) = \phi_0(s) + \mathcal{H}(s - x_2)(\phi_1 - \phi_0) \tag{21}$$

Thus, two equations arises on $[0, x_2]$ and $[x_2, L]$ as:

$$\frac{\partial^4 \phi_0}{\partial s^4} = \frac{(m_b + m_p)}{EI_1}\phi_0 \tag{22}$$

$$\frac{\partial^4 \phi_1}{\partial s^4} = \frac{(m_b)}{EI_2}\phi_1 \tag{23}$$

And, the continuity and boundary conditions read:

$$\phi_0(0) = 0 \tag{24}$$

$$\phi_0'(0) = 0 \tag{25}$$

$$\phi_1''(L) = 0 \tag{26}$$

$$\phi_1'''(L) = 0 \tag{27}$$

$$\phi_0(x_2) - \phi_1(x_2) = 0 \tag{28}$$

$$\phi_0'(x_2) - \phi_1'(x_2) = 0 \tag{29}$$

$$EI_1\phi_0''(x_2) - EI_2\phi_1''(x_2) = 0 \tag{30}$$

$$EI_1\phi_0'''(x_2) - EI_2\phi_1'''(x_2) = 0 \tag{31}$$

Thus, for the nth mode of the beam we can write:

$$\phi_{0n} = A_{1n}\cos(K_{1n}s) + B_{1n}\sin(K_{1n}s) + C_{1n}\sinh(K_{1n}s) + D_{1n}\cosh(K_{1n}s) \tag{32}$$

$$\phi_{1n} = A_{2n}\cos(K_{2n}s) + B_{2n}\sin(K_{2n}s) + C_{2n}\sinh(K_{2n}s) + D_{2n}\cosh(K_{2n}s) \tag{33}$$

A_{1n}, A_{2n}, B_{1n}, B_{2n}, C_{1n}, C_{2n}, D_{1n} and D_{2n} are constants to be determined thanks to the boundary and continuity conditions, we have:

$$K_{1n}^4 = \frac{(m_b + m_p)}{EI_1}\omega_{vn}^2 \tag{34}$$

$$K_{2n}^4 = \frac{m_b}{EI_2}\omega_{vn}^2 \tag{35}$$

Due to the bounadry and continuity conditions which are described Eqs. (24–31), one can obtain:

$$U_{8\times1} = \boldsymbol{G}X_{8\times1} \tag{36}$$

with:

$$U_{8\times1} = [\phi_0(0) \quad \phi_0'(0) \ \ldots \ EI_1\phi_0'''(x_2) - EI_2\phi_1'''(x_2)]^T \tag{37}$$

$$X_{8\times1} = [A_{1n} \quad B_{1n} \quad C_{1n} \quad D_{1n} \quad A_{2n} \quad B_{2n} \quad C_{2n} \quad D_{2n}]^T \tag{38}$$

For having non zero solution, determinant of the $\boldsymbol{G}$ matrix is set to be zero which leads to detection of system frequencies ω_{vn}. All constants of Eq. (33) can be expressed as functions of A_1. Then the nth mode function can be normalized to find A_1.

3.2 The Problem in Time

Let us suppose that the system is under base excitation. The modified version of Eq. (20) reads:

$$\begin{aligned} m(s)\ddot{v} + c_v\dot{v} - Q_v = \Big(& - D_\zeta(s)(v''' - v'v''^2) \\ & +(1-\mathcal{H}(s-x_2))\big(- T_{co}(s)[v''' + v'v''^2] + 6V_c v''v'''\big) + \lambda v' \Big)' \end{aligned} \tag{39}$$

where c_v and Q_v stand for damping and external excitation respectively. V_c is a piezoelectric constant. Let us project the system (39) on its nth mode, i.e. ϕ_n. It reads as:

$$M\ddot{g} + \mathcal{C}_v\dot{g} - Q_{vp} = T_v g + T_{vvv}g^3 + T_{vv2}g\,\overbrace{(g^2)}^{\ddot{}} + T_{vv1}g\,\overbrace{g^2}^{\dot{}} + T_{vvp}g^2 \tag{40}$$

with M, $\mathcal{C}_v$, T_v, T_{vvv}, T_{vv2}, T_{vv1} and T_{vvp} are constants. $\overbrace{\ }^{\ddot{}}$ and $\overbrace{\ }^{\dot{}}$ represent the second and first derivatives of the argument with respect to the time. We set Q_v as:

$$Q_{vp} = -m_b f\cos(\Omega t)\int_0^L \phi_n(s)ds \tag{41}$$

with Ω being the frequency of the external force, we are interested to study system behaviours around a 1:1 resonance, we set:

$$\Omega = \omega_{vn} + \sigma\epsilon^2 \tag{42}$$

with σ being the detuning parameter.

We use a multiple scale method to treat the problem by applying a very small bookkeeping parameter ϵ. We suppose the constants of the piezoelectric material are of order ϵ.

Different scales of time and its derivatives read ($j = 1, 2\ldots$):

$$T_j = \epsilon^j t \tag{43}$$

$$D_j = \frac{\partial}{\partial T_j} \tag{44}$$

And we set $v(s,t)$ in the form of series as:

$$v(s,t) = \phi(s)(\epsilon g_1(t) + \epsilon^2 g_2(t) + \cdots) \tag{45}$$

We suppose:

$$C_v = \mathcal{O}(\epsilon^2) \tag{46}$$

$$Q_v = \mathcal{O}(\epsilon^3) \tag{47}$$

At $\mathcal{O}(\epsilon)$ we have :

$$M D_0^2 g_1 = T_v g_1 \tag{48}$$

Thus:

$$g_1 = C_v \exp(i\omega_v T_0) + \overline{C}_v \exp(-i\omega_v T_0) \tag{49}$$

where C_v is the complex amplitude of g_1, $\overline{C}_v$ stands for its conjugates and:

$$\omega_v = -\sqrt{\frac{T_v}{M}} \tag{50}$$

At $\mathcal{O}(\epsilon^2)$:

$$M D_0^2 g_2 + 2M D_0 D_1 g_1 = T_v g_2 + T_{vvp} g_1^2 \tag{51}$$

Here, we use the Fredholm's alternative to impose the solvability condition, thus :

$$g_2 = P \exp(2i\omega_v T_0) + \overline{P} \exp(-2i\omega_v T_0) + N + \overline{N} \tag{52}$$

$$D_1 C_v = 0 \tag{53}$$

where P and N are complex constants and $\overline{P}$, $\overline{N}$ their complex conjugates. At $\mathcal{O}(\epsilon^3)$ system equations yields to:

$$\begin{aligned} M D_0^2 g_3 + 2M D_0 D_2 g_1 = {} & T_v g_3 + T_{vvv} g_1^3 + T_{vv2} g_1 D_0^2 g_1^2 + T_{vv1} g_1 D_0 g_1^2 \\ & + 2T_{vvp} g_1 g_2 + Q_{vp} - \mathcal{C}_v D_0 g_1 \end{aligned} \tag{54}$$

where T_v, T_{vvv}, T_{vv2}, T_{vv1}, T_{vvp} and $\mathcal{C}_v$ are defined in *Appendix 1*. We again use the alternative of Fredholm to have the equation of the solvability condition, and we suppose:

$$Q_{vp} = m_b \omega_{vn}^2 f \cos(\omega_{vn} T_0 + \sigma T_2) \int_0^L \phi_n(s) ds \tag{55}$$

Table 1 Characteristics of the multi-physics system

E_p(GPa)	E_b(GPa)	L(m)	b(m)	h_b(m)	h_p(m)	m(kg m^3)	m_p(kg m^3)
33	109	0.222	0.04	0.0064	0.005	9000	7800

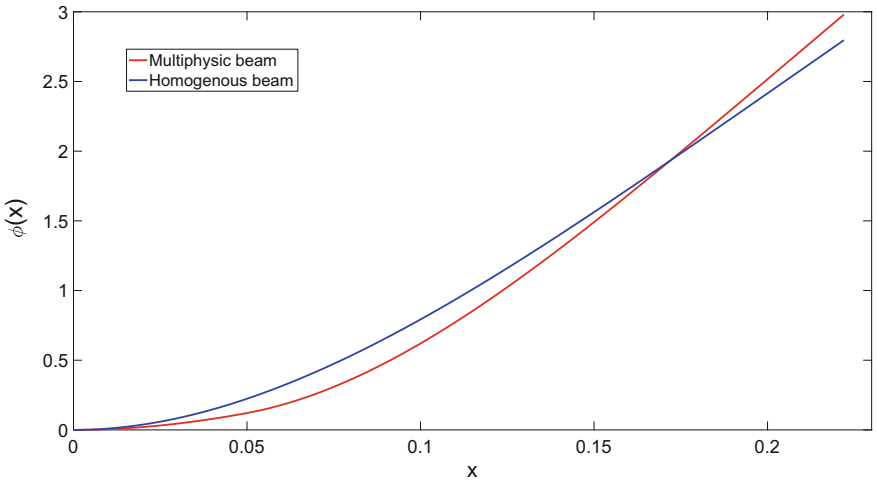

Fig. 4 First mode function for $\omega_{v1} = 607$ Hz: the blue line stands for the response of the homogeneous beam, the red line represents the overall mode of the multi-physics system

In Eq. (54), we suppose that $C_v = \dfrac{a}{2}\exp(i(\sigma T_2 - \gamma))$. We separate real and imaginary parts of the equation, then the following equation of order six in a is obtained.

$$\alpha_1 a^6 + \alpha_2 a^4 + \alpha_3 a^2 + \alpha_4 = 0 \tag{56}$$

where α_1, α_2, α_3 and α_4 are some constants defined in *Appendix 2*.

4 Numerical Results

Let us consider the piezoelectric material placed on a beam as shown in Fig. 3. Characteristics of the system are summarized in Table 1. We trace the two first modes of the multi-physic beam : $\omega_{v1} = 607$ Hz and $\omega_{v2} = 3350$ Hz. Corresponding modal responses are illustrated in Figs. 4 and 5. It is seen that the piezoelectric patch modifies the mode of the overall system.

For the problem in time, we treat the Eq. (56) in a by doing a change of variable $Z = a^2$ and solving the equation of the order three with the Cardano method. The

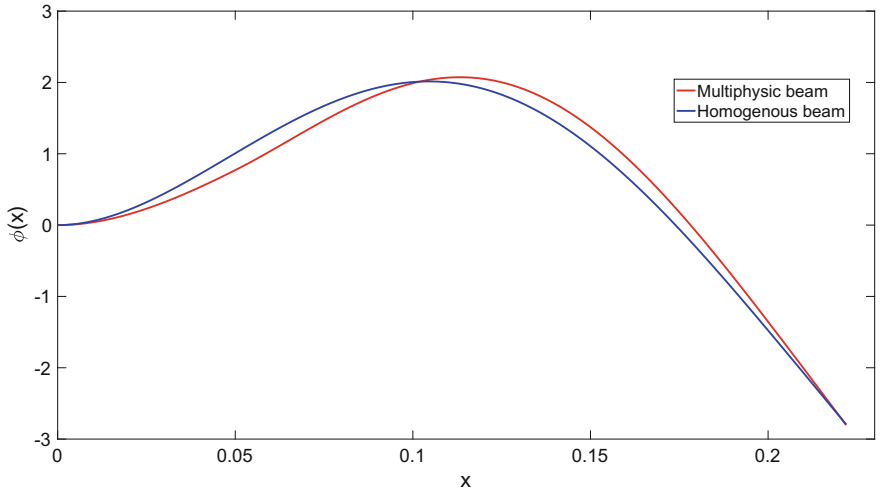

Fig. 5 Second mode function for $\omega_{v2} = 3350$ Hz: the blue line stands for the response of a homogeneous beam, the red line represents the overall mode of the multi-physics system

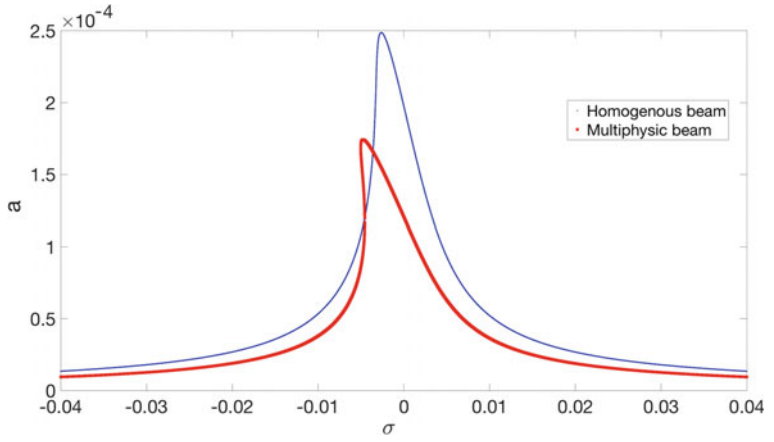

Fig. 6 Amplitude of the response of the displacement v around the first frequency, for $f = 2 \times 10^{-3}$ (see Eqs. (55) and (56)). The blue line corresponds to a homogenous beam, the red line corresponds to the multi-physic beam

results are illustrated in Fig. 6. We can see that the non-linear coefficient V_c coming from the piezoelectric material has a great influence on the non-linear behaviour of the beam with the piezoelectric patch.

5 Conclusion

Governing equations of a two-dimensional non-linear multi-physics beam are derived. The multi-physics system is composed of a homogeneous cantilever beam and a piezoelectric patch placed on the beam next to its clamped part. The spatio-temporal system variables are separated and modal responses of the overall system are obtained.

To treat temporal system variables, a multiple scale method in time is endowed, considering that a special mode of the system to be around the 1:1 resonance with the external base excitation. Then the global spatio-temporal system responses are traced. The main ideas of using piezoelectric patch on the beam are: (i) to change spatio-temporal responses of the beam, and (ii) to control/harvest its vibratory responses under externally induced excitations.

Acknowledgements The authors would like to thank and acknowledge the followings for supporting this research work: (i) the "Ministère de la Transition écologique et solidaire" and (ii) LABEX CELYA (ANR-10-LABX-0060) of the "Université de Lyon" within the program Investissement d'Avenir (ANR-11-IDEX-0007) operated by the French National Research Agency(ANR).

Appendix 1

$$M = \int_0^L m(s)\phi_n(s)^2 \, ds \tag{57}$$

$$\mathcal{C}_v = \int_0^L c_v\phi_n(s)^2 \, ds \tag{58}$$

$$T_v = \int_0^L -EI(s)\phi_n^{iv}(s)\phi_n(s) \, ds \tag{59}$$

$$T_{vvv} = \int_0^L -EI(s)[\phi_n'(s)\phi_n''^2(s) - \phi_n'^2(s)\phi_n'''(s)]'\phi_n(s) \, ds \tag{60}$$

$$T_{vv1} = \int_0^L [-\phi_n'(s) \int_0^L \frac{c_u}{2} \int_0^s \phi_n'^2(s) \, ds \, ds]'\phi_n(s) \, ds \tag{61}$$

$$T_{vv2} = \int_0^L [-\phi_n'(s) \int_0^L \frac{-m(s)}{2} \int_0^s \phi_n'^2(s) \, ds \, ds]'\phi_n(s) \, ds \tag{62}$$

$$T_{vvp} = \int_0^L 6V_c[\phi_n''(s)\phi_n'''(s)]'\phi_n(s) \, ds \tag{63}$$

Appendix 2

$$\alpha_1 = \left(\frac{w_{vn}}{2} T_{vv2} - \frac{3}{8} T_{vvv} - \frac{T_{vvp}}{4} \left(\frac{2}{T_v} + \frac{T_{vvp}}{T_v - 4Mw_{vn}^2} \right) \right)^2 \tag{64}$$

$$\alpha_2 = 2Mw_{vn}\sigma\sqrt{\alpha_1} \tag{65}$$

$$\alpha_3 = (Mw_{vn}\sigma)^2 + \frac{w_{vn}^2 \mathcal{C}_v^2}{4} \tag{66}$$

$$\alpha_4 = \left(\frac{m_b \omega_{vn} f}{2} \right)^2 \tag{67}$$

References

1. Badel, A., Sebald, G., Guyomar, D., Lallart, M., L E., Richard, C., Qiu, J.: Piezoelectric vibration control by synchronized switching on adaptative voltage sources : towards wideband semi-active damping. J. Acoust. Soc. Am. **119**, 2815–2825 (2006)
2. Ducarne, J., Thomas, O., Deü, J.: Structural vibration reduction by switch shunting of piezoelectric elements : modeling and optimization. J. Interll. Mater. Syst. Struct. **21**, 797–816 (2010)
3. Erturk, A., Renno, J.M., Inman, D.J.: Modeling of piezoelectric energy harvesting from an l-shaped beam-mass structure with an application to uavs. J. Interll. Mater. Syst. Struct. **20**, 529–544 (2009)
4. Yi, K., Monteil, M., Collet, M., Chesne, S.: Smart metacomposite-based systems for transient elastic wave energy harvesting. Smart Mater. Struct. **26**(035), 040 (2017)
5. Hodges, D.H., Ormiston, R.A., Peters, D.A.: On the nonlinear deformation geometry of euler-bernoulli beams. NASA Technical paper 1566 (1980)
6. Crespo Da Silva, M.R.M.: Non-linear flexural-flexural-torsional-extensional dynamics of beams-i. formulation. Int. J. Solids Struct. **24**, 1225–1234 (1988a)
7. Crespo Da Silva, M.R.M.: Non-linear flexural-flexural-torsional-extensional dynamics of beams-it. response analysis. Int. J. Solids Struct. **24**, 1235–1242 (1988b)
8. Pai, P.F., Nayfeh, A.H.: Three-dimensional nonlinear vibrations of composite beams-i. equations of motion. Nonlinear Dyn. **1**, 477–502 (1990)
9. Pai, P.F., Nayfeh, A.H.: Three-dimensional nonlinear vibrations of composite beams-ii. flapwise excitations. Nonlinear Dyn. **2**, 1–34 (1991a)
10. Pai, P.F., Nayfeh, A.H.: Three-dimensional nonlinear vibrations of composite beams-iii. chordwise excitations. Nonlinear Dyn. **2**, 137–156 (1991b)
11. Abdelkefi, A., Nayfeh, A., Hajj, M.: Effects of nonlinear piezoelectric coupling on energy harvesters under direct excitation. Nonlinear Dyn. **67**, 1221–1232 (2012a)
12. Abdelkefi, A., Nayfeh, A., Hajj, M.: Global nonlinear distributed-parameter model of parametrically excited piezoelectric energy harvesters. Nonlinear Dyn. **67**, 1147–1160 (2012b)
13. Bibo, A., Abdelkefi, A., Daqaq, M.: Modeling and characterization of a piezoelectric energy harvester under combianed aerodynamic and base excitations. J. Vib. Acoust. **137**(031,017) (2015). (12 pages)
14. Mam, K., Peigney, M., Siegert, D.: Finite strain effects in piezoelectric energy harversters under direct and parametric excitations. J. Sound Vib. **389**, 411–437 (2017)
15. Nayfeh, A., Pai, P.: Linear and Nonlinear Structural Mechanics. wiley series in nonlinear science edn. Wiley-Vch (2004)
16. IEEE standard on piezoelectricity. IEEE 176 (1987)

On Higher Order Effective Boundary Conditions for a Coated Elastic Half-Space

Julius Kaplunov, Danila Prikazchikov and Leyla Sultanova

Abstract Higher order effective boundary conditions are derived for a coated half-space. Comparison with the long wavelength expansion of the exact solution of a plane time-harmonic problem for the coating demonstrates the validity of the proposed formulation. At the same time the corrections to the simplest leading order effective conditions, earlier obtained in the widely cited paper (Bövik (1996). J. Appl. Mech. 63(1), 162–167.) [1], are proven to be asymptotically inconsistent.

1 Introduction

Thin films and coatings find numerous applications, including in particular, engineering and biological sciences, see e.g. [2–5]. The effect of a thin coating is often modeled by imposing the so-called effective boundary conditions along the surface of a substrate. These conditions first were derived in [6] using *adhoc* assumptions originating from the classical theory of plate extensions. Later on, it was suggested in [1] that the results of [6] are not consistent, and refined boundary conditions were proposed starting from rather heuristic arguments. The asymptotic procedure exposed in [7] justifies at leading order the consistency of the effective boundary conditions in [6] and also reveals that the extra terms in [1] are in fact of a higher order. Moreover, as it was briefly mentioned in [7], the development in [1] is not asymptotically consistent at the next order as well.

J. Kaplunov (✉) · D. Prikazchikov · L. Sultanova
School of Computing and Mathematics, Keele University, Keele, UK
e-mail: j.kaplunov@keele.ac.uk

D. Prikazchikov
e-mail: d.prikazchikov@keele.ac.uk

L. Sultanova
e-mail: l.sultanova@keele.ac.uk

I. V. Andrianov et al. (eds.), *Problems of Nonlinear Mechanics and Physics of Materials*, Advanced Structured Materials 94,
https://doi.org/10.1007/978-3-319-92234-8_25

Fig. 1 A coated half-space

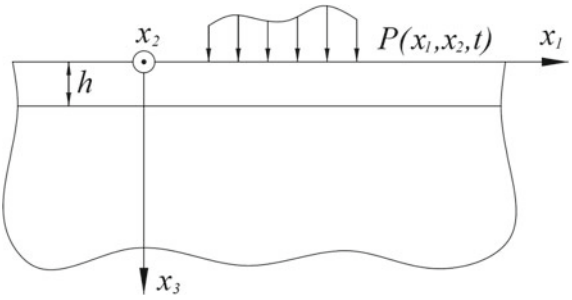

It is remarkable that the boundary conditions in [1] were exploited not only before but also after the publication of the critical comments in [7], e.g. see [8–10] along with [11–13]. This is partly an inspiration for revisiting the original problem for a coated elastic half-space aiming at establishing higher order effective conditions.

As in [7], we adapt the asymptotic methodology well established for the thin elastic structures, e.g. see [14, 15] and references therein. At leading order, we validate again the results in [6]. At next order, we arrive at refined effective conditions. They are tested by comparison with the exact solution of a plane strain time-harmonic problem. As it might be expected, the comparison demonstrates that the boundary conditions in [1] are not consistent at a higher order.

2 Statement of the Problem

We consider a linearly elastic isotropic layer of thickness h occupying the area $0 \le x_3 \le h$, lying on an elastic half-space $x_3 \ge h$. The prescribed vertical force $P = P(x_1, x_2, t)$ is acting on the free surface of the layer, see Fig. 1.

The 3D equations in linear elasticity can be written as

$$\begin{aligned} &\frac{\partial \sigma_{ii}}{\partial x_i} + \frac{\partial \sigma_{ij}}{\partial x_j} + \frac{\partial \sigma_{i3}}{\partial x_3} = \rho \frac{\partial^2 u_i}{\partial t^2}, \\ &\frac{\partial \sigma_{i3}}{\partial x_i} + \frac{\partial \sigma_{j3}}{\partial x_j} + \frac{\partial \sigma_{33}}{\partial x_3} = \rho \frac{\partial^2 u_3}{\partial t^2}. \end{aligned} \tag{1}$$

Here and below $i \ne j = 1, 2$ and $n = 1, 2, 3$, u_n are the displacements, σ_{in}, σ_{3n} are stresses, and ρ is the volume density. The constitutive relations are

$$\begin{aligned} &\sigma_{ij} = \mu \left(\frac{\partial u_i}{\partial x_j} + \frac{\partial u_j}{\partial x_i} \right), && \sigma_{ii} = (\lambda + 2\mu) \frac{\partial u_i}{\partial x_i} + \lambda \left(\frac{\partial u_j}{\partial x_j} + \frac{\partial u_3}{\partial x_3} \right), \\ &\sigma_{i3} = \sigma_{3i} = \mu \left(\frac{\partial u_i}{\partial x_3} + \frac{\partial u_3}{\partial x_i} \right), && \sigma_{33} = \lambda \left(\frac{\partial u_i}{\partial x_i} + \frac{\partial u_j}{\partial x_j} \right) + (\lambda + 2\mu) \frac{\partial u_3}{\partial x_3}, \end{aligned} \tag{2}$$

where λ and μ are the Lamé parameters. In addition, the wave speeds are given by

$$c_1 = \sqrt{\frac{\lambda + 2\mu}{\rho}}, \quad c_2 = \sqrt{\frac{\mu}{\rho}}. \tag{3}$$

In case of the coating, below we supply with suffix 0 the parameters in the Eqs. (1)–(3), using the notations ρ_0, λ_0, μ_0, c_{10} and c_{20}.

We impose the boundary conditions

$$\sigma_{33} = -P \quad \text{and} \quad \sigma_{i3} = 0 \tag{4}$$

at the surface of the coating $x_3 = 0$ and also assume continuity of the displacements u_n and stresses σ_{n3} along the interface $x_3 = h$.

The leading order effective boundary conditions on the surface of the substrate, modelling the effect of the coating, can be written as, see (3.18) in [7],

$$\begin{aligned} \sigma_{33} &= \rho_0 h \frac{\partial^2 u_3}{\partial t^2} - P, \\ \sigma_{i3} &= \rho_0 h \left[\frac{\partial^2 u_i}{\partial t^2} - c_{20}^2 \left(\frac{\partial^2 u_i}{\partial x_j^2} + 4(1 - \kappa_0^{-2}) \frac{\partial^2 u_i}{\partial x_i^2} + (3 - 4\kappa_0^{-2}) \frac{\partial^2 u_j}{\partial x_i \partial x_j} \right) \right], \end{aligned} \tag{5}$$

where $\kappa_0 = c_{10}/c_{20}$. In absence of surface loading ($P = 0$) these conditions coincide with those in [6] derived starting from the 2D theory of plate extension. More recent developments in [1], see also [9] treating a similar anisotropic problem, claim that the effective conditions (5) ignore several essential h-terms. The formulae (35) and (36) in [1] rewritten in the notation specified in this section, similarly to [7], can be presented as

$$\begin{aligned} \sigma_{33} &= \rho_0 h \frac{\partial^2 u_3}{\partial t^2} - \underline{h \left(\frac{\partial \sigma_{i3}}{\partial x_i} + \frac{\partial \sigma_{j3}}{\partial x_j} \right)}, \\ \sigma_{i3} &= \rho_0 h \left[\frac{\partial^2 u_i}{\partial t^2} - c_{20}^2 \left(\frac{\partial^2 u_i}{\partial x_j^2} + 4(1 - \kappa_0^{-2}) \frac{\partial^2 u_i}{\partial x_i^2} \right. \right. \\ &\quad \left. \left. + (3 - 4\kappa_0^{-2}) \frac{\partial^2 u_j}{\partial x_i \partial x_j} \right) \right] - \underline{h(1 - 2\kappa_0^{-2}) \frac{\partial \sigma_{33}}{\partial x_i}}. \end{aligned} \tag{6}$$

The underlined terms in formulae (6) do not appear in the effective conditions (5). The former may be also transformed to

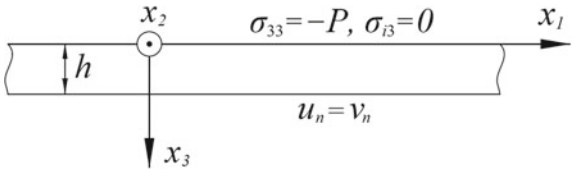

Fig. 2 Boundary value problem for a thin coating

$$\sigma_{33} = \rho_0 h \frac{\partial^2 u_3}{\partial t^2} - \rho_0 h^2 \left[\frac{\partial^3 u_i}{\partial t^2 \partial x_i} + \frac{\partial^3 u_j}{\partial t^2 \partial x_j} - c_{20}^2 \left(\frac{\partial^3 u_i}{\partial x_i \partial x_j^2} + \frac{\partial^3 u_j}{\partial x_i^2 \partial x_j} \right.\right.$$
$$\left.\left. +4(1-\kappa_0^{-2}) \left[\frac{\partial^3 u_i}{\partial x_i^3} + \frac{\partial^3 u_j}{\partial x_j^3} \right] + (3-4\kappa_0^{-2}) \left[\frac{\partial^3 u_j}{\partial x_i^2 \partial x_j} + \frac{\partial^3 u_i}{\partial x_i \partial x_j^2} \right] \right) \right]$$
$$+h^2(1-2\kappa_0^{-2}) \left(\frac{\partial^2 \sigma_{33}}{\partial x_i^2} + \frac{\partial^2 \sigma_{33}}{\partial x_j^2} \right), \tag{7}$$
$$\sigma_{i3} = \rho_0 h \left[\frac{\partial^2 u_i}{\partial t^2} - c_{20}^2 \left(\frac{\partial^2 u_i}{\partial x_j^2} + 4(1-\kappa_0^{-2}) \frac{\partial^2 u_i}{\partial x_i^2} + (3-4\kappa_0^{-2}) \frac{\partial^2 u_j}{\partial x_i \partial x_j} \right) \right]$$
$$-h^2(1-2\kappa_0^{-2}) \left(\rho_0 \frac{\partial^3 u_3}{\partial t^2 \partial x_i} - \left[\frac{\partial^2 \sigma_{i3}}{\partial x_i^2} + \frac{\partial^2 \sigma_{j3}}{\partial x_i \partial x_j} \right] \right).$$

It is already pretty clear at this stage that all extra h^2-terms in (7) can be neglected at leading order. In what follows, this observation is asymptotically justified. We also show below that h^2-terms in (7) are not identical to a proper asymptotic correction to (5).

3 Asymptotic Analysis

The aim of the paper is to determine an asymptotic correction to the leading order effective boundary conditions (5), in order to address consistency of (6), or equivalently, (7). Here we implement an asymptotic procedure similar to [7], modifying it slightly according to a more recent treatment in [16]. As usual, we study the boundary value problem for an elastic coating with the Dirichlet boundary conditions

$$u_n = v_n \tag{8}$$

at the interface $x_3 = h$, where $v_n = v_n(x_1, x_2, t)$ denote prescribed displacements, see Fig. 2.

We assume that the thickness of the coating h is small compared to typical wave length L, therefore, we introduce a geometric parameter given by

$$\varepsilon = \frac{h}{L} \ll 1. \tag{9}$$

We also specify dimensionless variables

$$\xi_i = \frac{x_i}{L}, \quad \eta = \frac{x_3}{h}, \quad \tau = \frac{t c_{20}}{L}. \tag{10}$$

According to the conventional asymptotic procedure, e.g. [7, 14], and ref. therein, we adopt the scaling

$$\begin{aligned} &u_n = L u_n^*, \qquad v_n = L v_n^*, \qquad P = \mu_0 \varepsilon p^* \\ &\sigma_{ii} = \mu_0 \sigma_{ii}^*, \quad \sigma_{ij} = \mu_0 \sigma_{ij}^*, \quad \sigma_{n3} = \mu_0 \varepsilon \sigma_{n3}^*, \end{aligned} \tag{11}$$

where all quantities with the asterisk are assumed to be of the same asymptotic order.

The Eq. (1) and the constitutive relations (2) rewritten in dimensionless form, become

$$\frac{\partial \sigma_{ii}^*}{\partial \xi_i} + \frac{\partial \sigma_{ij}^*}{\partial \xi_j} + \frac{\partial \sigma_{i3}^*}{\partial \eta} = \frac{\partial^2 u_i^*}{\partial \tau^2}, \tag{12}$$

$$\frac{\partial \sigma_{33}^*}{\partial \eta} + \varepsilon \left(\frac{\partial \sigma_{i3}^*}{\partial \xi_i} + \frac{\partial \sigma_{j3}^*}{\partial \xi_j} \right) = \frac{\partial^2 u_3^*}{\partial \tau^2}, \tag{13}$$

and

$$\sigma_{ij}^* = \frac{\partial u_i^*}{\partial \xi_j} + \frac{\partial u_j^*}{\partial \xi_i}, \tag{14}$$

$$\varepsilon \sigma_{ii}^* = (\kappa_0^2 - 2) \frac{\partial u_3^*}{\partial \eta} + \varepsilon \left(\kappa_0^2 \frac{\partial u_i^*}{\partial \xi_i} + (\kappa_0^2 - 2) \frac{\partial u_j^*}{\partial \xi_j} \right), \tag{15}$$

$$\varepsilon^2 \sigma_{i3}^* = \frac{\partial u_i^*}{\partial \eta} + \varepsilon \frac{\partial u_3^*}{\partial \xi_i}, \tag{16}$$

$$\varepsilon^2 \sigma_{33}^* = \kappa_0^2 \frac{\partial u_3^*}{\partial \eta} + \varepsilon (\kappa_0^2 - 2) \left(\frac{\partial u_i^*}{\partial \xi_i} + \frac{\partial u_j^*}{\partial \xi_j} \right), \tag{17}$$

with the transformed boundary conditions

$$\begin{aligned} &\sigma_{33}^* = -p^* \quad \text{and} \quad \sigma_{i3}^* = 0, \quad \eta = 0, \\ &\text{and} \\ &u_n^* = v_n^*, \quad \eta = 1. \end{aligned} \tag{18}$$

First, expressing $\dfrac{\partial u_3^*}{\partial \eta}$ from (17) and substituting the result into (15), we obtain

$$\sigma_{ii}^{*} = 4(1-\kappa_0^{-2})\frac{\partial u_i^{*}}{\partial \xi_i} + 2(1-2\kappa_0^{-2})\frac{\partial u_j^{*}}{\partial \xi_j} + (1-2\kappa_0^{-2})\varepsilon\sigma_{33}^{*}. \tag{19}$$

Next, we expand the displacements and stresses as

$$\begin{pmatrix} u_n^{*} \\ \sigma_{ii}^{*} \\ \sigma_{ij}^{*} \\ \sigma_{3i}^{*} \\ \sigma_{33}^{*} \end{pmatrix} = \begin{pmatrix} u_n^{(0)} \\ \sigma_{ii}^{(0)} \\ \sigma_{ij}^{(0)} \\ \sigma_{3i}^{(0)} \\ \sigma_{33}^{(0)} \end{pmatrix} + \varepsilon \begin{pmatrix} u_n^{(1)} \\ \sigma_{ii}^{(1)} \\ \sigma_{ij}^{(1)} \\ \sigma_{3i}^{(1)} \\ \sigma_{33}^{(1)} \end{pmatrix} + \varepsilon^2 \begin{pmatrix} u_n^{(2)} \\ \sigma_{ii}^{(2)} \\ \sigma_{ij}^{(2)} \\ \sigma_{3i}^{(2)} \\ \sigma_{33}^{(2)} \end{pmatrix} + \cdots \tag{20}$$

On substituting the latter into the Eqs. (12)–(17) and (19), we have at leading order

$$\begin{aligned} &\frac{\partial \sigma_{ii}^{(0)}}{\partial \xi_i} + \frac{\partial \sigma_{ij}^{(0)}}{\partial \xi_j} + \frac{\partial \sigma_{i3}^{(0)}}{\partial \eta} = \frac{\partial^2 u_i^{(0)}}{\partial \tau^2}, \\ &\frac{\partial \sigma_{33}^{(0)}}{\partial \eta} = \frac{\partial^2 u_3^{(0)}}{\partial \tau^2}, \\ &\sigma_{ij}^{(0)} = \frac{\partial u_i^{(0)}}{\partial \xi_j} + \frac{\partial u_j^{(0)}}{\partial \xi_i}, \\ &\frac{\partial u_n^{(0)}}{\partial \eta} = 0, \\ &\sigma_{ii}^{(0)} = 4(1-\kappa_0^{-2})\frac{\partial u_i^{(0)}}{\partial \xi_i} + 2(1-2\kappa_0^{-2})\frac{\partial u_j^{(0)}}{\partial \xi_j}, \end{aligned} \tag{21}$$

with the boundary conditions

$$\begin{aligned} &\sigma_{33}^{(0)} = -p^{*} \quad \text{and} \quad \sigma_{i3}^{(0)} = 0, \quad \eta = 0, \\ \text{and} \quad &u_n^{(0)} = v_n^{*}, \quad \eta = 1. \end{aligned} \tag{22}$$

Integrating the leading order Eq. (21) together with the boundary conditions (22), gives

$$u_n^{(0)} = v_n^{*}, \tag{23}$$

$$\sigma_{33}^{(0)} = \eta\frac{\partial^2 v_3^{*}}{\partial \tau^2} - p^{*}, \tag{24}$$

$$\sigma_{ii}^{(0)} = 4(1-\kappa_0^{-2})\frac{\partial v_i^{*}}{\partial \xi_i} + 2(1-2\kappa_0^{-2})\frac{\partial v_j^{*}}{\partial \xi_j}, \tag{25}$$

$$\sigma_{i3}^{(0)} = \eta\left[\frac{\partial^2 v_i^{*}}{\partial \tau^2} - \frac{\partial^2 v_i^{*}}{\partial \xi_j^2} - 4(1-\kappa_0^{-2})\frac{\partial^2 v_i^{*}}{\partial \xi_i^2} - (3-4\kappa_0^{-2})\frac{\partial^2 v_j^{*}}{\partial \xi_i \xi_j}\right]. \tag{26}$$

At next asymptotic order, the governing equations take the form

$$\frac{\partial \sigma_{ii}^{(1)}}{\partial \xi_i} + \frac{\partial \sigma_{ij}^{(1)}}{\partial \xi_j} + \frac{\partial \sigma_{i3}^{(1)}}{\partial \eta} = \frac{\partial^2 u_i^{(1)}}{\partial \tau^2}, \tag{27}$$

$$\frac{\partial \sigma_{33}^{(1)}}{\partial \eta} + \frac{\partial \sigma_{i3}^{(0)}}{\partial \xi_i} + \frac{\partial \sigma_{j3}^{(0)}}{\partial \xi_j} = \frac{\partial^2 u_3^{(1)}}{\partial \tau^2}, \tag{28}$$

$$\sigma_{ij}^{(1)} = \frac{\partial u_i^{(1)}}{\partial \xi_j} + \frac{\partial u_j^{(1)}}{\partial \xi_i}, \tag{29}$$

$$\sigma_{ii}^{(0)} = (\kappa_0^2 - 2)\frac{\partial u_3^{(1)}}{\partial \eta} + \kappa_0^2 \frac{\partial u_i^{(0)}}{\partial \xi_i} + (\kappa_0^2 - 2)\frac{\partial u_j^{(0)}}{\partial \xi_j}, \tag{30}$$

$$\frac{\partial u_i^{(1)}}{\partial \eta} + \frac{\partial u_3^{(0)}}{\partial \xi_i} = 0, \tag{31}$$

$$\kappa_0^2 \frac{\partial u_3^{(1)}}{\partial \eta} + (\kappa_0^2 - 2)\left(\frac{\partial u_i^{(0)}}{\partial \xi_i} + \frac{\partial u_j^{(0)}}{\partial \xi_j}\right) = 0, \tag{32}$$

$$\sigma_{ii}^{(1)} = 4(1 - \kappa_0^{-2})\frac{\partial u_i^{(1)}}{\partial \xi_i} + (1 - 2\kappa_0^{-2})\left(2\frac{\partial u_j^{(1)}}{\partial \xi_j} + \sigma_{33}^{(0)}\right), \tag{33}$$

with the boundary conditions

$$\sigma_{n3}^{(1)} = 0, \quad \eta = 0, \tag{34}$$

and

$$u_n^{(1)} = 0, \quad \eta = 1. \tag{35}$$

First, we obtain from (31) and (32), respectively, satisfying (35)

$$\begin{aligned} u_i^{(1)} &= (1 - \eta)\frac{\partial v_3^*}{\partial \xi_i}, \\ \text{and} \\ u_3^{(1)} &= (1 - 2\kappa_0^{-2})(1 - \eta)\left(\frac{\partial v_i^*}{\partial \xi_i} + \frac{\partial v_j^*}{\partial \xi_j}\right). \end{aligned} \tag{36}$$

Then, using (29), we have

$$\sigma_{ij}^{(1)} = 2(1 - \eta)\frac{\partial^2 v_3^*}{\partial \xi_i \partial \xi_j}. \tag{37}$$

Next, we deduce from (28) and (34)

$$\sigma_{33}^{(1)} = \frac{\eta}{\kappa_0^2}\left((\eta - 2 + \kappa_0^2 - \eta\kappa_0^2)\left[\frac{\partial^3 v_i^*}{\partial\xi_i\partial\tau^2} + \frac{\partial^3 v_j^*}{\partial\xi_j\partial\tau^2}\right] + 2\eta(\kappa_0^2 - 1)\left[\frac{\partial^3 v_i^*}{\partial\xi_i\partial\xi_j^2} + \frac{\partial^3 v_j^*}{\partial\xi_i^2\partial\xi_j} + \frac{\partial^3 v_i^*}{\partial\xi_i^3} + \frac{\partial^3 v_j^*}{\partial\xi_j^3}\right]\right). \tag{38}$$

As a result, (33) becomes

$$\sigma_{ii}^{(1)} = 2(\eta - 1)\left[2(\kappa_0^{-2} - 1)\frac{\partial^2 v_3^*}{\partial\xi_i^2} - (1 - 2\kappa_0^{-2})\frac{\partial^2 v_3^*}{\partial\xi_j^2}\right] + (1 - 2\kappa_0^{-2})\left[\eta\frac{\partial^2 v_3^*}{\partial\tau^2} - p^*\right]. \tag{39}$$

Therefore, (27) implies

$$\sigma_{i3}^{(1)} = -\eta\left[(\eta - 1 - \eta\kappa_0^{-2})\frac{\partial^3 v_3^*}{\partial\xi_i\partial\tau^2} + 2(\kappa_0^{-2} - 1)(\eta - 2)\left(\frac{\partial^3 v_3^*}{\partial\xi_i\partial\xi_j^2} + \frac{\partial^3 v_3^*}{\partial\xi_i^3}\right) - (1 - 2\kappa_0^{-2})\frac{\partial p^*}{\partial\xi_i}\right]. \tag{40}$$

Finally, substituting the leading order formulae (24) and (26) and $O(\varepsilon)$ corrections (38) and (40) into the expansions (20), we arrive at

$$\begin{aligned}
\sigma_{33}^* &= \eta\frac{\partial^2 v_3^*}{\partial\tau^2} - p^* + \varepsilon\frac{\eta}{\kappa_0^2}\left[(\eta - 2 + \kappa_0^2 - \eta\kappa_0^2)\left(\frac{\partial^3 v_i^*}{\partial\xi_i\partial\tau^2} + \frac{\partial^3 v_j^*}{\partial\xi_j\partial\tau^2}\right)\right. \\
&\left. + 2\eta(\kappa_0^2 - 1)\left(\frac{\partial^3 v_i^*}{\partial\xi_i\partial\xi_j^2} + \frac{\partial^3 v_j^*}{\partial\xi_i^2\partial\xi_j} + \frac{\partial^3 v_i^*}{\partial\xi_i^3} + \frac{\partial^3 v_j^*}{\partial\xi_j^3}\right)\right] + \ldots, \\
\sigma_{i3}^* &= \eta\left[\frac{\partial^2 v_i^*}{\partial\tau^2} - \frac{\partial^2 v_i^*}{\partial\xi_j^2} - 4(1 - \kappa_0^{-2})\frac{\partial^2 v_i^*}{\partial\xi_i^2} - (3 - 4\kappa_0^{-2})\frac{\partial^2 v_j^*}{\partial\xi_i\xi_j}\right] \\
&- \varepsilon\eta\left[(\eta - 1 - \eta\kappa_0^{-2})\frac{\partial^3 v_3^*}{\partial\xi_i\partial\tau^2} + 2(\kappa_0^{-2} - 1)(\eta - 2)\right. \\
&\left.\left(\frac{\partial^3 v_3^*}{\partial\xi_i\partial\xi_j^2} + \frac{\partial^3 v_3^*}{\partial\xi_i^3}\right) - (1 - 2\kappa_0^{-2})\frac{\partial p^*}{\partial\xi_i}\right] + \ldots.
\end{aligned} \tag{41}$$

The continuity of the displacements, see (8), and stresses at the interface $x_3 = h$ readily results in refined effective boundary conditions for the substrate $x_3 \geq h$. In the original variables they take the form

$$\begin{aligned}\sigma_{33} &= \rho_0 h\frac{\partial^2 u_3}{\partial t^2} - P + \frac{\rho_0 h^2}{\kappa_0^2}\left[2c_2^2(\kappa_0^2-1)\left(\frac{\partial^3 u_i}{\partial x_i \partial x_j^2} + \frac{\partial^3 u_j}{\partial x_i^2 \partial x_j}\right.\right.\\ &\quad \left.\left. + \frac{\partial^3 u_i}{\partial x_i^3} + \frac{\partial^3 u_j}{\partial x_j^3}\right) - \left(\frac{\partial^3 u_i}{\partial x_i \partial t^2} + \frac{\partial^3 u_j}{\partial x_j \partial t^2}\right)\right],\\ \sigma_{i3} &= \rho_0 h\left[\frac{\partial^2 u_i}{\partial t^2} - c_{20}^2\left(\frac{\partial^2 u_i}{\partial x_j^2} + 4(1-\kappa_0^{-2})\frac{\partial^2 u_i}{\partial x_i^2} + (3-4\kappa_0^{-2})\frac{\partial^2 u_j}{\partial x_i \partial x_j}\right)\right]\\ &\quad + \frac{\rho_0 h^2}{\kappa_0^2}\left[\frac{\partial^3 u_3}{\partial x_i \partial t^2} + 2c_2^2(1-\kappa_0^2)\left(\frac{\partial^3 u_3}{\partial x_i \partial x_j^2} + \frac{\partial^3 u_3}{\partial x_i^3}\right)\right] + h\frac{\kappa_0^2 - 2}{\kappa_0^2}\frac{\partial P}{\partial x_i}.\end{aligned} \tag{42}$$

Comparing these formulae at $P = 0$ with (7) we may expect that higher order h^2-terms will not coincide.

4 Comparison with the Exact Solution of a Plane Strain Problem

In order to validate the asymptotic results obtained in the previous section, let us consider a time-harmonic plane strain problem for the coating over the plane Ox_1x_3. In this case the displacements can be taken as

$$u_1 = \frac{\partial \varphi}{\partial x_1} + \frac{\partial \psi}{\partial x_3}, \quad u_3 = \frac{\partial \varphi}{\partial x_3} - \frac{\partial \psi}{\partial x_1}, \tag{43}$$

where φ and ψ are Lamé elastic potentials. The wave equations of motion become

$$\Delta\varphi - \frac{1}{c_{10}^2}\frac{\partial^2 \varphi}{\partial t^2} = 0, \quad \Delta\psi - \frac{1}{c_{20}^2}\frac{\partial^2 \psi}{\partial t^2} = 0, \tag{44}$$

where $\Delta = \dfrac{\partial^2}{\partial x_1^2} + \dfrac{\partial^2}{\partial x_3^2}$. The solutions of (44) are sought for in the form

$$\varphi = f(x_3)\mathrm{e}^{ik(x_1 - ct)}, \quad \psi = g(x_3)\mathrm{e}^{ik(x_1 - ct)}. \tag{45}$$

Substituting the latter into (44), we deduce

$$f(x_3) = A_1\mathrm{e}^{kx_3\alpha} + A_2\mathrm{e}^{-kx_3\alpha} \quad \text{and} \quad g(x_3) = A_3\mathrm{e}^{kx_3\beta} + A_4\mathrm{e}^{-kx_3\beta}, \tag{46}$$

where A_m, $m = 1, 2, 3, 4$, are arbitrary constants, and $\alpha = \sqrt{1 - \dfrac{c^2}{c_{10}^2}}$ and $\beta = \sqrt{1 - \dfrac{c^2}{c_{20}^2}}$.

We consider a traction free upper face ($P = 0$), i.e. at $x_3 = 0$

$$\sigma_{k3} = 0, \quad k = 1, 3, \tag{47}$$

imposing the boundary conditions (8) at the lower face $x_3 = h$ with

$$v_k = hB_k \mathrm{e}^{ik(x_1 - ct)}, \tag{48}$$

where B_k are certain prescribed values.

On satisfying the boundary conditions, we have

$$\begin{pmatrix} i\alpha & -i\alpha & \gamma^2 & \gamma^2 \\ \gamma^2 & \gamma^2 & -i\beta & i\beta \\ ik\mathrm{e}^{kh\alpha} & ik\mathrm{e}^{-kh\alpha} & \beta k\mathrm{e}^{kh\beta} & -\beta k\mathrm{e}^{-kh\beta} \\ \alpha k\mathrm{e}^{kh\alpha} & -\alpha k\mathrm{e}^{-kh\alpha} & -ik\mathrm{e}^{kh\beta} & -ik\mathrm{e}^{-kh\beta} \end{pmatrix} \begin{pmatrix} A_1 \\ A_2 \\ A_3 \\ A_4 \end{pmatrix} = \begin{pmatrix} 0 \\ 0 \\ hB_1 \\ hB_3 \end{pmatrix} \tag{49}$$

where $\gamma = \sqrt{1 - \dfrac{1}{2}\dfrac{c^2}{c_{20}^2}}$, and coefficients A_m expressed through the given constants B_k are presented in Appendix.

Then, substituting (45) and (46) into (43), we get

$$\begin{aligned} u_1 &= k\left[\beta(A_3\mathrm{e}^{2kx_3\beta} - A_4)\mathrm{e}^{-kx_3\beta} + i(A_1\mathrm{e}^{2kx_3\alpha} + A_2)\mathrm{e}^{-kx_3\alpha}\right], \\ u_3 &= k\left[\alpha(A_1\mathrm{e}^{2kx_3\alpha} - A_2)\mathrm{e}^{-kx_3\alpha} - i(A_3\mathrm{e}^{2kx_3\beta} + A_4)\mathrm{e}^{-kx_3\beta}\right]. \end{aligned} \tag{50}$$

Here and below the factor $\mathrm{e}^{ik(x_1 - ct)}$ is omitted. Next, using the expressions above and the constitutive relations (2), we have for the stresses at $x_3 = h$

$$\begin{aligned} \sigma_{33} &= 2\mu_0 k^2\left[\gamma^2(A_1\mathrm{e}^{2kh\alpha} + A_2)\mathrm{e}^{-kh\alpha} - i\beta(A_3\mathrm{e}^{2kh\beta} - A_4)\mathrm{e}^{-kh\beta}\right], \\ \sigma_{13} &= 2\mu_0 k^2\left[\gamma^2(A_3\mathrm{e}^{2kh\beta} + A_4)\mathrm{e}^{-kh\beta} + i\alpha(A_1\mathrm{e}^{2kh\alpha} - A_2)\mathrm{e}^{-kh\alpha}\right]. \end{aligned} \tag{51}$$

The last expressions can be expanded into asymptotic series in the small parameter $\varepsilon = kh \ll 1$ $\left(L = k^{-1} \text{ in } (9)\right)$ to get

$$\begin{aligned} \frac{\sigma_{33}}{\varepsilon^2\mu_0} &= -B_3\zeta^2 - iB_1\left[2 - \kappa_0^{-2}(2 + \zeta^2)\right]\varepsilon + \cdots, \\ \frac{\sigma_{13}}{\varepsilon^2\mu_0} &= B_1\left[4(1 - \kappa_0^{-2}) - \zeta^2\right] + iB_3\left[2 - \kappa_0^{-2}(2 + \zeta^2)\right]\varepsilon \\ &\quad - \frac{B_1}{3}\left[20 + \zeta^2(\zeta^2 - 8) + \kappa_0^{-2}(6\zeta^2 - 44) + 4\kappa_0^{-4}(\zeta^2 + 6)\right]\varepsilon^2 + \cdots, \end{aligned} \tag{52}$$

where the dimensionless velocity is

$$\zeta = \frac{c}{c_{20}}. \tag{53}$$

The asymptotic effective conditions (42) for the same displacements (48) prescribed at the lower face, become

$$\begin{aligned}
\sigma_{33} &= k^2h^2\rho_0\left[-B_3c^2 - iB_1kh\left[2c_{20}^2 - \kappa_0^{-2}(2c_{20}^2 + c^2)\right]\right],\\
\sigma_{13} &= k^2h^2\rho_0\left[B_1\left[4c_{20}^2(1-\kappa_0^{-2}) - c^2\right] + iB_3kh\left[2c_{20}^2 - \kappa_0^{-2}(2c_{20}^2 + c^2)\right]\right],
\end{aligned} \tag{54}$$

or, rewritten in terms of ε and ζ,

$$\begin{aligned}
\frac{\sigma_{33}}{\varepsilon^2\mu_0} &= -B_3\zeta^2 - iB_1\left[2 - \kappa_0^{-2}(2+\zeta^2)\right]\varepsilon,\\
\frac{\sigma_{13}}{\varepsilon^2\mu_0} &= B_1\left[4(1-\kappa_0^{-2}) - \zeta^2\right] + iB_3\left[2 - \kappa_0^{-2}(2+\zeta^2)\right]\varepsilon.
\end{aligned} \tag{55}$$

These formulae coincide with the two-term expansion of the exact solution (52). Thus, the validity of the asymptotic results in Sect. 3 is confirmed.

Let us now test the conditions in [1] in a similar manner. In case of the displacements (48) the relation (6) takes the form

$$\begin{aligned}
\sigma_{33} &= -\frac{h^2\rho_0\left[iB_1k^3h(4c_{20}^2 - c^2) + B_3c^2k^2\right]}{1 + k^2h^2(1-2\kappa_0^{-2})},\\
\sigma_{13} &= \frac{h^2\rho_0\left[B_1k^2(4c_{20}^2(1-\kappa_0^2) - c^2) + iB_3kh(1-2\kappa_0^{-2})\right]}{1 + k^2h^2(1-2\kappa_0^{-2})},
\end{aligned} \tag{56}$$

or, expanding the latter in ε,

$$\begin{aligned}
\frac{\sigma_{33}}{\varepsilon^2\mu_0} &= -B_3\zeta^2 - iB_1\left[4(1-\kappa_0^{-2}) - \zeta^2\right]\varepsilon + B_3\zeta^2(1-2\kappa_0^{-2})\varepsilon^2 + \cdots,\\
\frac{\sigma_{13}}{\varepsilon^2\mu_0} &= B_1\left[4(1-\kappa_0^{-2}) - \zeta^2\right] + iB_3\zeta^2(1-2\kappa_0^{-2})\varepsilon\\
&\quad + B_1(1-2\kappa_0^{-2})\left[4(\kappa_0^{-2}-1) + \zeta^2\right]\varepsilon^2 + \cdots.
\end{aligned} \tag{57}$$

These conditions coincide with the asymptotic expansion of the exact solution (52) only at leading order. This means that the effect of the underlined terms in (6) appears only at next order; in doing so, it is different from $O(\varepsilon)$ correction in the asymptotic expansion (52). As an illustration, in Fig. 3 for $\nu = 0.3$ we plot the normalized coefficients χ_{k3}^E and χ_{k3}^B, $k = 1, 3$, at ε-terms in (52) and (57). They are

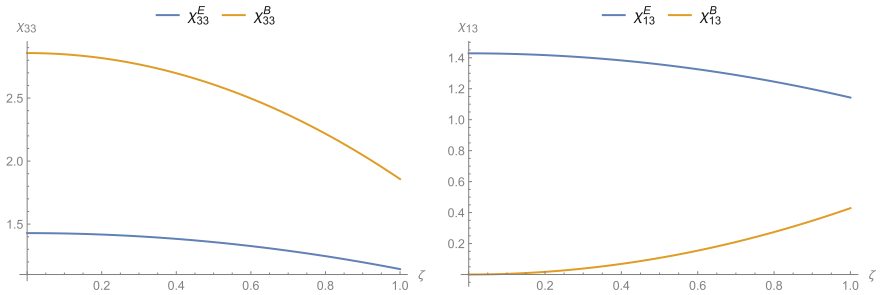

Fig. 3 Comparison of coefficients at ε-terms

$$\begin{aligned} \chi^E_{33} &= 2-\kappa_0^{-2}(2+\zeta^2), \quad \chi^B_{33} = 4(1-\kappa_0^{-2})-\zeta^2, \\ \chi^E_{13} &= 2-\kappa_0^{-2}(2+\zeta^2), \quad \chi^B_{13} = \zeta^2(1-2\kappa_0^{-2}). \end{aligned} \tag{58}$$

5 Conclusion

In this paper, we derive an asymptotic correction to the leading order effective boundary conditions for a coated elastic half-space. The derived conditions are tested by comparison with the exact solution of a plane time-harmonic problem. As a result, the formulation in [6] is validated at leading order, whereas its corrections proposed in [1] appears to be asymptotically inconsistent. The obtained conditions are of general interest for elastodynamics, e.g. for developing refined asymptotic models for surface waves, see [17, 18]. The latter provide a useful framework for modelling coated solids subject to high-speed moving loads, see [19, 20].

Acknowledgements This work has been supported by the Ministry of Education and Science of the Republic of Kazakhstan, Grant IRN AP05132743. The Keele University ACORN Scholarship for L. Sultanova is also gratefully acknowledged.

Appendix

The constants in (49) are

$$A_1 = h\frac{N_1}{D}, \quad A_2 = \mathrm{e}^{kh\alpha}h\frac{N_2}{D}, \quad A_3 = -h\frac{N_3}{D}, \quad A_4 = -\mathrm{e}^{kh\beta}h\frac{N_4}{D}, \tag{59}$$

where

$$
\begin{aligned}
N_1 &= iB_1\left(\mathrm{e}^{kh\alpha}(D_1\alpha\beta + D_2\gamma^4) - 2\mathrm{e}^{kh\beta}\alpha\beta\gamma^2\right)\\
&\quad -B_3\beta\left(\mathrm{e}^{kh\alpha}(D_2\alpha\beta + D_1\gamma^4) - 2\mathrm{e}^{kh\beta}\gamma^2\right),\\
N_2 &= iB_1\left(D_1\alpha\beta - 2\mathrm{e}^{kh(\alpha+\beta)}\alpha\beta\gamma^2 - \gamma^4 D_2\right)\\
&\quad +B_3\beta\left(D_1\gamma^4 - D_2\alpha\beta - 2\mathrm{e}^{kh(\alpha+\beta)}\gamma^2\right),\\
N_3 &= iB_3\left(\mathrm{e}^{kh\beta}(D_3\alpha\beta + D_4\gamma^4) - 2\mathrm{e}^{kh\alpha}\alpha\beta\gamma^2\right)\\
&\quad +B_1\alpha\left(\mathrm{e}^{kh\beta}(D_4\alpha\beta + D_3\gamma^4) - 2\mathrm{e}^{kh\alpha}\gamma^2\right),\\
N_4 &= iB_3\left(D_3\alpha\beta - 2\mathrm{e}^{kh(\alpha+\beta)}\alpha\beta\gamma^2 - \gamma^4 D_4\right)\\
&\quad -B_1\alpha\left(D_3\gamma^4 - D_4\alpha\beta - 2\mathrm{e}^{kh(\alpha+\beta)}\gamma^2\right),
\end{aligned}
\tag{60}
$$

and

$$
D = k\left[8\mathrm{e}^{kh(\alpha+\beta)}\alpha\beta\gamma^2 + D_2D_4(\alpha^2\beta^2+\gamma^4) - D_1D_3\alpha\beta(1+\gamma^4)\right],
$$

with

$$
D_1 = 1+\mathrm{e}^{2kh\beta},\quad D_2 = 1-\mathrm{e}^{2kh\beta},\quad D_3 = 1+\mathrm{e}^{2kh\alpha},\quad D_4 = 1-\mathrm{e}^{2kh\alpha}. \tag{61}
$$

References

1. Bövik, P.: A comparison between the Tiersten model and O(h) boundary conditions for elastic surface waves guided by thin layers. J. Appl. Mech. **63**(1), 162–167 (1996)
2. Chattopadhyay, D.K., Raju, K.: Structural engineering of polyurethane coatings for high performance applications. Prog. Polym. Sci. **32**(3), 352–418 (2007)
3. Hauert, R.: A review of modified DLC coatings for biological applications. Diam. Relat. Mater. **12**(3–7), 583–589 (2003)
4. Padture, N.P., Gell, M., Jordan, E.H.: Thermal barrier coatings for gas-turbine engine applications. Science **296**(5566), 280–284 (2002)
5. Veprek, S., Veprek-Heijman, M.J.: Industrial applications of superhard nanocomposite coatings. Surf. Coat. Technol. **202**(21), 5063–5073 (2008)
6. Tiersten, H.: Elastic surface waves guided by thin films. J. Appl. Phys. **40**(2), 770–789 (1969)
7. Dai, H.H., Kaplunov, J., Prikazchikov, D.: A long-wave model for the surface elastic wave in a coated half-space. Proc. R. Soc. Lond. A Math. Phys. Eng. Sci. **466**, 3097–3116 (2010). The Royal Society
8. Malischewsky, P.G., Scherbaum, F.: Love's formula and H/V-ratio (ellipticity) of Rayleigh waves. Wave Motion **40**(1), 57–67 (2004)
9. Niklasson, A.J., Datta, S.K., Dunn, M.L.: On approximating guided waves in plates with thin anisotropic coatings by means of effective boundary conditions. J. Acoust. Soc. Am. **108**(3), 924–933 (2000)
10. Wang, J., Du, J., Lu, W., Mao, H.: Exact and approximate analysis of surface acoustic waves in an infinite elastic plate with a thin metal layer. Ultrasonics **44**, e941–e945 (2006)
11. Godoy, E., Durán, M., Nédélec, J.C.: On the existence of surface waves in an elastic half-space with impedance boundary conditions. Wave Motion **49**(6), 585–594 (2012)
12. Pham, C.V., Vu, A.: Effective boundary condition method and approximate secular equations of Rayleigh waves in orthotropic half-spaces coated by a thin layer. J. Mech. Mater. Struct. **11**(3), 259–277 (2016)
13. Vinh, P.C., Xuan, N.Q.: Rayleigh waves with impedance boundary condition: formula for the velocity, existence and uniqueness. Eur. J. Mech.-A/Solids **61**, 180–185 (2017)
14. Aghalovyan, L.: Asymptotic Theory of Anisotropic Plates and Shells. World Scientific (2015)
15. Andrianov, I.V., Awrejcewicz, J., Manevitch, L.I.: Asymptotical Mechanics of Thin-Walled Structures. Springer Science and Business Media (2013)

16. Chebakov, R., Kaplunov, J., Rogerson, G.: Refined boundary conditions on the free surface of an elastic half-space taking into account non-local effects. Proc. R. Soc. Lond. A Math. Phys. Eng. Sci. **472**, 20150800 (2016). The Royal Society
17. Kaplunov, J., Prikazchikov, D.: Explicit models for surface, interfacial and edge waves. In: Craster, R., Kaplunov, J. (eds.) Dynamic Localization Phenomena in Elasticity, Acoustics and Electromagnetism, vol. 547, pp. 73–114. Springer, Berlin (2013)
18. Kaplunov, J., Prikazchikov, D.A.: Asymptotic theory for Rayleigh and Rayleigh-type waves. Adv. Appl. Mech. **50**, 1–106 (2017)
19. Erbaş, B., Kaplunov, J., Prikazchikov, D.A., Şahin, O.: The near-resonant regimes of a moving load in a three-dimensional problem for a coated elastic half-space. Math. Mech. Solids **22**(1), 89–100 (2017)
20. Kaplunov, J., Prikazchikov, D., Erbaş, B., Şahin, O.: On a 3D moving load problem for an elastic half space. Wave Motion **50**(8), 1229–1238 (2013)

Electrically Plane and Mechanically Antiplane Problem for an Inclusion with Stepwise Rigidity Between Piezoelectric Materials

Vladimir V. Loboda, Anna G. Kryvoruchko and Alla Ye. Sheveleva

Abstract An electrically insulated inclusion at the interface of two piezoelectric semi-infinite spaces under the action of antiplane mechanical and in-plane electric loadings is analyzed. One zone of the inclusion is absolutely rigid while the other part is mechanically soft. This problem is important for practical applications, but it has not been solved earlier at least in an analytical way. The presentations of all electro-mechanical quantities via sectionally-analytic vector-functions are obtained. With use of these presentations, the combined Dirichlet-Riemann boundary value problem is formulated and an exact analytical solution of this problem is found. On the base of this solution, the closed form analytical expressions for the required electro-mechanical quantities along the interface are derived. Particularly the stress jump along the mechanically rigid part of the inclusion is found and additionally the variation of this stress along its upper face is also given. The values of electromechanical quantities along the corresponding parts of the material interface are presented graphically. Singular points of the shear stress, strain and also the electric displacement and field are found and the corresponding intensity factors are determined. The dependence of the stress intensity factor on the intensity of the electric displacement and the relation of the rigid and soft zone lengths is investigated.

Keywords Piezoelectric material · Inclusion · Interface · Analytical solution

V. V. Loboda (✉) · A. G. Kryvoruchko
Department of Theoretical and Computational Mechanics, Oles Honchar Dnipro National University, Gagarin Avenue, 72, 49010 Dnipro, Ukraine
e-mail: loboda@dsu.dp.ua; lobvv@ua.fm

A. G. Kryvoruchko
e-mail: anna.kr@gmail.com

A. Ye. Sheveleva
Department of Computational Mathematics, Oles Honchar Dnipro National University, Gagarin Avenue, 72, 49010 Dnipro, Ukraine
e-mail: Shevelevaae@dnu.dp.ua

I. V. Andrianov et al. (eds.), *Problems of Nonlinear Mechanics and Physics of Materials*, Advanced Structured Materials 94,
https://doi.org/10.1007/978-3-319-92234-8_26

1 Introduction

Piezoelectric materials exhibit practically useful phenomenon because they produce an electric field when being deformed and undergo deformation when subjected to an electric field. Due to this intrinsic electro-mechanical coupling behaviour, piezoelectric materials have been widely used in modern technologies as sensors and actuators, being often adhered to substrates or embedded in polymer matrices. It is well known that piezoelectric ceramics are very brittle and susceptible to fracture. Although certain critical conditions might lead to the crack growth and propagation into the matrix, in many cases because of interface defects, e.g. interface inclusions, the fracture appear and grow from these defects leading to a progressive debonding. This important phenomenon has attracted certain attention in the scientific literature.

A conducting rigid line inclusion at the interface of two bonded piezoelectric materials was considered by Deng and Meguid [1]. Combining the analytic function theory and Stroh formalism the closed-form expressions for the field variables were found. The generalized two-dimensional problem of a dielectric rigid line inclusion, at the interface between two dissimilar piezoelectric media subjected to piecewise uniform loads at infinity, is studied by means of the Stroh theory by Gao and Fan [3]. The problem was reduced to the Hilbert problem and the closed-form expressions were obtained. The mixed boundary value problem for a debonded electrically conducting rigid line inclusion situated at the interface of two piezoelectric half planes was considered analytically by Wang and Shen [12] with use of the Stroh formalism. The model based on the assumption that all of the physical variables, i.e., tractions, displacements, normal component of electric displacements and electric potential, are discontinuous across the interface defect was analyzed in this work. An axisymmetric contact problem of a rigid inclusion embedded in the piezoelectric bimaterial frictionless interface under the action of far-field compression and electric displacement was studied by Eskandari et al. [2]. An arc-shaped conducting rigid line inclusion situated between a circular piezoelectric inhomogeneity and an unbounded piezoelectric matrix subjected to the uniform anti-plane shear stresses and in-plane electric fields at the infinity was considered by Wang and Schiavone [11].

It is worth to be noted that the mentioned results concerning the rigid inclusions at the interface between piezoelectric materials are obtained under the assumption that the inclusion is rigid along all it length. However in some cases important for practical applications the inclusion's rigidity can change from one its part to another. The mathematical model in such case becomes much more complicated, therefore, the associated analytical solutions has not been obtained yet to the authors knowledge. This important case of interface inclusion is studied in present paper and exact analytical solution for this case is obtained.

2 Basic Equations for a Piezoelectric Material Under Out-of-Plane Mechanical Loading and In-Plane Electric Loading

Constitutive relations for a linear piezoelectric material in the absence of body forces and free charges can be presented in the form by Pak [10]:

$$\Pi_{iJ} = E_{iJKl}\, V_{K,l}, \tag{1}$$

$$\Pi_{iJ,i} = 0, \tag{2}$$

where

$$V_K = \begin{cases} u_k, & K = 1, 2, 3, \\ \varphi, & K = 4, \end{cases} \tag{3}$$

$$\Pi_{iJ} = \begin{cases} \sigma_{ij}, & i, J = 1, 2, 3, \\ D_i, & i = 1, 2, 3;\ J = 4, \end{cases} \tag{4}$$

$$E_{iJKl} = \begin{cases} c_{ijkl}, & J, K = 1, 2, 3, \\ e_{lij}, & J = 1, 2, 3;\ K = 4, \\ e_{ikl}, & K = 1, 2, 3;\ J = 4, \\ -\varepsilon_{il}, & J = K = 4, \end{cases} \tag{5}$$

and u_k, φ, σ_{ij}, D_i are the elastic displacements, electric potential, stresses and electric displacements, respectively. Furthermore, c_{ijkl}, e_{lij} and ε_{ij} are the elastic, piezoelectric and dielectric constants, respectively. Small subscripts in (1)–(5) and afterwards are always running from 1 to 3, capital subscripts are ranging from 1 to 4 and Einstein's summation convention is used in (1), (2).

For the out-of-plane mechanical loading and in-plane electric loading assuming the material is transversely isotropic with the poling direction parallel to the x_3-axis one has

$$u_1 = u_2 = 0,\ u_3 = u_3(x_1, x_2),\ \varphi = \varphi(x_1, x_2).$$

Then using the contracted notation, whereby a pair of indices is changed into a single index according to the rule: $\underline{11} \to 1$, $\underline{22} \to 2$, $\underline{33} \to 3$, $\underline{23}$ or $\underline{32} \to 4$, $\underline{13}$ or $\underline{31} \to 5$, $\underline{12}$ or $\underline{21} \to 6$, the constitutive relations take the form:

$$\begin{Bmatrix} \sigma_{i3} \\ D_i \end{Bmatrix} = \mathbf{R} \begin{Bmatrix} u_{3,i} \\ \varphi_{,i} \end{Bmatrix}, \tag{6}$$

where $i = 1, 2$ and $\mathbf{R} = \begin{bmatrix} c_{44} & e_{15} \\ e_{15} & -\alpha_{11} \end{bmatrix}$.

Introducing the vectors

$$\boldsymbol{u} = [u_3, \varphi]^T, \ \boldsymbol{t} = [\sigma_{23}, D_2]^T, \tag{7}$$

one can write

$$\boldsymbol{t} = \mathbf{R}\boldsymbol{u}_{,2}. \tag{8}$$

Because u_3 and φ satisfy the equations $\Delta u_3 = 0, \ \Delta\varphi = 0$, i.e. they are harmonic, the vector $\boldsymbol{u}$ can be presented in the form

$$\boldsymbol{u} = 2\,\mathrm{Re}\,\boldsymbol{\Phi}(z) = \boldsymbol{\Phi}(z) + \overline{\boldsymbol{\Phi}}(\bar{z}), \tag{9}$$

where $\boldsymbol{\Phi}(z) = [\Phi_1(z), \ \Phi_2(z)]^T$ is an arbitrary analytic function of the complex variable $z = x_1 + ix_2$.

Substituting (9) in (8) and using the designation $\mathbf{Q} = i\mathbf{R}$, we arrive to the equations

$$\boldsymbol{t} = \mathbf{Q}\boldsymbol{\Phi}'(z) + \overline{\mathbf{Q}}\,\overline{\boldsymbol{\Phi}}'(\bar{z}). \tag{10}$$

Transform further the presentations (9) and (10). Taking into account that

$$\boldsymbol{u}' = \boldsymbol{\Phi}'(z) + \overline{\boldsymbol{\Phi}}'(\bar{z})$$

and introducing the vectors

$$\mathbf{v}' = [\sigma_{32}, -E_1]^T, \ \boldsymbol{P} = \left[u_3', D_2\right]^T, \tag{11}$$

one arrives to the following relations

$$\mathbf{v}' = \mathbf{A}\boldsymbol{\Phi}'(z) + \overline{\mathbf{A}}\,\overline{\boldsymbol{\Phi}}'(\bar{z}), \tag{12}$$

$$\boldsymbol{P} = \mathbf{B}\boldsymbol{\Phi}'(z) + \overline{\mathbf{B}}\,\overline{\boldsymbol{\Phi}}'(\bar{z}), \tag{13}$$

where $E_1 = \partial\varphi/\partial x_1$ is the electric field in the direction x_1 and the matrixes $\mathbf{A}$ and $\mathbf{B}$ have the form

$$\mathbf{B} = \begin{bmatrix} 1 & 0 \\ Q_{21} & Q_{22} \end{bmatrix}, \ \mathbf{A} = \begin{bmatrix} Q_{11} & Q_{12} \\ 0 & 1 \end{bmatrix}.$$

3 Bimaterial Case

Suppose that the plane (x_1, x_2) is composed of two half-planes $x_2 > 0$ and $x_2 < 0$. The presentation (12), (13) can be written for regions $x_2 > 0$ and $x_2 < 0$ in the form

$$\mathbf{v}^{(m)} = \mathbf{A}^{(m)}\boldsymbol{\Phi}^{(m)}(z) + \overline{\mathbf{A}}^{(m)}\overline{\boldsymbol{\Phi}}^{(m)}(\bar{z}), \quad \boldsymbol{P}^{(m)} = \mathbf{B}^{(m)}\boldsymbol{\Phi}'^{(m)}(z) + \overline{\mathbf{B}}^{(m)}\overline{\boldsymbol{\Phi}}'^{(m)}(\bar{z}), \tag{14}$$

where $m = 1$ for the region 1 and $m = 2$ for the region 2; $\mathbf{A}^{(m)}$ and $\mathbf{B}^{(m)}$ are the matrices $\mathbf{A}$ and $\mathbf{B}$ for the regions 1 and 2, respectively; $\boldsymbol{\Phi}^{(m)}(z)$ are arbitrary vector-functions, analytic in the regions 1 and 2, respectively.

Next we require that the equality $\boldsymbol{P}^{(1)} = \boldsymbol{P}^{(2)}$ holds true on the entire axis x_1.Then it follows from (14)

$$\mathbf{B}^{(1)}\boldsymbol{\Phi}'^{(1)}(x_1 + i0) + \overline{\mathbf{B}}^{(1)}\overline{\boldsymbol{\Phi}}'^{(1)}(x_1 - i0) = \mathbf{B}^{(2)}\boldsymbol{\Phi}'^{(2)}(x_1 - i0) + \overline{\mathbf{B}}^{(2)}\overline{\boldsymbol{\Phi}}'^{(2)}(x_1 + i0). \tag{15}$$

Here and thereafter a designation $F(x_1 \pm i0)$ means the limit value of a function $F(z)$ at $y \to 0$ from above or below of the x_1-axis, respectively. The Eq. (15) can be written as

$$\mathbf{B}^{(1)}\boldsymbol{\Phi}'^{(1)}(x_1 + i0) - \overline{\mathbf{B}}^{(2)}\boldsymbol{\Phi}'^{(2)}(x_1 + i0) = \mathbf{B}^{(2)}\boldsymbol{\Phi}'^{(2)}(x_1 - i0) - \overline{\mathbf{B}}^{(1)}\boldsymbol{\Phi}'^{(1)}(x_1 - i0).$$

The left and right sides of the last equation can be considered as the boundary values of the functions

$$\mathbf{B}^{(1)}\boldsymbol{\Phi}'^{(1)}(z) - \overline{\mathbf{B}}^{(2)}\boldsymbol{\Phi}'^{(2)}(z) \text{ and } \mathbf{B}^{(2)}\boldsymbol{\Phi}'^{(2)}(z) - \overline{\mathbf{B}}^{(1)}\boldsymbol{\Phi}'^{(1)}(z). \tag{16}$$

Due to last functions are analytic in the upper and lower planes, respectively, and using Liouville's theorem we find that each of these functions is equal to 0 for any z from the corresponding half-plane. Hence, we obtain

$$\overline{\boldsymbol{\Phi}}'^{(2)}(z) = \left(\overline{\mathbf{B}}^{(2)}\right)^{-1}\mathbf{B}^{(1)}\boldsymbol{\Phi}'^{(1)}(z) \text{ for } x_2 > 0, \tag{17}$$

$$\overline{\boldsymbol{\Phi}}'^{(1)}(z) = \left(\overline{\mathbf{B}}^{(1)}\right)^{-1}\mathbf{B}^{(2)}\boldsymbol{\Phi}'^{(2)}(z) \text{ for } x_2 < 0. \tag{18}$$

Further, we find the jump of the vector-function

$$\left\langle \mathbf{v}'(x_1) \right\rangle = \mathbf{v}'^{(1)}(x_1 + i0) - \mathbf{v}'^{(2)}(x_1 - i0), \tag{19}$$

when passing through the interface. Determining from the first formula (14)

$$\mathbf{v}'^{(m)}(z) = \mathbf{A}^{(m)}\boldsymbol{\Phi}'^{(m)}(z) + \overline{\mathbf{A}}^{(m)}\overline{\boldsymbol{\Phi}}'^{(m)}(\bar{z})$$

or

$$\mathbf{v}'^{(m)}(x_1 \pm i0) = \mathbf{A}^{(m)}\boldsymbol{\Phi}'^{(m)}(x_1 \pm i0) + \overline{\mathbf{A}}^{(m)}\overline{\boldsymbol{\Phi}}'^{(m)}(x_1 \mp i0), \tag{20}$$

and substituting in (19), one gets

$$\left\langle \mathbf{v}'(x_1) \right\rangle = \mathbf{A}^{(1)}\boldsymbol{\Phi}'^{(1)}(x_1 + i0) + \overline{\mathbf{A}}^{(1)}\boldsymbol{\Phi}'^{(1)}(x_1 - i0) - \mathbf{A}^{(2)}\boldsymbol{\Phi}'^{(2)}(x_1 - i0) - \overline{\mathbf{A}}^{(2)}\boldsymbol{\Phi}'^{(2)}(x_1 + i0).$$

Finding further $\boldsymbol{\Phi}'^{(2)}(x_1 - i0) = \left(\mathbf{B}^{(2)}\right)^{-1}\overline{\mathbf{B}}^{(1)}\overline{\boldsymbol{\Phi}}'^{(1)}(x_1 - i0)$ from (18) and substituting this expression together with (17) at $x_2 \to +0$ in the latest formula, leads to

$$\left\langle \mathbf{v}'(x_1) \right\rangle = \mathbf{D}\boldsymbol{\Phi}'^{(1)}(x_1 + i0) + \overline{\mathbf{D}}\,\overline{\boldsymbol{\Phi}}'^{(1)}(x_1 - i0),$$

where $\mathbf{D} = \mathbf{A}^{(1)} - \overline{\mathbf{A}}^{(2)}\left(\overline{\mathbf{B}}^{(2)}\right)^{-1}\mathbf{B}^{(1)}$.

Introducing a new vector-function, the last relation can be written as

$$\left\langle \mathbf{v}'(x_1) \right\rangle = \boldsymbol{W}^{+}(x_1) - \boldsymbol{W}^{-}(x_1), \tag{21}$$

where

$$\boldsymbol{W}(z) = \begin{cases} \mathbf{D}\boldsymbol{\Phi}'^{(1)}(z), & x_2 > 0, \\ -\overline{\mathbf{D}}\,\overline{\boldsymbol{\Phi}}'^{(1)}(z), & x_2 < 0. \end{cases} \tag{22}$$

The second relations (14) gives

$$\boldsymbol{P}^{(1)}(x_1, 0) = \mathbf{B}^{(1)}\boldsymbol{\Phi}'^{(1)}(x_1 + i0) + \overline{\mathbf{B}}^{(1)}\overline{\boldsymbol{\Phi}}'^{(1)}(x_1 - i0). \tag{23}$$

Determining further $\boldsymbol{\Phi}'^{(1)}(x_1 + i0)$ and $\overline{\boldsymbol{\Phi}}'^{(1)}(x_1 - i0)$ from (22) and substituting the obtained relations into (23), leads to

$$\boldsymbol{P}^{(1)}(x_1, 0) = \boldsymbol{S}\boldsymbol{W}^{+}(x_1) - \overline{\boldsymbol{S}}\boldsymbol{W}^{-}(x_1), \tag{24}$$

where

$$\boldsymbol{S} = \mathbf{B}^{(1)}\mathbf{D}^{-1} = \left[\mathbf{A}^{(1)}\left(\mathbf{B}^{(1)}\right)^{-1} - \overline{\mathbf{A}}^{(2)}\left(\overline{\mathbf{B}}^{(2)}\right)^{-1}\right]^{-1}. \tag{25}$$

It is found out that for the considered class of piezoelectric materials the matrix $\boldsymbol{S}$ has the following structure

$$\boldsymbol{S} = \begin{bmatrix} is_{11} & s_{12} \\ s_{21} & is_{22} \end{bmatrix}, \tag{26}$$

where all s_{kl} $(k, l = 1, 2)$ are real.

4 Formulation of the Problem for an Electrically Insulated Inclusion with Stepwise Changing Rigidity

Consider and electrically insulated inclusion $c \le x_1 \le b$ at the interface $x_2 = 0$. It is assumed that this inclusion is absolutely rigid for $c \le x_1 \le a$ and is mechanically "soft" at $a < x_1 < b$ $(a < b)$. Such situation can take place e.g. for thin mechanically "soft" interface layer adjacent with much more rigid inclusion which both have infinite lengths in the direction x_3 and the properties of electrical insulator (Fig. 1).

Then the boundary conditions at the interface are of the form

$$\varepsilon_{13}^{(1)} = \varepsilon_{13}^{(2)} = 0, \ D_2^{(1)} = D_2^{(2)} = 0 \text{ for } c < x_1 < a, \tag{27}$$

$$D_2^{(1)} = D_2^{(2)} = 0, \ \langle \sigma_{23} \rangle = 0 \ \langle \varepsilon_{13} \rangle = 0 \text{ for } a < x_1 < b, \tag{28}$$

$$\langle \sigma_{23} \rangle = 0, \ \langle D_2 \rangle = 0, \ \langle \varepsilon_{31} \rangle = 0, \ \langle E_1 \rangle = 0 \text{ for } x_1 \notin (c, b). \tag{29}$$

We also assume that a vector $\boldsymbol{P}^{\infty} = \left[\varepsilon_{13}^{\infty}, D_2^{\infty}\right]^T$ is prescribed at infinity. Consider (24) in the following expanded form

$$\begin{aligned} \varepsilon_{13}^{(1)}(x_1, 0) &= is_{11} W_1^+(x_1) + s_{12} W_2^+(x_1) + is_{11} W_1^-(x_1) - s_{12} W_2^-(x_1), \\ D_2^{(1)}(x_1, 0) &= s_{21} W_1^+(x_1) + is_{22} W_2^+(x_1) - s_{21} W_1^-(x_1) + is_{22} W_2^-(x_1), \end{aligned} \tag{30}$$

in which (26) was taken into account. Combining the Eq. (30) one arrives at the presentations

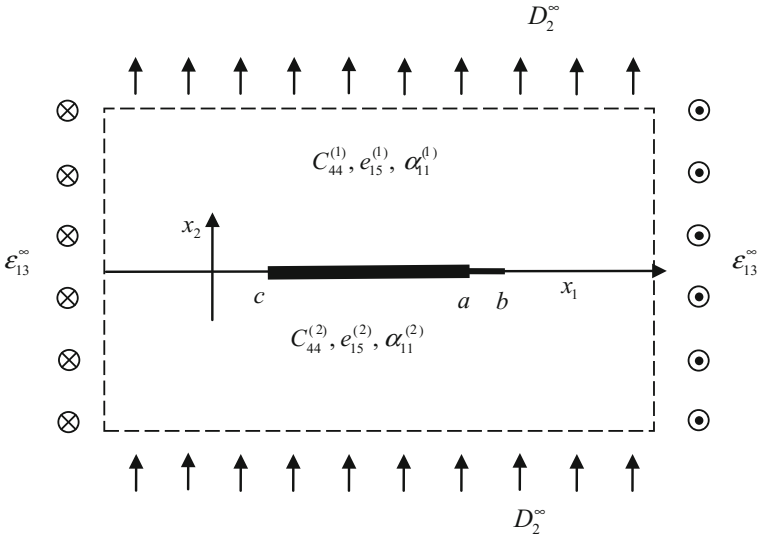

Fig. 1 An electrically insulated inclusion with stepwise changing rigidity

$$\varepsilon_{13}^{(1)}(x_1,0) - im_j D_2^{(1)}(x_1,0) = t_j\Big[F_j^+(x_1) + \gamma_j F_j^-(x_1)\Big], \tag{31}$$

where

$$F_j(z) = W_2(z) + is_j W_1(z), \tag{32}$$

and $t_j = s_{12} - m_j s_{22}$, $\gamma_j = -\big(s_{12} + m_j s_{22}\big)/t_j$, $s_j = (s_{11} + m_j s_{21})/t_j$, $m_{1,2} = \mp\sqrt{-\frac{s_{11}s_{12}}{s_{21}s_{22}}}$.

It follows from the last equations that $s_{1,2} = -m_{1,2}$, $\gamma_2 = 1/\gamma_1$, and the values $m_{1,2}$ are real.

Because according to (32) $F_j^+(x_1) - F_j^-(x_1) = W_2^+(x_1) - W_2^-(x_1) + is_j\big[W_1^+(x_1) - W_1^-(x_1)\big]$, then with use of (21) one gets

$$\langle -E_1(x_1,0)\rangle + is_j\langle\sigma_{23}(x_1,0)\rangle = F_j^+(x_1) - F_j^-(x_1). \tag{33}$$

It is sufficient to apply the relations (31), (33) in the following analysis only for $j = 1$, therefore, assuming $j = 1$, the Eqs. (31) and (33) can be presented in the form

$$\varepsilon_{13}^{(1)}(x_1,0) - im_1 D_2^{(1)}(x_1,0) = t_1\big[F_1^+(x_1) + \gamma_1 F_1^-(x_1)\big], \tag{34}$$

$$\langle -E_1(x_1,0)\rangle + is_1\langle\sigma_{23}(x_1,0)\rangle = F_1^+(x_1) - F_1^-(x_1), \tag{35}$$

where $m_1 = -\sqrt{-\frac{s_{11}s_{12}}{s_{21}s_{22}}}$, $s_1 = -m_1$.

Taking into account that for $x_1 \notin (c,b)$ the relationships $F_1^+(x_1) = F_1^-(x_1) = F_1(x_1)$ are valid, it follows from Eq. (34)

$$(1+\gamma_1)t_1 F_1(x_1) = \varepsilon_{13}^{(1)}(x_1,0) - im_1 D_2^{(1)}(x_1,0) \text{ for } x_1 \to \infty.$$

Using the fact that the function $F_1(z)$ is analytic in the whole plane cut along (c,b) and applying the conditions at infinity, one gets from the last equation

$$F_1(z)|_{z\to\infty} = \tilde{\varepsilon}_{13} - i\widetilde{D}_2, \tag{36}$$

where $\tilde{\varepsilon}_{13} = \frac{\varepsilon_{13}^{\infty}}{r_1}$, $\widetilde{D}_2 = \frac{m_1 D_2^{\infty}}{r_1}$, $r_1 = (1+\gamma_1)t_1$.

5 Absolutely Rigid Inclusion Along All Its Length

Consider now the case of an absolutely rigid inclusion along all its length. In this case $a = b$ and the interface conditions (27) and (29) should only be satisfied. Satisfying conditions (27) and (29) with use of (34) leads to the following equation

$$F_1^+(x_1) + \gamma_1 F_1^-(x_1) = 0 \text{ for } c < x_1 < a. \tag{37}$$

The solution of this equation under the condition at infinity (36) was found with use of [8] in the form

$$F_1(z) = \left(\tilde{\varepsilon}_{13} - i\tilde{D}_2\right)\frac{z - (a+c)/2 - i\varepsilon l}{\sqrt{(z-c)(z-a)}}\left(\frac{z-c}{z-a}\right)^{i\varepsilon}, \tag{38}$$

where $\varepsilon = \frac{1}{2\pi}\ln\gamma_1,\ l = b - c$.

The shear strain and electric displacement at the interface are obtained from (34) as follows

$$\varepsilon_{13}^{(1)}(x_1, 0) - im_1 D_2^{(1)}(x_1, 0) = \left(\varepsilon_{13}^{\infty} - im_1 D_2^{\infty}\right)\frac{x_1 - (a+c)/2 - i\varepsilon l}{\sqrt{(x_1-c)(x_1-a)}}\left(\frac{x_1-c}{x_1-a}\right)^{i\varepsilon} \text{ for } x_1 > a \tag{39}$$

and the electric field and the shear stress jumps are found from the formula (35) in the form

$$\langle -E_1(x_1, 0)\rangle + is_1\langle\sigma_{23}(x_1, 0)\rangle = -\frac{\varepsilon_{13}^{\infty} i + m_1 D_2^{\infty}}{t_1\sqrt{\gamma_1}}\frac{x_1 - (a+c)/2 - i\varepsilon l}{\sqrt{(x_1-c)(a-x_1)}}\left(\frac{x_1-c}{a-x_1}\right)^{i\varepsilon} \text{ for } c < x_1 < a. \tag{40}$$

Integrating the last relation, we obtain

$$\langle\varphi(x_1, 0)\rangle + is_1\langle\tilde{\sigma}_{23}(x_1, 0)\rangle = \sqrt{(x_1-c)(a-x_1)}\left\{\frac{\varepsilon_{13}^{\infty} i + m_1 D_2^{\infty}}{t_1\sqrt{\gamma_1}}\left(\frac{x_1-c}{a-x_1}\right)^{i\varepsilon}\right\} \text{ for } c < x_1 < a,$$

where $\langle\tilde{\sigma}_{23}(x_1, 0)\rangle = \int\langle\sigma_{23}(x_1, 0)\rangle\, dx_1$.

The jump of the electric potential over the inclusion can be easily found as real part of the last equation. It follows from Eqs. (38)–(40) that the oscillating singularity takes place at the crack tips in this case.

6 Solution of the Problem for an Electrically Insulated Inclusion with Stepwise Changing Rigidity

Consider now the problem formulated at the beginning of Sect. 3 (Fig. 1). Relations (21), (24) and, consequently, (34), (35) ensure satisfying equation $\boldsymbol{P}^{(1)}(x_1, 0) = \boldsymbol{P}^{(2)}(x_1, 0)$ for the whole interface and, accordingly, satisfying the second and third interface conditions (29). Further satisfaction of first and forth conditions (29) provides the analyticity of the function $F_1(z)$ for the whole plane with a cut along the segment (c, b) of the interface. Satisfying the remaining boundary conditions (27) and (28) with use of (34) and (35), one gets the following equations

$$F_1^+(x_1) + \gamma_1 F_1^-(x_1) = 0 \text{ for } c < x_1 < a, \tag{41}$$

$$\mathrm{Im}\left[F_1^+(x_1)+\gamma_1 F_1^-(x_1)\right]=0,\ \mathrm{Im}\left[F_1^+(x_1)-F_1^-(x_1)\right]=0 \text{ for } a<x_1<b.$$

The last two relations lead to the equation

$$\mathrm{Im}\, F_1^{\pm}(x_1)=0 \text{ for } a<x_1<b. \tag{42}$$

Relations (41) and (42) present the combined Dirichlet-Riemann boundary value problem. The solution of such problem was found and applied to the analysis of a rigid stamp by Nahnein and Nuller [9]. Concerning the problem of an in-plane interface crack, this solution has been developed by [7] and Kozinov et al. [5]. Using these results, an exact solution of the problem (41) and (42), satisfying the condition at infinity (36) as well as the condition of the electric potential uniqueness for overcoming the inclusion [4] and the requirement of its equilibrium, can be written in the form

$$F_1(z)=P(z)X_1(z)+Q(z)X_2(z), \tag{43}$$

where

$$P(z)=C_1z+C_2,\ Q(z)=D_1z+D_2,\ X_1(z)=ie^{i\chi(z)}/\sqrt{(z-c)(z-b)},$$
$$X_2(z)=e^{i\chi(z)}/\sqrt{(z-c)(z-a)},\ \chi(z)=2\varepsilon\ \ln\frac{\sqrt{(b-a)(z-c)}}{\sqrt{l(z-a)}+\sqrt{(a-c)(z-b)}},$$
$$C_1=-\widetilde{D}_2\cos\beta-\tilde{\varepsilon}_{13}\sin\beta,\ D_1=\tilde{\varepsilon}_{13}\cos\beta-\widetilde{D}_2\sin\beta,$$
$$C_2=-\frac{c+b}{2}C_1-\beta_1D_1,\ D_2=\beta_1C_1-\frac{c+a}{2}D_1$$

with

$$\beta=\varepsilon\ \ln\frac{1-\sqrt{1-\lambda}}{1+\sqrt{1-\lambda}},\ \beta_1=\varepsilon\sqrt{(a-c)(b-c)},\ \lambda=\frac{b-a}{l}.$$

Using the solution (43) together with formula (34), one gets

$$\varepsilon_{13}^{(1)}(x_1,0)-im_1D_2^{(1)}(x_1,0)=\left[\frac{Q(x_1)}{\sqrt{x_1-a}}+\frac{iP(x_1)}{\sqrt{x_1-b}}\right]\frac{r_1\exp[i\chi(x_1)]}{\sqrt{x_1-c}} \text{ for } x_1>b, \tag{44}$$

$$\varepsilon_{13}^{(1)}(x_1,0)=\frac{t_1P(x_1)}{\sqrt{(x_1-c)(b-x_1)}}\left[(1-\gamma_1)\cosh\chi_0(x_1)+(1+\gamma_1)\sinh\chi_0(x_1)\right]$$
$$+\frac{t_1Q(x_1)}{\sqrt{(x_1-c)(x_1-a)}}\left[(1+\gamma_1)\cosh\chi_0(x_1)+(1-\gamma_1)\sinh\chi_0(x_1)\right] \text{ for } a<x_1<b, \tag{45}$$

where $\chi_0(x_1)=2\varepsilon\tan^{-1}\sqrt{\frac{(a-c)(b-x_1)}{(b-c)(x_1-a)}}$.

Substituting the solution (43) into (35) gives the following formulas

$$-\langle E_1(x_1,0)\rangle + is_1\langle\sigma_{23}(x_1,0)\rangle = 2\sqrt{\alpha}\left[\frac{P(x_1)}{\sqrt{b-x_1}} - i\frac{Q(x_1)}{\sqrt{a-x_1}}\right]\frac{\exp\left[i\chi^*(x_1)\right]}{\sqrt{x_1-c}} \text{ for } c < x_1 < a, \tag{46}$$

$$-\langle E_1(x_1,0)\rangle = \frac{2}{\sqrt{x_1-c}}\left[\frac{P(x_1)}{\sqrt{b-x_1}}\cosh\chi_0(x_1) + \frac{Q(x_1)}{\sqrt{x_1-a}}\sinh\chi_0(x_1)\right] \text{ for } a < x_1 < b, \tag{47}$$

where $\chi^*(x_1) = 2\varepsilon\ \ln\frac{\sqrt{(b-a)(x_1-c)}}{\sqrt{l(a-x_1)}+\sqrt{(a-c)(b-x_1)}}$, $\alpha = \frac{(\gamma_1+1)^2}{4\gamma_1}$.

The analysis shows that the obtained solution has the oscillating singularity at the left end of the inclusion, which is similar to derived in Sect. 5. However, it is very important that this solution has the conventional square root singularity at the right crack tip and, therefore, commonly used intensity factors can be introduced. Thus, we introduce further the following mechanical strain and electrical displacement intensity factors (IFs)

$$K_\varepsilon = \lim_{x_1\to a+0}\sqrt{2\pi(x_1-a)}\varepsilon_{13}^{(1)}(x_1,0),\ \ K_D = \lim_{x_1\to b+0}\sqrt{2\pi(x_1-b)}D_2^{(1)}(x_1,0). \tag{48}$$

Using Eq. (45) and taking into account that $\chi_0(a) = \ln\sqrt{\gamma_1}$ one can find

$$K_\varepsilon = \frac{r_1 Q(a)}{\sqrt{a-c}}\sqrt{\frac{2\pi}{\alpha}}. \tag{49}$$

The intensity factor K_D can be found from the formula (44) and can be written in the form

$$K_D = -\frac{r_1}{m_1}\sqrt{\frac{2\pi}{l}}P(b). \tag{50}$$

It follows from Eq. (44) that the strain $\varepsilon_{13}^{(1)}(x_1,0)$ in the right neighborhood of the point b is finite, but Eq. (45) shows that in the left neighborhood of this point it is singular and the corresponding IF

$$K_{\varepsilon b} = \lim_{x_1\to b-0}\sqrt{2\pi(b-x_1)}\varepsilon_{13}^{(1)}(x_1,0)$$

is equal to

$$K_{\varepsilon b} = r_1\gamma_0\sqrt{\frac{2\pi}{l}}P(b) = -m_1\gamma_0 K_D, \tag{51}$$

where $\gamma_0 = \frac{1-\gamma_1}{1+\gamma_1}$. Thus, we have only two independent IFs at the points a and b. These IFs can be presented in the form

$$K_\varepsilon = \sqrt{\frac{\pi l}{2\alpha}}\Big[\sqrt{1-\lambda}\big(\varepsilon_{13}^{\infty}\cos\beta - m_1 D_2^{\infty}\sin\beta\big) - 2\varepsilon\big(\varepsilon_{13}^{\infty}\sin\beta + m_1 D_2^{\infty}\cos\beta\big)\Big], \tag{52}$$

$$K_D = \frac{1}{m_1}\sqrt{\frac{\pi l}{2}}\Big[\big(\varepsilon_{13}^{\infty}\sin\beta + m_1 D_2^{\infty}\cos\beta\big) + 2\varepsilon\sqrt{1-\lambda}\big(\varepsilon_{13}^{\infty}\cos\beta - m_1 D_2^{\infty}\sin\beta\big)\Big]. \tag{53}$$

It is worth to be mentioned that the identity

$$\alpha K_\varepsilon^2 + m_1^2 K_D^2 = \frac{\pi l}{2}\frac{(1-\lambda)(1+4\varepsilon^2)^2}{1+4\varepsilon^2-\lambda}\Big[\big(\varepsilon_{13}^{\infty}\big)^2 + m_1^2\big(D_2^{\infty}\big)^2\Big] \tag{54}$$

is valid.

Using of Eq. (36) for $x_1 \to a-0$ permits to obtain the following expressions of $\langle\sigma_{23}(x_1,0)\rangle$ via the stress intensity factor K_ε:

$$\langle\sigma_{23}(x_1,0)\rangle = -\frac{2\alpha}{r_1 s_1}\frac{K_\varepsilon}{\sqrt{2\pi(a-x_1)}} \text{ for } x_1 \to a-0. \tag{55}$$

7 Determination of the Stress and the Electric Fields at the Interface

The solutions obtained in the previous sections give only the jumps of the stress σ_{23} and the electric field E_1 over the material interface. It is clear that the actual values of these functions on the upper and lower faces of the inclusion and at it continuations is desirable to know. For this purpose in addition to the solution (43) the function $F_2(z)$, which is the solution of the problem of linear relationship

$$F_2^+(x_1) + \gamma_2 F_2^-(x_1) = 0 \text{ for } c < x_1 < a, \tag{56}$$

$$\operatorname{Im} F_2^{\pm}(x_1) = 0 \text{ for } a < x_1 < b, \tag{57}$$

with the condition at infinity

$$F_2(z)|_{z\to\infty} = \hat{\varepsilon}_{13} - i\widehat{D}_2, \tag{58}$$

should be used. The values $\hat{\varepsilon}_{13}$ and $\widehat{D}_2$ are defined as $\hat{\varepsilon}_{13} = \frac{\varepsilon_{13}^{\infty}}{r_2}$, $\widehat{D}_2 = \frac{m_2 D_2^{\infty}}{r_2}$, $r_2 = (1+\gamma_2)t_2$.

The solution of the problem (56)–(58) is very similar to (43), therefore, we will not present it here and only consider the properties of this solution in the following for each section of the interface.

Presenting (32) in the form

$$F_1(z) = W_2(z) + is_1 W_1(z),\ \ F_2(z) = W_2(z) + is_2 W_1(z) \tag{59}$$

and taking into account that $s_2 = -s_1$, one gets

$$W_1(z) = -i\frac{F_1(z) - F_2(z)}{2s_1},\ \ W_2(z) = \frac{F_1(z) + F_2(z)}{2}. \tag{60}$$

It follows from the Eq. (22)

$$\boldsymbol{\Phi}'^{(1)}(z) = \mathbf{D}^{-1}\boldsymbol{W}(z) \text{ for } x_2 > 0,\ \ \overline{\boldsymbol{\Phi}}'^{(1)}(z) = -\overline{\mathbf{D}}^{-1}\boldsymbol{W}(z) \text{ for } x_2 < 0.$$

Substituting these presentations into Eq. (20), one has

$$\mathbf{v}'^{(1)}(x_1 + i0) = 2\,\mathrm{Re}\big[\mathbf{A}^{(1)}\mathbf{D}^{-1}\boldsymbol{W}^{+}(x_1)\big]. \tag{61}$$

For the determination of (61) the expressions of $F_1^+(x_1)$ and $F_2^+(x_1)$ from (60) should be known.

With use of (21) and (59) and also the identities $\gamma_2 = \gamma_1^{-1},\ t_2 = -\gamma_1 t_1$ one gets for $x_1 \in (c, a)$

$$F_2^+(x_1) = \gamma_1^{-1}\overline{F_1^+(x_1)}.$$

It means that the formula (61) for $x_1 \in (c, a)$ can be written in the form

$$\left\{\begin{array}{c}\sigma_{23}(x_1, 0)\\ -E_1(x_1, 0)\end{array}\right\}^{+} = 2\,\mathrm{Re}\left[\mathbf{A}^{(1)}\mathbf{D}^{-1}\left\{\begin{array}{c} is_1^{-1}\left(\gamma_1^{-1}\overline{F_1^+(x_1)} - F_1^+(x_1)\right)\\ \gamma_1^{-1}\overline{F_1^+(x_1)} + F_1^+(x_1)\end{array}\right\}\right], \tag{62}$$

where one can get from (43)

$$F_1^+(x_1) = \sqrt{\gamma_1}\left[\frac{P(x_1)}{\sqrt{b - x_1}} - i\frac{Q(x_1)}{\sqrt{a - x_1}}\right]\frac{\exp[i\chi^*(x_1)]}{\sqrt{x_1 - c}} \text{ for } c < x_1 < a. \tag{63}$$

Taking into account the properties

$$X_1^{\pm}(x_1) = \frac{\pm e^{\pm\chi_0(x_1)}}{\sqrt{(x_1 - c)(b - x_1)}},\ \ X_2^{\pm}(x_1) = \frac{e^{\pm\chi_0(x_1)}}{\sqrt{(x_1 - c)(x_1 - a)}} \text{ for } x_1 \in (a, b),$$

one gets for this interval $F_2^+(x_1) = F_1^-(x_1)$ and the formulas (60), (61) can be written in the form

$$\left\{\begin{array}{c}\sigma_{23}(x_1, 0)\\ -E_1(x_1, 0)\end{array}\right\}^{+} = 2\,\mathrm{Re}\left[\mathbf{A}^{(1)}\mathbf{D}^{-1}\left\{\begin{array}{c} -is_1^{-1}\left(F_1^+(x_1) + F_1^-(x_1)\right)\\ F_1^+(x_1) - F_1^-(x_1)\end{array}\right\}\right] \text{ for } x_1 \in (a, b), \tag{64}$$

where it follows from (43) that

$$F_1^+(x_1)\{\pm\}F_1^-(x_1) = \frac{2}{\sqrt{x_1-c}}\left[\frac{P(x_1)}{\sqrt{b-x_1}}\left\{\begin{matrix}\sinh\\ \cosh\end{matrix}\right\}\chi_0(x_1) + \frac{Q(x_1)}{\sqrt{x_1-a}}\left\{\begin{matrix}\cosh\\ \sinh\end{matrix}\right\}\chi_0(x_1)\right] \text{ for } x_1 \in (a,b). \tag{65}$$

If $x_1 \notin (c,b)$ then $F_1^+(x_1) = F_1^-(x_1) = F_1(x_1)$. Analyzing (43) and the solution of the problem (56)–(58) one gets $F_2(x_1) = -\overline{F_1(x_1)}$ and the formulas (60), (61) attain the form

$$\left\{\begin{matrix}\sigma_{23}(x_1,0)\\ -E_1(x_1,0)\end{matrix}\right\} = 2\,\mathrm{Re}\left[\mathbf{A}^{(1)}\mathbf{D}^{-1}\left\{\begin{matrix}-is_1^{-1}\left(F_1(x_1)+\overline{F_1(x_1)}\right)\\ F_1(x_1)-\overline{F_1(x_1)}\end{matrix}\right\}\right] \text{ for } x_1 \notin (c,b). \tag{66}$$

Formula (43) for $F_1(x_1)$ is valid, in which x_1 instead of z should be taken.

Thus, the formulas (62), (64) and (66) define the shear stress and the electric field at the upper face of the material interface. Their values at the lower face in the intervals (c,a) and (a,b) can be found in a simple arithmetic way with use of the jumps (46) and (47).

Introduce further the following stress and electrical field intensity factors at the point a:

$$K_{23} = \lim_{x_1\to a-0}\sqrt{2\pi(a-x_1)}\,\sigma_{23}^{(1)}(x_1,0),\quad K_E = \lim_{x_1\to a-0}\sqrt{2\pi(a-x_1)}\,E_1^{(1)}(x_1,0).$$

Using the expressions (62), (63) one gets

$$\left\{\begin{matrix}K_{23}\\ K_E\end{matrix}\right\}^+ = 2\sqrt{2\pi}\,\frac{Q(a)}{\sqrt{\gamma_1(a-c)}}\,\mathrm{Re}\left[\mathbf{A}^{(1)}\mathbf{D}^{-1}\left\{\begin{matrix}-s_1^{-1}(1+\gamma_1)\\ i(1-\gamma_1)\end{matrix}\right\}\right]. \tag{67}$$

8 Numerical Illustration

The materials with the characteristics [6] $c_{44}^{(1)} = 43.7 \times 10^9$ Pa, $e_{15}^{(1)} = 8.12\,\mathrm{C/m^2}$, $\alpha_{11}^{(1)} = 7.86 \times 10^{-9}\,\mathrm{C/V\ m}$, $c_{44}^{(2)} = 44.6 \times 10^9$Pa, $e_{15}^{(2)} = 3.48\,\mathrm{C/m^2}$, $\alpha_{11}^{(2)} = 3.42 \times 10^{-9}\,\mathrm{C/V\ m}$ were chosen and $c = -10$ mm, $b = 10$ mm.

The results for the shear stress $\sigma_{23}(x_1,0)$ at $\varepsilon_{13}^{\infty} = 10^{-4}$, $D_2^{\infty} = 0.5 \times 10^{-2}\ \mathrm{C/m^2}$ are shown in Figs. 2 and 3 for the zones (c,a) and (a,b), respectively. Lines *I*, *II* and *III* correspond to a = 8, 6 and 4 mm, respectively. It is worth to mention that this stress has an oscillating square root singularity at the left tip of the inclusion and conventional square root singularity at both sides of the point a.

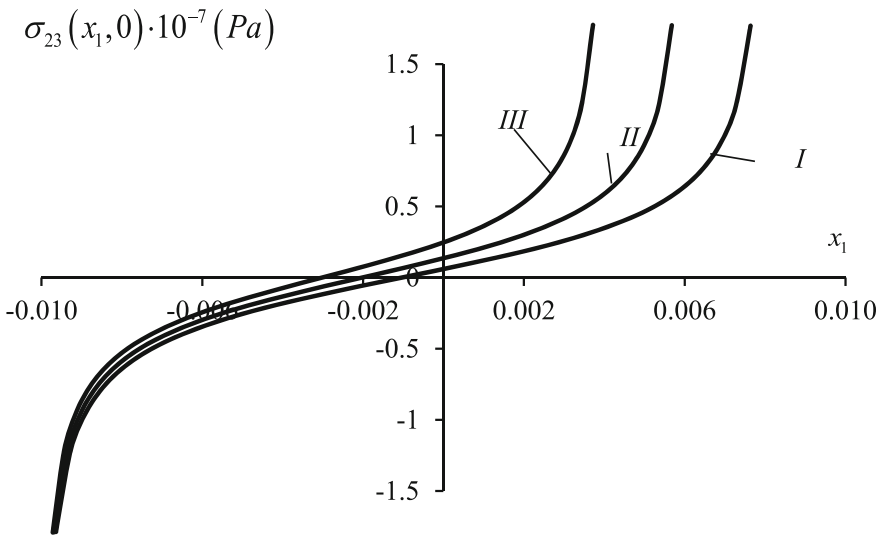

Fig. 2 Shear stress $\sigma_{23}^{(1)}(x_1, 0)$ variation in the zone (c, a)

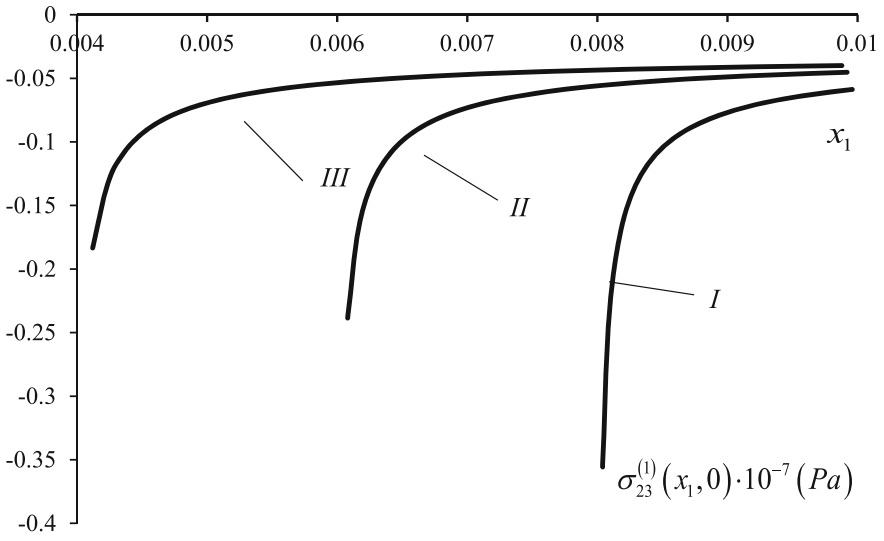

Fig. 3 Shear stress $\sigma_{23}^{(1)}(x_1, 0)$ variation in the zone (a, b)

The results of the shear strain $\varepsilon_{13}^{(1)}(x_1, 0)$ calculation for $x_1 \in (a, b)$ and $x_1 > b$ for the same strain and electric displacement at infinity as in Figs. 2, 3 are shown in Figs. 4, 5, respectively. The analysis showed that this strain is very large at the point a and then decreases on the distance from this point and further through the point b.

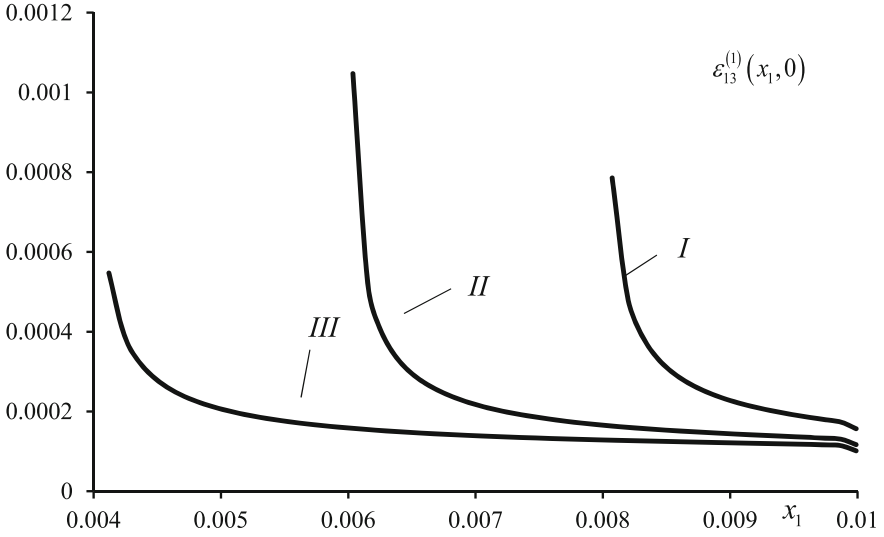

Fig. 4 Shear strain variation $\varepsilon_{13}^{(1)}(x_1, 0)$ in the zone (a, b)

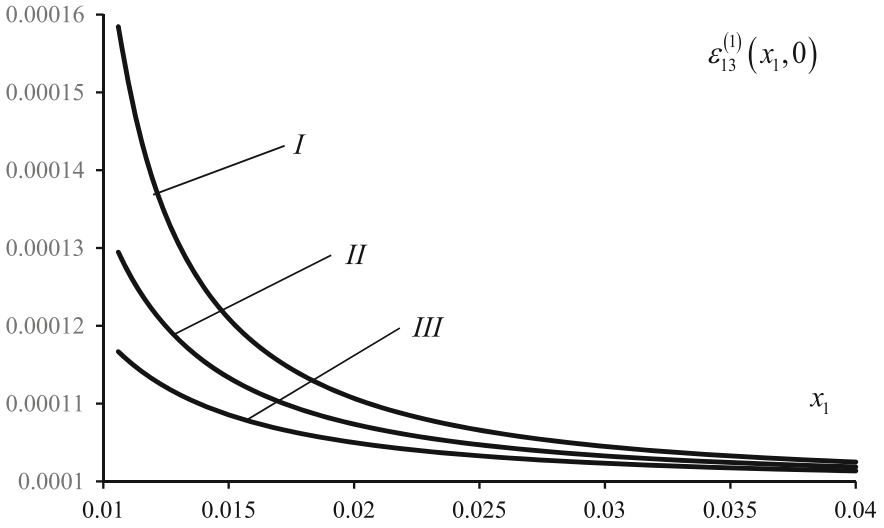

Fig. 5 Shear strain $\varepsilon_{13}^{(1)}(x_1, 0)$ variation for $x_1 > b$

Electric displacements $D_2^{(1)}(x_1, 0)$ for $x_1 > b$ at $\varepsilon_1^{\infty} = 10^{-6}$, $a = 6$ mm and $D_2^{\infty} = 0.5 \times 10^{-2}\,\mathrm{C/m^2}$ (line *I*), $0.25 \times 10^{-2}\,\mathrm{C/m^2}$ (*II*) and $10^{-3}\,\mathrm{C/m^2}$ (*III*) are shown in Fig. 6. It is seen from this figure that the electric displacements growth very fast at the inclusion tip because of singularity and tends to its nominal values for $x_1 \gg b$.

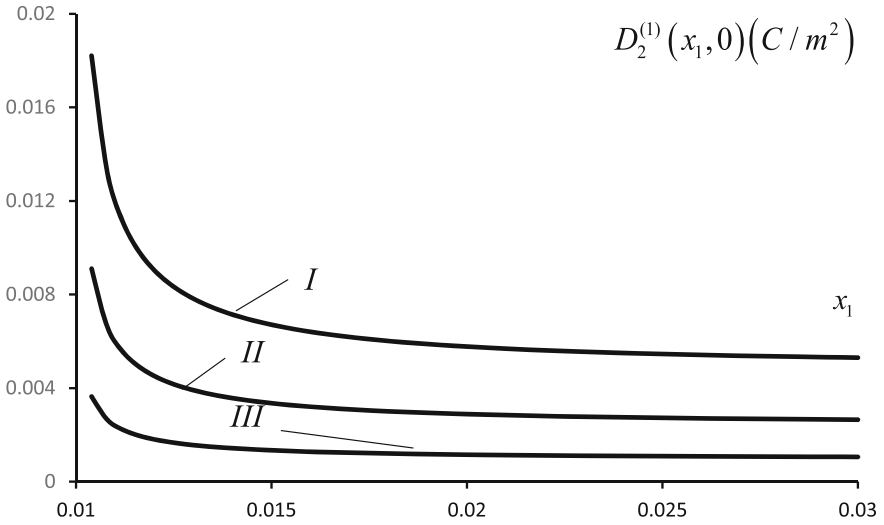

Fig. 6 Electric displacement variation $D_2^{(1)}(x_1, 0)$ for $x_1 > b$ and $\varepsilon_1^{\infty} = 10^{-6}$

Table 1 The variation of stress intensity factor K_{23} for $\varepsilon_{13}^{\infty} = 0.5 \times 10^{-6}$ and different λ and D_2^{∞}

$10^3 D_2^{\infty}\ [\mathrm{C}/m^2]$	λ		
	0.4	0.5	0.6
1	4495.83	3261.15	1785.9
0.75	4260.24	2770.25	976.77
0.5	4024.65	2279.36	167.64
0.4482	3975.83	2177.65	≈ 0
0	3553.47	1297.58	−1450.62
−0.6608	2930.76	≈ 0	−3589.31
−3.7709	≈ 0	−6106.84	−13655.2

The variation of stress intensity factor for the same bimaterial as above, $\varepsilon_{13}^{\infty} = 0.5 \times 10^{-6}$, $c = -10$ mm, $b = 10$ mm and different λ and D_2^{∞} are shown in Table 1. It can be seen from this results that the SIF K_{23} essentially depends both on the position of the point a and on the electrical displacement value. Moreover for each λ the magnitudes of D_2^{∞} are found for which K_{23} becomes equal to 0.

9 Conclusion

Two bonded piezoelectric semi-infinite spaces under the action of antiplane mechanical and in-plane electric loadings with an electrically insulated inclusion at the interface are analyzed. It is assumed that one zone of the inclusion is absolutely

rigid while the other part is mechanically soft. The presentations (34), (35) of the required electro-mechanical quantities via sectionally-analytic vector-functions are obtained. Satisfying the boundary conditions at the material interface the combined Dirichlet-Riemann boundary value problem (41), (42) is formulated and an exact analytical solution of this problem is found. Using this solution the closed form analytical expressions for the required electro-mechanical quantities at the interface are derived. Particularly the stress and the electric field jumps (46) along the mechanically rigid part of the inclusion is found and additionally the variation (62) of this functions along its upper face is also given.

The values of some electromechanical quantities along the corresponding parts of the material interface are also presented graphically for certain bimaterial, mechanically rigid and soft inclusion zone lengths. Singular points of the shear stress, strain and also the electric displacement and field are found and the corresponding intensity factors are determined. The dependence of the stress intensity factor on the intensity of the electric displacement and the relation on the rigid and soft zone lengths is investigated. It is particularly shown that the stress intensity factor of the shear stress essentially depends both on the position of the point a and on the electrical displacement value. Moreover, a suitable choice of the electric field permits to turn out this intensity factor to zero.

References

1. Deng, W., Meguid, S.A.: Analysis of conducting rigid inclusion at the interface of two dissimilar piezoelectric materials. J. Appl. Mech. **65**(1), 76–84 (1998)
2. Eskandari, M., Moeini-Ardakani, S.S., Shodja, H.M.: Axisymmetric contact of a rigid inclusion embedded at the interface of a piezoelectric bimaterial. Q. J. Mech. Appl. Math. **62**(3), 281–295 (2009)
3. Gao, C.F., Fan, W.X.: An interface inclusion between two dissimilar piezoelectric materials. Appl. Math. Mech. **22**(1), 96–104 (2001)
4. Knysh, P., Loboda, V., Labesse-Jied, F., Lapusta, Y.: An electrically charged crack in a piezoelectric material under remote electromechanical loading. Lett. Fract. Micromech. **175**(1), 87–94 (2012)
5. Kozinov, S., Loboda, V., Lapusta, Y.: Periodic set of limited electrically permeable interface cracks with contact zones. Mech. Res. Commun. **48**, 32–41 (2013)
6. Li, R., Kardomateas, G.A.: The mode III interface crack in piezo-electro-magneto-elastic dissimilar bimaterials. Trans. ASME **73**, 220–227 (2006)
7. Loboda, V.V.: The quasi-invariant in the theory of interface cracks. Eng. Fract. Mech. **44**, 573–580 (1993)
8. Muskhelishvili, N.I.: Some Basic Problems of Mathematical Theory of Elasticity, p. 707. Noordhoff International Publishing, Leyden (1977)
9. Nakhmein, E.L., Nuller, B.M.: Contact between an elastic half-plane and a partly separated stamp. J. Appl. Math. Mech. **50**(4), 507–515 (1986)
10. Pak, Y.E.: Linear electro-elastic fracture mechanics of piezoelectric materials. Int. J. Fract. **54**, 79–100 (1992)

11. Wang, X., Schiavone, P.: Debonded arc-shaped interface conducting rigid line inclusions in piezoelectric composites. C.R. Mech. **345**(10), 724–731 (2017)
12. Wang, X., Shen, Y.P.: Exact solution for mixed boundary value problems at anisotropic piezoelectric bimaterial interface and unification of various interface defects. Int. J. Solids Struct. **39**(6), 1591–1619 (2002)

Thermomechanical Coupling and Transient to Steady Global Dynamics of Orthotropic Plates

Valeria Settimi and Giuseppe Rega

Abstract Different reduced order models of thermomechanically coupled von Kármán shear indeformable plate with prescribed linear temperature along the thickness are comparatively investigated in terms of local and global dynamics exhibited in active thermal regime, under harmonic transverse and constant axial mechanical excitations. Two-d.o.f. one-way coupled models are then used for "economical" yet reliable numerical investigation of the nonlinear dynamic response in terms of the mechanical variable and of the dominant (membrane or bending) thermal variable, under the corresponding thermal excitations inducing variably rich scenarios of buckled mechanical response. Attention is focused on the important role played by global dynamics in unveiling the meaningful effects entailed on the structure steady mechanical response by the variably slow thermal transients taken into account by the thermomechanically coupled model.

1 Introduction

Thermomechanical coupling in laminated plates has been recently a matter of refined modeling at both the continuum and discretized level [5, 7], with a view to highlighting the relevant effects on the structure nonlinear dynamic response. Dealing with a reduced order model (ROM) of von Kármán shear-indeformable plate with one mechanical (mid-plane transverse displacement) and two thermal (membrane and bending) variables, the effects of thermoelastic coupling on mechanical vibrations in passive thermal conditions (i.e., with no thermal excitations) have shown to be relatively minor [5, 10], although the thermal variables dragged into the structure response by the directly excited mechanical variable exhibit distinct qualitative and

V. Settimi · G. Rega (✉)
Department of Structural and Geotechnical Engineering, Sapienza University of Rome, Rome, Italy
e-mail: giuseppe.rega@uniroma1.it

V. Settimi
e-mail: valeria.settimi@uniroma1.it

I. V. Andrianov et al. (eds.), *Problems of Nonlinear Mechanics and Physics of Materials*, Advanced Structured Materials 94,
https://doi.org/10.1007/978-3-319-92234-8_27

quantitative features, with the relevant coupling terms affecting the displacement in a different way [10]. The role of different variables/terms of coupling in the mechanical and thermal equations was also addressed [5], along with the possibility to refer to variably simplified models for catching some main aspects of the thermally affected mechanical response [6]. Based on preliminary results, no seemingly significant effects of thermoelastic coupling on mechanical vibrations were detected, even in the presence of a non-vanishing heat flow or of explicit thermal sources giving rise to a condition of active thermal dynamics [5].

However, more extended analyses conducted in the regime of full thermomechanical coupling have originated a meaningful set of outcomes where the much slower time scale over which thermal phenomena develop with respect to mechanical ones entails non-trivial steady effects on the structure overall response [11]. This influence has been highlighted by means of a systematic numerical investigation of the structure global dynamics, pursued through properly selected two-dimensional (2D) cross-sections of the actual 4D basins of attraction.

Global nonlinear dynamics plays a fundamental role in the analysis, control, and design of all engineering systems, as recently highlighted for a variety of them both with reference to specific mechanical/dynamical issues [2, 8, 9] and within a more general perspective [3]. For the considered thermomechanically coupled plate, even in passive thermal regime global analysis has allowed to detect and understand a substantially different scenario of dynamic response occurring in specific mechanical conditions (i.e., vanishing mechanical stiffness) between coupled and uncoupled models, due to the meaningful role played in the former just by the slow transient evolution of the system thermal dynamics [10]. When considering also thermal excitations in addition to mechanical ones, these slow transient effects on the steady structural response are seen to be more pervasive and systematic, as highlighted by the comprehensive investigation in [11].

The present work aims at overviewing some main effects of thermomechanical coupling in active thermal regime and in the presence of also a prescribed axial mechanical excitation, whose possible buckling effects may combine with thermal ones. Yet, for coupled systems, one main issue consists of preliminarily evaluating the relative importance of the various terms and variables of coupling in the governing equations, to the aim of a satisfactory — and more or less comprehensive — description of the system response. Dealing in particular with the thermomechanical interaction, fully [14] or (to a different extent) partially [1, 4, 12, 13] coupled analyses can indeed be pursued, with possibly different outcomes depending on the specifically considered situation or with an incomplete description.

Accordingly, the first part of this work (Sect. 2) is devoted to comparatively investigating some main local and global dynamical aspects of the structure nonlinear response as obtained with different ROMs ranging from the original, fully coupled, one with three degrees-of-freedom (d.o.f.) down to the simplest uncoupled mechanical model in which the presence of a coexisting active thermal environment is accounted for by merely including its known steady effect in the relevant equation of motion. This allows to properly identify the actual need and/or the possible added value (if any) of all workable models and to select a suitable one to be used for reliable

yet "economical" systematic investigations, based on the structural response aspects which one is interested in. Section 3 highlights the role played by global analysis in unveiling the effects of thermal transient on the structure steady dynamics, by considering two different kinds of thermal excitation entailing variably rich scenarios of buckled mechanical response.

2 Reduced Order Models and Their Comparative Outcomes

The thermomechanically coupled, geometrically nonlinear model here considered refers to a rectangular laminated plate in Fig. 1, of thickness h, and edge lengths a and b in the x and y directions, respectively. The plate is subjected to uniform compressive forces p_x and p_y on the plate edges, to distributed harmonic transverse mechanical excitation, and to thermal loadings. The model is derived within a unified modeling framework integrating mechanical and thermal aspects which is presented in [5, 10], to be referred for the formulation details. By considering classical displacements with von Kármán nonlinearities, along with a correspondingly consistent linear variation of the temperature along the thickness, and in the context of a minimal Galerkin discretization in conditions of no internal resonance between the transverse modes of the laminate, single-mode approximations are assumed for the transverse displacement w and the temperatures T_0 and T_1, while the in-plane displacement components are statically condensed. The subsequent nondimensionalization allows to obtain three coupled nonlinear ordinary differential equations for a simply supported orthotropic single-layer plate with movable and isothermal edges:

$$\ddot{W} + \bar{a}_{12}\dot{W} + \bar{a}_{13}W + \bar{a}_{14}W^3 + \bar{a}_{15}T_{R1} + \bar{a}_{16}W \cdot T_{R0} + \bar{a}_{17}\cos(t) = 0 \quad \text{(1a)}$$

$$\dot{T}_{R0} + \bar{a}_{22}\alpha_1 T_\infty + \bar{a}_{23}T_{R0} + \bar{a}_{24}\dot{W} \cdot W + \bar{a}_{25}e_0(t) = 0 \quad \text{(1b)}$$

$$\dot{T}_{R1} + \bar{a}_{32}T_{R1} + \bar{a}_{33}\dot{W} + \bar{a}_{34}e_1(t) = 0 \quad \text{(1c)}$$

in terms of the nondimensional reduced variables W (deflection of the center of the plate), T_{R0} (membrane temperature) and T_{R1} (bending temperature). Coefficients $\bar{a}_{ij}$ are defined in [10, 11], while the thermal excitations are represented by the constant thermal difference between plate and environment T_∞, and by the membrane and bending excitations e_0 and e_1 derived from body source thermal energies, whose distribution along the plate thickness is reported in Fig. 1.

In passive thermal regime, under specific conditions, the mechanical activation of thermal variables thanks to the coupling terms in the relevant equations may furnish contributions back to the mechanical equation able to modify the basins of attraction organization, highlighting the need to consider the two-way model to grasp the actual mechanical dynamics [10]. In the active thermal regime considered here, there are hints from [5] about the low role played in the mechanical response by both the non-directly excited thermal variables/equations (which govern the number of essential

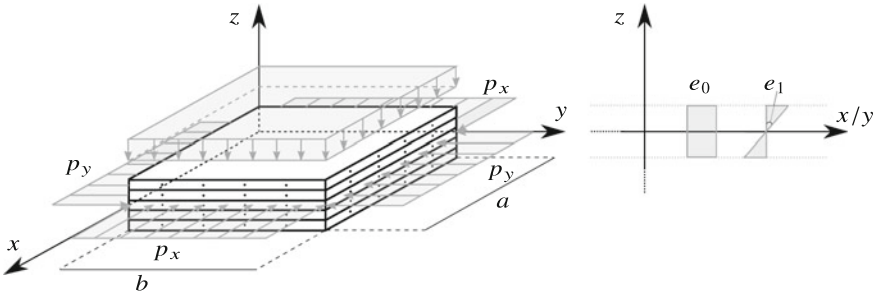

Fig. 1 Laminated rectangular plate subjected to various mechanical loads, and contributions to the overall thermal distribution along the plate thickness

thermal degrees of freedom) and the mechanical coupling terms in thermal equations (which govern the two-way coupling). To deeper investigate this aspect, and in order to detect the simplest model to be used to grasp the main thermomechanical features of the system response, it is of interest to develop a critical analysis of the various models derivable from the general system (1). To this aim, reference is made to an epoxy/carbon fiber composite plate of dimensions $a = b = 1\,m$ and $h = 0.01\,m$. The relevant mechanical and thermal properties are reported in [11], and furnish the following values of the equations coefficients

$$\bar{a}_{12} = 0.0592,\ \bar{a}_{13} = (1-p),\ \bar{a}_{14} = 0.6827,\ \bar{a}_{15} = -0.3674,\ \bar{a}_{16} = -0.9658,$$
$$\bar{a}_{17} = -f,\ \bar{a}_{22} = -1.4507,\ \bar{a}_{23} = 9.1137 \cdot 10^{-5},\ \bar{a}_{24} = 1.01 \cdot 10^{-4},$$
$$\bar{a}_{25} = -0.997719,\ \bar{a}_{32} = 7.8735 \cdot 10^{-4},\ \bar{a}_{33} = 8.8714 \cdot 10^{-4},\ \bar{a}_{34} = -12$$

obtained in primary resonance conditions, which represents the most critical situation for an externally forced system, as a function of the precompression p and of the harmonic forcing amplitude f. With respect to the latter, preliminary analyses in presence of the sole mechanical excitations [10] show the possibility to catch the main dynamical aspects of the system response also for low values of the amplitude f, which is therefore fixed to $f = 1$, and the ability of the precompression in inducing post-buckling behaviors for values higher than $p = 2.52$. In order to critically discuss the effects of the thermal excitations on the mechanical behavior of the plate, yet dealing with parameter values corresponding to physically admissible quantities, the precompression load is set to $p = 2.51$, i.e. a mechanical incipient but not yet triggered buckling configuration.

With the same objective, the thermal excitation is selected to reproduce the condition able to most affect the mechanical response of the system, i.e. to more quickly provide its contribution into the mechanical equation thanks to the coupling terms $\bar{a}_{15}$ or $\bar{a}_{16}$. Observing the linear thermal stiffnesses $\bar{a}_{23}$ and $\bar{a}_{32}$, it results that the membrane temperature evolution is much slower than the bending one ($\bar{a}_{23}/\bar{a}_{32} \cong 0.12$), thus slowing down the influence of the membrane excitations (T_∞ and e_0) on the mechanical vibrations [11]. For these reasons, the model comparison is developed

by considering the presence of a bending excitation e_1 with a linear variation along the thickness which reproduces a cooling of an external surface and an equivalent warming of the other.

The definition of the various, gradually simplified, models to be compared moves from the most general fully coupled, or in different words two-way (from thermal to mechanical, and from mechanical to thermal) coupled, 3 d.o.f. system (1) (***3-2*** model), which is able to comprehensively describe the thermomechanical behavior of the plate. Neglecting the mechanical contribution into the thermal equations, i.e. setting $\bar{a}_{24} = \bar{a}_{33} = 0$, a 3 d.o.f. one-way (from thermal to mechanical) coupled model can be obtained (***3-1*** model), while considering only the active thermal equation, i.e. eliminating Eq. (1b) from system (1), a 2 d.o.f. two-way model is defined (***2-2*** model). With further reductions, a 2 d.o.f. one-way model (***2-1*** model) can be deduced from ***2-2*** when neglecting the coupling term $\bar{a}_{33}$, up to the most simplified system composed of the sole mechanical equation (1a) (***1*** model) without membrane contributions ($\bar{a}_{16} = 0$) and with the bending thermal excitation taken into account by setting the T_{R1} value corresponding to the mean steady state response obtained from linearization of Eq. (1c):

$$T_{R1} = -\bar{a}_{34} e_1 / \bar{a}_{32} \tag{2}$$

Local and global dynamics of the five above described models are compared in terms of bifurcation diagrams, basins of attraction and temporal evolution of selected trajectories, as shown in Figs. 2, 3, 4, 5, 6 and 7. The outcomes of the bifurcation diagrams in terms of minimum and maximum value of the mechanical displacement W, obtained with the fully coupled ***3-2*** model and reported in Fig. 2, show that, starting from a pre-buckling scenario for $e_1 = 0$ with the sole existing P1 (thin black) cross-well solution, the addition of a positive/negative bending excitation

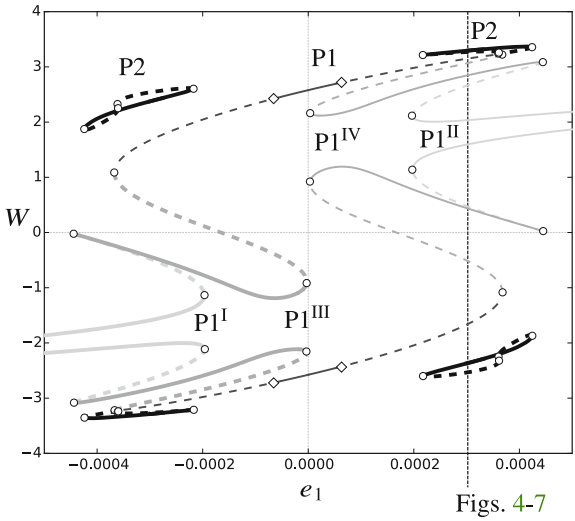

Fig. 2 Bifurcation diagrams of the displacement variable W as a function of thermal excitation e_1, for $p = 2.51$. Circle: saddle-node bifurcation; Diamond: period-doubling bifurcation

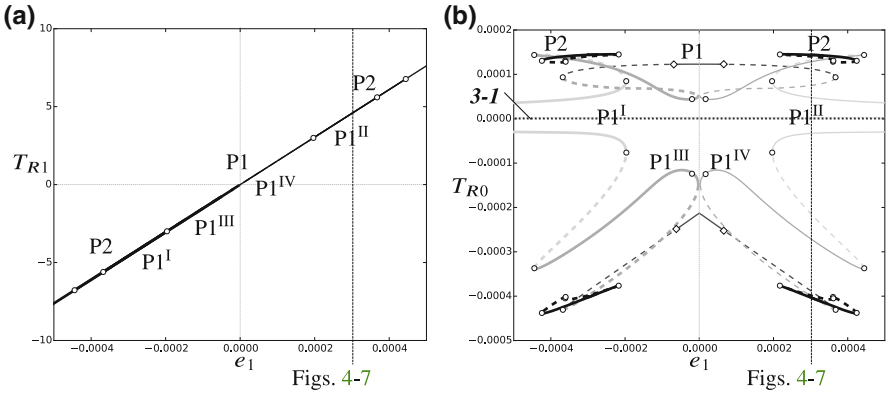

Fig. 3 Bifurcation diagrams of the thermal variables T_{R1} and T_{R0} as a function of thermal excitation e_1. **a** Bifurcation diagrams of the bending temperature T_{R1} furnished by the ***3-2***, ***3-1***, ***2-2***, ***2-1*** models. **b** Bifurcation diagrams of the membrane temperature T_{R0} furnished by the ***3-2*** and ***3-1*** models. Circle: saddle-node bifurcation; Diamond: period-doubling bifurcation

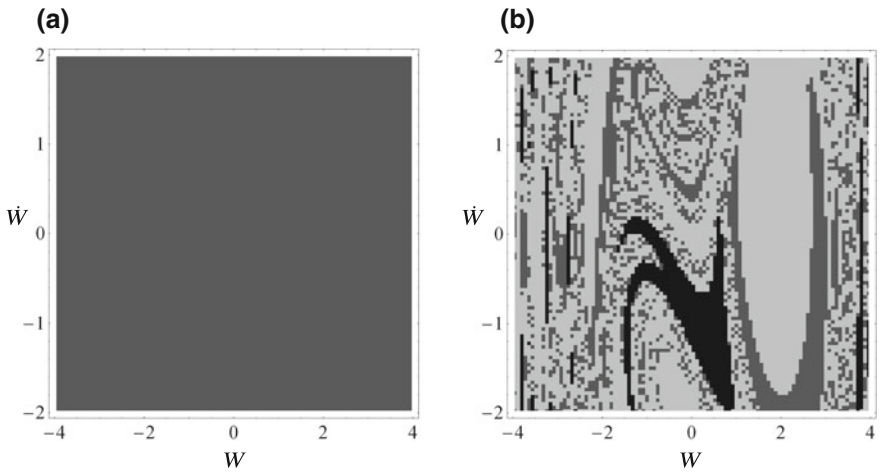

Fig. 4 Basins of attraction in the mechanical plane, for $p = 2.51$ and $e_1 = 3 \times 10^{-4}$. **a** Planar section of the basins of attraction for the ***3-2***, ***3-1***, ***2-2***, ***2-1*** models. **b** Basins of attraction for the ***1*** model. Light gray: basin of the low-amplitude buckled solution $P1^{II}$; Gray: basin of the high-amplitude buckled solution $P1^{IV}$; Black: basin of the period-2 solution P2

e_1 proves to be able to generate buckled responses, though confined around only one positive/negative equilibrium (i.e., in one of the two potential wells, in global dynamics terms), depending on the sign of e_1. Moreover, consistent with the physically expected effect of changing the sign of e_1, the overall scenario of the system mechanical response is antisymmetric, with the two stable low-amplitude buckled solutions ($P1^{I}$ thick/$P1^{II}$ thin light gray curves) existing in complementary ranges of the excitation, and with the high-amplitude ones ($P1^{III}$ thick/$P1^{IV}$ thin gray curves)

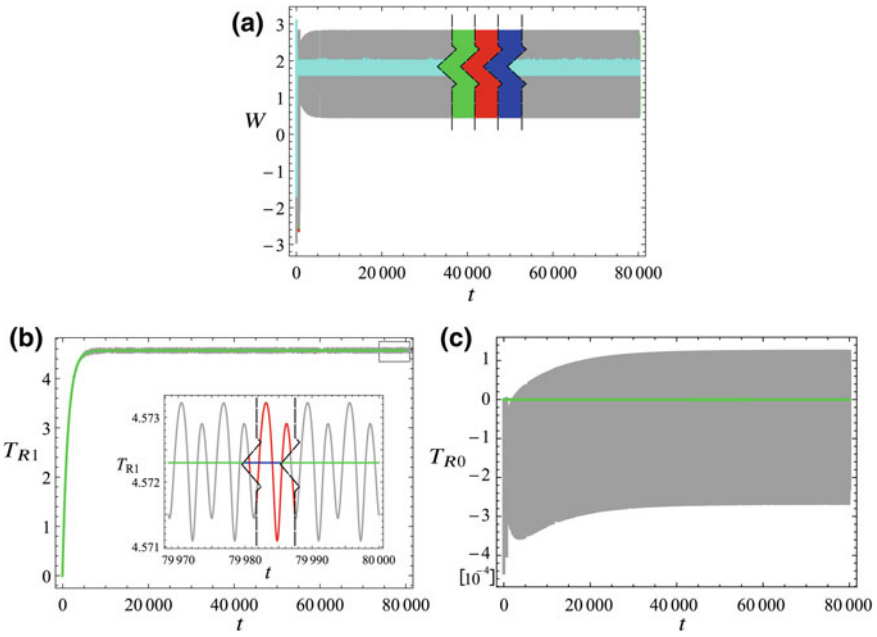

Fig. 5 Time histories of displacement and thermal variables, for $p = 2.51$, $e_1 = 3 \times 10^{-4}$ and trivial mechanical and thermal initial conditions. **a** Temporal evolution of the mechanical displacement W for ***3-2***, ***3-1***, ***2-2***, ***2-1***, ***1*** models. **b** Temporal evolution of the bending temperature T_{R1} for ***3-2***, ***3-1***, ***2-2***, ***2-1*** models. **c** Temporal evolution of the membrane temperature T_{R0} for ***3-2***, ***3-1*** models. Gray: ***3-2*** model; Green: ***3-1*** model; Red: ***2-2*** model; Blue: ***2-1*** model; Cyan: ***1*** model

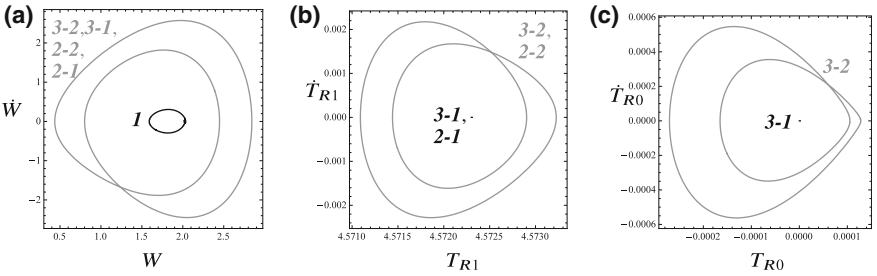

Fig. 6 Phase portraits and Poincaré maps in the mechanical and thermal planes, for $p = 2.51$, $e_1 = 3 \times 10^{-4}$ and trivial mechanical and thermal initial conditions. **a** Phase portraits in the mechanical plane $(W, \dot{W})$ for ***3-2***, ***3-1***, ***2-2***, ***2-1***, ***1*** models. **b** Phase portraits in the thermal plane $(T_{R1}, \dot{T}_{R1})$ for ***3-2***, ***3-1***, ***2-2***, ***2-1*** models. **c** Phase portraits in the thermal plane $(T_{R0}, \dot{T}_{R0})$ for ***3-2***, ***3-1*** models

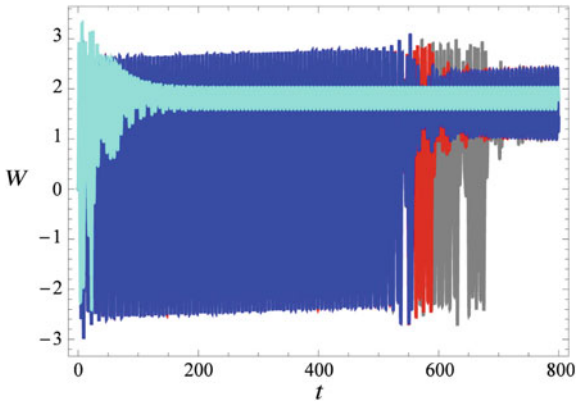

Fig. 7 Transient dynamics of the mechanical response, for $p = 2.51$, $e_1 = 3 \times 10^{-4}$ and trivial mechanical and thermal initial conditions. Gray: ***3-2*** model; Green: ***3-1*** model; Red: ***2-2*** model; Blue: ***2-1*** model; Cyan: ***1*** model

being confined in closer complementary ranges. As a consequence, for sufficiently high values of e_1, the system displays period-1 buckled solutions oscillating around one sole varied configuration, together with cross-well period-2 solutions P2 (thick black curves) confined in limited ranges of the positive/negative excitation values, thus highlighting the possibility to exploit the e_1 excitation to force the mechanical buckling around a selected equilibrium, according to its sign. The described behavior is exactly reproduced by all the four simplified models ***3-1***, ***2-2***, ***2-1***, ***1***, pointing out that the steady dynamics of the periodic responses, or in other words the system attractors, is insensitive to both the possibly different thermomechanical transient and coupling.

Instead, differences among the models responses can be caught if looking at the bifurcation diagrams in terms of the bending and membrane thermal variables T_{R1} and T_{R0}, displayed in Fig. 3. In fact, while the response of the directly activated bending variable T_{R1} (Fig. 3a) cannot be followed by the mechanical ***1*** model (though its value, as known parameter, can be deduced from Eq. (2)), the behavior of the dragged membrane temperature T_{R0} (Fig. 3b) can be described by the sole ***3-2*** and ***3-1*** models which include both the thermal variables. Moreover, with respect to the latter, the fully coupled ***3-2*** model demonstrates to be the only one able to correctly grasp its behavior, since the 3 d.o.f one-way model, although considering the membrane variable, furnishes identically null solutions due to the non-activation of Eq. (1b), which remains uncoupled and unforced. It is worth noting that the response in terms of membrane temperature is not affected by the sign of the excitation, i.e. it is symmetric with respect to the $e_1 = 0$ line, coherently with T_{R0} describing the thermal behavior in the plate mid-plane. Differently, the response of the bending thermal variable T_{R1} is organized along a straight line, due to the almost linear nature of the relevant thermal equation.

When considering also possible variations of the mechanical initial conditions, the comparison between coupled (i.e. ***3-2***, ***3-1***, ***2-2***, ***2-1***) and uncoupled ***1*** models highlights meaningful discrepancies. Figure 4 displays the basins of attraction (or the relevant cross sections in the mechanical plane, depending on the system d.o.f.'s)

realized, with trivial values of the thermal variables, after the application of a bending excitation $e_1 = 3 \cdot 10^{-4}$, corresponding to a power density linearly distributed along the thickness z of $8687.3 \cdot 10^3 \cdot z\, kW/m^3$. The coupled models, whose outcomes are coinciding and reported in Fig. 4a, provide discordant indications with respect to those furnished by the bifurcation diagrams, with a monostable behavior characterized by the sole (thin gray) high-amplitude buckled $P1^{IV}$ solution, without any evidence of the expected basins of attraction of the thin light gray $P1^{II}$ and of the thick black P2 responses. Conversely, the results obtained from the mechanical ***1*** model coherently identify all the three different basins with dominance of the $P1^{II}$ response and a markedly fractal organization.

The reasons of this disagreement have to be sought in the effect of the thermomechanical coupling together with the contemporary presence of slow and fast dynamics. To better understand the behavior of the coupled systems, in fact, it is worth noticing that the slowness of the bending thermal transient (which is taken into account by all the four models due to the combined presence of Eq. (1c) and term $\bar{a}_{15}$) causes the contribution of the e_1 excitation to be supplied gradually into the mechanical equation by means of the coupling term related to T_{R1}. On the other hand, the mechanical vibration is much faster than the thermal one and its transient, needed for reaching a stable solution, is very short. From a phenomenological viewpoint, it appears possible to neglect the mechanical transient and to look only at the attractor of the system, whose evolution with increasing values of the thermal bending excitation from zero to the selected value $e_1 = 3 \cdot 10^{-4}$ can be followed in the bifurcation diagram of Fig. 2. For low values of e_1, where the thin black P1 attractor is stable, the mechanical response is cross-well at least in its first initial steps, before possibly jumping to the coexisting gray buckled solution $P1^{IV}$ upon its onset. But when the bending excitation reaches a value ($e_1 \cong \pm 5.6 \cdot 10^{-5}$) providing a bending thermal variable T_{R1} in the mechanical equation such to instabilize the P1 response via period doubling bifurcation (see Fig. 2a), the mechanical trajectories are more likely to swiftly jump onto the $P1^{IV}$ buckled response. Since this solution is stable also after the arise of the further (thin light gray) buckled solution $P1^{II}$, the system response steadily remains on it in the whole considered cross-section of mechanical initial conditions. In contrast, the thermal transient is totally ignored in model ***1***, in which only the final value of the bending temperature evolution is added into the mechanical equation, and the system is able to display the basins of all the three solutions detected by the bifurcation diagram.

The effects of the various thermomechanical coupling terms can be further discussed by observing the temporal evolution of a single trajectory with fixed trivial initial conditions ($W = \dot{W} = T_{R0} = T_{R1} = 0$) followed by considering the five proposed models. Looking at the mechanical response in Fig. 5a, the outcomes confirm the coinciding behavior of the four coupled models which reach the steady high-amplitude gray $P1^{IV}$ solution, in contrast with the low-amplitude light gray $P1^{II}$ oscillation detected by the uncoupled ***1*** system, due to the fact that the selected mechanical initial condition belongs to different basins of attraction, as shown comparing the graphics of Fig. 4.

The evolution of the directly activated bending variable displayed in Fig. 5b, possibly followed only by the four coupled models, allows to point out the role played by the two-way coupling. In fact, despite the congruent steady value reached by all models, the periodic motion can be grasped by the sole gray ***3-2*** and red ***2-2*** ones, thanks to the oscillatory contribution provided by the mechanical response by means of the coupling term related to $\bar{a}_{33}$, while the one-way ***3-1*** and ***2-1*** models show a stationary solution. Moreover, due to the coinciding outcomes of the 3 d.o.f. and of the 2 d.o.f. (***3-2*** $\equiv$ ***2-2***, ***3-1*** $\equiv$ ***2-1***) models, it can be observed that the membrane thermal variable does not affect the behavior of the bending temperature.

Finally, as previously stated (see Fig. 3b), the dynamics of the dragged membrane temperature can be followed only if employing the fully coupled ***3-2*** model (see Fig. 5c), which is able to originate a non-null response by means of the $\bar{a}_{24}$ coupling term, while the other model that also contemplates the presence of the T_{R0} variable, i.e. the ***3-1*** model, provides null results due to the non-activation of Eq. (1b).

The characterization of the detected responses in the mechanical and thermal planes is reported in Fig. 6 in terms of phase portraits and Poincaré maps; here, the amplitude difference between the mechanical response identified by the coupled models and that determined by the mechanical ***1*** system is highlighted (Fig. 6a), and the very small amplitudes of the thermal variables are described (Fig. 6b, c).

In the light of the obtained results, and with the aim to focus the attention on the mechanical behavior of the thermomechanical plate, it can be thus convenient to work with the reduced 2 d.o.f. one-way ***2-1*** model, which is capable to correctly describe the response in terms of both transversal displacement and stationary bending temperature, while requiring a minor computational effort and a dimensionally lowered mathematical system with respect to the fully coupled one (1). Clearly, with this model, information about the oscillatory nature of the bending temperature, as well as any indication about the behavior of the membrane one, are neglected, which have however proved to be negligible.

As a conclusive analysis, it is of interest to comparatively summarize the transient dynamics of the mechanical response displayed by all the considered models, whose outcomes are presented in Fig. 7, which underline the influence of the coupling terms on the length of the non-stationary evolution. As shown, the shortest transient is relevant to the mechanical cyan ***1*** model, where the thermal contribution furnished by the bending excitation is entirely provided into the mechanical equation at the beginning of its time history. The two one-way models (green ***3-1*** and blue ***2-1***) display the same transient duration, due to the fact that the membrane thermal variable T_{R0}, although considered in the ***3-1*** model, is not activated by the excitation or by the coupling term, therefore having no influence on the displacement evolution. Instead, when the coupling terms are present also into the thermal equations, i.e., when considering the two-way gray ***3-2*** and red ***2-2*** models, the non-stationary dynamics lengthens, with the fully coupled ***3-2*** model which exhibits the longest transient thanks to the very slow contribution supplied by also the dragged membrane variable (whose slowness can be grasped by comparing the three graphics of Fig. 5).

3 Transient and Steady Global Dynamics Under Thermal Excitations

3.1 Bending

As shown in the previous section, the cross sections of the basins of attraction furnish, for the coupled models, contrasting results with respect to the outcomes provided by the bifurcation diagrams, due to the effect of the thermal transient into the evolution of the mechanical displacement.

Referring to the reduced 2 d.o.f. one-way ***2-1*** model formerly introduced, the matter can be better understood by also looking at different planar cross-sections of the 3D basins of attraction. In fact, the basin considered in Fig. 4a for null values of the thermal variable is certainly the reference natural one if thinking in purely mechanical terms; however, a more comprehensive description of the basins organization in the state space can only be obtained by considering planar cross-sections for also non-trivial values of the thermal variables. This is necessary mostly if being interested in grasping the final outcomes of the dynamics started with given initial conditions of the variable specifically governing the system response, which is here the bending temperature.

With application of the excitation value considered in Fig. 4, and looking at the final outcomes of the dynamics started with given T_{R1} initial conditions, Fig. 8a points out that relevant increasing values (Fig. 8b) succeed in catching the presence of also other basins of attraction, up to reproducing the response of the mechanical ***1*** model when the initial condition is set to the relevant regime value, as highlighted by the coincidence of results between Fig. 4b and the right panel of Fig. 8a. This is due to the progressive shortening of the transient dynamics as the thermal initial conditions become closer to the steady value to be attained, as shown in Fig. 8b, which corresponds to reduce the gap that the bending thermal variable has to cover.

To summarize this behavior, a cross section of the basins of attraction in the $(T_{R1}, \dot{W})$ plane is presented in Fig. 8c, which is obtained by fixing the mechanical initial condition to $W = 1.75$, within the buckled $\mathrm{P1^{II}}$ light gray basin at $T_{R1} = 3$ (see the mid panel of Fig. 8a). For initial T_{R1} lower than 3, the response of the coupled model always settles on the high-amplitude buckled $\mathrm{P1^{IV}}$ gray basin, due to the slow thermal contribution into the mechanical equation which is insufficient to move the response towards the other, yet existing, P2 and $\mathrm{P1^{II}}$attractors. For $3 < T_{R1} < 5$, the arise and enlargement of the low-amplitude $\mathrm{P1^{II}}$ light gray basin is highlighted, while for high T_{R1} initial conditions the latter becomes the only existing solution for the system, according to the outcomes of the bifurcation diagrams of Fig. 2 showing the $\mathrm{P1^{II}}$response as the only possible one for high values of the thermal excitation. In fact, setting a high T_{R1} initial condition corresponds to provide, in the first step of the system dynamical evolution, a high contribution into the mechanical equation by means of the coupling term related to $\bar{a}_{15}$. As a consequence, the displacement response is initially moved into the monostable range characterized by the $\mathrm{P1^{II}}$ solution, which therefore attracts all the trajectories regardless of the

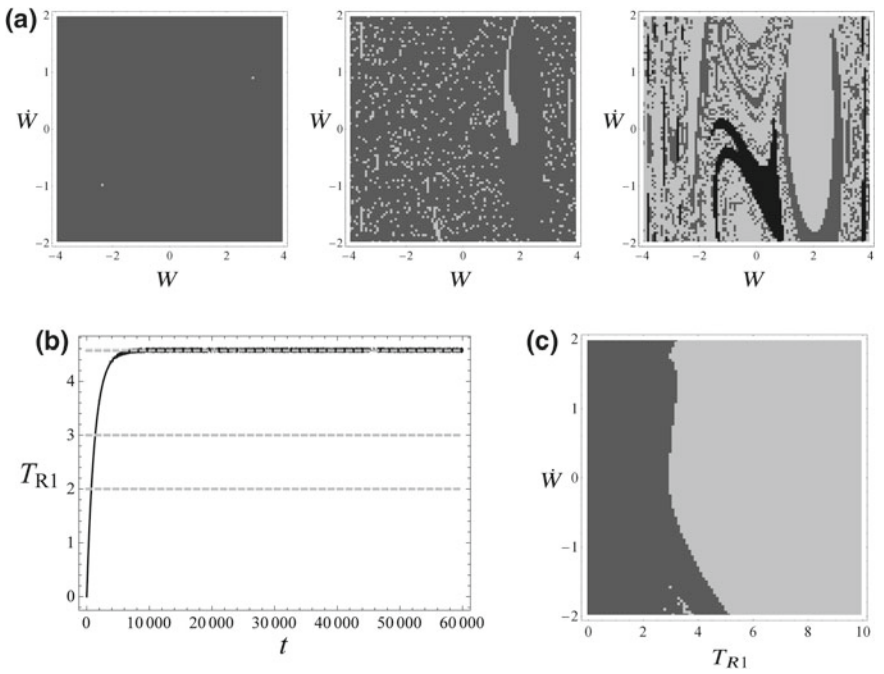

Fig. 8 **a** Cross sections of the basins of attraction of the thermomechanical model in the $(W, \dot{W})$ plane, with $p = 2.51$, $e_1 = 3 \times 10^{-4}$, $T_{R1} = 2.0$, $T_{R1} = 3.0$ and $T_{R1} = 4.57$.**b** Detection of the thermal initial conditions corresponding to the T_{R1} values in **a**, within the temporal evolution of the bending temperature variable. **c** Basin of attraction cross section in the $(T_{R1}, \dot{W})$ plane for $W = 1.75$. Light gray: basin of the low-amplitude buckled solution $P1^{II}$; Gray: basin of the high-amplitude buckled solution $P1^{IV}$; Black: basin of the period-2 solution P2

chosen initial velocity. Due to the fact that such solution is stable also when the thermal variable lowers and stabilizes around its steady value, it represents the only possible response of the system in the considered range.

3.2 Membrane

To critically discuss the effects of a membrane thermal excitation on the dynamical behavior of the system, two different kinds of thermal forcing can be considered according to the model, i.e. a time constant thermal difference T_∞ between plate and surrounding medium, which activates pure thermal convection on the external surfaces and pure internal thermal conduction, or a time-independent thermal excitation e_0, constant along the thickness, which can be physically obtained by exploiting the Joule effect due to the current passage in the plate (thanks, for example, to the insertion of conductive metallic fibers or carbon nanotubes into epoxy matrix, aimed

at enhancing its electrical conductivity). From linearization of Eq. (1b), and the subsequent substitution into Eq. (1a), a direct relation can be obtained among the two thermal excitations and also the mechanical precompression p:

$$e_0 = \frac{\bar{a}_{22}\,\alpha_1\,T_\infty}{\bar{a}_{25}} = -\frac{\bar{a}_{23}\,T_{R0}}{\bar{a}_{25}} = \frac{\bar{a}_{23}\,(p-1)}{\bar{a}_{16}\,\bar{a}_{25}} \tag{3}$$

It can be observed that e_0 and T_∞ produce the same effect on both the thermal and the mechanical vibrations, and, due to the coupling into the mechanical equation by means of a linear T_{R0} term, their action on the displacement variable corresponds to that of the precompression p. Such correspondence is stressed in the bifurcation diagram of the W displacement reported in Fig. 9a, obtained as a function of the two different (thermal e_0 and mechanical p) excitations, and, as done in the previous sections, by matching the zero of the thermal excitation with a p value corresponding to the incipient buckling ($p = 2.51$).

The results show the ability of e_0 in inducing a multistable post-buckling scenario, with the passage from the sole pre-buckling thin black P1 solution to the contemporary presence of two couples of buckled responses oscillating around varied positive/negative configurations of the plate, corresponding to low-amplitude buckled solutions (thick $P1^{I}$/thin $P1^{II}$ light gray curves) and to high-amplitude solutions (thick $P1^{III}$/thin $P1^{IV}$ gray curves) coexisting in a relatively wide range of the control parameters. The bifurcation diagram highlights also a globally symmetric behavior of the solutions of each couple with respect to the trivial equilibrium, coherently with the constant distribution of the membrane excitation along the plate thickness, and in contrast with what obtained from the application of the bending excitation previously described. Moreover, with respect to the results of Fig. 2, it is worth underlining that in this case the pre-buckling solution P1 is stable also in the post-buckling regime, where it becomes a high-amplitude cross-well solution oscillating around both the varied plate equilibria.

In particular, when a positive thermal excitation of $e_0 = 10^{-4}$ is applied, the system steady response is characterized by a multistable behavior including two pairs of buckled solutions, $P1^{III}$/$P1^{IV}$ and $P1^{I}$/$P1^{II}$, coexisting with the pre-buckling P1 response. However, the cross-section of the 3D basins of attraction with trivial values of the thermal variables displays a completely different scenario, as shown in Fig. 9b, in which the system behavior results to be monostable. The discrepancies between expected and obtained behaviors of the model can be understood by considering again the long thermal transient needed by the membrane temperature to attain its final steady value.

In fact, it entails, in the mechanical equation, a slow thermal contribution to the system overall stiffness up to reaching the value necessary to achieve the buckled configuration. As a consequence, the mechanical response in the very first initial steps of its temporal evolution falls onto the pre-buckling solution (black basin), which represents the only stable response for the system when no thermal excitation is applied, irrespective of the chosen mechanical initial conditions. Since it represents a robust attractor in the whole range of parameters here considered, the trajectories

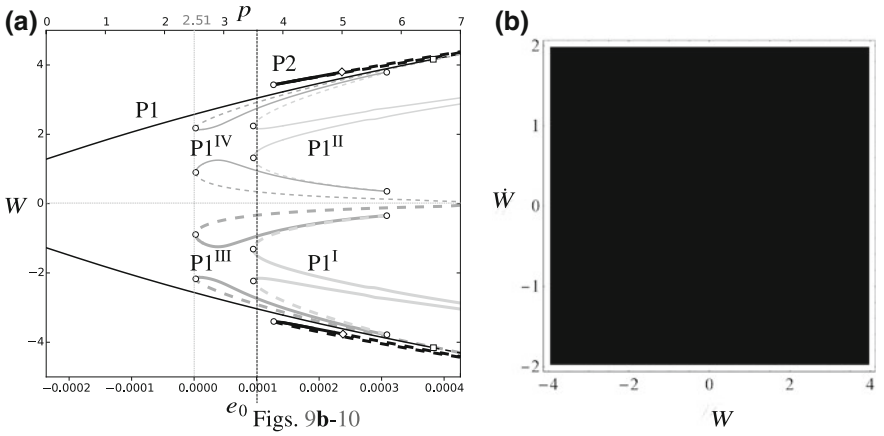

Fig. 9 **a** Bifurcation diagram of the W displacement as a function of the membrane excitation e_0 and of the mechanical precompression p. **b** Cross section in the mechanical plane of the 3D basins of attraction for $p = 2.51$ and $e_0 = 10^{-4}$. Black basin: pre-buckling solution P1

already settled on it do not modify their behavior also when other buckled responses arise in the 3D state space.

Also in this case, as seen before, changing the thermal initial conditions causes the arise and enlargement of the buckled $P1^{III}$ and $P1^{IV}$ basins of attraction (gray basins), and the subsequent birth of the low-amplitude buckled $P1^{I}$ and $P1^{II}$ basins (light gray basins), as shown in Fig. 10a for increasing values of T_{R0}. This behavior is well represented in Fig. 10c, where the section in the (T_{R0}-$\dot{W}$) plane is reported. The outcomes confirm the dependency of the mechanical response on the thermal initial values, and highlight a response similar to that obtained when analyzing the effects of the bending excitation (see Fig. 8c). However, here three regions can be detected, corresponding to qualitatively different responses of the system. For low values of T_{R0}, the mechanical displacement settles on the pre-buckling (black) P1 solution, while the basins of the high-amplitude buckled solutions $P1^{III}$ and $P1^{IV}$ appear and enlarge their compact part for $0.15 < T_{R0} < 1$, anyway coexisting with the pre-buckling one and showing a markedly fractal organization. For T_{R0} higher than 1, the low-amplitude buckled responses $P1^{I}$ and $P1^{II}$ (light gray basins) also arise and widen, with evident dominance of the one oscillating around the positive configuration, according to the chosen positive mechanical fixed initial condition $W = 2.0$. The region of high T_{R0} values (i.e.,$T_{R0} > 1.8$) is finally governed by the sole $P1^{II}$ basin, confirming the outcomes of the relevant bifurcation diagram of Fig. 9a which displays the presence of the sole buckled $P1^{I}$/$P1^{II}$couple for high values of the thermal dynamics.

As a final comment, it is worth noting that the fractal arrangement of the basins herein detected is not present in the previously analyzed bending forced case, due to the different kind of mechanical buckling (symmetric versus antisymmetric) achievable with the two thermal excitations. When the membrane variable is activated, in fact, the coexistence of several buckled solutions possibly reachable by the trajecto-

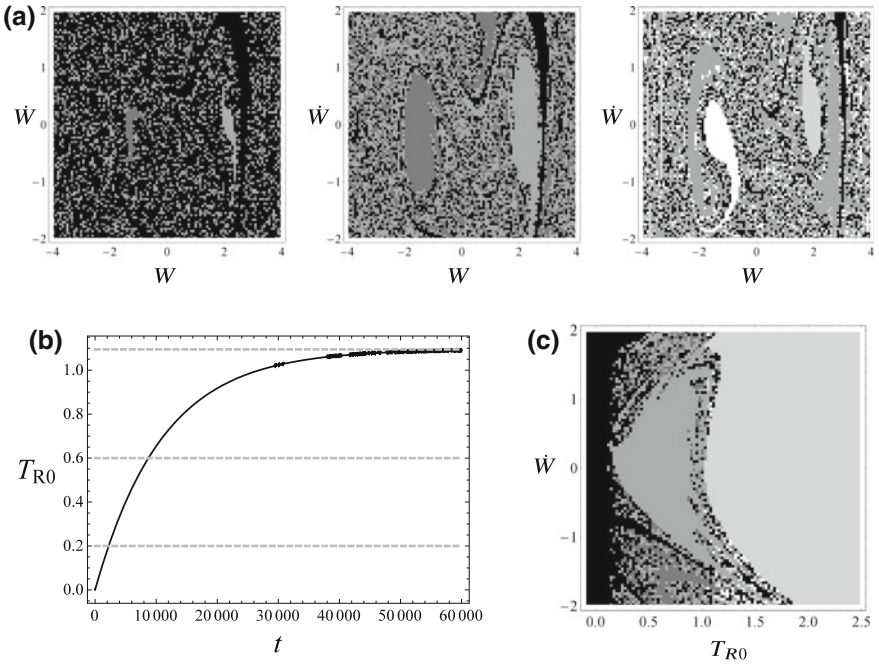

Fig. 10 **a** Cross sections of the basins of attraction of the thermomechanical model in the $(W, \dot{W})$ plane, with $p = 2.51$, $e_0 = 10^{-4}$, $T_{R0} = 0.2$, $T_{R0} = 0.6$ and $T_{R0} = 1.09475$. **b** Detection of the thermal initial conditions corresponding to the T_{R0} values in **a**, within the temporal evolution of the membrane temperature variable. **c** Basin of attraction cross section in the $(T_{R0}, \dot{W})$ plane for $W = 2.0$. Light gray: basin of the low-amplitude buckled solutions $P1^{II}/P1^{I}$; Gray: basin of the high-amplitude buckled solutions $P1^{IV}/P1^{III}$; Black: basin of the pre-buckling solution P1

ries causes the fractalization of the relevant basins, while the antisymmetric behavior of the bending variable strongly reduces the multistability region and the basins are organized in a more compact way.

4 Conclusions

Thermomechanical coupling of a reduced order model of von Kármán shear indeformable plate in active thermal regime and in the presence of an harmonic transverse mechanical excitation and a constant axial excitation has been addressed, focusing on both modeling aspects and phenomenological features of the transient and steady nonlinear dynamic response.

The first part of the work has been devoted to comparatively investigating some main local and global dynamical aspects of the response, as obtained with different reduced order models ranging from the original, fully coupled, model with one

mechanical (mid-plane transverse displacement) and two thermal (membrane and bending) variables, down to the simplest uncoupled mechanical model in which the presence of an active thermal environment is accounted for by merely including its known steady effect in the relevant equation of motion. Both the two-way (from thermal to mechanical, and from mechanical to thermal) and the one-way (from thermal to mechanical) coupling have been considered, along with intermediate (two-d.o.f.) models accounting for only the directly excited thermal equation/variable. This has allowed to evaluate the relative importance of the various terms and variables of coupling, in view of a satisfactory, and more or less comprehensive, description of the system dynamics. Based on the considered (membrane or bending) thermal excitation, the alternative two-d.o.f one-way coupled models obtained by skipping either one (bending or membrane, respectively) of the two thermal equations/variables and by neglecting the mechanical contribution into the remaining (membrane or bending) equation have been identified as the most "economical" ones to be used for a systematic numerical investigation aimed at reliably describing the response in terms of mechanical variable and of the dominant (membrane or bending) thermal one, although caught in its solely steady features.

In the second part of the work, the two alternative models have been used to investigate the plate dynamics under a bending or membrane thermal excitation, each one of them inducing a variably rich scenario of buckled mechanical responses. Attention has been focused on the important role played by global dynamics investigations in unveiling the meaningful effects entailed on the plate steady mechanical response by the variably slow thermal transients taken into account by the (though simplified) thermomechanically coupled model. For each of the considered excitations, these effects have been highlighted via a combined use of properly selected cross-sections of the 4D basin of attraction and of the transient time history of the corresponding thermal variable, by looking at the relevant outcomes against the local bifurcation scenario of the mechanical displacement.

Acknowledgements VS and GR acknowledge the financial support of PRIN 2015 "Advanced mechanical modeling of new materials and structures for the solution of 2020 Horizon challenge" (No. 2015JW9NJT).

References

1. Alijani, F., Bakhtiari-Nejad, F., Amabili, M.: Nonlinear vibrations of FGM rectangular plates in thermal environments. Nonlinear Dyn. **66**(3), 251–270 (2011)
2. Carvalho, E.C., Gonçalves, P.B., Rega, G.: Multiple internal resonances and nonplanar dynamics of a cruciform beam with low torsional stiffness. Int. J. Solids Struct. **121**, 117–134 (2017)
3. Rega, G., Lenci, S.: A global dynamics perspective for system safety from macro-to nanomechanics: analysis, control, and design engineering. Appl. Mech. Rev. **67**(5), 050802 (2015)
4. Ribeiro, P.: Thermally induced transitions to chaos in plate vibrations. J. Sound Vib. **299**(1), 314–330 (2007)
5. Saetta, E., Rega, G.: Unified 2D continuous and reduced order modeling of thermomechanically coupled laminated plate for nonlinear vibrations. Meccanica **49**(8), 1723–1749 (2014)

6. Saetta, E., Rega, G.: Modeling, dimension reduction, and nonlinear vibrations of thermomechanically coupled laminated plates. Procedia Eng. **144**, 875–882 (2016)
7. Saetta, E., Rega, G.: Third order thermomechanically coupled laminated plate: 2D nonlinear modeling, minimal reduction, and transient/post-buckled dynamics under different thermal excitations. Compos. Struct. **174**, 420–441 (2017)
8. Settimi, V., Rega, G.: Exploiting global dynamics of a noncontact atomic force microcantilever to enhance its dynamical robustness via numerical control. Int. J. Bifurc. Chaos **26**(07), 1630018 (2016)
9. Settimi, V., Rega, G.: Global dynamics and integrity in noncontacting atomic force microscopy with feedback control. Nonlinear Dyn. **86**(4), 2261–2277 (2016)
10. Settimi, V., Saetta, E., Rega, G.: Local and global nonlinear dynamics of thermomechanically coupled composite plates in passive thermal regime. Nonlinear Dyn. (2017). https://doi.org/10.1007/s11071-017-3648-1
11. Settimi, V., Rega, G., Saetta, E.: Avoiding/inducing dynamic buckling in a thermomechanically coupled plate: a local and global analysis of slow/fast response. Proc. R. Soc. A **20180206** (2018). http://dx.doi.org/10.1098/rspa.2018.0206
12. Shen, H.S., Xiang, Y.: Nonlinear vibration of nanotube-reinforced composite cylindrical panels resting on elastic foundations in thermal environments. Compos. Struct. **111**, 291–300 (2014)
13. Thanh, N.V., Khoa, N.D., Tuan, N.D., Tran, P., Duc, N.D.: Nonlinear dynamic response and vibration of functionally graded carbon nanotube-reinforced composite (fg-cntrc) shear deformable plates with temperature-dependent material properties and surrounded on elastic foundations. J. Therm. Stress. **40**(10), 1254–1274 (2017)
14. Yeh, Y.L.: The effect of thermo-mechanical coupling for a simply supported orthotropic rectangular plate on non-linear dynamics. Thin-Walled Struct. **43**(8), 1277–1295 (2005)

Appendix
Professional Life of Professor Leonid Isakovich Manevitch

Biographical Sketch of Leonid I. Manevitch

Leonid Isakovich Manevitch was born on April 2, 1938 in Mogilyov (Belarus). He got high education at the Faculty of Mechanics and Mathematics of Dnepropetrovsk State University (DSU) in 1954–1959. After graduating from the DSU, he worked as an engineer and the head of theoretical group in the Design Bureau Yuzhnoye" (1959–1964) and at the same time he studied in extramural postgraduate study in DSU. He got the degree of Candidate of Sciences (PhD) for his thesis on stability of shells in 1961. From 1964 till 1976 he worked in DSU as an Associate Professor, and then as a Full Professor at the Department of Applied Theory of Elasticity. In 1970 he received a degree of Doctor of Sciences for his dissertation devoted to asymptotic and group methods in the mechanics of deformable solids, and the title of Professor was conferred upon him in 1973. Since 1976, after moving to Moscow, he worked as a senior research fellow, and then as the head of the Physics and Mechanics of Polymers Division of the Chemical Physics Institute of the USSR Academy of Sciences. Since 1984 he also worked as a Professor at the Department of Polymer Physics at the Moscow Institute of Physics and Technology.

L. Manevitch's scientific activity was related to many areas of mechanics of deformable media, nonlinear dynamics and condensed matter physics. He obtained important and deep results in the asymptotic analysis of problems of strength and stability of anisotropic and reinforced plates and shells, in the asymptotic analysis of elasticity theory for anisotropic media, including theory of deformation and destruction of highly anisotropic composites. He has made significant contributions to the theory of nonlinear normal oscillations in essentially nonlinear systems, to nonstationary dynamics of nonlinear oscillatory systems; to molecular dynamics and physics of polymers and composite materials. He developed the theory of structural defects and structural transitions at the atomic level in molecular and polymer crystals, studied the transport and localization of energy in mechanical systems, polymer chains and nanotubes. These works have numerous applications to various fields of mechanics and physics, the theory of vibration protection and nanotechnology.

I. V. Andrianov et al. (eds.), *Problems of Nonlinear Mechanics and Physics of Materials*, Advanced Structured Materials 94,
https://doi.org/10.1007/978-3-319-92234-8

L.I. Manevitch is an active participant of many Russian and international symposia, conferences and congresses. As a guest speaker he repeatedly appeared at seminars of famous universities of the USA, Europe and Israel (Harvard University, Massachusetts Institute of Technology, Brown University, University of Illinois Urbana-Champaign, Delft University of Technology, Universities of Groningen, Ulm, Freiburg, Technion—Israel Institute of Technology, etc.).

His scientific results are presented in 20 monographs (in publishing houses Wiley, Springer, Kluwer, Imperial College Press, Nauka (Russia)) and in more than 350 publications.

L.I. Manevitch has a large number of disciples and followers. He was a supervisor on 38 candidate (PhD) dissertations, and 12 of his disciples became Doctors of Science. At present, L.I. Manevitch continues to work as the head of Physics and Mechanics of Polymers Laboratory of the Chemical Physics Institute of the Russian Academy of Sciences. This Laboratory under his leadership became one of the leading research teams in the field of solid polymer physics and nonlinear dynamics of molecular systems, which actively cooperates with famous research centers in USA, Italy, Israel, Germany.

Now L.I. Manevitch is active and full of creative ideas, as throughout his life.

List of Books of Professor Leonid I. Manevitch

(in reverse chronological order)

1. Manevitch L.I.: Interaction of Physics and Mathematics. Moscow-Izhevsk, Izhevsk Institute of Computer Researches (2018), 168 p. (in Russian).
2. Manevitch L.I., Kovaleva A.S., Smirnov V.V., Starosvetsky Yu.: Nonstationary Resonant Dynamics of Oscillatory Chains and Nanostructures. Singapore, Springer Nature (2017), 436 p.
3. Manevitch L.I., Gendelman O.V.: Analytically Solvable Models of Solid Mechanics. Moscow-Izhevsk, Izhevsk Institute of Computer Researches, (2016), 344 p. (in Russian).
4. Manevitch L.I., Gendelman O.V.: Tractable Models of Solid Mechanics. Formulation, Analysis and Interpretation. Berlin, Heidelberg, London, New York, Springer (2011), 302 p.
5. Manevitch L.I., Smirnov V.V.: Solitons in Macromolecular Systems. New York, Nova Science Publishers (2008), 134 p.
6. Manevich A.I., Manevitch L.I.: The Mechanics of Nonlinear Systems with Internal Resonances. Imperial College Press, London (2005), 250 p.
7. Andrianov I.V., Awrejcewicz J., Manevitch L.I.: Asymptotical Mechanics of Thin-Walled Structures. Berlin, Heidelberg, New York, Springer (2004), 535p.
8. Andrianov I.V., Barantsev R.G., Manevitch L.I.: Asymptotical Mathematics and Synergetics. Moscow, URSS (2004), 300 p. (in Russian).

9. Manevitch L.I., Andrianov I.V., Oshmyan V.G.: Mechanics of Periodically Heterogeneous Structures. Berlin, Heidelberg, New York, Springer (2002), 264 p.
10. Andrianov I.V., Manevitch L.I.: Asymptotology. Ideas, Methods, and Applications. Dordrecht, Boston, London, Kluwer Academic Publishers (2002), 252 p.
11. Awrejcewicz J., Andrianov I., Manevitch L.: Asymptotic Approaches in Nonlinear Dynamics: New Trends and Applications. Berlin, Heidelberg, New York, Springer-Verlag (1998), 350 p.
12. Vakakis A.F., Manevitch L.I., Mikhlin Yu.V., Pilipchuk V.N., Zevin A.A.: Normal Modes and Localization in Nonlinear Systems. New York, Wiley (1996), 552 p.
13. Andrianov I.V., Manevich L.I.: Asymptotology: Ideas, Methods, Results. Moscow, ASLAN (1994), 160 p. (in Russian).
14. Manevitch L.I., Pavlenko A.V.: Asymptotic Method in Micromechanics of Composite Materials. Kiev, Vyshchaya Shkola (High School) (1991), 132 p. (in Russian).
15. Andrianov I.V., Manevitch L.I.: Asymptotic Methods and Physical Theories. Moscow, Znanie (1989), 64 p. (in Russian).
16. Manevitch L.I., Mikhlin Yu.V., Pilipchuk V.N.: The Method of Normal Oscillations for Essentially Nonlinear Systems. Moscow, Nauka (1989), 216 p. (in Russian).
17. Andrianov I.V., Lesnichaya V.A., Loboda V.V., Manevitch L.I.: Investigation of Strength of Reinforced Shells of Engineering Structures. Kiev-Donetsk, Vyshchaya Shkola (High school) (1986), 104 p. (in Russian).
18. Andrianov I.V., Lesnichaya V.A., Manevitch L.I.: The Averaging Method in Statics and Dynamics of Ribbed Shells. Moscow, Nauka (1985), 222 p. (in Russian).
19. Manevitch L.I., Pavlenko A.V., Koblik S.G.: Asymptotic Methods in the Theory of Orthotropic Solids. Kiev, Vysshaya Shkola (High School) (1982), 152 p. (in Russian).
20. Mossakovskii V.I., Manevitch L.I., Miltzin A.M.: Modeling of Strength of Thin Shells. Kiev, Naukova Dumka (1977), 160 p. (in Russian).

The Scientific Contribution of Professor L. I. Manevitch

Scientific results obtained by Professor L.I. Manevitch (Manevich in some publications) are presented in 20 monographs and in more than 350 papers in peer reviewed journals. In this short review of his scientific activity we refer mainly to the monographs by Manevitch, his surveys papers and papers important from the point of view of the priority. These works contain detailed references to other Manevitch's publications.

I. Mechanics of Solids

Stability of Shells [1.1–1.18]

The first scientific works of L.I. Manevitch were devoted to structures stability problems, mainly related to cylindrical shells. It was due to traditions of the Dnepropetrovsk University scientific school (the direct teachers of L.I. were Prof. Yu.A. Shevlyakov and Academician V.I. Mossakovskii), and to his work at the Design Bureau "Yuzhnoye," which set him and his colleagues complex applied problems of design of reliable shell structures.

L.I. Manevitch's researches on shell buckling included both theoretical and experimental studies. The most important results obtained theoretically were connected with stability of cylindrical shells under bending and non-uniform compression in framework of the nonlinear theory [1.1–1.3]. In these papers, the lower critical load of a cylindrical shell was determined for pure bending and for non-uniform compression by applying the Rayleigh-Ritz method. It turned out that the inhomogeneity of the pre-buckling stress state of the structure plays a different role in shell bucking theory considering "small" or "large" perturbations. The results of these solutions were used later in the well-known monographs of A.S. Vol'mir, "Stability of Elastic Systems" (1963), "Stability of Deformable Systems" (1967) and others.

Along with these researches, a number of studies were carried out on the stability of smooth and reinforced shells (which had a predominantly applied orientation) within framework of the linear theory [1.4–1.7, 1.15, 1.17]. E.g., the complicated problem of buckling of the rocket structure consisting of a cylindrical tank with a spherical bottom connected to the cylinder by a circular ring, subjected to internal pressure, has been solved in [1.17]. At the same time, the analysis of the influence of various factors (weakened boundary conditions, parameters of reinforcing ribs, etc.) on the bearing capacity of the shells in the scope of various approximate versions of the shell theory ("semi-momentless" theory, structurally-orthotropic theory, certain simplified engineering schemes) served for L.I., perhaps, as the impetus to comprehend the importance of "asymptotic thinking", which allows to understand the complex picture of "play of forces" in the shells.

At the same time, in the Research Laboratory of Structures Strength and Reliability of the Dnepropetrovsk University, L.I. Manevitch, his colleagues and disciples carried out a wide range of experimental studies, which made the "Dnepropetrovsk school" known not only in the USSR but also abroad [1.8–1.13].

The extensive experiments made it possible to study the statistical properties of buckling loads of compressed cylindrical shells, evaluate separately the influence of various perturbing factors (initial imperfections, quality of the edges, etc.); to study the effect of reinforcements, combined loading, and the rigidity of the testing machine. The existence of different dimple-like *local* post-buckling equilibrium states of a compressed cylindrical shell has been experimentally revealed in [1.11, 1.13]. In addition, the external perturbation energy, necessary to snap

through from the initial shell state to a certain post-buckling one, has been determined [1.14, 1.16].

L.I. Manevitch's researches on stability, carried out in 1960–70s, were related to the most relevant directions and left a notable imprint in the shell buckling theory. We note that he also applied to the problems of the shell stability in the subsequent years [1.18].

Singular Asymptotics of Shells [1.19–1.30]

The first years of professional activity of L.M. were closely connected with the theory of shells. At 1960s the triumphant procession of FEM in Mechanics of Solids was just at the beginning, FEM codes (like ABAQUS, ANSYS) did not exist, and the possibilities of computer technology were very limited. The analysis of shells, especially ribbed ones, presented serious difficulties. Recall that the shell theory can be interpreted as a part of the theory of elasticity for bodies, in which two sizes significantly exceed the third one (thickness of the shell). As a result, a natural small parameter appears in the equations, viz. the shell thickness to its radius ratio h/R. Asymptotic methods in theory of shells are therefore quite adequate both physically and mathematically. The asymptotic theory of isotropic shells was well developed, but its generalization to reinforced shells was a non-trivial problem. L. M. pointed out that some of the dimensionless parameters in the initial equations (for example, the ratio of the flexural stiffness' in different directions) are of the order h/R. This fact made possible to obtain new non-trivial asymptotics of the boundary value problems of ribbed shells [1.19]. A complete classification of possible limit systems was obtained on the basis of the Newton polygon method and its generalizations.

Asymptotic analysis for the most frequently used boundary conditions made it possible to formulate simplified boundary value problems of order lower than the original ones. Linear and nonlinear problems of statics, dynamics and stability were considered. The main results were collected in [1.20].

V.V. Bolotin and, independently, Keller J.B. and Rubinow S.I. proposed an effective asymptotic method for solving linear dynamical problems of the theory of plates and shells with complicated boundary conditions (dynamic edge effect or Keller-Rubinow wave method). L.M. by means of thin energetic estimates has generalized the method to the nonlinear case [1.21]. Such a generalization, in particular, allowed to take a fresh look at normal modes of nonlinear oscillations of distributed systems and to obtain them analytically for complicated boundary conditions [1.22–1.24].

After the appearance of powerful FEM codes, satisfying the demands of engineering practice, interest to the theory of shells weakened significantly. The nano-revolution revived the interest to nano-shells. Experiments showed an interesting feature of nano-shells: they remain elastic at considerable deformations. Thus, the main role in their description is played by geometric nonlinearity. Using this observation L.M. and his coauthors have obtained interesting results [1.25–1.30].

Homogenization [1.31–1.35]

L.M.'s research in the field of homogenization was initiated by the problems of ribbed shells analysis. The mathematical apparatus was based on asymptotic methods for PDE with rapidly oscillating right-hand sides and boundary conditions. Note that the works by N.S. Bakhvalov appearing at the same time were based on the so-called Bakhvalov's ansatz, and the works of the French school used the multi-scale approach. The important features of L.M.'s work were the analytical solution of cell problems and the analytical description of the boundary layers [1.31–1.35].

Composites [1.36–1.38]

After moving to Semenov Institute of Chemical Physics in Moscow (1976) L.M. began activity in the theory of composite materials, which was new field for him. A lot of his papers were devoted to the determination of the effective characteristics of layered, fibrous and particle-filled composites for an elastic or elastoplastic matrix with the complicated interface between the inclusions and the matrix [1.36, 1.34]. For densely packed, high-contrast composites the percolation theory was used. Numerical results were compared with experimental data [1.37, 1.38].

Anisotropic Theory of Elasticity [1.39–1.45]

As shown by L.M., the boundary value problems of plane and spatial axisymmetric elasticity theory in the case of strong anisotropy can be reduced asymptotically to successively solved Laplace's equations. For the plane problem, this gives possibility to use complex analysis effectively, and for the spatial problem, the method of integral transforms. There have been obtained approximate analytical solutions of the contact problems with unknown boundary between the contact regions, problems of the transfer of static and dynamic loads by elastic elements to plane and spatial elastic and viscoelastic orthotropic bodies [1.39–1.41], problems of the adhesive strength and failure of fibrous composites [1.42–1.45].

1.1. Shevlyakov, Yu.A., Manevitch, L.I.: Stability of a cylindrical shell during bending, Reports of the Academy of Sciences of the Ukrainian SSR, 5, 605–608 (1960) (in Ukrainian).
1.2. Manevitch, L.I.: On local stability of shells under non-uniform loading. Reports of the Academy of Sciences of the Ukrainian SSR, 8, 1018–1021 (1961) (in Ukrainian).
1.3. Manevitch, L.I.: On the stability of a cylindrical shell under uneven axial compression. Proceedings of the conference on the theory of plates and shells. (Kazan, 1960), 226–232 (1960) (in Russian).
1.4. Manevitch, L.I., Stezhko, A.V.: Effect of boundary conditions on the vibration frequencies and critical stresses of a cylindrical shell. Soviet Applied Mechanics, 4(3), 7–10 (1968).
1.5. Manevitch, L.I., Stezhko, A.V.: Investigation of the stability of a cylindrical shell reinforced at the edges by elastic frames. Hydroaeromechanics and the Theory of Elasticity, Dnepropetrovsk, DGU, 8, p. 92–98 (1968) (in Russian).

1.6. Manevitch, L.I., Grishchak, V.Z.: Investigation of the bearing capacity of reinforced cylindrical shells under combined loading taking into account the discrete arrangement of the frames. Hydroaeromechanics and the Theory of Elasticity. Dnepropetrovsk, DGU, 8, 72–83 (1968) (in Russian).
1.7. Manevitch, L.I., Grishchak, V.Z.: Influence of longitudinal tensile loads on the stability of cylindrical shells under the influence of external pressure, Soviet Applied Mechanics, 6(8), 829–833 (1970).
1.8. Manevitch, L.I., Miltsyn, A.M., Mossakovskii, V.I., Prokopalo, E.F., Smelyi, G.N., Sotnikov, D.I.: Experimental study of the stability of smooth cylindrical shells of various scales under axial compression. "Mekhanika. Tverdogo Tela" [Mechanics of Solids], 5, 180–184 (1968) (in Russian).
1.9. Manevitch, L.I., Prokopalo, E.F.: On the statistical properties of the bearing capacity of smooth cylindrical shells. In: "Problems of reliability in construction mechanics", Vilnius, 182–187 (1968) (in Russian).
1.10. Heizenblazen, R.E., Manevitch, L.I., Mossakovskii, V.I., Prokopalo, E.F.: On the influence of initial perturbations on the stability of smooth cylindrical shells. Izv. AN SSSR, Mekhanika Tverdogo Tela [Mechanics of Solids], 6, 180–184 (1969) (in Russian).
1.11. Mossakovskii, V.I., Manevitch, L.I., Prokopalo, E.F.: Investigation of post-critical behaviour of cylindrical shells. In: Reports of the USSR Academy of Sciences, 206(2), 297–298 (1972) (in Russian).
1.12. Manevitch, L.I., Mossakovskii, V.I., Prokopalo, E.F.: Experimental study of the influence of the rigidity of the testing machine on the stability of cylindrical shells under axial compression. Izv. AN SSSR, Mekhanika Tverdogo Tela [Mechanics of Solids], 6, 152–154 (1973) (in Russian).
1.13. Manevitch, L.I., Mossakovskii, V.I., Prokopalo, E.F.: Experimental study of the postcritical behaviour of shells. Izv. AN SSSR, Mekhanika Tverdogo Tela [Mechanics of Solids], 10 (1) 163–168 (1975) (in Russian).
1.14. Mossakovskii, V.I., Manevich, L.I., Evkin, A.Yu.: Investigation of post-buckling equilibrium forms of a compressed cylindrical shell. Soviet Applied Mechanics, 11(11), 1155–1159 (1975).
1.15. Andrianov, I.V., Manevitch, L.I.: Investigation of stability of eccentrically stiffened circular cylindrical and conical shells with free in circumferential direction butt-ends. Hydroaeromechanics and the Theory of Elasticity, 21, 139–142 (1976) (in Russian).
1.16. Evkin, A.Yu., Krasovsky, V.L., Manevitch, L.I.: Stability of longitudinally compressed shells under quasi-static local disturbances. Izv. AN SSSR, Mekhanika Tverdogo Tela [Mechanics of Solids], 13(6) 95–100 (1978) (in Russian).
1.17. Manevitch, L.I., Pis'mennaya L.E.: Stability of composite shells. Soviet Applied Mechanics, 16 (2), 140–145 (1980).
1.18. Manevitch, L.I., Gendelman, O.V.: Local buckling of reinforced cylindrical shells. VII Symposium Statecznosci Konstrukcji, Poland, Bielsko-Biala, 27–31 (1994).

1.19. Manevitch, L.I., Pavlenko, A.V.: Asymptotical analysis of equations of the excentrically stiffened cylindrical shells theory. Theory of Plates and Shells. Moscow, Nauka, 185–190 (1971) (in Russian).
1.20. Andrianov, I.V., Lesnichaya, V.A., Loboda, V.V., Manevitch L.I.: Investigation of Strength of Reinforced Shells of Engineering Structures. Kiev-Donetsk, Vyshchaya Shkola (High school), 104 p. (1986) (in Russian).
1.21. Andrianov, I.V., Manevitch, L.I., Kholod, E.G.: On the nonlinear oscillation of rectangular plates. Structural Mechanics and Theory of Structures 5, 48–51 (1979) (in Russian).
1.22. Andrianov, I.V., Lesnichaya, V.A., Manevitch, L.I.: Homogenization Methods in Statics and Dynamics of Ribbed Shells. Moscow, Nauka, 221 p. (1985) (in Russian).
1.23. Andrianov, I.V., Awrejcewicz, J., Manevitch, L.I.: Asymptotical Mechanics of Thin-Walled Structures: A Handbook. Berlin, Heidelberg, Springer (2004).
1.24. Awrejcewicz, J., Andrianov, I. V., Manevitch, L.I.: Asymptotic Approaches in Nonlinear Dynamics: New Trends and Applications. Heidelberg, Berlin, New York: Springer-Verlag (1998).
1.25. Smirnov, V.V., Shepelev, D.S., Manevitch, L.I.: Localization of bending vibrations in the single-wall carbon nanotubes. Nanosystems: Physics, Chemistry, Mathematics **2** (2), 102–106 (2011).
1.26. Strozzi, M., Manevitch, L.I., Pellicano, F., Smirnov, V.V., Shepelev, D.S.: Low-frequency linear vibrations of single-walled carbon nanotubes: Analytical and numerical models. J. Sound Vibr. **333**, 2936–2957 (2014).
1.27. Smirnov, V.V., Shepelev, D.S., Manevitch, L.I.: Localization of low- frequency oscillations in single-walled carbon nanotubes. Phys. Rev. Lett. **113,** 135502 (2014).
1.28. Smirnov, V.V., Manevitch, L.I., Strozzi, M., Pellicano, F.: Nonlinear optical vibrations of single-walled carbon nanotubes. 1. Energy exchange and localization of low-frequency oscillations. Physica D **325**, 113–125 (2016).
1.29. Kaplunov, J., Manevitch, L.I., Smirnov, V.V.: Vibrations of an elastic cylindrical shell near the lowest cut-off frequency. Proceedings of Royal Society A **472**, 1–11 (2016).
1.30. Strozzi, M., Smirnov, V.V., Manevitch, L.I., Milani, M., Pellicano, F.: Nonlinear vibrations and energy exchange of single-walled carbon nanotubes. Circumferential flexural modes. J. Sound Vibr. **381,** 156–178 (2016).
1.31. Manevitch, L.I., Kovaleva, A., Smirnov, V., Starosvetsky, Yu.: Nonstationary Resonant Dynamics of Oscillatory Chains and Nanostructures. Singapore, Springer Nature (2018).
1.32. Andrianov, I.V., Manevitch, L.I.: Classification of approximate equations for discretely stiffened shells. Hydroaeromechanics and the Theory of Elasticity, Dnepropetrovsk, DGU, **15**, 115–122 (1972) (in Russian).
1.33. Andrianov, I.V., Manevitch, L.I.: Calculation of the strain-stress state of orthotropic strip, stiffened by ribs. Mechanics of Solids **10** (4), 125–129 (1975).

1.34. Andrianov, I.V., Lesnichaya, V.A., Manevitch, L.I.: Homogenization Methods in Statics and Dynamics of Ribbed Shells. Moscow, Nauka (1985) (in Russian).
1.35. Manevitch, L.I., Andrianov, I.V., Oshmyan, V.G.: Mechanics of Periodically Heterogeneous Structures. Berlin, Heidelberg, New York, Springer (2002).
1.36. Andrianov, I.V., Manevitch, L.I.: Homogenization method in the theory of shells. Advances in Mechanics **6**(3/4), 3–29 (1983) (in Russian).
1.37. Knunyants, N.N., Lyapunova, M.A., Manevitch, L.I., Oshmyan, V.G., Shaulov, A.Yu.: Modeling the effect of a nonideal adhesive bond on the elastic properties of a dispersively filled composite. Mechanics of Composite Materials **22**(2), 162–165 (1986).
1.38. Gai, M.I., Manevitch, L.I., Oshmyan, V.G.: Percolation effects in the mechanics of composite materials. Mechanics of Composite Materials **26**(3), 310–314 (1990).
1.39. Gai, M.I., Zelenskii, E.S., Manevitch, L.I., Oshmyan, V.G., Sochnev, V.I., Sulyaeva, Z.P., Turusov, R.A.: Elastic characteristics of randomly nonuniform composites. Mechanics of Composite Materials **23**(2), 172–178 (1987).
1.40. Manevitch, L.I., Pavlenko, A.V., Shamrovskii, A.D.: Application of the group theory methods to the dynamical problems for orthotropic plates. In: Proceedings of the 7th All-Union Conference on Plates and Shells (Dnepropetrovsk, 1969). Moscow, Nauka, 408–412 (1970) (in Russian).
1.41. Manevitch, L.I., Pavlenko, A.V., Shamrovskii, A.D.: The approximate solution of the theory of elasticity contact problem for anorthotropic strip reinforced by ribs. Hydroaeromechanics and the Theory of Elasticity, Dnepropetrovsk, DGU, 13, 102–112 (1971) (in Russian).
1.42. Manevitch, L.I., Pavlenko, A.V.: Transmission of a dynamic load by a longitudinal stiffener on an elastic orthotropic plate. Mechanics of Solids **10** (2): 100–106 (1975).
1.43. Manevitch, L.I., Gendelman, O.V.: Tractable Models of Solid Mechanics: Formulation, Analysis and Interpretation. Berlin, New York, Springer (2011).
1.44. Manevitch, L.I., Pavlenko, A.V.: Asymptotic Methods in Micromechanics of Composite Materials. Kiev, Naukova Dumka (1991) (in Russian).
1.45. Manevitch, L.I., Pavlenko, A.V., Koblik, S.G.: Asymptotic Methods in the Theory of Elasticity of Orthotropic Body. Kiev – Donetsk, Vyshcha Shkola (1979) (in Russian).

II. Nonlinear Normal Vibration Modes

The first work by L.I. Manevitch (with Yu.K. Privarnikov) on vibrations and stability of rods under dynamic loading was published in 1966 [2.1]. In this work the essential role of inertial nonlinearity was highlighted, and it was sudden to that

period. A necessity of effective calculation of fundamental frequencies and corresponding normal vibration modes of a missile resulted to the idea of using geometric symmetry in disposition of side units of the missile. Initially, the symmetry group representations were used by L.I. Manevitch and S.A. Vladimirov in problems of linear elastic vibrations. Meanwhile, even elastic joints between the missile units contain nonlinear elements, so, it prevents to use the symmetry group representations. Therefore L.I. Manevitch and M.A. Pinsky proposed the approach based on classification of subgroups of the discrete groups of symmetry. It permits to determine nonlinear normal vibration modes which are invariant with respect to the selected subgroups. Obtained results were presented, in particular, in [2.2], then they were included to some books concerned with nonlinear vibration modes [2.9, 2.10].

In the middle of the 60th, after acquaintance with works by R.M. Rosenberg, generalizing the concept of nonlinear normal modes (NNMs) to essential nonlinear systems, co-publications by L.I. Manevitch and B.P. Cherevatzky, relating to this topic, appeared. Here the traditional approach based on the classical small parameter method was used to construct NNMs [2.3]. It was considered also so-called "degenerative" two-DOF systems having strongly different inertial characteristics. It permits to distinguish both non-local and localized vibration modes. There was also carried out an investigation of resonance regimes in nonlinear non-autonomous systems by using the concept of nonlinear normal vibration modes [2.4].

Other direction in the theory of NNMs is relative to analysis of trajectories of such solutions in the system configuration space. These investigations were begun by L.I. Manevitch and Yu.V. Mikhlin. As a result, a new approach on construction of these trajectories in conservative finite-DOF systems, closed to generating ones, which permit normal vibrations with rectilinear trajectories, was proposed. Such generating systems can be non-linearized ones, in particular, homogeneous systems which potential is an even homogeneous function of positional coordinates. To construct the weakly curvilinear trajectories, the double power series both by the small parameter and by some selected generalized coordinate, were used [2.5]. Result of investigation was a direct generalization of classical results by A.M. Lyapunov (concerned with quasilinear case) to essentially nonlinear systems.

Two different projects dealing with non-local dynamic effects were initiated by L.I. Manevitch together with V.N. Pilipchuk in late 70th. The main question under investigation was whether the concept of NNMs is actually applicable to vibrating systems with multiple equilibrium positions and/or stiff barriers. Besides, both types of systems were found to have some common basis due to the fact that impact interactions with stiff barriers admit interpretation as transitions to new potential wells after unfolding the configuration space in a specific mirror-like way. The corresponding dynamics are of practical interest due to the possibility of snap-through phenomena in shallow shells incorporated, for instance, in different triggering devices. In this case, an adequate description was achieved using the manifold of equilibrium positions of perfectly flexible degenerated structures as a basis solution for some type of "global linearization" [2.6, 2.7]. Such manifolds are

essentially curvilinear with asymptotically zero velocity of motions along them. Further, let us note publication [2.8] as one of the first unless the very first work introducing the NNMs for impact dynamics of multiple degrees-of-freedom systems. This work deals with the model of string with discrete massive attachments moving between two stiff barriers. In particular, it was suggested to model the impact interactions by means of high degree monomials in order to avoid difficulties at numerical simulation. More importantly, unfolding the configuration space revealed hidden spatial symmetries associated with nonlinear local modes. Such "additional" local modes appear to co-exist with conventional NNMs dictated by explicit spatial symmetries. Transition to infinite chains led to solutions describing solitary waves (solitons) within the class of weakly modulated standing waves. Energy localization effects were analyzed in survey [2.9], where the difference between nonlinear localization and stochastic Anderson's localization was analyzed.

Main aspects of the theory of nonlinear normal and local modes and their stability have been summarized in monographs [2.6, 2.10]. Later, in the book [2.11] interaction of NNMs under internal resonance conditions was studied in autonomous and non-autonomous discrete two-degree-of-freedom systems, infinite chains of particles, and continuous systems, including circular rings and cylindrical shells. Interaction of NNMs in the case of simultaneous internal and external resonances at forced oscillations, bifurcations of the steady-state modes and their stability were systematically studied in this book.

2.1. Manevich, L.I., Privarnikov, Yu.K.: Nonlinear vibrations and stability of bars under dynamic loading. Soviet Applied Mechanics (Prikladnaya Mekhanika) **2** (12), 35–39 (1966).
2.2. Manevich, L.I., Pinsky, M.A.: On nonlinear normal vibrations in systems with two degrees of freedom. Soviet Applied Mechanics (Prikladnaya Mekhanika) **8** (9), 83–90 (1972).
2.3. Manevich, L.I., Cherevatzky, B.P.: On approximate determination of normal vibrations in nonlinear systems close to symmetric and homogeneous ones. Hydro- and Aeromechanics and Theory of Elasticity, Dnepropetrovsk University **12**, 121–128 (1970) (in Russian).
2.4. Manevich, L.I., Cherevatzky, B.P.: Resonant modes in nonlinear systems with two degrees of freedom. Soviet Applied Mechanics (Prikladnaya Mekhanika) **9** (11), 1210–1215 (1973).
2.5. Manevitch, L.I., Mikhlin, Yu.V.: On periodic solutions close to rectilinear normal vibration modes. Applied Mathematics and Mechanics (PMM USSR) **36** (6), 1051–1058 (1972).
2.6. Manevitch, L.I., Mikhlin, Yu.V., Pilipchuk, V.H.: The Method of Normal Vibrations for Essentially Nonlinear Systems. Nauka, Moscow (1989) (in Russian).
2.7. Manevitch, L.I., Pilipchuk, V.N.: Non-linear vibrations of a three-element mechanical system with several equilibrium positions, Soviet Applied Mechanics (Prikladnaya Mekhanika), **17** (2), 97–103 (1981).

2.8. Vedenova, E.G., Manevitch, L.I., Pilipchuk, V.N.: Normal oscillations of a string with concentrated masses on non-linearly supports, Applied Mathematics and Mechanics (PMM USSR) **49** (2), 203–211 (1985).
2.9. Manevitch, L.I., Pilipchuk, V.N.: Localized vibrations in linear and non-linear chains. Advances in Mechanics **13** (3/4), 107–134 (1990) (in Russian).
2.10. Vakakis, A.V., Manevitch, L.I., Mikhlin, Yu.V., Pilipchuk, V.N., Zevin, A. A.: Normal Modes and Localization in Nonlinear systems. Wiley, New-York (1996).
2.11. Manevich, A.I., Manevitch, L.I.: The mechanics of nonlinear systems with internal resonances. Imperial College Press, London (2005).

III. Nonstationary Processes in Essentially Nonlinear Systems

Major progress in theoretical study of energy transport in essentially nonlinear systems has been achieved, since it was realized the most efficient transport usually occurs in conditions of resonance. This observation allows one to treat the system in the vicinity of the resonance manifold, and to restrict the consideration by averaged equations of motion (sometimes referred to as slow-flow equations). This crucial simplification often allows reduction of dimensionality and gives rise to conservation laws absent in the complete system beyond the resonance manifold. In particular case of conservative system with two degrees of freedom, the existence of additional integral of motion in the approximation with isolated resonance implies complete integrability. This classical result has been first formulated in quasilinear setting and dates back to Birkhoff's theory of normal forms.[1] In papers[2] the aforementioned approach was used for exploration of beatings in a spring pendulum in conditions of 1:2 resonance. Recent application[3] addresses propagation of asymmetric Gaussian beams in nonlinear waveguides.

The method of normal forms in its traditional setting requires from the system to be quasilinear. However, it is common to use formally similar methods for exploration of nonlinear systems far beyond the quasilinear regime. Harmonic balance with slowly varying amplitudes[4] is a profound example of such approach. It lacks rigorous mathematical justification, but often provides reliable results and is widely used in engineering. Mathematically equivalent approximations can be

[1]Birkhoff, G.: Dynamical Systems. AMS, Providence, p. 82 (1927), Moser, J.: Stable and random motions in dynamical systems. Princeton UP (1973); Verhulst, F.: Phil. Trans. **290**, 435–465 (1979).
[2]Augusteijn, M.F., Breitenberger, E.: J. Math. Phys. **21**, 462—471 (1980), Breitenberger, E., Mueller, R.D.: J. Math. Phys. **22**, 1196–1210 (1981).
[3]Ianetz, D., Schiff, J.: Chaos 28 (1), 013116 (2018).
[4]Hayashi, Ch.: Nonlinear Oscillations in Physical Systems. Princeton UP (2014).

conveniently formulated in terms of complex variables. Early examples of this sort are the models with self-trapping[5] and rotating-wave approximation[6] in the lattice dynamics.

L.I. Manevitch, with multiple collaborators, substantially reformulated this approach, expanded it and converted into a powerful tool for exploration of non-stationary processes in a multitude of physical contexts. In recent papers, the method is commonly referred to as complexification-averaging (CxA) [3.1–3.6].

The CxA approach comprises two main features:

Presentation of the slow-flow system in terms of complex variables. This feature should be, first of all, viewed as mathematical convenience, since from fundamental point of view the slow-flow equations are similar to those delivered by conventional harmonic balance with slowly varied amplitudes. However, the simplification is substantial and by no means occasional. Recently it was demonstrated that it is in fact a particular case of canonical transformation to action-angle variables.[7]

Topology of special phase trajectories. The aforementioned integrability of the slow flow of 2DOF Hamiltonian systems with isolated resonance allows considering the averaged problem on the phase plane. Commonly, the planar phase portraits are characterized by their special invariant submanifolds, such as (in the considered Hamiltonian case) fixed points and separatrices, that is, homoclinic/heteroclinic orbits of the saddles. However, in order to consider the non-stationary processes, one should look at other individual orbits on the resonant manifold, that approximately conform to particular initial conditions for the original problem. For particular case of initial excitation of a single element of the system, L.I. Manevitch coined the term ***Limiting Phase Trajectory (LPT)***. The LPT approximately describes the slow evolution of the selected phase trajectory. Qualitative modification of the response for given initial conditions (for instance, the transition from localization to beating) corresponds to passage of the LPT through the saddle point. In other terms, for particular values of parameters that correspond to the transition, the LPT coincides with a (part of) separatrix in the system. From common viewpoint, such event is not classified as global bifurcation, since for different initial conditions the transition will occur at different hypersurface in the space of parameters. In the same time, physical significance of such transitions is apparent.

It should be mentioned, that the idea of complexification appeared first, and was instrumental in exploration of targeted energy transfer in systems with nonlinear energy sinks. The concept of LPT was used in diverse physical settings, including small-size oscillatory systems [3.1, 3.2, 3.6, 3.7], systems with local and nonlocal sonic vacuum [3.5, 3.9], one-dimensional and quasi-one-dimensional nonlinear lattices [3.10, 3.11], systems with self-excitation [3.12, 3.13], auto-resonance

[5]Eilbeck, J.C., Lomdahl, P.C., Scott, A.C.: Physica D **16,** 318–338 (1985).
[6]Flach, S., Gorbach, A.: Phys. Rep. **467**, 1–116 (2008).
[7]Gendelman, O.V., Sapsis, T.P.: ASME J. Appl. Mech. **84**, 011009, 1–9 (2017).

[3.14, 3.15], system exhibiting Landau-Zener effect [3.16, 3.17]. More recent achievements include dynamical transitions in strongly nonlinear forced pendula [3.6, 3.18], Frenkel-Kontorova model [3.19] and nonlinear vibrations of carbon nanotubes [3.20–3.22].

3.1. Manevitch, L.I.: The description of localized normal modes in a chain of nonlinear coupled oscillators using complex variables. Nonlinear Dynamics, **25**, 95–109 (2001).
3.2. Manevitch, L.I.: Complex representation of dynamics of coupled nonlinear oscillators, In: Uvarova, L., Arinstein, A.E., Latyshev, A.V. (eds.), Mathematical Models of Non-Linear Excitations. Transfer, Dynamics, and Control in Condensed Systems and Other Media, pp. 269–300. Springer, New York (1999).
3.3. Manevitch, L.I.: New approach to beating phenomenon in coupled nonlinear oscillatory chains, Archive of Applied Mechanics, **77**, 301–312 (2007).
3.4. Manevitch, L.I.: A concept of limiting phase trajectories and description of highly non-stationary resonance processes, Applied Mathematical Sciences, **9**, 4269–4289 (2014).
3.5. Manevitch, L.I., and Gendelman, O.V.: Tractable Models of Solid Mechanics, Springer, Berlin (2011).
3.6. Manevitch, L.I., Kovaleva, A., Smirnov, V. and Starosvetsky, Y.: Nonstationary Resonant Dynamics of Oscillatory Chains and Nanostructures, Springer, Singapore (2018).
3.7. Manevitch, L.I. and Kovaleva, A.: Nonlinear energy transfer in classical and quantum systems. Phys. Rev. *E* **87**, 022904, 1–12 (2013).
3.8. Manevitch, L.I. and Musienko, A.I.: Limiting phase trajectories and energy exchange between an anharmonic oscillator and external force. Nonlinear Dynamics, **58**, 633–642 (2009).
3.9. Manevitch, L.I. and Vakakis, A.F.: Nonlinear oscillatory acoustic vacuum. SIAM J. Appl. Math. **74**(6), 1742–1762 (2014).
3.10. Manevitch, L.I. and Smirnov, V.V.: Limiting phase trajectories and thermodynamics of molecular chains. Phys. Doklady **55,** 324–328 (2010).
3.11. Manevitch, L.I. and Smirnov, V.V.: Limiting phase trajectories and the origin of energy localization in nonlinear oscillatory chains. Phys. Rev. *E* **82**, 036602 (2010).
3.12. Kovaleva, M.A., Manevitch, L.I. and Pilipchuk, V.N.: New type of synchronization for auto-generator with hard excitation. J. Exp. Theor. Phys. **116**, 369–377 (2013).
3.13. Manevitch, L.I., Kovaleva, M.A. and Pilipchuk, V.N.: Non-conventional synchronization of weakly coupled active oscillators, Europhysics Letters, **101**, 50002, 1–5 (2013).
3.14. Kovaleva, A. and Manevitch, L.I.: Emergence and stability of autoresonance in nonlinear oscillators. Cybern. Phys. **2**, 25–30 (2013).

3.15. Kovaleva, A. and Manevitch, L.I.: Limiting phase trajectories and emergence of autoresonance in nonlinear oscillators. Phys. Rev. *E***88**(1–6), 024901 (2013).
3.16. Kosevich, Y.A., Manevitch, L.I., and Manevitch, E.L.: Vibrational analogue of nonadiabatic Landau– Zener tunneling and a possibility for the creation of a new type of energy trap. Phys. Usp. **53,** 1281–1286 (2010).
3.17. Manevitch, L.I., Kosevich, Y.A., Mane, M., Sigalov, G., Bergman, L.A. and Vakakis, A.F.: Towards a new type of energy trap: classical analog of quantum Landau-Zener tunneling. Int. J. Non-Linear Mech. **46**, 247–252 (2011).
3.18. Manevitch, L.I., Smirnov, V.V. and Romeo, F.: Stationary and non-stationary resonance dynamics of the finite chain of weakly coupled pendula. Cybern. Phys. **5**(4), 130–135 (2016).
3.19. Smirnov, V.V. and Manevitch, L.I.: Large-amplitude nonlinear normal modes of the discrete sine lattices. Phys. Rev. *E***95**, 022212 (2017).
3.20. Smirnov, V.V., Shepelev, D.S. and Manevitch, L.I.: Localization of low-frequency oscillations in single-walled carbon nanotubes. Phys. Rev. Lett. **113,** 135502 (2014).
3.21. Smirnov, V.V., Manevitch, L.I., Strozzi, M., Pellicano, F.: Nonlinear optical vibrations of single-walled carbon nanotubes. 1. Energy exchange and localization of low-frequency oscillations. Physica D **325**, 113–125 (2016).
3.22. Manevitch, L.I., Smirnov, V.V., Strozzi, M. and Pellicano, F.: Nonlinear optical vibrations of single-walled carbon nanotubes, International Journal of Non-Linear Mechanics, **94**, 351–361 (2017).

IV. Physics of Solid Polymers

Theoretical analysis of the molecular mechanisms of mobility of polymer crystals, semicrystalline polymers and polymeric glasses, as well as of nano-objects (graphene, nanotubes) and DNA-like biomolecules, carried out under supervision of L. Manevitch at the N.N. Semenov Institute of Chemical Physics of the Russian Academy of Sciences. This analysis was a development of preceding investigations on nonlinear dynamics of finite-dimensional mechanical systems [4.1, 4.2]. The development is based on the fact that a knowledge of the spectrum of nonlinear excitations is a necessary condition for the adequate theoretical description of the molecular mechanisms of the primary physical and chemical processes, such as relaxation, melting, thermal conductivity, mechanodestruction, plastic deformation, polarization, topochemical polymerization etc., in solid polymers and ordered biomolecules. The main results are presented further.

1. **Dynamical models of localized nonlinear excitations and point topological defects in polymer crystals and molecular chains [4.3–4.9]**.

An explicit representation of topological solitons and localized nonlinear excitations (breathers) was first obtained in a molecular chain having the non-rectilinear configuration, in the framework of realistic three-dimensional molecular dynamics (MD) models. The velocity and temperature dependences of their parameters were determined; the inter-soliton and soliton-phonon interactions were investigared; a possibility of formation and propagation of bound states, so-called "soliton molecules", was predicted.

Some regularities in propagation of the soliton excitations in extended polymer chains were revealed using the MD approach. The localized nonlinear excitations in the inhomogeneous model of the double helix DNA molecule were simulated and a possibility of formation and propagation of the topological solitons and breathers mostly in one chain was shown.

2. **Molecular mechanisms of physical processes in polymer crystals, semicrystalline polymers, polymer glasses and molecular chains [4.10–4.16]**.

Based on the obtained information on the spectrum of nonlinear excitations, a detailed study of the mobility of polymer chains in crystal together with the found earlier temperature dependence of the mobility was made. Basing on the analysis of experimental NMR data, a new molecular model describing both the diffusion of chains between crystalline and amorphous phases, and the dielectric mechanical relaxation in polyethylene and semicrystalline polymers was proposed. Besides, the problem of structural transformations in premelting of crystalline polyethylene was formulated and studied.

Along with the obtained analytical description of dislocations in polymer crystals, the molecular dynamics simulation of both edge and screw dislocations in such crystals was first carried out; a mobility of the dislocations was studied and the corresponding yield strength was calculated. On the basis of the concept of such modes responsible for the anomalies of the low-temperature properties of glasses a continuum model of a low-frequency localized mode in polymer glasses was developed; estimates of their yield strength were first obtained.

Taking into account the regularities of the propagation of solitons in extended polymer chains, the possible molecular mechanisms of their mechanodeconstruction was revealed. Based on the obtained information on characteristics of nonlinear localized excitations in DNA molecule, the energy comparison of possible mechanisms for openings of the DNA double helix was made.

3. **Continuum models of a polymer crystal [4.17–4.19]**.

Applying the asymptotic method developed in monographs [4.20, 4.21] to highly anisotropic media, on the basis of data on the structure of the polyethylene crystal and on the interchain interaction potentials, it was first proposed equations of the continuous media motion in which stiffness characteristics are expressed through molecular parameters both in the long-wave, and short-wave regions of the vibrational spectrum.

4. **Solitons in nondegenerate bistable systems [4.22–4.26]**.

A theory of topological solitons in molecular chains with a nondegenerate bistable interaction potential was developed. The theory extends the soliton concept to description of conformational transitions (in particular, in DNA) and to solid-phase chemical reactions like to topochemical polymerization of crystalline diacetylene, or like to solid-phase detonation. The fundamentally two-stage nature of the propagation of the soliton excitation was revaled. In the first stage there is a transformation of the system from the initial state to the region of attraction of the final state with conservation of the Lagrange function. In the second stage, at a sufficiently large distance from the front, the system transforms to the final state (relaxation with the release of energy). Using the developed theory, it was shown the molecular mechanisms of the above-mentioned physical and chemical processes.

5. **Localized excitations and physical processes in nanostructures [4.27–4.30]**.

The experience accumulated at the Institute of Chemical Physics on the investigation of nonlinear dynamics and molecular mechanisms of physical and mechanical processes in solid polymers led to the statement of a number of problems that are fundamentally important for such nano-objects as the graphene layer and the carbon nanotube. Localized excitations in these nanostructures were first revealed. A process of thermal conductivity of nanotubes, which is a direct development of the research on thermal conductivity of quasi-one-dimensional lattices, was also modeled. The investigation confirms that in both the cases the localized modes play a primary role in the molecular mechanism of the energy transfer process. On the other hand, the analysis of nonlinear localized modes allows to reveal a possible intercalation mechanism of anisometric silicate nanoparticles in polymer nanocomposites.

4.1. Manevitch, L.I., Mikhlin, Yu.V., Pilipchuk, V.N.: The Method of Normal Vibrations for Essentially Nonlinear Systems. Moscow, Nauka (1989) (in Russian).
4.2. Vakakis, A.V., Manevitch, L.I., Mikhlin, Yu.V., Pilipchuk, V.N., Zevin, A. A.: Normal Modes and Localization in Nonlinear systems. New-York, Wiley (1996).
4.3. Manevitch, L.I., Ryvkina, N.G.: Nonlinear dynamics of polymer crystals: Soliton models of structural defects in the polyethylene crystals. Progr. Colloid Polym. Sci. **80,** 78–82, 1989.
4.4. Ginzburg, V.V., Manevitch, L.I.: On the theory of dislocations in polymer crystals. Polymer Science A Physics, Chemistry **34** (9), 782–785; Dislocation dipols in polymer crystals. Ibid, 786–788 (1992).
4.5. Manevitch, L.I., Savin, A.V.: Solitons in a polyethylene crystal: isolated chain in transconformation, Phys. Rev. E **4**, 4713–4722, 1997.
4.6. Savin, A.V., Manevitch L.I.: Solitons in a polyethylene crystal: a chain surrounding by immobile neighbors. Phys Rev B **58,** 17, 11338–11400, 1998.

4.7. Zubova, E.A., Manevitch, L.I., Balabaev, N.K.: Vacancy mobility in polymer crystals. J. Exp. Theor. Physics **88**(3), 586–589 (1999).
4.8. Savin, A.V., Manevitch, L.I.: Solitons in spiral polymeric macromolecules. Phys. Rev. E **61** (6), 7065–7075, (2000).
4.9. Manevitch, L.I., Savin, V.A., Lamarque, C-H.: Analytical study and computer simulation of discrete optical in a zigzag chain. Phys Rev B **74**, 014305, (2006).
4.10. Ginzburg, V.V., Manevitch, L.I.: Vacancies in a polyethylene crystal. Fizika Tverdogo Tela (Physics of the Solid State) **32** (8), 2414 –2419 (1990).
4.11. Enikolopyan, N.N., Manevitch, L.I., Zarkhin, L.S.: Nonlinear dynamics and the problem of polymer fracture. J. Appl. Pol. Sci. **39**, 2245 (1990).
4.12. Ginzburg, V.V., Manevitch, L.I.: On the theory of melting polymer crystals. Colloid and Polymer Science **269**, 867–872 (1991).
4.13. Gendelman, O.V., Manevitch, L.I.: New model of plastic deformation of disordered systems. J. Phys. Cond. Matter **5** (11) 1633–1642 (1993).
4.14. Gendelman, O.V., Manevitch, L.I.: Exact soliton-like solutions in generalized dynamical models of a quasi-one-dimensional crystal. J. Exp. Theor. Physics **85** (4), 824–826 (1997).
4.15. Musienko, A.I., Balabaev, N.K., Manevich, L.I.: Microscopic mechanism of plastic deformation in a polyethylene crystal. Doklady Physical Chemistry **372** (4/6), 92–94 (2000).
4.16. Zubova, E.A., Balabaev, N.K., Manevitch L.I.: Molecular mechanisms of the chain diffusion between crystalline and amorphous fractions in polyethylene. Polymer **48** (6), 1802–1813 (2007).
4.17. Gendelman, O.V., Manevitch, L.I.: The description of polyethylene crystal as a continuum with internal degrees of freedom. Int. J. Solids Struct. **33** (12) 1781–1798 (1996).
4.18. Gendelman, O.V., Manevitch, L.I.: Linear and nonlinear excitations in a polyethylene crystal. 1. Vibrational modes and linear equations. Macromol. Theory Simul. **7**, 579–590 (1998).
4.19. Manevitch, L.I., Gendelman, O.V., Savin, A.V.: Nonlinear normal modes (breathers) and chaotic motions in oscillatory chains. In: *Solid mechanics and its application*, Springer, **122**, 59–69 (2005).
4.20. Manevitch, L.I., Pavlenko, A.V., Koblik, S.G.: Asymptotic Methods in the Theory of Elasticity of Orthotropic Bodies. Kiev-Donetzk, Viszha Shkola (1979) (in Russian).
4.21. Manevitch, L.I., Pavlenko, A.V.: Asymptotic Methods in Micromechanics of Composite Materials. Kiev, Naukova Dumka (1991) (in Russian).
4.22. Manevitch, L.I., Smirnov, V.V.: Propagation of exothermic reactions in condensed matter. Phys. Lett. **A 165** (5/6) 427–432 (1992).
4.23. Manevitch, L.I., Savin, A.V., Smirnov, V.V., Volkov, S.N.: Solitons in nondegenerate bistable systems. Physics Uspekhi **37** (9), 859–879 (1994).
4.24. Manevitch, L.I., Sigalov, G.M.: Solitonic mechanism of structural transformations in a non-degenerate chain of particles with anharmonic and competing interactions. Phys. Let. A **210** (6), 423–428 (1996).

4.25. Manevitch, L.I., Smirnov, V.V.: Collective interactions in solid-phase chemical processes expressed through non-linear dynamics of crystals. Chem. Rev. **23**, part 2, 1–22 (1998).
4.26. Manevitch, L.I., Sigalov, G.M., Savin, A.V.: Topological solitons in non-degenerate one-component chains. Phys Rev E **65**, 036618 (2002).
4.27. Manevitch, L.I., Savin, A.V.: Nonlinear modes and energy transfer in polymer chains. Polymer science. Series A, Chemistry, physics **47** (5), 499–523 (2005).
4.28. Ginzburg, V.V., Gendelman, O.V., Manevitch, L.I.: Simple "kink" model of melt intercalation in polymer-clay nanocomposites. Phys. Rev. Lett. **86** (22), 5073–5075 (2001).
4.29. Gendelman, O.V., Manevitch, L.I., Manevitch, O.L.: Solitonic mechanism of structural transition in polymer–clay nanocomposites, J. Chem. Phys. **119,** 1066–1069 (2003).
4.30. Manevitch, L.I., Smirnov, V.V.: Localized nonlinear oscillations of a planar zigzag. Doklady Physical Chemistry **413** (1), 69–73 (2007).

V. Nonlinear Chains
Quasi-One-Dimensional System

The problems dealing with the nonlinear dynamics of the oscillatory chains (the nonlinear lattices), perhaps, are in the most priority of the L. Manevitch's scientific interests. Two reasons of this can be found. First of them is that such systems allow us to understand many fundamental principles of the "nonlinear world". The second reason results from the wide variety of the quasi-one dimensional nonlinear models, which arise as a consequence of the attempts to describe the polymeric systems in solid state. Four main coupled directions in the L. Manevitch's works can be formulated as follows: (i) the linear and non-linear dynamics of the complex structured chains; (ii) the dynamics of the bi-stable systems with the non-degenerated states; (iii) the energy transfer and localization in the discrete systems under conditions of the resonant interactions; (iv) the essentially nonlinear one-dimensional chains with vibro-impact interactions.

Historically, the vibro-impact nonlinear chains have been the first objects in the class of the one-dimensional discrete systems considered by Manevitch with coauthors. Two types of the soliton-like solutions have been revealed. First of them can be found if the continuum approximation is valid for the envelope of the NNM with highest frequency [5.1, 5.2], and it is an extension of the envelope solitons in the quasilinear chain (see, i.e., [5.3]) onto the strongly nonlinear case.

If the continuum approximation does not work even for the envelope of this NNM the essentially discrete localized excitations (the discrete breathers), which are often called as the Intrinsic Localized Modes (ILM) have been revealed for the

first time. [5.1]. The further development may be found in [5.4] where the exact solution for the linear chain vibrating between two rigid walls is presented.

The nonlinear lattices with a complex structure are in the focus of the Manevitch's interests for a long time. The one-dimensional chains with the identical oscillators cannot demonstrate many peculiarities which are typical for the complex structured systems like the polymeric molecules and crystals. The first reason is the non-trivial geometry of the polymers, which is often specified by the zigzag or spiral conformations. Even this peculiarity leads to the essential geometric nonlinearity in the respective dynamical models and its domination over the physical nonlinearity leads to absence of the compression solitons in the zigzag chains. Instead of the latter one can observe the tension solitons.

However, not only the complex geometry is the issue of the intricacy of the polymer chain description. The macromolecular systems show the strong hierarchy of the interactions from the hard covalence bonds up to the weak intermolecular interactions. On the one hand this hierarchy allows us to consider the polymer systems like one-dimensional, but on the other hand it leads to the many coupled degrees of freedom. The development of the classical models of the intricate molecular system needs in the separation of the various interactions taking into account the differences between the potential forces. By this way, we should distinct the "valence angle" and "conformation angle" variables, the tension and twist of the chain, the effective forces acting from the molecular environment, etc. Such an approach is specific for the molecular dynamic simulations and it is *a priori* suitable for the development of the analytical studying.

The nonlinear dynamical models of the polymer molecules and crystals have been studied in the series of the papers of Manevitch with co-workers [5.6–5.8]. The first models of the vacancies and dislocations have been developed in these works. The detailed investigations of the dynamics of the zigzag chain with and without of the crystal environment were performed in coauthorship with A. Savin [5.9]. The results obtained in the study of the polyethylene molecules were expanded into the analogues of the PE molecule, but with more complicated spiral structure, the polythetraftorethylene (PTFE). It was shown that the torsion solitons are appended to the spectrum of the nonlinear localized excitations in the crystal of PTFE. The breather-like excitations in the realistic models of the polymeric chains of zigzag and spiral conformations have been described for the first time in [5.10, 5.11]. These breathers exist in the vicinity of the low-frequency edge of the oscillation spectrum and correspond to the transversal optical-type vibrations of the planar zigzag accompanied by the longitudinal ones.

The development of the theory of the plastic deformation and the phase transitions in the polymer crystals needs in the study of the elementary events of these processes . Such events are the motion of the crystal defects—the point-like vacancies and line dislocations [5.12, 5.13]. These defects can be described as the soliton-like excitations in the polymer chain, but the influence of the molecular surrounding should be taken into account [5.14–5.16]. The presence of the environment effects not only on the characteristics of the soliton, but leads to some qualitative changes. The requirement of keeping the crystalline order results in the

soliton's topological charge. The specific property of the topological soliton (like the kinks in Frenkel-Kontorova model)) is the subsonic velocity of the propagation, while the dynamic solitons (in the Fermi-Pasta-Ulam (FPU) or Toda lattices) move with the supersonic velocities only. The weakness of the intermolecular forces in the polymeric crystal sometimes does not suppress the supersonic velocities of the solitons, but provides the non-zero topological charge [5.17, 5.18]. One should note that it was very fruitful association of the analytical study and molecular dynamical modelling for the study of the deformation of the polymeric solids. The majority of the analytical findings mentioned above have been verified by the numerical experiments [5.12, 5.14, 5.15, 5.17].

At the same time the dynamical linear theory of the polymer crystals was developed in [5.20, 5.21]. The theory is based on the realistic molecular structure and the potentials of the interaction between the macromolecules of the flexible polymers in the crystalline states. The numerical simulations help to understand the main peculiarities of the systems under consideration. The resulting theory takes into account both the hierarchy of the interactions in the polymer crystal and the specific internal degrees of freedom of the macromolecules. The asymptotic continuum description of the dynamics of polymer crystals contains the main elastic characteristics expressed via the microscopic values which are the structural constants and parameters of the interaction potentials.

Talking about the polymeric chains in the researches of Prof. Manevitch, one should say about the works dealing the most intricate polymeric molecule - the DNA. The dynamics of the double strand DNA in the framework of the FK model has been proposed by L. Yakushevich. In the paper [5.22] much more detailed analysis of the DNA dynamics was performed in the framework of the mentioned model, but the further research allowed to extend the model essentially [5.23]. More realistic model of the DNA has been developed, and such significant processes as heat transfer and structural transitions have been investigated [5.26]. The model of the DNA denaturation via the formation of the breather-like excitation has been evolved [5.24]. These researches resulted in the construction of the coarse-grained DNA model, which allows to study the structural transitions in the DNA more effectively [5.25, 5.27].

The problem of the supersonic propagation of the chemical reactions in solid media arises in the study of the solid explosives detonation, chemical transformation under high pressure in combination with shear deformation, some topochemical reactions, etc. Main question was: why the propagation appears as a stationary process in spite of the energy is released permanently? The detonation wave theory has been developed by Ya. Zeldovich under assumption that the thermodynamical equilibrium is achieved in the front due to the compression of the reagents by the shock wave. However, the numerical simulations performed by M. Peyrard with co-workers and L. Manevitch with co-workers show that no equilibrium in the reaction front exists and the explosion energy is released at some distance after the front. The difficulty of the problem consisted in that the transition occurs between two stationary states with different energies. Such transitions do not described in the framework of the dynamics of the conservative systems [5.28]. The solution of the

problem has been found in the series of the papers [5.29 and references herein], where it was shown that the process of the propagation of the exothermical transition is two – stage one. The first stage consists in the dynamical renormalization of the states' energies that the transition turns out to be possible. The intermediate state is specified by the same value of the Lagrange function of the system as that in the metastable state . It is important that the velocity of the front propagation turns out to be supersonic and unique. The second stage is observed in the numerical simulations as the instability of the intermediate state with the transformation of the reaction energy into the kinetic energy of the reaction products. The close problem arises in the model of the "one-dimensional" glass by Reichert and Schilling. Using the approach mentioned above, Manevitch with co-workers studied the mechanism of the transitions and revealed the elementary excitations which are responsible for these processes [5.30].

However, the study of the martensite transitions and the processes of the collapse of the carbon nanotubes shows that the exothermic transitions in the solids can propagate with the subsonic velocities escorted by the "oscillating tail", which starts from the front immediately. It is notable, that the energy of the oscillations is not equal to the energy, which is released in the front. It may be both smaller and greater than the latter. This problem has been solved in the work [5.31], were the inequality of the energies has been explained by a difference of the front velocities and the group velocity of the oscillations.

It is necessary to single out the series of works dealing with new paradigm of the non-stationary nonlinear dynamics—the Limiting Phase Trajectory (LPT) concept. This paradigm issues from the well-known phenomenon—the beating in the system of two weakly coupled identical oscillators. The idea by Manevitch consists in that the beating represents the fundamental essentially non-stationary process, which is responsible for the energy exchange between some clusters of the particles (*coherent domains*) [5.33]. The necessary condition for this is the resonance between the Nonlinear Normal Modes (NNMs) which correspond to synchronized (coherent) motions of the particles, i.e., a closeness of their frequencies. It means that additional, slow time scale, depending on the difference of the NNMs frequencies, appears alongside with fast time scale which is determined by the period of one of the resonating NNMs. In this new time scale the NNMs can be considered as stationary (quasi-equilibrium) states. Among all other non-stationary solutions, the Limiting Phase Trajectory (LPT) describing the beating phenomenon, can be singled out. To clarify the fundamental role of LPTs in non- stationary resonance dynamics it is important to remind that NNMs, which correspond to fundamental stationary processes, do not take part in the energy exchange. Only a combination of resonating (coherent) NNMs, which form a wave packet, can make this due to periodic interference of the resonating NNMs on each cluster (a combination of two resonating NNMs is the limit case of such wave packet). Thus, the beats and LPTs which describe them turn out to be fundamental non-stationary processes whose role in the strongly non-stationary resonance dynamics is similar to the role of NNMs in the stationary or non-stationary but non-resonance dynamics. An extension to multi-particle chains leads to notion of coherence domains (consisting

of certain number of particles) the energy exchange between which is described by LPTs. (In the two-particle model the coherence domains are the particles themselves). One should notice that the essential progress in the analysis of the resonant dynamics turns out to be possible due to asymptotic approach, which is based on the complex representation of the equations of motion [5.3] and multiple scale asymptotic expansions in the framework of the LPT and coherence domains concept.

The nonlinear dynamics of the various quasi-one-dimensional discrete systems with using this concept has been studied for the quite number of the nonlinear chains (the FPU, FK, Klein-Gordon, and sine-lattices, as well the system with the "sonic vacuum") and nanostructures [5.33–5.46]. It was shown that the evolution of the LPT reflects the processes of the energy exchange and localization in the system [5.32, 5.33]. If the LPT passes through both domain states, the energy exchange is possible. However, the modulation instability of the zone-bounded normal mode leads to the creation of the separatrix, which can coincide with the LPT at the certain value of the oscillation amplitude. In further, the full energy exchange turns out to be forbidden and the energy is localized in the one of the coherent domains. Here one should notice two fundamental features of the LPT. First, the LPT is responsible for the non-stationary (pulsing) localization of the oscillation energy, while the normal modes correspond to the stationary one. It is important to note that this phenomenon is a general one for the wide class of the nonlinear chains and nanostructures (in particular, carbon nanotubes [5.38, 5.39]). The second peculiarity is that the LPT like the normal modes can be an attractor, if a weak dissipation is put in the system [5.45]. All advances in the non-stationary resonant dynamics of the nonlinear systems are discussed in the recent monograph [5.46] in detail.

5.1. Vedenova, E.G., Manevich, L.I., Nisichenko, V.P., Lysenko, A.S.: Solitons in substantially nonlinear one-dimensional chain. J. Appl. Mech. Tech. Physics **24**(6), 910–914 (1983).
5.2. Vedenova, E.G., Manevich, L.I., Pilipchuk, V.N.: Normal oscillations of a string with concentrated masses on nonlinearly elastic supports. J. Appl Math. Mech. **9** (2), 153–159 (1985).
5.3. Manevitch, L.I.: The description of localized normal modes in a chain of nonlinear coupled oscillators using complex variables. Nonlinear Dynamics **25**, 95–109 (2001).
5.4. Gendelman, O.V., Manevitch, L.I.: Discrete breathers in vibroimpact chains: analytic solutions. Phys Rev E **78** (2), 026609 (2008).
5.5. Manevitch, L.I., Ryvkina, N.G.: Nonlinear dynamics of polymer crystals. Soliton models of structural defects in the polyethylene crystals. Relaxation in Polymers, 78–82 (1989).
5.6. Ginzburg, V.V., Manevich, L.I.: Vacancies in a polyethylene crystal. Fizika Tverdogo Tela (Physics of the Solid State) **32** (8), 2414 –2419(1990).
5.7. Manevitch, L.I., Ryvkina, N.G.: Soliton model of structural defects in a polyethylene crystal. Polymer Science USSR **32** (3), 489–495 (1990).

5.8. Manevitch, L.I.: Solitons in the physics of polymers. Int. J. Polymer Mat. **15** (34), 256 (1991).
5.9. Savin, A.V., Manevitch, L.I., Christiansen, P.L., Zolotaryuk, A.V.: Nonlinear dynamics of zigzag molecular chains. Physics Uspekhi **42** (3), 245–260 (1999).
5.10. Savin, A.V., Manevitch, L.I.: Solitons in the spiral polymeric macromolecules. A chain surrounded by immovable neighbors. Phys Rev B **63** (2), 224303 (2001).
5.11. Manevitch, L.I., Gendelman, O.V., Savin, A.V.: Nonlinear normal modes and chaotic motions in oscillatory chains. IUTAM Symposium "Chaotic Dynamics and Control of Systems and Processes in Mechanics", Rome, Italy, 8–13 June 2003, eds. by G. Rega and F. Vestroni, Berlin, Springer-Verlag, 59 (2003).
5.12. Balabaev, N.K., Gendelman, O.V., Mazo M.A., Manevich, L.I.: Modeling twist domain walls in polyethylene crystals. Polymer Science, Series A, Polymer Physics **38** (4), 418–422 (1996).
5.13. Savin, A.V., Manevich, L.I.: Structural transformations in crystalline polyethylene: role of topo- logical solitons in premelting. Polymer Science, Series A, Polymer Physics **40**, 545–554 (1998).
5.14. Zubova, E.A., Balabaev, N.K., Manevich, L.I., Tsygurov, A.A.: Dynamics of twist point defects with stretching in a polymer crystal. J. Exp Theor Phys **91** (3), 515–523 (2000).
5.15. Zubova, E.A., Balabaev, N.K., Manevitch, L.I.: Diffusion of topological solitons and dielectric c relaxation in a polymeric crystal. J. Exp Theor Phys **94** (4), 759–769 (2002).
5.16. Musienko, A.I., Balabaev, N.K., Manevitch, L.I.: Modeling of screw dislocation dynamics in crystalline polyethylene. Doklady Physical Chemistry **384** (13), 101–103 (2002).
5.17. Balabaev, N.K., Gendelman, O.V., Manevitch, L.I.: Supersonic motion of vacancies in a polyethylene crystal. Phys Rev E **64**, 036702 (2001).
5.18. Musienko, A.I., Manevich, L.I.: Classical mechanical analogues of relativistic effects. Physics Uspekhi **47** (8), 797–820 (2004).
5.19. Gendelman, O.V., Manevich, L.I.: Exact soliton-like solutions in generalized dynamical models of a quasi-one-dimensional crystal. J. Exp Theor Phys **85** (4), 824–826 (1997).
5.20. Gendelman, O.V., Manevitch, L.I.: Linear and nonlinear excitations in a polyethylene crystal. 1. Vibrational modes and linear equations. Macromolecular theory and simulations **7** (6), 579–589 (1998).
5.21. Gendelman, O.V., Manevitch, L.I.: Linear and nonlinear excitations in a polyethylene crystal. 2. Nonhomogeneous states and nonlinear excitations. Macromolecular theory and simulations **7** (6), 591–598 (1998).
5.22. Yakushevich, L.V., Savin, A.V., Manevitch, L.I.: Nonlinear dynamics of topological solitons in DNA, Phys Rev E **66** (1), 016614 (2002).

5.23. Kovaleva, N.A., Savin, A.V., Manevitch, L.I., Kabanov, A.V., Komarov, V. M.: Topological solitons in an inhomogeneous DNA molecule. Polymer Science. Series A, Polymer Physics **48** (3), 278–293 (2006).
5.24. Kovaleva, N.A., Manevich, L.I., Musienko, A.I., Savin, A.V.: Low frequency localized oscillations of the DNA double strand, Polymer Science. Series A, Polymer Physics A **51** (7), 833–847 (2009).
5.25. Savin, A.V., Mazo, M.A., Kikot, I.P., Manevitch, L.I., Onufriev, A.V.: Heat conductivity of the DNA double helix. Phys Rev B **83** (24), 245406 (2011).
5.26. Manevitch, L.I., Savin, A.V.: Nonlinear modes and energy transfer in polymer chains. Polymer science. Series A, Chemistry, physics **47** (5), 499–523 (2005).
5.27. Kikot, I.P., Savin, A.V., Zubova, E.A., Mazo, M.A., Gusarova, E.B., Manevitch, L.I.: New coarse grained DNA model. Biophysics **56** (3), 387–392 (2011).
5.28. Enikolopyan, N.S., Manevitch, L.I., Smirnov, V.V.: Effect of the ordering of elementary excitations on the chemical processes in solid state. Khimicheskaya Fizika (Russian Journal of Physical Chemistry B) **10** (3), 389–398 (1991).
5.29. Manevich, L.I., Savin, A.V., Smirnov, V.V., Volkov S.N.: Solitons in nondegenerate bistable systems. Physics Uspekhi **37** (9), 859–879 (1994).
5.30. Manevitch, L.I., Sigalov, G.M., Savin, A.V.: Topological solitons in non-degenerate one-component chains. Phys Rev E **65** (3), 036618 (2002).
5.31. Smirnov, V.V., Gendelman, O.V., Manevitch, L.I.: Front propagation in a bistable system: How the energy is released, Phys Rev E **89** (5), R050901 (2014).
5.32. Manevitch, L.I.: New approach to beating phenomenon in coupled nonlinear oscillatory chains. Archive Appl Mech **77** (5), 301–312 (2007).
5.33. Manevitch, L.I., Smirnov, V.V.: Limiting phase trajectories and the origin of energy localization in nonlinear oscillatory chains. Phys Rev E **82** (3), 036602 (2010).
5.34. Manevitch, L.I., Smirnov, V.V.: Limiting phase trajectories and thermodynamics of molecular chains. Doklady Physics **55** (7), 324–328 (2010).
5.35. Manevitch, L.I., Smirnov, V.V.: Resonant energy exchange in nonlinear oscillatory chains and limiting phase trajectories: from small to large systems. A.F. Vakakis, ed., Advanced Nonlinear Strategies for Vibration Mitigation and System Identification/Berlin: Springer, 207–258 (2010).
5.36. Smirnov, V.V., Manevitch, L.I.: Limiting phase trajectories and dynamic transitions in nonlinear periodic systems. Acoustical Physics **57** (2), 271–276 (2011).
5.37. Kovaleva, A., Manevitch, L.I.: Resonance energy transport and exchange in oscillator arrays. Phys Rev E **88** (2), 022904 (2013).
5.38. Smirnov, V.V., Shepelev, D.S., Manevitch, L.I.: Localization of Low-Frequency Oscillations in Single-Walled Carbon Nanotubes. Phys Rev Lett **113**, 135502 (2014).

5.39. Smirnov, V.V., Manevitch, L.I., Strozzi, M., Pellicano, F.: Nonlinear optical vibrations of single- walled carbon nanotubes. 1. Energy exchange and localization of low-frequency oscillations. Physica D **325**, 113–125 (2016).
5.40. Manevitch, L.I., Smirnov, V.V., Romeo, F.: Stationary and non–stationary resonance dynamics of the finite chain of weakly coupled pendula. Cybernetics and Physics, **5**(4), 130–135 (2016).
5.41. Manevitch, L.I., Vakakis, A.F.: Nonlinear oscillatory acoustic vacuum. SIAM J. Appl. Math. **74**, 17421762 (2014).
5.42. Kikot, I.P., Manevitch, L.I., Vakakis, A.F.: Non-stationary resonance dynamics of a nonlinear sonic vacuum with grounding supports. J. Sound and Vibration **357**(2), 349–364 (2015).
5.43. Zhang, Z., Koroleva, I., Manevitch, L.I., Bergman, L.A., Vakakis, A.F.: Nonreciprocal acoustics and dynamics in the in-plane oscillations of a geometrically nonlinear lattice. Phys Rev E 94 (3), 032214 (2016).
5.44. Smirnov, V.V., Manevitch, L.I.: Large-amplitude nonlinear normal modes of the discrete sine lattices. Phys Rev E **95**, 022212 (2017).
5.45. Manevitch, L.I., Kovaleva, M.A., Pilipchuk, V.N.: Nonconventional synchronization of weakly coupled active oscillators. Europhys. Lett. **101** (5), 50002 (2013).
5.46. Manevitch, L.I., Kovaleva, A.S., Smirnov, V.V., Starosvetsky, Yu.: Nonstationary Resonant Dynamics of Oscillatory Chains and Nanostructures. Springer Nature Singapore Pte Ltd, Singapore (2017).

VI. Methodology of Science

Any serious researcher tries to determine the place of his work in the general picture of the world, within the framework of a certain metatheory. L.M. has a pronounced desire for philosophy of science, that is why the interest of L.M. in asymptotology (the term proposed by Kruskal, see WIKI) is not incidental. “Asymptotic description is not only a convenient tool in the mathematical analysis of nature, it has some more fundamental significance” (K. Friedrichs). This point of view is popularized in the books [6.1, 6.2] by L.M. with co-authors, based on the belief: “The book of Nature is written in the language of asymptotology”.

However, the interests of L.M. in the field of methodology of science are not limited to asymptotology. A number of published articles presented in the collection [6.3] discuss the role of various number systems, nonlinear elementary excitations, thermodynamic arrow of time, wave-particle duality, and quantum-classical analogies in understanding and adequately describing physical reality. Situations are considered where the interaction of physics and mathematics turned out to be of fundamental importance, but its implementation or ignoring was determined by the philosophical mentality of outstanding researchers or the scientific community as a whole.

6.1. Andrianov I.V., Manevitch L.I.: Asymptotology. Ideas, Methods, and Applications. Dordrecht, Boston, London. Kluwer Academic Publishers (2002), 252 p.
6.2. Awrejcewicz J., Andrianov I., Manevitch L.: Asymptotic approaches in nonlinear dynamics: new trends and applications. Berlin-Heidelberg –New York, Springer-Verlag (1998), 350 p.
6.3. Manevitch L.I.: Interaction of Physics and Mathematics. Moscow-Izhevsk: Izhevsk Institute of Computer Researches (2018), 168 p. (in Russian).